LA-3770

MASTER

PROCEEDINGS

of the

APS TOPICAL CONFERENCE

on

PULSED HIGH-DENSITY PLASMAS

September 19-22, 1967

LOS ALAMOS SCIENTIFIC LABORATORY
of the
University of California
LOS ALAMOS • NEW MEXICO

UNITED STATES
ATOMIC ENERGY COMMISSION
CONTRACT W-7405-ENG. 36

DISCLAIMER

This report was prepared as an account of work sponsored by an agency of the United States Government. Neither the United States Government nor any agency Thereof, nor any of their employees, makes any warranty, express or implied, or assumes any legal liability or responsibility for the accuracy, completeness, or usefulness of any information, apparatus, product, or process disclosed, or represents that its use would not infringe privately owned rights. Reference herein to any specific commercial product, process, or service by trade name, trademark, manufacturer, or otherwise does not necessarily constitute or imply its endorsement, recommendation, or favoring by the United States Government or any agency thereof. The views and opinions of authors expressed herein do not necessarily state or reflect those of the United States Government or any agency thereof.

DISCLAIMER

Portions of this document may be illegible in electronic image products. Images are produced from the best available original document.

LEGAL NOTICE

This report was prepared as an account of Government sponsored work. Neither the United States, nor the Commission, nor any person acting on behalf of the Commission:

A. Makes any warranty or representation, expressed or implied, with respect to the accuracy, completeness, or usefulness of the information contained in this report, or that the use of any information, apparatus, method, or process disclosed in this report may not infringe privately owned rights; or

B. Assumes any liabilities with respect to the use of, or for damages resulting from the use of any information, apparatus, method, or process disclosed in this report.

As used in the above, "person acting on behalf of the Commission" includes any employee or contractor of the Commission, or employee of such contractor, to the extent that such employee or contractor of the Commission, or employee of such contractor prepares, disseminates, or provides access to, any information pursuant to his employment or contract with the Commission, or his employment with such contractor.

This report expresses the opinions of the author or authors and does not necessarily reflect the opinions or views of the Los Alamos Scientific Laboratory.

Printed in the United States of America. Available from Clearinghouse for Federal Scientific and Technical Information National Bureau of Standards, U. S. Department of Commerce Springfield, Virginia 22151

Price: Printed Copy $3.00; Microfiche $0.65

LA-3770
UC-20, CONTROLLED
THERMONUCLEAR PROCESSES
TID-4500

PROCEEDINGS

of the

APS TOPICAL CONFERENCE

on

PULSED HIGH-DENSITY PLASMAS

held at the

LOS ALAMOS SCIENTIFIC LABORATORY

of the

UNIVERSITY OF CALIFORNIA

Los Alamos, New Mexico

September 19-22, 1967

Report distributed: September 29, 1967

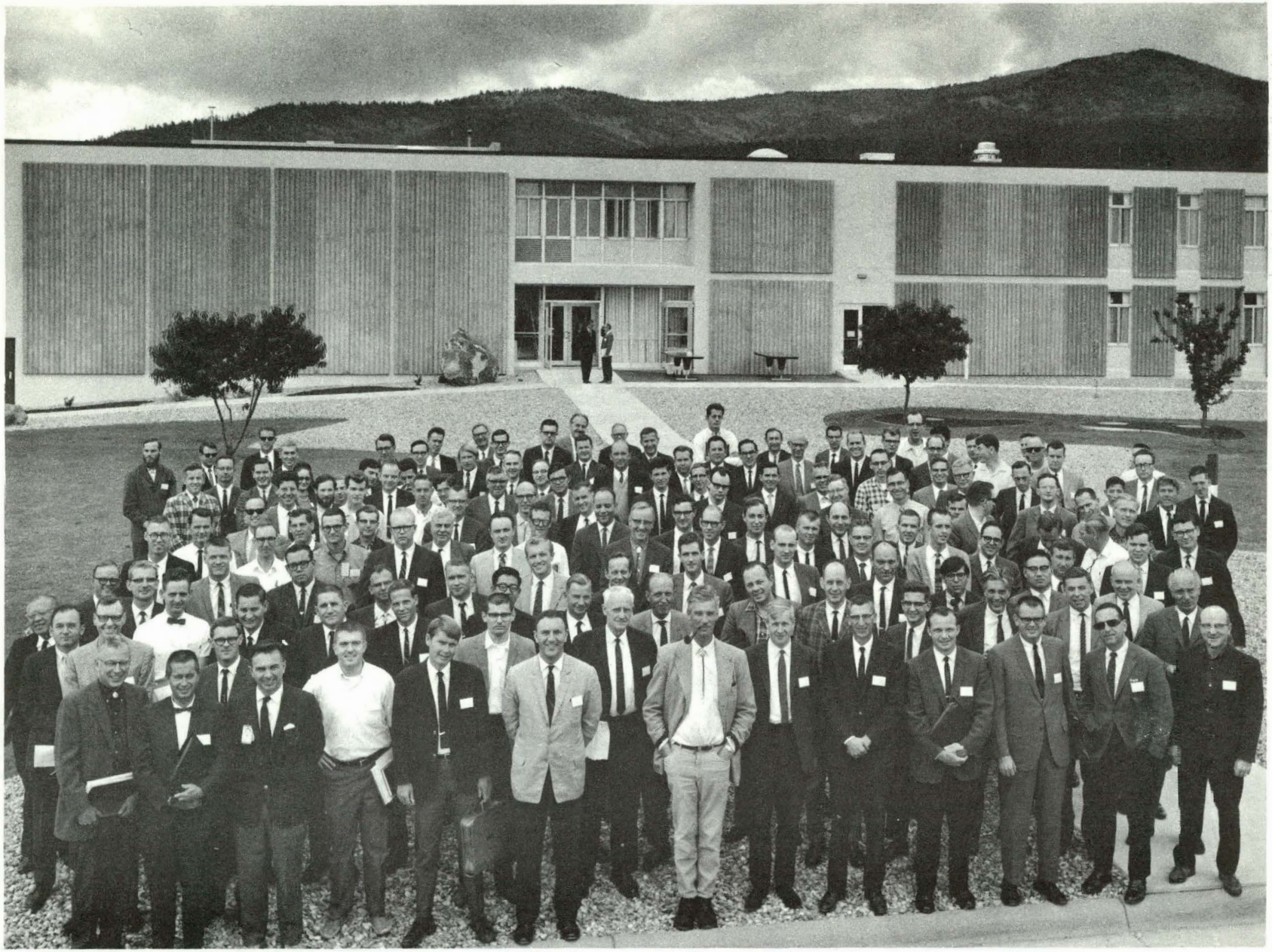

Participants in APS Topical Conference on Pulsed High-Density Plasmas, September 19-22, 1967.

AMERICAN PHYSICAL SOCIETY

TOPICAL CONFERENCE ON PULSED HIGH-DENSITY PLASMAS

LOS ALAMOS SCIENTIFIC LABORATORY

UNIVERSITY OF CALIFORNIA

LOS ALAMOS, NEW MEXICO

SEPTEMBER 19-22, 1967

PROGRAM

Tuesday, September 19, 9:00 a.m.

Welcoming Address: N. E. Bradbury, Director
Los Alamos Scientific Laboratory

THETA PINCHES I

Chairman, J. L. Tuck

A1* SURVEY ON THE LINEAR THETA PINCH WORK IN GARCHING, E. Fünfer, Institut für Plasmaphysik, Garching bei München, Germany (Invited Paper).

A2 OBSERVATIONS IN AN 8-METRE THETA PINCH, H. A. B. Bodin and A. A. Newton, Culham Laboratory, Abingdon, Berkshire, England.

A3 FARADAY ROTATION MEASUREMENTS ON THE SCYLLA IV THETA PINCH, R. F. Gribble, E. M. Little, and W. E. Quinn, Los Alamos Scientific Laboratory.

A4 STUDY OF TRAPPED REVERSE FIELD CONFIGURATIONS IN A LINEAR THETA PINCH EXPERIMENT, A. Kaleck, H. Kever, L. Könen, P. Noll, K. Sugita, F. Waelbroeck, and H. Witulski, Institut für Plasmaphysik der Kernforschungsanlage, Jülich, Germany.

A5 MEASUREMENTS OF PLASMA DENSITY AND END LOSSES IN A LARGE THETA-PINCH, E. A. McLean, A. D. Anderson, and H. R. Griem, Naval Research Laboratory.

A6 EVIDENCE FOR LONG-TIME CONFINEMENT OF DENSE PLASMA BY MEANS OF TWO θ PINCHES AND A CUSP (CHALICE), G. Yevick, R. Harvey, M. Schiff, and H. Opat, Stevens Institute of Technology.

A7 END STABILIZATION EFFECT IN THE SLOW THETA PINCH, Shigeo Hamada, Tetsu Miyamoto, Haruyuki Ohnishi, and Masatomo Sato, Nihon University, Tokyo, Japan.

A8 THETA PINCH WITHOUT THE INTERACTION BETWEEN PLASMA AND NEUTRALS AT THE ENDS, S. Kawasaki and T. Uchida, Institute of Plasma Physics, Nagoya University, Nagoya, Japan.

Tuesday, September 19, 2 p.m.

HIGH-BETA PLASMA THEORY

Chairman, J. L. Johnson

B1* STABILITY OF THE THETA PINCH, John Wesson, Culham Laboratory, Abingdon, Berkshire, England (Invited Paper).

B2 HYDROMAGNETIC EQUILIBRIUM OF A FINITE BETA TOROIDAL PLASMA COLUMN, J. L. Johnson, R. L. Morse, and W. B. Riesenfeld, Los Alamos Scientific Laboratory.

B3 LONGITUDINAL FINITE AMPLITUDE WAVES IN A COLLISIONAL PLASMA, H. Kever, Institut für Plasmaphysik der Kernforschungsanlage, Jülich, Germany.

B4 TWO DIMENSIONAL EQUILIBRIUM FOR HIGH BETA MIRROR DEVICES INCLUDING PARTICLE LOSS, W. Grossmann, Jr., and J. P. Freidberg, Courant Institute, New York University.

B5 THETA-PINCH LOSS RATE ASSOCIATED WITH HIGH-β COLLISIONLESS EQUILIBRIUM CONFIGURATIONS, Ralph W. Kilb, General Electric Research and Development Center.

B6 CONTINUUM EQUATIONS FOR FINITE BETA PLASMA SYSTEMS, P. L. Auer and R. E. Kinsinger, Cornell University.

B7 Z-DEPENDENT MARGINAL STABILITY OF THE RIGID ROTOR MODEL OF A HIGH-BETA THETA PINCH, J. P. Freidberg and R. L. Morse, Los Alamos Scientific Laboratory.

B8 TURBULENT HEATING OF A SHOCKED MAGNETIZED PLASMA, O. K. Mawardi and R. M. Scott, Case Institute of Technology.

Wednesday, September 20, 9 a.m.

DENSE PLASMA FOCUS

Chairman, W. H. Bostick

C1* SOME CHARACTERISTICS OF THE DENSE PLASMA FOCUS, J. W. Mather, P. J. Bottoms, and A. H. Williams, Los Alamos Scientific Laboratory (Invited Paper).

C2 DYNAMICS AND NEUTRON EMISSION OF A PLASMA FOCUS EXPERIMENT, C. Patou, A. Simonnet, and J. P. Watteau, C.E.A., Paris 15ème, France.

C3 PRODUCTION OF NEUTRONS BY A NON-CYLINDRICAL Z PINCH, A. Coudeville, A. Jolas, and J. P. Watteau, C.E.A., Paris 15ème, France.

C4 DETAILED MEASUREMENT OF THE X-RAY EMISSION SPECTRA OF HIGH DENSITY KILOVOLT PLASMAS, E. H. Beckner, Sandia Laboratory.

C5 THE FORMATION AND BREAK-UP OF THE PINCH IN THE PLASMA FOCUS EXPERIMENT, J. W. Long, N. J. Peacock, P. D. Wilcock, and R. J. Speer, Culham Laboratory, Abingdon, Berkshire, England.

C6 NEUTRON AND X-RAY PRODUCTION IN A FOCUSED Z-PINCH, D. A. Meskan, H. L. van Paassen, and G. G. Comisar, Aerospace Corporation.

C7 COAXIAL SNOWPLOW DISCHARGE, D. Butler, I. Henins, J. Marshall, and R. Morse, Los Alamos Scientific Laboratory.

Wednesday, September 20, 2 p.m.

THETA PINCHES II

Chairman, H. R. Griem

D1 ION HEATING IN THE EARLY STAGES OF A VERY FAST THETA PINCH, U. Schumacher, R. Wilhelm, and H. Zwicker, Institut für Plasmaphysik, Garching bei München, Germany.

D2 SPACE-TIME RESOLVED MACH-ZEHNDER INTERFEROMETER MEASUREMENTS OF CROSS-SECTIONAL ELECTRON DISTRIBUTION IN θ-PINCH PLASMA, H. N. Roberts (Introduced by Arwin A. Dougal), F. Weigl, and A. A. Dougal, University of Texas.

D3 MEASUREMENT OF THETA-PINCH END LOSS USING A GAS LASER INTERFEROMETER, K. S. Thomas, Los Alamos Scientific Laboratory.

D4 A LOW ENERGY HIGH EFFICIENCY THETA PINCH, A. W. DeSilva and H.-J. Kunze, University of Maryland.

D5 BREMSSTRAHLUNG OF DENSE HOT PLASMA IN THE WAVELENGTH RANGE 0.25 to 20 μ, P. Bogen, K. H. Dippel, and D. Rusbüldt, Institut für Plasmaphysik der Kernforschungsanlage, Jülich, Germany.

D6 DIRECT MEASUREMENT OF MASS PICKUP IN A LOW ENERGY THETA PINCH, Robert W. Harris, Sandia Laboratory.

D7 THE INFLUENCE OF STRONG MAGNETIC MIRRORS ON STABILITY AND CONTAINMENT OF A THETA PINCH PLASMA, A. Heiss, H. Herold, and E. Unsöld, Institut für Plasmaphysik, Garching bei München, Germany.

Thursday, September 21, 9 a.m.

GUNS AND INJECTION

Chairman, F. H. Coensgen

E1* IMPULSION HEATING OF PLASMA IN THE BILLE-EN-TÊTE EXPERIMENT, P. Evrard, J. Jacquinot, C. Leloup, J. P. Poffé, M. de Pretis, and F. Waelbroeck, Association Euratom-CEA sur la Fusion, Fontenay-aux-Roses, France (Invited Paper).

E2 COAXIAL GUN DEVELOPMENT, I. Henins, P. S. Henry, J. Lohr, and J. Marshall, Los Alamos Scientific Laboratory.

E3 PROPERTIES OF THE SPOKES IN COAXIAL AND PARALLEL-PLATE PLASMA ACCELERATORS, W. Prior, W. H. Bostick, L. Grunberger, P. Palmadesso, and J. Zorski, Stevens Institute of Technology.

E4 DEPOLARIZING CURRENTS IN A DENSE PLASMA INJECTED ALONG A DOUBLE BEND MAGNETIC FIELD, D. Véron (Introduced by P. Hubert), Association Euratom-CEA sur la Fusion, Fontenay-aux-Roses, France.

E5 PREIONIZATION PHENOMENA IN PLASMA ACCELERATOR, T. N. Lie, M. J. Rhee, and C. C. Chang, Catholic University of America.

E6 TRANSIENT SPECTRAL STUDY OF DISCHARGES IN COAXIAL PLASMA GUNS, Charles J. Michels and Henry J. Hettel, NASA-Lewis Research Center.

E7 INVESTIGATIONS OF A CESIUM PLASMA ACCELERATOR WITH OPTICAL DIAGNOSTICS IN THE VISIBLE AND VACUUM ULTRAVIOLET, D. R. Simon, D. A. Hill, and M. E. Levy, Vitro Laboratories.

E8 EXPERIMENTAL INVESTIGATIONS OF NORMAL IONIZING SHOCK WAVES, Leslie S. Levine and Robert A. Gross, Columbia University.

E9 COMPARISON OF ION PROBE AND DOUBLE LANGMUIR PROBE MEASUREMENT ON PLASMA BLOBS, D. G. Fearn (Introduced by F. L. Ribe) and E. R. Wooding, Royal Holloway College, University of London, London, England.

Thursday, September 21, 1:30 p.m.

Excursion to Bandelier National Monument and Barbeque Dinner

Thursday, September 21, 7:15 p.m.

THEORY; LASER PRODUCED PLASMAS

Chairman, P. L. Auer

F1 NUMERICAL CALCULATIONS IN MAGNETOHYDRODYNAMICS, Klaus Hain, Naval Research Laboratory.

F2 COMPUTER SIMULATIONS OF THE THETA-PINCH, T. A. Oliphant, Jr., Los Alamos Scientific Laboratory.

F3 SHEATH STABILITY, R. L. Morse, Los Alamos Scientific Laboratory

F4 A VARIATIONAL APPROACH TO THE CLASSIFICATION OF NONLINEAR MAGNETOHYDRODYNAMIC WAVES AND PLASMOIDS, D. R. Wells, University of Miami, and J. Norwood, Jr., NASA Langley Research Center.

F5 LASER IRRADIATED SINGLE PARTICLE PLASMAS, A. F. Haught and D. H. Polk, United Aircraft Research Laboratories.

F6 LASER - THERMONUCLEAR FUSION EXPERIMENT, J. C. Bryner and G. H. Sichling, North American Aviation, Inc.

Friday, September 22, 9 a.m.

THETA PINCHES III

Chairman, Betsy Ancker-Johnson

G1 THE 15-METER SCYLLAC THETA PINCH, E. L. Kemp, W. E. Quinn, F. L. Ribe, and G. A. Sawyer, Los Alamos Scientific Laboratory.

G2 ANISOTROPY AND ITS RELAXATION IN A FAST MEGAJOULE THETA PINCH, C. Andelfinger, E. Fünfer, G. Lehner, F. Pohl, U. Seidel, J. Sommer, and M. Ulrich, Institut für Plasmaphysik, Garching bei München, Germany.

G3 COLUMBA - A HIGH TEMPERATURE Z-PINCH EXPERIMENT, J. A. Phillips, A. E. Schofield, and J. L. Tuck, Los Alamos Scientific Laboratory.

G4 "LONG-CUSP" CONTAINMENT EXPERIMENT, T. K. Allen, H. Coxell, M. Hill, and I. J. Spalding, Culham Laboratory, Abingdon, Bershire, England.

G5 HARD CORE THETA-PINCH WITH REVERSE TRAPPED MAGNETIC FIELD, A. C. Kolb, M. P. Young, and E. A. McLean, Naval Research Laboratory.

G6 HARD CORE θ-PINCH AND ITS TOROIDAL EQUILIBRIUM, S. Yoshikawa, Princeton University.

Friday, September 22, 2 p.m.

MISCELLANEOUS TOPICS

Chairman, R. F. Taschek

H1 OBSERVED ANOMALOUS PLASMA LOSS FROM A MINIMUM-B SYSTEM, F. H. Coensgen, W. F. Cummins, R. E. Ellis, F. R. Kovar, and W. E. Nexsen, Jr., Lawrence Radiation Laboratory.

H2 BREAKDOWN AND PREIONIZATION STUDIES FOR A MEGAJOULE THETA PINCH AT LOWER DENSITIES, A. Eberhagen, W. Köppendörfer, and M. Münich, Institut für Plasmaphysik, Garching bei München, Germany.

H3 AN EXPLOSIVE GENERATOR-POWERED θ-PINCH, D. B. Thomson, R. S. Caird, K. J. Ewing, C. M. Fowler, and W. B. Garn, Los Alamos Scientific Laboratory, J. C. Crawford and R. A. Damerow, Sandia Corporation.

H4 THEORY OF INERTIAL CONFINEMENT OF DENSE PLASMAS, J. G. Linhart, Ch. Maisonnier, and J. P. Somon, Laboratori Gas Ionizzati, Frascati, Italy.

H5 PULSED, HIGH DENSITY ELECTRON-HOLE PLASMAS IN THE LINEAR PINCH, W. S. Chen and B. Ancker-Johnson, Boeing Scientific Research Laboratories and University of Washington.

H6 PREIONIZATION STUDIES IN A LARGE INVERSE PINCH, F. Y. Sorrell, G. C. Vlases, and E. A. Crawford, University of Colorado.

H7 HIGH DENSITY PLASMA INDUCED BY PULSED MICROWAVE, R. D. Block, D. L. Rode, and O. K. Mawardi, Case Institute of Technology.

* Indicates Invited Papers

WELCOMING ADDRESS

by

N. E. BRADBURY, DIRECTOR
LOS ALAMOS SCIENTIFIC LABORATORY

Ladies and Gentlemen, it is a great pleasure for me to add my welcome to that of Jim Tuck's for this Topical Conference at Los Alamos on Pulsed High-Density Plasma Physics. It gives me particular pleasure to do this for two reasons: Los Alamos has a reputation across the world, I suppose, for its work in nuclear weapons and this reputation sometimes exceeds and overshadows its reputation for all the work it does in other fields. It gives me, therefore, particular pleasure to have people here from across the world and from across the country talk about some of the other sorts of things that Los Alamos does and to see the sort of place it is. There is also another widespread misapprehension about Los Alamos which has it located in the middle of a howling desert. I think you can see from this morning's weather that it is not quite the case.

The particular problems of plasma physics are highly exciting and challenging in their own right and as such would be well worthy of the study of physicists. The fact that some day in some way, I believe, this area of physics will eventually pay off enormously for mankind only adds to its great scientific interest.

Because the importance of your talks and of the program with its long-range objectives in both application and in scientific understanding, and the importance of our being able to talk to each other from across the world here at Los Alamos, I, as Director of the Laboratory, find it a particularly great pleasure in having you with us today and for the next few days. I would like to express my personal wish that your conference be productive and that the activities in which you engage outside of the conference room will be no less pleasant and enjoyable. Thank you for coming.

ACKNOWLEDGEMENTS

The topical conference on Pulsed High-Density Plasmas was held on 19-22 September 1967 in Los Alamos with about 175 conferees in attendance. The organizing committee consisted of the following persons: A. S. Bishop (AEC Washington), R. H. Lovberg (University of California, La Jolla), and H. Dreicer, J. Marshall, J. A. Phillips, F. L. Ribe, W. B. Riesenfeld, and J. L. Tuck (at whose original suggestion the conference was organized). Local arrangements were made primarily by H. Dreicer, F. L. Ribe, and G. A. Sawyer.

Particular thanks are due J. W. McDonald, the editor of these proceedings. His patient and effective labors, together with those of L. W. Riedel, have allowed us to distribute this report with extraordinary speed. For handling the numerous arrangements regarding the holding of the conference we are particularly indebted to R. Y. Porton and the following members of the Public Relations staff: Mrs. Faith Stevens, P. G. Smith, and R. W. Brashear. Particular thanks are due the following Sherwood ladies for their aid in many ways: Mesdames Gladys Alexander, Elizabeth Pohlmann, Barbara Ray, and Harriett Sass. Audio-visual facilities were handled by A. C. Anderson, L. C. Burkhardt, R. O. Holm, T. D. Langham, and P. H. Snowden.

F. L. Ribe
Chairman, Organizing Committee

SURVEY OF THE LINEAR THETA PINCH WORK IN GARCHING +)

by

E. Fünfer
Institut für Plasmaphysik
Garching b. München, Germany

ABSTRACT

The main objectives are very hot, high β-plasmas, collisionless compression and turbulent heating, and M&S experiments.
Low filling densities down to 10^{12} cm^{-3} are required and preionization becomes a severe problem. Therefore three different methods were investigated: the high frequency theta pinch with dynamically confined plasma, the high-voltage z-pinch with short current pulse and the photoionization by strong ultraviolet radiation.
In the main discharge highly anisotropic plasmas with ion temperatures of several keV can be observed. The time behaviour of the anisotropy is compared with theoretical considerations. Electron temperatures of some 100 eV were found by laser scattering experiments. The values from X-ray absorption were much higher and not reproducible. Coherent laser scattering at 90° with a theta pinch of high density and low temperature allowed the measurement of spectrally resolved ion and satellite lines.
The influence of mirrors on end losses and stability has been studied. The plasma remains stable in the low pressure regime for a low impurity level.
Two-dimensional programmes are treated: a (r,z) programme for end losses and thermal conductivity and a (r,φ) programme for plasma rotation. A programme for collisionless compression with a phenomenological friction term was also treated.
A preliminary linear M&S experiment (Limpus) on Isar I showed no noticeable difference in its behaviour as compared with a straight coil.

Our main interest is devoted to very hot and dense high β-plasmas, collisionless compression and turbulent heating, and M&S experiments. The experiments were performed with the capacitor banks Isar I, III and IV and a bank for turbulent heating experiments. Fig. 1 shows the parameters of the banks. Isar IV is suitable for studying the initial dynamic behaviour. Isar I has a relatively long confinement time, and the effects of end losses, relaxation and instabilities can be observed. Isar III is more flexible than Isar I, and so the influence of mirrors on end losses and instabilities was studied.

Preionization

The highest ion energies are obtained in the low pressure regime. Here, the conditions for good preionization, namely a high degree of ionization, high conductivity, low trapped fields and small amounts of impurities, are not easy to fulfil. Three methods are investigated, the high frequency theta pinch, the z-pinch and ultraviolet preionization.

High Frequency Theta Pinch

We used a method where the frequency of the compressing B-field was in the region of the frequency of the radial plasma oscillations[1]. When the plasma oscillates in phase with the compressing

field, violent contact with the tube walls occurs and a high degree of impurities is observed. When the frequency is raised, the plasma can no longer follow the magnetic forces and is dynamically confined around the coil axis. Proper controlling of the magnetic field amplitude, frequency and filling pressures higher than 30 μ, results in a well-confined and fairly clean plasma. When the plasma hits the wall an impurity level of about 2 percent oxygen is found, and when the plasma is confined the level drops by an order of magnitude.

A magnetohydrodynamical three fluid model[2] including the neutral gas component is applied to calculate the radial density distribution as a function of time. The results agree qualitatively with the experimental effects[1].

Z-Pinch Preionization

In the low pressure regime, fast theta pinch preionization became unsatisfactory and we used a succession of two high-voltage z-pinches of short duration[3]. A reduction of contamination by an order of magnitude was obtained.

Ultraviolet Preionization

All these methods fail at densities below 10^{14} cm^{-3}, which are used in collisionless compression experiments. Here, preionization by strong ultraviolet radiation is applied[4]. The ultraviolet radiation source must fulfil the following conditions: The radiation pulse should be short compared with the recombination time of the ionized deuterium, which is about a few μsec. As much as possible of the radiation intensity should lie below the limit of ionization of deuterium (800 Å). Theoretical considerations[5] indicate that a deuterium plasma with high density and temperature above 3 eV yields the most effective radiation. Two fast, high voltage z-pinches on each end of the theta-pinch coil are triggered simultaneously (Fig. 2). By a pulsed gas inlet, a gas pressure well above the filling pressure for the theta pinch is produced in the z-pinch regions. The degree of ionization in the centre of the coil is about 5%.

Early Phases of a Very Fast Theta Pinch

The above-mentioned double z-pinch preionization is adopted in the Isar I, III and IV experiments. During the first implosion, the magnetic field was measured by probes in Isar IV. The width of the current layer is fairly large and decreases with increasing pressure. The reason for this field diffusion is not yet clear. It is of interest that the magnetic field on the axis remains well below 100 G up to the first compression. Further experiments aim at an improvement of the preionization.

Anisotropy and Relaxation

It seems reasonable to assume a highly anisotropic plasma in our experiments, and we looked for methods of measuring anisotropy and relaxation. The high neutron yield allows two different neutron diagnostic methods:

1. Measurement of the neutron energy distribution with nuclear plates. For an anisotropic plasma, the energy spectrum depends on the direction of observation. Side-on one measures the perpendicular, end-on the parallel temperature of the plasma. A perpendicular ion temperature of about 4 keV was measured.

2. The anisotropy of the neutron flux. The differential cross section for the $d(d,n)He^3$ is anisotropic. An anisotropic plasma therefore produces an anisotropic neutron flux[6]. With two scintillators side- and end-on, the neutron flux ratio as a function of time was measured. From the experiments it follows that the flux ratio, i.e. the anisotropy, rises rapidly to a maximum well before the field maximum and then falls relatively fast. This slope cannot be explained only by ion-ion collisions. Because T_e/T_i is small, electron-ion collisions must be considered,

too. The theoretical results[7], obtained from the Fokker-Planck equation are applied to the Isar I data (Fig. 3)[8].

End losses are measured with a Mach-Zehnder interferometer. The time behaviour of the total number of particles yields, at least qualitatively, the parallel velocity of particles and consequently the parallel temperature $T_{i\parallel}$. A collisionless outflow of particles parallel to the magnetic field is assumed.

End Losses with Mirrors

The influence of mirrors on confinement time and stability was studied in Isar III[9]. Mirror ratios up to R = 3 were applied. The filling pressure varied from 10 μ to 40 μ. The ion temperatures lie between 0.5 and 2 keV. For all mirror ratios no instabilities could be seen in smear camera pictures during the observation time of about 5 μsec. Rotational instabilities occasionally arise with and without mirrors. Also in a very short mirror, instabilities are indicated by an abnormally high loss rate. These effects are not yet fully understood.

As in Isar I, the loss rate can be described by collisionless outflow along the field lines. In contrast, however, to Isar I, the experimental values of Isar III agree with the assumption that $T_{i\parallel} = T_{i\perp}$. This seems reasonable considering the influence of mirrors.

It follows from these experiments that the confinement time t_N rises about proportionally to the mirror ratio. With R = 3, for instance, $t_N \approx 7.5$ μsec is measured, instead of $t_N \approx 2$ μsec for R = 1.

In Fig. 4 t_N is plotted as a function of R for different initial pressures. The measured values are compared with calculated values from the collisionless outflow model and from the magnetohydrodynamic model of Taylor and Wesson[10]. These results seem encouraging enough to continue the Isar I relaxation studies with mirror coils.

Laser Scattering Experiments

Ion temperatures on Isar III were obtained from forward laser scattering[11]. In another experiment[12] we fulfilled the condition for cooperative scattering by reducing the Debye length, whereas the scattering angle was 90°. This means a plasma of high density and low temperature. The spectrum of the ion line was measured as well as the position and half-width of the satellite lines. The spectrum was obtained from a single discharge with an error of $\pm$ 5 percent. Fig. 5 and Fig. 6 show examples.

Theoretical curves according to the Salpeter theory are properly fitted to the experimental values. The theory now yields the parameter β, a function of α and the ratio T_e/T_i. The shape, the half-width, the total intensity of the ion and satellite lines and the frequency distance between ion and satellite lines yield the ion and electron temperature and density.

The theory assumes a number of electrons in the Debye sphere $nD^3 \gg 1$. In these experiments nD^3 varies between 2 and 10. Even for $nD^3 = 2$, agreement within $\pm$ 5 percent between theory and experiment is found. The theory holds also for a few electrons in the Debye sphere.

Two-Dimensional Programmes

A two-dimensional programme with rotational symmetry (r,z) has been developed for the computation of end losses in theta pinches with and without mirrors[13]. In a first stage, a relatively simple plasma model is used. It is a one-fluid model with isotropic pressure and infinite electrical conductivity. Furthermore radial equilibrium for all times is assumed. The influence of thermal conductivity is taken into account, however.

It appears interesting to compare the results for zero thermal conductivity with those for nonzero conductivity. For a special case (Isar III, B_m = 70 kG,

$n = 6 \cdot 10^{16}$ cm^{-3}, T = 400 eV, coil length = 30 cm), the confinement times with and without thermal conductivity are 1.7 μsec and 1.3 μsec respectively. It is a general feature that thermal conductivity increases the confinement time as a consequence of the reduced temperature. In Fig. 7 the density along the axis is shown as a function of time. With conductivity, the density increases even initially and falls slowly as compared with the case of zero conductivity. The temperature, on the other hand, falls to lower values with conductivity. The pressure shows similar behaviour. Fig. 8 presents the energy losses as a function of time with and without conductivity. With conductivity the rate of energy losses is larger in the early phases of the pinch. The results agree qualitatively with the experimental values in Isar III with a mirrorless coil. This comparison is preliminary, however, and a final comparison will be made once a two-fluid model with anisotropic pressure has been included in the programme.

A two-dimensional (r, φ) programme has also been developed[14]. A set of two-fluid equations, including thermal conductivity, Hall term, exchange of energy between ions and electrons, finite electrical conductivity etc. is used. The programme has been applied to the problem of plasma rotation induced by superimposed magnetic fields perpendicular to the axis. The computations concern the first implosion in Isar III for different filling pressures and trapped fields from -1 kG to +1 kG and perpendicular fields from 0.1 - 1 kG. The result is that the plasma does not rotate like a rigid body. The rotational velocity changes its sign as a function of radius at least once. An example is given in Fig. 9. Here $n \cdot v_\varphi$ is plotted as a function of r and φ. The rotational velocity develops in about 10^{-7} sec and reaches values of the order of 10^6 cm/sec.

Collisionless Compression and Turbulent Heating

In fast theta pinches at low densities the collisionless processes are important. In order to evaluate the influence of a two-stream instability on the structure of a strong, nonstationary compression pulse, a numerical programme was treated[15]. It uses a two-fluid model for a cylindrical plasma including effects of electron inertia and describes the action of the instability by a phenomenological friction term. This friction term limits the azimuthal electron speed to a critical value which, in turn, is connected with the electron temperature and changes, therefore, with heating by friction and compression.

This friction term may or may not prevent density profiles, radial velocity and pressure from running into a discontinuity. This is demonstrated in the density profile of Fig. 10. The density n/n_o is plotted over the radius r/R_o at different dimensionless times τ. At $\tau = 2.4$ the density profile exhibits a sharp peak. Here, fluid elements coming from behind the wave with higher velocities tend to overturn the preceeding ones.

These theoretical predictions are being investigated in a fast theta pinch at low densities between 10^{12} - 10^{14} cm^{-3}.

The "Limpus" Experiment

As mentioned in the beginning, we shall also have to study toroidal pinches in the future. One possibility is offered by the M&S principle[16]. A preliminary experiment with a linear, corrugated coil (Limpus) has been performed on Isar I[17]. As in a straight coil, instabilities could be observed in the Limpus experiment at 20 μ, but not at 10 μ. Further experiments with higher corrugation amplitudes are planned.

+) This work was performed as part of the joint research program of the Institut für Plasmaphysik, Garching and Euratom.

References

1 G. Decker, Z.f.Physik (1967), in press
2 D. Düchs, Comptes Rendus de la VIe Conf. Int. Phen. Ion. dans les Gas, Vol. 2, 567, Paris (1963)
3 U. Schumacher and R. Wilhelm, Paper presented at Tagung d. Deutsch. Phys. Ges., Kiel (1966), Phys. Verhndl. 5, (1966)
4 G. Hofmann, to be published
5 G. Hofmann and F. Pecorella, to be published
6 G. Lehner and R. Pohl, Report IPP 1/6o (1967), to be published Z.f.Physik
7 G. Lehner, Z.f.Physik, 1967 (in press)
8 C. Andelfinger et al., Report IPP 1/67 (1967)
9 A. Heiss et al., these proceedings
1o J.B. Taylor, J.A. Wesson, Nucl. Fus. 5, 159 (1965)
11 B. Kronast et al., Phys. Rev. Let. 16, 1o82 (1966)
12 H. Röhr, Dissertation TH Munich (1967) to be published
13 F. Hertweck and W. Schneider, Paper presented at 2nd Europ. Conf. on Contr. Fus. and Plasma Phys., Stockholm (1967)
14 D. Düchs, to be published
15 R. Chodura, Paper presented at 1st Europ. Conf. on Plasma Phys. and Contr. Nucl. Fus. Res., Munich (1966)
16 F. Meyer and H.U. Schmidt, Z.f.Naturf. 13a, 1oo5 (1958)
17 C. Andelfinger et al., Report IPP 1/55 (1966)

Exper.	W kJ	U_o kV	B kG	$\dot{B}$ G/sec	E_φ kV/cm	L_a nHy	Coil l(cm)	Coil d(cm)	T/2 µsec	T_c /e µsec
Isar I	2670	40	178	$2.9\cdot10^{10}$	0.7	5.1	150	10	19	105
Isar II	500	2x40	90	$5.2\cdot10^{10}$	1.0	8	100	10	5.2	≈50
Isar III	80	40	80	$4\cdot10^{10}$	1.0	20	30	7	5	30
Isar IV	115	2x40	230	$2.2\cdot10^{11}$	2.8	7.5	14	7	3.4	50
Turb. Heat. Exper.	9.6	2x40	13	$3.4\cdot10^{10}$	1.4	2x7	60	15.8	12	8

Fig. 1. Linear theta pinch experiments at Garching.

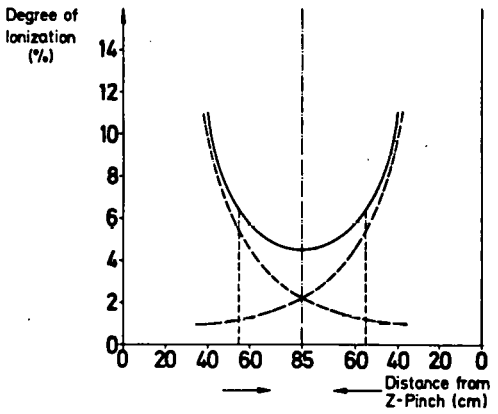

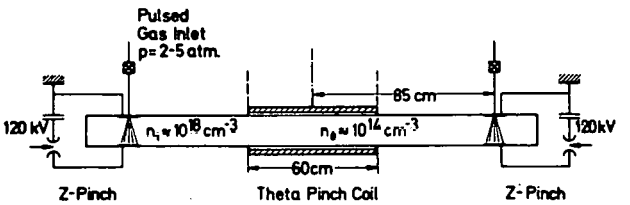

Fig. 2 Experimental arrangement of UV-preionization and measured degree of ionization

Fig. 2. Experimental arrangement of UV-preionization and measured degree of ionization.

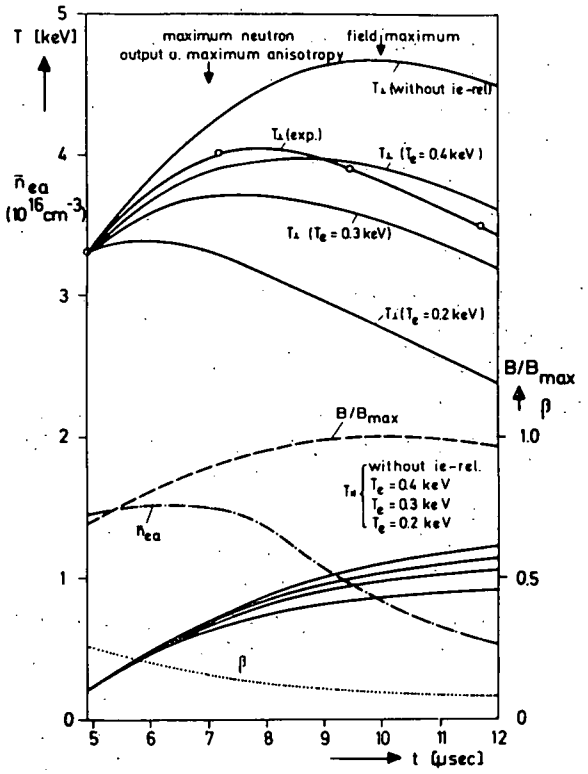

Fig. 3. Comparison between experimental and theoretical values of the temperatures concerning experiments on Isar I.

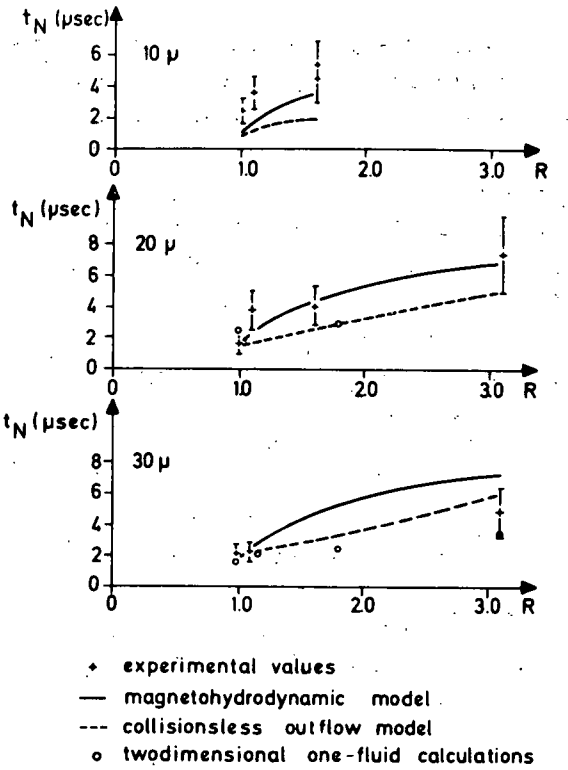

Fig. 4. Containment time t_N as a function of the mirror ratio R for different initial pressures.

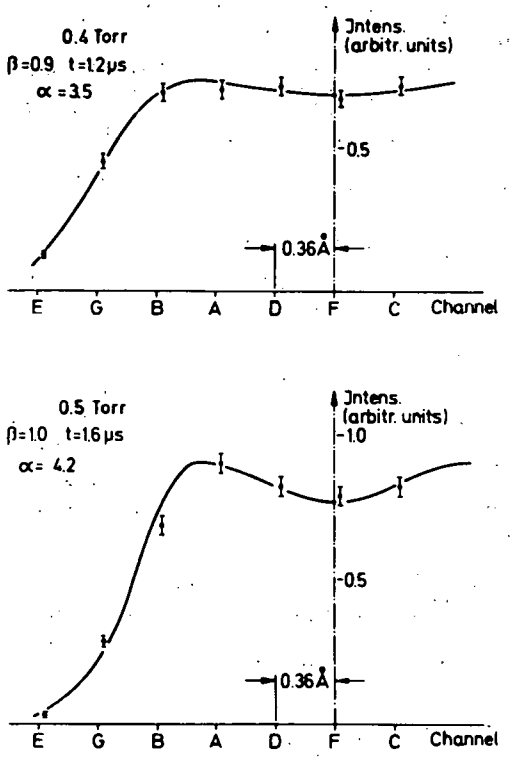

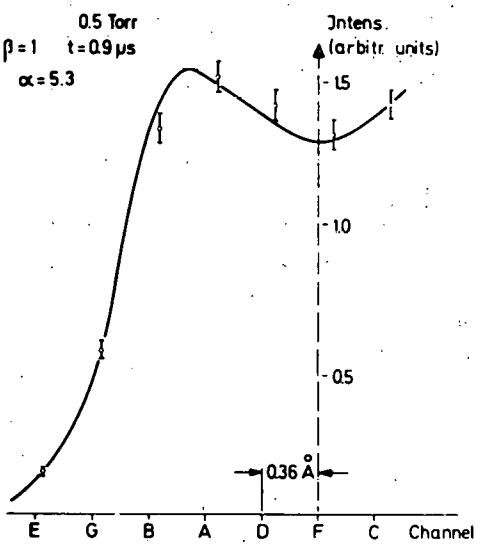

Fig. 5. Spectra of ion lines at various plasma parameters.

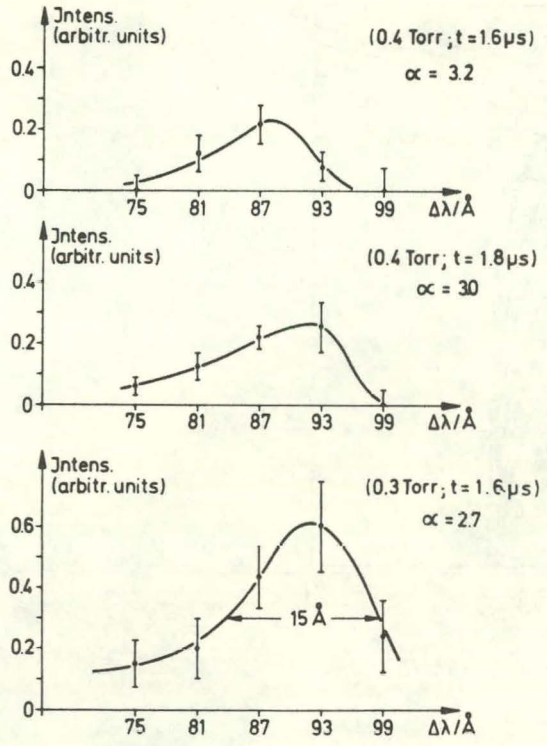

Fig. 6. Examples for satellite lines.

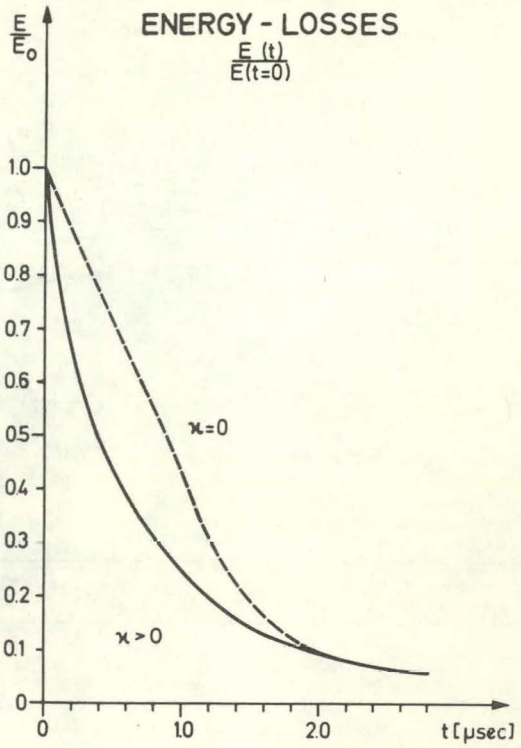

Fig. 8. Energy losses with and without conductivity $\varkappa$ as a function of time.

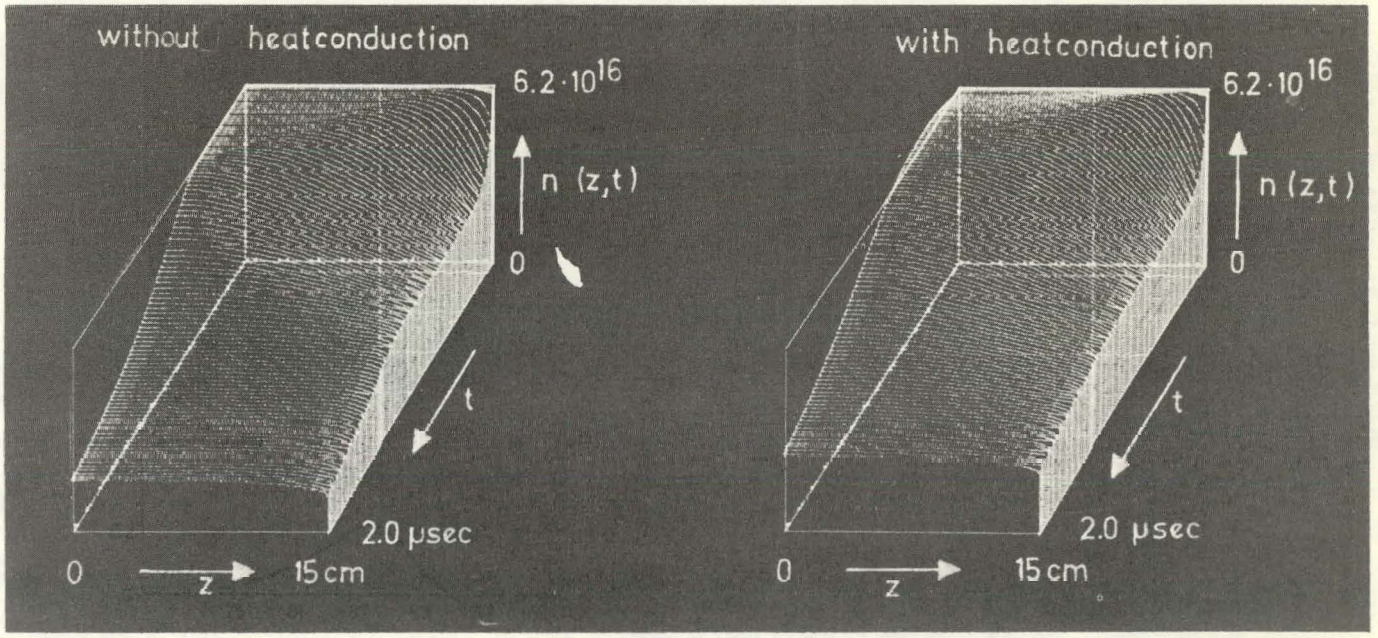

Fig. 7. Density profile as a function of time.

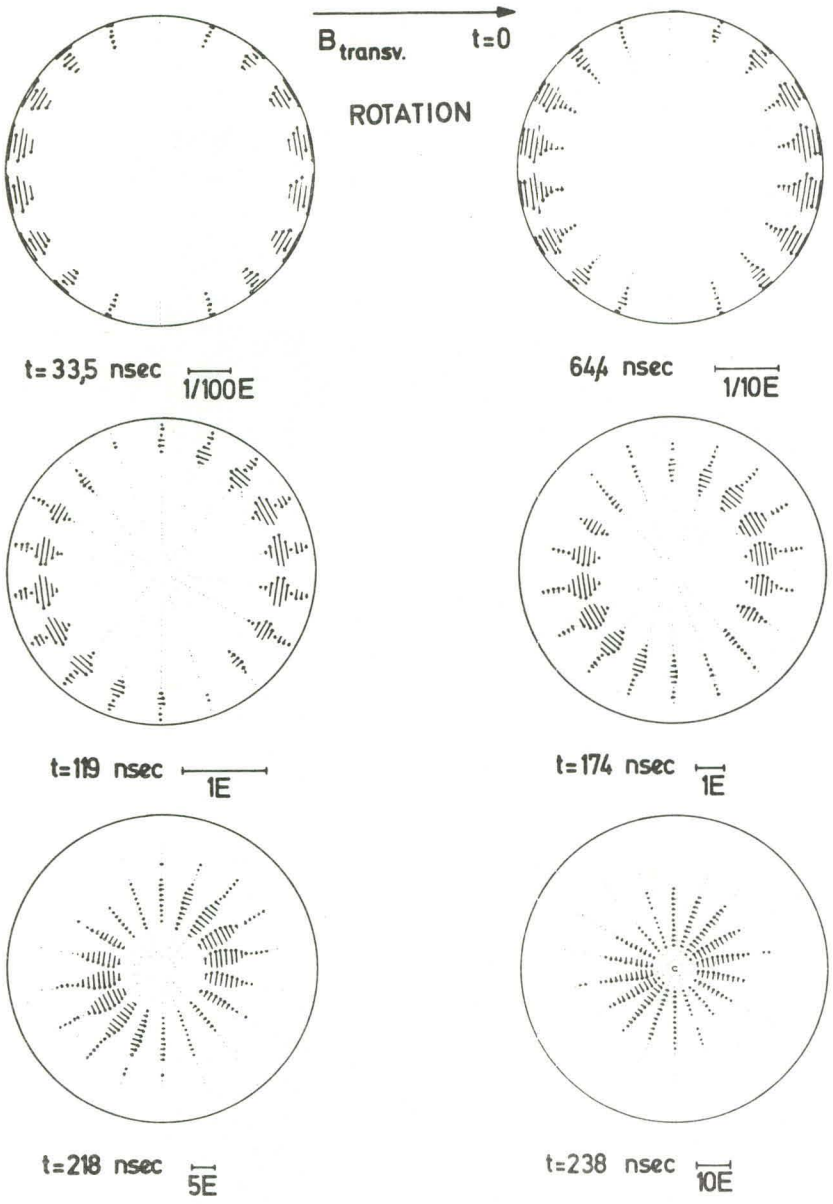

Fig. 9. $n \cdot v_\varphi$ as a function of radius, angle and time.

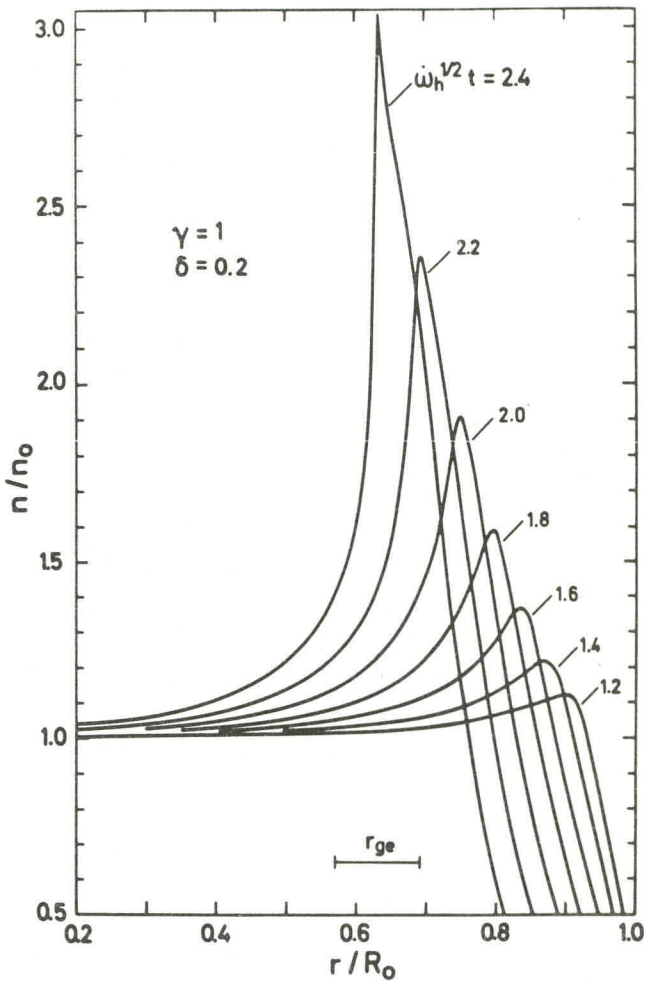

$$B_o = 0$$

$$\dot{\omega}_h = \frac{e \cdot \dot{B}_a}{(m_i \cdot m_e)^{1/2}}$$

$$\sigma = \frac{c}{\omega_{pe} \cdot R_o}$$

Fig. 10. Density profiles at various times τ.

OBSERVATIONS IN AN 8-METRE THETA PINCH

by

H.A.B. Bodin and A.A. Newton

Culham Laboratory, Abingdon, Berkshire, England

This paper describes experiments using a coil 8-metres long and 11 cms in diameter. The magnetic field reaches 25 kG at 40 kV and decays when crowbarred with at time constant of 160 μsec. The plasma temperature is ~ 100 eV and density ~ 3×10^{16} cm^{-3} on axis. The plasma in the midplanc is unaffected by the ends for long relative times.

The plasma remains close to the tube axis along its length for some tens of μsecs, showing only slight transverse motion. An axisymmetric magnetic field perturbation was produced in the midplane after the implosion, and the observed growth and propagation of the m = 1 instability agreed with ideal hydromagnetic theory. Higher modes were not observed. It was shown by analysing the radial density distribution that the diffusion rate was least when the discharge was quiescent; much faster diffusion rates were observed when there were radial accelerations due to the implosion, oscillations or rotation.

INTRODUCTION

The problems of heating, energy loss and particle flow in the theta-pinch[1-4] have been extensively studied. Some results have been reported on stability[5-8] but little on diffusion[9]; even with coils up to 2 metres long the interpretation of these results has been confused by the influence of the ends. The purpose of the present experiment is to study hydromagnetic stability and diffusion in a long coil where the effect of the ends can be neglected for relatively long times.

The principle of the stability experiment is to create an axisymmetric magnetic field perturbation in the mid-plane of the coil and to compare the observations of plasma instability with the theoretical predictions. In particular, the growth of m = 1 will be compared with ideal hydromagnetic theory and the damping of higher modes by non-ideal effects will be studied. The ends are expected to influence the stability in a time $t_A = \frac{\ell}{2V_A} = 20$ μsecs.

In the diffusion experiment the electron density distribution is measured in the mid-plane as a function of time and compared with the computations using the Hain-Roberts[10] code and assuming classical or other resistivities. The time available for this experiment is that for which the profile is uninfluenced by particle end losses, i.e. $t_s = \frac{\ell}{2C_s} = 40$μsec, where C_s is the sound speed.

These experiments are being carried out using a coil 8-metres long energised by the Culham megajoule bank[11]. The electron temperature is measured by Thomson scattering using a twelve channel spectrophotometer[12] and electron density distribution with a calibrated image converter camera. Bank and plasma parameters are summarised in Table I.

At all voltages the discharge column remains close to the axis along its length, showing slight transverse motion. Fig.1(upper) shows stereoscopic streak photographs taken in the mid-plane (the unequal intensity is an instrumental effect); Fig.1 (lower) shows photographs taken of the same discharge at three other axial positions. Ultimately a low amplitude instability, consisting of a mixture of m = 1 and m = 2 is observed, which is associated with rotation. The onset time of this instability,which grows simultaneously along the plasma, is very approximately equal to the Alfvén transit time from the ends to the mid-plane. At 34 kV the instability appears at 30 μsecs.

The remainder of this paper concerns times before the appearance of the above instability.

HYDROMAGNETIC STABILITY EXPERIMENT

A local axisymmetric magnetic field perturbation was generated near the mid-plane of the coil by firing the crowbar switch of one electrically

isolated coil section, 25 cm long, before peak field. Details have already been published[12].

The growth of the $m=1$ instability was computed[13,14] using a normal mode analysis and the hydromagnetic model. The amplitude of the instability as a function of axial distance, z, and time, t, was predicted in the form $\xi(z,t) = \xi(z)e^{\omega t}$, using the mathematical form shown in Fig.2. Computations have been carried out for a range of values of δ and β, which were measured. The calculation integrates along the length of the plasma, averaging regions of stable and unstable curvature and includes the effect of plasma loading outside the unstable region. Thus the growth rates are much less than those obtained from the simple expression using the local curvature and Alfvén speed. Fig.2 shows theoretical growth times for $\beta = 0.8$ as a function of δ; the results are only weakly dependent on β except when $\beta \to 1$.

Fig.3 shows streak photographs taken simultaneously in the unstable region (measured $\delta \approx 1$) and at three other axial positions. It is seen that an $m=1$ instability grows in the unstable region, and the displacement due to the instability propagates down the column and arrives at the three positions shown in the lower picture at successively later times. Fig.4 is a log plot of the amplitude of the instability in the unstable region as a function of time showing exponential growth with a characteristic time of 3 μsec and is in satisfactory agreement with the theory. Fig.5 shows the propagation of the $m=1$ motion along the column; the onset time is plotted as a function of the distance from the perturbed region, and it is seen that data from two discharges lie approximately on a straight line. The propagation velocity lies between 25 and 30 cm/μsec, compared with the theoretical value of $V_A(2-\beta)^{\frac{1}{2}} = 24$ cm/μsec.

Higher modes were not observed during the exponetial growth of $m=1$ although on ideal MHD theory they grow faster than $m=1$, the difference being small for a diffuse density distribution. The absence of such modes is attributed to finite Larmor radius[15] stabilisation, since the stability condition is easily satisfied for the theoretical growth rate. The subsequent appearance of $m=2$ during rotation arises because the rotational destabilising force is stronger than that due to field curvature; the finite Larmor radius stability condition for a rotating plasma is marginally unsatisfied. It is possible to identify the limits in which finite Larmor radius effects give stability.

DIFFUSION EXPERIMENT

At times earlier than 2 μsec field diffusion is observed to proceed at a rate much greater than classical. This accounts for the fact that β is only about 0·65. The profile shows a diffuse current sheath whereas ideal hydromagnetic theory predicts a thin sheath. Computations using the Hain-Roberts code with an artificial resistivity, chosen to give the effective diffusion coefficient the Bohm scaling and magnitude, show much better agreement with the experiment, particularly in the outer regions. It should be noted that to obtain agreement it is necessary to change the scaling of the resistivity as well as its magnitude.

To investigate diffusion at later times, computations were started at 5 μsec, inserting experimental values of the temperature and the density distribution as the initial conditions. The calculation uses the measured external magnetic field variation, classical resistivity, and assumes no energy loss. This last assumption is important since an energy loss tends to cancel profile changes due to diffusion. Fig.6 shows the results at 20 μsec from the start of the discharge. The agreement between the calculated profile and the experimental points is good at most radii. The discrepancy near the axis shows that there is some energy loss. The same computation was run using an artificial resistivity chosen to give a diffusion coefficient of 1/10th the Bohm value, and the profile obtained in this way departed from the experimental points by 15% at 20 μsec. Ultimately the experimental profile shows diffusion and differs from that predicted by the classical computation; this departure appears a few microseconds before the instability of the plasma is seen on photographs.

CONCLUSIONS

An axisymmetric magnetic field perturbation was generated in the mid-plane of the coil after the radial implosion; an $m=1$ instability grew exponentially in the unstable region with a growth time in agreement with the computations based on hydromagnetic theory. The $m=1$ motion due to this instability

propagated along the column with a velocity close to that predicted by theory. Higher modes ($m \geq 2$) were not observed at this time and this was attributed to finite Larmor radius stabilisation.

Diffusion was studied by measuring the time variation of the radial density distribution in the mid-plane. When the discharge is experiencing a radial acceleration due to the implosion or oscillations (in the early stages) or rotation (in the later stages) the density distribution shows diffusion at a rate much faster than classical. The time variation of the density distribution in intermediate stages, when the discharge is steady, was compared with computations which started at 5 μsec, using experimental values as initial conditions and the measured time variation of the external field. The calculations assumed classical resistivity and no energy loss, which is important since an energy loss tends to cancel profile changes due to diffusion. The experimental points lie close to the theoretical profile.

ACKNOWLEDGEMENTS

The authors wish to thank their colleagues whose intensive efforts made it possible to obtain the results presented in this paper, and J.A. Wesson for discussions on the stability.

REFERENCES

1. BODIN. H.A.B. et al. IAEA Conference on Plasma Physics and Controlled Fusion Research, Culham, 1965. Proceedings vol.1, pp.193-221.

2. QUINN. W.E. et al. As above. Proceedings vol.1, pp.237-247.

3. ANDELFINGER. C. et al. As above. Proceedings, vol.1, pp.249-260.

4. GREEN, T.S. et al. Physics of Fluids (to be published).

5. BODIN, H.A.B., NEWTON, A.A. and PEACOCK, N.T. Nuclear Fusion, 1, 139 (1961).

6. BODIN, H.A.B. and NEWTON, A.A. Physics of Fluids, 6, 1338, (1963).

7. LITTLE, E.M. et al. Nuclear Fusion Supplement, Part 2, p.497. (1962)

8. KOLB, A.C., THONEMANN, P.C. and HINTZ, E. Physics of Fluids, 8, 1347, (1965).

9. BODIN, H.A.B. and DANCY, D.J. Culham Laboratory Report CLM-P 133 (1967).

10. HAIN, K. et al. Z. fur Naturforschung, 15A, 1039 (1960).

11. McCORMICK, N.R. Culham Laboratory Report CLM-P 130, 1967.

12. WATSON, J.L. and BEACH, A.D. AWRE Reports nos. O-66/66 and O-42/67.

13. HAAS, F.A. and WESSON, J.A. Culham Laboratory Report CLM-P 136, (1967).

14. WESSON, J.A. Private Communication.

15. HEYWOOD, G.C.H. and BODIN, H.A.B. Culham Laboratory Report CLM-P 134, 1967.

16. ROSENBLUTH, M.N. et al. Nuclear Fusion Supplement, Pt.1, 143, (1962).

TABLE I

8-METER EXPERIMENT - PARAMETERS

BANK

Energy	= 1·1 MJ
Voltage	= 40 kV
Capacity	= 1382 μF
Inductance	= 2·8 nH
Added Inductance	= 3·4 nH
Total Inductance (including coil)	= 7·98 nH

ELECTRICAL CHARACTERISTICS

Ringing

Half period	= 10·5 μsec
Peak current	= 15·3 Megamps
Peak field	= 25·1 Kilogauss
Initial dB/dt	= $8·2 \times 10^9$ g/sec
Initial E_θ field	= 250 volts/cm

COIL

Length (32 sections)	= 7·72 meters
Bore	= 11 cm
Tube bore	= 8·3 cm

Crowbar

Time to 1/e	= 158 μsec
Ripple	= ± 15%

MAGNETIC FIELD WAVEFORM

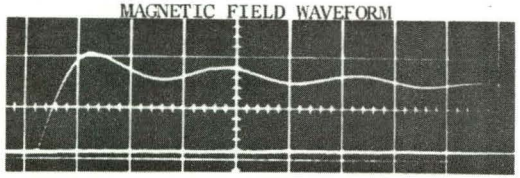

NOMINAL PLASMA CHARACTERISTICS

Initial filling pressure	p_o	= 20 μHg
Temperature	$T_i = T_e$	= 100 eV
Electron density on axis,	n_e	= 3×10^{16}/cc
Beta	β	= 0·5-0·8
Plasma radius,	r_p	= 1 - 2 cm
Ion Larmor radius	r_{Li}	= 1 mm
Mean free path	λ	= 4 mm
Ion-electron equipartition time,	t_{eq}	= 1 μsec
Cyclotron frequency/collision frequency	$\omega_{ce}\tau_{ei}$	= 300
Sound speed,	c_s	= 10^7 cm/sec
Alfvén speed,	V_A	= $2·10^7$ cm/sec
Sound transit time	t_s	= 40 μsec
Alfvén time,	t_A	= 20 μsec
Thermal conduction cooling time	t_c	= 500 μsec

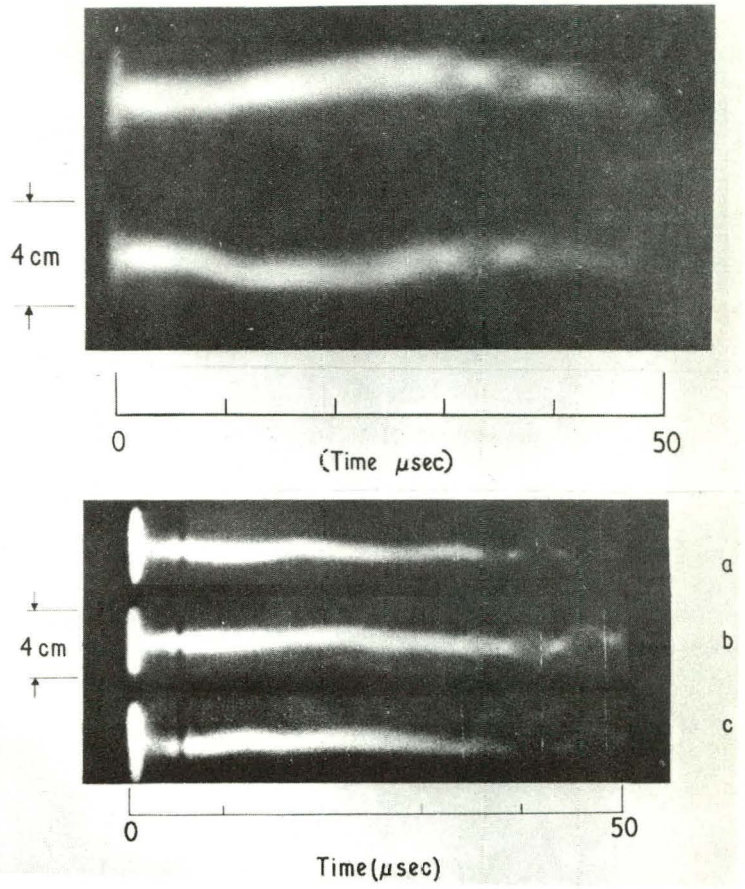

Fig. 1. Streak photographs at different axial positions.

Upper: Stereo view in mid-plane
Lower: (a) 75 (b) 175 (c) 225 cm from the end of the coil.

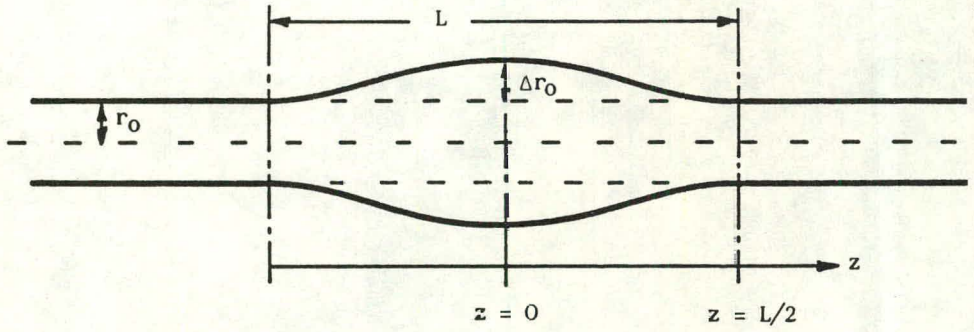

$$r = r_o\left[1 + \delta\left(1 + \cos\frac{2\pi z}{L}\right)\right]^{+\,L/2}_{-\,L/2}, \quad \delta = \frac{1}{2}\frac{\Delta r_o}{r_o}$$

THEORETICAL INSTABILITY GROWTH TIMES FOR LOCAL PERTURBATION

δ	τ (μsec)	ℓ_e/L	τ/τ_A
0·2	14·0	12	10·8
0·4	5·5	4·7	4·2
0·6	4·0	3·5	3·2
0·8	3·65	3·1	2·8
1·0	3·5	3·0	2·7

τ = growth time of instability
L = length of unstable region = 25 cm
ℓ_e = e-folding distance for amplitude of instability in z direction
$\tau_A = L/V_A$
V_A = Alfven speed = 2×10^7 cm/sec
$\delta = 1/2\ \Delta r/r_o$

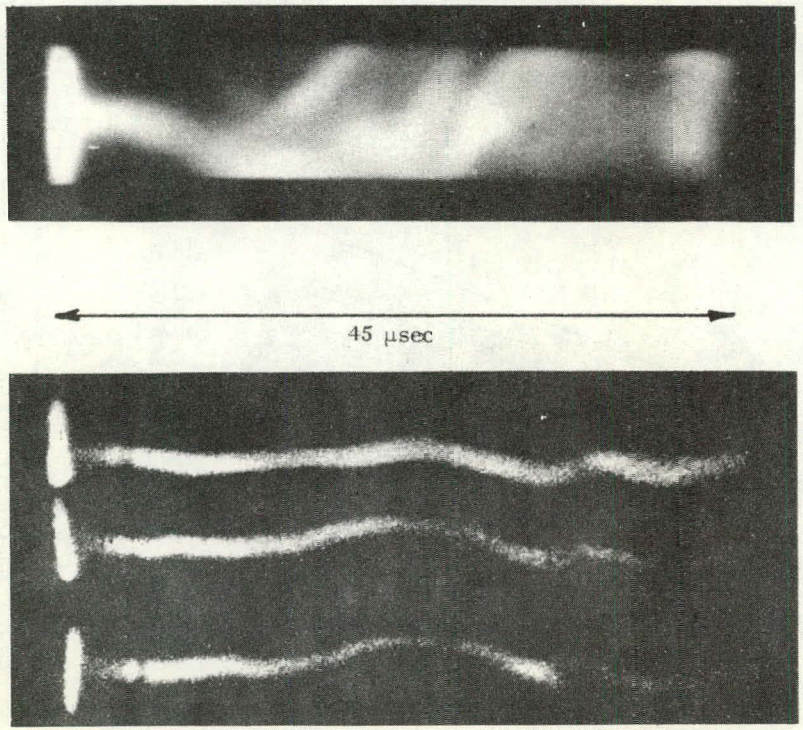

Fig. 3. Streak photographs showing the growth (upper) and propagation (lower) of an m = 1 instability.

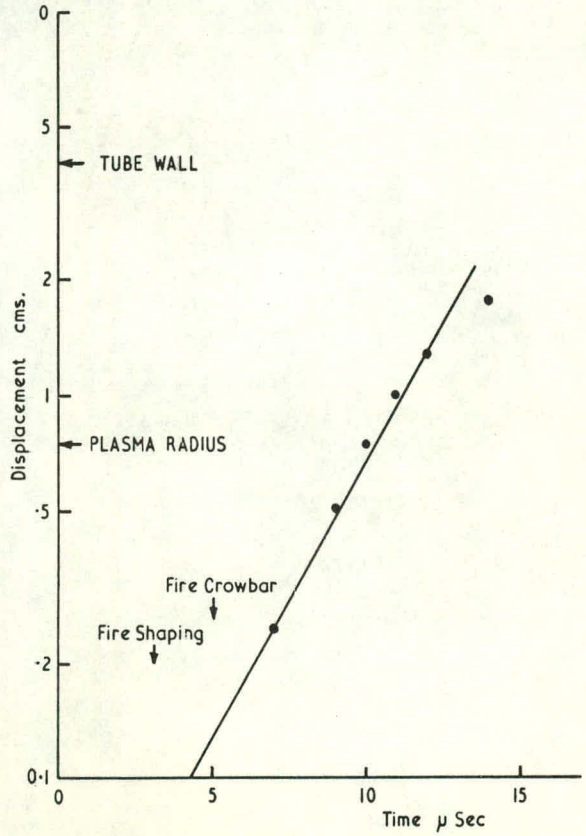

Fig. 4. Growth of m = 1 instability.

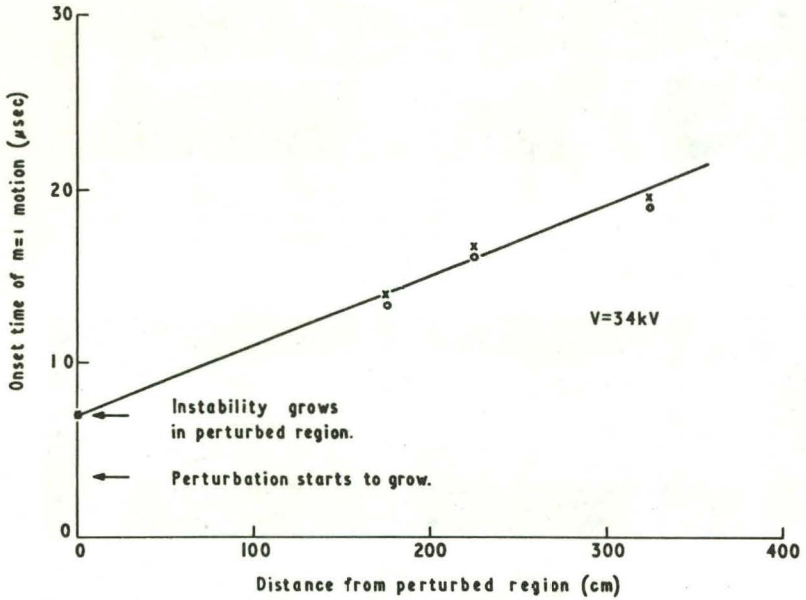

Fig. 5. Propagation of m = 1 instability along the plasma column.

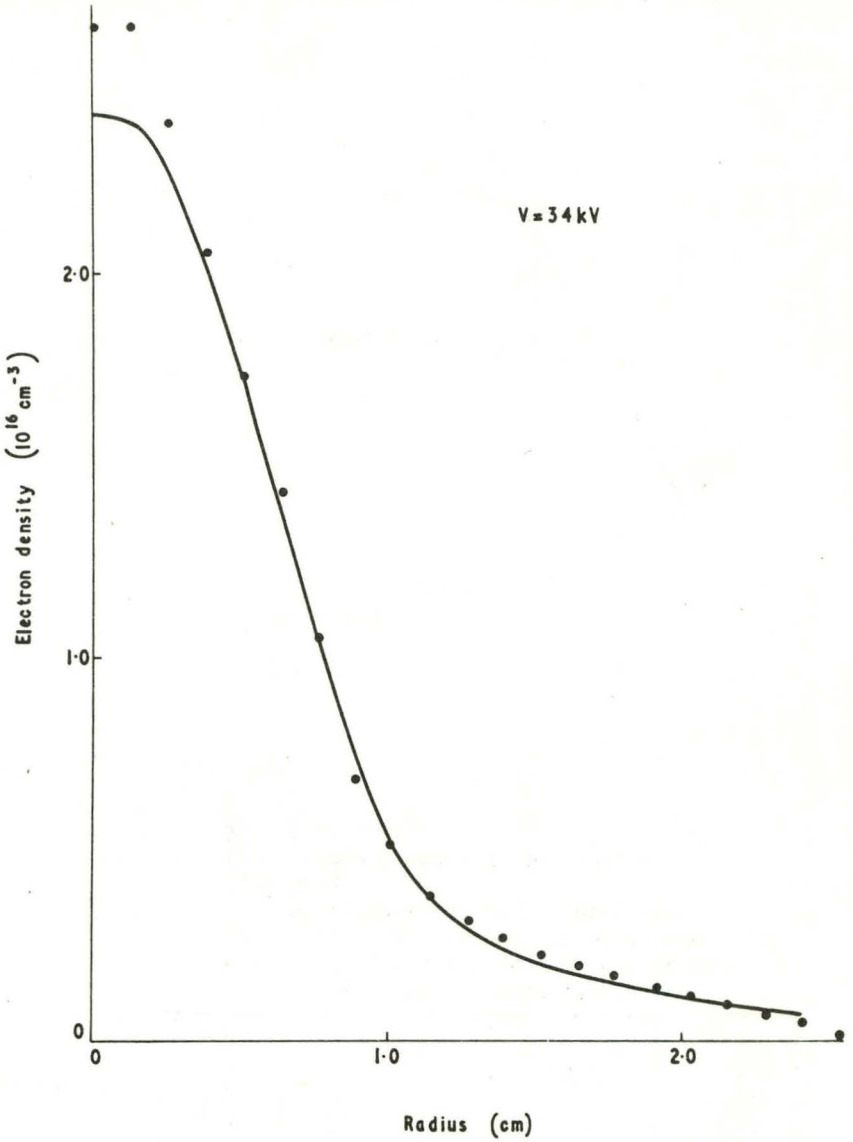

Fig. 6. Electron density distributions at 20 μsec, theory and experiment.

FARADAY ROTATION MEASUREMENTS ON THE SCYLLA IV THETA-PINCH*

by

R. F. Gribble, E. M. Little, and W. E. Quinn

Los Alamos Scientific Laboratory, University of California
Los Alamos, New Mexico

ABSTRACT

Faraday rotation measurements have been combined with Mach-Zehnder interferometer measurements to yield the value of the internal magnetic field B_i in the Scylla IV plasma as a function of time and radius. Since the Faraday rotation is proportional to $\int B_i(\ell) n_e(\ell) d\ell$ and the Mach-Zehnder interferometer provides $\int n_e(\ell) d\ell$, the data yield the average value of the internal magnetic field $B_i(r)$ which exists over the plasma length ℓ at the radius r. The measurements of $B_i(r)$ are combined with those of the external magnetic field B_e to determine the average plasma β as a function of radius, $\beta = 1 - B_i^2(r)/B_e^2$. The Faraday rotation measurement employs a 1.5-mm diameter beam of visible radiation (6328 Å) from a HeNe gas laser as a plasma magnetic-field probe and a calcite Wollaston prism as the polarization analyzer with silicon diode detectors. In the low-pressure plasma regime (10 to 25 mtorr) the β values in the central plasma core (~ 5-mm diameter range between 0.9 and 1.0 with initial reversed bias magnetic fields and values between 0.7 and .95 without bias fields. Radial profiles of β averaged over the plasma length have been obtained at various times during the discharge. A combination of β, n, and T_e in the simple pressure balance yields ion temperatures in the 2 to 10 keV region.

I. INTRODUCTION

A measurement of the Faraday rotation of a plane polarized wave propagating through a plasma-magnetic field medium can be used to determine the integral of the product of the magnetic field and plasma density over the length of the media. Such rotation measurements have been performed on plasmas in small theta-pinch devices by Dougal, et al.[1]; Falconer and Ramsden[2]; and Bogen and Rusbüldt[3]. These measurements have used the 3.39 μ radiation of HeNe gas lasers except for reference 2, which employed the 6328 Å emission of a gas laser. With 3.39 μ, the measurement is difficult due to refractive effects ($\alpha \lambda^2$) of the plasma, combined with extremely non-uniform sensitivity over the small active surface area of the InAs infrared detectors. The 6328 Å radiation reduces this limitation through the λ^2 dependence of the plasma refractive effects and through the much greater area, sensitivity and uniformity of response of detectors available in the visible region. A disadvantage of the use of the shorter wavelength is the λ^2 dependence of the Faraday rotation.

Faraday rotation measurements with 6328 Å radiation have been combined with Mach-Zehnder interferometer observations to determine the average magnetic field as a function of radius in the plasma of the Scylla IV theta pinch[4]. These measurements also give the average plasma β, the ratio of plasma pressure to external magnetic field pressure, as a function of radius; the plasma density; and with the assumption of a simple pressure balance between plasma and magnetic field, the perpendicular plasma temperature, "$T_\perp$".

II. METHOD

The Faraday rotation measurement employs the visible radiation (6328 Å) from a HeNe gas laser as

a plasma - magnetic field probe. The plane of polarization of the laser beam, propagating parallel, or anti-parallel, to the magnetic field in the plasma region, rotates as

$$\theta_R = 1.5 \times 10^{-15} \lambda^2 \int_o^L B_i n_e d\ell \text{ (degrees)}, \quad (1)$$

where B_i is the magnetic field (gauss), n_e the plasma electron density (cm^{-3}), L the plasma length (cm), and λ the wavelength of the laser beam (cm). Since the Faraday rotation is proportional to $\int B_i(\ell) n_e(\ell) d\ell$ and the Mach-Zehnder interferometer provides $\int n_e(\ell) d\ell$, the determination of B_i from the combined measurements assumes that

$$\int B_i(\ell) n_e(\ell) d\ell = \bar{B}_i(r) \int n_e(\ell) d\ell \quad (2)$$

and that this $\bar{B}_i(r)$ is the magnetic field which exists over the major portion of the plasma length at the radius r.

With a Faraday laser beam of 1.5-mm diameter and with fast detectors and wide band amplifier, θ_R can be measured as a function of both space (radius) and time. A series of interferograms taken on the same discharge provides the time as well as radial space resolution of $\int n_e d\ell$.

These measurements of B_i can be combined with that of the external magnetic field B_e to determine the average plasma β as a function of radius,

$$\beta = 1 - B_i^2/B_e^2 . \quad (3)$$

These measurements can also be used to obtain the plasma temperature at a given radius averaged over the length of the plasma from pressure balance with the magnetic field. From pressure balance,

$$K(T_e + T_i)_\perp = \frac{1}{8\pi n} (B_e^2 - B_i^2) = \frac{\beta}{n} \frac{B_e^2}{8\pi} \quad (4)$$

where B_e is the external magnetic field and it is assumed that $n_e = n_i = n$.

III. EXPERIMENTAL ARRANGEMENT

A schematic diagram of the Faraday-rotation experimental arrangement is shown in Fig. 1. A 70-mW HeNe gas laser at 6328 Å sends a plane polarized light beam through the plasma region parallel to the axis of the one-m length, 10.2-cm diameter, compression coil, into a polarization analyzer, and onto a pair of silicon detectors. In order to accommodate the Mach-Zehnder interferometer on the machine simultaneously with the Faraday arrangement, the Faraday beam probe is turned through 90° by a small mirror just before entering the coil between the Mach-Zehnder mirror and the end of the coil. As the Faraday beam leaves the coil, it is reflected out of the interferometer's path by the tilted Mach-Zehnder interferometer filter. Two narrow band interference filters in series, with transmissions peaked at 6328 Å, serve to reject the plasma light as well as the 6943 Å laser light of the interferometer. The polarization analyzer consists of a 13° calcite Wollaston prism which splits the plane polarized laser beam into two perpendicular components of polarization.

The silicon detectors consist of a selected, matched pair of photoconductive detectors with 20 V/W sensitivity, a measured rise time of 0.1 μsec, and a measured variation in sensitivity over the 0.7-cm diameter active area of less than 2%. Each detector monitors one component of the laser beam. A wide band, high common mode rejection ratio, integrated amplifier provides a difference signal from the two detectors. The Faraday rotation is proportional to the ratio of the difference to the equivalent sum of the detector signals after amplification.

The resolution of the Faraday rotation is determined by the signal to noise ratio of the laser-electronic system and by the almost completely unpredictable effects of the beam refraction by transverse electron density gradients in the plasma. The signal to noise ratio limitation is determined by the laser power and the 3-mV peak to peak noise at the differential amplifier output. With 23-mW incident on the prism, the minimum resolvable rotation is 4×10^{-3} degrees, which corresponds to a minimum resolvable product of internal magnetic field B_i in kG and electron density n_e' in number of 6943 Å Mach-Zehnder fringes of 2.3 (kG) (fringes). With the plasma length and densities in the Scylla IV device, this corresponds

to a magnetic field of ~ 0.3 kG, which is 0.3% of the maximum compression field.

Radial profile data of B_i and β were obtained by scanning the radial dimension of the plasma shot-by-shot with the 1.5-mm diameter laser beam. Approximately 6 discharges were taken for each radial position of the laser beam, which was moved in 2-mm increments. Since the plasma column moves a few millimeters in the radial direction during a given discharge, the data are analyzed and averaged according to the measured position of the laser beam relative to the axis of the plasma. Optical systems with image converter cameras record the Mach-Zehnder interferograms with time resolutions of 50 nsec and provide 4 interferograms at selected times during the discharge.

IV. RESULTS

Faraday measurements on the Scylla IV plasma have been performed in the low-pressure regime with initial filling pressures of 10, 15, and 25 mT and with magnetic bias fields of 0, -1.2, and -2.4 kG. Measurements were made at 1.4, 2.4, 3.4, and 4.4 μsec after the application of the main magnetic field ($\tau/4$ = 3.7 μsec). Radial profiles of B_i, β, n_e, and "$T_\perp$" are shown in Figs. 2 and 3 for an initial filling pressure of 15 mT and with initial bias fields of zero and -1.2 kG. The error bars of the plots represent the average deviations from discharge to discharge. The graphs of Fig. 4 compare the radial plasma β profiles at different times during the discharge. In both cases, with and without B_o, the β profiles are relatively flat in the central plasma region during the earlier portion of the discharge (~ 1.4 μsec). Without B_o, the β profile becomes more triangular in time with the value of β on the axis remaining high. With B_o, the profiles also decrease in radial extent, but possess more of a parabolic shape. It is interesting that the radial extent of the β profiles, Fig. 4., increases slightly after the magnetic field maximum, indicating some radial expansion of the plasma as the magnetic field decreases.

In general β increases with increasing filling pressures (10 to 25 mT) and with increasing negative bias fields. For example, with 25 mT initial deuterium filling pressure and a negative bias of 2.4 kG, β remains greater than 0.95 for 4.4 μsec. There is a good correlation between β and the neutron emissions; the higher the β, the greater the neutron yield.

The β values (and the neutron yields) appear to depend on the condition of the discharge tube. In a relatively new, "conditioned" tube, the β values near the plasma axis were greater than 0.9 with zero bias fields and greater than 0.95 with bias fields over the 4.4-μsec observation time. The data presented in Figs. 2-4 were taken in the same discharge tube, but after many discharges, and resulted in lower β values.

V. DISCUSSION

The characteristics of the radial β profiles are in qualitative agreement with Morse's theory[5,6], which treats the adiabatic relaxation of an initially thin sheath to a thickness of the order of an ion collisionless skin depth $\lambda_i = c/\omega_{pi}$ and allows the external field to penetrate the plasma. This relaxation discharges the radial electrostatic fields necessary to maintain a sheath thickness $< \lambda_i$, and propagates in from the end as an azimuthally symmetric torsional Alfvén wave whose axial velocity varies with radius and has a mean transit time of about 1 μsec.

An ion distribution function which is a function of the constants of particle motion, $\varepsilon = M\bar{V}^2/2$ and $P_\theta = Mr(V_\theta + A_\theta)$, represents a stationary solution of the Vlasov equations. Hence an essentially Maxwelliam distribution might be hypothesized in which P_θ (and hence radial) dependence is built into the temperature, "$T"(P_\theta)$, in order to explain the observed experimental results. An equally plausible explanation can be based on a type of isothermal distribution function of which the following is a convenient analytic example:

$$f_o(\varepsilon,P_\theta) \sim \exp\{-[\varepsilon + \omega P_\theta + P_\theta^2/2Mr_o^2]/T\}, \quad (5)$$

where ω and r_o are simple rotation and transverse anisotropy parameters respectively. This gives a density and mean current velocity

$$n(r) = \frac{n_o}{(1 + r^2/r_o^2)^{\frac{1}{2}}} \exp\{[\omega^2 r^2 + 2\omega r(1 + r^2/r_o^2)A_\theta - r^2 A_\theta^2/r_o^2]/u^2\} \quad (6)$$

$$V_c = -(\omega r + r^2 A_\theta^2/r_o^2)/(1 + r^2/r_o^2). \quad (7)$$

Here $T = Mu^2/2$, $A_\theta(r = 0) = 0$ and $A_\theta(r)$ is given by Maxwell's $\vec{\nabla} \times \vec{B}$ equation. In the limit ($r_o^2 \to \infty$) it can be shown that

$$\frac{"T"}{T} = a^2 + b^2 e^{-\alpha^2 r^2}, \quad (8)$$

where a^2, b^2 and α^2 are positive constants related to n_o, T, ω and B_z, owing to the dominance of the centrifugal force term $r^2\omega^2$ in the exponent. This "T" distribution decreases with increasing r in contradiction to the experimental results. For finite r_o^2, as opposed to the rigid-rotation limit $r_o \to \infty$, the coefficient $(1 + r^2/r_o^2)^{-\frac{1}{2}}$ in front of the exponential in n(r) causes n(r) to decrease with increasing r, which is the desired result. For sufficiently small r_o^2, profiles of "T" resembling the experimental results can be obtained. The mechanism responsible for the decrease of n(r) with radius is the combined effect of cylindrical geometry and a transverse anisotropy in the pressure tensor; when f_o is written out in terms of velocity components it is seen that there are really two transverse temperatures, $T_r = T$ and $T_\theta = T/(1 + r^2/r_o^2)$.

REFERENCES

1. A. A. Dougal, J. P. Craig and R. F. Gribble, Phys. Rev. Letters 13, 1 (1964).
2. I. S. Falconer and S. A. Ramsden, Bull. Am. Phys. Soc. 10, 219 (1965).
3. P. Bogen and D. Rusbüldt, Phys. Fluids 9, 2296 (1966).
4. F. C. Jahoda, E. M. Little, W. E. Quinn, F. L. Ribe, and G. A. Sawyer, J. Appl. Physics 35, 2351 (1964).

   E. M. Little, W. E. Quinn, and G. A. Sawyer, Phys. Fluids 8, 1168 (1965).
5. R. L. Morse, Phys. Fluids (to be published).
6. The following discussion is due to R. L. Morse.

* Work performed under the auspices of the U. S. Atomic Energy Commission.

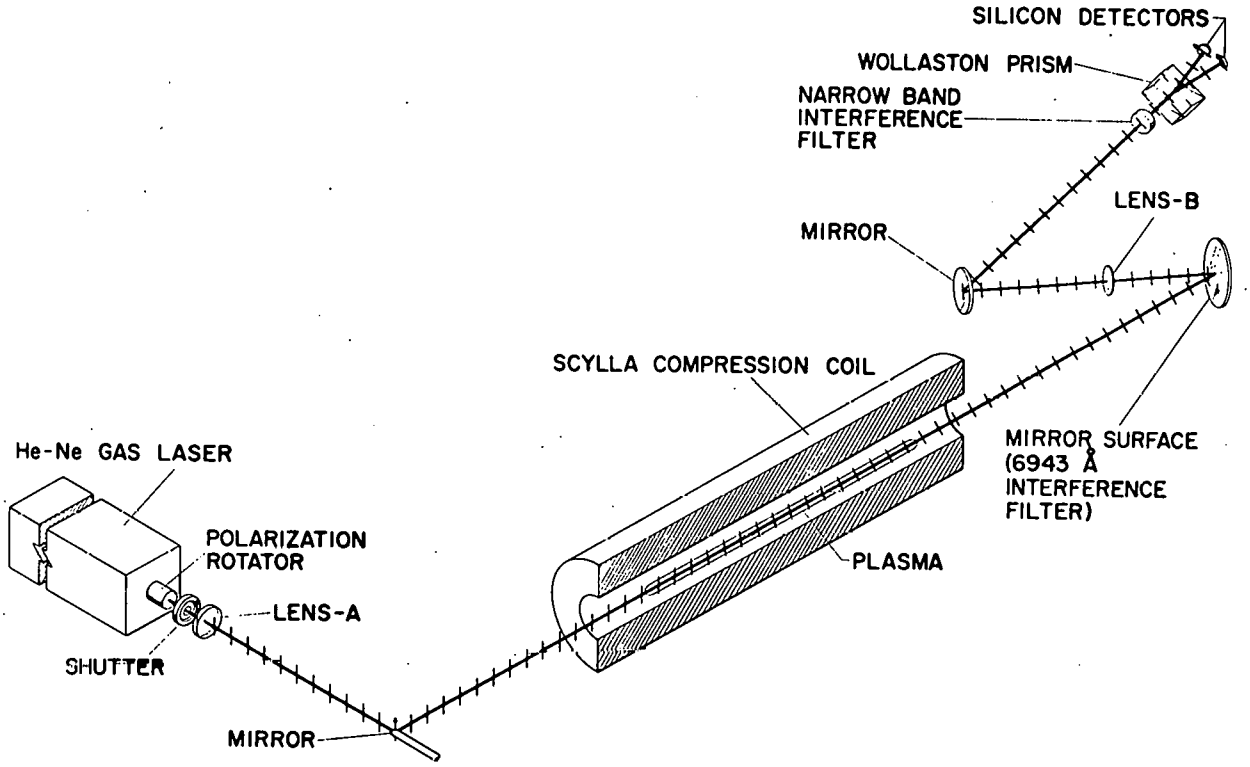

Fig. 1. Diagram of the experimental arrangement of the Faraday rotation apparatus.

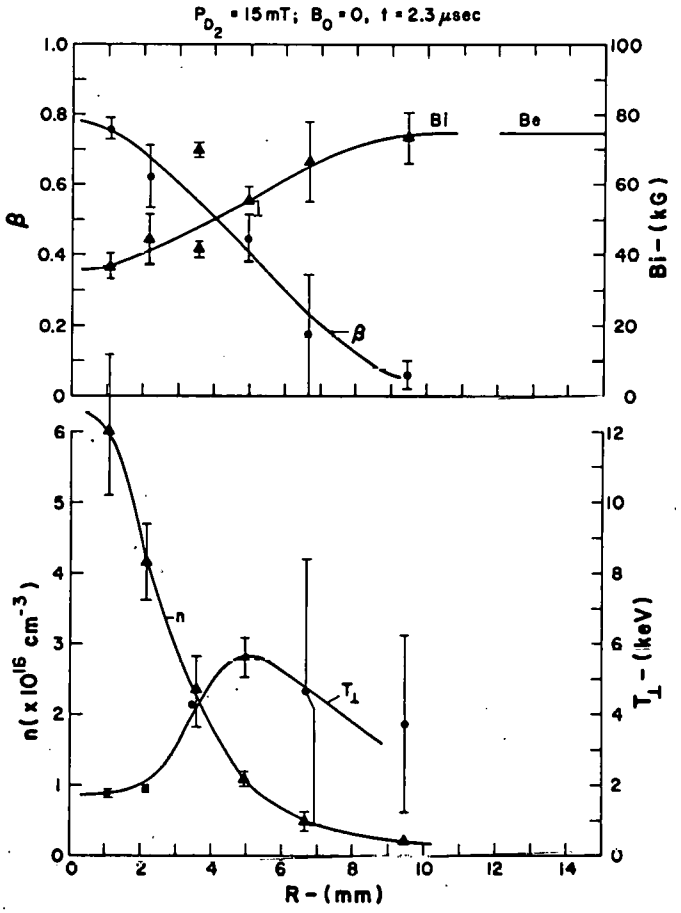

Fig. 2. Radial profile graphs of B_i and β (upper plot) and n and T (lower plot) as a function of plasma radius at 2.3 μsec after the beginning of the discharge with a deuterium filling pressure of 15 mT and zero bias field.

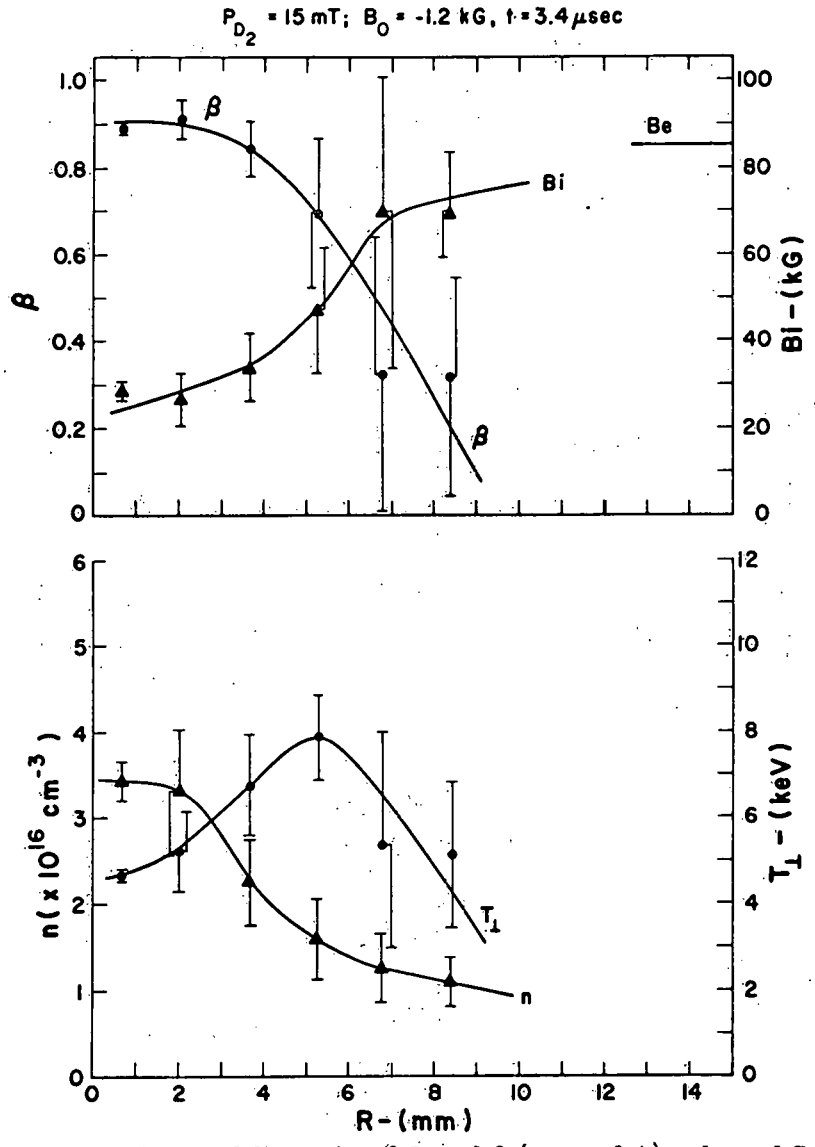

Fig. 3. Radial profile graphs of B_i and β (upper plot) and n and T (lower plot) as a function of plasma radius at 3.4 μsec after the beginning of the discharge with a deuterium filling pressure of 15 mT and a -1.2 kG magnetic bias field.

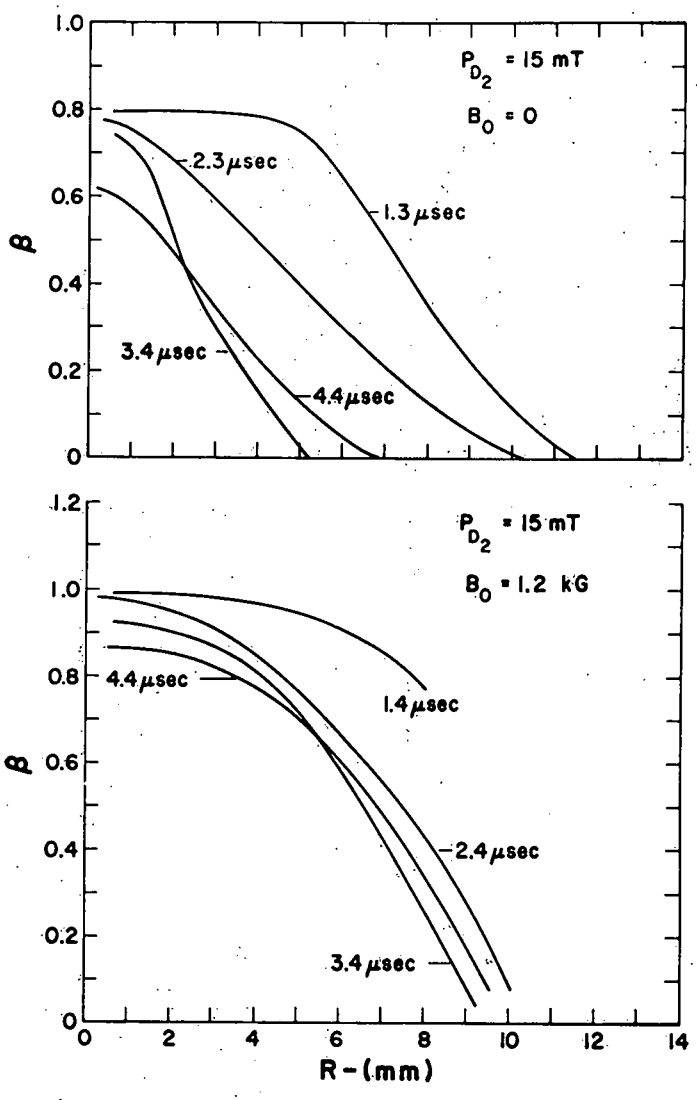

Fig. 4. Radial profile graphs of β as a function of radius at various times during the discharge with deuterium filling pressures of 15 mT and with zero bias field (upper plot) and with -1.2 kG magnetic bias field (lower plot).

STUDY OF TRAPPED REVERSE FIELD CONFIGURATIONS IN A LINEAR THETAPINCH EXPERIMENT

A. Kaleck, H. Kever, L. Könen, P. Noll, K. Sugita, F. Waelbroeck, H. Witulski

Institut für Plasmaphysik der Kernforschungsanlage Jülich des Landes Nordrhein-Westfalen e.V.

ASSOCIATION EURATOM-KFA

ABSTRACT

At the 120 cm long thetapinch experiment (Julietta), the decay of closed field configurations produced by compressing plasmas with reverse bias field and their axial evolution have been studied by simultaneous measurements of continuum radiation profiles at different axial positions and with a set of compensated loops. For typical discharge conditions with reduced energy (50 mTorr D_2, 1.9 kG bias field, B_{max} = 35 kG, half period 11 μs, T_e = 250 eV, $n_e = 5 \cdot 10^{16}$ cm^{-3}), the antiparallel magnetic flux stays roughly constant during the adiabatic compression and decompression phases in agreement with numerical calculations. After a fast axial contraction, the length of the configuration remains approximately constant ($\approx 2/3$ of the coil length) and the axial homogeneity is fair. For other initial conditions (larger D_2-pressure and/or with weaker preionization) strong axial inhomogeneities of the plasma diameter and of the diamagnetism are observed which can result from end effects (axial waves), from field inhomogeneities at the observation windows, or from inherent instabilities. When the condenser bank energy is increased to 600 kJ, axial variations are more pronounced and plasma rotations are detected after the peak compression.

Introduction

The large thetapinch experiment (Julietta) is presently used to investigate the stability of configurations with trapped reverse magnetic fields. In principle, a set of closed field lines could be produced within the plasma by using a bias field which is antiparallel to the compression field. If there were no instabilities, this plasma should escape by classical diffusion across the field into field lines which are closed outside the compression coil, and by subsequent axial flow. This process is rather slow and a certain axial confinement of the plasma could then be expected.

An axial splitting of the plasma into fragments mostly ascribed to the resistive tearing mode instability has been observed in some rather low temperature thetapinch plasmas[1, 2], in other experiments it has not been detected[3, 4]. Another instability splits the plasma radially into threads which usually rotate around each other. The rotation is often assumed to cause an m = 2 instability.

In order to detect such incipient instabilities and to follow the disappearance of the closed

field configuration we examined the plasma distribution by a number of simultaneous localized measurements all along the plasma column which is produced within a coil 120 cm long and 10.5 cm in diameter.

Diagnostics

In the first experiments, simultaneous streak pictures were made with a rotating mirror camera. After a relative intensity calibration with a pulsed light source and Abel inversion, relative radial electron density profiles can be obtained if the plasma is axisymmetric. From these, the radial magnetic field distribution, the trapped reverse flux and the total flux displacement can be evaluated as long as a reverse flux (implying a neutral sheath with B = 0) exists, and assuming that the temperature is reasonably uniform.

Side-on radiation profiles are also obtained with a modified T.V.-camera[5] looking radially and perpendicularily to the streak camera. The T.V.-camera is opened typically for 50 nsecs at one time during the discharge, and the light intensity distribution is stored as an electrical charge distribution. This information is read later by an electron beam and selected "lines" can be displayed directly on an oscilloscope. This video signal is, within experimental errors, proportional to the light intensity and can be used directly for Abel inversion.

The magnetic flux displaced by the plasma was measured by compensated magnetic loops at 6 axial positions. In contrast to the light measurements, the loops produce some axial integration over a length of about one coil diameter.

Soft X-ray detectors, monochromators, and in some cases an axial Michelson interferometer completed the set of diagnostics.

Plasma Production

Four condenser banks are normally discharged into the compression coil: first a preionization bank (700 kc) 50 μs later, almost simultaneously, the preheat bank (400 kc, 3 kG peak field) and the bias field bank, and 20 μs still later, when the bias field has reached about 2 kG, the main bank.

Most experiments are carried out with 50 mTorr initial deuterium pressure. Axial interferometric and side-on radiation measurements show that, when the main bank is fired, the preheated plasma is about 5 mm detached from the wall by the slowly rising bias field. The contact with the vessel is then reduced during the field reversal time when the plasma is radially unconfined. Nevertheless, the main discharges with reverse bias field are often considerably more contaminated by oxygen (about 1%) than discharges without bias field (about .3%) when no field reversal occurs.

Experimental Results

Two typical discharges without and with reverse bias field are shown in figs. 1 and 2. At maximum compression ($\approx$5 μs), the diameter and the displaced flux decrease smoothly from the midplane to the coil ends without bias field (flow losses). With reverse bias field, the loop signals are larger and indicate a sharp axial boundary between -38 and -54 cm resulting probably from the axial contraction which is produced by the tension of the closed field lines. Abel inversion of the light intensity profiles shows that the radial electron density distribution presents a dip on the axis indicating a trapped reverse field even during the decompression phase till about 2 μs before the end of the half cycle.

Radial density and magnetic field distributions of a similar discharge, obtained at 3 different

times at the center window, are shown in fig. 3. The magnetic flux displacements calculated from the radial field distributions are in fair agreement with the loop signal at z = -6 cm. During the field reversal time and the irreversible implosion, the initial negative magnetic flux (90 kG cm^2) decreases to about 20 kG cm^2. It remains thereafter constant within the experimental errors.

The evolution of a radial distribution for parameters which are close to those measured at 2.3 μs (fig. 3) has been calculated (fig. 4) from a simplified model which predicts that the reverse flux should decrease slowly. At first sight the plasma behaves in rough agreement with the predictions based on classical resistivity. However, end effects, and also axial waves, initial nonuniformities and incipient instabilities have not been taken into account.

In fact, the axial homogeneity of such "smooth" discharges with reverse bias field is only fair. In these first experiments the loops and windows were not sufficiently closely spaced to tell whether this resulted from axial motions, conncected to the initial phase or from incipient instabilities. Without preionization or at larger initial pressure, axial splitting of the plasma into fragments has often been observed. With stronger compression rotation and m = 2 instabilities occur after peak compression.

The experiments were recently resumed using a modified set-up: a low-inductance crow-bar system was incorporated, the coil ends were modified, the coil was provided with 15 evenly spaced narrower windows and with 16 magnetic loops (fig. 5). Simultaneous observation at 8 windows by the T.V.-camera was achieved (fig. 5) and orthogonally, streak pictures were made radially at the same axial positions.

The following preliminary results were obtained:

1. The plasma drift was considerably reduced.
2. The 16 loops allow an accurate reconstruction of constrictions and axial motions in agreement with optical observations: in the example illustrated on fig. 6 and 7; plasma bulges develop near the column ends which contract with an initial velocity of about $8 \cdot 10^6$ cm/s to roughly 1/3 rd of the coil length at maximum compression. Later, the plasma rotates, splits into two filaments and reexpands axially.
3. In other discharges, preferentially without preionization, strong radial constrictions and break-up into fragments were often observed. The instability is first detected shortly after the initial implosion and the splitting is essentially completed after about 2 μs, in order of magnitude agreement with the theoretical rise time of tearing-mode resistive instabilities[6] for these experimental conditions. On the other hand, the growth rate of these instabilities should increase with stronger compression; experimentally no new radial constriction appears after 2 μs whereas the compression increases. Moreover, after conditioning of the discharge tube, it seems that fewer constrictions develop. This suggests that these constrictions might result from rather pronounced initial axial inhomogeneities.

Literature

1 H.A.B. Bodin, Nucl. Fusion 3 (1963) 215

2 A. Eberhagen et al., Nucl. Fusion 4 (1964) 296

3 P. Bogen et al., Nucl. Fusion 4 (1964) 131

4 A.C. Kolb et al., Plasma Physics and Controlled Nuclear Fusion Research, Vol. I (1966) 261

5 W. Hopmann, KFA-Bericht Jül-290-PP (1966)

6 H.P. Furth et al., Phys. Fluids 6 (1963) 459

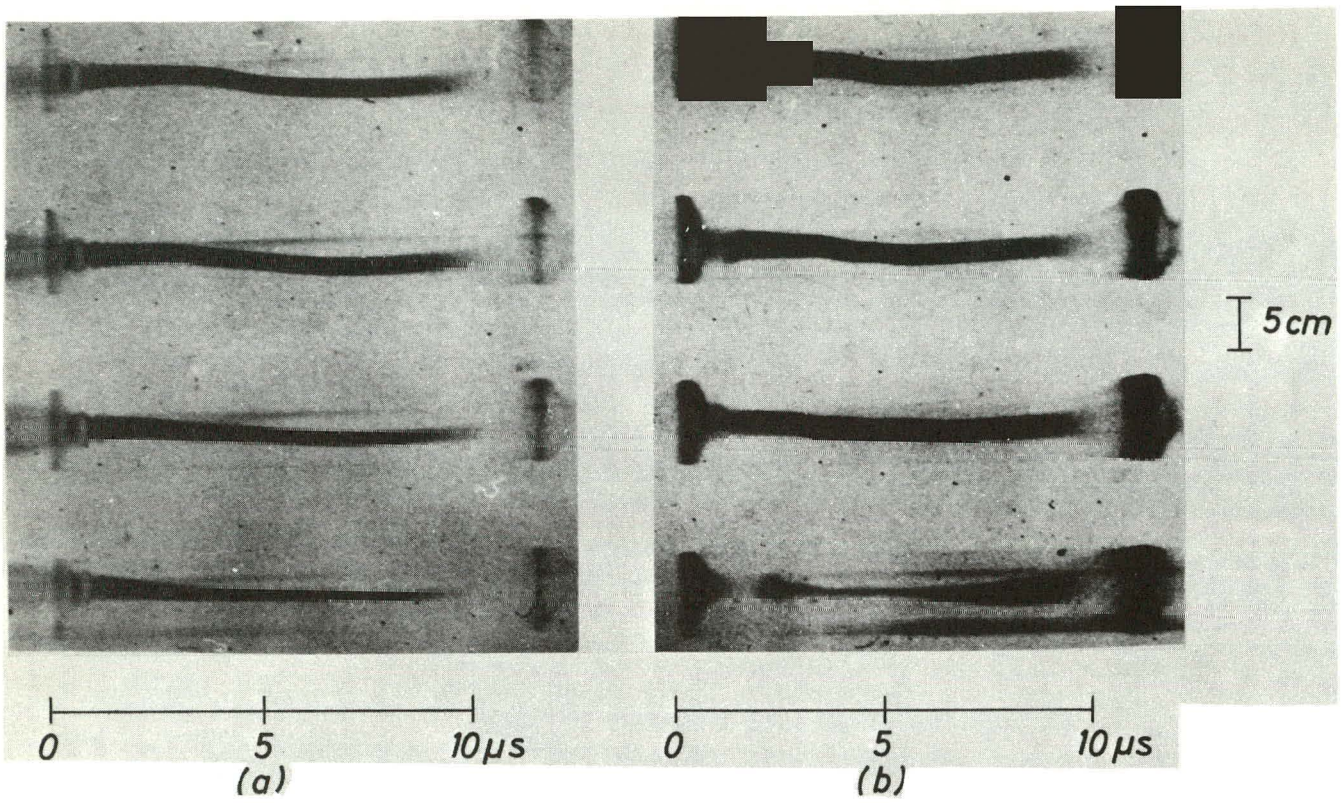

Fig. 1 Streak photographs of discharges in 50 mTorr D_2 taken in the midplane z = 0 (top) and at the axial positions z = -16, -32, and -48 cm (bottom). a) B_z = 0, b) B_z = -1.9 kG. The peak field is 35 kG at 5 μs.

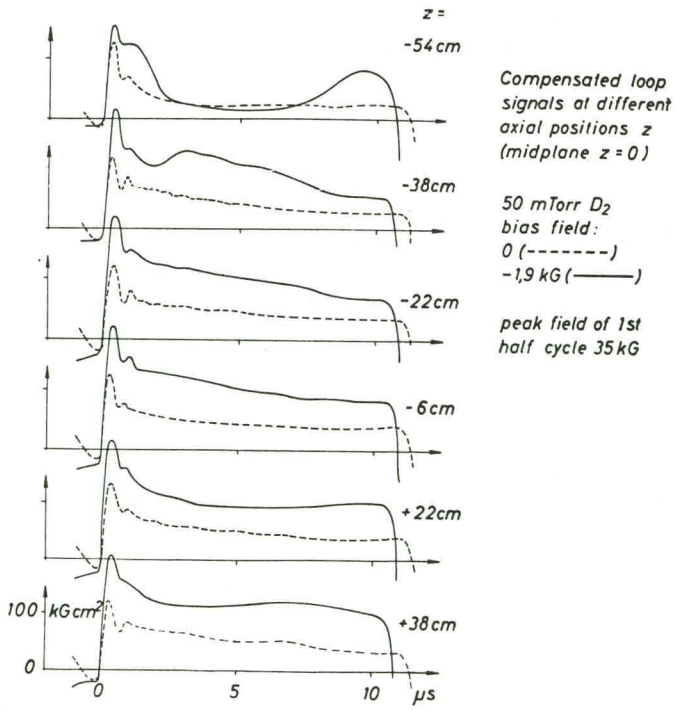

Fig. 2 Loop signals of the same discharges as fig. 1 taken at 6 axial positions. The plotted signals are not corrected for the slight miscompensation of the loops. In fact, without bias field the corrected signals decrease as one goes from -6 to +22 and +38 cm.

Fig. 3 Radial magnetic field- and electron density distributions in the midplane at 3 different times evaluated from streak photographs (—) and from the T.V.-camera signal (---) of a discharge in 50 mTorr D_2 with B_z = - 1.9 kG (B_{max} = 35 kG at 5 μs). T_e was measured axially by soft X-ray absorption. The electron density N_{max} was calculated from pressure balance assuming $T_i = T_e$ and $\partial T/\partial r = 0$.

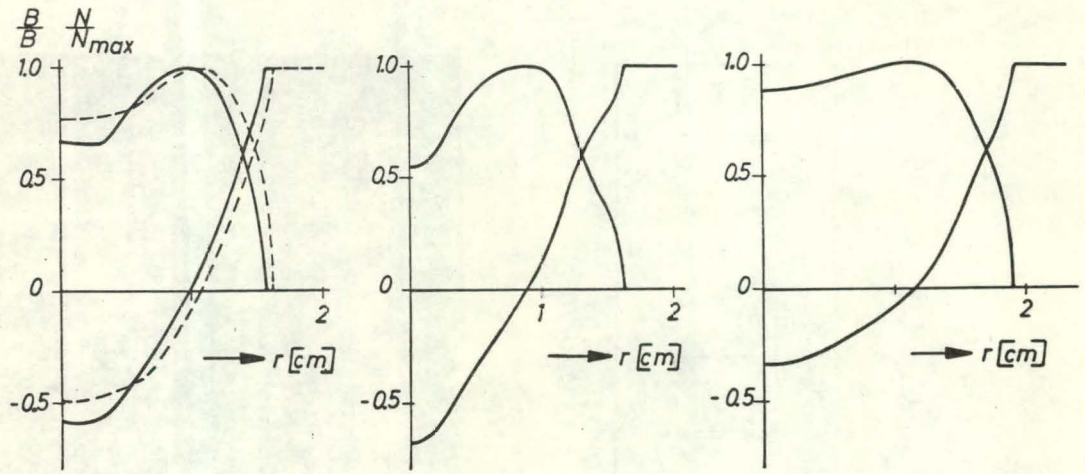

t =	2.3 μs	4 μs	7 μs
B_a =	21 kG	31 kG	27,5 kG
$T_e \approx$	150 eV	280 eV	270 eV
$N_{max} \approx$	3.7×10^{16} cm^{-3}	4.3×10^{16} cm^{-3}	3.5×10^{16} cm^{-3}

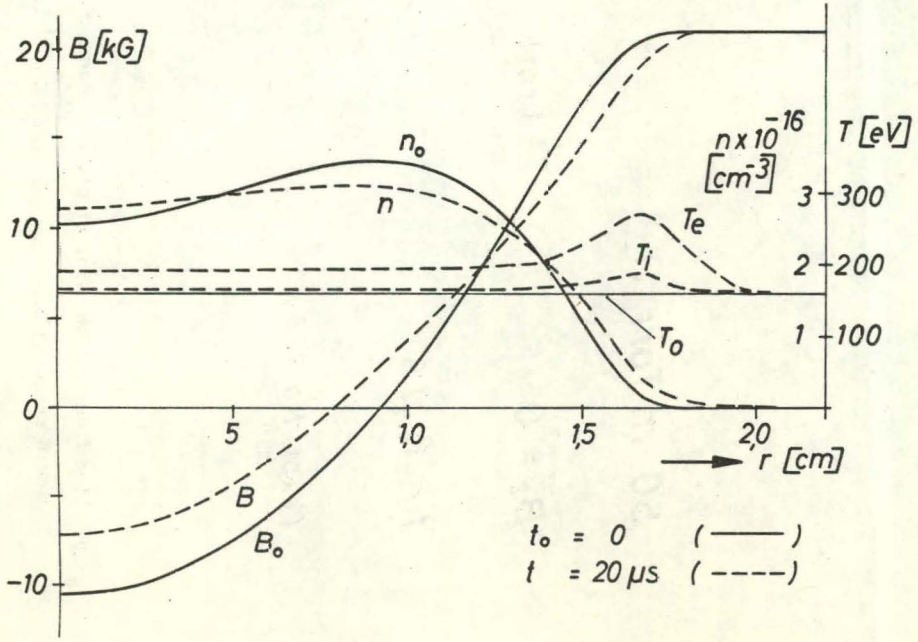

Fig. 4 Computed change of an initial radial distribution which is close to that measured at 2.3 μs (B_o = initial magnetic field, n_o = electron density, T_o = electron- and ion temperatures). No energy losses, zero axial gradients and a constant external magnetic field were assumed.

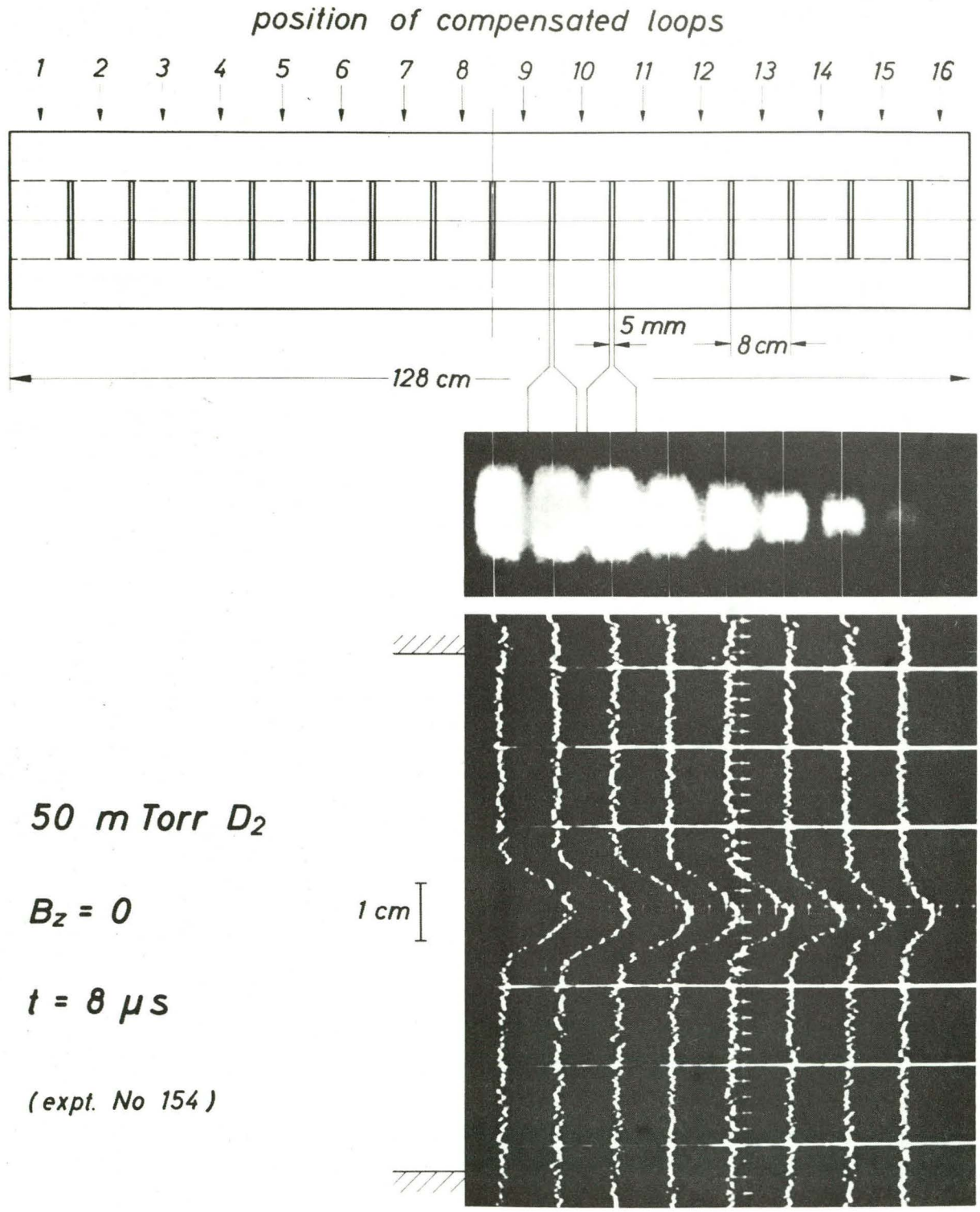

Fig. 5 Modified coil showing position of compensated loops and windows. Below: a T.V.-camera picture and 8 selected video signals taken on a discharge without bias field.

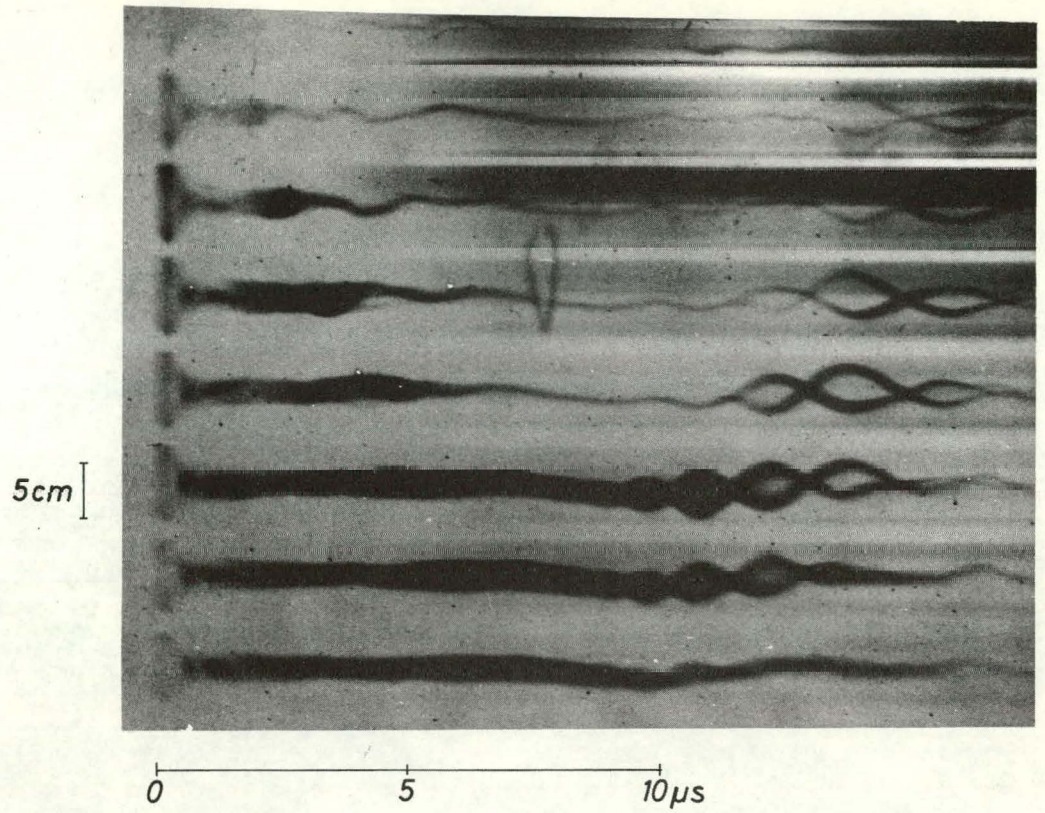

Fig. 6 Streak photograph of a discharge in 50 mTorr D_2 with 2.2 kG reverse bias field observed simultaneously at 8 axial positions from the coil end (top) to the midplane (bottom). Peak field 48 kG at 6.5 μs.

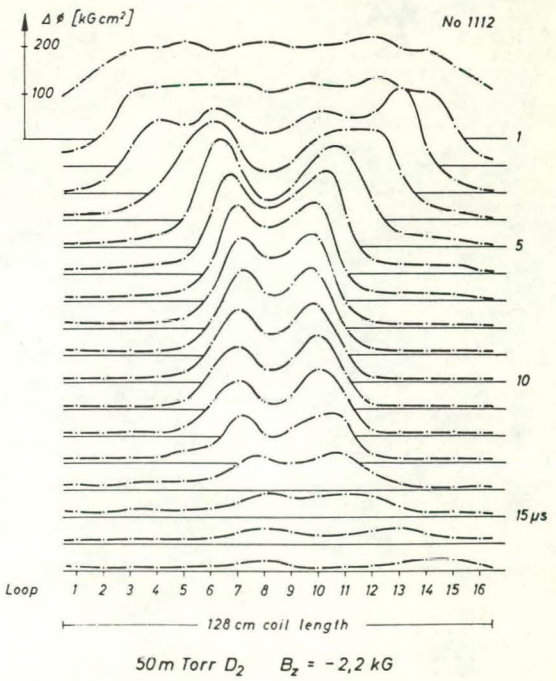

Fig. 7 Evolution of the axial distribution of magnetic flux displacement obtained by loops for the same discharge as fig. 6.

MEASUREMENT OF PLASMA DENSITY AND PARTICLE LOSSES IN A LARGE THETA PINCH

by

E. A. McLean, A. D. Anderson, and H. R. Griem*
Naval Research Laboratory
Washington, D. C. 20390

ABSTRACT

Particle containment times (~25 μsec) have been measured in $\beta \simeq 0.4$–0.5 and $B \simeq 1$ plasmas produced with initial reverse fields. Flow through the constricted ends of the dense plasma column does not always account for the observed particle loss rate. However, there is direct photographic evidence for plasma leaving the coil region along the field lines, presumably after radial diffusion across field lines along the plasma column. This radial diffusion is found to be slower than Bohm diffusion by an order of magnitude (or more) for $\beta \simeq 1$. In another experiment with a larger tube diameter and a lower β, after the first 10-15 μsec the loss time is consistent with "Bohm times" of $\tau \sim r^2/4D_B$. The loss rate during the first 10-15 μsec appears to be considerably lower but has not yet been established quantitatively.

Introduction

While there is no question that theta pinches provide an efficient means of producing high-temperature and high-density plasmas, with ratios of plasma pressure to external magnetic pressure (β) approaching unity in many cases, the factors which limit plasma confinement in such devices are not yet resolved. If the plasma is macroscopically stable, two mechanisms of plasma losses are competing with each other; namely, streaming of dense plasma through the ends of the plasma column and radial diffusion. The latter may again be followed by axial streaming which would, however, generally occur through a much larger cross section and therefore be at a much lower density than the constricted flow mentioned above.

To estimate the loss rate due to flow out the constricted ends of a plasma column it is necessary to invoke a model. If the area of the bulk of the plasma column is $A_p = \pi r^2$, and the effective end aperture is A_e, then the confinement time is of the order

$$\tau_z \simeq \frac{\ell}{2v} \frac{A_p}{A_e} \quad , \tag{1}$$

where ℓ is the length of the column and v is the flow speed through the end aperture.

If the mean-free-paths are short compared to the length of the end "nozzles", as in the present experiments, the plasma flows sonically through the ends as

$$v = \left(\frac{\gamma P}{\rho}\right)^{\frac{1}{2}} = \left(\frac{5}{3} \frac{k(T_e + T_i)}{m_i}\right)^{\frac{1}{2}} \tag{2}$$

* Department of Physics and Astronomy, University of Maryland

(If the mean-free-paths are long, then the characteristic velocity is about one-fourth the above.)

There is also an uncertainty in estimating the effective aperture A_e. If one ignores sheath problems

$$A_e \approx \pi\rho^2, \tag{3}$$

where ρ is the radius of the plasma column near the coil ends. Taylor[1], however, has included the effect of conservation of angular momentum on particles free-streaming along a sheath into a point cusp. Under these circumstances the loss rate is almost identical to losses through a ring cusp of radius r. The effective aperture is approximately

$$A_e \simeq \pi\left(\frac{3\pi}{2}\right)^{\frac{1}{2}} \rho_c r, \tag{4}$$

where ρ_c is the ion Larmor radius at the point cusp and r is the mean plasma radius. Setting $A_e \equiv 2\pi r\rho$, the effective "leakwidth" ρ is

$$\rho \approx \left(\frac{3\pi}{8}\right)^{\frac{1}{2}} \rho_c \approx \rho_c. \tag{5}$$

Thus the uncertainty in the aperture can be estimated from the ratio between (3) and (4) using (5)

$$\frac{\rho^2}{2r\rho_c} .$$

Characteristic times for radial particle losses are, on the other hand, estimated by

$$\tau_r \simeq \frac{r^2}{4D} , \tag{6}$$

where D is the diffusion coefficient, and the numerical factor actually depends somewhat on the radial density profile (assumed here to be parabolic). Were collective effects dominant, these could presumably lead to some fraction of the Bohm diffusion coefficient

$$D_B \simeq \frac{c\,k\,T}{16\,e\,B} . \tag{7}$$

The object of the present experiment was to separate axial and radial losses and to determine the effective diffusion coefficient. For some of the experimental conditions reported previously[2], this separation proved rather difficult because containment times associated with end losses estimated according to Eq. (1) were quite close to observed containment times, or because these times were limited by the onset of a rotating flute instability. To improve this situation, experiments were performed with larger coil diameters corresponding to small stray transverse fields and therefore less rotation. Moreover, especially when both the coil and tube diameters were increased, the resulting plasma diameter became larger along most of the plasma column, but remained about the same near the ends. This leads to a substantial increase of the factor A_p/A_e in Eq. (1) and, accordingly, also of the estimated axial loss time. Since the actual containment times only increased by small factors, a less ambiguous determination of radial diffusion losses is now possible.

Experiments

The Pharos theta-pinch experiment has been described previously[2], the only essential changes being in the coil (d_c) and tube (d_t) diameters. These changed from d_c = 10.5 cm, d_t = 8.4 cm to (a) d_c = 13.5 cm, d_t = 8.4 cm, and (b) d_c = 19 cm, d_t = 17 cm. A negative bias field of ~4kG is imbedded in a theta-pinch preheater discharge in ~ 60 mTorr D_2. The main compression field rises in 10-15 μsec. Measurements of radial density profiles as a function of time were obtained for case (a) from streak-camera records of the visible bremsstrahlung emission taken simultaneously through various slots in the 180-cm long coil, which was split into nine sections. Similar data for case (b) have not been fully analyzed. This photographic technique, which was put on an absolute scale by comparison with a photoelectric continuum monitor, is described in detail elsewhere[3]. Results, e.g. for case (a) above, at a main bank energy of 1.3MJ corresponding to a maximum field B of ~55kG are present in Figs. 1 and 2. The approximately flat-topped appearance of the radial profiles is characteristic of high-β plasmas, and it is seen that the density gradient extends over about half the plasma radius.

From the plot of the total number of electrons versus time in Fig. 2 an e-folding time of ~24 μsec may be estimated, which agrees rather well with visual estimates made directly from the streak records.

A sequence of streak photographs for the large diameter coil case (b) for various bank energies corresponding to maximum fields of 30, 45 and 55kG, respectively, is shown in Fig. 3. It is seen that the plasma radius varies slowly along the axis but decreases by a factor $\gtrsim 2$ at a distance 70 cm from the midplane of the coil. Also, the plasma radius remains almost constant from 5 to 15 μsec, and the average density changes by less than about 20% during this period. But then plasma is rapidly lost in the following 10-20 μsec.

To determine the fate of the plasma lost from the dense column, image-converter photographs were taken viewing the discharge vessel side-on just outside the compression coils. As shown in Fig. 4 plasma emerges from the coil region as early as 3 μsec from the initiation of the main discharge, following the field lines toward the walls. While these pictures certainly demonstrate that the plasma escapes out the ends and not to the walls interior to the coil, they cannot be used to decide whether the effective loss aperture corresponds to the minimum radius of the dense column or to a much larger aperture filled by radial diffusion across the field lines.

Results and Discussion

Measured containment times for cases (a) and (b) are summarized in Table 1 together with experimental conditions near peak field.

TABLE 1*

Case	a	b(1)	b(2)	b(3)
β	~1	0.4	0.4	0.5
d_c	13.5	19	19	19
d_t	8.4	17	17	17
B[kG]	55	55	45	30
T[eV]	300	200	150	100
N[cm^3]	1.4×10^{17}	8×10^{16}	7×10^{16}	6×10^{16}
r	0.7	1.8	1.9	1.8
ρ	0.35	0.6	0.7	0.8
τ_{exp}	24	~20	~20	~20
τ_{th}	3	19	20	17
τ_z	14	40	35	30
τ_r	4	35	45	40

*(a) Times expressed in μsec and lengths in cm.

(b) The dense plasma column is ~150 cm long in all cases.

(c) The containment time τ_{exp} for case (b) is taken to be the time duration of rapid decay after the time of peak field. τ_z is obtained from Eqs. (1), (2), and (3).

(d) d_c and d_t are the coil and tube diameter, N the average density (radial average at midplane), ρ is the minimum radius at the end and r is a mean radius averaged over the length of the column.

(e) $\frac{1}{\tau_{th}} = \frac{1}{\tau_z} + \frac{1}{\tau_r\ (\text{Bohm})}$

(f) The temperature for case (a) was determined with an estimated accuracy of 20% from x-ray bremsstrahlung measurements[4]. For case b(3) the decay time of the CV lines at 2271Å was used[2,5] to determine T_e to 20%. For cases b(1) and b(2) the temperature was scaled according to $\sim B^{4/5}$ for adiabatic compression with allowance for slight changes in initial heating.

For case (a), where the radial and axial distributions have been measured the estimated time τ_z is

$$\tau_z \approx \frac{\ell}{2\bar{v}} \quad \frac{A_p}{A_e} = \frac{150}{2 \times 22} \left(\frac{0.7}{0.35}\right)^2 = 14\ \mu\text{sec},$$

which is somewhat less than the observed containment time of 24 μsec. [If the free flow assumption were valid ($\bar{v}_z = \bar{v}/4$), then τ_z = 50-60 μsec, which is long compared to the confinement time.] Allowing for a factor two uncertainty in the measured containment time and considering the above axial loss time τ_z to be an upper limit, we therefore conclude that the radial loss rate is an order of magnitude or more below the Bohm diffusion rate.

For case (b), where the average plasma radius is increased to ~ 2 cm (the maximum radius at the midplane varies between 2-3 cm typically) the loss rate after peak field is about a factor of two faster than is expected for flow out the ends of the constricted column. The loss over and above the usual end loss characterized by τ_z can be accounted for by radial diffusion at the Bohm rate.

During the first ~15 μsec of the discharge in the large diameter tube the streak photographs indicate that the loss rate is considerably less. A detailed analysis is required to determine the effective diffusion coefficient. This should be possible because of the delayed onset of the rotating flute instability following a relatively long (~25 μsec) quiescent period.

References

1. J.B. Taylor, "Steady State Model of Cusp Losses," Culham Laboratory Report No. CLM-R58 (March 1966)
2. A. C. Kolb, W.H. Lupton, R.C. Elton, E.A. McLean, M. Swartz, M.P. Young, H.R. Griem, and E. Hintz, Plasma Physics and Controlled Nuclear Fusion Research (International Atomic Energy Agency 1966), Vol. I, p. 261.
3. E.A. McLean, Appl. Optics, Dec. 1967 issue.
4. R.C. Elton, unpublished data
5. H.-J Kunze, A.H. Gabriel, and Hans R. Griem, Phys. Fluids (submitted).

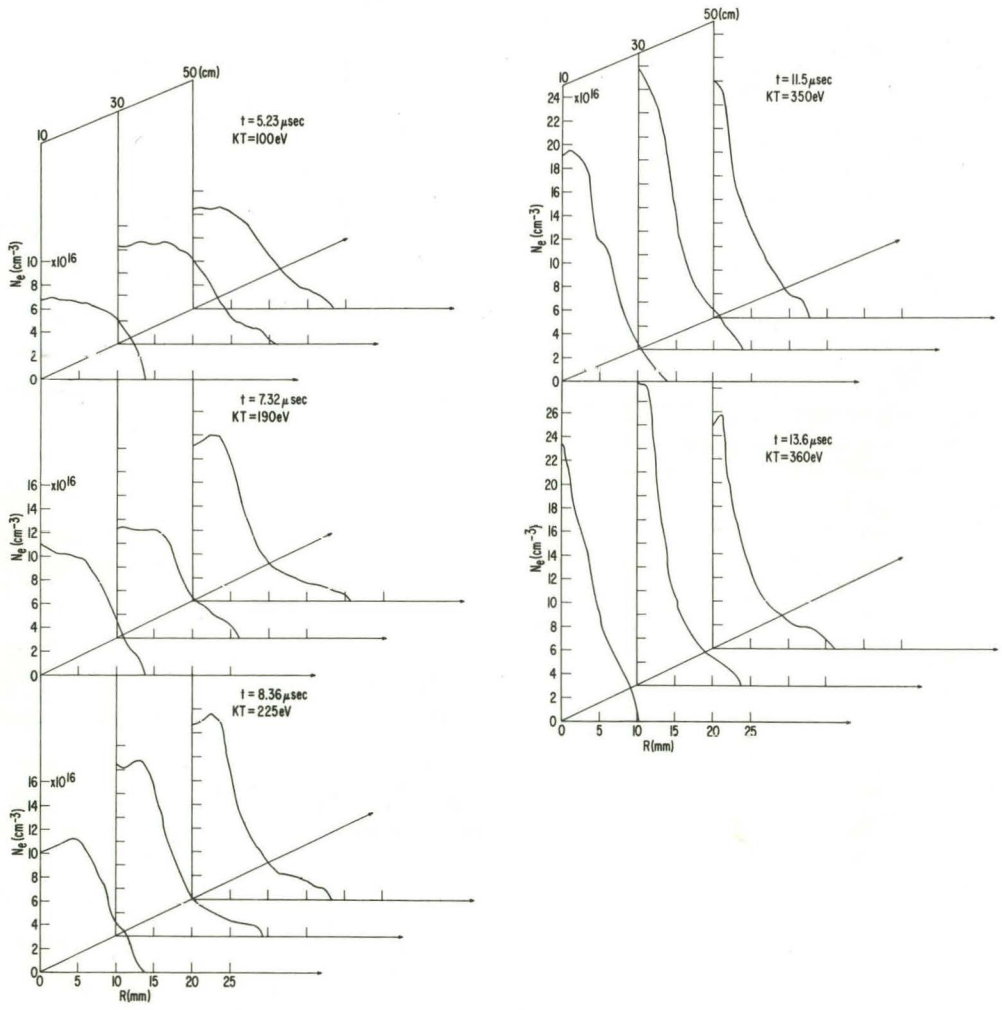

Fig. 1. Electron density distributions for case (a) as described in Table 1.

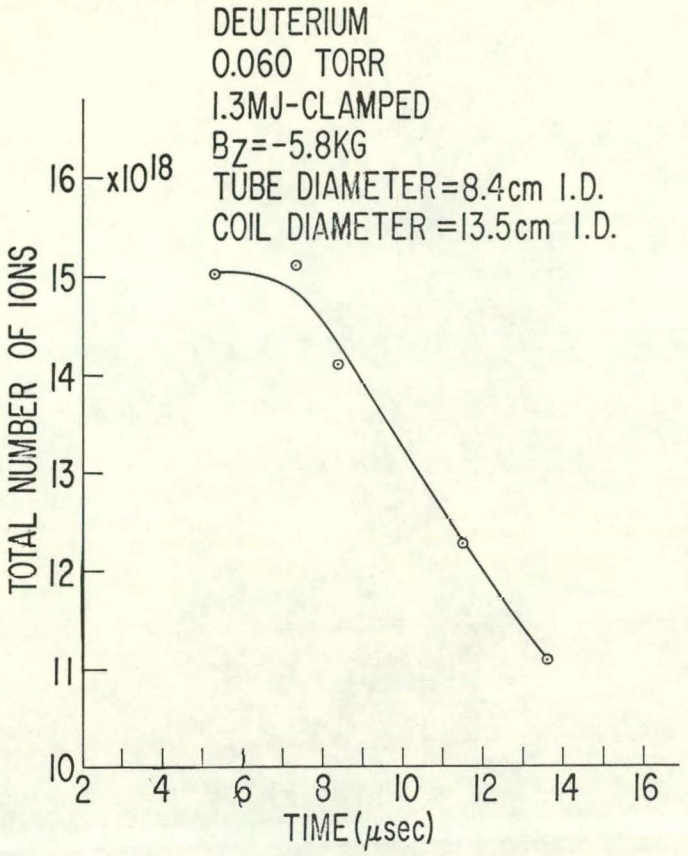

Fig. 2. Total number of electrons in the dense plasma column versus time.

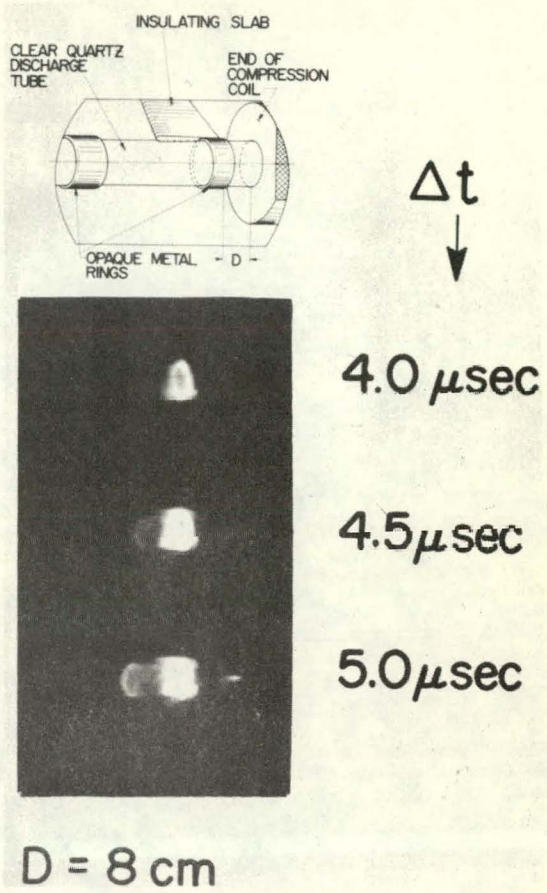

Fig. 4. Image-converter photographs of plasma emerging from the coil ends. D = 8 cm.

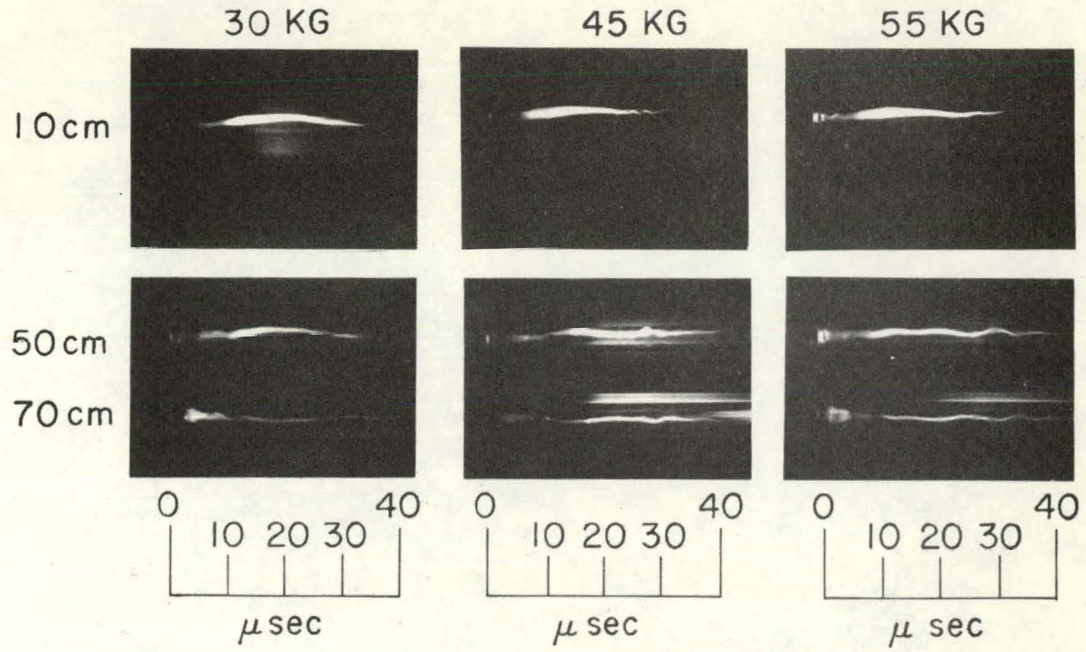

Fig. 3. Streak records for cases (b) as described in Table 1.

EVIDENCE FOR LONG-TIME CONFINEMENT OF DENSE PLASMA BY MEANS OF TWO θ PINCHES AND A CUSP, (CHALICE)*

by

George Yevick, Robin Harvey, Morton Schiff, and Henry Opat
Stevens Institute of Technology
Hoboken, New Jersey

ABSTRACT

Experimental evidence is presented for the confinement of plasmas having densities greater than 3×10^{16} particles per cc. and confinement times at least 20 microseconds by means of two θ-pinches and a cusp (Project CHALICE). Two-color Mach-Zehnder streak interferograms are taken looking down the length of the system. The streak itself lasts for 100 microseconds and a plot of time-dependent radial density is obtained. (Unfortunately, we have not yet measured the plasma temperature.) The deuterium is preheated with a 7.5μf capacitor-powered, weak, linear pinch. The two θ-pinches are produced by a fast θ-pinch Bank (64μf) with rise times of 1μ second and then crowbarred. Simultaneously with the θ-pinch Bank a Cusp Bank (135μf) is switched on. The half life of the crowbarred magnetic field of the Cusp Bank is 50 microseconds. At the present time, we are operating at low voltages, yielding magnetic fields of 20 kilogauss for θ-pinch Bank and 27 kilogauss, Cusp Bank, at the line escape of the cusp. We have taken Mach-Zehnder data with all possible combinations of the three banks. Only the combination of preheater, θ-pinch, and Cusp Bank yields a dense, long confinement-time plasma.

I. INTRODUCTION

Project Chalice is concerned with the production, injection, and confinement of hot, dense plasma. The production of the hot plasma occurs in two stages. First, a weak linear pinch is created to preheat the plasma. In the second stage, a pair of opposed θ-pinch coils generates two hot, dense plasmas.

Magnetic fields produced by the θ-pinch coils form a cusp region in the equatorial plane. Because of the extreme rapidity of the θ-pinch Bank, it is necessary to have a slow Cusp Bank specifically for confining the plasma produced in the θ-pinch region (See Fig. (1)) possessing a long decay time for confinement purposes.

At the two outer ends of the system, there exist strong permanent mirrors (measured mirror ratio 1.9). Now, by careful timing and by virtue of the radial dependence of the fields due to the Cusp Bank at the cusp point ends of the θ-pinch coils, we are able to generate dynamically vanishing mirrors. The "dynamic mirrors" first

*Supported by the United States Atomic Energy Commission under contract No. AT(30-1)-2582. This is report no. SIT-2582-24.

confine the plasma in the two θ-pinch regions and then effectively open up to allow injection into the cusp region.

The experimental set-up is completed. All experiments are done with deuterium gas utilizing pressures from 50 to 300 microns. Diagnostic tools incorporate two-color Mach Zehnder frame and streak interferometry, spectroscopic streak, integrating and high speed neutron-detectors, and calibrated deuterium line intensity. In process of completion is an X-ray bremstrahlung spectrometer.

II. EXPERIMENTAL SET-UP

(A) Description of System

Fig. (1) illustrates the configuration of Project Chalice. The main parameters of the system are as follows:

	Pre-Heater	θ-pinch Bank	Cusp Bank
Capacitance (μf)	7.5	64	135
Voltage Range [Nominal] (kv)	3-7[5]	5-30[10]	5-15 [5]
B at [Nominal Voltage] (kg)	3 (pinch)	20	27 (line) 13 (pt.)
Rise Time (μsec)	4	1	9
Crowbar Time (T_e) (μsec)	-	1/2 cycle (chopped)	60

The length of the Z pinch is 18 in. long. The two θ-pinches are each 4" long with a useable diameter of 1.75". The glass tube is made to follow the field lines in the cusp region with an effective separation between the cusp coils (line escape) of 0.5". The distance between escapes is about 1". A somewhat complete description of the system is to be found in Refs. (1 and 2).

(B) Dynamic Mirrors

The magnetic field configuration due to the three banks is complicated both in space and time. Some idea of the fields are shown in Fig. (2). At the time of initiation of the θ-pinch, the dominant field is the slower cusp-field which has risen to roughly one-half full value. Near the dipolar cusp-coils, the fields fall off as 1/r; whereas in the solenoidal θ-pinch region, the fields are uniform. When the plasma commences to implode near the wall, it sees two types of effective mirrors, the fixed mirrors at the outside ends and the high field at the entrance to the cusp. As it continues to implode, not only do the θ-pinch fields increase and thereby decrease the effect of the dynamical mirror, but also at the same time the plasma cylinder collapses into low B regions in the point escape domain. When the internal θ-pinch fields become higher than the confining cusp fields, injection takes place. The plasma enters the cusp but sees at the line escape a field which is twice as high as the field it overcame at the point escape. Upon rebounding, cusp fields have increased and the plasma is trapped. Afterwards, the cusp bank is crowbarred.

(C) Mach Zehnder Interferometer

Using an intense pulsed white light source,[3] we are able to do two-color, long time interferometry (See Fig. (3)). The difficult task of finding white light fringes is achieved with the aid of rubber bands. Frame and streak interferometry is accomplished with an image converter-camera for a large range of time scales. "Infinite" and multiple fringe data were taken. The plasma was viewed lengthwise through the mirrors. This reduced the visible diameter to 7/8"

The fringe shifts seen in Figs. (4) are proportional to the total number of electrons in the path of the beam. If λ is in cm. and N is the density in cm^{-3}, the fringe shift is given by $s = -4.5 \times 10^{-14} \lambda \int_0^L N_e \, dz$. Knowing the fringe shift we can obtain the product of electron density and the assumed length of the plasma. The latter is in the ratio of 18:10:1 for the preheater θ-pinch and cusp regions respectively.

III. EXPERIMENTAL RESULTS

A typical sampling of data is to be found in Figs. (4 to 6).

(A) Preheater

The value of the magnetic field chosen was such as to minimize field trapping. The timing of the θ-pinch Bank was found previously[4] to be conditioned by the necessity for prohibiting the plasma from hitting the walls, thereby introducing impurities. A typical trace of the preheater alone

is shown in Fig. (4b). The pinch radius is around 0.5 cm (occuring at 1 μsec) and expands to the walls at about 2.5 μsec, prior to which time the θ-pinch Bank goes into action. The plasma density as shown in Fig. (5) is 0.5×10^{16} particles per cc^3 at that time.

From the measurement of the ratio of the intensities of H_α to H_β we know that the temperature is above 1 ev. The data is consistent with the assumption that the preheater plasma is roughly 50% ionized. (See Fig. (5)).

(B) Preheater Plus Cusp Bank

In brief the effect of the cusp bank is to moderate slightly the visible fluctuations of the preheater plasma. (See Fig. 4.c) There appears to be negligible confinement presumeably because of no trapping. Decay time is around 6 μsec.

(C) θ-Pinch Bank Alone

Fig. (4d) shows that the θ-pinch Bank produces plasma which lasts only for the duration of the magnetic field (2 μsecs).

(D) Preheater Plus θ-Pinch Bank

Figs. (4a and 5) are an expanded view exhibiting magneto-hydrodynamic oscillations. We observe that after the θ-pinch ceases, the plasma returns to the preheater condition as shown in Fig. (4e) as if no effect were produced by the θ-pinch bank.

(E) θ-Pinch Bank Plus Cusp Bank

We immediately observe from Fig. (4f) that nothing much transpires.

(F) Preheater Plus θ-Pinch Bank Plus Cusp Bank

In Figs. (4g, h, i) we see a distinct qualitative difference from all the above events. The plasma apparently is trapped and the confinement time of 30 μsecs. corresponds to roughly the B^2 decay time of the Cusp Bank. In these three figures (Figs. (4 g, h, i)), the voltage ratio of the θ-pinch and Cusp Banks was 2:1. When the ratio was changed to 3:2 (Fig. (4j)), the efficacy of confinement was greatly reduced. Trapping appears to be negligible.

(G) Temperature Measurements

We have succeeded only in measuring the temperature of the preheater by comparing the intensity of the H_α to H_β. The measurements show the preheater plasma to be above 1 ev. Experiments are now in progress to measure high temperatures by means of differential absorption of the bremstrahlung.

(H) Neutron Detection

Fracture of the intricately-shaped tube due of mechanical shock caused by firing of the θ-pinch and Cusp Banks has been a serious problem. This has prevented us from going to high voltages. (We are in the process of switching to a ceramic tube). We estimate that we are 5 kv below the threshold of neutron production[5].

IV. INTERPRETATION OF DATA

Unfortunately, we have no knowledge of the plasma temperature at the present time. Nor do we have any direct information differentiating the plasma density in the cusp from the plasma elsewhere.*

Furthermore, studies of the plasma impurities by means of spectroscopic streak were carried out over a year ago under slightly different circumstances. These experiments showed that proper timing of the events yields negligible impurities. However, we believe that reconfirmation of these experiments are advisable in order to exclude the possibility that impurity plasma is being generated.

Keeping the above in mind, we would like to interpret the data in the following way. From Fig. (6), we observe that a fringe shift of approximately 1.5 fringes prevails with the proper combination of preheater plus θ-pinch Bank plus Cusp Bank for an e-folding time of 30 microseconds. This fringe shift is not to be found with any other combination, nor with an improper ratio of voltages between θ-pinch and Cusp Bank.

*This requires Mach-Zehnder interferometry through the cusp equatorial plane-an experiment which we hope to carry out in the near future.

There are three possibilities for the disposition of plasma in the tube at the time when only crowbarred cusp fields are present. (a) Plasma is confined between the two outside θ-pinch mirrors; (b) Plasma is contained in the cusp only; (c) or some combination.

In Case a, the density n would be 4×10^{16} per cm^3, Case (b) $n = 3 \times 10^{17}$ per cm^3. The argument against Cases (a) and (c) is that the magnetic fields due to the Cusp Bank in the θ-pinch were not strong enough to contain any plasma when the ratio of Cusp Bank to θ-pinch Bank was too high for injection (e.g. θ-pinch Bank 10 kv and Cusp Bank 7.5 (Fig. 4 j) - no trapping, whereas θ-pinch Bank 10 kv and Cusp Bank 5, we obtain trapping Fig. (4.g)). Furthermore, it is unlikely that, by changing the parameters away from the optimum, the impurity content should change drastically.

We therefore conclude that case (b) is most probable. This corresponds to an $n \gtrsim 10^{17}$ and a τ of 30 μsec.

ACKNOWLEDGMENT

We should like to express our deepest thanks to Dr. Sergio Martellucci of the Laboratorio Gas Ionizzati, Frascati, Italy for his guidance in optical matters and in particular for the construction of the Mach Zehnder.

1 Proceedings of 1965 Symposium on Engineering Problems of Controlled Thermonuclear Research, Livermore, California, CONF-750512, p. 35

2 Proceedings of 1966 Symposium on Engineering Problems of Controlled Thermonuclear Research, Oak Ridge, Tenn. CONF. 661016, p 209, 221, 315.

3 Martellucci, S., and Pence, E., Rev. Sci. Inst., 37, 786, 1966.

4 Chalice Annual Report, SIT 2582-19, 1965-66, Chap. 2

5 Mather, J. W., Nuclear Fusion, 1, 233, 1961.

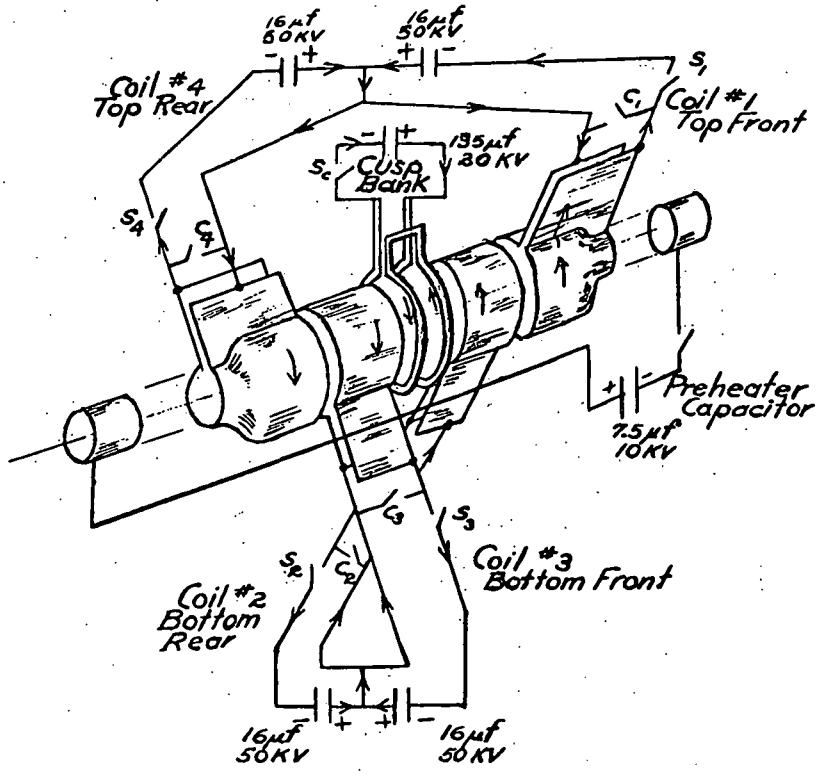

Figure 1. Schematic diagram of Project Chalice.

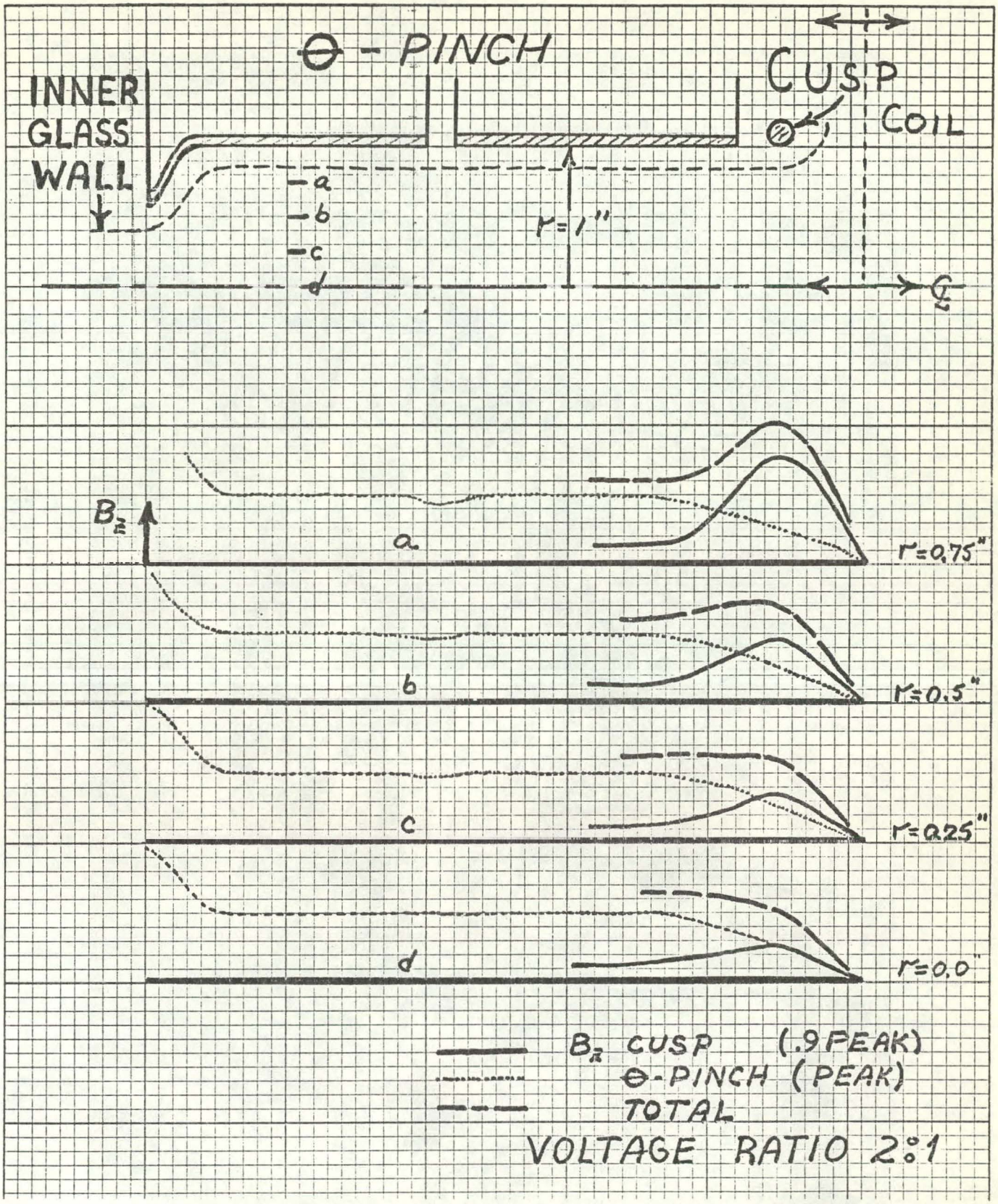

Figure 2. Dynamic mirror and magnetic fields. The fields due to the θ pinch and cusp banks are shown at an intermediate stage where the mirror has vanished at r = 0.25R. If the plasma cylinder had imploded to this diameter it would now be able to enter the cusp. The fields at the cusp line escape, are however, twice as high as they are at the injection point and so the plasma is trapped.

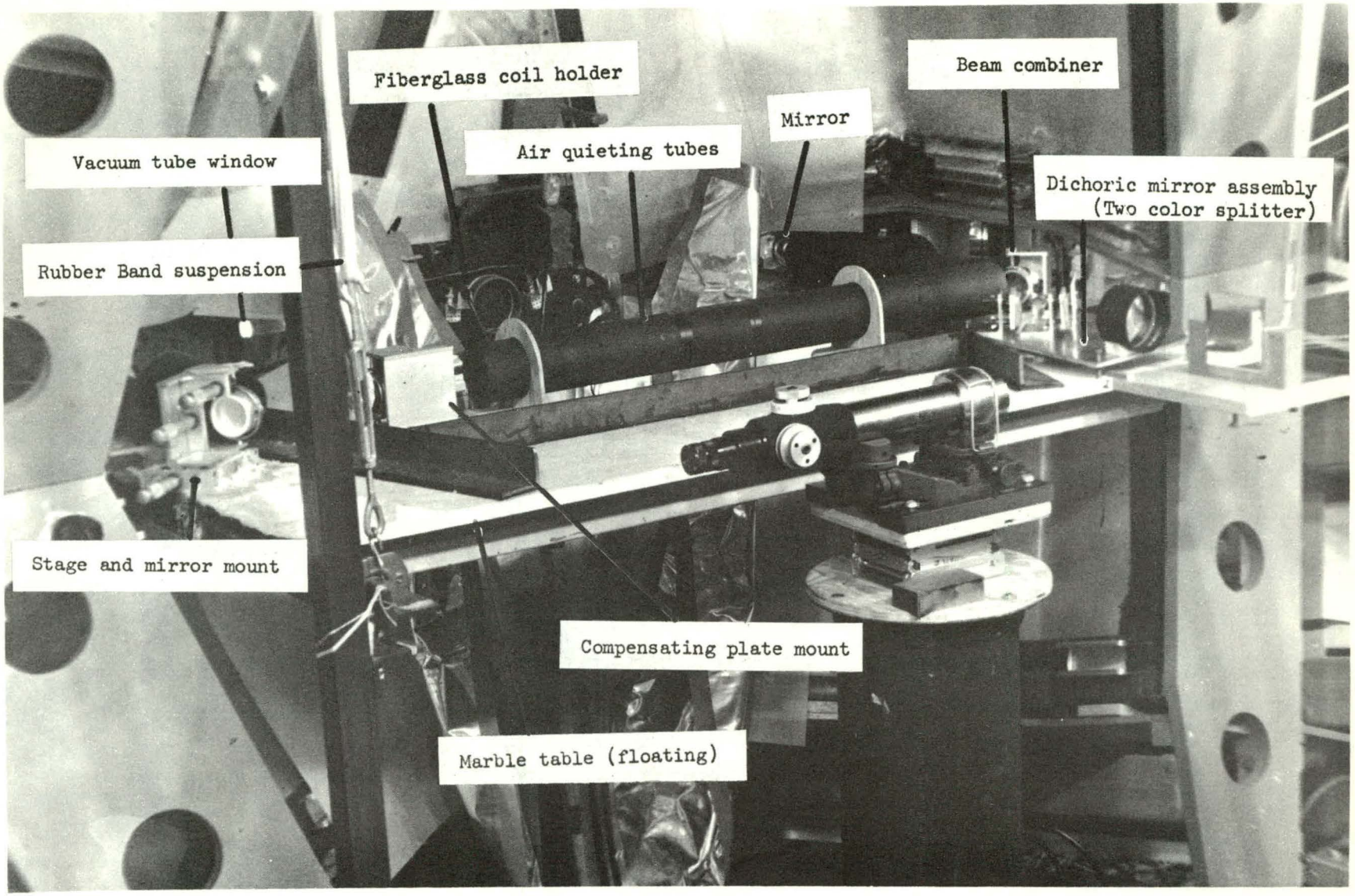

Figure 3. The Mach Zehnder interferometer.

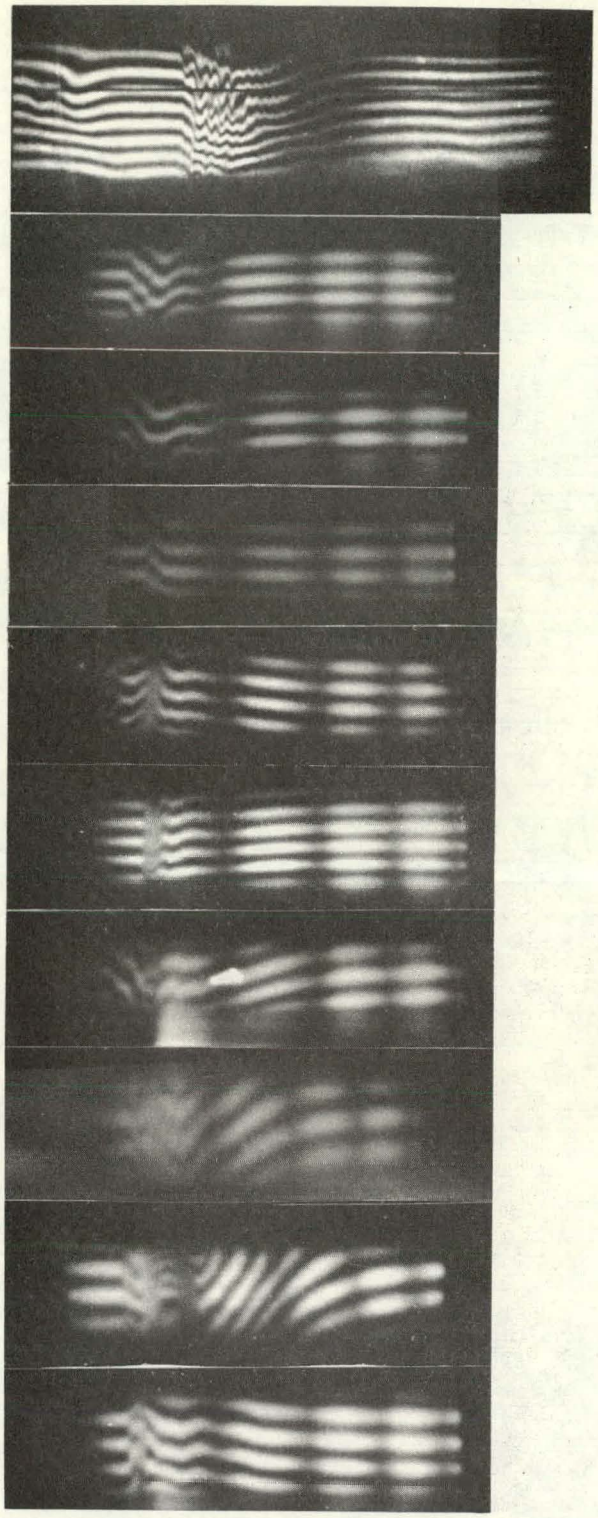

	PREHEATER	θ-PINCH	CUSP
a	5 kv	10 kv	0 kv
b	5	0	0
c	5	0	5
d	0	5	0
e	5	10	0
f	0	10	5
g	5	10	5
h	5	15	7.5
i	5	15	7.5
j	5	10	7.5

Figure 4. Interferograms. Figure 4a is a 10-μsec streak (diameter in the vertical direction) while Figs. 4b to 4j are 90-μsec streaks. The vertical bands are modulations of the light source which serve as time marks (20 usec apart in Figs. 4b through 4j). Fringe shifts in some of the interferograms are not traceable momentarily. The proper fringe number is ascertained with a control shot and an isodensitometer using as a reference the beginning and end of the photograph where there are no shifts. Simultaneous records were made in two colors (only one shown) as a further control.

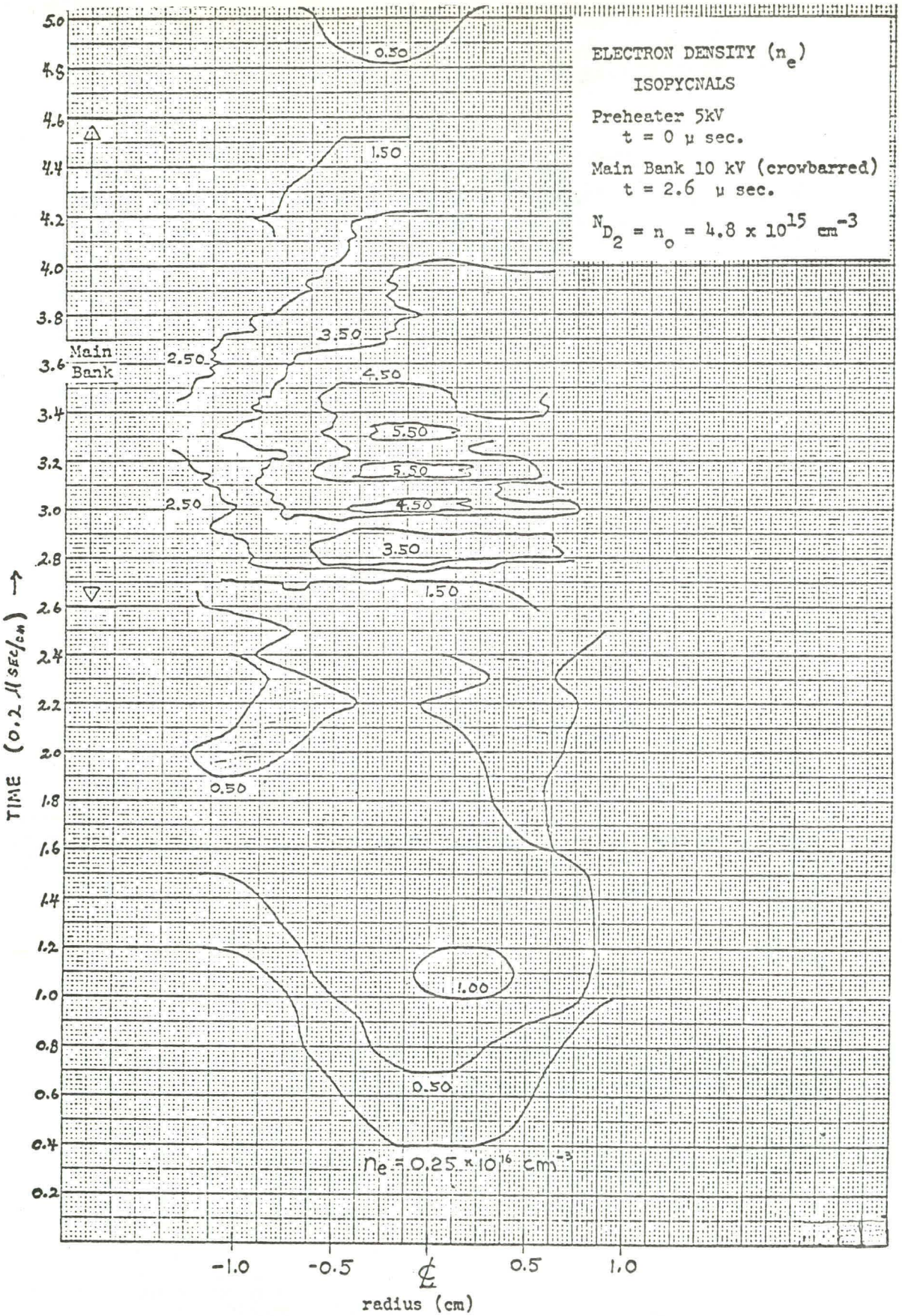

Figure 5. Electron density isopycnals. The fringes shown in Fig. 4a are transferred to electron density as a function of time and space.

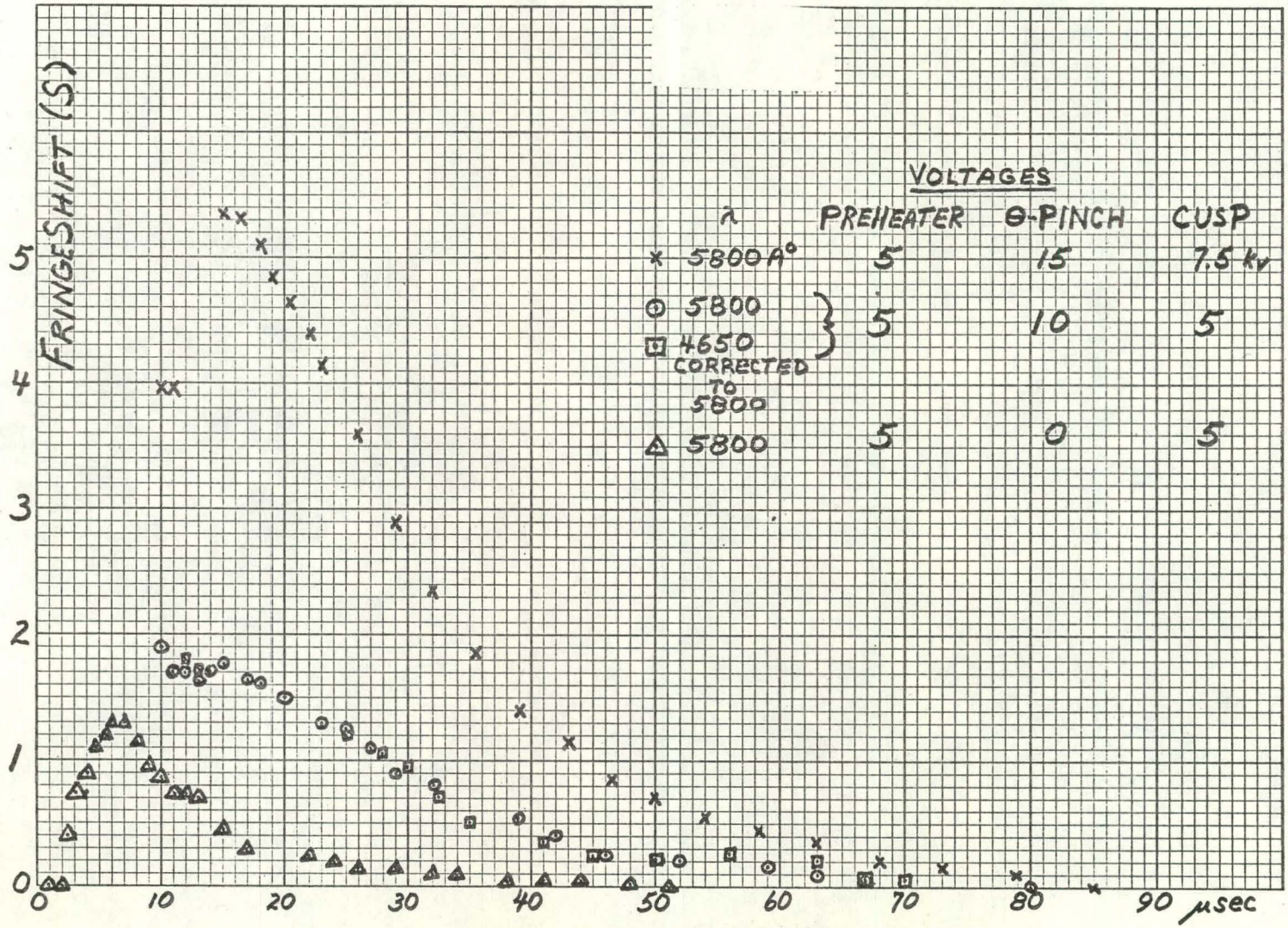

Figure 6. Fringe shift plots. The events shown in Figs. 4c, 4g, and 4i are compared.

END STABILIZATION EFFECT IN THE SLOW THETA PINCH

by

Shigeo Hamada, Tetsu Miyamoto, Haruyuki Ohnishi
and Masatomo Sato
Department of Physics and Atomic Energy Research Institute,
College of Science and Engineering, Nihon Universtty, Tokyo

ABSTRACT

Existence of a stabilization effect due to the plasma near and outsides mirror points is shown by experiments dispacing a driving magnetic field or excluding the outer plasma by glass plates. The effect is not the so-called line tying effect. Effects of an inclined glass plate and afunnel shaped glass cone were examined. The former pushes the plasma column towards the side of the obtuse angle between its surface and lines of force, and the latter stabilizes the plasma. Theoretical results are briefly described in stability of an unsteady plasma flow along lines of force and in a motion of unsteady plasma string. The results are consistently compared with the experimental results.

INTRODUCTION

A plasma in an axially symmetric mirror field has been frequently found to be stable or less unstable than theoretical predictions. Several stabilizing effects, e.g. viscous damping[1] and finite Larmor radius effect[2], have been proposed. These are concerning with an equilibrium plasma contained between both the mirror points. Little attention has been paid to plasmas outsides the mirrors. In case of a fluid like plasma, the equilibrium state required by stability theories, however, does not exist and a considerable amount of the plasma flows out the mirrors. A main purpose of this work is to show that the exteror plasma in the slow theta pinch plays an important role in stabilization of the plasma.

EXPERIMENTAL ARRANGEMENT

Device and Plasma

A multi-turn coil which was 370mm in length and 140mm in inner diameter was used in connection to a 32μF-25kV capacitor bank through an air gap. Two configurations of magnetic field, which were available with the same coil were used. One had a mirror ratio 1.4 a half period 60μs and the maximum field 15kG. and the other had no mirror, a half period 75μs . andthe maximum field 15kG . Discharges were carried out without preheating in a volume of Helium gas within a range of initial pressure 50 – 200mT. Peak temperature and density of the plasma were estimated within a range of 10 -30eV and about or below 10^{16} particles/cm^3, respectively.

Arrangements

The coil was made movable in relation to the axis of a discharge chamber which was 100mm in inner diameter, 1500mm in length and made of pyrex glass. An artificial field asymmetry, therefore, could be introduced by displacement of the coil axis.In order to investigate effects of exclusion of the

outer plasmas on drift and stability, vertical glass plates, an inclined glass plate or a funnel shaped glass cone were put on various positions in the discharge chamber. Schematic arrangements of a series of experiments are shown in fig. 1 . Observations were made by means of a high speed framing camera, radially and axially.

EXPERIMENTAL RESULTS

Case (a) in fig. 1

Both the cases of mirror and straight fields were examined but any essential difference was not observed. Initial contractions of the plasmas occurred at the third half cycle, but were incomplete so that the intensities of light were considerably weak and the plasmas were very unstable. At the fourth half cycle, a slowly growing flute like instability appeared. At the fifth and subsequent half cycles, the instability disappeared and the shapes of the cross sections of the plasma column were kept circular during each half cycle.

Case (b) in fig. 1

The coil axis was parallelly displaced from the chamber axis by 10 mm.. Photographs in fig. 2. were taken at the fifth half cycle in the case of mirror and show the following typical behaviors. The plasma initially contracts to a neighbourhood of the chamber axis, and then, drifts towards and beyond the coil axis and returns again past it, with a slight deformation and a rotation. The path of the drift motion seem to be spiral, frequently. Time variation of column position is shown in fig. 3 . The drift velocity increases with the number of the half cycle and is greater in the case of straight field than in the case of mirror. The direction of the drift show that the plasma is stabilized particularly against the m= 1 mode of perterbation.

Case (c) in fig. 1

Observations were made in cases of L = -40mm, 0mm and 80mm, where L was the distance of each of the glass plates measured outwardly from the nearest mirror point. Photographs taken at the sixth half cycle are shown in fig. 4. In the case of L = 80 mm, the plasma column still drifts towards the coil axis. In the case of L = 0mm, the cross section of the plasma column is violently deformed and its drift motion is not clearly seen. In the case of L = -40mm, it can be seen, in spite of violent deformation, that the plasma drifts towards the chamber wall in the opposite side of the coil axis. This inversion of direction of drift was confirmed also by side-on photographs, and showed that the excluded outer plasmas played an important role in stability. Possibility of the so-called line tying effect is excluded in this experiment because that effect should stabilize the plasma, also in the case of L = -40mm.

Case (d) in fig. 1

In order to examine an influence of the glass plates to the motion of the plasma column, axial and side-on observations were made in this arrangement. The glass plate was placed at a mirror point so that its surface made an angle 70° with the coil axis. The plasma column was pushed towards the side of the obtuse angle as expected,[3] with a velocity 7 x 10 cm/sec. The directions of drift in the case (c) were always towards the opposite side of the obtuse angle, and therefore, the inversion of driction of drift was due to the very exclusion of the outer plasmas.

Case (e) in fig. 1

A funnel shaped glass cone was placed near a mirror point. Photographs taken at the sixth half cycle are shown in fig. 5a and ,for comparison, photographs taken with an arrangement in which the glass cone was replaced by a vertical glass plate are shown in fig. 5b. The photographs in fig. 5a show that the plasma is considerably stable and does not drift, in contrast to the photographs in fig. 5b.

THEORETICAL RESULTS

Here, we will describe our theoretical results obtained in a limiting case of low β.

Method

The fluid velocity $\vec{v}$ is decomposed into $\vec{v}_{11} + \vec{v}_{\perp} = \vec{v}_{11} + B \times \nabla\psi/B^2$ where $\vec{v}$ is the component of v parallel to the line of force, $\vec{v}_{\perp}$ the component of $\vec{v}$ perpendicular to the line of force, $\vec{B}$ the magnetic field and ψ the electric potential. Behaviors of ψ corresponds to the interchange motion of the plasma.
B. B. Kadomtsev deduced equations to ψ, with use of which we are able to make an analysis of our problems.[5]

Stability of Unsteady Flow along Lines of Force

Assuming an axial symmetry and sharpness of the plasma boundary, designating the displacement of the boundary to the m-mode of perterbation by bm, and making use of a near axis approximation obtained the following equation to bm(t).

$$\ddot{b}_m - \frac{S}{V}\dot{b} + m\frac{P^*}{V}b = 0 \qquad (1)$$

V, S, P are defined as follows

$$V = \int \frac{\rho}{B^3}\, d\lambda, \quad S = \int \frac{2\rho v_{11}}{B^3}\, d\lambda$$
$$P^* = \int \frac{2p+\rho v_{11}^2}{B^3 Rr}\, d\lambda \qquad (2)$$

where ρ is the plasma density, p the plasma pressure, R the curvature radius of the line of force taking minus sign in case of convex curvature, r the distance from the line of force to the fied axis and $-\lambda$ the magnetic potential. In the equation (1), V, S, P^* should take values calculated with use of unperterbed ρ, p, v_{11} at the boundary. When we put $v_{11} = 0$, the equation (1) yields a Rosenbluth stability condition $P^* > 0$.[4] In case of $v_{11} \neq 0$, damping or reactive term $\frac{S}{V}\dot{b}$ which is a Corioli force due to change of direction of field line moving with the plasma appears. Furthermore, a centrifugal force $\rho v_{11}^2/R$ plays an important role, particularly, in outer part where p is smaller than ρv_{11}^2.

Motion of a Plasma String

The following equation has been derived.

$$\ddot{\vec{r}} - \frac{S}{V}\dot{\vec{r}} + \frac{P}{V}\vec{r} = 0 \qquad (3)$$

where $\vec{r}$ is the position vector of the string in the center plane perpendicular to the field axis.

A Quasi Steady Model

The plasma flow and sign and time dependance of V, S, P^* have been calculated with use of a quasi steady model. The plasma is concluded to subject to a damping force proportional to v_1 and an attractive force proportional to the distance from the field axis. This is consistent with the experimental results.

REFERENCES

1) H.A.B.Bodin et al : Nuclear Fusion 1 139 (1961).

2) M.N.Rosenbluth et.al.: Nuclear Fusion Suppl. part 1 143 (1962).

3) S.A.Colgate and S.Yoshikawa: Phys.Fluid 7 1877 (1964).

4) M.N.Rosenbluth and C.L.Longmire : Annals phys. 1 120 (1957).

5) B.B.Kadomtsev : Plasma physics and the problem of controlled thermonuclear reaction. Vol. 4 17 (1959).

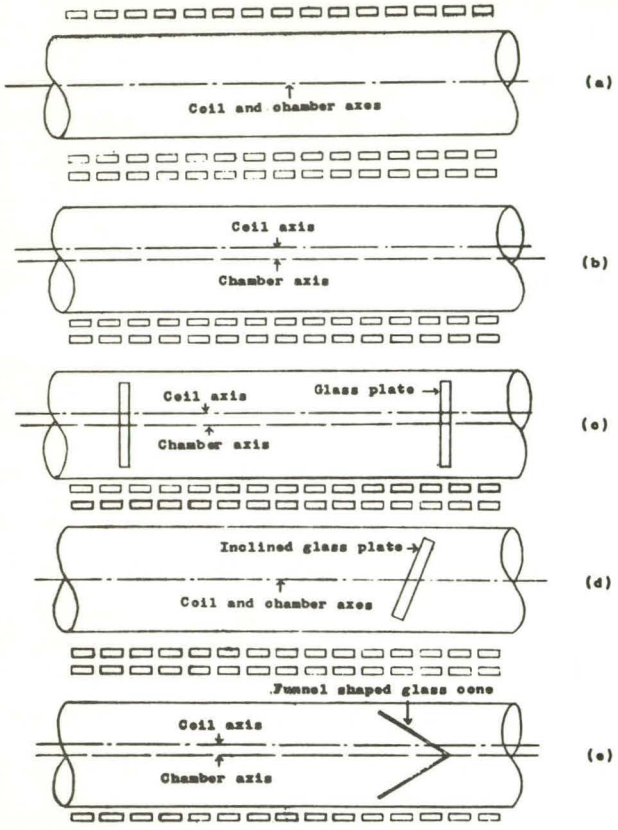

Fig. 1. The arrangement of the coil, the chamber and insulators in series of experiments (a) - (e).

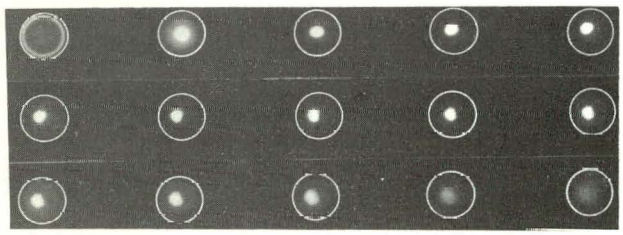

Fig. 2. Axial photographs at initial pressure 50mT and for the fifth half cycle, when the coil axis was displaced from the chamber axis by 10mm.

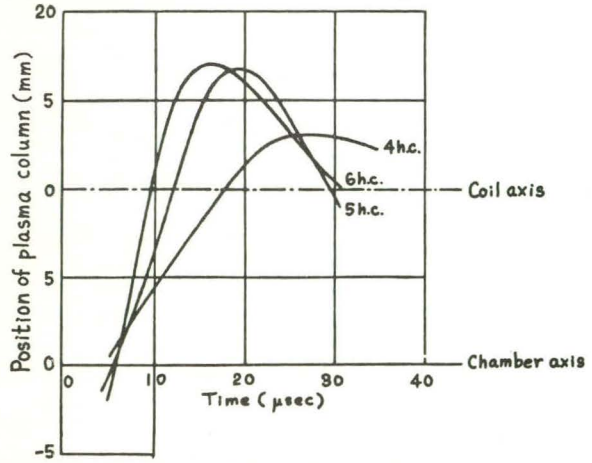

Fig. 3. Time variation of the column positions averaged axially.

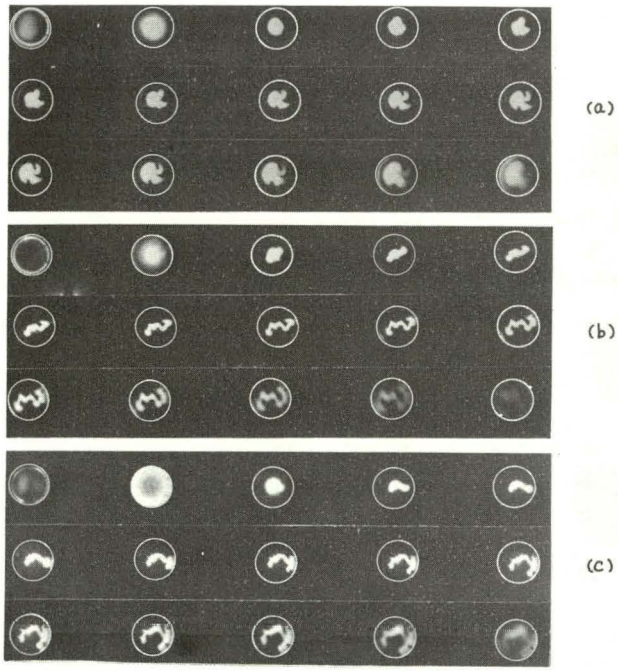

Fig. 4. Typical photographs in the case (c). Initial pressure 100mT and the fifth half cycle. Position of glass plate: (a) L = 80mm (b) L = 0mm and (c) L = -40mm.

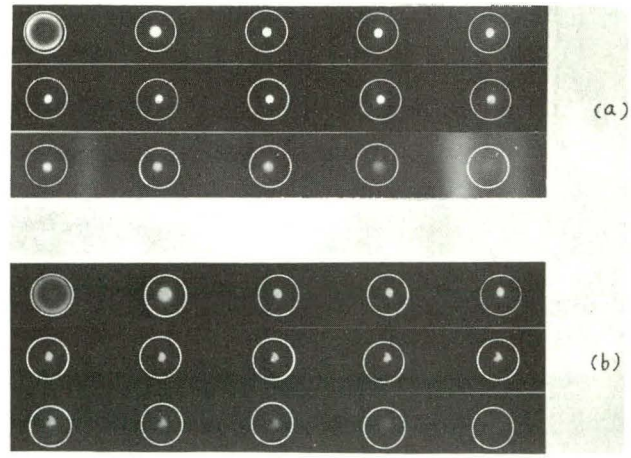

Fig. 5. (a) The funnel shaped glass cone was displaced from the coil axis by 10mm. Initial pressure 100mT and the six half cycle. (b) A vertical glass plate instead of the funnel shaped glass cone was placed at the same position.

THETA PINCH WITHOUT THE INTERACTION BETWEEN PLASMA AND NEUTRALS AT THE ENDS

by

S. Kawasaki and T. Uchida
Institute of Plasma Physics
Nagoya University
Nagoya, Japan

ABSTRACT

A theta pinch system where there was no interaction between the plasma and the neutrals remaining at the ends of the coil, was realized in success, using the high speed gas injection system set in the middle of the coil. The typical character of the experiment is that the distribution of the gas is localized in a sufficiently long coil, so that we can get rid of the effect of the neutrals which would remain in the ordinary theta pinch. Helium plasma produced is compressed by a magnetic field with a peak value of 23Kgauss. The single turn coil used here is 80cm long and 10cm in diameter. The plasma produced in the coil is about 60cm long and seems relatively stable except a slight lateral drift to the wall, which might be due to the effect of the gas injector. The results of the preliminary experiments are given.

1. INTRODUCTION

Since 1960 we have been studying a mechanism of shock phenomenon in the collision dominant plasma flow by the interaction with a magnetic barrier in our experimental system called BSG(MACETIE).[1] We have already reported about such a shock phenomenon[2)3)] and now are planning to repeat the same experiment, using higher temperature plasma in view of its greater interest for the nuclear fusion.

The fast theta pinch system which has been constructed as a plasma source in the experiment has such a particular character as the gas distribution should be localized only within a certain region in the discharge coil, in the initial stage of the gas discharge. The restriction gives us many difficulties in the design and the arrangement of the system but brings the greater advantage in the study of theta pinch so that we can treat the distributions of magnetic fields and of the plasma as two relatively independent factors. With the system, we would be able to research the phenomenon concerning with the "end loss" in the theta pinch by more direct methods, and its clarification is also necessary for understanding of our whole experiments. We shall report here the construction of the theta pinch system and the results of the preliminary experiments.

2. THEORETICAL BACKGROUND

The problem of the "end loss" in the theta pinch has been discussed by many authors.[4)5)] Wesson analysed the hydromagnetic equations of the one dimensional transient flow and Bodin et al. found the qualitative consistence between Wesson's theory and their results about the end loss in their long theta pinch system. Many important simplifications, however, were made in their analysis according to the model which they adopted. There is a possibility that the physical mechanisms which had not yet been taken account of, might take important role. For example recently Mosse[6)] treated this problem with another method.

One of the most principal objects in our experiments is to understand the features of the plasma expanding into the weaker magnetic field from the strong one[1)] in the transient state, which is related with the above problem closely. This has also been analyzed theoretically by the theoretical nembers associated with BSG experiments.[7)] So we have wished to obtain the experimental results which we could compare with the theory.

With our experimental system, the end loss of the confined plasma could be measured by the more direct method such as the probe, optical, μ-wave or other technique, not by the indirect method in which the loss rate was estimated only through the containment time of the plasma.

3. EXPERIMENTAL DESIGN

1. Coil and Discharge System

We used the single turn coil 80cm long and 10cm in dia. which has relatively large aspect ratio and no mirrors. This coil is divided into 16 sections and there are slits 5mm width between the sections. The electrical parameters of the coil and the discharge system are listed in Table I.

Table I

Electrical Characteristics of Discharge System

Voltage	20 kV
Capacity	210μF(7μF x 30)
No. of Trigger Generators	2
No. of Main Spark Gaps	30
Bank Inductance	10nH (Includes 7nH inductance of cables and spark gaps)
Coil Inductance	12nH
Total Inductance	25nH
Half Period	6.5μs
Peak Current	1.5MA
Peak Magnetic Field	23kG
Peak Electric Field	150V/cm (at the wall of the chamber)

A relatively wide space in the middle of coil is prepared for a fast acting gas valve. The decrease of the magnetic field in the center of the coil on the middle plane owing to the wide gap is about 20%. The discharges were induced by the discharge of 210μF, 20kV condenser bank through the coil. The period of the discharge was 13.2 μsec and the peak magnetic field in the first half cycle is 23Kgauss. The peak voltage in the azimuthal direction at the wall of the discharge chamber takes the relatively low value of 150 Volts/cm. In order to minimize the bank inductance, we used 30 parallel circuits separately switched by the spark gap mounted to each condenser, which were designed to have such a character that they could be operated easily simultaneously. Total and coil inductance were 25nH and 12nH respectively. Fig.1 shows the diagram of the discharge circuit. We have prepared the preionization system and the crowbar facility which consisted of two vacuum graded switches equipped with a titanium washer gun as a trigger circuit. These system, however, were not used in the preliminary experiments.

2. Fast Acting Valve

In order to inject the gas into discharge tube rapidly, the fast acting valve which is drived electro-magnetically is attached to the center of the tube, through the slit of the coil. The cross section of the valve is shown in Fig.2. Using this valve, the Helium gas of 0.5atm.cc can be introduced into the tube in 350μsec. After 800μsec from the beginning of its injection, the gas was distributed almost uniformly in azimuthal direction. The valve can be operated independently of the main discharge circuit. The schematic figure of the whole system is shown in Fig.3.

4. PRELIMINARY EXPERIMENTS

1. General Aspects of Plasma

The preliminary experiments were made using the bank at 15kV with a corresponding peak magnetic field of 18Kgauss and with no preionization, in order to test the possibility of the operation in this type of the theta pinch and to research the existence of the characteristics of the plasma which was particular in this system. The values of helium gas pressure at the beginning of discharges were varied in the range of 50~200mTorr in view of the convenience of the observation. These values, however, were estimated by the measurements with the fast ionization gauge of Marshall type and its correct calibration has not yet done. The distribution of the gas in the discharge chamber was nealy uniform within 5% in the region -30~30cm in z-direction and decreased remarkably outside the region. We didnot use the orifice to make the distribution localize more distinctly, lest it should cause the complicated phenomena.

An example of high speed streak photographs which were taken in the perpendicular direction with the axis of the discharge chamber is shown in

Fig.4. It shows that plasma was produced at the beginning of the second half cycle and that there was no instability until the end of that cycle in any case. The photographs and the double magnetic loop signals reveal that the mean implosion velocities are in the range 6 ~ 8cm/μsec at the first implosion at the initial gas pressures we used.

The framing photograph which was taken also in the perpendicular direction is shown in Fig.5. So far as concerning with our results of the experiments gained until now, the axial motions of the plasma, for example, the axial contractions which have been reported frequently[8] have not been seen. Nor we have been able to find any instability in the axial direction. The framing photograph taken in the axial direction, however, seems that the plasma shows a slight movement in the radial direction after its compression stage (Fig.6). The direction of the drift is fixed in all cases independently of the initial gas pressures and the other parameters, so it might be due to the nonuniformity of the magnetic field which might be caused by the misalignment of the coils or the existence of the fast acting valve close to the coils, although the direction of the drift accorded neither with that of the current feeders nor of the gas inlet.

2. The Diamagnetic Signal of the Plasma

Balanced magnetic loops[9] and internal magnetic search coils were used for studying the general features of plasma. These signals show that at the beginning of the third half cycle the plasma was produced more strongly and suggest the necessity of preionization (See Fig.7). These signals were measured in the range 0 ~ 30cm in the axial direction and no remarkable difference could be seen among them. The results of these measurements show that the plasma trapped the reverse field in the pressure range we used.

From the frequency of the radial oscillation which are seen in these signals we can determine the line mass density to be equivalent to about 80mTorr at the initial pressure of 100mTorr. There is an error in the gas collection effeciency owing to the inaccuracy of the initial gas pressure. The more detailed analysis of these signal will be done after applying the crowbar facility and the preheating system into this scheme.

5. CONCLUSION

We could realize our particuler scheme of the theta pinch which has such a charactar as the distribution of gas was localized within the coil initially and so there might be no interaction between the plasma and the neutral gas remaining in the ends. No serious effects to the plasma has been seen. The plasma was relatively stable and it seems that there is no reason why we cannot expect to gain the high temperature stable plasma in this system, although the characters of the plasma obtained have not yet analysed in detail. We would suggest that our results implied that our plasma revealed the unique characteristics in the movement in the axial direction.

REFERENCES

1) T. Uchida et al., Nuclear Fusion 5 63 (1965)

2) APS Bulletin, Miyamoto's lecture in Plasma Physics Division of APS, Boston meeting (1966)

3) to be submitted in Nuclear Fusion

4) T. S. Green, Phys. Fluids 6 864 (1963)

5) H. A. B. Bodin, T. S. Green, A. A. Newton, G. B. F. Niblett and J. A. Reynolds, Culham Conference CN21/34 (1965)

6) R. L. Morse, Phys. Fluids 9 2536 (1966)

7) to be submitted in Proc. Phys. Soc. Japan

8) H. B. B. Bodin et al., Nuclear Fusion Suppl. Part 2 511 (1962)

9) T. S. Green, Nuclear Fusion 2 1, 2, 92 (1962)

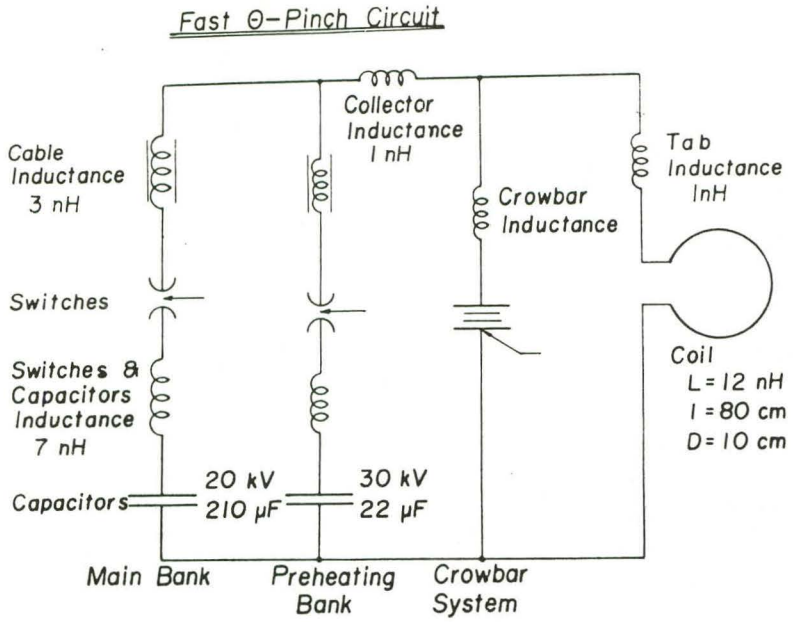

Fig. 1. Diagram of discharge circuit.

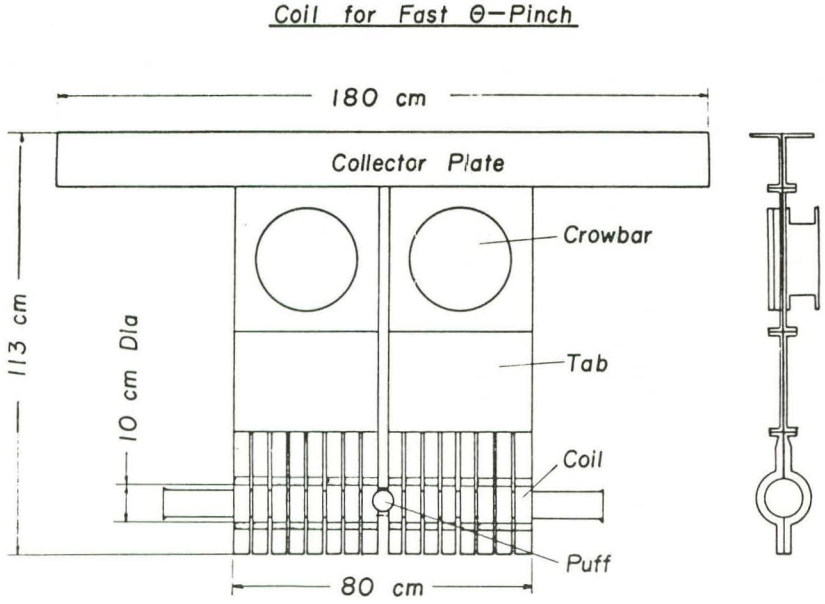

Fig. 3. Schematic figure of whole system.

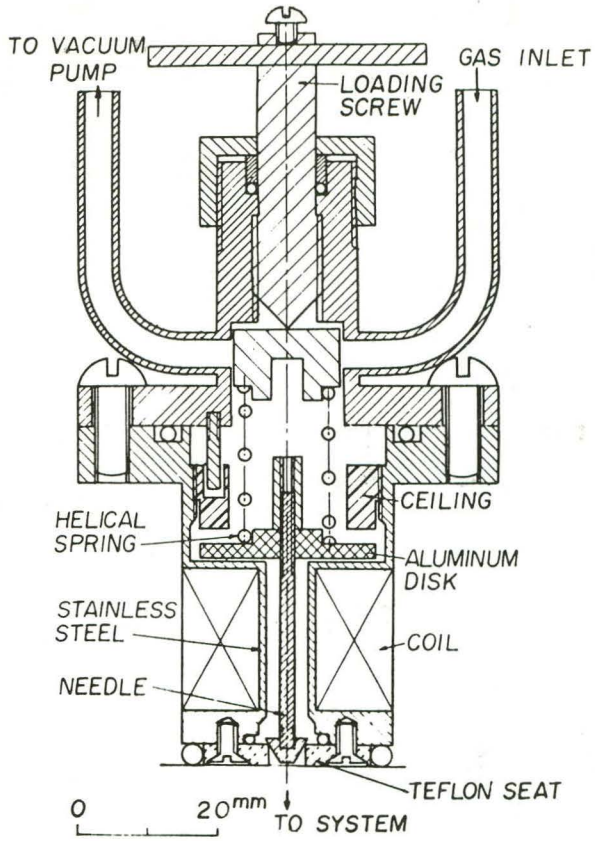

Fig. 2. Cross section of fast-acting valve.

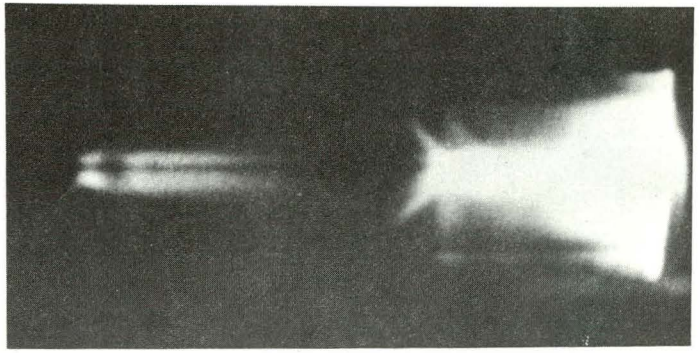

Fig. 4. Streak photograph taken in the direction perpendicular to the axis of the discharge coil.

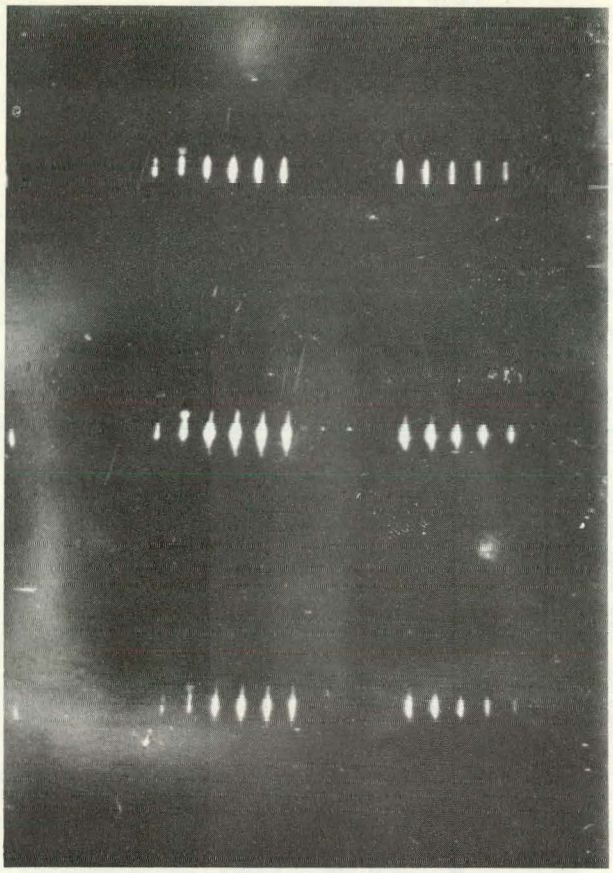

Fig. 5. Framing photographs taken in the direction perpendicular to the axis of the discharge coil at 8 μs, 10 μs and 12 μs after the triggering of starting switch, respectively.

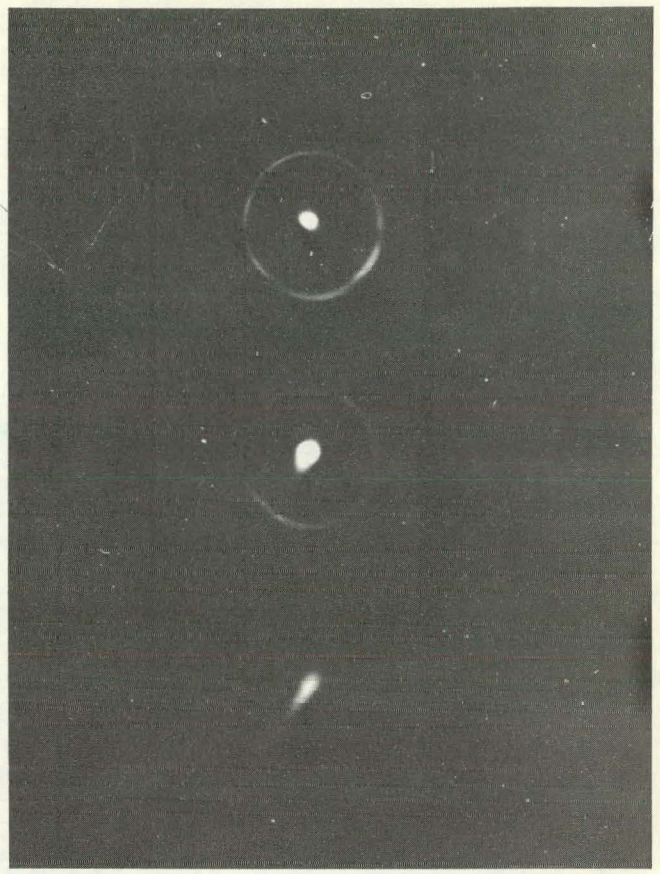

Fig. 6. Framing photographs taken in the axial direction at 8.2 μs, 10.2 μs and 12.2 μs after the triggering of starting switch, respectively.

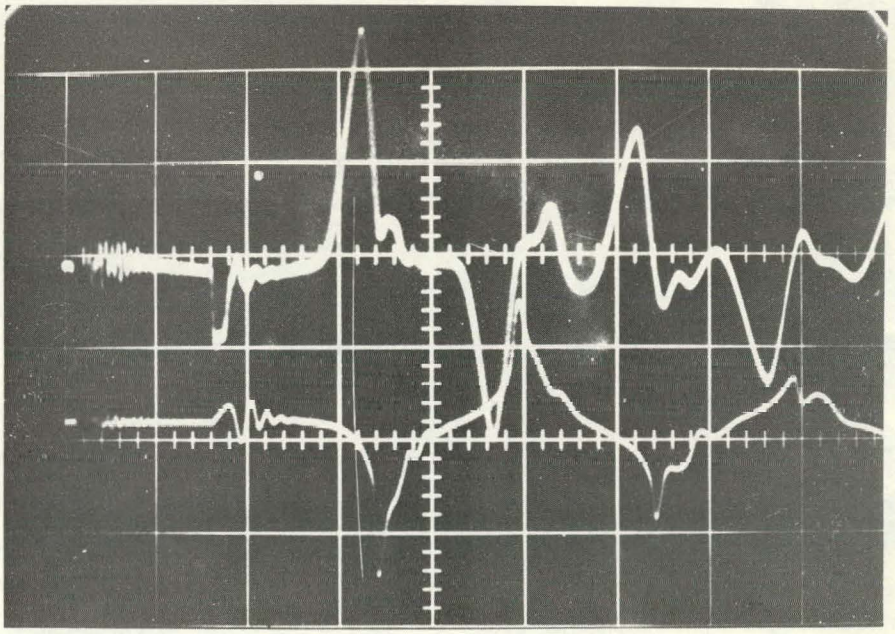

Fig. 7. Signals of balanced magnetic loops (upper one, 0.2 V/div.) and internal magnetic search coil (lower one, 1 V/div.). Time sweep: 5 μsec/div.

STABILITY OF THE THETA-PINCH

by

John Wesson
United Kingdom Atomic Energy Authority
Culham Laboratory
Abingdon, Berkshire.

ABSTRACT

In a toroidal theta-pinch it is inevitable that regions having favourable stability properties alternate along its length with regions having unfavourable stability properties. Owing to the complexity of such configurations it is useful to consider a linear theta-pinch with similar properties. The simplest case is that of an axisymmetric pinch which is periodic along its length and which has no axial current. The purpose of this paper is to summarise the known hydromagnetic stability properties of this configuration.

1. Introduction

As a result of the unavoidable end losses from a straight theta-pinch, estimates of the length of a conceivable thermonuclear power reactor are of the order of hundreds of metres (see appendix). It is possible to remove this loss and to reduce the length by forming a toroidal pinch. The conditions for such equilibria have been discussed by Meyer and Schmidt[1] and Wobig[2]. In such a system the plasma surface has a corrugated form and therefore stabilising and destabilising regions alternate. This configuration is rather complicated theoretically and it is useful to consider a linear analogue. This is provided by a straight axisymmetric pinch in which the pinch radius varies periodically along its lenth thus introducing regions of favourable and unfavourable curvature. The purpose of this paper is to summarise the known hydromagnetic stability properties of this configuration[2,3,4,5].

The stability of the theta-pinch has been studied by setting up a simple model and then determining the change in potential energy δW arising from a displacement of the plasma. After describing the model and the method of the calculation, the general expression for δW will be given. This will include the variation with β and the effect of the coil. The most important results derivable from this expression will then be described by starting from the simplest case $\beta = 1$ without the effect of a coil and subsequently considering the effect of reducing β below unity and of the proximity of the coil. Finally a method of dynamically stabilising all the unstable modes will be described.

2. The Theta-pinch Model

We assume that the theta-pinch has a sharp boundary, the plasma pressure being constant inside the plasma radius $R(z)$ where z is the axial co-ordinate (see Fig.1). The plasma is taken to be compressible and perfectly conducting and has a trapped magnetic field $\underline{B}_i$ and an external field $\underline{B}$. The problem of the stability of a general axisymmetric system of this kind is very difficult. It is made tractable however by the assumption that the wavelength λ of R is sufficiently large that $\epsilon \sim \frac{2\pi R}{\lambda} \ll 1$.

The equilibrium is defined by specifying the radius R as a function of z. The other equilibrium quantities are then determined by expanding the appropriate equations in ϵ. In leading order the external and internal axial components of the magnetic field, B and B_i, are both functions of z. (The subscripts z are avoided for convenience as we shall, in this paper, only be concerned with the z components) B_i is determined from R by the flux conservation equation

$$\pi R^2(z) . B_i(z) = \Phi$$

where Φ is the trapped flux. The external field B is related to B_i, and hence to R, by the pressure

balance relation

$$\frac{1}{8\pi} B^2(z) = p + \frac{1}{8\pi} B_i{}^2(z).$$

We shall define β by

$$\beta(z) = 8\pi p/B^2(z).$$

The external magnetic field $\underline{B}(r,z)$ is completely determined by specifying $R(z)$ and the pressure p. This field may then be regarded as being produced either by a coil lying on a stream surface of the field, or by a cylindrical coil with the appropriate current distribution.

3. Application of the Energy Principle

A cylindrical theta-pinch is stable to all wavelengths $2\pi/k$ of the normal mode e^{ikz} but the $k = 0$ mode is only marginally stable. We might expect therefore that long wavelength modes will be the most dangerous when R is made periodic. This is, in fact, found to be the case and we can therefore make use of a long wavelength expansion in determining the perturbations about the equilibrium. It is then possible to solve for the radial dependence of the perturbations which minimise change in potential energy δW. After integrating over r and θ its final form is [4]

$$\delta W = \frac{1}{8}\int B^2 \beta \xi^2 R\frac{d^2R}{dz^2}\, dz +$$

$$\frac{1}{8m}\int B^2 \left[\frac{d}{dz}(R\xi) - 2(1-\beta)\,\xi \frac{dR}{dz} \right]^2 \frac{1+(R/R_w)^{2m}}{1-(R/R_w)^{2m}}\, dz +$$

$$\frac{1}{8m}\int B^2 (1-\beta)\left[R\frac{d\xi}{dz} - \xi\frac{dR}{dz} \right]^2 dz \qquad (1)$$

where R_w is the coil radius, $\xi(z)$ is the radial displacement of the surface and perturbed quantities are taken to vary as $e^{im\theta}$ (only $m > 0$ being considered). The three integrals arise from the surface, vacuum and plasma respectively. The surface term is a measure of the average curvature of the "magnetic hill" on which the plasma rests and is the only destabilising contribution. The vacuum and plasma terms are always stabilising and result from bending the magnetic field lines. The worst perturbations are found to be incompressible so that, in contrast to similar low β cases, δW has no contribution from the internal energy of the plasma itself.

4. Discussion of Stability

We first consider $\beta = 1$ and neglect the effect of the coil, that is we take $R/R_w \to 0$. Equation (1) then becomes

$$\delta W = \frac{1}{8m}\int B^2 \left[\left(R\frac{d\xi}{dz}\right)^2 - (m-1)\left\{\frac{dR^2}{dz}\,\xi\,\frac{d\xi}{dz} + \left(\frac{dR}{dz}\,\xi\right)^2\right\}\right] dz$$

Two results may now be deduced from this equation. Firstly, for $m = 1$, $\delta W \geq 0$ and the system is marginally stable to this mode since δW may be reduced to zero by taking $\frac{d\xi}{dz} = 0$. Secondly, the trial function ξ = constant makes $\delta W < 0$ for all $m > 1$ so that these modes are unstable.

The physical explanation of these results is as follows. The magnetic field increases away from the plasma in regions where $\frac{d^2R}{dz^2} > 0$ and decreases away from it where $\frac{d^2R}{dz^2} < 0$. The appropriate average over these regions gives a resultant field decreasing away from the plasma. The instability for $m > 1$ arises through the resulting decrease in the potential energy when the plasma surface is displaced. This displacement of the plasma involves some line bending and this is an effect which tends to stabilise the system. The energy required for this bending is greater for the lower m - numbers. This is because the perturbed magnetic potential falls off as r^{-m} and consequently the volume in which the magnetic energy is changed increases with decreasing m. It turns out that for $m = 1$ this effect is just sufficient to stabilise the mode.

The next question to consider is what effect a reduction of β below unity has on stability, this being particularly important in the case of $m = 1$. Taking $\beta \simeq 1$ and putting $\frac{d\xi}{dz} = 0$ in equation (1) gives

$$\delta W = \frac{\xi^2}{8m}\int B^2 \left(\frac{dR}{dz}\right)^2 \left\{ -(m-1) + (m-3)(1-\beta)\right\} dz$$

Thus the $m = 1$ mode becomes unstable if β is reduced below 1.

We now consider the possibility that the reduction in the stability of the $m = 1$ mode arising from β not being equal to 1 may be compensated by a stabilising effect due to the proximity of the coil. This should result in a critical β above which the pinch will be stable to $m = 1$. We shall now determine an upper limit for this β. In order to do this we introduce the small parameter $\Delta = (R/R_w)^2$ which we take to be of order $(1-\beta)$. Expanding

equation (1) in Δ leads, in zero order, to

$$\delta W_o = \pi \int \beta B^2 R^2 \left(\frac{d\xi_o}{dz}\right)^2 dz$$

where subscripts denote the order in Δ. δW_o is minimised to zero by ξ_o = constant so that to first order we have

$$\delta W = \delta W_1 = 2\pi \int \beta B^2 \left(\frac{dR}{dz}\right)^2 \xi_o^2 \left[\left(\frac{R}{R_w}\right)^2 - (1-\beta)\right] dz.$$

Thus the m = 1 mode is stable if $(1-\beta) < (R/R_w)^2$ for all z, that is if

$$\frac{B_i}{B} < \frac{R}{R_w}$$

everywhere. It can also be shown that a necessary condition for stability is

$$\beta > \frac{1}{1 + (R/R_w)^{2m}}$$

for some z. For small R/R_w this reduces to the requirement that $(B_i/B) < (R/R_w)^m$ somewhere. This condition for stability is very stringent even for the most stable mode, m = 1. For $R_w = 5R$ the stability requirement for this mode is $\beta > 0.96$.

In order to check that these conclusions are not a result of the assumption of a sharp boundary, a necessary stability condition for a diffuse radial pressure profile was derived with qualitatively similar results[4].

An estimate of the growth rate $i\omega$ of the m = 1 mode, for the profile $R = R_o(1 + \delta \cos kz)$, has been made[4] and the result is

$$\omega^2 = -(k\delta)^2 \frac{B^2}{4\pi\rho} \frac{\beta(3-2\beta)}{1-\beta+F} \left\{1 + (1-2\beta)F\right\}$$

where the density ρ was assumed to be constant across the pinch, and

$$F = \frac{1 + (R_o/R_w)^2}{1 - (R_o/R_w)^2}$$

5. Dynamic Stabilisation

The results presented so far show that a periodic, static theta-pinch is hydromagnetically very unstable, the m = 1 mode being very difficult to stabilise and m > 1 almost impossible. This leads to a consideration of the possibility of stable non-static systems. In particular a method of dynamically stabilising the present model of a $\beta = 1$ theta pinch has been found which stabilises all the unstable modes.

The method of stabilisation may be described as follows. Consider a linear pinch with a periodic surface profile and corresponding periodic external magnetic field produced by a coil having the appropriate current distribution. As we have seen, in the absence of wall stabilisation this system is unstable for m > 1 and marginally stable for m = 1. Now consider a system in which this magnetic field configuration and surface profile are made to propagate along the pinch with a velocity V by suitably alternating part of the current in the coil. It is found that if $|V| > |V_A|$ then all $m \geq 1$ are stable, where $V_A^2 = B^2/4\pi\rho$, B being the mean value of the magnetic field at the surface of the plasma and ρ the plasma density.

More precisely the plasma profile is taken to have the form $R = R_o(1 + \delta f(z - Vt))$ where f is a periodic function of wavelength λ and $1 \gg \delta \gg 2\pi R/\lambda$. The plasma is taken to be incompressible for simplicity but we note that in the static case the incompressible modes were the most unstable. As in the static problem it is found that the most dangerous modes are of long wavelength, all modes except those for which $kR \ll \delta$ being stable where k is an axial wave-number characterising the mode. The criterion which must be satisfied for these modes to be stable and therefore for the system to be stable is

$$\frac{1}{4}\left[\left(4\frac{V^2}{V_A^2} - \frac{1}{8}\right)^2 + \frac{63}{64}\right] + \left[\frac{(m-\frac{1}{2})V_A^2 + (m-\frac{7}{2})V^2}{(V^2 - V_A^2)V_A^2}\right]^2 > 0$$

and this is clearly satisfied when $V^2 > V_A^2$.

The implication of this result for the toroidal theta-pinch is that it leads to the conjecture that the equilibrium profile, which is necessarily periodic and unstable, may be stabilised if the profile is made to propagate round the torus with sufficiently high velocity.

It should be noted that the m = 0 mode has not been considered and although this mode is stable without dynamic stabilisation the possibility of

introducing instability cannot be ruled out.

It is also possible that although the present model for the plasma allows the wave to propagate without accelerating the plasma this may not be the case for an actual plasma. An interesting possibility is that a standing wave might provide similar stabilising effects without being vulnerable to this objection.

6. Comment

The present state of our knowledge of the hydromagnetic stability of the theta-pinch is fairly encouraging. Although the theory is so far only exploratory it does seem that it might be possible to remove the instability of the static pinch by dynamic stabilisation. It is also possible that finite Larmor radius stabilisation may prove to be an important effect. However so little is known about the non-hydromagnetic instabilities in a theta-pinch that there is no reason to be confident about its overall stability properties. A theoretical understanding of this problem would require an extensive programme of research and this is hardly begun.

Acknowledgment

Most of the work reviewed in this paper was carried out in collaboration with Dr. F.A. Haas. The author is grateful to Dr. Haas for several helpful discussions.

References

1. F. Meyer & H.U. Schmidt, Z.Naturforsch 13a p.1005, 1958.
2. H. Wobig, Institute for Plasmaphysik (Garching) Report IPP6/53, 1966.
3. F.A. Haas & J.A. Wesson, Phys.of Fluids 9, p.2472, 1966.
4. F.A. Haas & J.A. Wesson, Phys.of Fluids, to be published, 1967, and Culham Laboratory Report CLM-P136, 1967.
5. F.A. Haas & J.A. Wesson, To be published.
6. J.B. Taylor, Culham Laboratory Report CLM-R58, 1966.

Appendix

We assume that the pinch has a radius R and a length L and that along this length the kinetic pressure 2nkT (n is the ion density and $T_i = T_e$) is balanced by the magnetic pressure $B^2/8\pi$. The pinch is terminated by mirror fields of magnitude B_m.

The effective loss area of each end of the pinch is[6]

$$\frac{3\pi c R}{eB_m}\left(\frac{\pi M k T}{2}\right)^{\frac{1}{2}}$$

when M is the ion mass. This area is approximately $2\pi R \times$ the Larmor radius of the ions in the mirror field. The total number of ions is $N = \pi R^2 L n$ and the initial loss rate is given by

$$\frac{dN}{dt} = 2 \times \tfrac{1}{4} n \left(\frac{8 k T}{\pi M}\right)^{\frac{1}{2}} \times \frac{3\pi c R}{eB_m}\left(\frac{\pi M k T}{2}\right)^{\frac{1}{2}}.$$

Thus the containment time

$$\tau = \frac{N}{dN/dt} = \frac{e}{3ck}\frac{RLB_m}{T}.$$

If a criterion of the form $n\tau = \mathcal{L}$ is satisfied then

$$L = \frac{3ck}{e}\frac{\mathcal{L}T}{RB_m n}$$

and using the pressure balance relation we obtain

$$L = \frac{48\pi ck^2}{e}\frac{\mathcal{L}T^2}{RB_m B^2}$$

$$= 2 \times 10^{-10}\frac{\mathcal{L}T^2}{RB_m B^2}$$

If $\mathcal{L} = 10^{15}$ sec.cm^{-3}, $T = 10^8$ °K, R = 10 cm. and $B_m B^2 = 10^{16}$ gauss^3 then L = 200 metres.

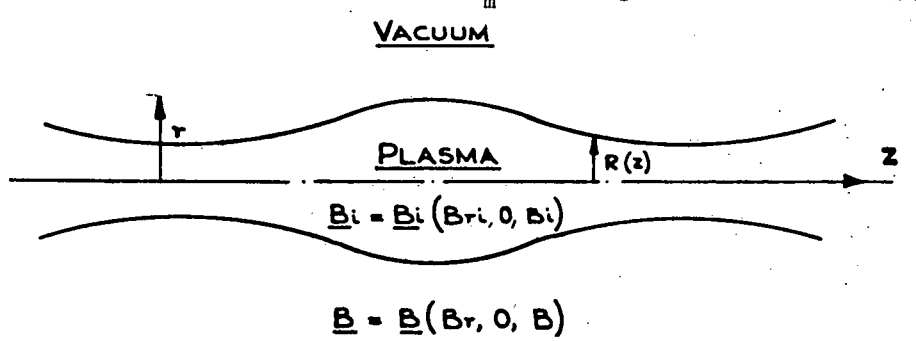

Fig. 1. Diagram of periodic theta-pinch

HYDROMAGNETIC EQUILIBRIUM OF A THIN-SKIN, FINITE BETA TOROIDAL PLASMA COLUMN

by

J. L. Johnson†, R. L. Morse, W. B. Riesenfeld
Los Alamos Scientific Laboratory, University of California
Los Alamos, New Mexico

†Princeton University Plasma Physics Laboratory,
on loan from Westinghouse Research Laboratories

ABSTRACT

We discuss an analytic approach to the problem of describing the toroidal equilibrium of a finite beta plasma column in the hydromagnetic approximation. The thickness of the sheath region separating the plasma from the external magnetic field is assumed to be negligibly small compared to all other dimensions (the "thin-skin" approximation). The deviations of this interface from toroidal cylindrical shape are treated by perturbation theory, a procedure which is consistent with the usual series expansion in powers of reciprocal aspect ratio. The formalism provides analytic expressions for the auxiliary currents necessary to produce equilibrium in toroidal theta pinch systems such as Scyllac.

INTRODUCTION

The analysis of high β systems, in which the plasma currents generate magnetic fields of the same order of magnitude as the externally applied fields, poses special difficulties both with respect to equilibrium and stability aspects of the problem. A major achievement in the analysis of toroidal high β devices was the demonstration, by construction[1] and by calculation,[2] that an equilibrium unity β plasma with a sharp boundary separating the plasma from the field exists. Although this type of configuration can be successfully investigated by numerical techniques,[3] engineering design is greatly facilitated by an analytic formulation.

We restrict the discussion to systems in which all magnetic field lines close upon themselves after traversing the torus azimuthally. The hydromagnetic equilibrium problem consists of finding solutions of the system of equations

$$\vec{\nabla} p = \vec{j} \times \vec{B} \tag{1}$$

$$4\pi \vec{j} = \text{curl } \vec{B}, \tag{2}$$

with closed toroidal constant pressure surfaces, where p is the plasma pressure, $\vec{j}$ the electric current density, and $\vec{B}$ the magnetic field. In equilibrium, surfaces of constant pressure must coincide with surfaces of constant $\oint \frac{d\ell}{B}$

$$p = p\left(\oint \frac{d\ell}{B}\right) \tag{3}$$

in order that there be no net charge build-up on any flux tube.[4] Integration of Eqs. (1) and (2) in the thin-skin limit leads to the jump condition

$$B_{out}^2 - B_{in}^2 = 8\pi p, \tag{4}$$

where B_{out} and B_{in} are the field magnitudes just outside and inside of the interface. For reasons of tractability p is assumed to be constant within the

plasma.

In toroidal systems the azimuthal field is inversely proportional to the radial distance from the toroidal major axis, so that the constant $\oint d\ell/B$ surfaces would be cylinders concentric with the major axis and thus would not close upon themselves within the machine. In low β stellarators the problem is overcome by applying rotational transforms.[5,6] In high β systems with closed field lines additional magnetic fields must be applied to ripple the field lines so that inner lines with higher field values are lengthened and constant $\oint d\ell/B$ surfaces are changed into toroids.

We adopt a conventional toroidal coordinate system with metric of form

$$d\ell^2 = dr^2 + r^2 d\theta^2 + (1 - \frac{r}{R}\cos\theta)^2 dz^2 . \qquad (5)$$

The gradient operator is then given by

$$\vec{\nabla} = \hat{e}_r \frac{\partial}{\partial r} + \hat{e}_\theta \frac{1}{r}\frac{\partial}{\partial \theta} + \hat{e}_z \frac{1}{1 - \frac{r}{R}\cos\theta}\frac{\partial}{\partial z} \qquad (6)$$

where the $\hat{e}_i$ are the appropriate unit vectors. We assume that the aspect ratio is large and retain terms only to first order in a/R, where a is the unperturbed minor radius of the plasma column. The curvature term in the azimuthal field is of form

$$B_z(a,\theta,z) = B^{(o)}(1 + \frac{a\cos\theta}{R} + \ldots) . \qquad (7)$$

To compensate for this term in the magnetic pressure B^2, we superpose a ripple field of general form $\vec{B}^{(\delta)}(r,\theta)\sin k_s z$, where δ labels the magnitude of the field line excursions and $k_s = s/R$, s integral. The z-independent term in B^2 immediately imposes the ordering

$$\left[\frac{B^{(\delta)}}{B^{(o)}}\right]^2 \sim \frac{a}{R}, \qquad (8)$$

implying that a/R is a second order term with respect to the ripple field amplitudes or with respect to the field line excursion parameters. The latter are taken to be the formal expansion parameters of our theory.

TOROIDAL EQUILIBRIUM FOR A PLASMA COLUMN OF ARBITRARY β

The plasma is assumed to have a sharp boundary surface $r(\theta,z) = a + \delta a(\theta,z)$, where we take δa to be zero at z = 0. Inside this surface the magnetic field is of form

$$\vec{B}_{in} = B_{in}^{(o)} \vec{\nabla}\Big[z(1 + E^{(2)}) + \sum_{\ell,s} \frac{1}{k_s} A_{\ell s}^{(1)} I_\ell(k_s r)\cos\ell\theta \cos k_s z + \sum_{\ell,s} \frac{1}{2k_s} A_{\ell s}^{(2)} I_\ell(2k_s r)\cos\ell\theta \sin 2k_s z + \ldots \Big] \qquad (9)$$

where the superscripts on the amplitudes refer to the perturbation order. We have explicitly retained a second-order correction $E^{(2)}$ to the unmodulated part of the azimuthal field component. For the magnetic field outside of the plasma we write

$$\vec{B}_{out} = B_{out}^{(o)} \vec{\nabla}\Big\{ z + \sum_{\ell s} \frac{1}{k_s}\Big[C_{\ell s}^{(1)} I_\ell(k_s r) + D_{\ell s}^{(1)} K_\ell(k_s r)\Big]\cos\ell\theta \cos k_s z + \sum_{\ell s} \frac{1}{2k_s} D_{\ell s}^{(2)} K_\ell(2k_s r)\cos\ell\theta \sin 2k_s z + \ldots \Big\} . \qquad (10)$$

I_ℓ and K_ℓ are the modified Bessel functions of order ℓ, and the notation is standard. Special choices have been made for the phases of the various trigonometric functions appearing in Eqs. (9) and (10). It turns out that the general superposition of fields with differing k_s wavenumbers is superfluous; solutions of Eqs. (3) and (4) can be found for a given k, with the second-order coefficients $A_\ell^{(2)}$ and $D_\ell^{(2)}$ properly chosen to compensate for the z-dependences.

It is convenient to define the plasma beta as

$$\beta \equiv \frac{8\pi p}{B_{out}^{(o)2}} , \qquad (11)$$

and to introduce the notation

$$I^{(\ell)} \equiv \frac{I_\ell(ka)}{ka\, I_\ell'(ka)} . \qquad (12)$$

By integrating the equations for the field lines just inside and outside of the plasma boundary we can relate the field amplitudes to the shape of the boundary. We find that

$$\delta a(\theta,z) = a \sum_{\ell=0}^{\infty} \delta_\ell \cos\ell\theta \sin kz, \tag{13}$$

where

$$\delta_\ell = \frac{1}{ka} A_\ell^{(1)} I_\ell'(ka) = \frac{1}{ka}\left[C_\ell^{(1)} I_\ell'(ka) + D_\ell^{(1)} K_\ell'(ka)\right]. \tag{14}$$

Here the prime stands for differentiation with respect to the argument kr of the Bessel functions. The pressure balance condition (4) then becomes, up to first order in the ripple parameters δ_ℓ, the following:

$$B_{in}^{(o)2} = (1 - \beta) B_{out}^{(o)2} \tag{15}$$

$$C_\ell^{(1)}(ka) + D_\ell^{(1)} K_\ell(ka) = (1 - \beta)(ka)^2 \delta_\ell I^{(\ell)}. \tag{16}$$

Eqs. (14) and (16) furnish a complete specification of the first-order fields in terms of δ_ℓ:

$$A_\ell^{(1)} = \frac{ka\delta_\ell}{I_\ell'(ka)}$$

$$C_\ell^{(1)} = (ka)^2 \delta_\ell K_\ell(ka)\left[1 - (1-\beta)\frac{I_\ell(ka)K_\ell'(ka)}{I_\ell'(ka)K_\ell(ka)}\right] \tag{17}$$

$$D_\ell^{(1)} = -\beta (ka)^2 \delta_\ell I_\ell(ka).$$

The component of $\vec{B}$ normal to the boundary, given by $B_r - B_z ka \sum_\ell \delta_\ell \cos\ell\theta \cos kz$, vanishes on each side of the boundary because of Eq. (14) and thus is continuous.

To construct the equations which determine the δ_ℓ's we consider the pressure balance condition to second order:

$$\frac{2(1 - \beta)E^{(2)}}{\beta} = \frac{2a\cos\theta}{R} - \frac{1}{4}(ka)^2 \sum_{\ell=0}^{\infty}\sum_{m=0}^{\infty} \delta_\ell\delta_m \Big\{[1 + (1 - \beta)(\ell m + k^2a^2) I^{(\ell)}I^{(m)}] \cos(\ell - m)\theta + [1 - (1 - \beta)(\ell m - k^2a^2) I^{(\ell)}I^{(m)}]\cos(\ell + m)\theta\Big\}. \tag{18}$$

The second-order field $E^{(2)}$ is chosen to satisfy the θ-independent part of Eq. (18). The δ_ℓ's can then be adjusted to cancel the $\cos\theta$, $\cos2\theta$, ... terms. For simplicity we assume $ka < 1$ and use the small argument expansion for the Bessel functions. There results the following infinite set of coupled equations for the δ_ℓ's:

$$\begin{aligned}
&2(3 - 2\beta)\delta_o\delta_1 + (2 - \beta)\sum_{\ell=1}^{\infty} \delta_\ell\delta_{\ell+1} = \frac{4}{k^2aR} \\
&\frac{1}{2}\beta\,\delta_1^2 + 2(2 - \beta)\delta_o\delta_2 + (2 - \beta)\sum_{\ell=1}^{\infty} \delta_\ell\delta_{\ell+2} = 0. \\
&\frac{2}{3}(5 - 2\beta)\,\delta_o\delta_3 + \beta\,\delta_1\delta_2 + (2 - \beta)\sum_{\ell=1}^{\infty} \delta_\ell\delta_{\ell+3} \\
&\cdots \\
&2\left[1 + \frac{2}{n}(1 - \beta)\right]\delta_o\delta_n \\
&+ \frac{1}{2}\beta\sum_{\ell=1}^{n-1} \delta_\ell\delta_{n-\ell} + (2 - \beta)\sum_{\ell=1}^{\infty} \delta_\ell\delta_{\ell+n} = 0.
\end{aligned} \tag{19}$$

Furthermore, it can be proved by direct calculation that the conditions (19), which remove the θ-dependence from the right-hand-side of Eq. (18), are precisely the conditions to make $\oint d\ell/B$ constant over the perturbed boundary to second order in δ_ℓ. Thus the field distribution satisfies the equilibrium conditions (3) and (4).

DETERMINATION OF THE FIELDS

The set of equations (19) can be solved systematically for the δ_ℓ's by introducing a small ordering parameter ϵ and assuming that

$$\frac{\delta_\ell}{\delta_o} \sim \epsilon^\ell. \tag{20}$$

We solve to a given order in ϵ by neglecting higher order terms in a given equation and by truncating the system of equations at the line in which each of the terms exceeds the given order in ϵ. The system of equations then becomes finite, with the number of unknown quantities δ_ℓ/δ_o equal to the number of

equations. For example, to third order we obtain the solution

$$\frac{\delta_1}{\delta_o} = \frac{2}{(3-2\beta)k^2 aR\delta_o^2}\left[1 + \frac{\beta}{2(3-2\beta)^3(k^2 aR\delta_o^2)^2}\right]$$

$$\frac{\delta_2}{\delta_o} = -\frac{\beta}{(2-\beta)(3-2\beta)^2(k^2 aR\delta_o^2)^2} \qquad (21)$$

$$\frac{\delta_3}{\delta_1} = \frac{3\beta^2}{(2-\beta)(5-2\beta)(3-2\beta)^3(k^2 aR\delta_o^2)^3} \quad .$$

The ordering parameter

$$\epsilon = \frac{2}{(3-2\beta)k^2 aR\delta_o^2}$$

can indeed be made small for Scyllac design values. But the ordering procedure works even when $\epsilon \sim 1$. By writing $\delta_\ell/\delta_o = c_\ell \epsilon^\ell$ one can derive recursion relations for the c_ℓ's from which one can deduce that these are rapidly decreasing functions of ℓ, even in the unity β case. In the latter case, for instance, one obtains $c_1 = 1$, $c_2 = -\frac{1}{4}$, $c_3 = \frac{1}{8}$, $c_4 = -\frac{5}{64}$, $c_5 = \frac{7}{128}$, ... Thus the convergence of the series for a given δ_ℓ/δ_o is rapid for all reasonable ϵ. The presence of a δ_o term is essential for this convergence; if one assumes that the dominant cancellation of the $2a\cos\theta/R$ arises from an interference between $\ell = 1$ and $\ell = 2$ fields, for example, then no convergence is obtained: one can show that there exist δ_ℓ's of arbitrarily large ℓ values having the same magnitude as δ_2.

THE CURRENT SOURCES

From the regularity properties of the Bessel functions it follows that in general the $C_\ell^{(1)}$ terms represent fields created by currents in external conductors while the $D_\ell^{(1)}$ terms are generated by the plasma surface currents, at least in so far as the equilibrium is a stable one. To make an analytical estimate of the size of the external currents needed, we assume that the latter are surface currents flowing on a shell of radius $\rho > a$. The field components external to the plasma which the external current must generate, have form

$$\vec{B} = B^{(o)}\vec{\nabla}\left[\frac{C_\ell}{k} I_\ell(kr)\cos\ell\theta\cos kz\right] .$$

By writing a similar expression for the field outside of the current shell, matching boundary conditions at $r = \rho$, and eliminating C_ℓ by means of Eq. (17), we obtain the linear current density flowing in the shell:

$$\vec{J} = \frac{B^{(o)}\delta_\ell (ka)^2 K_\ell(ka)}{4\pi k\rho K_\ell'(k\rho)}\left(\hat{e}_\theta \cos\ell\theta \sin kz\right.$$

$$\left. - \hat{e}_z \frac{\ell}{k\rho}\sin\ell\theta\cos kz\right). \qquad (22)$$

For simplicity we have set $\beta = 1$ in the above expression. These currents can be quite large, especially if a/ρ is small. By using the small argument limits of the Bessel functions we may conclude that these multipole currents do not form a divergent sequence, provided that

$$\frac{\delta_\ell}{\delta_o} \lesssim \left(\frac{a}{\rho}\right)^\ell , \qquad (23)$$

a requirement that can be satisfied by imposing the restriction

$$\rho \lesssim (ka)^2 R\delta_o^2 . \qquad (24)$$

DISCUSSION

Our discussion of toroidal equilibrium treats a highly idealized plasma model. At best it can only furnish general analytical guidelines for the design of high β toroidal systems. At worst it may founder against the rock of plasma instabilities. While such systems can be made stable against general magnetohydrodynamic interchanges, localized ballooning modes are known to develop in the unfavorable bumpy regions and growth rates for the higher modes have been estimated.[7] The question of stability with respect to a rigid outward ($m = 1$) displacement is open, and the subject of microinstabilities for a more realistic plasma model is virtually untouched.

An uncomfortable feature of our results is that an $\ell = 0$ field, which is energetically costly to set up, is necessary. (The field and plasma must be compressed rather than merely distorted). This necessity is a consequence of our mathematical perturbation formalism and the need to achieve

convergence, and does not necessarily imply than an $\ell = 1, 2, \ldots$ system is physically impossible.

The assumption of a sharp plasma boundary is a drastic one, yet seems to be necessary for an analytical tractability; attempts to generalize the Meyer-Schmidt equilibrium to a diffuse boundary have proved futile.

One of the authors, J. L. J., wishes to thank the Los Alamos Sherwood group for the hospitality extended to him during July-August of 1967.

This work was partially supported by the U. S. Atomic Energy Commission, Contract No. AT(30-1)-1238 with Princeton University.

REFERENCES

1. F. Meyer and H. U. Schmidt, Zeit. f. Naturforschung 13a, 1005 (1958).
2. D. Pfirsch and H. Wobig, Plasma Physics and Controlled Nuclear Fusion Research, IAEA Vienna (1965) p. 757.
3. T. Oliphant, Los Alamos Scientific Laboratory Report, to be issued.
4. B. B. Kadomtsev, Plasma Physics and the Problem of Controlled Thermonuclear Reactions, ed. M. A. Leontovich, Pergamon Press, New York (1960), Vol. IV, p. 17.
5. J. M. Greene and J. L. Johnson, Advances in Theoretical Physics, ed. K. A. Brueckner, Academic Press, New York (1965), Vol. 1, p. 195.
6. V. D. Shafranov, Reviews of Plasma Physics, ed. M. A. Leontovich, transl. Consultants Bureau, New York (1966) Vol. 2, p. 103.
7. R. L. Morse, Los Alamos Scientific Laboratory Report LA-3442-MS (1966).

LONGITUDINAL FINITE AMPLITUDE WAVES IN A COLLISIONAL PLASMA

by

H. Kever

Institut für Plasmaphysik der Kernforschungsanlage Jülich des
Landes Nordrhein-Westfalen
ASSOCIATION EURATOM-KFA

ABSTRACT

Steady nonlinear waves of finite amplitude which propagate along a constant magnetic field in an initially cold and uniform plasma are considered under conditions where collisions, either binary or collective, between ions and electrons cannot be neglected. In the literature, these waves have been studied for the case of a cold and collisionless plasma by Montgomery[1] and by Saffman[2]. In the present analysis, the assumption of negligible plasma pressure has been retained, the effect of collisions is taken into account through a collisional term which is proportional to the drift velocity between the ions and electrons. The structure of these waves has been investigated under the assumption that the collisional term is small, and an asymptotic solution has been obtained of first order in the ratio of the effective collision frequency and the cyclotron frequency of the electrons in the unperturbed magnetic field. From this solution the scaling lengths within the wave, the angle of rotation of the magnetic field and the amount of heating are inferred.

1. For the longitudinal waves considered in the following, the direction of propagation is parallel to an uniform magnetic field, and the components of the magnetic field perpendicular to the direction of propagation are disturbances connected with the passage of the wave. In ref. 2 it has been shown that for a cold and collisionfree plasma there exist a constant profile solution for the magnetic field which is similar in shape to the transverse solitary waves. The amplitude of the magnetic field perpendicular to the direction of propagation turns out to be, for waves of moderate strength, of about $\frac{1}{2}\,(m_+/m_-)^{1/2}$ times the strength of the uniform magnetic field.

The question arises about the structure of such waves in the presence of dissipation. Another problem is the heating through such waves when, due to dissipative mechanism within the plasma, e.g. collisions between particles, part of the energy of the transverse magnetic field is being transformed into thermal energy. To study the influence of dissipation, a frictional term in the equation of motion has been chosen which is based on the assumption of binary collisions between

ions and electrons. This may serve presumably as well as a model for a plasma when the friction between ions and electrons is caused by collective interactions. Only the weak collisional case is treated, since it is assumed that the collision frequency is small. The pressure of the plasma is regarded to be much smaller than the pressure of the magnetic field, therefore the kinetic pressure has been neglected in the equations of motion.

2. The wave field is considered in the wave system, which is moving with constant velocity U along the initial and uniform magnetic field $\underline{B}_o = (B_o,o,o)$. We write $\underline{B}_w = (o,B_y,B_z)$ for the magnetic part of the wave. The equations of motions for the ions are written in the form

$$m_+ \frac{du_+}{dt} = e(E+v_+B_z-w_+B_y) - \nu_c m_{red}(u_+-u_-)$$

$$(1)\quad m_+ \frac{dv_+}{dt} = e(w_+B_o-u_+B_y) - \nu_c m_{red}(v_+-v_-)$$

$$m_+ \frac{dw_+}{dt} = e(u_+B_y-v_+B_o) - \nu_c m_{red}(w_+-w_-)$$

where ν_c is the collision frequency and m_{red} the reduced mass of ions and electrons. A similar set of equations holds for the electrons, with e,m_+ replaced by $-e,m_-$. Instead of using the Poisson-equation to determine the electrostatic field E, the quasineutrality assumption for the particle densities n_+ and n_- is adopted. From the system of Maxwell's equations only those relating the magnetic field with the current densities need to be retained

$$(2)\quad \frac{dB_y}{dx} = \mu_o en(w_+-w_-),\quad \frac{dB_z}{dx} = -\mu_o en(v_+-v_-).$$

As in the case of no collisions, the constants of motion from the equation of continuity and eqs. (1,2) become

$$(3)\quad F = nu,\quad P = m_t uF + B_y^2/2\mu_o + B_z^2/2\mu_o$$

$$P_y = (m_+v_++m_-v_-)F - \frac{B_oB_y}{\mu_o}$$

$$P_z = (m_+w_++m_-w_-)F - \frac{B_oB_z}{\mu_o}$$

where $m_t = m_++m_-$ is the total mass.

According to the boundary conditions ahead of the wave at $x = -\infty$, the values of these constants are

$$(4)\quad F = n_oU_o,\quad P = m_tUF,\quad P_y = P_z = o.$$

With t as independent variable defined through $dt = u^{-1}dx$, the system of equations can be reduced (ref. 1) to two coupled equations for the components B_y,B_z of the magnetic field $\underline{B}_w$:

$$(5)\quad \frac{d^2B_y}{dt^2} = \frac{\mu_oe^2}{m_+m_-}\{-B_y\frac{B^2}{2\mu_o} + (P-\frac{B_o^2}{2\mu_o})B_y - \frac{B_o}{e\mu_o}(m_+-m_-)\frac{dB_z}{dt}\} - \nu_c\frac{dB_y}{dt}$$

$$(6)\quad \frac{d^2B_z}{dt^2} = \frac{\mu_oe^2}{m_+m_-}\{-B_z\frac{B^2}{2\mu_o} + (P-\frac{B_o^2}{2\mu_o})B_z + \frac{B_o}{e\mu_o}(m_+-m_-)\frac{dB_y}{dt}\} - \nu_c\frac{dB_z}{dt}.$$

Upon introducing cylindrical coordinates for the magnetic field, i.e. $B_y = B\cos\phi$, $B_z = B\sin\phi$, the eqs. (5,6) can be written in a more convenient form. In addition, it is convenient to use the following notations

$$\Omega = \frac{eB_o}{(m_+m_-)^{1/2}},\quad \alpha = \frac{m_+-m_-}{2(m_+m_-)^{1/2}},$$

and normalized variables

$$s = \Omega t,\quad \nu = \nu_c/\Omega,\quad b_y = B_y/B_o,\quad b_z = B_z/B_o$$

$\dot{\phi}, \dot{b}$ represent derivatives with respect to s. The eqs. (5,6) are transformed to

$$(7) \qquad \frac{d}{ds}\left(b^2(\dot{\phi}-\alpha)\right) = -\nu b^2\dot{\phi}$$

$$(8) \quad \frac{d}{ds}\left\{\frac{1}{2}(\dot{b}^2+b^2\dot{\phi}^2) + V(b)\right\} = -\nu(\dot{b}^2+b^2\dot{\phi}^2)$$

where $V(b) = -\frac{1}{2}\left(\frac{\mu_o P}{B_o^2}-1\right)b^2 + \frac{1}{8}b^4$

is the potential of the motion of the magnetic field.

3. In order to obtain the structure of the wave under the influence of a small frictional term, the solutions to the eqs. (7,8) shall be determined up to first order in the normalized collision frequency ν. To accomplish this, the solutions to zero order are required. Therefore, we discuss the solutions of the eqs. (7,8) for $\nu = o$ as far as the results are pertinent to the intended application. Upon dropping the terms proportional to ν, the integration of the eq. (7) yields immediately

$$(9) \qquad b^2(\dot{\phi}-\alpha) = C_1 \ .$$

Since the boundary condition at $s = -\infty$ is $b^2 = o$, the constant C_1 of integration in eq. (9) is zero. This result is independent of the particular value of $\dot{\phi}=\alpha$ (as long as this value remains finite). For a non-trivial solution with $b^2 \neq o$, the value of $\dot{\phi}-\alpha$, as a consequence of $C_1 = o$, must therefore be zero throughout the wave. So, for finite amplitude solutions, there is a rotation of the magnetic field with constant rate $\alpha\Omega$ which persists at $x = -\infty$.

With the value of $\dot{\phi}$ being determined, again using the boundary conditions ahead of the wave, the eq. (9) can be written

$$(10) \qquad \dot{b}^2 + 2V_\alpha(b) = o$$

where the potential $V_\alpha = -\frac{1}{8}(K^2b^2-b^4)$, $K^2 = 4\left(\frac{\mu_o P}{B_o^2} - 1 - \alpha^2\right)$ is the sum of the expression V and the contribution $\alpha^2b^2/2$ from the rotation of the magnetic field. The function V_α is zero at the initial singular point $b = o$ and at the point $b = K$; therefore K is the maximum value of the transverse component of the magnetic field. For a real disturbance, the condition $K^2 > o$ must be satisfied. In terms of the original variables, this requires

$$(11) \qquad \frac{\mu_o P}{B_o^2} > 1+\alpha^2 = \frac{(m_+ + m_-)^2}{4m_+m_-} \ .$$

It is convenient to define the Mach-number of the wave through the hybrid Alfvén speed $\tilde{v}_A$, i.e. $\tilde{M} = U/\tilde{v}_A$, where

$$\tilde{v}_A = \frac{B_o}{(4\mu_o \frac{m_+m_-}{m_+ + m_-} n_o)^{1/2}} \sim \frac{1}{2}\left(\frac{m_+}{m_-}\right)^{1/2} v_A$$

and v_A is the usual Alfvén velocity. Accordingly, the condition for a disturbance of constant profile to propagate along a magnetic field is $\tilde{M} > 1$, and so is formally the same as for a transverse wave. An upper bound on $\tilde{M}$ is given because the velocity of the particles along the magnetic field has everywhere the same direction, since F, as a constant, has everywhere the same sign. Therefore

$$Fu_{min} = P - \frac{B_{max}^2}{2\mu_o} > o,$$

and this leads to $\tilde{M}^2 < 2$.

Equ (10) can be solved through quadrature. If the origin of the coordinate system is chosen to coincide with the maximum of the magnetic field, the solution is

$$(12) \qquad b = K \operatorname{sech}\left(\frac{1}{2}Ks\right),$$

where $K^2 = \frac{(m_+ + m_-)^2}{m_+ m_-} (\hat{M}^2 - 1)$.

The magnetude of the magnetic field vector perpendicular to the direction of propagation has the same bell-shaped profile as that known from the transverse solitary wave. In the next section, the solution of eqs. (7,8) for small but finite ν are considered.

4. First, eq. (7) can be integrated formally and after applying the boundary condition $\dot{\phi} = \alpha$ at $s = -\infty$, is used to obtain asymptotic expansions for $\dot{\phi}$. Upon substituting in the integrand for $\dot{\phi}$, one obtains to first order in ν

$$(13) \qquad \dot{\phi} = \alpha - \alpha \frac{\nu}{b^2} \int_{-\infty}^{s} b^2 ds' .$$

For consistency with the neglections of terms of second order in ν, the magnetic field (12) of zero order in ν must be inserted into eq. (13). The integration can be carried out; the result is

$$(14) \quad \dot{\phi} = \alpha \left\{1 - 2 \frac{\nu K}{b^2} \left[1 - \left(1 - \frac{b^2}{K^2}\right)^{1/2}\right]\right\} .$$

This means that only a small difference between $\dot{\phi} = \alpha$ and the actual value of $\dot{\phi}$ has developped at the first relative maximum of the magnetic field, since $\dot{\phi} \sim \alpha (1 - 2 \frac{\nu}{K})$ for $b \sim K$. The eq. (8) gives through integration

$$(15) \quad \dot{b}^2 + b^2 \dot{\phi}^2 + 2V = -2\nu \int_{-\infty}^{s} (\dot{b}^2 + b^2 \dot{\phi}^2) ds' .$$

Upon substituting for $\dot{\phi}$ from eq. (13), the contributions from $\dot{\phi}$ which are of first order in ν cancel on both sides of eq. (15); therefore eq. (15) becomes, up to terms of second order in ν,

$$(16) \quad \dot{b}^2 + 2V_\alpha = -2\nu \int_{-\infty}^{s} \dot{b}^2 ds' .$$

This equation contains only $b(s)$ as dependent variable, so the problem becomes tractable by means of standard methods. Again, for consistency with the omission of terms of order ν^2 and higher ones, the integral in eq. (16) has to be evaluated with the magnetic field in zero order. This yields

$$(17) \quad \dot{b}^2 + 2V_\alpha = \begin{cases} -\frac{\nu}{3} K^3 \left\{1 - (1 - b^2/K^2)^{3/2}\right\}, & \dot{b} > 0 \\ -\frac{\nu}{3} K^3 \left\{1 + (1 - b^2/K^2)^{3/2}\right\}, & \dot{b} < 0 . \end{cases}$$

The expression in the second line on the right hand side is valid in the interval after the magnetic field has attained its first relative maximum. To first order, the values b_1, b_2 where the magnetic field becomes steady, are given by

$$(18) \quad b_1^2 = K^2 \left(1 - \frac{4\nu}{3K}\right), \quad b_2^2 = 4\nu K/3 .$$

The difference in the variable s between these two points where $\dot{b} = 0$, is

$$(19) \qquad s = \int_{b_2}^{b_1} db / (-\dot{b}) .$$

For an estimate of order of magnitude, one takes $\dot{b} = (-2V_\alpha)^{1/2}$, i.e. considers the effect of ν on the distance between the two neighbouring turning points where the magnctic field has a relative maximum or minimum, as determined by the limits of integration. The result is

$$(20) \qquad S = K^{-1} \log (3K/\nu) .$$

For the spacing between the first relative maximum and minimum of the magnetic field, eq. (20) leads to

$$L = \frac{c}{\omega_p (\hat{M}^2 - 1)} \log \frac{\omega_{ce}}{\nu} (\hat{M} - 1)^{1/2} .$$

5. Considering the structure of eq. (16), one finds that the solution b performs a number of oscillations of decreasing amplitude around an average value and ends up in an equilibrium state $\dot{b} = o$ where $V'_\alpha(b) = o$. The value of the magnetic field is found to be $b_1^2 = K^2/2$. When the magnetic field becomes steady, b^2 in eq. (7) for an order of magnitude evaluation can assumed to be constant. It follows

$$\dot{\phi} = \dot{\phi}(s_o)\ e^{-\nu(s-s_o)} \tag{21}$$

so that $\dot{\phi}$ asymptotically tends to zero. If the region of validity of this exponential decrease is extended to $s_o = o$, the angle between the direction of the transverse component of the magnetic field at the first relative maximum and in the final state becomes $\phi = \nu^{-1}\alpha$, which is the angle of rotation during one collision time.

With the value of the transverse component of the magnetic field in the final state being known, the amount of energy dissipated in the wave can be calculated from the equation for energy conservation between states of uniform flow. For the density Q of energy dissipated in the final state, one obtains

$$Q = \frac{1}{16}\,\frac{m_+}{m_-}\,\frac{(M^2-1)^2}{3M^2+1}\,\frac{B_o^2}{2\mu_o} \tag{22}$$

Eq. (22) holds for waves which are not too weak, i.e. when $M-1 >> 2(m_-/m_+)^{1/2}$. When the energy Q is completely converted into thermal energy, the kinetic pressure is an order of magnitude smaller than the pressure of the transverse magnetic field. Despite the smallness of the kinetic pressure, a more refined model would still require the inclusion of finite pressure as well as the consideration of the dependence of the collision frequency on the parameters of the problem.

References

1 D. Montgomery, Phys. Fluids 2,581(1959)
2 P.G. Saffman, J. Fluid Mech. 21,16(1961)

TWO DIMENSIONAL EQUILIBRIUM FOR HIGH BETA MIRROR DEVICES INCLUDING PARTICLE LOSS

by

W. Grossmann, Jr. and J. P. Freidberg

Courant Institute of Mathematical Sciences
New York University
New York, New York

ABSTRACT

Two dimensional equilibrium for high beta mirror devices are found by solving the Vlasov equation and Amperes law self-consistently. Particle loss is taken into account self-consistently by allowing particles to exist only outside of the local loss cone angle. It is found that for a given set of plasma parameters and applied mirror ratio that (1) solutions only exist below some critical value of β, (2) in certain cases the solutions show a non-uniqueness related to the question of stability.

I. INTRODUCTION

In this paper we describe a theoretical approach to the calculation of high β, two-dimensional self-consistent plasma equilibria such as might exist in axisymmetric theta-pinch and magnetic mirror machines. More specifically, we are interested in solutions to the Vlasov equations representing a "long thin" plasma confined by magnetic mirrors. The development of a theta-pinched plasma is described theoretically by a number of mathematical models, all professing varying degrees of success. Essentially, all of these theories depend heavily on numerical codes, and the agreement between theory and experiment is generally of a qualitative nature. In the present work, a mathematical model is postulated using a suitable mathematical definition of a "long thin" plasma. The resulting equilibrium solutions indicate that in high β plasmas a given applied mirror ratio results in enhanced containment due to the effect of significant induced self mirroring fields. Further, the equilibrium solutions predict for a given mirror ratio and a given set of plasma parameters a maximum value of β above which equilibrium solutions do not exist.

II. FORMULATION OF THE PROBLEM

We consider the following physical model for a long thin high β plasma confined by magnetic mirrors. We asume that in equilibrium the plasma is described by a distribution function whose loss cones are empty. Necessary in our analysis is the assumption of axial symmetry. Further we assume the electrons are collision-dominated and the ions collisionless. The electrons serve to neutralize space charge electric fields and the ions are assumed to carry all the plasma current. Finally the externally applied mirror field is assumed generated in such a manner that any variation in the z direction occurs over a distance much larger than the plasma diameter. This small z variation is physically what is meant by a "long thin" plasma. We leave a detailed discussion of the validity of the above assumptions to a later paper.

The mathematical model we choose to study is given by the steady state Vlasov equation and Ampere's law written as:

$$\bar{v} \cdot \nabla f + \frac{e}{m} \bar{v} \times \bar{B} \cdot \nabla_v f = 0 \qquad (1)$$

$$\nabla \times \bar{B} = \mu_o J = e\mu_o \int \bar{v} f \, d\bar{v} \qquad (2)$$

In the above equations the mathematical definition of a long thin plasma is equivalent to setting $(\partial B/\partial z)/(\partial B/\partial r) \sim 0(\epsilon)$ where $\epsilon \ll 1$. Two exact constants of the motion are the particle energy and the canonical angular momentum. We further

postulate an adiabatic invariant in the form of the particle magnetic moment. We choose a modified form of a rigid rotor distribution function, the pure form of which is an exact solution to Eq. (1). Our chosen distribution function is then only an adiabatically correct solution to Eq. (1) and is given for the equilibrium model as

$$f = N_o\left(\frac{m}{2\pi KT}\right)^{3/2} \exp\left(\frac{-(E + \omega P_\theta)}{KT}\right)(1-\frac{\mu^*}{\mu})^P U(1-\frac{\mu^*}{\mu}) \quad (3)$$

where $\mu = m\frac{V_\perp^2}{2B}$, $\mu^* = E/B_{max}$ and $U(1-\frac{\mu^*}{\mu})$ is a step function denoting the absence of particles in a symmetric cone of half angle α^*, α^* being the local velocity space loss cone angle. The function $(1 - \frac{\mu^*}{\mu})^P$ where P is an arbitrary positive number is a function which is necessary to smooth the distribution function near the loss cone angle in order to obtain equilibrium solutions. Introducing the magnetic vector potential $\bar{A}$, polar coordinates, invoking symmetry and the "long thin" definition, Eq. (2) to lowest order in ϵ reduces to

$$\frac{\partial}{\partial r}\frac{1}{r}\frac{\partial}{\partial r} rA_\theta = \mu_o e N_o \omega r S_J. \quad (4)$$

$$\exp\left\{-\frac{2\, e\omega r\, A_\theta + m\omega^2 r^2}{2\, KT}\right\}$$

$$S_J = \frac{e^{-a^2}}{2}\int_{\alpha^*}^{\pi/2} d\alpha\, e^{\frac{a^2 \sin^2\alpha}{2}} \sin^3\alpha \left(1 - \frac{\sin^2\alpha^*}{\sin^2\alpha}\right)^P$$

$$\left[(3 + 2a^2\sin^2\alpha) I_o\left(\frac{a^2\sin^2\alpha}{2}\right)\right.$$

$$\left. + (1 + 2a^2\sin^2\alpha) I_1\left(\frac{a^2\sin^2\alpha}{2}\right)\right] \quad (5)$$

and $a^2 = (m\omega^2)/2KT$. The integration limit for Eq. (5) is found from the definition of $\sin^2\alpha^* = B(r,z)/B_{max}(r',z')$. It is seen that in the "long thin" plasma model the z variable enters into the solution of Eq. (4) only as a parameter.

If the following new variables are defined

$$\psi = \frac{rA_\theta - r^2 B_o(Z)/2}{r_r^2 B_o(0)}, \quad X = \frac{r^2}{2r_r^2},$$

$$r_r^2 = \frac{m\, KT}{e^2 B_o^2(0)}$$

$$M(Z) = \frac{B_o(Z)}{B_o(0)}, \quad \gamma = \frac{\omega m}{e B_o(0)}, \quad \lambda = \frac{2 N_o KT \mu_o}{B_o^2(0)}$$

Equation (4) becomes:

$$\frac{\partial^2 \psi}{\partial X^2} = \frac{\gamma\lambda}{2} \exp\left[-\gamma(\psi + (M(Z) - \gamma) X)\right] S_J \quad (6)$$

which represents a two point boundary value problem subject to the conditions that

$\psi(x = 0, z) = 0$ [No flux on center line]

$\frac{d\psi}{dx}(x \to \infty, z) = 0$ [No induced field at $r \to \infty$].

III. GENERAL PROPERTIES OF THE SOLUTION

Before proceeding to numerical calculations we first note the following rather general properties of the solutions to Eq. (6).

1) The total magentic field is a monotone increasing function of radius. This results from the fact that $\psi > 0$.

2) It can be shown that P must be greater than 1/2 in order for equilibrium solutions to exist. For P less than 1/2, the plasma is subject to mirror type instabilities near the mirror end. This effect was pointed out to us by R. L. Morse.

3) It can be shown numerically and in some special cases analytically that there results two solutions to Eq. (6) satisfying the given boundary conditions. That is, the solution to Eq. (6) is non-unique. One solution corresponds to a monotone decreasing density distribution and a magnetic field with positive bias. The other solution corresponds to a non monotone density distribution and a magnetic field distribution which can exhibit negative bias. A stability analysis indicates that the former solution is stable to Z-dependant marginal modes and the latter solution is unstable to these modes. Hereafter we only consider the stable (monotone density) solutions.

4) Finally and perhaps the most important property exhibited by the solutions suggested to us by Ralph Kilb is the following. For an infinite mirror ratio it can be shown that for solutions to Eq. (6) to exist at the center plane of the plasma (Z = 0) then $\lambda < (1-\gamma)^2$. In this case λ represents the actual ratio of plasma to magnetic pressure. This criterion is related to the difficulty in satisfying pressure balance. For any finite mirror ratio however, it is found that solutions to Eq.(6)

only exist below some critical value of β which is less than λ because of the reduction in plasma density due to finite loss cones. That is, our solutions predict a maximum β which can be found during equilibrium conditions for a given applied mirror ratio.

IV NUMERICAL EXAMPLE

In Fig. 1 we show the calculated values of this maximum value of β for a given set of plasma parameters λ, γ, P and applied mirror ratio. Here β is defined as $\beta = 1 - B^2(r = 0)/B^2(r = \infty)$ and includes the plasma centrifugal pressure. These curves were calculated for the optimum case of $\lambda = (1-\gamma)^2$ and represent the highest possible β one might expect. It is interesting to note that even though at short times the β of a theta pinch plasma is essentially unity this theory predicts that a much lower β will exist for equilibrium times, e.g. $\beta \sim .24$ for $M = 1.25$.

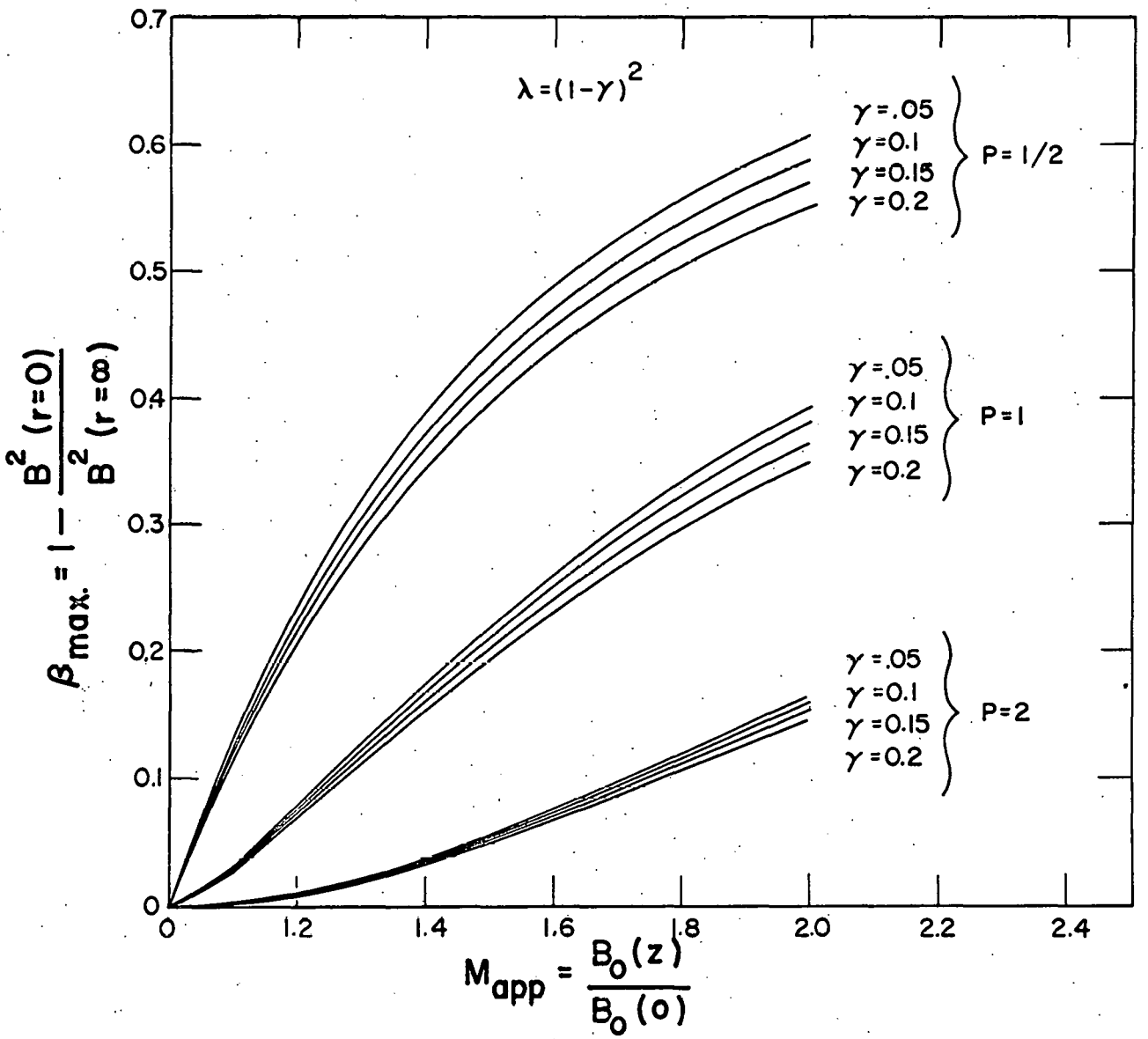

Fig. 1 - Calculated values of maximum β versus applied mirror ratio for various values of plasma parameters.

THETA-PINCH LOSS RATE ASSOCIATED WITH HIGH-β COLLISIONLESS EQUILIBRIUM CONFIGURATIONS

by

Ralph W. Kilb
General Electric Research and Development Center
Schenectady, New York

ABSTRACT

Numerical studies of equilibrium configurations in a collisionless high-β θ-pinch showed that some regimes did not have solutions. A guiding center fluid approach was used with $P_\perp(B)$ and $P_{||}(B)$. With $\beta > 0.3$ and an empty loss cone, solutions could not be found, apparently because the plasma did not satisfy the ellipticity condition[1] $\partial/\partial B[P_\perp(B) + B^2/8\pi] > 0$. This criterion is closely related[1] to the "mirror instability" which occurs when $P_\perp/P_{||}$ is too large. However, numerical solutions can be found when the loss cone is populated to a minimum level which will satisfy the ellipticity criterion. From the required loss cone population, one may compute an e-folding loss time τ, which yields $\tau \sim 1$ μsec for our θ-pinch. This compares with an experimental $\tau \sim 1.8$ μsec during the high-β phase of the pinch. Following Grad,[1] we speculate that during the high-β phase some microinstability (perhaps of the Post-Rosenbluth loss cone type) continuously fills the loss cone. The associated high loss rate may stop when the plasma-β falls to ~1/4, where ellipticity is satisfied with zero loss cone level. This late stage may correlate with the second quarter cycle of our θ-pinch where the neutron yield and end loss measurements seem to indicate better containment after the plasma-β and density have fallen sharply.

[1] H. Grad, NYO-1480-50, Eq.(9.18) and p 76.

A theoretical study of the axial variation of the plasma in the G.E. high power θ-pinch was undertaken using the "Guiding Center Plasma" (GCP) equations for the ions and assuming a quasi-equilibrium. It soon emerged that equilibrium solutions did not exist for high-β plasmas when the mirror loss cone was empty. J. Freidberg and W. Grossman pointed out to me that a general theory[1] of Grad predicts instabilities in such a situation. These instabilities can pump ions into the loss cone in an attempt to produce a velocity distribution satisfying local stability, but this same pumping causes macroscopic plasma loss out the mirrors.

The GCP equations are used because the collision time for ions (6-20 μsec) is considerably longer than their cyclotron time (<0.5 μsec) and transit time (~ 0.5 μsec). Thus μ and J are adiabatic constants, if one bars microinstabilities. In contrast, the electron collision time (~ 0.01 μsec) is extremely short compared to the observed particle loss time (~ 1.8 μsec), so the electron velocity distribution is isotropic and MHD equations are appropriate for elec-

trons. One consequence is that $\nabla_{\parallel} P_e$ must be balanced by an electrostatic $\nabla_{\parallel}\varphi$. Assuming T_e is constant along the field line, integration of $\nabla_{\parallel} P_e = en\nabla_{\parallel}\varphi$ yields:

$$\varphi(z) - \varphi(0) = \frac{T_e}{e} \ell n \left[\frac{n(z)}{n(0)}\right] \qquad (1)$$

Thus a measurement of $n(z)$ directly yields $\varphi(z)$. In our θ-pinch,[2] $T_e \approx 0.3$ keV and a ten-fold drop in density would correspond to $\Delta\varphi \approx -0.7$ keV. Such a potential drop is small, but not completely negligible, compared to the mean ion energy of ~ 3 keV. However, the retention of the electrostatic potential would considerably complicate the following ion equations, so we henceforth assume $\varphi(z) \equiv 0$ but still employ an isotropic P_e.

The "trapped" ion distribution at the centerplane is assumed to be separable: $f_1(E,\theta) = N_1 g(E)\, h(\theta)$. For $h(\theta)$ a diffusion distribution[3] is approximated (for mirror ratio <10) by:

$$h(\theta) = \frac{\sin\theta - \sin\theta_c}{1 - \sin\theta_c} \qquad (2)$$

where θ_c is the loss cone angle given by $\sin^2\theta_c = B_c/B^*$. Here B_c is the centerplane field, and B^* is the mirror field in the plasma.

For g(E) we use the approximate mirror distribution:[4]

$$g(E) \propto E \exp\{-E/T_i\} \qquad (3)$$

In addition to $f_1(E,\theta)$, we assume that the microinstabilities superimpose a Maxwellian ion distribution:

$$f_2(E,\theta) = \frac{N_2\sqrt{E}}{2(\pi T_i)^{3/2}} e^{-E/T_i} \qquad (4)$$

and use the normalization $\int f_i(E,\theta)dE \sin\theta \cdot d\theta d\varphi = N_i$. Assuming that μ and E are constants of the motion, we use Longmire's method[5] to find the density and pressure along the field line as a function of B(z) in the plasma. After straightforward, but extensive, algebra we obtain for the region inside the mirror:

$$n(B) = N_2 + \frac{N_1}{D}\left[\sqrt{\frac{B^*}{B}} \arctan\sqrt{\frac{B^*}{B} - 1} - \sqrt{1 - \frac{B}{B^*}}\right]$$

$$P_\perp(B) = T_e n(B) + N_2 T_i + \frac{4}{3}\frac{N_1 T_i}{D} \times$$

$$\left[\frac{9}{8}\sqrt{\frac{B^*}{B}} \arctan\sqrt{\frac{B^*}{B} - 1} - \left(\frac{7}{8} + \frac{1}{4}\frac{B}{B^*}\right)\sqrt{1 - \frac{B}{B^*}}\right]$$

$$P_\parallel(B) = T_e n(B) + N_2 T_i + \frac{4}{3}\frac{N_1 T_i}{D} \times$$

$$\left[\frac{3}{4}\sqrt{\frac{B^*}{B}} \arctan\sqrt{\frac{B^*}{B} - 1} - \left(\frac{5}{4} - \frac{1}{2}\frac{B}{B^*}\right)\sqrt{1 - \frac{B}{B^*}}\right]$$

$$D \equiv \sqrt{\frac{B^*}{B_c}} \arctan\sqrt{\frac{B^*}{B_c} - 1} - \sqrt{1 - \frac{B_c}{B^*}}$$

For the external region beyond the mirror peak we find:

$$n(B) = N_2\left(1 - \sqrt{1 - B/B^*}\right)$$

$$P_\perp(B) = T_e n(B) + T_i N_2\left[1 - (1 + 0.5B/B^*)\sqrt{1 - B/B^*}\right]$$

$$P_\parallel(B) = T_e n(B) + T_i N_2\left[1 - (1 - B/B^*)^{3/2}\right]$$

Neglecting field curvature, momentum balance transverse to the plasma requires:

$$\frac{B_v^2}{8\pi} = p^* \equiv P_\perp(B) + \frac{B^2}{8\pi} \qquad (5)$$

where $B_v(z)$ is the vacuum magnetic field. Specification of β, T_e, N_1, N_2, and $B_v(z)$ then yields B_c, B^* and T_i by applying Eq.(5) at the centerplane and mirror peak. Variation of the plasma B from B_c to B^* now allows one to locate the z-positions by relating $p^*(z)$ from Eq.(5) to $B_v(z)$. However, when β is high and the loss cone is

empty (N_2=0), p* actually decreases for $B \approx B_c$ and therefore it is impossible to match p* against a smoothly rising $B_v(z)$. Thus a quasiequilibrium exists only if $\partial p^*/\partial B \geq 0$, which is the ellipticity condition required by Grad.[1] He also conjectures that microinstabilities occur if $\partial p^*/\partial B < 0$, but the GCP theory does not yield an explicit growth rate. However, since the microinstabilities are outside the scope of the GCP theory, they seem likely to be of the order of the ion cyclotron frequency or higher. Examples are the instabilities of Harris,[6] of Dory, Guest and Harris,[7] and of Post and Rosenbluth.[4] Speculating that the growth rate is large enough to create a locally stable velocity distribution such that $\partial p^*/\partial B = 0$, we may use this as a criterion to solve for the minimum N_2 for a given set of plasma conditions T_e, β, n(0) and $B_v(z)$. These calculations have been done for our θ-pinch conditions, and show that for $\beta > 0.5$ one must have $N_2 > N_1$ if $\partial p^*/\partial B = 0$ at the centerplane. From N_2 and the integrated density along the field line one may now compute an e-folding loss time, which generally is ~ 1 μsec as compared to the observed time of ~ 1.8 μsec in the first quarter cycle of our θ-pinch.[2]

Figure 2 shows the computed axial variation of n(z) and B(z) for the experimental $B_v(z)$, T_e, n(0) and $\beta \approx 0.97$ at 3 μsec ($\sim$ 1/8 cycle). The stability criterion $\partial p^*/\partial B = 0$ requires $N_2/N_1 = 25$, which means a nearly Maxwellian distribution with a corresponding short e-folding time $\langle \tau \rangle$. Note that n(z) is nearly constant up to the mirror because of the nearly Maxwellian distribution. The relative plasma radius R(z)/R(0) was derived by using flux conservation. A preliminary comparison with experiment can be made by comparing with the axial variation of bremsstrahlung. The light intensity relative to the center plane is proportional to $n^2(z)R(z)/n^2(0)R(0)$. This is plotted in Fig. 2, and shows a drop of ~ 2 in light intensity at the mirror versus the centerplane.

Figure 3 shows a side-on view of the plasma at 3 μsec. The light intensity along the axis seems to be roughly consistent with the n^2R curve in Fig. 2, thus indicating that the loss cone is well-populated as we conjecture.

Figure 4 shows the computed axial variation at 8 μsec ($\sim$1/4 cycle), by which time extensive particle loss has significantly lowered the plasma β. The stability criterion now requires only $N_2/N_1 = 0.05$, with a corresponding increase in e-folding to 6.9 μsec. The experimental neutron rate and D^+ ejection rate[2] seem to indicate better containment at this time. Note that n(z) decreases nearly linearly from the centerplane because of the diffusion distribution h(θ). This results in a sharp decrease in n^2R along z, which correlates with the "fireball" appearance of our θ-pinch plasma at late times as shown in Fig. 5. The low light intensity at the mirror relative to the centerplane in Fig. 5 indicates that the GCP equations are indeed appropriate and that the plasma is not dominated by collisions or microinstabilities.

Further calculations showed that for $\beta < 0.3$ the loss cone could now be empty (N_2=0) and yet satisfy $\partial p^*/\partial B > 0$.

To summarize, the GCP approximation for the ions in a high-β θ-pinch shows that a quasi-equilibrium does not exist because $\partial/\partial B[P_\perp(B) + B^2/8\pi] < 0$ near the centerplane

when the loss cone is empty. Adopting Grad's conjecture[1] that this implies microinstabilities, one may assume that these instabilicreate a Maxwellian distribution and populate it to a level which satisfies the ellipticity condition $\partial p^*/\partial B = 0$. Associated with the Maxwellian distribution is an e-folding loss rate which gives $\langle\tau\rangle \approx 1\,\mu$sec for our θ-pinch when $\beta > 0.5$. However, when $\beta < 0.3$ the loss cone can be empty and yet satisfy $\partial p^*/\partial B > 0$. Thus intermediate-β plasmas ($\beta < 0.3$) should show improved containment, in the GCP approximation. Preliminary data for our θ-pinch appears to correlate with these calculations, but additional data (such as a laser determination of n(z) on the axis at successive times) is required before a definite judgement can be made. The GCP theory leads one to expect a lower loss rate after the β falls to ~ 1/4 in a clamped θ-pinch or in a sustained field θ-pinch.

I am indebted to L. M. Goldman for several discussions and for providing Figs. 3 and 5.

REFERENCES

1. H. Grad "The Guiding Center Plasma" NYO-1480-50. Also in Proc. of Symposia in Appl. Math., 18, 162-248 (1967), Section 9.

2. R. L. Bingham, L. M. Goldman, R. W. Kilb, Plasma Phys. and Cont. Nucl. Fusion Res., Vol. I, IAEA, Vienna(1966), pp.301-314.

3. D. J. BenDaniel and W. Carr, UCRL-5859 (1960).

4. R. F. Post and M. N. Rosenbluth, Phys. Fluids, 9, 730-749 (1966).

5. C. L. Longmire, Elementary Plasma Physics, Interscience (1963) Sect.3.5.

6. E. G. Harris, Phys. Rev. Lett. 2, 34 (1959); and J. Nucl. Energy Part C, 2 138-145 (1961).

7. R. A. Dory, G. E. Guest, E. G. Harris, Phys. Rev. Lett. 14, 131 (1965).

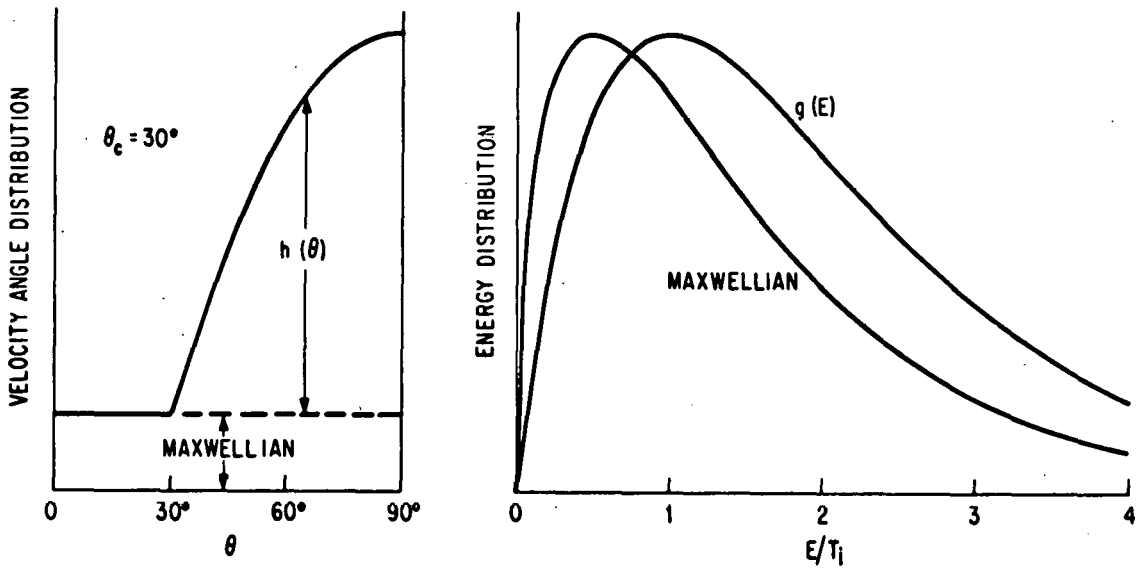

Fig. 1. Velocity angle distribution resulting from combined diffusion distribution h(θ) and Maxwellian distribution. Also mirror distribution g(E) and Maxwellian distribution versus E/T_i.

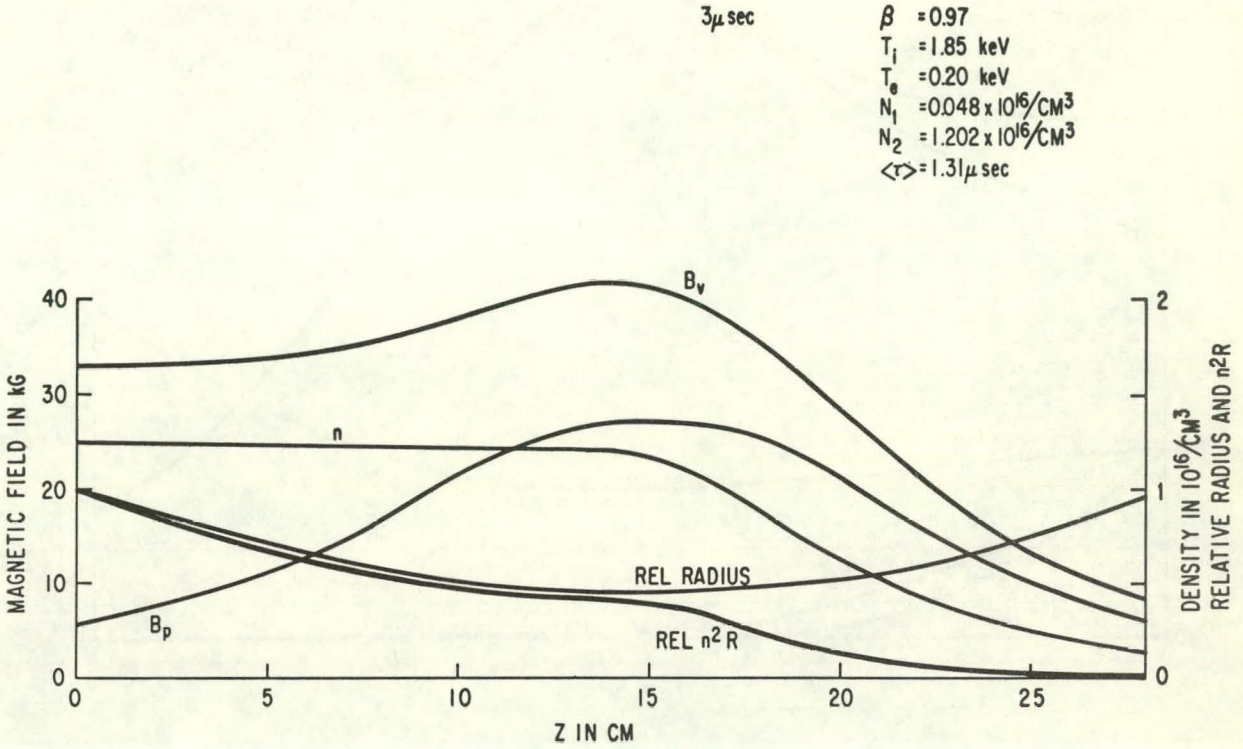

Fig. 2. Computed quasi-equilibrium plasma parameters for our θ-pinch at 3 μsec (~1/8 cycle) versus z. Note that n is nearly constant up to the mirror peak at z = 14, because $N_2/N_1 \approx 25$ so the distribution is nearly Maxwellian.

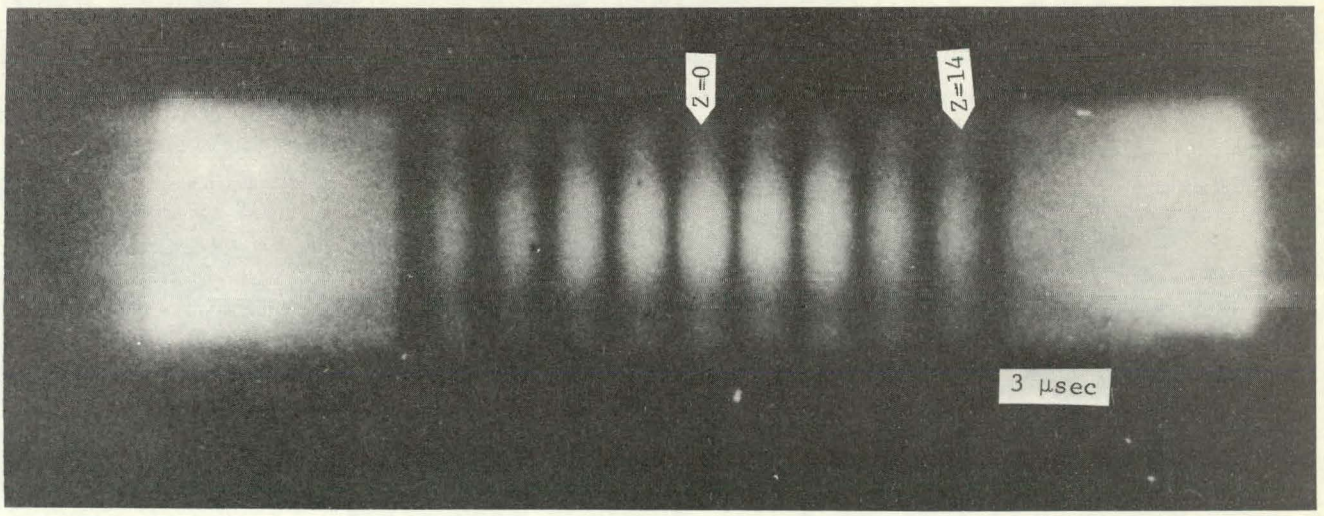

Fig. 3. Side-on view of plasma at 3 μsec. Note that the axial variation of the light intensity is roughly consistent with the computed n^2R curve in Fig. 2.

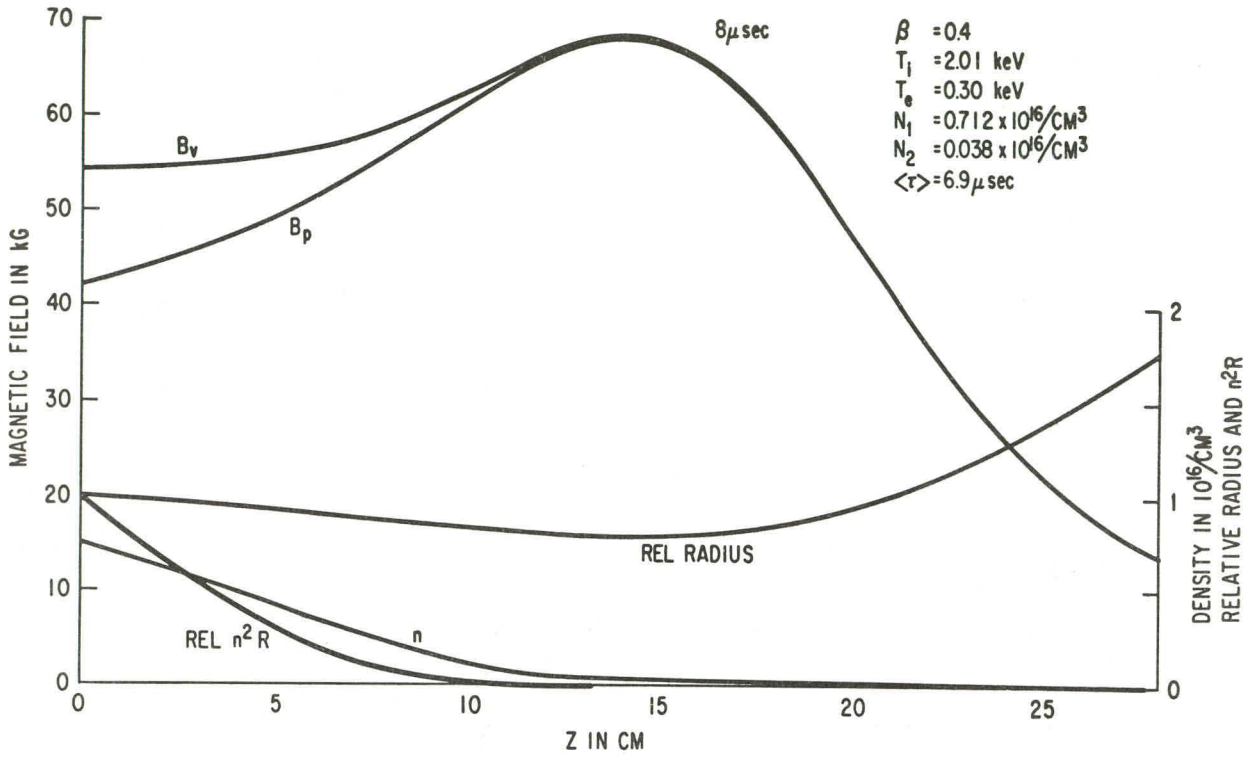

Fig. 4. Computed quasi-equilibrium plasma parameters at 8 μsecs (~1/4 cycle) versus z. Here n drops linearly with z because of the predominant diffusion distribution h(θ).

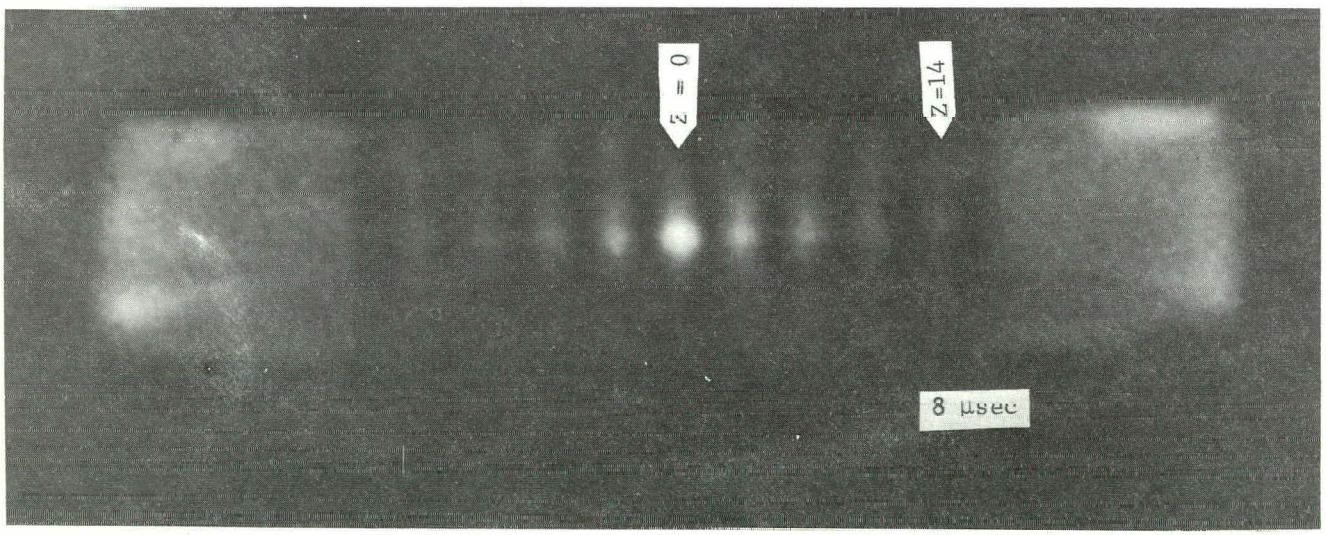

Fig. 5. Side-on view of plasma at 8 μsec. The large difference in light intensity at the centerplane and mirror peak indicates that the loss cone is highly depopulated.

CONTINUUM EQUATIONS FOR FINITE BETA PLASMA SYSTEMS*

by

P. L. Auer and R. E. Kinsinger
Cornell University
Ithaca, New York

ABSTRACT

A method of expansion has been developed earlier by one of us for solving the Vlasov equation. This method resembles CGL but takes into special account the effect of electric fields produced by space charge separation. We consider a plane disturbance propagating perpendicular to an axial magnetic field. In this case our method leads to a renormalized precession frequency and particle orbits which are distorted from circular into elliptical shape. The expansion is carried out to second order in the smallness parameter and a closed set is obtained which differs in certain respects from results of conventional CGL approach as well as from FLR results. The reason will be discussed in some detail. A single fluid formulation is obtained and examined with a view to understanding the role of finite beta in dynamic situations which produce strong gradients in the magnetic field and in the plasma properties.

I. Introduction

It has been shown previously[1] that in the presence of strong space charge forces a special technique must be employed for the expansion of the Vlasov equation. For finite beta systems supporting strong disturbances as in theta pinches or under conditions where formation of collision-free-shocks may be expected, the role of space charge forces must be taken into account in lowest order.

Consider, for example, a plasma in an axial magnetic field in which a plane disturbance propagates in the x direction. In this event all macroscopic quantities may vary in the x-t plane, where t is time. Excluding motion along the magnetic field line produces ideal axial symmetry. The field configuration becomes

$$\bar{E} = [E_x(x,t), E_y(x,t), 0]$$
$$\bar{B} = [0, 0, B(x,t)] \quad . \tag{1}$$

Introduce the distribution function $f(x,\dot{x},\dot{y},t)$; it satisfies the Vlasov Equation

$$\left\{\frac{\partial}{\partial t}+\dot{x}\frac{\partial}{\partial x}+\frac{e}{M}\left[E_x+\frac{1}{c}\dot{y}B\right]\frac{\partial}{\partial \dot{x}}+\frac{e}{M}\left[E_y-\frac{1}{c}\dot{x}B\right]\frac{\partial}{\partial \dot{y}}\right\}f = 0 \tag{2}$$

where $\dot{x},\dot{y}$ are the microscopic velocities and phase space coordinates, as well, while e and M are the charge and mass of the plasma species and c is the velocity of light.

In the presence of strong space charge fields the particle orbits are ellipses rather than circles and the precession frequency ω is given by

$$\omega^2 = \Omega[\Omega+v'] \equiv \alpha^2\Omega^2$$
$$\Omega = \frac{eB}{Mc} \tag{3}$$

where v is the y component of drift and prime denotes partial derivative with respect to x. The drift velocity is readily computed by methods given previously.

$$\bar{v}_D \equiv [u(x,t), v(x,t), 0] \tag{4}$$
$$v(x,t) = -\frac{cE_x(x,t)}{B(x,t)}$$
$$u(x,t) = \frac{1}{\alpha^2\Omega}\left[\frac{e}{M}E_y(x,t)+\frac{\partial}{\partial t}v(x,t)\right] \tag{5}$$

* This work was supported by the AEC under Contract No. AT(30-1)-3782.

II. Adiabatic Expansion

The adiabatic invariant, as may be expected, is given by the area of the orbit normal to the magnetic field; and for the elliptic orbit under discussion it becomes

$$J = \frac{M}{2\omega}\{[\dot{x}-u]^2+\alpha^{-2}[\dot{y}-v]^2\} \ . \qquad (6)$$

Introduce J (except for factor of M/2) and the orbital polar angle θ as the appropriate phase space variables in place of $\dot{x},\dot{y}$. The normalization becomes

$$\int\int_{-\infty}^{\infty} d\dot{x}d\dot{y} f_{old}(x,\dot{x},\dot{y},t) = \frac{\Omega}{2}\alpha^2 \int_0^{\infty} dJ \int_0^{2\pi} d\theta f_{new}(x,J,\theta,t) \qquad (7)$$

and the Vlasov Equation as given by (2) becomes transformed for the new distribution function

$$\omega\frac{\partial}{\partial\theta}f+\mathcal{L}(x,J,\theta,t)f = 0 \qquad (8)$$

where the linear operator $\mathcal{L}$ takes the form

$$\mathcal{L} \equiv \frac{d}{dt}+\cos\theta\sqrt{\omega J}\,\frac{\partial}{\partial x} + \sum_{n=1}^{3}[a_n(J,x,t)\cos n\theta\frac{\partial}{\partial J}+b_n(J,x,t)\sin n\theta\frac{\partial}{\partial\theta}]$$

$$a_1 = -2\frac{\dot{u}}{\omega}\sqrt{\omega J}-\frac{1}{2}\sqrt{\omega}J^{3/2}\frac{\partial}{\partial x}\ell n\ \alpha^3\omega^2$$

$$a_2 = J\frac{d}{dt}\ell n\alpha^3\Omega = -2Jb_2$$

$$a_3 = \frac{1}{2}\sqrt{\omega}J^{3/2}\frac{\partial}{\partial x}\ell n\alpha = -2Jb_3$$

$$b_1 = \frac{\dot{u}}{\sqrt{\omega J}}-\frac{1}{4}\sqrt{\omega J}\frac{\partial}{\partial x}\ell n\alpha$$

$$\frac{d}{dt} = \frac{\partial}{\partial t}+u\frac{\partial}{\partial x} \qquad (9)$$

and dot denotes the operator d/dt.

The adiabatic expansion consists of ordering terms in $1/\omega$; thus

$$f = f_0+f_1+\cdots$$

$$\frac{\partial f_0}{\partial\theta} = 0$$

$$\frac{\partial f_1}{\partial\theta} = -\frac{1}{\omega}\mathcal{L}f_0; \text{ etc.} \qquad (10)$$

The expansion scheme is completed once we impose the boundary condition that be periodic in the interval $0\leq\theta\leq 2\pi$. This, in turn requires

$$0 = \int_0^{2\pi}\mathcal{L}f_n d\theta \ ; \ n = 0,1,\ldots \ . \qquad (11)$$

III. Zero Order Results

On the basis of (10) and (11) we find

$$\frac{\partial}{\partial\theta}f_0 = 0 = \frac{d}{dt}f_0$$

$$f_0 = F(J) \ . \qquad (12)$$

The fact that in lowest order f is an arbitrary function of J confirms that J is in fact the appropriate adiabatic variable.

From (12) and (7) we can readily compute moments in lowest order and thereby produce zero order continuum formulations; in addition to drift quantities already defined, we have

$$\rho \equiv \langle M\rangle = \text{mass density} = \alpha^2\left(\frac{n_0}{B_0}\right)B$$

$$P_{xx} \equiv \langle M(\dot{x}-u)^2\rangle = \text{pressure component in drift frame} = \alpha^3\left(\frac{P_0}{B_0^2}\right)B^2$$

$$P_{yy} \equiv \langle M(\dot{y}-v)^2\rangle = \alpha^2 P_{xx}$$

$$\text{etc.} \qquad (13)$$

In the above, angular brackets denote average over the distribution and zero subscript denotes the uniform, time independent plasma state (reference state).

The zero order results obtained to this point may be summarized in the form

$$E_x = -\frac{1}{c}vB$$

$$u' = -\frac{d}{dt}\ell n\rho$$

$$v' = -\Omega_0\left(\frac{B}{B_0}-\frac{\rho}{\rho_0}\right)$$

$$\frac{d}{dt}\left(\frac{P_{xx}}{\rho\omega}\right) = 0 \ . \qquad (14)$$

The above yield the familiar expression for the space charge electric field, the fact that flux is not conserved in lowest order, and an adiabatic equation of state appropriate to non-circular orbits. In addition, Maxwell's equations provide

$$\frac{\partial B}{\partial t}+\frac{\partial}{\partial x}cE_y = 0$$

$$\frac{\partial B}{\partial x} = -\frac{4\pi}{c}J_y \qquad (15)$$

having neglected displacement current. Assuming a quasi-neutral plasma, the last equation and the second of equation (14) combine

$$\frac{\partial}{\partial x}[\frac{1}{n}\frac{\partial B}{\partial x}] = 4\pi(\frac{1}{m}+\frac{1}{M})\frac{e^2B_0}{c^2}[\frac{B}{B_0}-\frac{n}{n_0}] \qquad (16)$$

where n is the plasma density and M is the ion mass.

It is instructive to make an estimate at this point for the correction factor as defined by (3). For an Adlam-Allen pulse, as an example, we have an exponential tail

$$B \sim \exp\{-(1-A^{-2})^{\frac{1}{2}}\frac{\omega_p x}{c}\}$$

where A is the alfven mach number and ω_p the plasma frequency in the undisturbed region. Substituting into (14) and (16) yields that $\alpha \sim 1/A$ where this estimate has validity for a cold plasma in the region $1\leq A<2$. This example serves to illustrate the not insignificant corrections introduced by strong space charge forces for relatively weak disturbances. However, the role of finite β corrections is not revealed by this example. In order to produce a closed set of equations including finite β contributions it is necessary to proceed explicitly to second order and implicitly to third order.

IV. First Order Results

In first order we obtain corrections to the zero order drift approximation. From the structure of the equations (8-11) we can write

$$f_1 = -\sum_{m=1}^{3}\frac{1}{m\omega}\sin m\theta\int_0^{2\pi}\frac{d\theta'}{\pi}\cos m\theta'\mathcal{L}f_0$$

$$= -\sum_{m=1}^{3}\frac{1}{m\omega}a_m\frac{\partial F}{\partial J}\sin m\theta \qquad (17)$$

Define

$$V_y \equiv \frac{\langle\dot{y}-v\rangle}{\langle 1\rangle}$$

$$P_{xy} \equiv M(\dot{x}-u)(\dot{y}-v) \qquad (18)$$

and we obtain in first order

$$u+\frac{1}{\rho}P'_{xx} = \Omega V_y^{(1)}$$

$$P_{xy} = -\frac{d}{dt}(\frac{P_{xx}}{2\Omega})$$

$$= [\frac{u'}{2\Omega}-\frac{\dot{\alpha}}{2\omega}]P_{xx} \cdot \qquad (19)$$

For a quasi-neutral plasma the first of these yields a momentum equation for the fluid

$$n(m+M)\dot{u}+\frac{\partial}{\partial x}[P_{xx}^{elec}+P_{xx}^{ion}]$$

$$= \frac{1}{c}J_yB = -\frac{1}{8\pi}\frac{\partial}{\partial x}B^2 \qquad (20)$$

while the second of equations (19) yields the now familiar finite larmor radius "pseudo viscosity" term along with corrections proportional to (α-1).

In this order we also find heat flow terms which we do not bother to write out at this time.

V. Second Order Results

In second order we have a homogeneous correction, f_{20}, to the energy, as well as additional flow corrections

$$f_2 = f_{20}+\sum_{m=1}^{6}\frac{1}{m\omega}\cos m\theta\int_0^{2\pi}\frac{d\theta'}{\pi}\sin m\theta'\mathcal{L}(\theta')f_1(\theta')$$

$$= \sum_{m=0}^{6}f_{2m}(J,x,t)\cos m\theta \cdot \qquad (21)$$

The kinetic equation for f_{20} becomes

$$\frac{d}{dt}f_{20} = -\frac{1}{2\pi}\int_0^{2\pi}\mathcal{L}(\theta)\sum_{m=1}^{3}f_{2m}\cos m\theta d\theta$$

$$= -\frac{1}{2}\sqrt{\omega J}f'_{21} - \frac{1}{2}\sum_{m=1}^{3}[a_m\frac{\partial}{\partial J} - mb_m]f_{2m} \quad . \quad (22)$$

From the above, we obtain to second order

$$\frac{\partial}{\partial x}[v+V_y^{(1)}+\frac{1}{\rho}\frac{\partial}{\partial x}(\frac{P_{xx}}{2\Omega})] = -\Omega_0[\frac{B}{B_0}-\frac{\rho}{\rho_0}]$$

$$\rho u+\rho V_x^{(2)} = \rho_0[\frac{c}{B_0}E_y+\frac{1}{\Omega_0}(\frac{\partial v}{\partial t})] + \frac{\rho_0}{\Omega_0}\frac{d}{dt}[V_y^{(1)}+\frac{1}{\rho}\frac{\partial}{\partial x}(\frac{P_{xx}}{2\Omega})] \quad (23)$$

where $\rho V_x \equiv \langle M(x-u)\rangle$.

In second order the diagonal element of the stress tensor may be written as

$$P_{xx}^{(2)} = -\frac{3}{2}\frac{P_{xx}^{(0)}}{\alpha^2\Omega}\frac{\partial}{\partial x}[V_y^{(1)}] + \frac{1}{2\sqrt{\omega}}\frac{d}{dt}[\frac{\sqrt{\omega}}{\alpha^2\Omega}P_{xy}]+0(\beta^2); \quad (24)$$

and we do not bother to write out other elements of the stress tensor or the heat flow tensor at this time.

VI. Application to Adlam-Allen Pulses

Consider a quasi-neutral plasma of electrons of mass m and single charged positive ions of mass M. Treat a stationary disturbance with velocity u_0, in the wave frame

$$m(x)V_x(x) = n_0u_0 = n^{(0)}(x)u(x) \quad , \quad (25)$$

where n_0 is the undisturbed plasma density and u(x) is the zero order drift approximation to the third velocity $V_x(x)$. The above equation, as it stands, is correct to all orders.

Momentum balance provides

$$u(x)+V_x^{(2)}(x) = u_0-\frac{1}{n_0(m+M)u_0}[\frac{B^2(x)-B_0^2}{8\pi}+\sum_{+,-}'P_{xx}-P_0] \quad (26)$$

where P_{xx} is to be calculated to second order and subscript zero denotes values in the undisturbed fluid. The induction equation becomes in second order

$$\frac{d^2}{dt^2}[B+\frac{2\pi}{B}\sum_{+,-}'P_{xx}^{(0)}] = \frac{\omega_p^2}{c^2}[u(x)B(x)-u_0B_0] + u_0B_0\sum_{+,-}'\frac{4\pi e^2}{M_\pm c^2}\dot{n}^{(0)}V_x^{(2)} \quad (27)$$

where $d/dt \equiv u(x)d/dx$ in the wave frame and ω_p is the plasma frequency in the undisturbed region.

Finally, we have for each species

$$V_x^{(2)} = -\frac{u(x)}{u_0\Omega_0}\frac{d}{dt}[\frac{\dot{u}}{\Omega}+\frac{\Omega^{-2}}{2n_0Mu_0}\frac{d}{dt}(\Omega P_{xx}^{(0)})]$$

$$P_{xx} = \frac{P_0}{B_0^2}\{\alpha^3B^2[1-\frac{3/2}{u_0\Omega_0}\frac{d}{dt}(\frac{\dot{u}}{\Omega})] - \frac{1}{u_0\Omega_0^2}\frac{B_0}{\sqrt{\omega}}\frac{d}{dt}[\sqrt{\omega}u\frac{d}{dt}(\alpha^3B)]\}+0(\beta^2). \quad (28)$$

We also have

$$\alpha \equiv \frac{\omega}{\Omega} = [\frac{u_0B_0}{u(x)B(x)}]^{\frac{1}{2}} \quad .$$

The above set is complete to second order in the adiabatic parameter; we have exhibited all terms explicitly to order β.

The full non-linear set has not yet been solved. However, in the linear approximation we find a shift in the scale length from ω_p/c to $(8/\beta_+)^{\frac{1}{2}}\omega_{p+}/c$ for $\beta_+ > 8m/M$, in agreement with earlier results obtained directly from the Vlasov Equation.

REFERENCE

(1). P. L. Auer, Phys. Fluids 5, 1091 (1962).

Z-DEPENDENT MARGINAL STABILITY OF THE RIGID ROTOR MODEL OF A HIGH BETA THETA-PINCH*

by

J. P. Freidberg and R. L. Morse

Los Alamos Scientific Laboratory, University of California
Los Alamos, New Mexico

ABSTRACT

One dimensional equilibria in a cylindrical geometry are found for an infinitely long high β theta-pinch. The solutions are obtained by calculating a current using a rigid rotor distribution function (which is an exact solution to the Vlasov equation), and then solving self-consistently with Ampere's law. It is found, that for a given set of parameters which describe the plasma there exist two solutions to the equations. Solution I corresponds to the case of a monotonically decreasing density with radius, while solution II describes a density which first rises and then decreases monotonically. A z-dependent marginal stability analysis of these two solutions indicates the following:

1. No z-dependent marginal states exist for Solution I.
2. A z-dependent marginal state exists for $k_z = 0$ for the special case in which Solutions I and II coalesce.
3. For Solution II a marginal, z-dependent state exists for some specific value of $k_z^2 > 0$, denoted by k_m^2.

This indicates that Solution II is not a satisfactory equilibrium. Estimates of unstable growth rates will be given for $k_m^2 > k_z^2 > 0$. Comparison will be made with numerical simulation.

I. INTRODUCTION

We investigate the marginal stability of a high β, axisymmetric theta pinch with respect to z-dependent perturbations. The plasma is assumed to behave according to the following model. The ions are collisionless and their behavior is described by the Vlasov equation.

The electrons are assumed cold and therefore, in the equilibrium they carry no currents but serve to produce charge neutrality. For perturbations of the type considered here, the electrons can move along field lines and neutralize any ion space charge which tends to form. Hence we assume $\nabla \cdot \underline{E} = 0$. By assuming a specific form for the equilibrium distribution function, a rigid rotor distribution,[1] we are able to show the following:

1. For the given distribution function and boundary conditions, there are two possible equilibrium solutions; that is the solution is non-unique.
2. For one of these solutions, there is no marginal state.
3. For the special case, when the plasma parameters are such that both solutions coalesce, there is a marginal state for $k_z = 0$.
4. For the second solution, a marginal state exists for sufficiently small k_z. Also, a formula is derived relating this value of k_z to the plasma parameters.

II. EQUILIBRIUM SOLUTIONS

The equations describing the equilibrium are given by

$$\underline{v} \cdot \nabla f + \frac{e}{m} \underline{v} \times \underline{B} \cdot \nabla_v f = 0 \qquad (1)$$

$$\nabla \times \underline{B} = \mu_o \int \underline{v}\, f\, d\underline{v} \qquad (2)$$

For the case of an axisymmetric, z independent equilibrium, there are three exact constants of the motion, given by

$$\mathcal{E} = \frac{m}{2}\,(v_r^2 + v_\theta^2 + v_z^2)$$

$$p_\theta = r(mv_\theta + e A_\theta)$$

$$v_{\shortparallel} = v_z$$

It is well known that any f which is a function of $\mathcal{E}$, p_θ and $v_{\shortparallel}$ is a solution to Eq. (1). As stated in the introduction, we choose for our equilibrium f, denoted by f_o, a rigid rotor distribution function given by

$$f_o(\mathcal{E},p_\theta,v_{\shortparallel}) = N_o\left(\frac{m}{2\pi\kappa T}\right)^{3/2} \exp\left[-(\mathcal{E} + \omega p_\theta)/\kappa T\right]$$

where N_o, T, and ω are constants.

We next calculate the current density $\underline{J}_o$, by integrating over all velocities, and set $\underline{B} = \nabla \times A_\theta$. Substituting this into Eq. (2) yields

$$\frac{d}{dr}\frac{1}{r}\frac{d}{dr}\,rA_\theta = \mu_o e N_o \omega r \exp\left[-\frac{e\omega r A_\theta}{\kappa T} + \frac{m\omega^2 r^2}{2\kappa T}\right] \qquad (3)$$

Denoting the applied magnetic field at $r \to \infty$ by B_o and introducing the following normalizations,

$$r_L^2 = \frac{m\kappa T}{e^2 B_o^2} \qquad x = \frac{r^2}{2r_L^2}$$

$$\gamma = \frac{\omega}{eB_o/m} \qquad \psi = \frac{rA_\theta - r^2 B_o/2}{r_L^2 B_o}$$

$$\beta = \frac{N_o \kappa T}{B_o^2/2\mu_o}$$

into Eq. (3) gives

$$\frac{d^2\psi}{dx^2} = \frac{\beta\gamma}{2} \exp\{-\gamma[\psi + (1-\gamma)\,x]\} \qquad (4)$$

Here ψ represents the induced magnetic flux due to plasma currents. (Note that the relationship between Larmor radius scale length, r_L and the collisionless skin depth, $r_o = c/\omega_{pi}$ is $r_L = r_o\sqrt{\beta/2.}$) The boundary conditions on ψ are

$$\psi(0) = 0 \qquad (5\text{-a})$$

$$\frac{d\psi}{dx}(\infty) = 0 \qquad (5\text{-b})$$

The first condition corresponds to zero induced flux at the origin, while the second to zero induced magnetic field at $r \to \infty$. To solve this equation, we assume $\psi(o) = 0$, and $d\psi(x)/dx = A$. We can then integrate this equation by standard techniques. After obtaining this solution we compute $d\psi(\infty)/dx$ and determine A such that $d\psi(\infty)/dx = 0$. The results of these computations are given below

$$\psi(x) = -(1-\gamma)\,x - \frac{1}{\gamma}\left[\frac{\ell n(1-\gamma)^2}{\beta} - 2\ell n \cosh\left[\frac{\gamma(1-\gamma)}{2}\,x + x_o\right]\right] \qquad (6)$$

$$x_o = \pm \tanh^{-1}\left[1 - \frac{\beta}{(1-\gamma)^2}\right]^{\frac{1}{2}} \qquad (7)$$

$$A = -(1-\gamma) \pm \sqrt{(1-\gamma)^2 - \beta} \qquad (8)$$

As stated previously there are two values of A, (which correspond to two values of magnetic field on axis) which satisfy conditions 5-a and 5-b. It can easily be shown that the solution with the + sign corresponds to monotonic decreasing density, and positive magnetic bias at r = 0. The other solution corresponds to an increasing and then monotonic decreasing density and has positive or reverse magnetic bias depending on whether $\beta > 1 - 2\gamma$ or $\beta < 1 - 2\gamma$ respectively.

III. STABILITY OF THE FIRST SOLUTION

The equations for the perturbed distribution function f_1, and the perturbed flux ψ_1, are determined by the standard technique of first integrating along the zeroth order orbit to obtain f_1, and then integrating f_1 over velocities to obtain $\underline{J}_1$. This computation is greatly simplified if we consider the marginal state (i.e. perturbation of the type $e^{i\omega t}$ with $\omega \to 0$) and allow only z dependent perturbations of the form $\psi_1(x,z) = \psi_1(x)e^{ik_z z}$. The simplification that arises, results because under these assumptions p_θ remains constant for all particles, by symmetry, and it can be shown that energy is conserved for all particles except a resonant class whose contribution is vanishingly small. It follows from the constancy of phase space density

near a particle (Liouville's theorem) that the same distribution function, $f(\mathcal{E},p_\theta)$, describes the plasma before and after the perturbation. Using this information it can be shown that the equation for the perturbed flux is given by

$$\frac{d^2\psi_1}{dx^2} - \left[\frac{k_z^2}{x} - \gamma\,\psi_o''(x)\right]\psi_1 = 0 \qquad (9)$$

subject to $\psi_1(o) = 0$ $\frac{d\psi_1}{dx}(\infty) = 0$, and where ψ_o is related to the equilibrium ψ, (given by Eq. 6)), by $\psi_o(x) = \psi(x) + (1-\gamma)x$. Also, z has to be normalized to r_L. In order to show that the solution corresponding to monotonic decreasing density is marginally stable, we multiply Eq. (9) by ψ_1^* and then integrate between any two values of x, denoted by x_1 and x_2. After several integrations by parts Eq. (9) can be put in the following form

$$-k_z^2\int_{x_1}^{x_2}\frac{|\psi_1|^2\,dx}{x} - \int_{x_1}^{x_2}\left|\psi_1' - \frac{\psi_o''}{\psi_o'}\psi_1\right|^2 + \left(\psi_1^*\psi_1' - \frac{|\psi_1|^2\psi_o''}{\psi_o'}\right)\Bigg|_{x_1}^{x_2} = 0 \qquad (10)$$

For the solution corresponding to monotonic decreasing density, (i.e. $x_o > 0$) it can easily be shown that $\psi_o' > 0$. Hence we can set $x_1 = 0$, and $x_2 = \infty$ in Eq. (10), whereby the endpoint contribution vanishes and we can solve for k_z^2 as follows

$$k_z^2 = -\frac{\int_o^\infty\left|\psi_1' - \frac{\psi_o''}{\psi_o'}\psi_1\right|^2 dx}{\int_o^\infty\frac{|\psi_1|^2}{x}\,dx} < 0$$

Clearly no marginal state exists. This argument does not apply to the other solution (i.e. $x_o < 0$) since in this case $\psi_o'(x) = 0$ at $x = -2x_o/\gamma(1-\gamma)$.

IV. MARGINAL STATE FOR $k_z = 0$

We show here that a marginal state exists for $k_z = 0$, for the special case when the two equilibrium solutions coalesce (i.e. $x_o = 0$). To do this, we set $k_z = 0$ in Eq. (9), introduce a new independent variable $y = x\gamma(1-\gamma)/2$, and make use of the fact that

$$\psi_o'(y) = \frac{2}{\gamma}\tanh(y + x_o)$$

$$\psi_o''(y) = \frac{2}{\gamma}\operatorname{sech}^2(y + x_o)$$

Eq. (9) then reduces to

$$\psi_1'' + 2\operatorname{sech}^2(y + x_o)\psi_1 = 0 \qquad (11)$$

where $'$ now denotes differentiation with respect to y. It can be shown that the solution to this equation is given by

$$\psi_1(y) = C_1\tanh(y + x_o) + C_2[(y + x_o)\tanh(y + x_o) - 1] \qquad (12)$$

and

$$\frac{d\psi_1(y)}{dy} = C_1\operatorname{sech}^2(y + x_o) + C_2[\tanh(y + x_o) + (y + x_o)\operatorname{sech}^2(y + x_o)] \qquad (13)$$

Applying the conditions $\psi_1(0) = 0$ and $d\psi_1(\infty)/dy = 0$ yields

$$C_1\tanh x_o + C_2(x_o\tanh x_o - 1) = 0$$

$$C_2 = 0$$

Clearly, for non-trivial solutions to exist, $\tanh x_o = 0$ or $x_o = 0$. Hence, when both solutions coalesce, corresponding to $x_o = 0$, there is a marginal state for $k_z = 0$.

V. MARGINAL STATE FOR THE SECOND SOLUTION

In this section we show that a marginal state exists for the solution with $x_o < 0$, by solving Eq. (9) via an expansion in terms of the parameter x_o. Again introducing the variable y, we are interested in the solution to the following equation

$$\psi_1'' - \left(\frac{k'^2}{y} - \gamma\,\psi_o''\right)\psi_1 = 0 \qquad (14)$$

where $k'^2 = 2k_z^2/[\gamma(1-\gamma)]$. A simple expansion in terms of k'^2 will not work, since regardless of how small k'^2 is, the large y behavior is determined by this term. To remedy this we set

$$\psi_1(y) = \xi^{\frac{1}{2}}K_1(\xi^{\frac{1}{2}})\phi(y) \qquad (15)$$

where $\xi = 4k'^2 y$, K_1 is the modified Bessel function and $\xi^{\frac{1}{2}} K_1(\xi^{\frac{1}{2}})$ satisfies Eq. (14) with $\gamma \Psi_o'' = 0$. Substituting Eq. (15) into Eq. (14) yields the following equation for ϕ

$$\phi'' - \frac{4k'^2 K_o(\xi^{\frac{1}{2}})}{\xi^{\frac{1}{2}} K_1(\xi^{\frac{1}{2}})} \phi' + \gamma \Psi_o'' \phi = 0 \qquad (16)$$

subject to $\phi(0) = 0$ $\phi'(\infty) = 0$. We now expand ϕ, k'^2 and Ψ_o'' as series in x_o as follows

$$\phi = \phi_o + x_o \phi_1 + x_o^2 \phi_2 \ldots .$$
$$k'^2 = x_o \alpha_1 + x_o^2 \alpha_2 \ldots .$$
$$\gamma \Psi_o'' = 2 \operatorname{sech}^2 y - x_o \, 4 \operatorname{sech}^2 y \tanh y \ldots .$$

Substituting, we find that the lowest and first order equations are given by

$$\phi_o'' + 2 \operatorname{sech}^2 y \phi_o = 0 \qquad (17)$$

$$\phi_1'' + 2 \operatorname{sech}^2 y \phi_1 = 4 \operatorname{sech}^2 y \tanh y \phi_o + \frac{4K_o(\xi^{\frac{1}{2}})}{\xi^{\frac{1}{2}} K_1(\xi^{\frac{1}{2}})} \phi_o' \alpha_1 \qquad (18)$$

The solution to Eq. (17), satisfying the conditions on ϕ is given by $\phi_o = \lambda \tanh y$ where λ is an arbitrary constant. We now let

$$\phi_1 = C_1 \tanh y + C_2 (y \tanh y - 1) + \tanh y \int_o^y \frac{dy'}{\tanh^2 y''} \int_o^{y'} B(y'') dy''$$

Substituting into Eq. (18) yields

$$B(y) = \lambda \left[4 \operatorname{sech}^2 y \tanh^3 y + \frac{4K_o(\xi^{\frac{1}{2}})}{\xi^{\frac{1}{2}} K_1(\xi^{\frac{1}{2}})} \tan h \, y \operatorname{sech}^2 y \, \alpha_1 \right]$$

Applying the boundary conditions on ϕ we find

$$\phi_1(0) = - C_2 = 0$$

$$\phi_1'(\infty) = \int_o^\infty B(y) \, dy = 0$$

The second condition can only be satisfied if α_1 is chosen appropriately. Doing this results in the following relationship between x_o and k'^2 to lowest order.

$$x_o = \frac{k'^2}{\alpha_1} = - 4k'^2 \int_o^\infty \frac{K_o(\xi^{\frac{1}{2}})}{\xi^{\frac{1}{2}} K_1(\xi^{\frac{1}{2}})} \tanh y \operatorname{sech}^2 y \, dy \qquad (19)$$

This curve is plotted in Fig. 1. Also superimposed, are values of k'^2 determined by direct numerical solutions to Eq. (14) on the CDC 6600 computer. From Fig. 1 it is seen that a marginal state exists if $x_o < 0$ and that the marginal wavenumber, given by Eq. (19) agrees fairly well with the computed value for sufficiently small x_o.

REFERENCES

1 N. N. Komarov and V. M. Fadeev, JETP 14, 378 (1962).

* Work performed under the auspices of the U. S. Atomic Energy Commission.

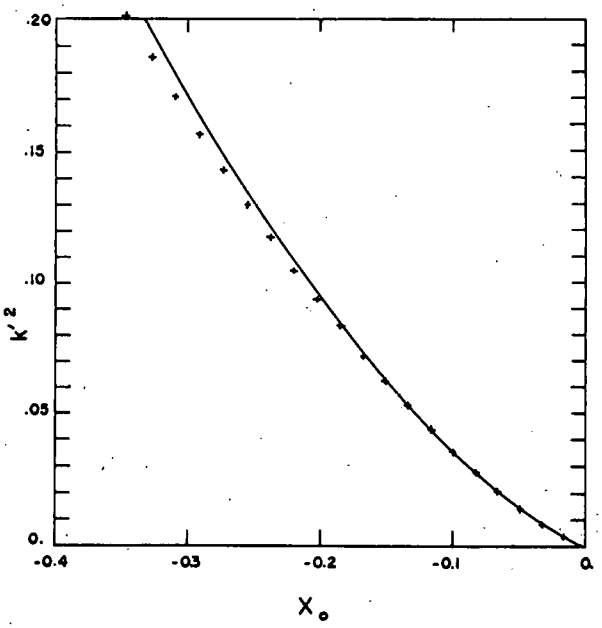

Fig. 1. Plot of the theoretical and numerical values of k'^2 vs x_o.

TURBULENT HEATING OF A SHOCKED MAGNETIZED PLASMA*

by

O. K. Mawardi and R. M. Scott
Case Western Reserve University

ABSTRACT

This paper describes a study in progress on strong shock waves in a magnetic field. The aim of this work is to make investigations on the observed heating of the plasma downstream of the shock. This anomalous behavior is ascribed to an ion-ion two stream instability which causes the onset of turbulence in the plasma. The turbulent character of the shock is inferred from the thickness of the shock front and diffusion of the trapped magnetic field. Comparison of theory with experiments is discussed.

Introduction

As a result of intensive research effort, the shock tube has become a very versatile and reliable tool for the study of high temperature plasmas. Since the theory of non-linear waves is quite complex, it is of advantage to concentrate on one-dimensional problems where the mathematics is more tractable. Accordingly, great care has been taken to improve the performance of a shock tube to be able to produce in the laboratory, shock waves under conditions closely approximating the idealized theory.

Two shock geometries have been considered in great details; the cylindrical[1] and the plane[2] shock fronts. These two cases, of course, refer to two separate physical conditions and both have relative merits in as far as the study of the dynamics of the shock is concerned. Plane shocks, in a magnetized plasma, however, have the advantage of exhibiting a steady structure under certain flow regimes of upstream Alfvèn Mach number[3,4]. Consequently plane waves lend themselves to easier interpretations.

*Supported in part by the National Science Foundation and by the Cambridge Air Force Research Center.

This paper describes a series of investigations which were originally undertaken to verify the classical theory of strong hydromagnetic plane shocks in a magnetized plasma. An anomalous heating of the plasma which was observed is ascribed to a turbulent heating phenomenon. This is discussed in details.

The device used in the experiment is shown in schematic form in Fig. 1. The operating parameters are summarized in Table 1. The short coaxial gun initiates the shock wave which travels down the tube. A bias axial magnetic field confines the plasma away from the walls of the shock tube and prevents rapid cooling of the plasma. An azimuthal bias field provides a magnetic field normal to the direction of propagation of the shock front. All the experimental work reported here was performed on hydrogen.

Magnetic probes were used to measure the current sheet as a function of time and axial position. The shot-to-shot reproducibility was quite satisfactory. The electric fields inside the plasma were measured by means of a differential probe similar to the one used by Burkhardt and Lovberg[5].

Table 1

Cathode radius	6.80 cm
Anode radius	5.90 cm
Length of gun	6.04 cm
Main energy-storage capacitance	3.4 kilojoules
Initial capacitor voltage	10 kilovolts
Time to $I_{max.}$	3.4 μsec.
Axial bias field	2.92 kilogauss
Azimuthal bias field	0.90 kilogauss
Gas pressure	3.3×10^{-1} torr

The electron temperature and electron density in the shock front were estimated from measurements of the shape and intensity of the Balmer Beta line in hydrogen. A 3/4 meter monochrometer was set at a wavelength and the shock tube fired. The intensity at a particular wavelength versus time was read from a 551 Tektronix oscilloscope. The monochrometer was moved to a new wavelength and the processes repeated. The information was fed into a computer program which plotted the intensity versus wavelength at a particular time. From these plots, the width of the H_β line was measured, and from the width the density determined. The temperature was determined from the ratio of the integrated line intensity to the continuum intensity around the line. The determination is based on the work presented by Griem[6] and assume L.T.E.

Experimental Results

Systematic mapping of the magnetic field inside the gun were performed. Fig. 2, shows a typical set of oscillograms for the azimuthal (B_θ) , axial magnetic (B_z) fields as well as for the output of a photomultiplier registering the intensity of the luminous front.

Spatial plots of B_θ (Fig. 3) derived from the oscillograms show the time evolution of the current sheet associated with the shock. The shock structure (temperature and electron density) is shown in Fig. 4.

In order to check whether the dynamics of the shock followed a classical behavior, the theory of a one dimensional blast wave in a magnetized plasma was developed.[7] Whereas reasonable agreement was observed for a shock wave in an unmagnetized plasma[8] there was serious discrepancy between the classical theory and the experimental findings.

Several comments on these points of departure are in order. Typical values for the shock thickness observed are of the order of 2 cms. Now according to classical theory[9] the thickness of the shock front in a plasma magnetohydrodynamics weak shock wave propagating across a magnetic field is given by

$$\Delta \sim \frac{\eta_m}{u(m-1)} \qquad (1)$$

where $\eta_m = \frac{1}{\mu_o \sigma}$ is the magnetic viscosity for the plasma, u the velocity of the shock front and m is the Alfvènic Mach number. Using the measured electrons temperature it is found that the predicted value is a few millimeters, which falls short of the observed thickness.

Two other points which also are difficult to explain with the classical theory are the rapid diffusion of the magnetic field (and associated heating of the electrons) and the appearance of ordered fluctuations at the lower Mach numbers in both B_θ and B_z . At higher Mach number ($\sim$3) the fluctuations appear to be damped out.

Collective Effects in Shocks

Several estimates for the shock thickness have been obtained by means of the so-called "laminar theory."[10] In this theory the plasma is assumed cold, i.e., its pressure p is much smaller than $\frac{B^2}{2\mu_o}$. To prevent the onset of instabilities downstream of the shock, the shock velocity has to be less than the thermal velocity of the electrons. Sagdeev[10] has shown that this requires the Mach number not to exceed $1 + \frac{3}{8}\left(\frac{2\mu_o nkT}{B^2}\right)^{1/3}$. For higher Mach numbers, the non-linear character of the instabilities which set in will quickly render the plasma flow turbulent. Now for the laminar regime the expected shock thickness is of the order

$$\Delta \sim \frac{u}{\bar{\nu}_{ei}} \qquad (2)$$

where u is the shock velocity $\bar{\nu}_{ei}$ is the mean electron-ion collision frequency in the front. As this predicts a value much too smaller than the thickness observed ($u \sim 4 \times 10^6$ cm/sec ; $\nu_{ei} \sim 10^{10}$) Sagdeev's theory does not apply here.

A possible explanation for this anomalous behavior is ascribed to the large axial ion current which can exist in the case considered. Lovberg[12] had offered the suggestion that important ion-currents parallel to the flow can occur whenever the shock front is an ionization shock front moving in cross electric and magnetic field. The origin of such a current is akin to a polarization current and is given by[13]

$$j_p = nev_p = \frac{nm}{B^2}\frac{\partial E_x}{\partial t} \doteq \frac{nm}{B^2} u \frac{dE_x}{dx} \qquad (3)$$

where v_p is the velocity of the particles, m the mass of the charged particles and x is in the direction of plasma flow. Since the current is proportional to the mass, the ions contribution is much larger than that of the electrons. This ion velocity which is associated with the newly formed ions will lead to an instability whenever this velocity exceeds the thermal velocity of the background ions downstream of the shock. It is therefore, proposed that the onset of this instability will cause the flow regime to be turbulent even though the Mach number is below the critical value obtained by Sagdeev.

A rough estimate of the frequency of this instability will be obtained following similar arguments developed by Kadomtsev[14] which is followed closely. The problem is idealized to that of an ion flux in the x-direction and of uniform density. A constant magnetic field is in the z-direction. All quantities are assumed to be varying as $e^{-i\omega t+i(qz+kx)}$. The linearized equations for the conservation of momentum of the electrons are given by

$$\begin{aligned} -i\omega v_x + \frac{ic_e^2 k}{\omega}(kv_x + qv_z) &= -\frac{e}{m_e}E_x + \frac{eB}{m_e}v_y \\ -i\omega v_y &= \frac{e}{m_e}E_y - \frac{eB}{m_e}v_x \qquad (4) \\ -i\omega v_z + \frac{ic_e^2 k}{\omega}(kv_x + qv_z) &= -\frac{e}{m_e}E_z \end{aligned}$$

In the above equations, v_x, v_y, v_z refer to electron velocities along the three directions, C_e correspond to the velocity of sound for the electrons and E_x, E_y, E_z are the three components of the electric field. The fluctuating density and pressure was eliminated by invoking the acoustic approximation $p_e = nm_e c_e^2$ and the equation for the conservation of particles.

Neglecting the displacement current and requiring that the axial component for the current is contributed mainly by the ions one readily finds

$$\begin{aligned} \nabla x \nabla x \underline{E} &= -\mu_o \frac{\partial}{\partial t}\underline{J} \\ &= -i\mu_o \omega e n \underline{v} + i\omega\mu \qquad (5) \end{aligned}$$

The total current $\underline{J}$ consists of an electronic term and an ionic term $\underline{j}_i$. This latter current is a polarization current and has only an x-component. It is given by

$$j_i = -i\omega\varepsilon E_x \qquad (6)$$

The dielectric constant ε of the ions is a function of the frequency and will lead to a dispersion relation defining the instabilities. Assuming the ions to move behind the shock with a velocity v_o and with an average density n then the perturbation will introduce a fluctuation v_i and n_i. The conservation of ions is expressed by

$$i\omega v_i + ik\left(v_i v_o + \frac{c_i^2}{n} n_i\right) = \frac{e}{m_i} E_x \qquad (7)$$

where C_i is the ions sound velocity. The ion current is on the other hand

$$j_i = e(n_i v_x + n v_o) \qquad (8)$$

Manipulation of equations (6) to (8) leads to

$$\varepsilon = \frac{n_i e^2}{m_i} \frac{1}{(\omega - kv_o)^2 - k^2 c_i^2} \qquad (9)$$

When an ion stream is now superimposed (as is the case corresponding to the freshly produced ions), one obtains for the dielectric constant

$$\varepsilon = \frac{e^2}{m_i}\left(\frac{n_i}{(\omega - kv_o)^2 - k^2 c_i^2} + \frac{n_i^*}{(\omega - kv_o^*)^2 - k^2 c_i^2}\right) \qquad (10)$$

where n_i^* and v_o^* are the density and velocity of the ions in the beam.

The dispersion relation for the plasma is now obtained by eliminating $\underline{E}$ and $\underline{v}$ from (4) and (5) and using the value of ε obtained in (10). A simple case was discussed by Kadomtsev in which

$v_o^* = -v_o$ and $n_i^* = \frac{n}{2}$. The dispersion relation he finds is

$$(\omega^2x^2-\omega_c^2 \cdot \frac{q^2}{k^2})[(\omega^2-k^2v_o^2)^2-2k^2c^2(\omega^2+k^2v_o^2)+k^4c_i^4] - \\ - \frac{m_e}{m_i}(\omega^2+k^2v_o^2-k^2c_i^2)\cdot[\omega^2\omega_c^2x+c_e^2k^2(\omega^2x^2-\omega_c^2\frac{q^2}{k^2})] = 0 \quad (11)$$

In the above $\omega_c = \frac{eB}{m_e}$ and, $x = \frac{\omega_p^2}{c^2k^2}$, the plasma frequency is given by $\omega_p^2 = \frac{ne^2}{m\varepsilon_e}$. One of the roots of interest correspond to the long wave length limit for which q/k tends to zero. It is thus approximately found that this root is

$$\omega^2 \approx \frac{m_i}{m_e}\frac{\omega_c^2}{x} \quad (12)$$

Choosing a wave length of the order of a few millimeters (which is observed), the frequency predicted by (13) is a few megacycles which is reasonably close to the frequency observed. The proposition of ion induced instabilities is plausible since the ion's thermal velocity is considerably lower than that of the electron's and as stated above appreciable ion currents are obtained.

On the basis of these arguments, it appears that the thickness of the shock front should be set by a turbulent process associated with the ions. An approximate estimate of the thickness can be obtained by visualizing the moving ions as "colliding" with the small scale fluctuations produced by the instability. The ions distribution function f can be expressed by $f_o + f_i$ where f_i is the perturbation of f_o and which is caused by the fluctuations. The function f_i satisfies the Fokker-Planck equation

$$\frac{\partial f}{\partial t} \sim \frac{\partial}{\partial v}(D\frac{\partial f}{\partial v}) \quad (13)$$

where D the coefficient of diffusion in velocity space. This coefficient is given by[15]

$$D = \frac{2\pi e^2}{\varepsilon_o m}\int dk\, W(k,v) \quad (14)$$

where W is the transverse energy density to the magnetic field. Using (13) and (14), one can estimate roughly the time needed to make the ions isotropic, as a result of these collision with the fluctuating field. This time is

$$\tau = \frac{\langle v^2\rangle}{D} \quad (15)$$

The coefficient D can be calculated from quasi-linear theory. In the same reference (15) it is given by

$$D = \frac{2\pi e^2}{\varepsilon_o m^2}\int dk\, \frac{U(k)}{|v - \frac{d\omega(k)}{dk}|} \quad (16)$$

In the above formula $\omega = \omega(k)$ is the dispersion relation for the plasma and has already been derived in (12). The term U(k) is taken approximately as $\langle \frac{\tilde{B}^2}{2\mu_o}\rangle \delta(k)$, where $\tilde{B}$ is the fluctuating magnetic field. Combining (15) and (16) one finds that in the limit of large wave number

$$\tau = \frac{m\varepsilon_o}{\pi e^2}\frac{\frac{1}{2}m\langle v^2\rangle}{\langle\frac{\tilde{B}^2}{2\mu_o}\rangle}v_t \quad (17)$$

where v_t is an effective transit velocity of the ions in the shock front. Assuming equipartition of the trapped magnetic energy between the ions and the electrons, then direct measurement of the magnetic field fluctuations shows that

$$\langle\frac{\tilde{B}^2}{2\mu_o}\rangle / \frac{1}{2}m\langle v^2\rangle \sim \frac{1}{200}.$$

The shock thickness is now given from (17) by $\frac{v_t}{\tau}$ computer to be 2.8 cm which compares reasonably well with the measured value of 2.2 cm.

REFERENCES

1. See for instance: K. Hain and A. C. Kolb Nuclear Fusion Suppl. Part II, 1962, p. 561; S. C. Lin Jour. Appl. Phys. 25, 54 (1959).
2. K. O. Friedrichs Los Alamos Report LAMS-2105 Sept. 1954; P. Germain Revs. Modern Phys. 32, 951 (1960).
3. J. E. Anderson "Magnetohydrodynamic Shock Waves," (M.I.T. Press, Cambridge, Mass., 1963) p. 31 ff.
4. R. Z. Sagdeev "Reviews of Plasma Physics" (Consultant Bureau, New Yoek, 1966) p. 23 ff.

5. L. C. Burkhardt and R. H. Lovberg Phys. Fluids 5, 341 (1962).

6. H. R. Griem, Plasma Spectroscopy, McGraw-Hill Book Co., New York, p. 281 (1964).

7. O. K. Mawardi, One dimensional blast wave theory in a magneto-plasma. Tech. Rept. No. A-55, July 1967 Plasma Research Program, Case Inst. of Technology.

8. R. H. Block "The Onset of an Electromagnetically Driven Shock" Tech. Rept. No. A-23, July 1963, Plasma Research Program, Case Inst. of Technology.

9. H. W. Liepmann and J. D. Cole in "Plasma Dynamics" (Addison-Wesley, Reading Mass. 1960) p. 198 ff.

10. R. Z. Sagdeev Zh.T.F. 31, 1185 (1961) (Soviet Phys. Technical Phys. 6, 867 (1962)); M. Camac et al., Zs.F. Naturforschg. 13 a, 916, (1958).

11. See Ref. 4.

12. See Ref. 5.

13. C. L. Longmire "Elementary Plasma Physics" (Interscience Publ., New York 1963) p. 31.

14. B. B. Kadomtsev in "Plasma Physics and the Problem of Controlled Thermonuclear Reactions" (pergamon Press, New York, 1960) Vol. IV, p. 431.

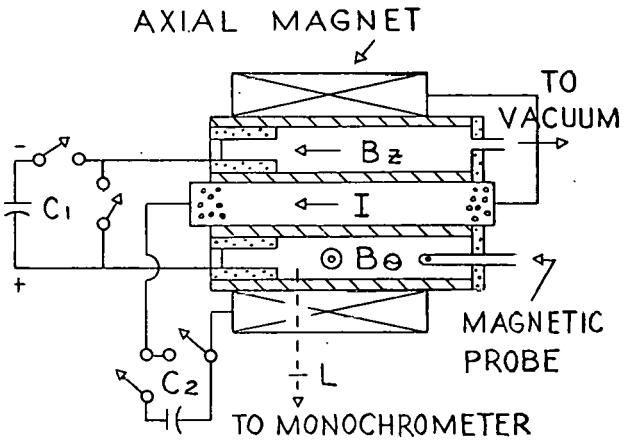

Fig. 1. C1 is 56 μfd, C2 is 14 μfd.

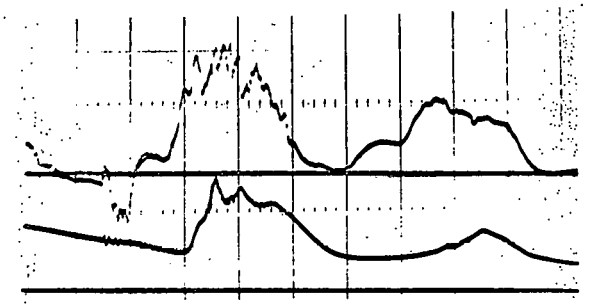

Fig. 2a. Top: E_z Probe (18 v/div); bottom: B_θ probe (1.12 kgauss/div). Time scale: 2 μsec/div. This shows the fluctuations in the fields.

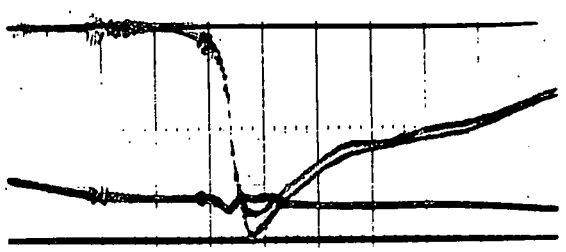

Fig. 2b. Top: Intensity of luminous front. Time scale: 2 μsec/div.

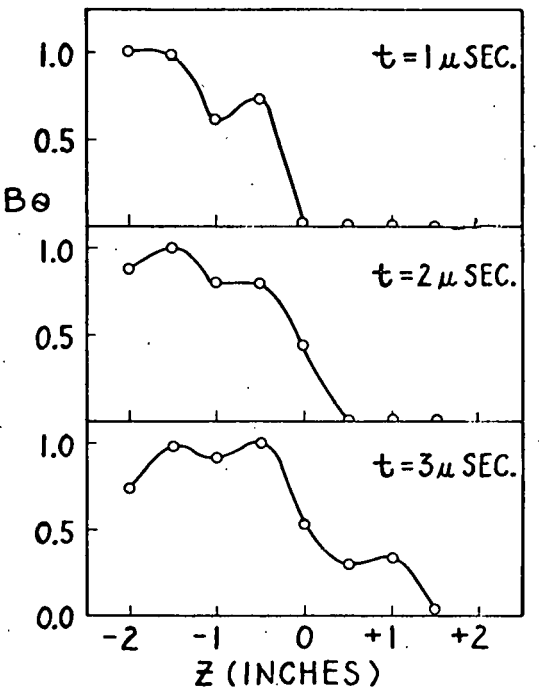

Fig. 3. Spatial dependence of azimuthal magnetic field B_θ at different times. Reference point zero corresponds to muzzle end of gun.

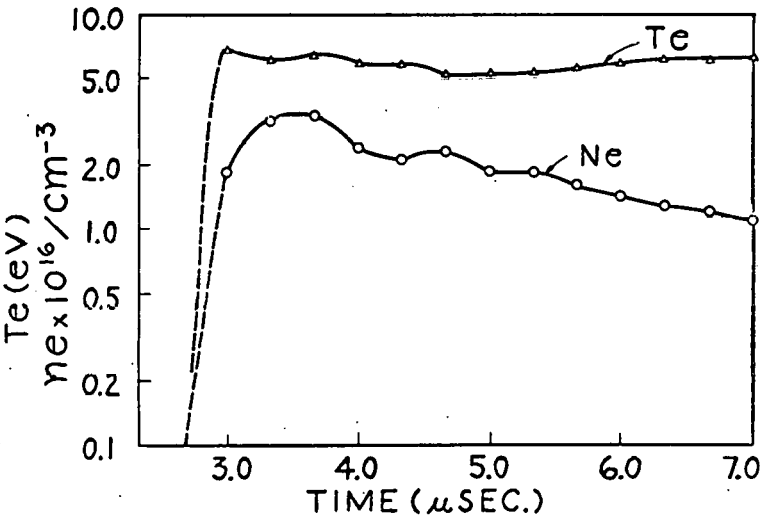

Fig. 4. Profile of electron density (n_e) and temperature (T_e) 2.5 cm from muzzle of gun. Values plotted correspond to a space average and have been estimated by method described in text.

SOME CHARACTERISTICS OF THE DENSE PLASMA FOCUS*

J. W. Mather, P. J. Bottoms, and A. H. Williams
Los Alamos Scientific Laboratory
University of California
Los Alamos, New Mexico

ABSTRACT

The production of hot dense deuterium plasmas $2 \times 10^{19} < n < 2 \times 10^{20}$ with electron temperatures $T_e > 5$ keV have been reported[1,4] using a combination of hydromagnetic plasma acceleration and the fast z pinch effect. The electrical resistance of the current sheath during the acceleration phase and final collapse process has been measured. Values of resistance prior to the moment of collapse and during the last few tenths of centimeters of radial collapse are $\sim 50 \times 10^{-6}$ ohms and $\sim 8 \times 10^{-3}$ ohms respectively. The former value corresponds to $T_e \sim 60$ eV. The plasma emits a copious supply of X-rays with energies up to ~ 60 keV. If X-rays of energies $\gg 60$ keV are produced[2], their contribution appears negligible in comparison. A bent crystal X-ray spectrometer is being used to determine the spectral distribution of the X-ray source. The results if obtained will be discussed. Hydrodynamic models[10] are now available which show qualitatively the dynamical behavior of the dense plasma focus device; however, the heating of the plasma electrons to temperatures $T_e \sim 5$ keV is not predicted by these models ($\omega\tau > 1$). Other heating schemes will be discussed.

INTRODUCTION

The production of hot dense plasmas have been reported[1-4] using a combination of hydromagnetic plasma acceleration and the fast z-pinch effect. The compressive force produced by the self magnetic field of the axisymmetric current sheath rapidly heats the deuterium ions in a few tenths of microseconds or less during the collapse process. Average collapse velocities reach $4\text{-}5 \times 10^7$ cm/sec whereas instantaneous sheath velocities $> 6 \times 10^7$ cm/sec would be predicted in the last few millimeters of radius due to the inverse radius squared dependence of the driving magnetic field pressure. Due to the two dimensional character of the compression f (rz), it is expected that a major fraction of the gas encountered in the collapse is ejected or caused to stream away from the dense plasma region. Plasma densities of $n \geq 2 \times 10^{19}$ particles/cc and millimeter dimensions suggest that only a fraction ($\sim 2\text{-}5\%$) of the gas is actually trapped by the sheath during the collapse process.

*Work performed under the auspices of the U. S. Atomic Energy Commission and Defense Atomic Support Agency.

THE APPARATUS

The schematic diagram of the experimental arrangement is shown in Fig. 1. A detailed description of the apparatus and the general layout of the electrical circuit and condenser bank is described elsewhere.[1] The condenser energy ranges from ~ 18 kJ to 43 kJ. The outer and inner electrode diameter are typically 10 and 5 cm respectively with a length of ~ 17.5 cm. The outer electrode is either of honeycomb construction or fabricated in squirrel cage geometry. Deuterium pressures range from 4-12 torr. The dynamical behavior[5] of the current sheath is determined from the current, voltage and plasma sheath resistance measurements. A typical current (upper) and voltage (lower) signal is shown in Fig. 2. The sharp drop in the current at peak current time and the simultaneous increase in the voltage (V) measured at the breech characterizes a large inductive change due to the rapid collapse of the current sheath off the end of the electrode. Sweep speed is 0.5 μsec/cm. The actual voltage V_p appearing across the plasma sheath during the pinch stage is related to V by $V_p = V\, L_T/L_e$ where L_T is the sum of the discharge and external inductances and L_e is the external inductance. This ratio is typically ~ 3. In Fig. 2, the voltage

scale is 12 kV per large division.

ENERGY DISTRIBUTION OF NEUTRONS

The study of the neutron energy spectrum from the plasma focus should in principle help in determining whether an accelerated or thermal mechanism is responsible for neutron production. Although past neutron flux measurements[3,4] have indicated a spatial neutron isotropy ≥ 95%, there seems to be some question as to the neutron energy spread. Very preliminary neutron energy measurements in the 0-90° and 0-180° directions indicate that the energy spread is ≤ 10%.[6] Some measurements are as low as 2%. If one examines the maximum increase in neutron velocity $\Delta v \sim 1.2 \times 10^8$ cm/sec in terms of an acceleration of a deuteron into a target deuteron at rest (target theory), then the deuteron in the laboratory frame would be required to have ~ 50 keV. On the other hand if the neutrons are emitted from a dense thermal plasma which is moving as a whole away from the center electrode, (boiler mechanism), a value of ~ 12.5 keV would be calculated for each deuteron in the moving plasma. Since the spatial anisotropy of neutron production is ≤ 5% and since one would expect a greater anisotropy (~ 30% in the 0-180° direction) under a target theory assumption, the moving dense thermal plasma mechanism is favored. From Fig. 4b, the velocity of the on-axis high density region during the last few moments of collapse may reach $7\text{-}9 \times 10^7$ cm/sec during neutron production. This mechanism may account in part for the observed neutron energy shifts.

GENERAL REMARKS ON X-RAYS

At least two sources of intense X-rays are evident in the plasma focus discharge. Pinhole camera X-ray photographs, one of which is shown in Fig. 3 shows that X-ray emission comes from the face of the positive center electrode and from the plasma foci formed ~ 1-2 cm away. Negative center electrodes reduce the surface emission to a negligible value. By virtue of the fact that pinch voltages V_p of the order of 60-100 kV are generated by the collapsing current sheath, it is reasonable to expect that some fraction of the plasma electrons in the sheath will be accelerated toward the electrode. In this case the x-ray emission would be characterized by the ordinary thick target bremstrahlung in addition to the fluorescent radiation.

If all the electrons in the current sheath (~ 500 kA) are accelerated to 50 kV in a time of 50 ns into a tungsten target, then a thick target calculation would yield ~ 4 joules of x-rays. This estimate, although reasonable, would require ~ 1300 joules of high energy electrons. Since the energy supplied to the fast collapse comes primarily from the stored inductive energy behind the current front, it would seem difficult to obtain an additional 1300 joules and still maintain energy balance.[6] Nevertheless, because of the complexity of the problem, this possibility remains.

A bent crystal x-ray spectrometer[7] has been designed to study the x-ray spectral distribution from the plasma. Bent crystals of Mica and LiF[8] are used to cover the energy range from ~ 0.7 keV to 25 keV. The diffracting surface is placed ~ 35 cm from the axis of the discharge and a two aperture collimator defines the x-ray beam so that ≈ 3 mm of the plasma source can be seen. The spectrometer is movable along the axis of the chamber with a micrometer screw to obtain a mapping of the region of x-rays. The spectrometer can be evacuated to reduce the air absorption at lower energies. A thin aluminum foil fits over the last aperture to provide a vacuum and light seal.

This type of spectrometer has the advantage of surveying many energies with good dispersion for a few discharges, however, it has the disadvantage of low reflection efficiency. For example, with reflection efficiences of 10^{-3} - 10^{-5}, a primary photon beam intensity in the neighborhood of 10^{10} - 10^{12} photons/cm^2 is required.

In the first use of this instrument which employed a Mica crystal (2d spacing = 19.9 A°), no characteristic lines were observed of brightness above the general background. The background film density in this case was abnormally high to draw any firm conclusion. Investigation of the background intensity was made by studying the intensity of X-rays emitted through the Pyrex glass chamber wall. From the intensity versus absorber thickness of copper and lead, values of X-ray energies in the vicinity of 50 - 60 keV are indicated. The X-ray intensity was recorded by calibrated ionization chambers over an intensity ratio of ~ 100. If

higher energies are present, their contribution to the intensity is small. A check of the X-ray intensity was made also with thermoluminescent (TLD) LiF detectors[9] which have an approximate flat response over the range of 10 keV to 1 MeV. Typical values of the X-ray intensity at a distance of ~ 11 cm from the tube axis ranged from 6-10R per discharge. The TLD detector is in the form of a 1 cm diameter disc of Teflon ~ 5 mils thick in which is embedded LiF crystals. The intensity of the 50-60 keV X-rays appear to come from a central source extending a distance of ~ 3-4 cm beyond the end of the central electrode.

THEORETICAL STUDY

A preliminary study[10] of the dense plasma focus discharge has been made using a two-dimensional (2D) magnetohydrodynamic code. Some results of this study are shown in Fig. 4 and 5 which pertain to the most interesting and least understood region of the dense plasma discharge. The inclusion of this work is not to be construed as a final or complete discussion of the phenomena but rather to show some of the plasma characteristics that are not experimentally complete. Much of the information calculated such as the rate of change of the tube inductance, sheath velocity, kinetic energy and the time history of the sheath resistance during the passage of the current sheath in the accelerator has been omitted simply on the basis that the experimental results and the calculations are in good agreement. These experimental qualities have been reported.[5]

The 2D formulation utilizes Eulerian hydrodynamics with variable grid mesh size. In those regions of interest, smaller mesh is used. The code treats both ions and electrons as fluids with temperatures T_i and T_e, assumes that the outer electrode is impervium and acts as a heat sink, ie, it is a boundary condition on the problem, assumes that the electrons lose energy by radiation, includes thermal conduction by electrons but not by ions and that the ohmic heating is due to a resistance given by the $T_e^{3/2}$ relationship of Spitzer. The discharge is started at the breech by providing a conducting layer of ~ 1 eV temperature. Maxwell's equation determine the magnetic fields. No material is assumed to come from the surface of the electrodes to be part of pressure balance.

The gas sheath profiles, not shown here, show that the current flows mostly in the forward part of the sheath and that very little current is in the gas near the wall. This result has been obtained with magnetic probes.[1] The calculation indicates that the sheath thickness is ~ 1 cm midway in the annular region and that the frontal part is canted backwards from the inner to the outer electrode. T_e and T_i at the midpoint of the sheath increases from ~ 18 - 25 eV during the acceleration phase; the sheath velocity is ~ 10 cm/μsec.

Figure 4b shows a r, z plot of the current paths at and beyond the end of the center electrode. The solid and dotted lines refer to the forward and rear portion of the current sheath respectively. Four such configurations are shown; one prior to collapse at 2.97 μsec and three at times of 3.22, 3.28 and 3.29 μsec during the collapse stage. It is curious that two high density regions form, one on-axis and one off-axis. No explanation at this time is offered for this result.

Figure 4a shows the z position dependence of the gas density, electron temperature and the ion temperature at a time of 3.2 μsec. The gas density ($\sim 10^{-8}$ gr/cc) near the face of the center electrode actually falls below ambient (2×10^{-7} gr/cc) but increases to a peak density of 1.8×10^{-6} gr/cc at ~ 2 cm from the electrode. If the low mass density near the electrode is true, then current starvation would cause large voltages to be generated. It appears experimentally that sufficient gas density may be produced by the vaporization of the electrode surface due to the inward sweeping of the collapsed current across the electrode. The peak density of 1.8×10^{-6} gr/cc is low by a factor of ~ 30 if the measured density[3,11] of ~ 2×10^{19}/cc is correct. The peak electron temperature of 0.87 keV is low compared to experimental values of 5-7 keV. The plasma focus discharge is a copious emitter of x-rays some of which comes from a hot plasma. The 2-D code, at least at this stage, can not develop high electron temperatures. This is due in part to the fact that the collisional mean free path is much longer than the dimensions of the plasma, ie, $\omega\tau \gg 1$. At this stage a pure hydrodynamic electron heating process is probably not valid. This result does not detract from the over-

all success of the code, rather it means that other heating processes must be considered during the last moments of collapse in order to achieve high electron temperatures. The ion temperature at 3.2 μsec drops within a distance of ~ 1/2 cm from 26 to ~ 2 keV. Part of the ion curve not included here, extends into low density regions behind the current front to larger temperature values. The temperature in these regions are not believed -- in the future, the inclusion of the ion conduction and viscosity terms may reduce the effect considerably.[12] At z ~ 2 cm T_i ~ 1.5-2 keV.

Figure 5 shows the time history of neutron production and the trajectories of the off-axis and on-axis high ρ regions. The z coordinate is measured from the center electrode. There is general motion of the dense region; the velocity of the on-axis region at first moves slower than the off-axis region but eventually the velocity of the off-axis region decreases almost to zero. The on axis velocity at the time of neutron emission increases to ~ 8 x 10^7 cm/sec and becomes larger later. This motion could produce the so called moving "boiler" mechanism of neutron production. Some of the neutron energy measurements indicate such a mechanism. The neutron production of 2×10^{10} neutrons is in good agreement with the experimental results (~ 10^{10}) within a factor of 2-3. The neutron production is calculated by integrating $n^2 \langle \sigma v \rangle$ over the axial region extending from the center electrode. The contribution to the neutron pulse is small in the regions of high T_i and low density. By and large the emission is produced near z ~ 2 cm for a T_i ~ 1.5 keV and a mass density of ~ 1.8 x 10^{-6} gr/cc.

SUMMARY

The determination of the neutron energy spectrun should lead to a better understanding of the mechanisms responsible for neutron production. In addition to the target theory and the moving thermal plasma (boiler) mechanism, there may be other exotic schemes which involve plasma vortices.[12]

The spectral distribution of X-rays and their time dependence as a function of distance from the center electrode should help immeasurably in the understanding of X ray production from the plasma focus. It would seem that the addition of small percentages of high Z contaminants to the deuterium plasma focus should increase the X-ray output.

ACKNOWLEDGMENTS

The authors wish to express their thanks to J. LeBlanc and J. Wilson for the magnetohydrodynamic study of the plasma focus and for permission to include pertinent data herein. The authors are grateful to R. Henson for his collaboration and to G. Livermore, J. Murphy and L. Mitchell for their invaluable technical assistance.

REFERENCES

1. Mather, J. W., Physics of Fluids 8, 366 (1965).
2. Filippov, N. V., Filippova, T. I., & Vinogradov, V. P., Nuclear Fusion Suppl. Pt. 2 577 (1962).
3. Mather, J. W., Plasma Physics & Controlled Nuclear Fusion Vol. II, IAEA 389 (1966). (See additional references noted there).
4. Filippov, N. V., & Filippova T. I., Plasma Physics & Controlled Nuclear Fusion Vol. II, IAEA (1966).
5. Mather, J. W. and Bottoms, P. J., Los Alamos Scientific Laboratory Report LA-DC 8229, Phys. of Fluids (In Press) 1967.
6. See papers of this conference.
7. Henke, Burt, Dept. of Physics, Pomona College, Calif. (Private Communication) 1966.
8. Birks, L. S., U.S. Naval Research Laboratory (Private Communication) 1967.
9. Bemis, E., Los Alamos Scientific Laboratory (Private Communication) 1967.
10. This work is included in part through the courtesy of J. LeBlanc and J. Wilson, Livermore Radiation Laboratory (Private Communication) 1967.
11. Mather, J. W., Los Alamos Scientific Laboratory Report LA-3334 MS (1965).
12. Bostick, W. H.; Prior, W., Grundberger, L., and Emmert, G., Physics of Fluids 9, 2078 (1966).

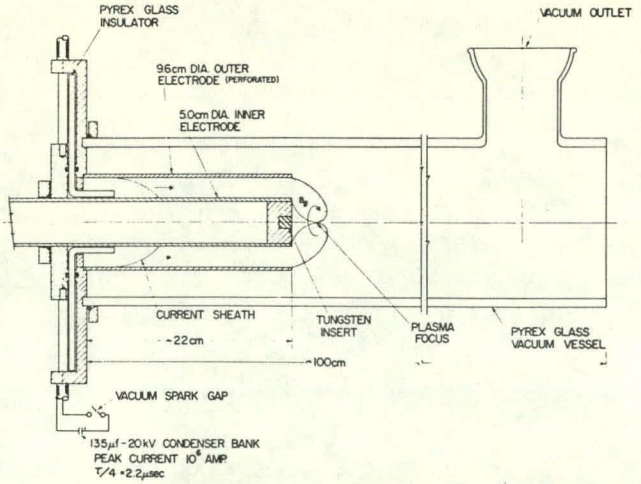

Fig. 1. Schematic diagram of the plasma discharge.

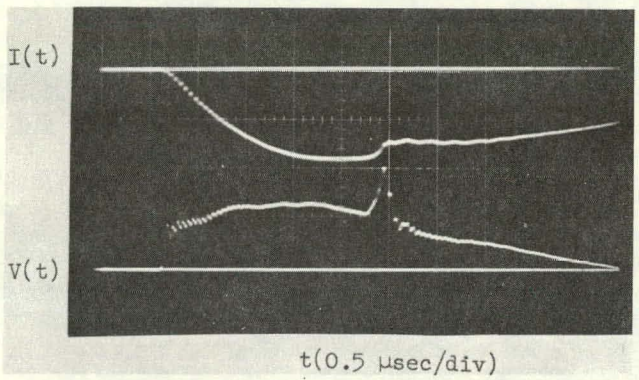

Fig. 2. Breech voltage (lower) and current (upper) signals. Sweep speed: 0.5 μsec/cm. Voltage calibration: 15 kV/cm.

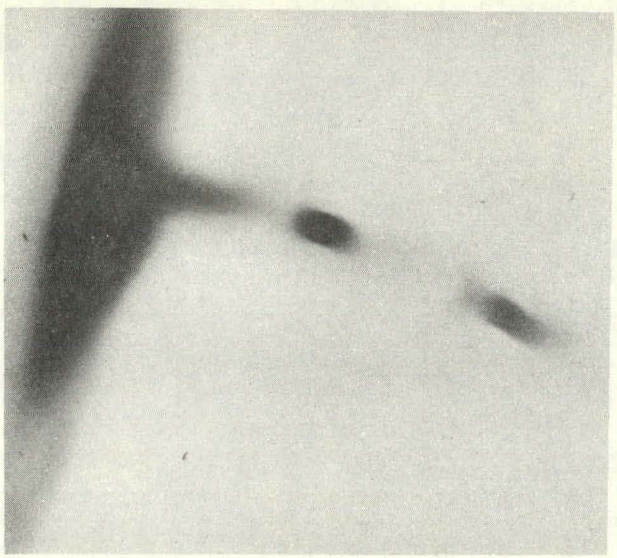

Fig. 3. Soft x-ray pinhole camera photograph. Center electrode is at left.

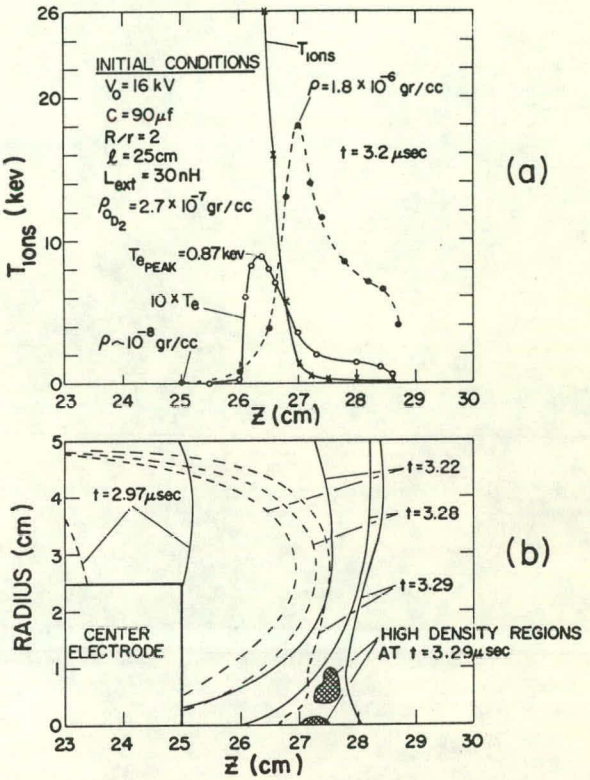

Fig. 4. Results of 2-D computation
a. T_i, T_e and mass density ρ versus position from center electrode.
b. Current paths during collapse - the solid and dotted lines represent the front and back, respectively, of the current sheath. The shaded areas are the on and off axis high ρ position.

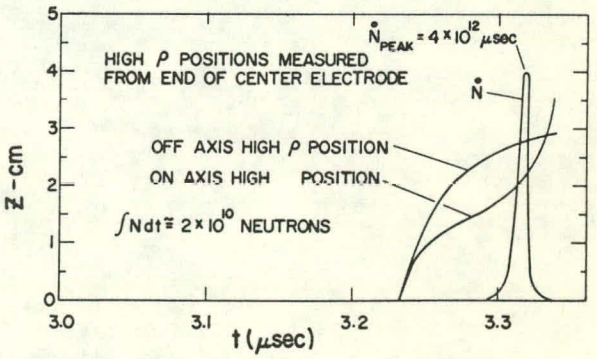

Fig. 5. Results of 2-D computation: high ρ positions and neutron rate versus time.

DYNAMICS AND NEUTRONS EMISSION OF A PLASMA FOCUS EXPERIMENT

by

C. PATOU, A. SIMONNET, J.P. WATTEAU

C.E.A., B.P. 511-15 PARIS 15ème FRANCE

ABSTRACT

A coaxial non cylindrical discharge is produced in an experimental apparatus similar to that of MATHER /1/.

The snow-plow model was used to study the dynamics of the discharge in its two phases : axial acceleration followed by a radial compression in front of the inner electrode. The mass accelerated in the first phase is not dragged along in the radial compression which occurs at peak current. The efficiency of the heating is due to the small mass of plasma which is compressed in the second phase. The stored magnetic energy is partially transferred to the plasma at the end of the compression and the measured neutron yield seems to increase with the part of the magnetic energy transferred.

A study of the neutron yield was done on two hundred shots with the following experimental conditions = 18 kV voltage, 15 kJ energy, 500 kA peak electrical current, 3.3 Torr total filling pressure. Experiments were made either with pure deuterium or with a 50/50 mixture of deuterium and tritium. With pure deuterium the average yield is 1.4×10^9 neutrons. It is half when adding 0.6 per cent of Xenon, while the dispersion is three times smaller. With deuterium and tritium the neutron yield is approximately thirty times larger. The neutron durations are 80 ns with deuterium and 40 ns with deuterium and tritium.

INTRODUCTION

A coaxial non-cylindrical electrical discharge energized by a capacitor bank is produced in an experimental apparatus similar to that of MATHER /1/. An axial motion along the electrodes is followed by a radial compression before the inner electrode. The parameters have been chosen so that the electrical current reaches its peak value when the radial compression begins. They are : filling pressure 3.3 Torr, bank capacity 90 uF, charging voltage 18 kV and positive polarity on the inner electrode.

DYNAMICS AND ENERGY BALANCE

The snow-plow model /2/ was applied separately to the axial motion and to the radial compression.

Axial motion

The magnetic piston is a plasma annulus guided by the two coaxial electrodes. The annulus is divided in elementary annuli of unit width supposed independant of one another. Their motion is then purely axial and for the one of radius r_o the equation is

$$\frac{d}{dt}\left[2\pi r_0 \rho_0 z \frac{dz}{dt}\right] = 2\pi r_0 \frac{\mu_0}{2}\left(\frac{I}{2\pi r_0}\right)^2 \qquad (1)$$

in which ρ_0 is the gas density

Computations were done using the measured electrical current curve for various values of r_o. They indicate the piston reaches the open end of the electrodes 2.1 μs after the electrical breakdown. The measured value obtained from a framing camera is 2.2 μs and it corresponds to the zero value of $\frac{dI}{dt}$. This simple theoretical model gives good account of the dynamics and the energy balance to the exception of the front curvature. But this curvature is made to agree with experiment in a two dimensions snow-plow model /3/ in which the front location at different times has been shown (fig. 1).

Radial compression

Dynamics (fig. 2). When the plasma reaches the electrodes end we assume its motion goes on axially with the exception of a small part that is then

radially compressed. Let m_o and v_o be its mass and its initial radial velocity. The motion equation is

$$\frac{d}{dt}\left\{\left[m_o + \pi\rho_o\left(R_c^2 - R^2\right)\right]\frac{dR}{dt}\right\} = -2\pi R\,\frac{\mu_o}{2}\left(\frac{I}{2\pi R}\right)^2 \quad (2)$$

in which the initial value of radius R is R_c the inner electrode radius. Let I_M be the current peak value and t_c, α , β defined by,

$$\frac{\mu_o}{2}\left[\frac{I_M}{2\pi R_c}\right]^2 = \frac{\rho_o}{2}\left[\frac{R_c}{t_c}\right]^2 \qquad \alpha = \frac{m_o}{\pi R_c^2 \rho_o} \quad (3)$$

$$\beta = \frac{v_o}{\left(R_c/t_c\right)} \quad (4)$$

In the calculation we took

$$I = I_M\left[1 - \frac{0.2\,t}{t_c}\right]$$

which takes into account the current decrease. Equation (2) was computed for various values of α and β . For α = 0.1 and β = 0 the theoretical and experimental variations of R (t) approximately coincide (fig. 3). The α value shows that a very small part of the plasma gathered during the axial motion is taken in the radial compression.

Energy balance. Fig. 4 shows the oscillograms of the current derivative ($\frac{dI}{dt}$) and the voltage across the electrodes at the insulator end (V). From these were calculated the variations of the current I of the chamber inductance ℓ and of the energy E brought to the plasma during the compression. The energy increase is

$$\Delta E = \int_{t_o}^{t} VI\,dt - \frac{1}{2}\left[\ell I^2 - \ell_o I_M^2\right] \quad (5)$$

in which t_o is the start of the compression. At $t = t_o$, I_M = 500 kA, $\ell = \ell_o$ = 25 nH.

Δ E is mainly due to the decrease during the compression of the magnetic energy stored by the circuit in the phase of axial motion. Fig. 5 shows that the neutron yield grows with the energy brought to the plasma during the compression phase.

NEUTRON EMISSION

Chamber filled with deuterium

At every shot the neutron number N is measured by activation (Rhodium and Silver) with 15 per cent accuracy. The lecture of nuclear plates (Ilford 400 μ) led to a value of N in agreement with that found by activation. The following procedure is used for measurements. The gas is changed every ten shots. The statistics (fig. 6) is done on 160 shots, three of which were below the detection threshold (10^7 neutrons in 4π ster.). Fig. 6a shows the number of shots versus neutron yield. The most probable value is 1.4×10^9 neutrons per shot. The first shot after a new filling gives 3×10^9 neutrons on an average.

In a similar experiment with different geometrical dimensions however FILIPOV [4], [5] noticed that adding 2 per cent Xenon to deuterium makes the discharge stabler and increases the neutron yield. When we add 0.6 per cent Xenon the discharge is indeed more reproducible as well as the neutron emission (fig. 6b). But the most probable value of N is half. We were not able to increase N in varying the xenon quantity for the chosen parameters.

A neutron yield larger than 10^7 usually occurs when $\frac{dI}{dt}$ reaches its minimum value. The concurrence is better than 5 ns in most shots. But the emission can start up to 20 ns before this time. When there is just one neutron pulse, its mean rise time and half width are 40 ns and 80 ns respectively.

Chamber filled with a deuterium-tritium mixture

The total pressure is kept at the same value (3.3 Torr) as well as the other parameters. Two mixtures were used : one with 10 per cent tritium (DT 10) and the other with 50 per cent tritium (DT 50). We measured the number of neutrons whose energy is larger than 8 MeV by copper activation. The maximum yield observed for DT 50 is 2.10^{11} neutrons.

The average neutron yield is proportional to 1, 10, 30 for deuterium, DT 10, DT 50, respectively. These figures are consistant with those obtained from nuclear plates. If a thermonuclear origin is assumed at the same temperature 1 keV in all three cases, the ratios should be 1, 15, 35. They would become 1, 35, 100 at temperature 5 keV.

With the DT 50 mixture the pulse rise time and half-width are about 20 ns and 35 ns respectively. These measurements differ from those MATHER[6] obtained with the same mixture. He found the neutron yield to be 100 times larger than with deuterium and the pulse to last 300 ns approximately.

CONCLUSION

The snow-plow model explains the axial motion and it seems to show that at the end of this phase a small part of the gathered plasma only is radially compressed before the inner electrode. The neutron emission increases with the energy transfered to the plasma during the radial compression but its characteristics are different from those already published by other authors.

REFERENCES

/1/ MATHER (J.W.).- High density deuterium plasma focus.- Physics of Fluids Vol. 8, n° 2, 1965, p. 367.

/2/ ROSENBLUTH (M.), GARWIN (R.), ROSENBLUTH (A.) Infinite conductivity theory for the pinch.- Los Alamos Scientific Laboratory, Report LA 1850, 1954.

/3/ COUDEVILLE (A.), JOLAS (A.), WATTEAU (J.P.).- Production of neutrons by a non-cylindrical Z pinch.- Pulsed High Density Plasmas Conference, Los Alamos, September 19-22, 1967.

/4/ FILIPOV (NV), FILIPOVA (TI).- Phenomena following the formation of a dense plasma focus in the cumulation of a non-cylindrical Z pinch.- LATR 6526, 1965.

/5/ FILIPOV (NV), FILIPOVA (TI), VINOGRADOV (VP).- Conference on Plasma Physics and Controlled Nuclear Fusion Research, CN 10/226, Saltzburg 1961.

/6/ MATHER (J.W.).- High density deuterium plasma focus.- CN 21/80, Culham 1965.

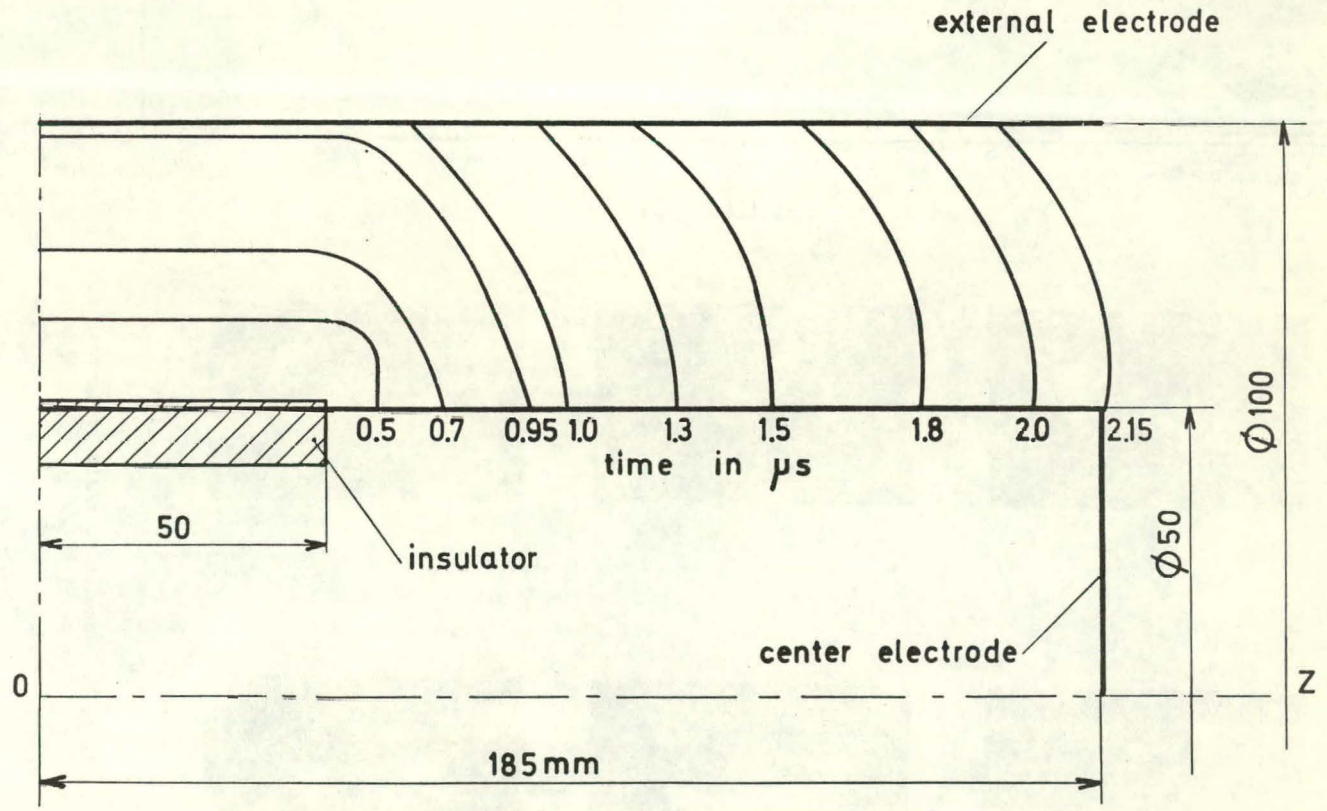

Fig. 1 Front location at different times of the axial motion obtained from two dimensions snow-plow model.

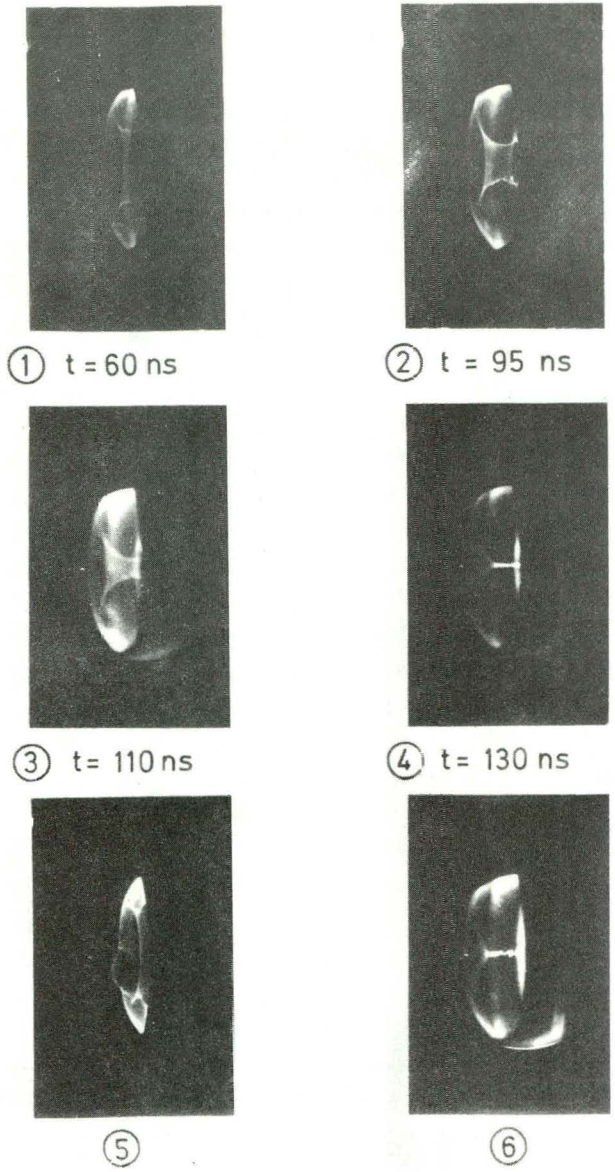

Fig. 2 1, 2, 3, 4 Dynamics of radial compression
5, 6 Instabilities of plasma front
(time exposure 1 ns).

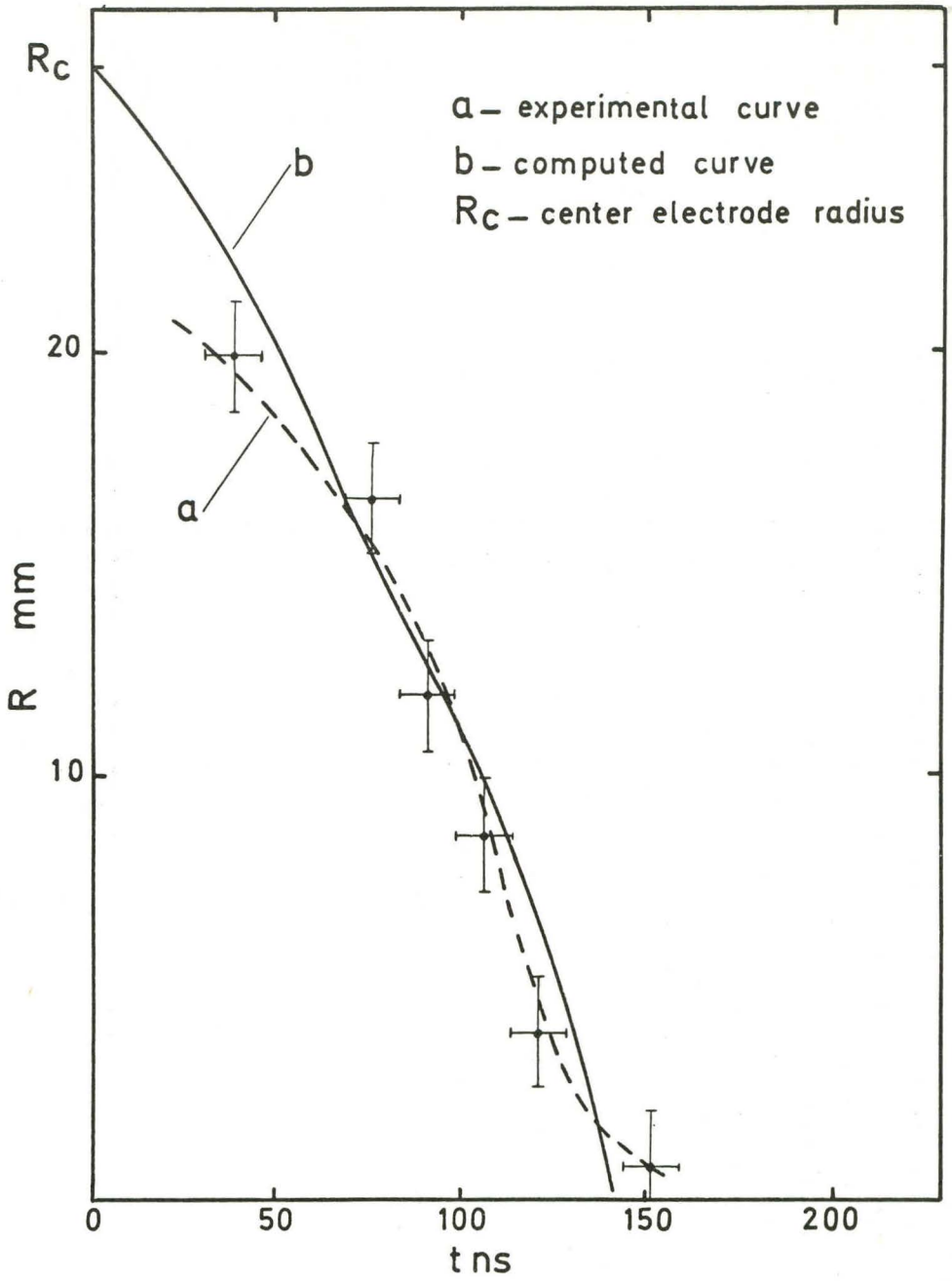

Fig. 3 Radius of discharge versus time.

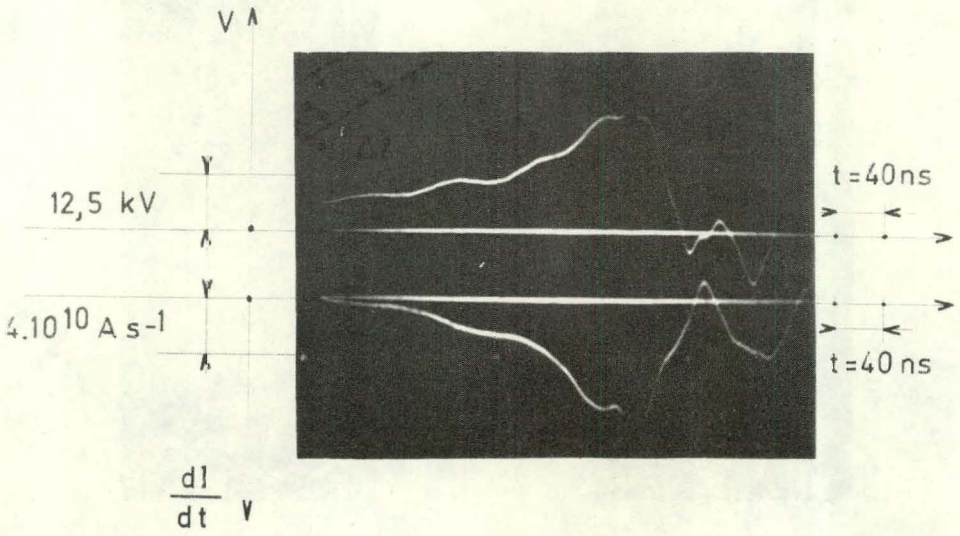

Fig. 4 Typical oscillograms of V and $\frac{dI}{dt}$ for radial compression.

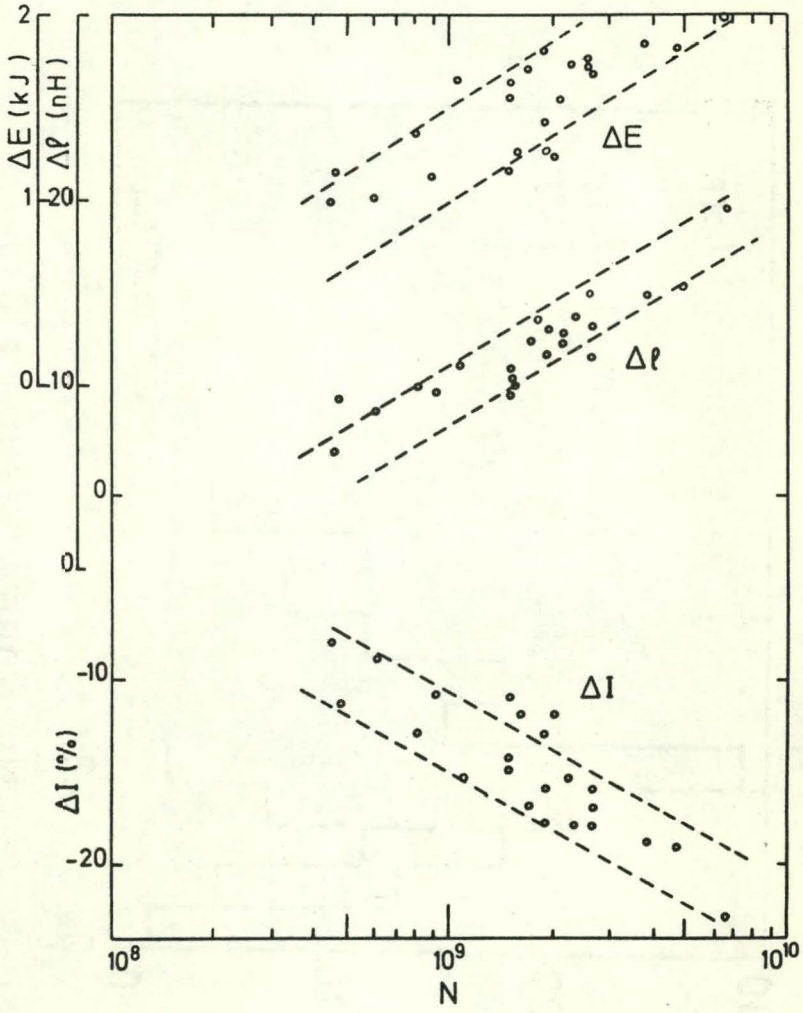

Fig. 5 Variation of current I, inductance ℓ and energy E during the radial compression versus the neutron yield N.

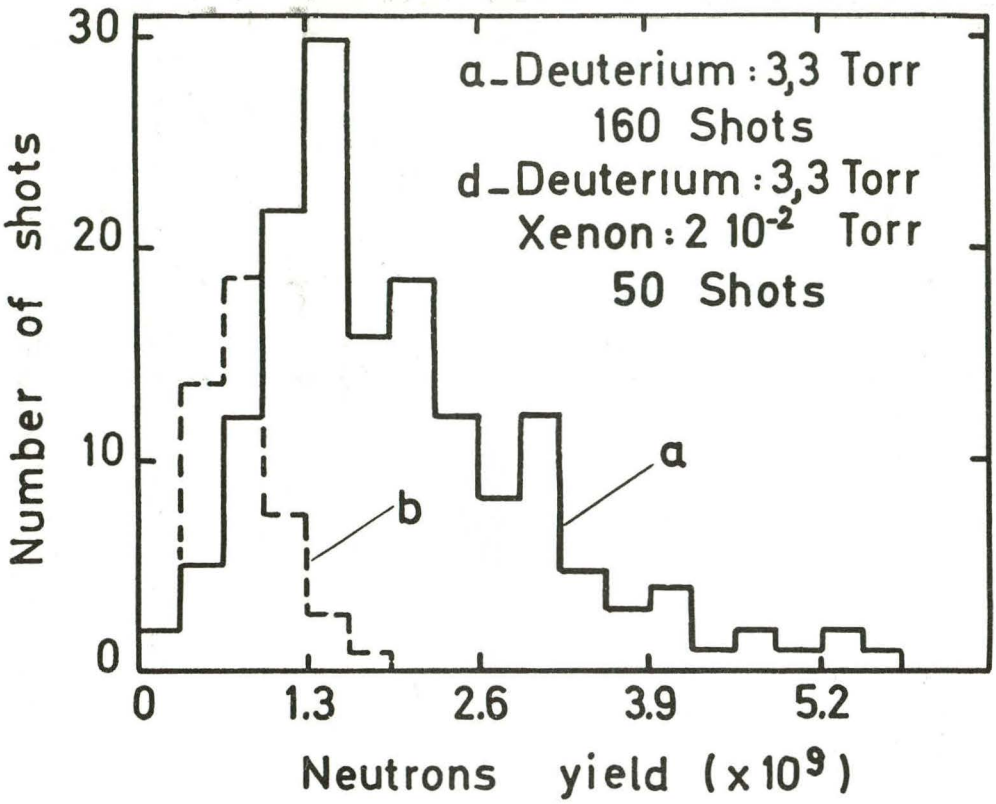

Fig. 6 Statistics of neutron emission.

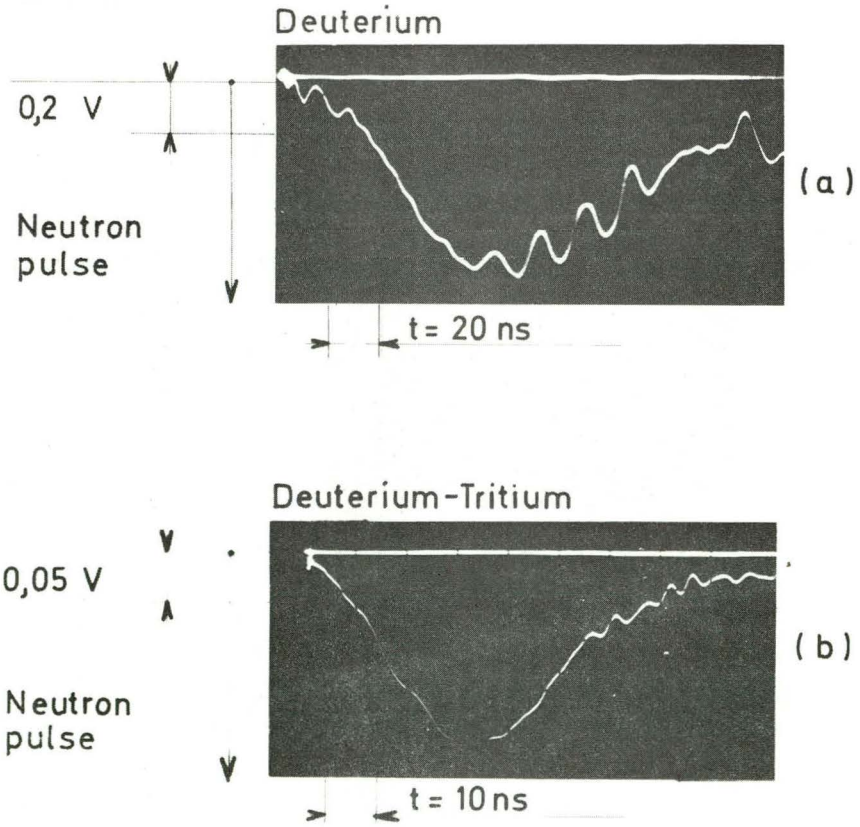

Fig. 7 Typical oscillograms of neutron pulse.

PRODUCTION OF NEUTRONS BY A NON-CYLINDRICAL Z PINCH

by

A. COUDEVILLE, A. JOLAS, J.P. WATTEAU

C.E.A., B.P. 511-15 PARIS 15ème FRANCE

ABSTRACT

To gather the plasma of a Z pinch a non-cylindrical insulator shape was used. The pyrex chamber has two symmetrical narrowings where the pinch effect develops more rapidly. In order to explain the discharge dynamics a two dimensions snowplough model was developed. The system of momentum and electrical equations was solved with calculations performed on computers. To check the validity of the model the shape of the plasma column and the current are compared with experimental data from framing pictures and electrical measurements. A comparison can be made with other non-cylindrical discharges like those studied by FILIPOV and MATHER. With a 1 torr deuterium pressure and an energy of 3 kJ, when the current reaches 100 kA a fast and strong decrease of the current derivative together with a simultaneous pulse of up to 5.10^6 neutrons are observed. Tentative explanations are proposed.

INTRODUCTION

To realize a cusped geometry in which $\beta = 1$ a z pinch plasma is confined by an increasing cusp magnetic field /1/. To gather the plasma in the center of the confinement region we gave the plasma chamber a non-cylindrical shape. A two dimensions snowplough model was used to study the discharge dynamics. In particular experimental conditions a neutron emission is observed.

EXPERIMENT

The discharge chamber made of pyrex is swollen in its center part with two symmetrical narrowings (fig. 1-a). It is one meter long, 18 cm in mean diameter, and filled with 1 torr deuterium. A 90 kV 14 kJ capacitor bank produces a current I of 190 kA with an initial rise time of 3.10^{11} A.s^{-1}. Framing pictures of the discharge (10 ns exposure time) show that the compression is faster in the narrowings (fig. 2). A pressure gradient occurs along the axis that causes the ejection of plasma on both sides of the two narrowings and generates axial shock waves. Part of the plasma jets from the two narrowings is gathered in the cusp confinement region.

DISCHARGE DYNAMICS

The discharge being non-cylindrical a two dimensions snowplough model is used. The current sheath motion can be described as follows (fig. 1-b). A point M of the current sheath originated in M_o at the internal insulator surface. M_o is defined by parameter λ. M is then a function of λ and time t. The mass dm of a current sheath element corresponding to $d\lambda$ is equal to :

$$dm = \int_o^t \rho . 2\pi r \left| \frac{\partial \vec{OM}}{\partial \lambda} d\lambda \times \frac{\partial \vec{OM}}{\partial t} dt \right|$$

in which ρ is the specific mass of the gas. The force $\vec{df}$ acting on this element is :

$$\vec{df} = 2\pi r \left| \frac{\partial \vec{OM}}{\partial \lambda} \right| d\lambda . \frac{\mu_o}{2} \left(\frac{I}{2\pi r} \right)^2 \vec{n}$$

in which $\mu_o = 4\pi . 10^{-7}$, and $\vec{n}$ is a unit vector normal to the current sheath and directed towards the plasma. The trajectory of any point M is given by the snowplough equation /2/,

$$\frac{d}{dt} \left[\frac{\partial \vec{OM}}{\partial t} . \int_o^t r . \left| \frac{\partial \vec{OM}}{\partial \lambda} \times \frac{\partial \vec{OM}}{\partial t} \right| dt \right] = \frac{\mu_o}{8\pi^2 \rho} . \left| \frac{\partial \vec{OM}}{\partial \lambda} \right| . \frac{I^2}{r} . \vec{n} \quad (1)$$

The equation of the electrical circuit is :

$$V_o - \frac{1}{C} \int_o^t I dt = RI + \frac{d(LI)}{dt} \quad (2)$$

in which V_o and C are the bank charging voltage and capacity, R and L the resistance and inductance (functions of time). Equations (1) and (2) are linked by terms I and L. At first equation (1) was numerically solved in which I was the experimentally measured current. The system of equations (1) and (2) was then solved with constant R. Figures (3) and (4) show reasonable agreement between the luminous front and the computed current sheath in the narrowings of the chamber, particularly for their minimum radius r_m (fig. 3).

NEUTRON EMISSION

This discharge is non-cylindrical as in the focus experiments of FILIPOV and MATHER /3/ /4/ and we were induced to look for a neutron emission with particular initial conditions.

The discharge chamber used is two times smaller and energized by another 50 kV - 37 kJ capacitor bank. A BF_3 counter and a scintillator give the neutron yield N and its derivative $\frac{dN}{dt}_{V_o}$. When pressure ranges from 1 to 2 torr and V_o from 10 to 15 kV, a neutron yield up to 5.10^6 is measured. The neutron pulse has an average 200 ns width and is simultaneous with the $\frac{dI}{dt}$ and discharge voltage V pulses (fig. 5).

Tentative explanations

The current sheath dynamics is computed from the preceding two dimensions snowplough model with constant R. Let us introduce the compression ratio τ_m (initial to final radius) corresponding to the minimum narrowing radius r_m (t), and the mass ρ_e, the kinetic energy e_c and the inelastic collisions energy e_T per unit length of the current sheath. Figure 6 indicates for V_o = 14 kV the shape of the current sheath and the location of mass and energies at time t = 1,3 µs for which τ_m = 52. The plasma energy is located in the narrowings but the final density and temperature of 10^{20} cm^{-3} and 37 eV cannot explain a thermonuclear neutron emission.

Comparison is made between measured (a) and computed (b) curves of I and $\frac{dI}{dt}$ (fig. 7). The derivatives do not superimpose due to the instantaneous conduction assumed in the computation. It is experimentally progressive, and in equation (2) the resistive term RI is larger than the inductance one $\frac{d(LI)}{dt}$ during t_R = 250 ns for which the current sheath starts to move radially. A t_R translation makes the two $\frac{dI}{dt}$ curves coincide (dotted curve). When the current sheath reaches the axis (t = 1,5 µs) they become different again as the experimental compression ratio τ_m is limited by the plasma pressure. The framing pictures show that the plasma column then stretches along the axis in each narrowing until an instability occurs (t = 1,8 µs) and breaks it apart. This produces a pulse on the (a) $\frac{dI}{dt}$ curve which would be obtained for high τ_m values (fig. 7 curve (b)) without instability of the current sheath.

From measured electrical values and computed density and temperature the calculated neutron yield of a m = 0 instability in the narrowing center is 10^5. This value is a lower yield since the current of accelerated particles is supposed to be limited by space charge /5/.

CONCLUSION

In experiments of references /3/, /4/, it is hard to ascertain the neutron origin. In the case of this experiment a thermonuclear origin seems impossible. A m = 0 instability fits better with the measured neutron yield.

REFERENCES

/1/ WATTEAU (J.P.).- Experiments with pulsed magnetic cusps.- The Physics of Fluids, Volume 4, number 5, May, 1961, p. 607

/2/ ROSENBLUTH (M.), GARWIN (R.), ROSENBLUTH (A.).- Infinite conductivity theory of the pinch.- LASL 1850, September 14, 1954.

/3/ FILIPOV (N.V.), FILIPOVA (T.I.), VINOGRADOV (VP) Nuclear Fusion Suppl., Pt 2, 1962, p. 577.

/4/ MATHER (J.W.).- High density deuterium plasma focus.- Conference on Plasma and Controlled Nuclear Fusion Research CN-21/80, Culham 1965.

/5/ ANDERSON (O.A.) and al.- Neutron production in linear deuterium pinches.- Physical Review, Volume 110, number 6, June 15, 1958.

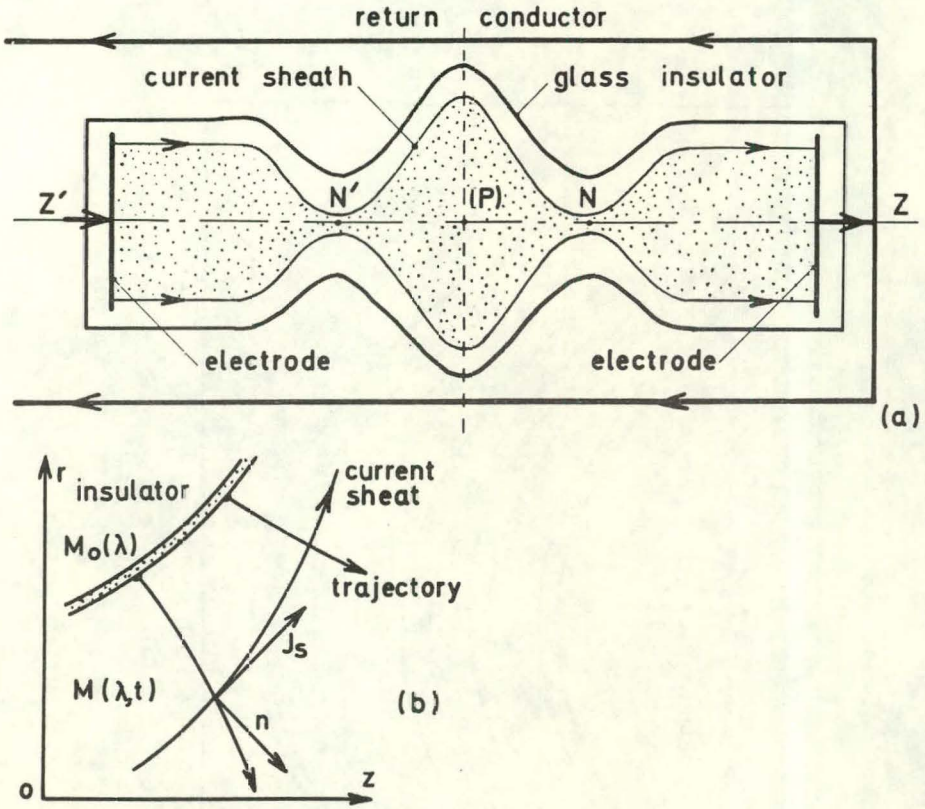

Fig. 1. (a) Non cylindrical discharge chamber (b) Coordinates system of the two dimensions snowplough model. (J_S surface current density).

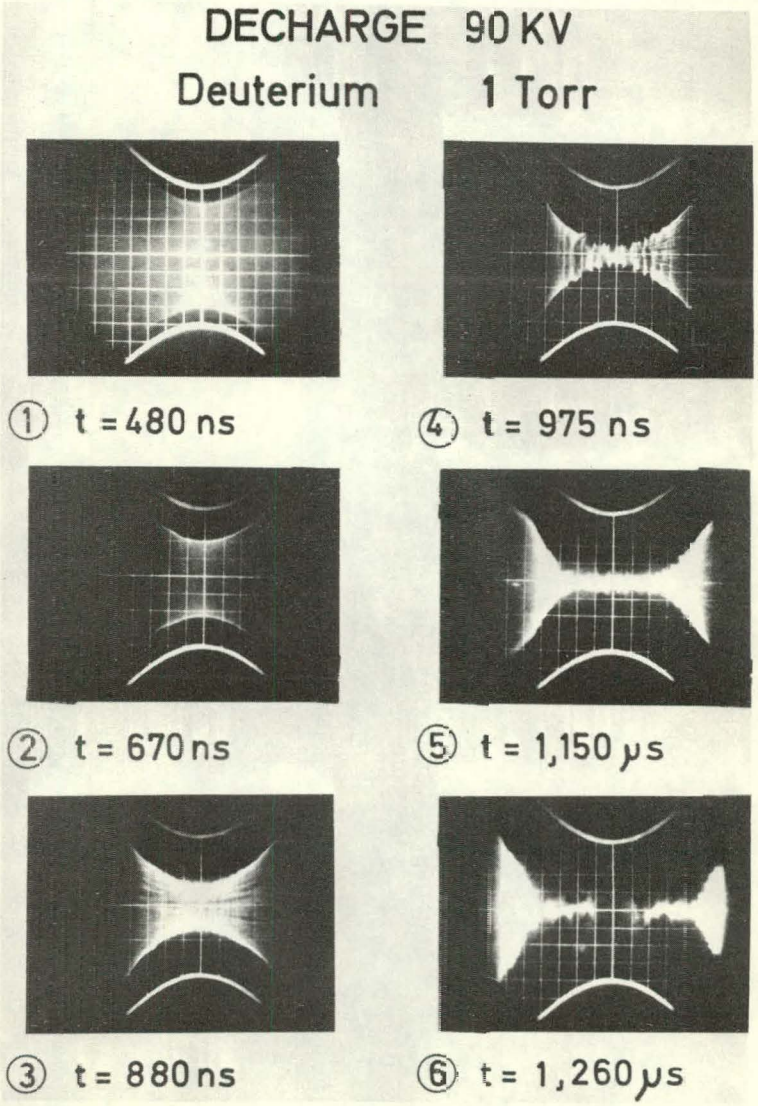

Fig. 2. Discharge current sheath development in a narrowing.

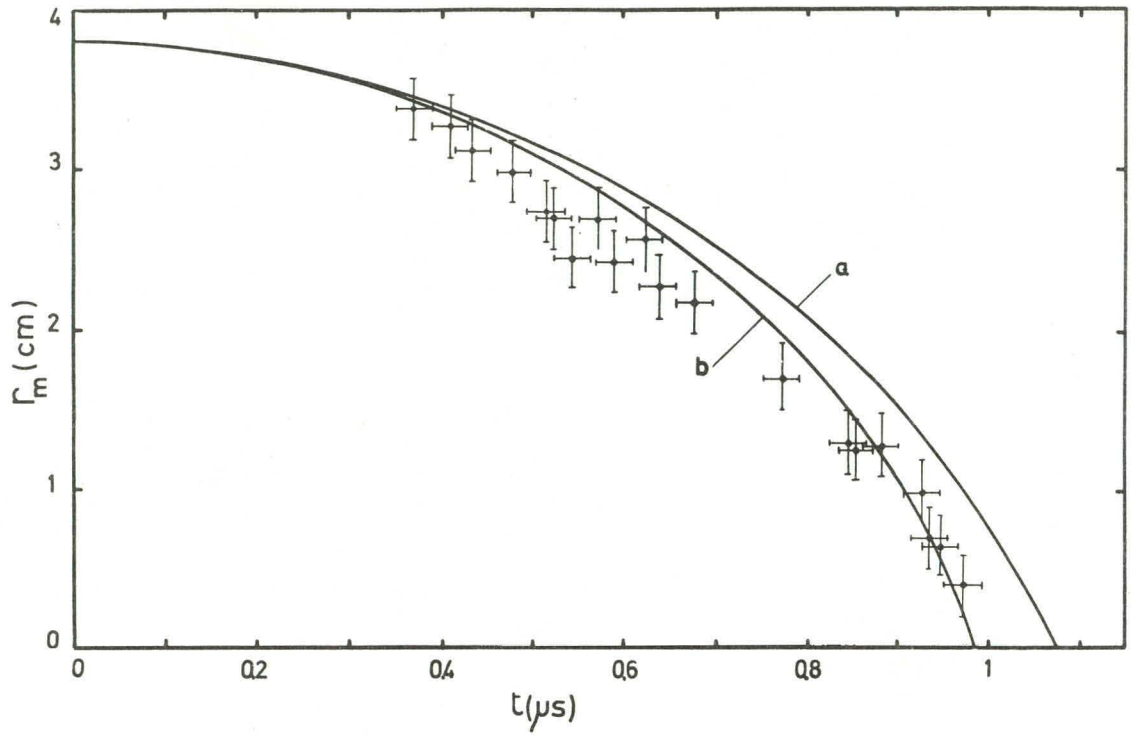

Fig. 3. Time variation of the minimum radius r_m (t) in a narrowing:
- dots: experimental values
- curve a: computed from measured current
- curve b: computed from momentum and electrical equations.

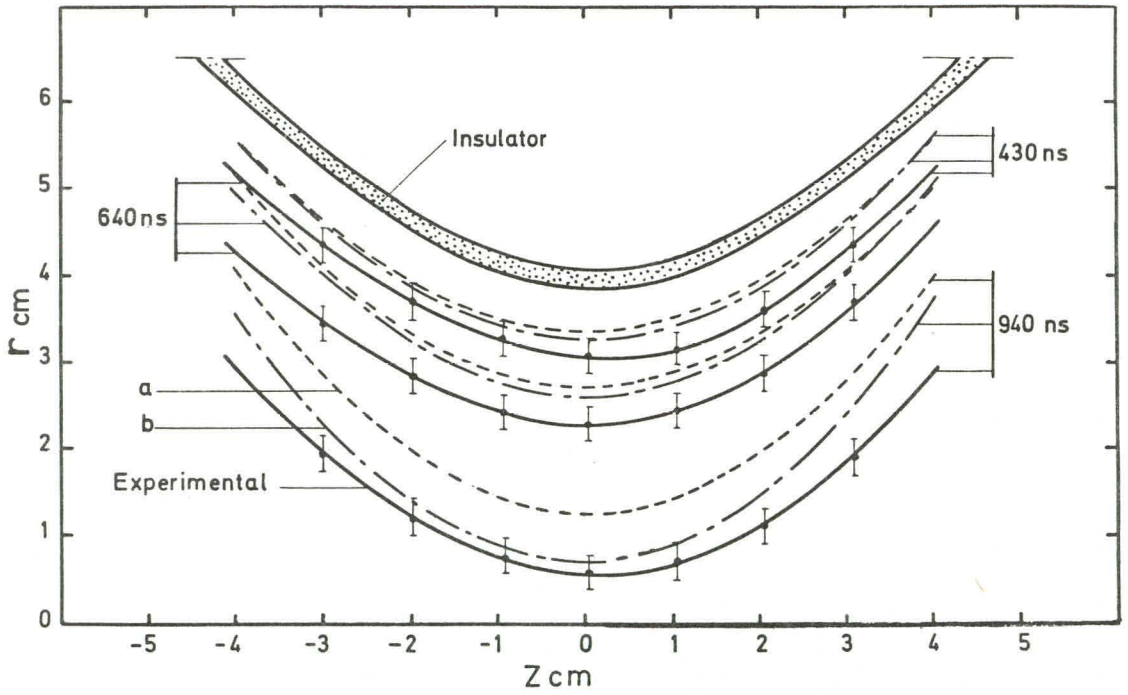

Fig. 4. Computed current sheath compared with the experimental one in a narrowing:
- curve a: computed from measured current
- curve b: computed from momentum and electrical equations.

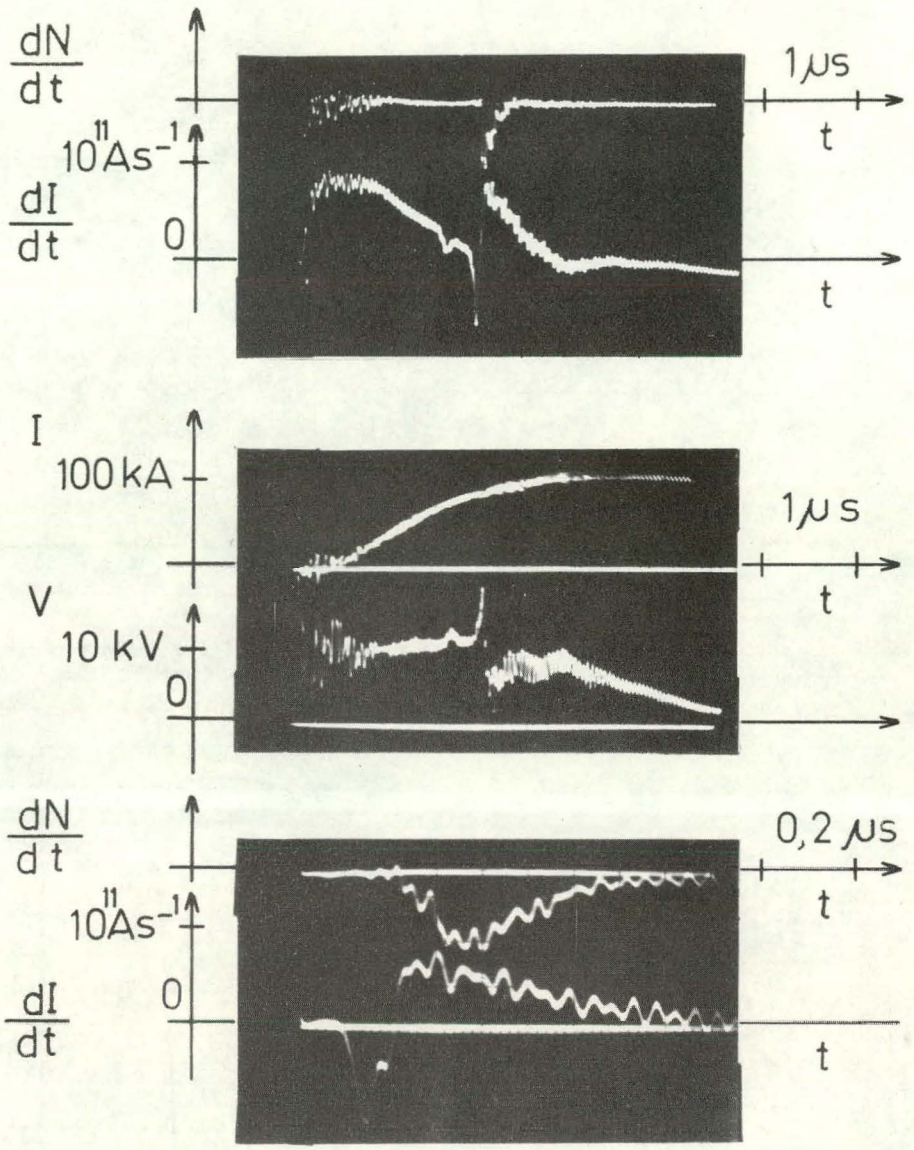

Fig. 5. Neutron pulse $\frac{dN}{dt}$, current derivative $\frac{dI}{dt}$, current I and discharge voltage V oscillograms for the following conditions: discharge length 50 cm, 1 torr deuterium, 14 kV, 3 kJ.

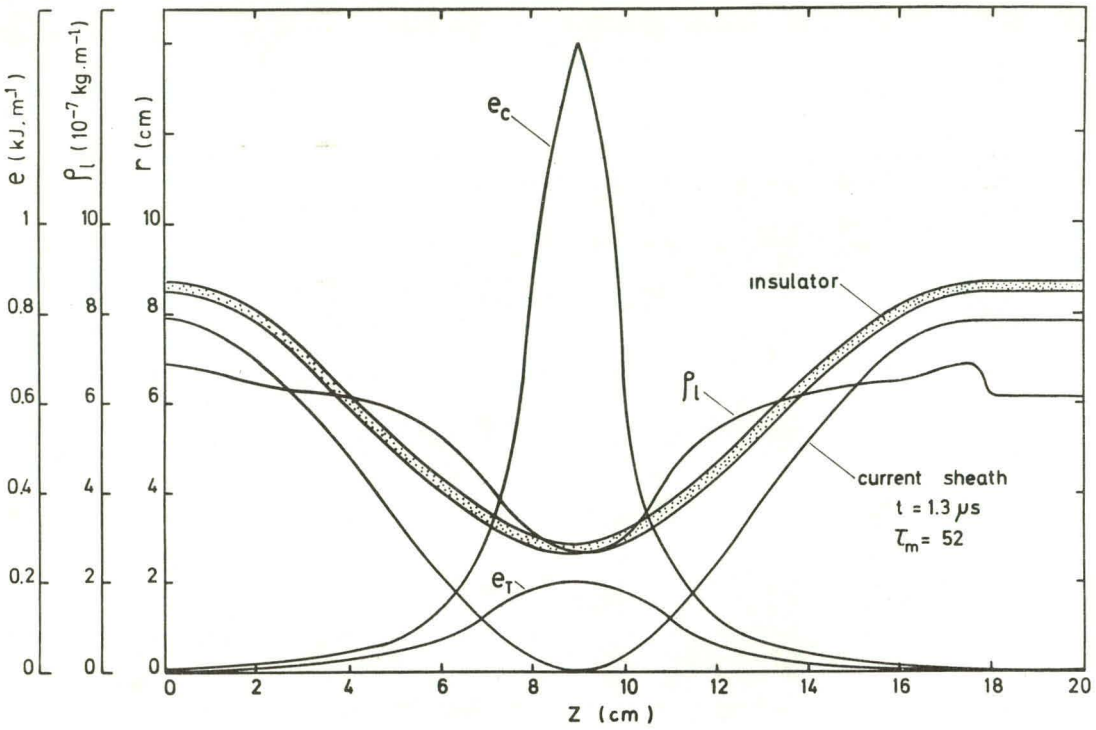

Fig. 6. Discharge shape and specific mass ρ_ℓ, kinetic energy e_c, and inelastic collisions energy e_T per unit length of the current sheath at time t = 1.3 μs when $\tau_m = 52$.

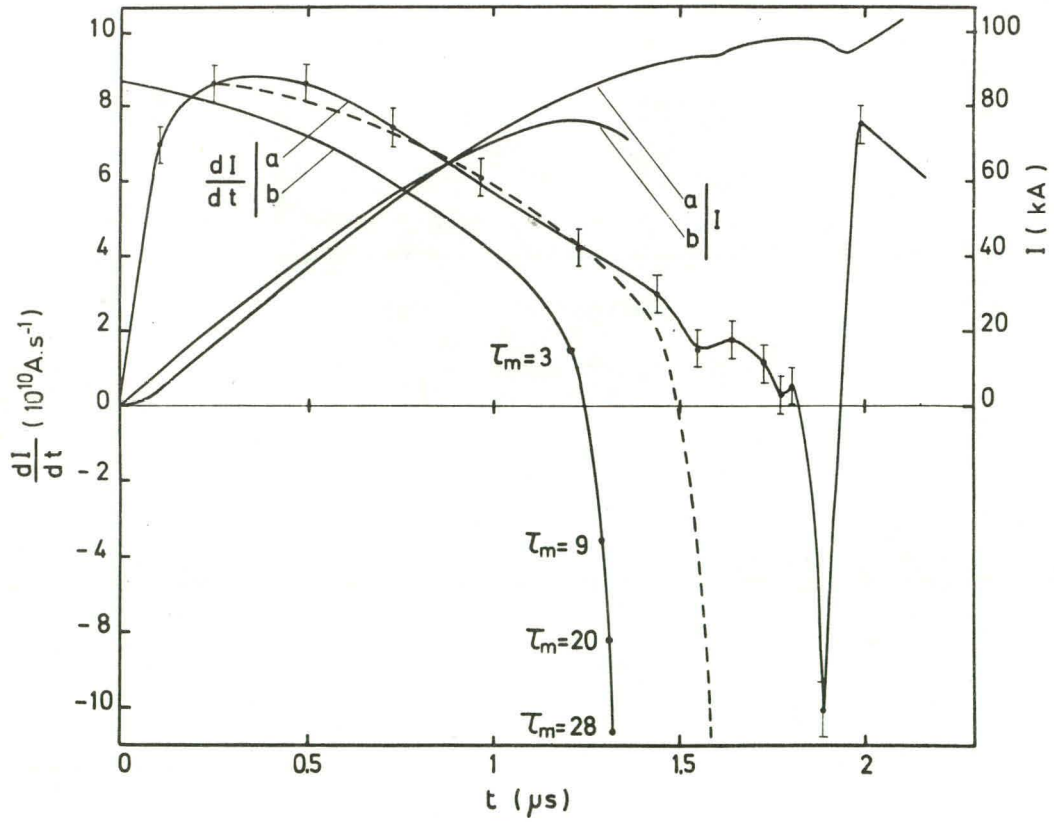

Fig. 7. Current I and its derivative $\frac{dI}{dt}$: (a) from experiment (b) computed.

DETAILED MEASUREMENT OF THE X-RAY EMISSION SPECTRA OF HIGH DENSITY KILOVOLT PLASMAS*

by

E. H. Beckner
Sandia Laboratory
Albuquerque, New Mexico

ABSTRACT

The X-ray emission spectra of dense, hydrogenic kilovolt plasmas produced in a coaxial discharge tube have been measured in detail, utilizing a crystal diffractometer for line identification and Li-drifted germanium detectors for absolute continuum measurements. In previous work it was found that these plasmas generally contain nontrivial quantities of copper contaminant ions; in this paper precise identification is reported of the dominant lines observed in the emission spectra of these plasmas. Since there is a significant relationship between the radiation intensity and the polarity of the center electrode of the discharge tube, both positive and negative modes of operation have been studied and X-ray intensities correlated with neutron emission rates. In both modes of operation two or more distinct X-ray pulses are generally observed: the first pulse possesses a source "temperature" in excess of 100 keV, and appears to be a simple continuum without observable lines; subsequent pulses possess strong Cu-line radiation in addition to continuum radiation corresponding to electron temperatures of 20-50 keV. Neutron emission is observed only at the time of the first X-ray pulse. In neither mode of operation can the X-ray emission rate and spectra be described as arising simply from plasma bremsstrahlung processes in the neutron-producing deuterium plasma.

INTRODUCTION

Coaxial discharge tubes have been shown to be capable of producing high temperature, dense plasmas.[1,2] The details of the plasma production mechanisms in these tubes, however, have remained obscure; this fact has prevailed, to be sure, in spite of extensive diagnostic efforts.[3-5] The work reported in this paper is an extension of previous studies of the neutron and X-ray emission spectra and intensities observed from these plasmas.[3] A crystal diffraction spectrometer has been utilized to obtain identification of line radiation arising from contaminant copper ions (electrode material); in addition, Li-drifted germanium detectors have been used to determine the magnitude and shape of the continuum spectra. Measurements of this latter type previously were made with silicon detectors which were significantly transparent to X-rays of

*This work was supported by the United States Atomic Energy Commission.

$E \gtrsim 15$ keV. The newly-developed germanium detectors are fully opaque to X-ray energies of almost 100 keV. In addition to these techniques, a thick pilot-B scintillator was employed to cover the X-ray range $100 < E < 500$ keV.

Much of the present work has, additionally, been devoted to a comparative study of the radiation spectra obtained from these tubes under both positive and negative center electrode operation. This was done primarily because it was felt that contributions to the spectra from contaminant ions would be reduced in the negative C.E. mode. Mather showed several years ago that the X-ray intensity in the two cases was substantially different,[1] and at first glance this appears reasonable if merely sufficient voltage appears across the tube electrodes to accelerate electrons to energies greater than the ionization potential of the electrode atoms. In fact, however, the actual phenomena are considerably more complicated--due, in part, to the fact that the processes which accompany the collapse of the current structure are unavoidably nonequilibrium in nature. These facts notwithstanding, we find both distinct similarities (emission of $E > 100$ keV X-rays coincident with neutron production) and differences (positive C.E. operation yields a factor of fifty more Cu-line radiation than negative C.E.) in the two modes of operation.

EXPERIMENTAL DETAILS

These experiments were conducted in an open-ended coaxial discharge tube made of oxygen-free copper, with outer electrode diameter of 10 cm and inner electrode diameter of 5 cm. Both electrodes were 25 cm long, with the outer electrode perforated to provide ~50% transparency. The insulator was made of pyrex. The energy source was a 150μF capacitor bank charged to 18 kV, switched with a wide dielectric switch. The combined bank and switch inductance was 7 nH. Peak current through the tube was approximately 750 kA.

Detailed measurements of the X-ray emission spectra were made with an LiF crystal diffractometer, which possessed resolution of 0.20° ($\Delta\lambda \simeq .007$Å at 1.5Å). Time resolution was accomplished with a pilot-B crystal-photomultiplier tube combination which possessed an inherent pulse width of <20 ns. Absolute X-ray intensity measurements were made with Li-drifted germanium detectors[6] which had an active thickness of 1.05 mm (50% absorbing to X-rays of ~90 keV). These detectors possessed rise and fall times of less than 5 ns. K-edge filter techniques were employed with these detectors to determine the shapes of the continuum emission spectra[3] (absorbers used were Ti, V, Fe, Ni, Cu, Zr, Mo, Pd, Ag). Additionally, a thick pilot-B crystal mounted on a photomultiplier tube was employed to measure X-radiation from $100 < E < 500$ keV.

Neutron detection was accomplished with a pilot-B-photomultiplier tube for time resolution, and an Ag-activated-proportional counter array for absolute determination.

EXPERIMENTAL RESULTS

Positive Center Electrode

This is the mode of operation in which these tubes are recognized to operate most easily and efficiently, and our first studies were of this mode. We display in Fig. 1 a typical set of experimental results for operation at 5 Torr D_2. Results in hydrogen are extremely similar, except for the neutron pulse.

It is necessary to discuss separately observations made of the first radiation pulse and those of later pulses. The first X-ray pulse, which is coincident in time with the neutron pulse and with the sharp

voltage spike which accompanies the collapse of the current column, is found to best be described as arising from continuum radiation of $T_e \sim 200$ keV. The voltage spike is measured to be in excess of 30 kV, with this value necessarily inductively reduced by at least a factor of four due to the fact that the probe is located at the base of the tube and the voltage source at the end of the electrodes. Although the details of the phenomenon remain obscure, it seems that this first, hard X-ray pulse and the voltage spike are of common origin--that being the violent collapse of the plasma current column.

Subsequent radiation pulses contain both line and continuum components. In Fig. 2 we show detailed measurements of the X-ray spectrum at $t \simeq 2.7$ μsec. Necessarily, these data are obtained from a large number of shots, with each data point obtained on a different shot and normalized against total X-ray intensity received by a solid state detector. Although the diffractometer slits prevented direct detection of radiation from the tube electrodes, the dominant line radiation is seen to be that from copper ions in low ionization states. That the copper radiation arises from a variety of ionized species is indicated by the fact that the lines are substantially broadened and shifted. This line radiation is so strong (~50% of the total emission intensity) that the Ge-detector/filter techniques lose their sensitivity insofar as continuum shape, and hence T_e, determinations are concerned.

Negative Center Electrode

The basic phenomena observed in this mode of operation are quite similar to those observed with +C.E., though all radiation quantities are found to be reduced in amplitude. Figure 3 shows a typical set of data obtained in this mode wherein electrons move toward the outer electrode rather than the center electrode. The X-radiation intensity is seen to be diminished by more than a factor of 25, while the neutron production is down by about a factor of ten. The amplitudes of the first, hard, X-ray pulses were not obtained on a relative intensity basis for the two modes of operation.

Figure 4 displays the LiF crystal diffractometer data for -C.E. operation. The total intensity was diminished sufficiently in this mode to make shot-to-shot variations more obvious; however, the fact remains that copper line radiation was definitely present in the late-time pulses, though we could not identify copper lines in the first pulse (if it existed) due to difficulties associated with shielding from the hard X-rays. The line radiation data in Fig. 4, like those in Fig. 2, show substantial broadening and imply that the radiation arises from numerous stages of ionization. It is clear, additionally, that the stages of ionization are not exceptionally high, because the observed line radiation is located nearer to the location of K_α (cold copper) than the theoretical location of the resonance helium-like copper line. The data in Fig. 4 suggest the presence of the resonance H-like Cu XXIX line at 1.44Å. However, the apparent line is sufficiently misplaced, and the results sufficiently difficult to duplicate, to discourage identification as such.

CONCLUSIONS

We have attempted, for both modes of operation, to compare neutron and X-ray radiation rates and spectra to see if the radiation source can be described simply. It seems that at no time in these discharges is it possible to confidently describe these plasmas as thermal in nature. It may be, and indeed should be, that the ions or electrons possess, independently,

Maxwellian distributions of particle velocities. The particles do not, however, appear at any time to achieve a condition in which $T_e = T_i$. This fact is demonstrated most vividly in the data of Fig. 3, wherein we found X-radiation (second pulse) arising from electrons possessing energies of 30-50 keV while apparently no neutrons were being produced. One must admit the possibility that the two particle groups possess a common temperature during the first pulse (where we know $E_e > 100$ keV), but until more is known about the details of the phenomena which generate the plasmas, it seems highly unlikely that such is the case. Specifically, electrons or ions at temperatures of 100 keV and densities of even 10^{20} cm^{-3} require longer than 10^{-9} and 10^{-7} seconds, respectively, to achieve Maxwellian distributions of each particle group. To transfer energy from one group to another at these temperatures is just not possible on the present time scales.

REFERENCES

1. J. W. Mather, Phys. Fluids 8, 366 (1965).
2. N. V. Filippov, V. P. Filippova, and V. P. Vinogradov, Nucl. Fusion Suppl. Pt. 2, 577 (1962).
3. E. H. Beckner, J. Appl. Phys. 37, 4944 (1966).
4. P. J. Bottoms, R. M. Henson, and J. W. Mather, Bull. Am. Phys. Soc. II, 12, 713 (1967).
5. E. H. Beckner, Rev. Sci. Instr. 38 507 (1967).
6. Solid State Radiations, Inc., Los Angeles, Calif.

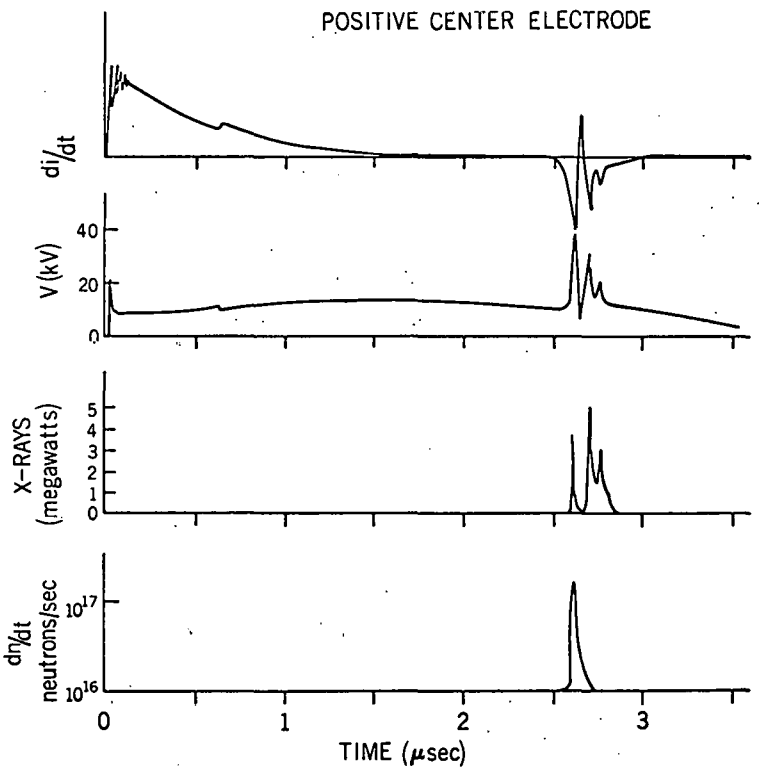

Figure 1. Typical data for tube operation with positive C.E. Voltage is measured across the transmission plates at the base of the tube. The X-ray intensity is the total radiation emitted for $1 < E < 100$ keV, as measured with the germanium detectors; consequently, the amplitude of the first pulse is somewhat incorrectly represented, since at this time $E > 100$ keV.

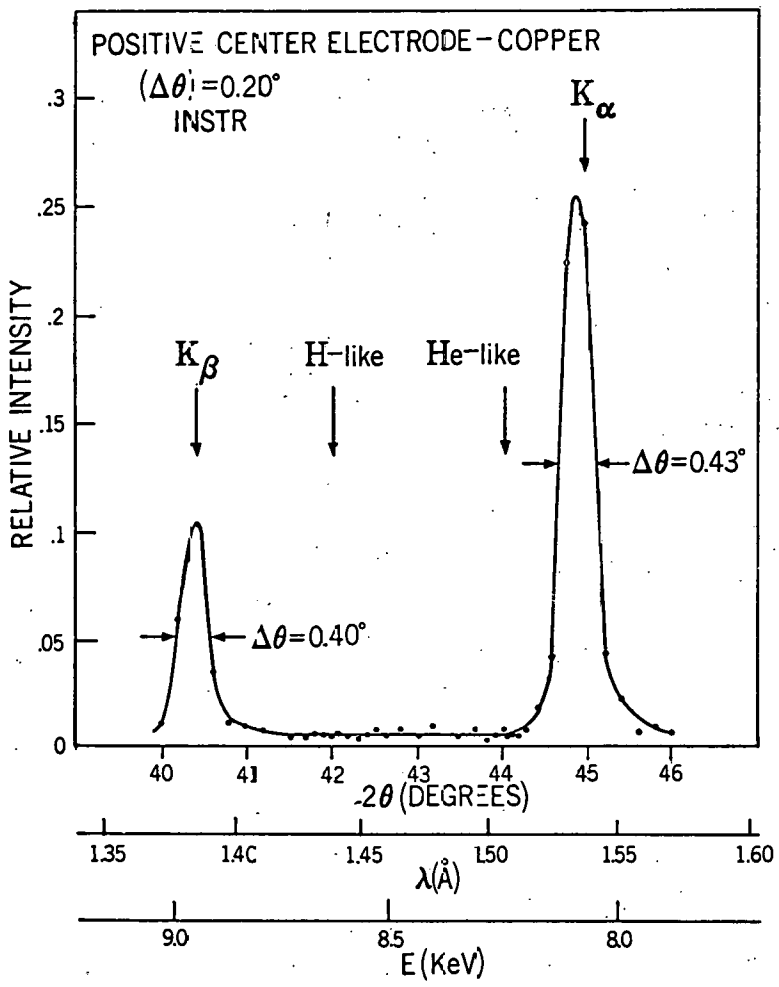

Figure 2. X-ray emission spectrum at t ≃ 2.7 μsec (second pulse) obtained with an LiF crystal diffractometer possessing measured resolution of 0.20° at 2θ = 45°.

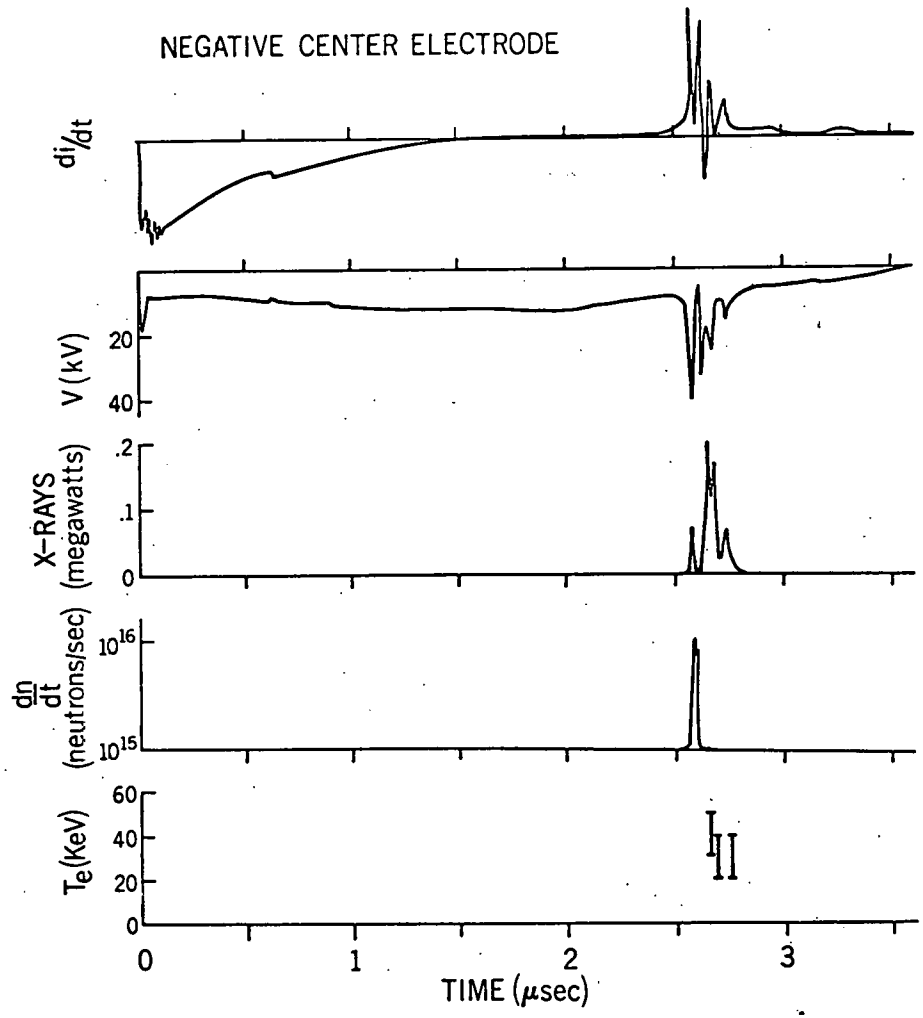

Figure 3. Typical data for tube operation with negative C.E. All measurements were made in the same manner as those in Fig. 1. The electron temperatures shown for the second and subsequent pulses are based on K-edge filter techniques and an assumed continuum shape corresponding to simple plasma bremsstrahlung. Since the line radiation in these data accounted for ~10% of the total radiation, these temperature assignments are felt to be reasonably meaningful.

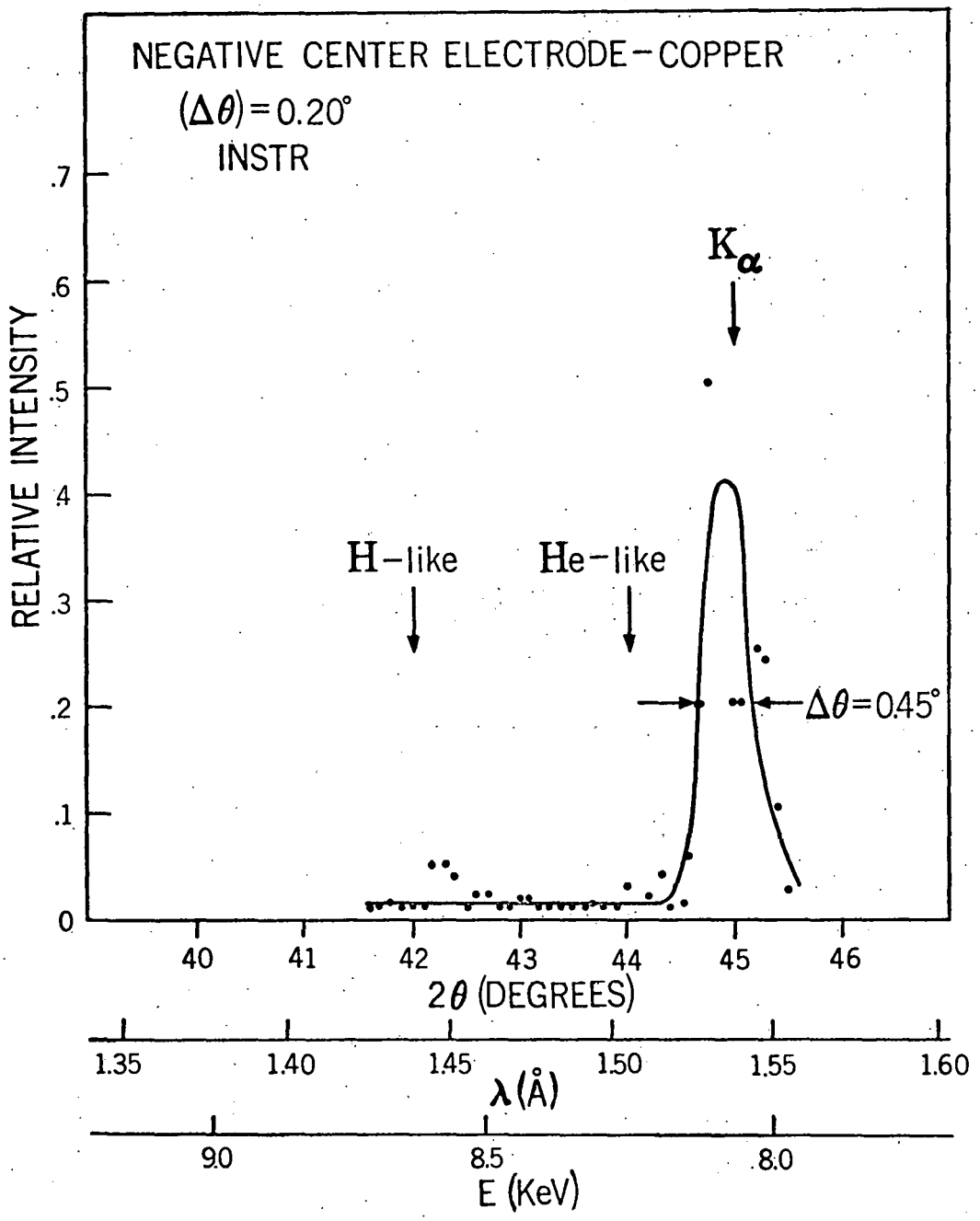

Figure 4. X-ray emission spectrum at t ≈ 2.7 μsec (second pulse) for negative center electrode operation.

THE FORMATION AND BREAK-UP OF THE PINCH IN PLASMA FOCUS

By

J.W. Long, N.J. Peacock, P.D. Wilcock

Culham Laboratory, Abingdon, Berks., England

R.J. Speer

Imperial College, London, England

ABSTRACT

A superdense pinch[1,2] is generated in an open-ended, metal walled tube between coaxial electrodes. The collapse of the current sheath at the open end of the electrodes and the formation and breakup of the focus is studied using an image-converter camera with a 10 nsec exposure, X-ray pinhole photography and grazing-incidence spectroscopy.

The current sheath collapses radially to a narrow filament, 0.5 mm in diameter in less than 10^{-7} sec. Due to the initial forward momentum the filament rapidly elongates, travelling 2 or 3 cm axially in 2×10^{-7} sec. Instabilities of the m = 0 type with growth times less than 0.5×10^{-7} sec break up the plasma locally. The filament is sustained however by further compressions and the total 'sustainment time' can last up to 3×10^{-7} sec. i.e. the duration of the thermal X-ray and neutron emission.

The plasma has an electron temperature of several keV and a density greater than 10^{19} cm^{-3}. The addition of a few per cent heavy gas prolongs the lifetime of the filament and markedly increases the X-ray emission. Resonance lines and free-bound recombination continua at wavelengths < 10 Å in H- and He- like ions of these added gases confirm a relatively high electron temperature in the pinch.

INTRODUCTION

Fillipov et al[1] and Mather[2] have described versions of a metal-walled, coaxial plasma gun which produces a dense pinch when operated in D_2 gas at about 1 torr pressure or higher. The present paper is primarily concerned with the evidence from image-converter pictures and X-ray pinhole pictures for the formation and localised breakup in a similar pinched plasma. The electro-magnetic spectrum at wavelengths < 10 Å has been recorded with grazing-incidence grating spectrographs while the absolute flux has been measured using band-pass transmitting foils and surface barrier detectors.

DISCHARGE APPARATUS

The dimensions of the discharge chamber and the coaxial electrodes (the inner is electrically the anode) are shown in Fig.1. The coaxial gun operates in a static gas filling of between 0.3 and 3 torr D_2 and is driven by a capacitor bank of 21.6 kJ at a voltage of 30 kV. The peak current of 800 kA is reached 2.6 μsec after initiation. The current sheath forms initially across the pyrex insulation shown in Fig.1 and is driven down the coaxial system by the self $\vec{j} \times \vec{B}$ force reaching the open end of the gun at peak current. The effect of the collapse of the unconstrained plasma current sheath at the open end of the electrode system is to introduce a high impedence into the electrical circuit. The circuit waveforms and the X-ray emission are shown in Fig.2 where a high voltage spike (several times the applied voltage) and a drop in the circuit current (as much as 50%) are always associated with the other symptoms of an active focus such as a high neutron flux ($\gg 10^8$ neutrons/discharge) and copious X-ray emission. The apparent delay in the neutrons relative to the X-ray emission in Fig.2 is due to the difference in times of flight of the photons and neutrons.

The energy transferred to the plasma, assuming pressure balance, is

$$W_p = \tfrac{1}{2} L_1 (I_1^2 - I_2^2)/(1 + 2 \log R_o/r_p);$$

$(R_o/r_p)^2$ is the radial compression, L_1 is the circuit inductance before collapse and I_1 and I_2 are the currents before and after collapse. The larger the current depression the greater is the energy transferred to the plasma. The addition of a few per cent heavy gas to the D_2 filling caused a large depression in current at the focus (Fig.2) and markedly increased the energy input into the plasma and its duration in time. X-ray emission was also much more intense and the plasma was spatially more reproducible. The neutron yield is observed to increase

by up to a factor of 2 with the addition of 1% of argon[3]. In this paper most of the results therefore were taken with a percent or more of heavy gas addition.

THE FORMATION AND BREAKUP OF THE FOCUS

Fig.3 shows four discharge sequences taken with 1.5% of argon addition to the D_2 filling. The non-cylindrical implosion of the current sheath is clearly observed to generate a 'fountain' of plasma with the 'jet' momentarily anchored to the central electrode. Axial motion of the fountain is preserved however as the plasma front, which is surprisingly flat, travels forward at a speed of $\approx 10^7$ cm/sec.

The 'jet' or plasma filament should be hydromagnetically unstable with instability growth times of the order of 10 nsec, i.e. $2 r_p/v_s = 0.1 \times 10^{-7}$sec.; v_s being the sound speed on the plasma. The m = 0, or sausage instability will have the fastest growth rate. From Fig.3 the growth times for the sausage instability is < 50 nsec. That part of the plasma filament nearest the electrode is compressed first and breaks up earliest. An appreciable fraction of the current is still carried by the focus however since the magnetic field is responsible for subsequent compression and instabilities in the axially growing column. Although time integrated the X-ray pinhole pictures (Fig.4) effectively give a time-resolved record in the X-ray light from the plasma, since the location of maximum compression travels axially along the filament. Pictures D and E (Fig.4) show clearly the same compression and breakup of the filament as is seen in the visible time-resolved pictures. The severe erosion of the centre electrode due to electron bombardment and the high flux of X-rays with hardness characteristic of the anode material show that the compressed plasma is electrically connected to the anode and acts like the cathode of an X-ray tube. The total duration of the voltage spikes and of the neutron and X-ray emission is thus to be associated with the total sustainment time of the plasma filament.

ELECTRON TEMPERATURE

The relative intensity of the radiation transmitted through thin foils of Ni, Al and Be, was compared with that expected from a computed energy spectrum to give estimates of the electron temperature[4]. The reverse-biased, p-n junction surface-barrier detectors with depletion layers of 80 μ were screened from X-ray emission from the anode. The temperature with 3% added argon was 1.5 ± 0.7 keV. Absolute measurement of the photon flux[5] assuming a conversion efficiency of 3.6 eV/ion pair indicated a plasma ion density greater than 10^{19} cm^{-3}. In pure D_2, T_e was less than a factor of two higher.

THE EMISSION SPECTRUM IN THE X-RAY REGION

The use of diffraction gratings to disperse the radiation has the advantage that over an extended energy range the spectrum is recorded in one exposure. The lower wavelength limit is limited by the grating cut-off $\lambda_c(\text{Å}) \approx 10 \times \theta^o$ where $(90 - \theta^o)$ is the angle of incidence on the grating. To record the emission at $\lambda < 20$ Å the diffraction gratings were used at a grazing angle of $\leq 2^o$.

The two-metre instrument[6] with an Au-coated grating blazed for 80 Å, was used for wavelengths down to ~7 Å. For wavelengths shorter than this an NPL plane diffraction grating[7] was employed with 2' collimation of the source and with a grazing angle ~ 10', (Fig.6). The irreproducible motion of the source and the finite collimation limited the resolution to $\frac{\lambda}{\Delta\lambda} \lesssim 18$.

When 1% of argon or xenon was added to the D_2 gas filling, a continuum was observed on the 2-metre spectrograph increasing in intensity towards $\lambda_c \sim 7$(Å). Since $T_e(\text{keV}) = 6.19/\lambda(\text{Å})$ this sets a lower limit of the electron temperature at 0.88 keV. The addition of larger concentrations of impurities produced dominantly free-bound and line radiation, (Fig.5) and the plasma is radiation cooled in this case. The absorption at 8 Å (Fig.5) is due to a 5 μ filter of aluminium. Assuming a constant instrument response, the flat continuum (Fig.5) between 8 or 9 Å, when compared to the product of the transmission of the Al filter and the exponential decrease in the energy in the free-bound continuum, gives a temperature of the order of 800 eV. The intensity of the upper members of the Lyman series of NeX[8] and the intensity ratio of the 13.44Å($1s2p\ ^3P_1 - 1s^2\ ^1S_0$)/ 13.54Å($1s2p\ ^1P_1 - 1s^2\ ^1S_0$) in NeIX[9] (Fig.5) both indicate a considerably higher collision rate than in a theta pinch plasma.

For the plasma focus conditions the coupled equations describing the relative ion population have been solved and it is found for example that with a

few per cent impurities a steady state is reached in 0.1 μsec, with the radiation spectrum dominated by H- and He-like ions. The steady state computed spectrum for 1% A, $n_e = 10^{19}$ cm^{-3}, $T_e = 2$ keV, is invoked to explain the features recorded with the plane grating at $\lambda < 7$Å, (Fig.6) from a single discharge in an argon-doped plasma. The strong line feature at 3.9Å seen in 4 orders on the original plate is accounted for by a blend of AXVIII, Lyα at 3.75Å and AXVII $1s2p\ ^1P_1 - 1s^2\ ^1S_0$ at 3.96 Å. X-ray transitions at 4.2Å in neutral argon cannot account for this feature. The broad weaker feature at shorter wavelengths (Fig.6) is due to free-bound continua and higher-excited levels of H- and He-like argon ions.

A line feature observed between 1.3 and 1.5Å was spatially located only within 5 mm of the centre copper electrode and hence is most probably due to X-radiation rather than optical resonance lines in H- and He-like Cu. Furthermore no resonance lines in Li-like copper which lie between 8Å and 9Å were observed.

CONCLUSIONS

The plasma temperature in pure D_2 is about 3 keV. The compressed filamentary plasma is unstable, breaks-up by m = 0 stabilities and reforms downstream several times as it is carried forward by its initial momentum. The total duration of the X-ray and the neutron emission is a measure of the sustainment rather than the containment time of the plasma. Spectroscopic measurement of the optical transitions indicate an approach to steady state excitation conditions in the plasma at a density $> 10^{19}$ cm^{-3}. There is thus time for an electron ion relaxation and a thermal distribution of plasma particles.

REFERENCES

1. FILIPPOV, N.V., FILLIPOVA, T.I. and VINOGRADOV, V.P. (1962) Nucl. Fusion Suppl. Pt.2, pp.577-587.

   FILIPPOV, N.V. and FILIPPOVA, T.A. (1965) Report I.A.E. 913, I.V. Kurchatov Institute, Moscow, pp.1-15.

   KOLESNIKOV, Yu.A., FILIPPOV, N.V. and FILLIPPOVA, T.I. (1966) Ibid. Report 18/904.

2. MATHER, J.W. (1965) Physics of Fluids, vol.8, no.2, pp.366-377.

   Culham Conference in Plasma Physics and Controlled Nuclear Fusion Research, (1965) Paper CN-21/80. Proceedings published by I.A.E.A., Vienna, (1966).

3. VASILJEV, A.P. and FILIPPOVA, T.I. (1967), 289. 8th International Conference on Ionization Phenomena. I.A.E.A. Vienna.

4. STRATTON, T.F. (1965) 'Plasma Diagnostic Techniques', chapter 8, Academic Press.

5. BECKNER, E.H. (1966) Journal Applied Physics. vol.37, no.13, pp.4944-4952.

6. GABRIEL, A.H., SWAIN, J.R. and WALLER, W.A. (1965) Journal Scientific Instruments, vol.42, pp.94-97.

7. FRANKS, A. and LINDSEY, K. (1967) Journal Scientific Instruments. (In the press).

8. SAWYER, G.A., JAHODA, F.C., RIBE, F.L. and STRATTON, T.F. (1962) Journal Quantitative Spectroscopy Radiative Transfer. vol.2, pp.467-475.

9. ELTON, R.C. and KOPPENDORFER, W.W. (1967), 450, 8th International Conference on Ionization Phenomena, I.A.E.A., Vienna.

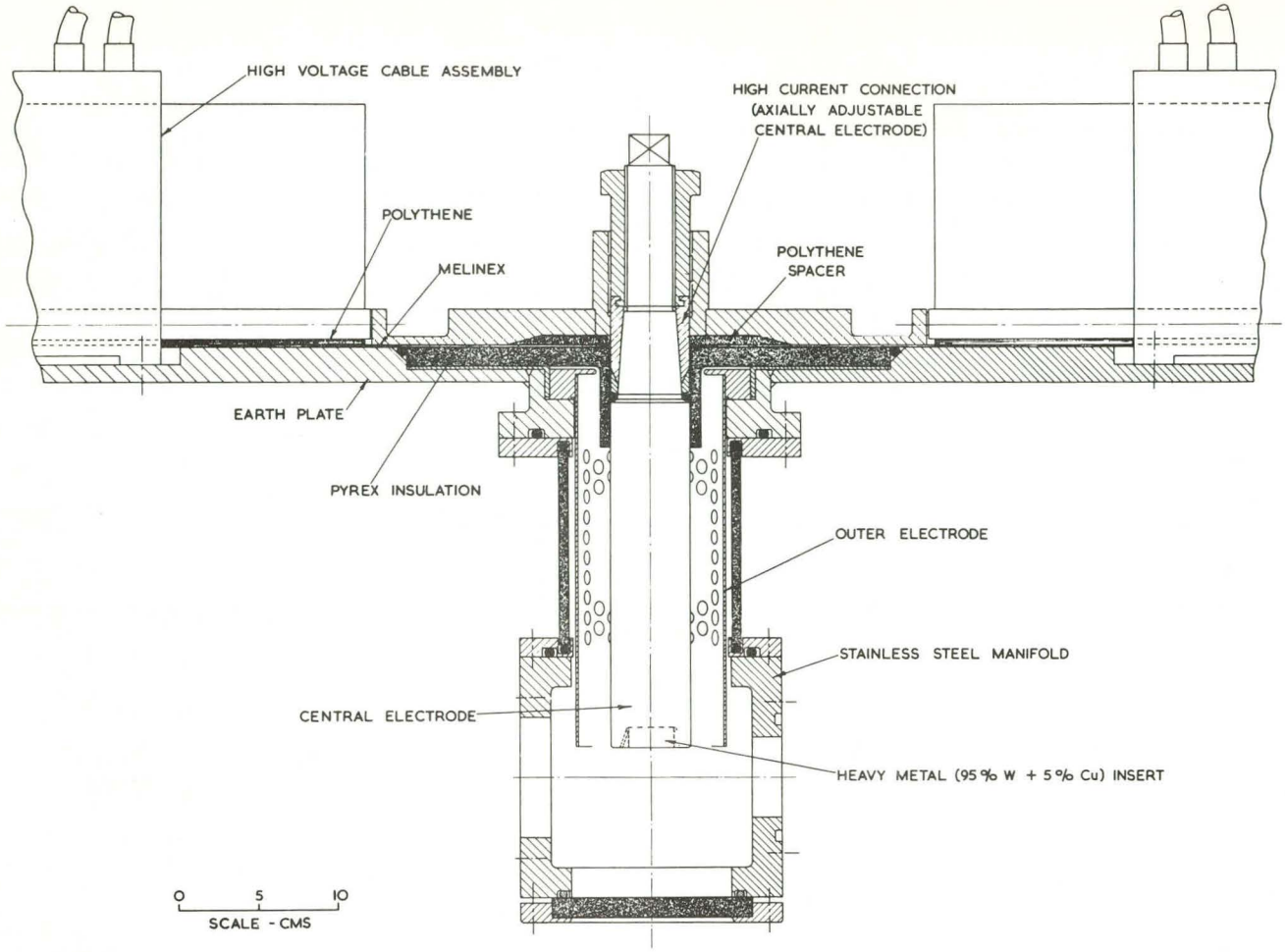

Fig.1 Schematic diagram of plasma focus

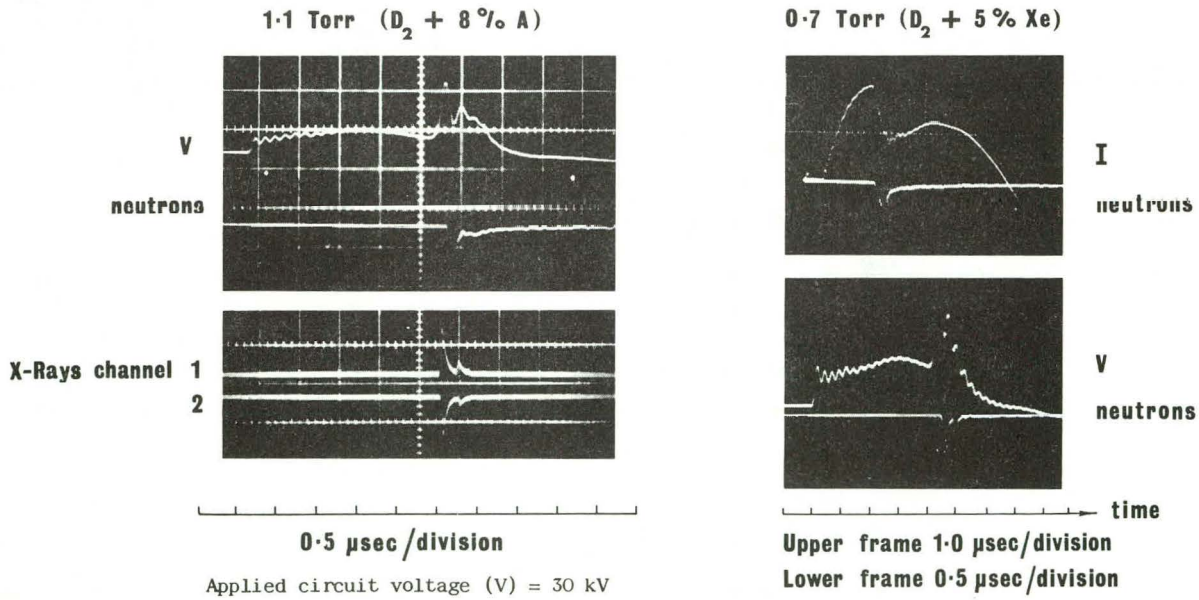

Fig.2 Plasma focus waveforms

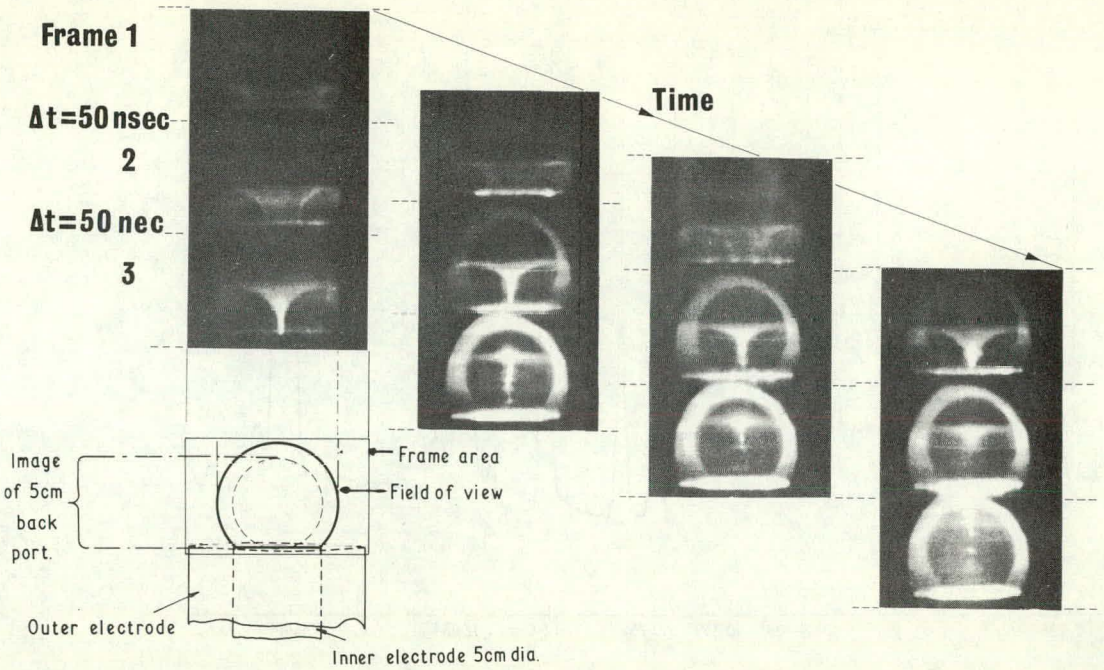

Fig.3 Image converter sequences of four discharges in plasma focus (V_b = 28 kV) p_o = 1.1 torr (D_2 + 1.5%A) 10 nsec exposures, 50 nsec between exposures.

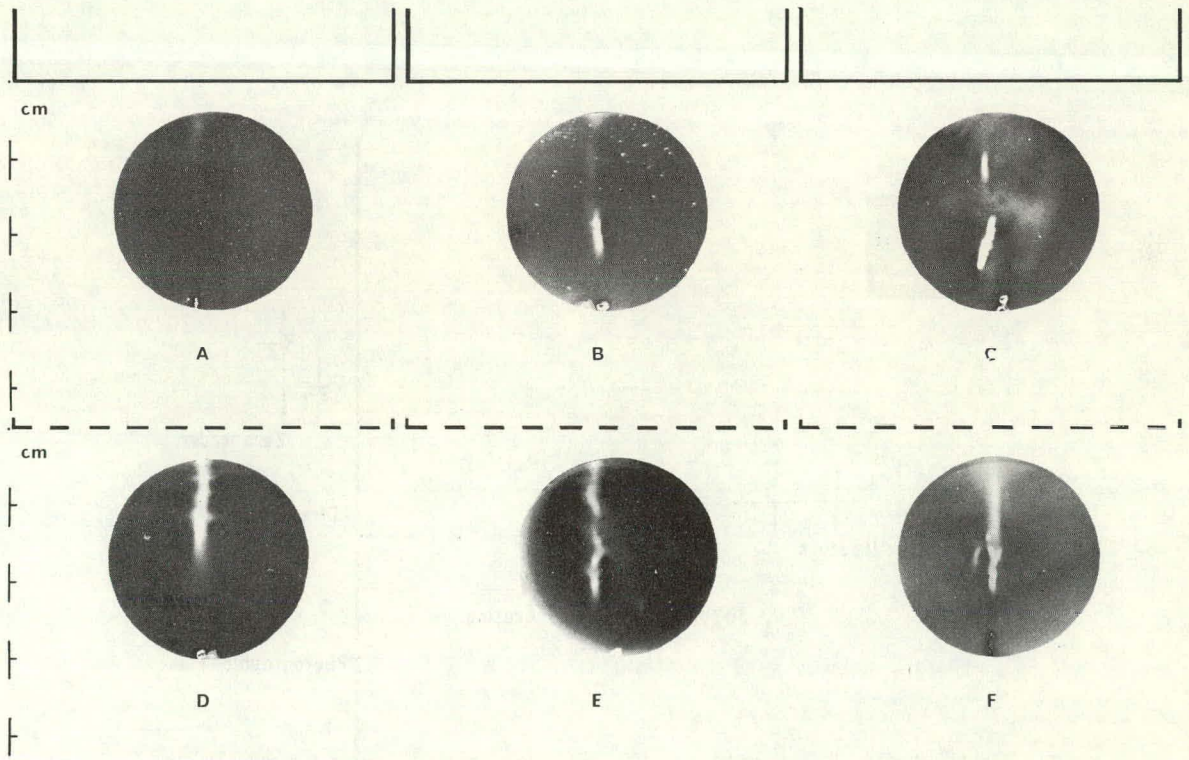

Fig.4 Pinhole camera pictures in X-ray light from plasma focus. Dimensions of central electrode is shown with plasma to scale. (Visible light screened by 2·68 mg cm^2 Al) Initial gas filling (A) 1·6 Torr D_2; (B) 1·0 Torr (D_2 + 8% N_e); (C) 1·0 Torr (D_2 + 10% A); (D) 1·1 Torr (D_2 + 40% H_e); (E) 1·2 Torr (D_2 + 10% X_e); (F) 1·05 Torr (D_2 + 3% A), two discharges.

CR 67/132

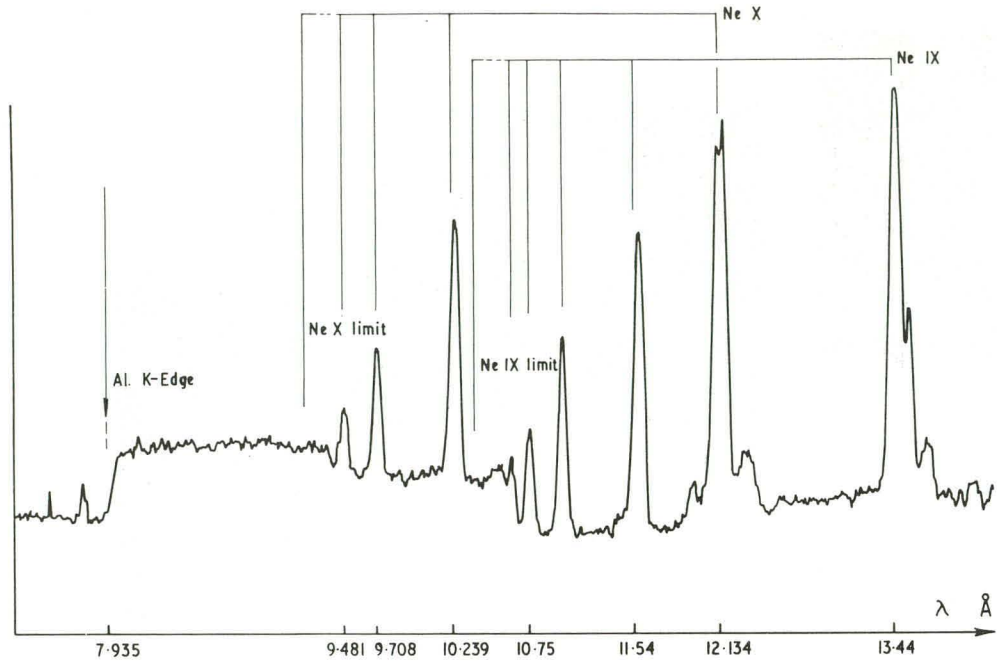

Fig.5 Spectrum of plasma focus in neon at 1·0 Torr. Dispersion is second order on 2 metre Rowland circle at 2^{o} grazing angle. A 5 micron thick filter of Al transmits only the He-like and H-like ion features of neon.

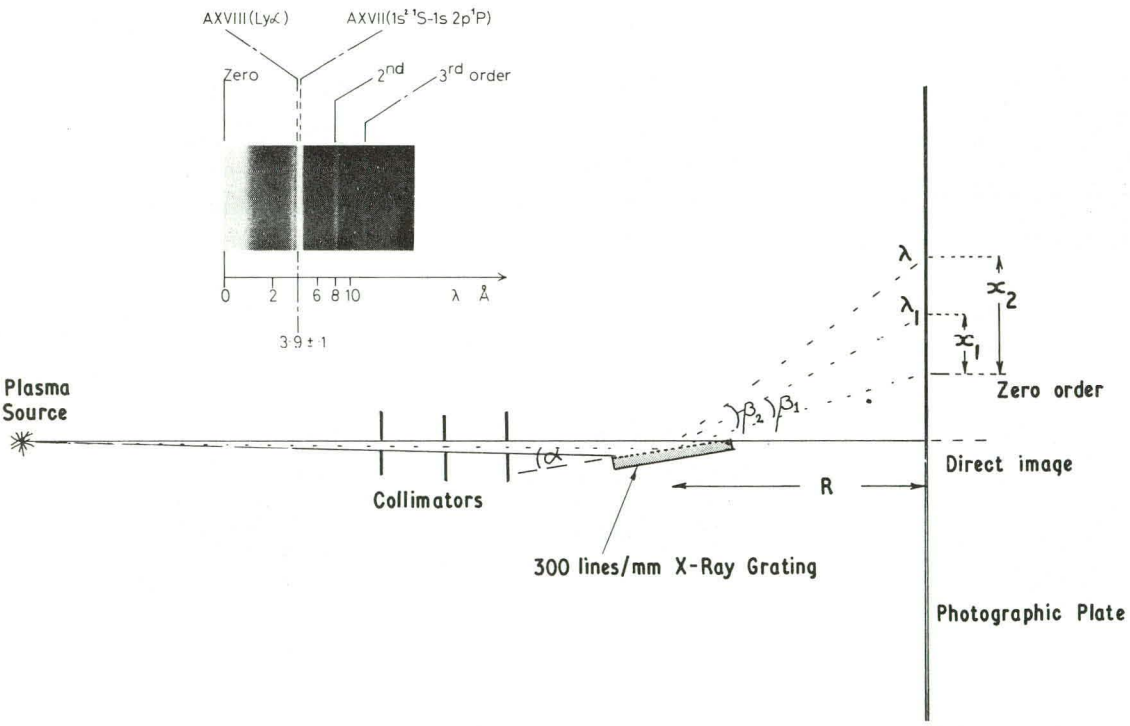

Fig.6 Soft X-ray spectrum of plasma focus taken with plane, etched grating at 10 arc minutes grazing angle and 2 arc minutes collimation of source. Pressure filling 1·3 Torr D_2 + 10% Argon.

CR 67/132

NEUTRON AND X-RAY PRODUCTION IN A FOCUSED Z-PINCH

by

David Allan Meskan, H. L. van Paassen, and G. G. Comisar
Aerospace Corporation, Los Angeles, California

ABSTRACT

Diagnostic studies were made of the neutrons and x rays produced by a paraboloidal geometry Z-pinch device (700 mTorr D_2, 15 kJ). The neutron energy spectra at 0 and 180 deg relative to the electric field applied at the pinch axis were obtained by nuclear emulsion techniques; they resemble the spectra obtained for linear pinches. The energy anisotropy can be explained in terms of a 90- to 130-keV deuteron beam that strikes stationary deuterons. Ross filters reveal complex x-ray spectra from 7 to 88 keV, while absorber studies reveal x radiation up to 350 keV. The spectrum from 7.11 to 29.2 keV is insensitive to neutron yield and fits the function $\omega^{-1.7}$, as does plasma bremsstrahlung from the electron energy distribution $E^{-2.2}$. The relationship between the power-law spectrum and MHD current turbulence theories is discussed. An x-ray tube spectrum typical of a copper anode bombarded by a 30- to 50-keV electron beam is superimposed on the continuum. The presence of energetic x rays and fast deuterons is not consistent with the boiler model of neutron production recently proposed by the Fillipovs.

I. INTRODUCTION

Pulsed high-density deuterium plasmas with kilovolt temperatures may be generated by coaxial accelerators[1, 2] or metal-walled discharges.[3, 4] Despite extensive diagnostic studies of such devices,[1-6] the mechanisms of neutron and x-ray production are not well understood. For example, early work at the Kurchatov Institute[3] indicated the generation of fast deuterons by an acceleration mechanism while later work there[4] points toward a traveling thermonuclear reaction ("boiler" model), and recent work at Los Alamos lends support to the model of a stationary thermonuclear reaction. This paper discusses measurements of neutron and x-ray energies that were performed in the exploration of these questions. The results of these measurements are in accord with an acceleration mechanism.

II. APPARATUS

The paraboloidal pinch geometry[7] is shown in Fig. 1. Deuterium gas fills the volume between the inner copper anode and the outer copper cathode. Closing the air gap switch introduces the voltage of the 15-kJ capacitor bank across the electrodes. A current sheet develops across the pyrex insulator at the base of the anode and is driven toward the apex of the apparatus by J × B forces. Maximum compression of the quasi-cylindrical imploding shock-front occurs 3 to 5 μsec after breakdown, in agreement with snow-plow theory.[1] A peak current of 300,000 A is achieved during the maximum compression.

Three events are observed within 50 nsec of the current peak: (1) a discontinuity in the current, (2) a burst of neutrons, and (3) a burst of x rays. Typical operation at 18 kV and 700 mTorr gives neutron yields between 5×10^7 and 10^9 n/burst with an average value of 3×10^8. The neutron yield is reduced by the substitution of a hollow, constant radius, cylindrical inner electrode containing a nuclear emulsion. The total x-ray flux through the 0.125-in.-thick beryllium window is 100 erg/cm^2.

III. NEUTRON ENERGY SPECTRUM

The neutron energy spectrum was measured for the purpose of identifying the mechanism responsible for the production of neutrons. The energy of the neutron in MeV from the D(d, n)He^3 reaction can be approximated from

$$E_n = 2.45 + 1.1E_d^{1/2}\cos\theta \qquad (1)$$

where E_d is the energy of the incident deuteron and θ is the angle between the velocity vectors of this deuteron and the neutron. In a thermonuclear reaction, there is not a preferred direction and the resultant spatially isotropic neutron energy distribution has a maximum at 2.45 MeV. Conversely, when there is a preferred deuteron energy and direction, the observed anisotropic neutron energy distribution allows calculation of E_d from Eq. (1) if θ is known.

Moving thermonuclear reactions also produce anisotropic energy distributions.[4] The energy of a neutron produced by a translating D-D reaction is given by

$$E_n = 2.45 + 2.2\, E_{d'}^{1/2} \cos\theta' \qquad (2)$$

where $E_{d'}$ is the energy of a deuteron pair moving with the translational velocity of their center of mass and θ' is the angle between the velocity vectors of the center of mass and the neutron.

The decision to use nuclear emulsions for energy spectrum measurements was based on the success other groups have had in using this technique on plasma devices.[3] Ilford K2 200-μ emulsions mounted on 1-in. × 3-in. glass slides were positioned as indicated in Fig. 1. Each emulsion was surrounded by lead shielding with a minimum thickness of 0.3 in. to prevent x-ray fogging of the emulsion. The pinch was then fired 100 times for a total yield of 6×10^9 neutrons. (Largest single burst yield: 2×10^8 neutrons.) After development, both emulsions were scanned over 1-mm × 12-mm strips along their axes.

The energy spectrum of recoil protons whose tracks made an angle ψ of 30 deg or less with the accelerator's axis is shown in Fig. 2 with the theoretical spectrum that would result from a monoenergetic neutron beam at 2.45 MeV. A substantial anisotropy is shown to exist in the neutron energy distribution. By assuming that the neutrons were produced on the accelerator's axis, the neutron energy is obtained from that of the recoil proton from the relationship $E_n = E_p \sec^2\psi$. The corresponding neutron energy spectra is also shown.

The measured spectra negate the possibility of neutron production by stationary thermonuclear reactions. Assuming that individual deuterons were accelerated to an energy E_d before striking stationary target deuterons allows one to estimate $\bar{E}_d$, the deuteron energy corresponding to the peak energy $\bar{E}_n$ of the neutron energy spectra. Equation (1), $2.75 \lesssim E_n(0\text{ deg}) \lesssim 2.85$ MeV, and $2.05 \lesssim \bar{E}_n(180\text{ deg}) \lesssim 2.15$ MeV give $90 \lesssim \bar{E}_d \lesssim 130$ keV. Although the peak for the 0-deg spectrum appears to be somewhat higher than 2.85 MeV, this does not affect the conclusion that many deuterons must have been moving along the axis with energies of ~100 keV in order to produce the observed spectra.

The Fillipov model of a plasma "blob" with thermonuclear temperature that moves axially with high velocities must also be considered. The estimates of $\bar{E}_n$ and Eq. (2) give $\bar{V}_t = (2E_{d'}/M)^{1/2} = 2 \times 10^8$ cm/sec, which is a rather high velocity since it corresponds to the velocity of the "blob." X-ray pinhole camera pictures do not show the smearing that is expected from a hot plasma moving at 10^8 cm/sec.

The measured neutron and recoil proton energy spectra therefore indicate a mechanism that accelerates deuterons axially to energies on the order of 100 keV.

IV. X-RAY MEASUREMENTS

Preliminary x-ray measurements made using aluminum absorbers with Kodak Type F film as the detector revealed the presence of soft x rays with photon energies < 15 keV and hard x rays with energies between 29 and 41 keV. (X rays with energies higher than ~350 keV were also detected.) The intensity of the hard component was proportional to the neutron yield of the shot.

Ross x-ray filters were designed to measure the x-ray spectrum in the following intervals: 7.1 to 8.3, 8.3 to 9.0, 14 to 20, 20 to 25.5, 25.5 to 29.2, 40.4 to 67.4, and 67.4 to 88 keV. The gaps in spectral coverage occur because of the difficulty in obtaining thin foils of certain

elements. During exposure, the filters and film detectors were on the device axis 53 cm from the anode.

The intensity and spectral distribution between 7.1 and 29.2 keV was not a function of neutron yield. The standard deviation of the x-ray intensity in each of the measured photon energy intervals between 7.1 and 29.2 keV was about 30%, while the standard deviation in the neutron yield was over 90%. Also, the spectrum showed no significant change when hydrogen was substituted for deuterium.

When the data from each shot were plotted, it was found that the flux in erg/cm^2-keV could be represented by $F = a\omega^{-s}$ where $\hbar\omega$ is the photon energy in keV. The composite spectrum in Fig. 3 includes data from 31 deuterium firings. This spectrum, typical of the spectra from individual shots, is described by $F = 430\,\omega^{-1.7}$.

Only one of the 31 shots in this series had sufficient intensity for Ross filter analysis above 29.2 keV and yielded more than 10^9 neutrons. Its spectrum differed from that of the other shots in two respects: a 45-keV radiation peak was superimposed on the ω^{-s} distribution, and the 7.1 to 8.3 and 8.3 to 9.0 keV filters detected an increase in fluorescence radiation.

A multiple pinhole x-ray camera with Ross filters was used to measure the position, distribution, and spectrum of the x-ray source. The source, a thin sheet of variable and complex structure that at times resembled a stellar nebula was located within 0.05 in. of the anode surface. The small point sources are believed to be associated with irregularities in the granular surface of the anode.

The radiation from any region of the anode surface is anisotropic with minimum intensity in the direction of the surface normal. Radiation at 45 deg is typically 3.5 × greater than at 90 deg. A spectral map of the surface could not be made since the images made by pinholes with different Ross filters were at different angles relative to the anode surface.

V. DISCUSSION OF THE POWER-LAW SOFT X-RAY SPECTRUM

The ω^{-s} variation of the described continuous x-ray energy spectrum may indicate turbulent plasma heating. An electron distribution f(E) produces the bremsstrahlung power spectrum[8]

$$I(\omega) = c\int_{\hbar\omega}^{\infty} f(E)\,\log_e\left[(E/\hbar\omega)^{1/2} + (E/\hbar\omega - 1)^{1/2}\right] E^{-1/2}\,dE \qquad (3)$$

A non-Maxwellian electron distribution of the power law form $f(E) \propto E^{-\gamma}$ gives

$$I(\omega) = c'\omega^{-\gamma+1/2}\int_1^{\infty} X^{-\gamma-1/2}\log_e\left[X^{1/2} + (X-1)^{1/2}\right] dX \qquad (4)$$

where the integral has a finite value for $\gamma > 1/2$. Comparison of Eq. (4) with the soft x-ray data ($s = 1.7 \pm 0.3$) leads to the identification $\gamma = s + (1/2)$, and, consequently, the electron distribution $f(E) \propto E^{-2.2 \pm 0.3}$.

Syrovatskii[9] has recently developed a general model for turbulent heating of electrons. This model considers a volume of high-temperature plasma with a total energy density $W_t = W_m + W_k + W_f$, where $W_m = H^2/8\pi$ is the magnetic energy density, $W_k = 1/2\,\rho u^2$ is the kinetic energy density of the turbulent background plasma, and $W_f = NE$ is the energy density of N fast particles of average energy E. A steady state is maintained if the loss of dN fast particles is compensated by an energy gain $dW_t = E\,dN$. The balance relation obtained by assuming $W_f/W_t = \epsilon$ is

$$1/\epsilon\ d(NE) = 1/\epsilon\ (E\,dN + N\,dE) = E\,dN \qquad (5)$$

which has the solution $N = CE^{-1-\delta}$, where $\delta = \epsilon/(1-\epsilon)$ is the ratio of the fast particle energy to the remaining energy. The corresponding differential energy spectrum is

$$dN = f(E)\,dE = CE^{-\gamma}$$

where $\gamma = 2 + \delta$. At this point, Syrovatskii assumes strict equipartition of energy between the three modes and sets $\delta = 1/2$ to get $\gamma = 2.5$. This value is in excellent agreement with cosmic ray data. However, the theory of magnetohydrodynamical turbulence is presently in an uncertain

state with regard to the question of energy equipartition.[10] For example, the work of Chandrasekhar[11] indicates a fine-scale mode of turbulent energy transfer for which $W_m = 2.6W_k$. This gives $\delta = (1 + 2.6)^{-1} = 0.28$ and $\gamma = 2.28$, in good agreement with the $\gamma = 2.2 \pm 0.3$ electron energy distribution inferred from the soft x-ray data.

Theories based upon general thermodynamic considerations[9] yield $\gamma = 2 + (\kappa - 1)^{-1}$, where $\kappa = 2$ or 5/3 corresponding to two- or three-dimensional adiabatic processes, respectively, leads to $\gamma = 3$ or $\gamma = 7/2$, in apparent disagreement with the bremsstrahlung interpretation. Likewise, Kurchatov's hypothesis[12] concerning the presence of acceleration mechanisms of the Fermi type[13] leads to $\gamma = 1 + (\alpha\tau)^{-1}$, where the parameters α and τ are sensitive to local plasma conditions, contrary to the experimental observation that the spectra are quite insensitive to neutron yield. Consequently, these electron heating theories seem less appropriate than the described turbulent mechanism.

VI. CONCLUSIONS

It has been shown that the production of neutrons is the paraboloidal Z-pinch can be best described in terms of acceleration of deuterons to energies on the order of 100 keV. Plasma instabilities have been postulated by numerous investigators as the source of the electric fields that cause this acceleration.

It has also been demonstrated that models of turbulence exist that can explain the observed x-ray spectrum. The same plasma instabilities required for the acceleration of deuterons could also be the source of turbulence. It is thus concluded that under present operating conditions, a mechanism that gives rise to plasma instabilities and results in an extremely turbulent plasma, not a thermonuclear reaction, is operative.

Important questions remain unanswered. Recent x-ray absorber and Ross filter measurements have indicated a change in the spectrum as the neutron yield increases above 10^9 n/burst. Does this mean that the conclusions reached here are only valid for relatively small energy inputs and low neutron yields? What are the details of the instabilities? What are the dynamics of the pinch during all phases of the discharge and how does it differ from right cylindrical coaxial focused pinches?

All of these questions will be studied with the aid of a new device being constructed that will have a similar geometry, 5 times greater energy input, and much greater diagnostic accessibility.

ACKNOWLEDGEMENT

The authors wish to thank Dr. V. Josephson and M. H. Dazey for their contributions.

This work was supported by the U. S. Air Force under Contract No. AF 04(695)-1001.

REFERENCES

1. J. W. Mather, Phys. Fluids 8, 366 (1965).
2. J. W. Mather, Proc. Conf. Plasma Physics and Controlled Nuclear Fusion Res. (International Atomic Energy Agency, Vienna, 1966) Vol. II, p. 389.
3. A. M. Andrianov, et al., Geneva Conf. on Peaceful Uses of Atomic Energy (United Nations, N. Y., 1958), paper 2301; N. V. Fillipov, T. I. Fillipova, and V. P. Vinogradov, Nucl. Fusion Supplement 2, 277 (1962).
4. N. V. Fillipov and T. I. Fillipova, Ref. 2, p. 405.
5. E. H. Beckner, J. Appl. Phys. 37, 4944 (1966); Rev. Sci. Instr. 38, 507 (1967).
6. R. H. Lovberg, Phys. Fluids 8, 177 (1965).
7. V. Josephson, "Tri-Dimensional Plasma Compression Assemblies," TR-669(6550-10) -2, Aerospace Corp. (December 1965).
8. W. Heitler, The Quantum Theory of Radiation, (Oxford Univ. Press, 1954) 3rd ed. p. 246.
9. S. I. Syrovatskii, Sov. Phys. JETP 13, 1257 (1961).
10. T. G. Cowling, Magnetohydrodynamics (Interscience, N. Y., 1957), Chapt. 5.
11. S. Chandrasekhar, Proc. Roy. Soc. A233, 330 (1955).
12. I. V. Kurchatov, Nucleonics 14 (6), 36 (1956)
13. V. L. Ginzburg and S. I. Syrovatskii, The Origin of Cosmic Rays (Macmillan Co., N. Y., 1964), translated by H. S. W. Massey and D. ter Haar, Secs. 9 and 16.

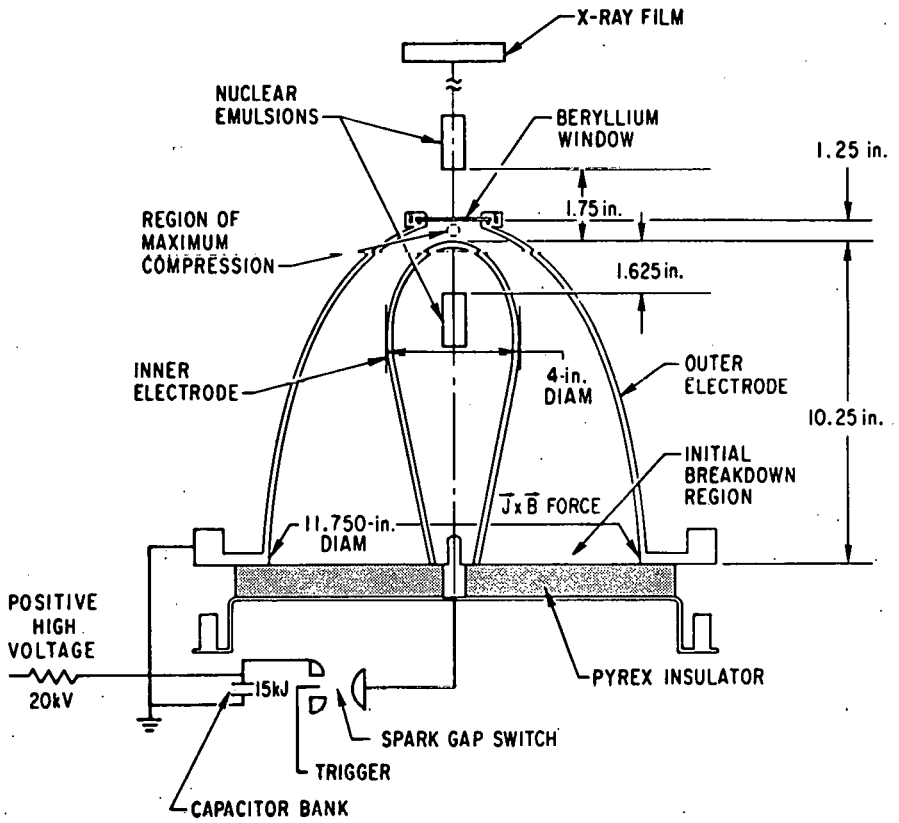

Fig. 1. Paraboloidal pinch geometry

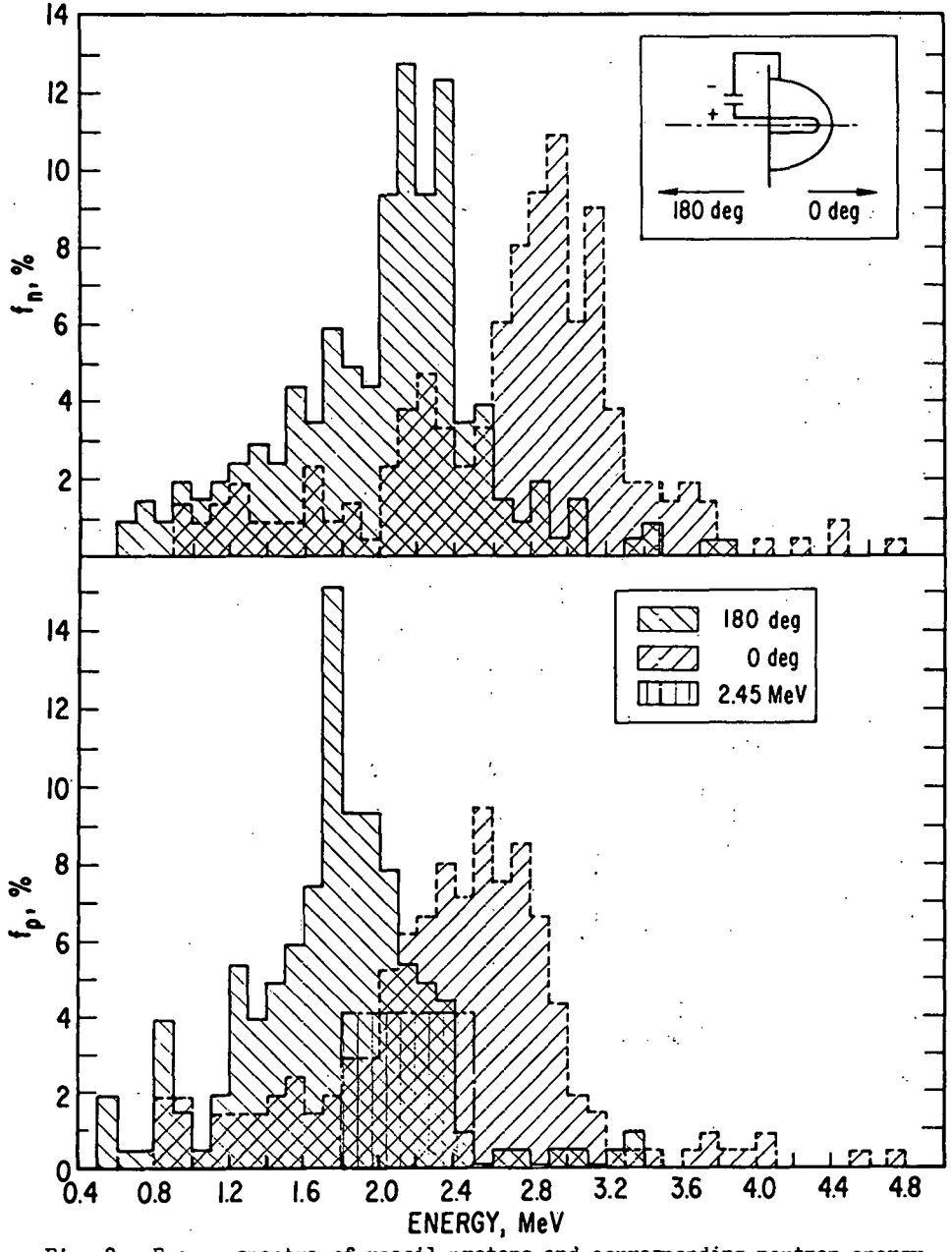

Fig. 2. Energy spectra of recoil protons and corresponding neutron energy

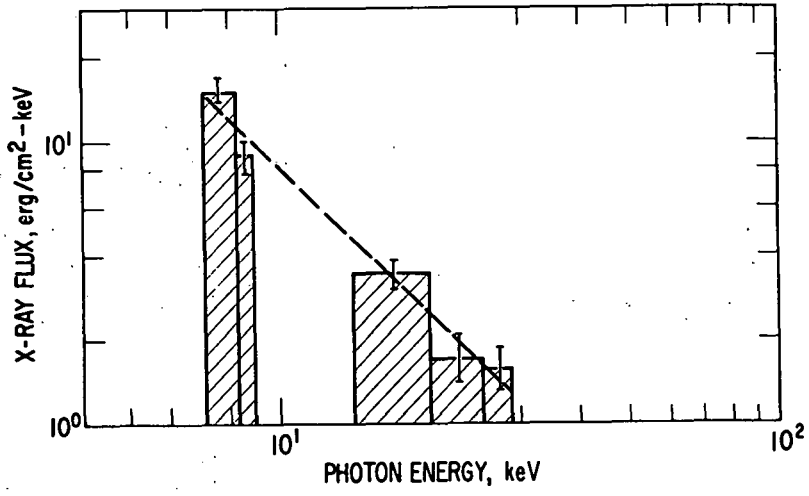

Fig. 3. Composite x-ray spectrum for 31 shots at 18 and 19 keV with deuterium at pressures between 650 and 780 mTorr

NEUTRON AND X-RAY PRODUCTION IN A FOCUSED Z-PINCH (PAPER C6)

David Allan Meskan, G. G. Comisar, and H. L. van Paassen

ERRATA

Abstract:

Line 11 should read, "current MHD turbulence"

Section II:

Para 3, line 10 should read "The x-ray flux measured 50 cm from the 0.125-in. -thick. . ."

Section III:

Para 5, Line 8: Change "E_n" to "$\bar{E}_n$"

Section IV:

Para 4, Line 5: Change "31" to "26"

Para 5, Line 1: Change "31" to "26"

Section V:

Equation (3) should read:

$$I(\omega) = C\int_{\hbar\omega}^{\infty} f(E)\,\log_e\left[\left(\frac{E}{\hbar\omega}\right)^{1/2} + \left[\left(\frac{E}{\hbar\omega}\right) - 1\right]^{1/2}\right] E^{-1/2}\,dE$$

Para 2, Line 17: $dN = f(E)\,dE = CE^{-\gamma}\,dE$

Section VI:

Para 1, Line 2: Change "is" to "in"

Fig. 3, Caption: Change "31" to "26"

COAXIAL SNOWPLOW DISCHARGE*

By

T. D. Butler, I. Henins, J. Marshall and R. Morse
Los Alamos Scientific Laboratory, University of California
Los Alamos, New Mexico

ABSTRACT

A coaxial type discharge system has been operated without an outer electrode and with static fillings of several different gases over wide ranges of filling densities. Plasma light photographs and magnetic probe analysis show a sharply defined current and plasma layer for most operating conditions. A cylindrical snowplow model for the plasma layer gives reasonable quantitative agreement with all phases of the discharge including the period during which the plasma layer leaves the end of the center electrode and forms a pinch on the center axis of the system. Experimental and theoretical numerical results will be shown.

I. INTRODUCTION

The coaxial plasma discharge has been employed as a plasma accelerator[1,4] and a plasma focus.[2] In the latter mode of operation the system is given a static gas filling. An axially symmetric discharge is seen to form at the current feed end between the inner and outer electrodes and to propagate to the open end where a z-pinch is formed. This paper describes an experimental and theoretical study of a static filled system in which the outer coaxial electrode is removed and replaced by a less obstructive current return as shown in the cross section of the experimental apparatus, Fig. 1. The outer electrode is thought to hamper diagnosis and analysis of the discharge without significantly changing its behavior because material in the sheath moves radially outward (see below). With this change the shape of the discharge could be seen from side on photographs, eg., Fig. 2. This device was supplied by various combinations of 20 kV capacitors switched by ignitrons and totaling up to 830 μf. Shots were fired in H_2, D_2, He and A with peak currents from about 200 to 500 kA and filling pressures from 0.04 to 30. torr.

At times when the current is changing slowly and the sheath is well removed from the rear insulator but not yet to the end of the cylindrical electrode, its structure can be approximated by a modified Newtonian equilibrium model in which a shocked layer or sheath is stationary in a frame moving axially with a uniform velocity, u. In this frame cold gas of density ρ_0 impinges with pure axial velocity -u on the front of the sheath, which can be shown to be thin compared to other lengths in the problem (mainly because of large density ratios across hypersonic shocks). The back of the sheath is supported by the pressure of the purely azimuthal vacuum magnetic field,

$$P_B = B_0^2 r_0^2/8\pi r^2$$

where r is the radius of a point on the sheath and r_0 and B_0 are the radius of the electrode and the magnetic field at its surface, respectively. A mass, momentum and energy conserving time independent calculation with this model shows that equilibrium can be achieved if the sheath is normal to the inner electrode at the point of contact and if the angle of its backward slant relative to a radius line, θ, increases monotonically with distance from the electrode. Material which enters the sheath moves outward along the sheath with a local flow velocity

v(s) where s is arc length along the sheath from the electrode. In the lab frame material is continually being collected, pushed forward and to the outside by the advancing sheath in the manner of a snowplow. The sheath thickness, $\theta(s)$ and v(s) are zero at the electrode and increase in proportion to $\sqrt{s}$ for small s/r_0. For larger s/r_0 the sheath thickness is sometimes sensitive to the ratio of directed ion energy, $Mu^2/2$, to ionization potential. The $\theta(0) = 0$ boundary condition may be taken from a fluid mechanical cavitation argument applied to the point of contact or from the agreement of the sheath velocity predicted from this assumption,

$$u^2 = B_0^2/8\pi\,\rho_0,$$

with experimental results over a range of conditions (Fig. 4). It is assumed throughout that the plasma behaves like a classical conducting fluid driven by a magnetic piston. These assumptions are based on the magnitude of the ion-ion and ion-neutral (elastic and charge exchange) cross sections for the energies considered and the resulting relatively small values of mean free paths and c/ω_{pi} for the densities considered.

Time dependent solutions of the same theoretical model problem have been computed using a two dimensional cylindrically symmetric PIC[3] code. The PIC method (Particle-in-Cell), which is a mixture of Lagrangian and Eulerian techniques, was used because of its ability to handle compressible fluid flow and the field-plasma free surface. The plasma was treated as an inviscid, non-heat conducting fluid with the polytropic gas equation of state

$$P = (\gamma - 1)\rho I$$

where P is pressure, γ the ratio of specific heats, ρ is the density and I the internal energy. Ionization energy was neglected. Runs were made with $\gamma = 4/3$ and $5/3$. The free surface boundary condition was satisfied by using the vacuum field pressure (above) in every cell containing no particles. A time independent B_0^2 was used for this purpose. To start the PIC computations, two cells were evacuated at the intersection between the rear return electrode and the cylindrical electrode. The latter electrode was treated as a rigid boundary in the calculations.

II. RESULTS

Figure 2 shows two approximately corresponding sequences of pictures. In the first row are plasma light photographs from the experiment run with a peak current of 400 kA and a filling pressure of 2 torr of deuterium. The second row shows computer plots of the particles at different times (arbitrary dimensionless time units) during a PIC run simulating the experimental situation. Current traces show that the current was sufficiently slowly varying at the time of the first experimental picture to allow comparison with equilibrium theory and the corresponding picture obtained from the constant current PIC computation. Figure 3 shows a plot of the center lines of the three sheaths. The PIC line bends over more than the others near the back because the necessary shortness of the mesh in z prevents this part of the computation from being in equilibrium. The pure stationary result, which in principle goes on to s, $r \to \infty$, and $z \to -\infty$, was obtained from integrating the exact equations numerically with the help of the asymptotic solution near s = 0. The two predicted sheath thicknesses are in better than order of magnitude agreement with one another and with the experiment but the agreement is not as good as it is for the shape of the sheath.

Sheath velocities were determined by focusing two photomultiplier telescopes at points a few centimeters apart on the electrode and determining the transit interval from scope traces. The results are shown in Fig. 4 for deuterium. Different shots are plotted against $I/\sqrt{P}$ where I is total current and P is filling pressure. This is proportional to $B_0/\sqrt{\rho_0}$. As discussed above, if the $\theta(0) = 0$ boundary condition applies, u should vary linearly with this ratio. The theoretical velocities are given by the dashed line which lies reasonably close to the experimental points. Note that most of these velocities correspond to D_2 energies which are larger than the total D_2 dissociation and ionization potential.

When the sheath passes over the end of the electrode, a rapidly accelerating z-pinch-like collapse toward the center axis begins. This is caused by the r_0^2/r^2 dependence of the magnetic pressure and is reflected in the relatively short time intervals between the later pictures in the two sequences in Fig. 2.

The PIC code developed radial collapse velocities as large as six times the equilibrium u values.

At the time in a deuterium shot when the collapse reaches the axis, $\sim 10^9$ neutrons are produced. No effort was made to increase this yield.

The last frame in each sequence shows a bubble which forms very rapidly starting from the time when the radial collapse reaches the center axis. In the experiment this rather striking feature continues its rapid, approximately hemispherical expansion until its diameter is several times that of the electrode.

An explanation of the formation of the bubble is provided by the PIC results. The large axial pressure gradient generated by the radial collapse of the sheath causes a jetting of the relatively high temperature plasma into the undisturbed gas along the axis. The converging sheath aids in the focusing as well as the enhancement of the jet. When the jet penetrates the front of the converging sheath, the plasma in the jet expands under a radial hydrodynamic pressure gradient. This expansion is later enhanced by the presence of the magnetic field which contributes to an inverse z-pinch effect in the same manner as occurs initially along the outer surface of the electrode.

ACKNOWLEDGMENTS

The authors are indebted to A. A. Amsden for his assistance with the PIC calculations. This work was performed under the auspices of the United States Atomic Energy Commission.

REFERENCES

1. I. Henins and J. Marshall, "Coaxial Gun Development," APS Topical Conference on Pulsed High Density Plasmas (September 1967).
2. J. W. Mather, P. J. Bottoms, and A. H. Williams, "Some Characteristics of the Dense Plasma Focus," APS Topical Conference on Pulsed High Density Plasmas (September 1967).
3. A. A. Amsden, "The Particle-in-Cell Method for the Calculation of the Dynamics of Compressible Fluids," Los Alamos Scientific Report LA-3466 (1966).
4. F. J. Fishman and H. Petschek, "Flow-Model for Large Radius-Ratio Magnetic Annular Shock-Tube Operation," Phys. Fluids 5, 632 (1962).

* Work performed under the auspices of the U. S. Atomic Energy Commission.

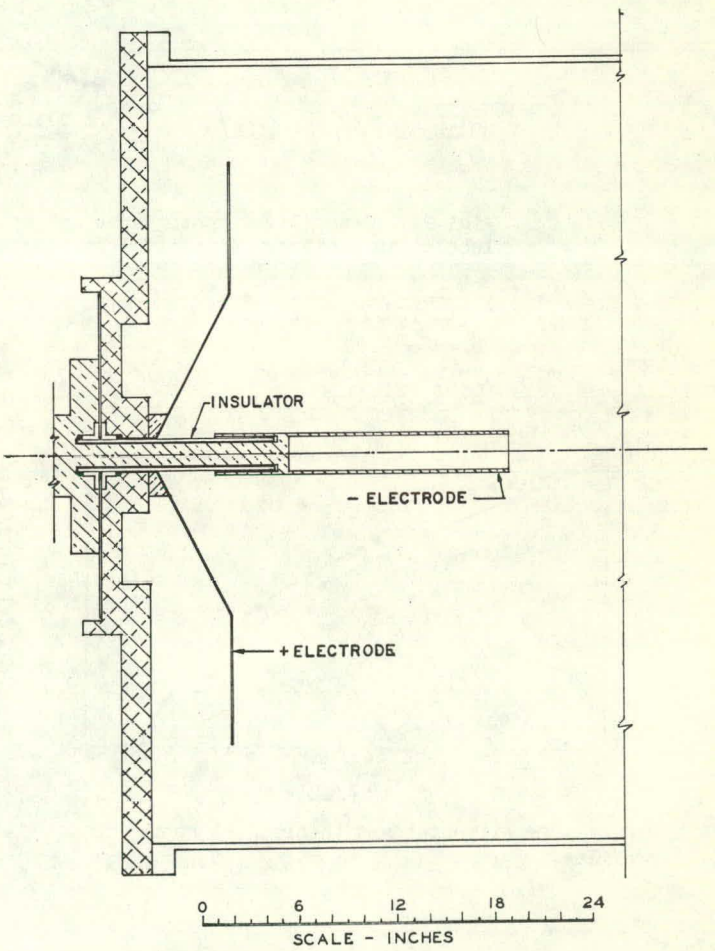

Fig. 1. Experimental apparatus seen in cross section through center line.

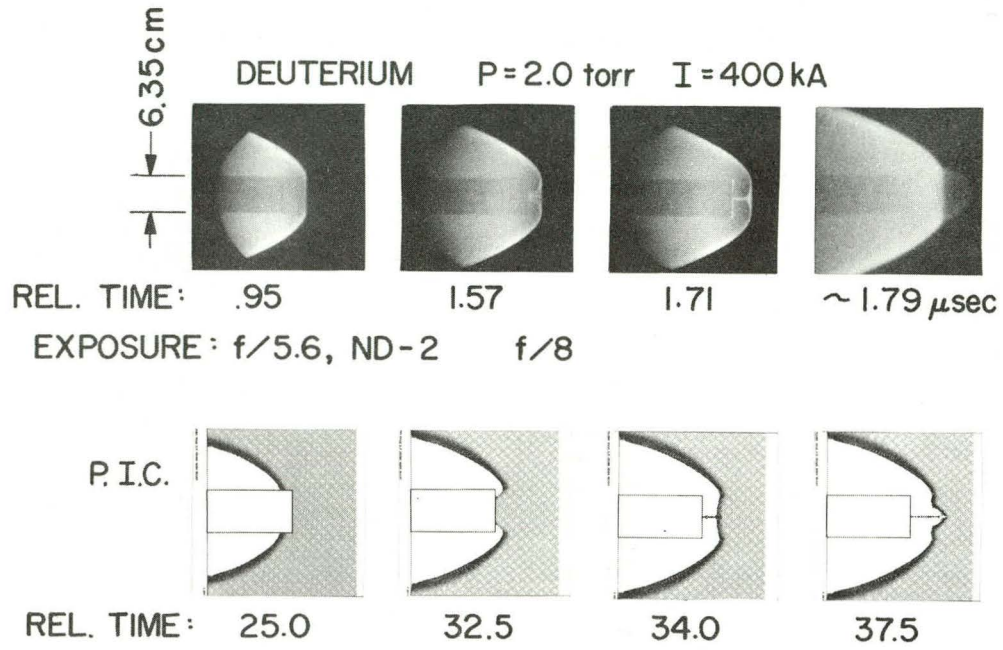

Fig. 2. Plasma light photographs and approximately corresponding P.I.C. pictures labeled in arbitrary dimensionless time units.

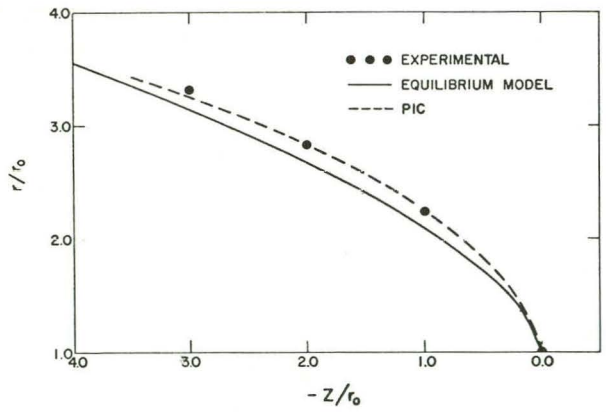

Fig. 3. Experimental and theoretical shock profiles.

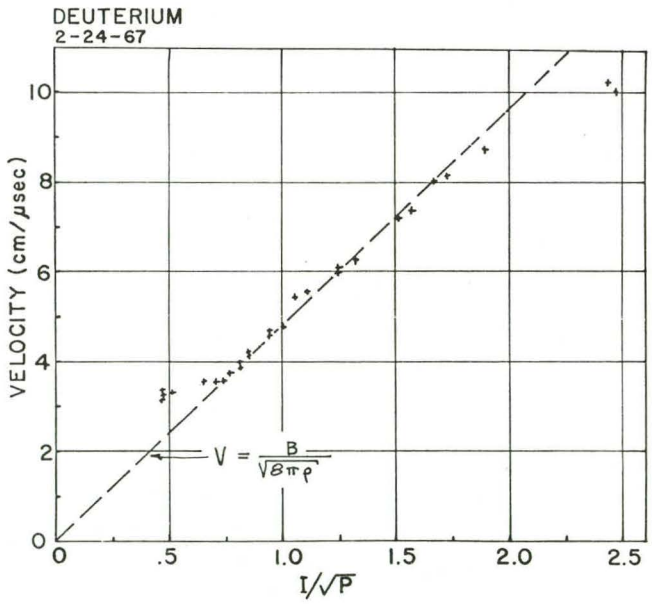

Fig. 4. Axial shock velocities before end-collapse for different parameters - velocities on dashed line agree with normal incidence boundary condition.

ION HEATING IN THE EARLY STAGES OF A VERY FAST THETA PINCH +)

by

U. Schumacher, R. Wilhelm, and H. Zwicker
Institut für Plasmaphysik
Garching b. München, Germany

ABSTRACT

In a theta pinch with fast rising magnetic field (dB/dt = (1.3 - 2.1) x 10^{11} G/s) ion energies in the keV-region were obtained already after the first compression. At filling pressures of 20 mtorr these energies were indicated by neutron production at the end of the implosion. The velocity distribution function of the ions seems to be nearly monoenergetic. Probe measurements during the implosion show that the current carrying layer decreases with increasing filling pressure (10 - 60 mtorr D_2). The axial region, however, remains free of field up to the first compression.

Introduction

The purpose of these investigations was to produce a strong implosion wave in a theta pinch with a rapidly increasing magnetic field and hence to achieve correspondingly high energy gain of the ions.

Simple estimates show that the first compression should already lead to ion energies in the keV region for initial densities of over 10^{15} cm^{-3}.

In an attempt to find whether this high ion heating is suitable as a starting point for the further adiabatic compression, a major part of the investigation was concentrated on the early stages of the discharge.

The subsequent plasma heating was studied up to the field maximum. Because of the relatively short compression coil, however, the influence of end losses has to be taken into account before this time.

Apparatus

In a theta pinch coil 7 cm in diameter and 14 cm long, magnetic field rises of (1.3 - 2.1) x 10^{11} G/sec (without plasma) are achieved for voltages of 50 - 80 kV. About 80% of the stored energy of 45 - 115 kJ is transferred to the coil, resulting in a maximum field of 145 - 230 kG. Damage to the vessel is considerably reduced by switching a crowbar in the current maximum. For the preionization we use a 120 kV z-pinch with a single current pulse, thereby achieving a mean degree of ionization of about 50% [1].

Measurements

Initial measurements were made at filling pressures of 10 - 60 mtorr deuterium and a voltage of 50 kV. Information on the early stages of the compression was first obtained by diamagnetic probe measurements and direct magnetic field measurements in the plasma. In Fig. 1 the region of the current carrying sheath is plotted as a function of time for three different initial pressures. A sharp inner boundary of the sheath is given by the point at which the magnetic field indicated by the inner probe rises practically from zero (curve A). The second curve (B) shows the outer boundary obtained from the diamagnetic signals. The important result to be noted in these measurements is that for all three initial pressures the axial regions remain practically fieldless ($B < 100$ G) up to the first compression. On

the other hand, the width of the plasma region permeated by the magnetic field increases strongly with decreasing initial pressure. This spread of the current carrying sheath, which at a filling pressure of 10 mtorr extends almost to the wall, should be accompanied by a possibly considerable reduction of the energy increase. It was attempted experimentally to determine the magnitude of the ion energy achieved in the implosion. A mean ion energy in the keV region should be indicated by noticeable neutron emission.

As Fig. 2 shows, such neutron emission was already detected at the end of the implosion for small initial densities. Here the plasma compressions, determined from diamagnetic signals, and the time behaviour of the neutron flux are plotted for a filling pressure of 20 mtorr deuterium. There is a pronounced neutron peak, which is correlated with the first maximum compression. With the electron density of 1×10^{16} cm^{-3}, determined spectroscopically from laser scattering[2] and Stark broadening of D_β, and with a rough volume estimate from diamagnetic signals one obtains ion energies of about 1.6 keV at the time of the first compression. A monoenergetic one-dimensional ion distribution function was taken as a basis for the rate coefficients $\langle \sigma v \rangle_n$ of neutron production. Because of the steepness of the $\langle \sigma v \rangle_n$-curves in this energy range, uncertainties in the electron density and volume determination hardly affect the ion energy obtained in this way. On the other hand, the type of distribution function assumed has more influence on the value of the mean ion energy. A monoenergetic two-dimensional distribution function gives an ion energy of 1.8 keV, while the values obtained with Maxwell-like distributions are up to a factor of 2 smaller.

The subsequent behaviour of the ion energy in the adiabatic phase was determined in the usual way from the neutron flux and the density. Laser measurements and the determination of the bremsstrahlung, which is possible in the later stages, give the electron density in the axial region (Fig. 3).

Assuming a parabolic density distribution up to a radius R

$$n(r) = n_0 \cdot \left(1 - \left(\frac{r}{R}\right)^2\right)$$

from the diamagnetic signal

$$\Delta\phi = \pi \cdot R^2 \cdot B_0 - \int_0^R B(r) \cdot 2\pi r \cdot dr$$

the pressure equilibrium

$$\frac{B_0^2}{2\mu_0} = n(r) \cdot \left[E_i + kT_e\right] + \frac{B^2(r)}{2\mu_0}$$

and the total neutron flux

$$N = \frac{l}{2} \int_0^R \langle \sigma v \rangle_n \cdot n^2(r) \cdot 2\pi r \cdot dr$$

we determined the ion energy, which is assumed to be constant over the radius. Here n_0 is the density on the axis, R the plasma radius, B_0 the external magnetic field, B(r) the magnetic field strength at radius r, E_i and kT_e the ion energy and electron temperature respectively. The length of the plasma was found from z-resolved diamagnetic signals and from neutron flux measurements and continuum radiation in planes at various distances from the coil centre.

The results obtained on evaluating the ion energy are shown in Fig. 4a for a filling pressure of 20 mtorr. These depend very slightly on the assumed density distribution.

The continuous curve is obtained for a two-dimensional monoenergetic ion velocity distribution, the broken curve is obtained for a two-dimensional Maxwellian. Fig. 4b shows the time behaviour of the value of β in the axial region.

Assuming a Maxwell distribution of the ions one obtains in the early stages values for β which are scarcely compatible with the zero field measured direct. On the other hand, the β-curve for the monoenergetic distribution function of the ions is consistent with the zero field found in the axial region.

Because of end losses, the further adiabatic heating of the plasma could only be followed up to the field maximum.

A rough impression of the end losses can be obtained from Fig. 5, which shows the decrease of the plasma volume with time, this being determined by spatially resolved diamagnetic probe measurements.

It can be seen that the field inhomogeneity at the coil ends leads to plasma losses, which results in the plasma length decreasing immediately after the implosion. A strong decrease of the cross-sectional area begins only towards the end of the quarter-cycle. Since the density on the axis remains almost constant during the adiabatic compression, the midplane region should remain largely unaffected by end losses for a fairly long period.

Results

In a theta pinch with a stored energy of only 45 kJ, ion energies in the keV region could already be achieved in the implosion phase by means of a fast rising magnetic field. On further compression this energy rises to some keV for densities of about 3×10^{16} cm^{-3}.

These energy data depend, however, on the type of velocity distribution function of the ions. It seemed reasonable in the implosion phase to assume a mono-energetic one-dimensional distribution function to determine the energy of the ions. A two-dimensional monoenergetic distribution function does not yield a very much higher energy anyhow.

For the following phases of the discharge the behaviour of β indicates that the high-energy components of the velocity distribution are absent at first and that the distribution function is also described better here by a monoenergetic distribution.

However, especially at low initial densities there is a strong spread of the current carrying sheath, the cause of which is still not clear. There is thus a lower density range for which optimum plasma heating does not seem possible under these conditions.

+) This work was performed as part of the joint research program of the Institut für Plasmaphysik, Garching and Euratom.

References

1 U. Schumacher and R. Wilhelm, paper presented at the Frühjahrstagung der DPG, Kiel 1966

2 The laser scattering measurements were made by P. Grund.

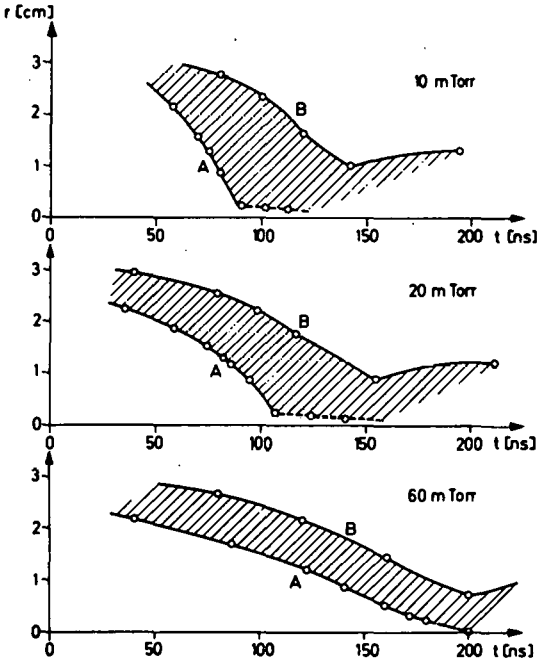

Fig. 1 Current layer as a function of time

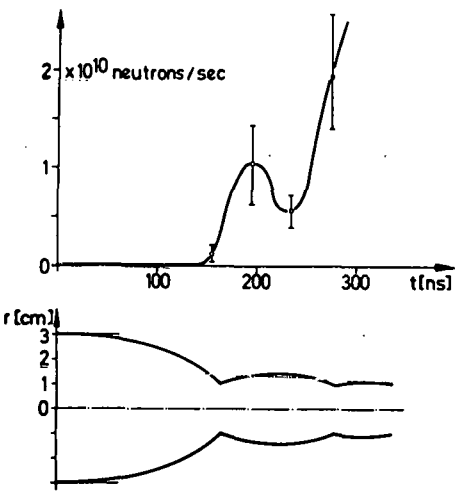

Fig. 2 Neutron emission and plasma compressions at 2o mtorr

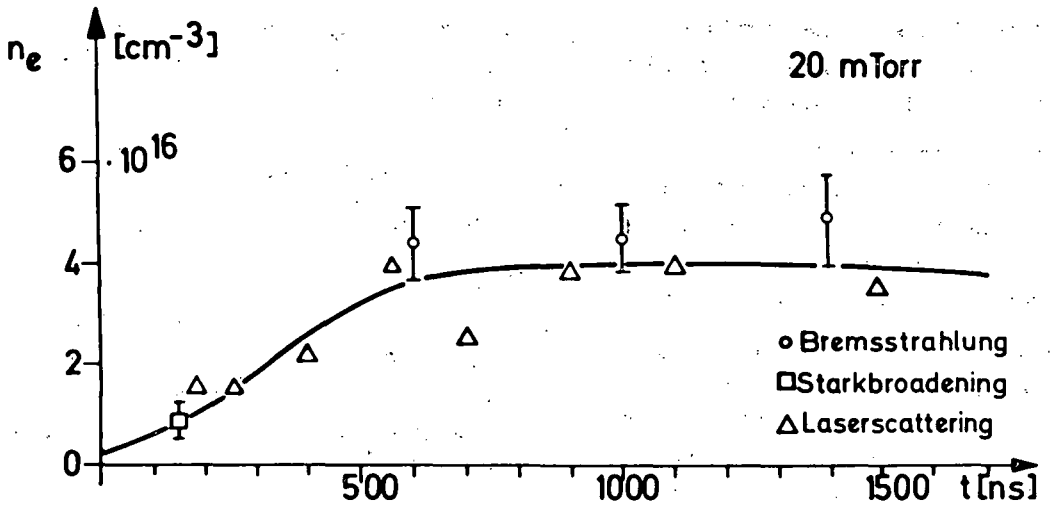

Fig. 3 Electron density at the axis in the midplane versus time

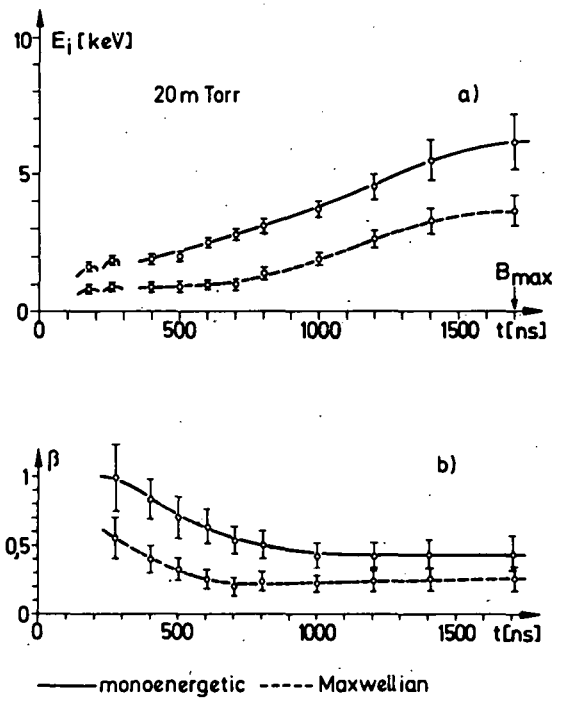

Fig. 4 Time behaviour of ion energy (a) and (b)

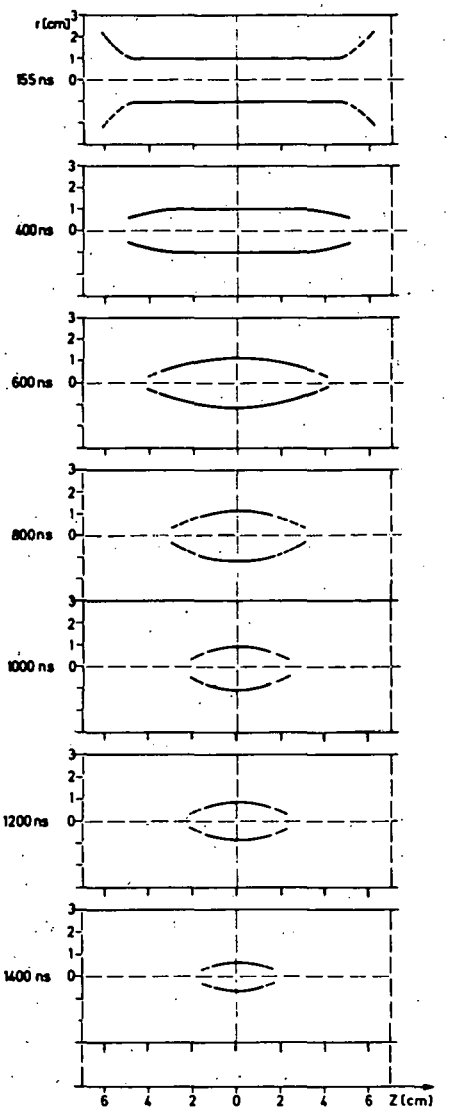

Fig. 5 Plasma volume as a function of time at 2o mtorr

SPACE-TIME RESOLVED MACH-ZEHNDER INTERFEROMETER MEASUREMENTS OF CROSS-SECTIONAL ELECTRON DISTRIBUTION IN θ-PINCH PLASMA

by

Howard N. Roberts (Introduced by Arwin A. Dougal),
Frederic Weigl, and Arwin A. Dougal
Department of Electrical Engineering and
Laboratories for Electronics and Related Science Research
The University of Texas, Austin 78712

ABSTRACT

A 2" ID quartz tube with quartz end windows is closely encircled by a 20 cm coil (1.15 mirror ratio) in a four-stage, 30 kJ θ-pinch (3.0 μsec quarter period). A 175 MW giant pulse (15 nsec) ruby laser illuminates the interferometer. A distinct density minimum persists on the plasma axis as late as 3.2 μsec into the main compression for initial deuterium pressures of 0.05 - 0.1 Torr, reverse bias fields of 2 - 6 kG, and peak fields of 17 - 60 kG. Measurable neutron emission consistently begins within 0.2 μsec of the time the density minimum vanishes (typically 1.2 - 1.6 μsec after main field initiation). Peak densities observed are 2 - 30 x 10^{16}cm^{-3}. Near 1.0 μsec after initiation of main compression 6-10 rotating flutes appear and remain until about 2.0 μsec. The e-folding times of plasma density are 2 - 12 μsec prior to peak compression and 0.4 - 3.0 μsec afterwards. These loss rates agree within 50% to predictions of free flow through an orifice the size of an ion Larmor orbit. Correlation to analytical predictions of electron distribution by a Hain-Roberts code in which the coordinates move with the current sheath is within 20%.

INTRODUCTION

The Mach-Zehnder interferometer measurements resolve electron distributions over the entire plasma cross-section at variable times in the plasma history. This technique is applied to a wide range of plasma conditions, including the very hot neutron producing plasmas.

EXPERIMENTAL ARRANGEMENT

Figure 1 depicts the arrangement of the Mach-Zehnder interferometer for studying the θ-pinch plasma. The time resolving neutron detector is also shown in position in Fig. 1.

A block diagram of the four-stage θ-pinch with pertinent information included is presented in Fig. 2. The one-turn coil is 20 cm long, with a 5.47 cm bore and an effective mirror ratio of 1.15. It closely encircles a 76 cm long, 5.04 cm ID quartz tube with high quality quartz end windows.

Because of essentially 100% preionization by the preheater capacitor bank (giving initial electron and ion temperatures of about 2 eV),[1] excellent shot to shot repeatability prevails.

INTERPRETATION OF INTERFEROMETRIC MEASUREMENTS

The theory of a Mach-Zehnder interferometer is well known.[2,3] For dense, fully ionized deuterium plasma the index of refraction to a good approximation depends only on the electrons and is given by

$$\mu = 1 - \frac{1}{2}\frac{\omega_p^2}{\omega^2} \quad \text{for } \omega >> \omega_p,$$

where ω_p is the electron plasma frequency and ω is the frequency of the laser radiation (λ = 6943 Å). The change in effective path length introduced by a plasma of length L is given by

$$\frac{\Delta L}{\lambda} = \int_0^L \frac{\mu - 1}{\lambda} d\ell = \frac{r_e \lambda}{2\pi} \int_0^L n_e(r,\ell) d\ell \equiv F(r)$$

where $n_e(r,\ell)$ is the electron density, r_e is the classical electron radius, and $F(r)$ is the total number of "fringe shifts" observed at any point of interest in the plasma cross-section. Thus

$$\int_0^L n_e(r,\ell)\, d\ell = 3.2 \times 10^{17} F(r) \quad cm^{-2} \quad (1)$$

EXPERIMENTAL OBSERVATIONS

Time resolving series of plasma interferographs for the first half-cycle of the main compression (0 to 6 μsec) were obtained for the following parameter ranges: initial deuterium pressures of 0.05 to 0.10 Torr; reverse bias fields of 2 to 6 kG; and peak forward fields of 17 to 60 kG. In the following discussions time zero is always the instant the main field current rise begins.

Axial Density Minimum

For all cases examined a density minimum persisted on the plasma axis at least until 1.2 μsec and as late as 3.2 μsec. In about 30% of the cases a density minimum reappeared at about 4.0 μsec. The density minimum prior to the peak in the B-field (3.0 μsec) is attributed to reverse bias field trapping. This interpretation is supported by single-pass Faraday rotation measurements made independently on this plasma.[4] Kerr cell photographs of plasma luminosity show clearly that the plasma is less luminous on axis during periods when a density minimum exists. The recurrence of an axial density minimum near 4.0 μsec is attributed to a higher end-loss rate on the plasma axis (since the loss-cone is centered on the axis). A sequence of interferographs and their resulting density profiles are presented in Fig. 3. The density minimum can be seen to dissipate near 1.5 μsec and instabilities (to be discussed later) are apparent.

Neutron Emission Correlation

For neutron producing plasma conditions (peak fields > 50 kG, reverse bias of 4 to 6 kG, pressures < 0.08 Torr), the time resolved relative neutron yield was measured and interferographs were obtained simultaneously. Correlation of the results reveals that the neutron emission consistently begins within 0.2 μsec after the axial density minimum vanishes (typically near 1.4 μsec for such plasmas). More than mere coincidence may be involved. It is proposed that the forward field has diffused through the slightly resistive plasma by that time and intermixes with the trapped reverse bias field. The resulting rapidly changing B-fields in the plasma as the reverse bias field is annihilated generate a strong azimuthal E-field. The currents which result produce additional ohmic heating.[5] Thus the energy stored in the trapped bias field (50 to 100 joules) is converted to kinetic energy and provides quite a large burst of energy in a short interval (effectively about a 50 MW power level). Further investigations of this phenomenon are planned.

Peak Densities Observed

The electron density for 100% ionization at 0.1 Torr initial pressure is $6.4 \times 10^{15} cm^{-3}$. Peak densities observed were from 2 to $30 \times 10^{16} cm^{-3}$ for 0.1 Torr and 2 to $3.4 \times 10^{16} cm^{-3}$ for 0.05 Torr. The peak densities observed increased as the compression field intensity was increased and decreased as the reverse bias field intensity was increased. Peak densities decreased rapidly as the initial pressure was lowered. Peak densities at 0.10 Torr were about 6 to 8 times greater than at 0.05 Torr. Correspondingly, plasma diameters increased as the pressure was lowered between 0.1 and 0.05 Torr indicating higher average temperatures for the lower pressures.

Instabilities Observed

In all cases examined, multi-flute type instabilities formed near 1.0 μsec. The flutes

(typically 6 to 10 of them at first) begin as periodic perturbations of the plasma boundary. Typically by about 1.5 μsec the surface perturbations appear to have become "arms" reaching out of the plasma at various axial and azimuthal positions with a somewhat periodic location azimuthally. There are typically 6 to 16 such "arms" which extend outward radially near the plasma surface but appear to bend in both the azimuthal and axial directions as they reach out(especially so for the 2 kG reverse bias cases). The bulk of the plasma remains stable in the presence of the still rising compression field. Very low collision rates are expected for these plasmas. Thus runaway electrons can result in the region of B-field intermixing and are believed to be the cause of the arms observed.[5] As the reverse bias field intensity is increased from 2 to 6 kG, the duration and degree of activity of the arms decreases markedly. The flutes and arms which form between 1.0 and 2.0 μsec do not appear to rotate. Furthermore, the first surface perturbation consistently starts at the same azimuthal location (about 150° from the feed slot). At about 4.0 to 4.5 μsec the plasma column begins to acquire one or more forms of the "kink" instability. In some cases it appears to be a helix with the helical axis roughly coincident with the unperturbed plasma axis. In other cases the ends of the column appear to bend away from the axis in opposite radial directions. And in still other cases 2 or 3 sinusoidal type bends develop along the axis. The kinked plasmas tend to rotate azimuthally about a center of mass as the amplitudes of the kinks grow. The column encounters the wall typically at about 5 to 6 μsec. Until this contact with the wall is made essentially no electron concentrations have developed at the wall.

Plasma End-loss Rates

End-loss is essentially the only loss mechanism in this device. By exploiting the azimuthal symmetry of the bulk of the plasma, the total number of electrons (N_e) present at the instant each interferograph was taken can be estimated without knowledge of a plasma length.[6] Integrating Eq. (1) over the plasma cross-section results in

$$N_e = 2.0 \times 10^{18} \int_0^{r_0} F(r)\, r\, dr \qquad (2)$$

where r_0 is the plasma radius. A digital computer was employed to integrate numerically the density profile data, $F(r)$, obtained from each interferograph. Some of the results are presented in Fig. 4. The e-folding times for the cases examined were 2 to 12 μsec prior to peak compression (τ_1) and 0.4 to 3.0 μsec afterwards (τ_2). Prior to 2.5 μsec in three of the cases the τ_1's were much larger (17 to 50 μsec). But for these three cases the τ_2's were 1.0 μsec or less. The very hot (neutron producing) plasmas tended to have the higher loss rates ($\tau_1 \sim 2.0$ μsec, $\tau_2 \sim 0.7$ μsec). The 4 kG reverse bias cases consistently had the largest τ_1's. By employing the analytical predictions of ion temperatures based on a Hain-Roberts code which uses Lagrangain coordinates centered on the current sheath, an estimate of the ion thermal speed can be obtained. Then for the plasma before 3.0 μsec, a simplified analysis of free flow through an orifice (as set down by Little, et. al.[6]) leads to predictions of the radius of the orifice which are typically within 50% of the size of the computed ion Larmor radius.

Plasma Drifts

In all cases examined the plasma tended to drift toward the feed slot after 3.0 μsec. The drift rate was always less than 3 mm per μsec.

Correlation to Analytical Predictions

Experimental measurements of the frequency of radial oscillation of the current sheath at the end of its implosion and of the radial position of the annulus of maximum particle density are readily obtainable. The radial oscillation frequencies in all cases examined vary from 8 to 20 MHz and agree with analytical predictions of the previously

mentioned computer code to within 20%. The rate of implosion and radial position of the current sheath during radial oscillations at the end of the implosion also agree to the analytical results to within 20% for the cases examined. Experimentally, the peak electron densities at 0.10 Torr initial pressure and 50 kG peak field vary from 0.8 to 3.0 x 10^{17} cm^{-3} as the reverse bias is decreased from 6 to 2 kG. The theory predicts a range of 1 to 2 x 10^{17} cm^{-3} for similar parameters.

SUMMARY

A density minimum is found to persist in reverse bias plasmas and is attributed to reverse bias field trapping. Dissappearance of the density minimum near the time of onset of neutron emission is interpreted as an indication of interdiffusion of the forward and reverse field in the plasma with the resulting conversion of the reverse field potential energy into particle kinetic energy. Lower peak densities and larger plasma diameters at lower pressures are indicative of higher average plasma temperatures at the lower pressures. Instabilities before 3.0 μsec are attributed to runaway electron effects. Rotating kink type instabilities are observed after 3.0 μsec. Plasma end-loss rates prior to 3.0 μsec agree to within 50% to predictions of free flow through an orifice the size of an ion Larmor orbit. The plasma was observed to drift slowly toward the feed slot after 3.0 μsec. Analytical predictions of plasma motion and distribution typically agree to experimental observations to within 20%.

REFERENCES

1. R. F. Gribble and A. A. Dougal, Bull. Am. Phys. Soc. II, 8, 131 (163).

2. F. D. Bennet, J. Appl. Phys. 22, 184 (1951).

3. M. Francon, Optical Interferometry, (Academic Press, New York, 1966), p. 97.

4. A. A. Dougal, J. P. Craig, and R. F. Gribble, Phys. Rev. Letters 13, 156 (1964).

5. S. Glasstone and R. H. Lovberg, Controlled Thermonuclear Reactions (D. Van Nostrand, Inc., Princeton, N. J., 1960), p. 120.

6. E. M. Little, W. E. Quinn, and G. A. Sawyer, Phys. Fluids 8, 1168 (1965).

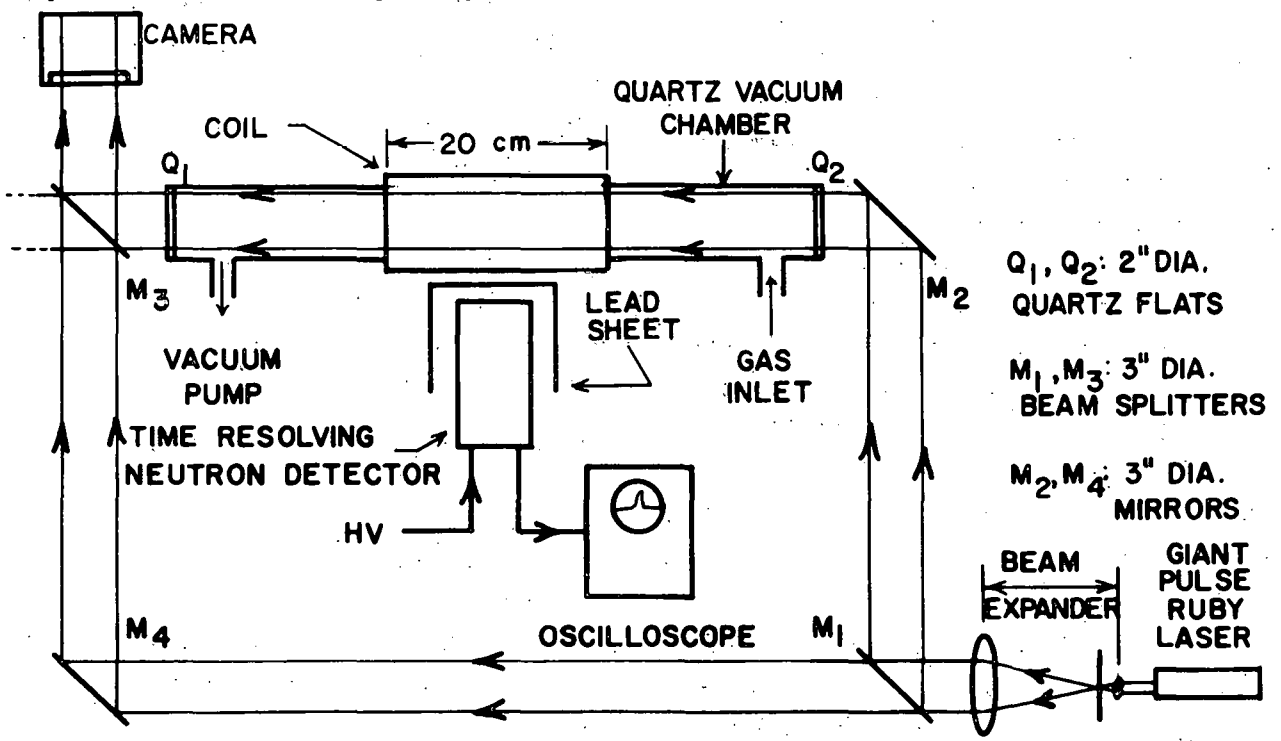

Fig. 1. Arrangement of the Mach-Zehnder interferometer and the neutron detector on the θ-pinch.

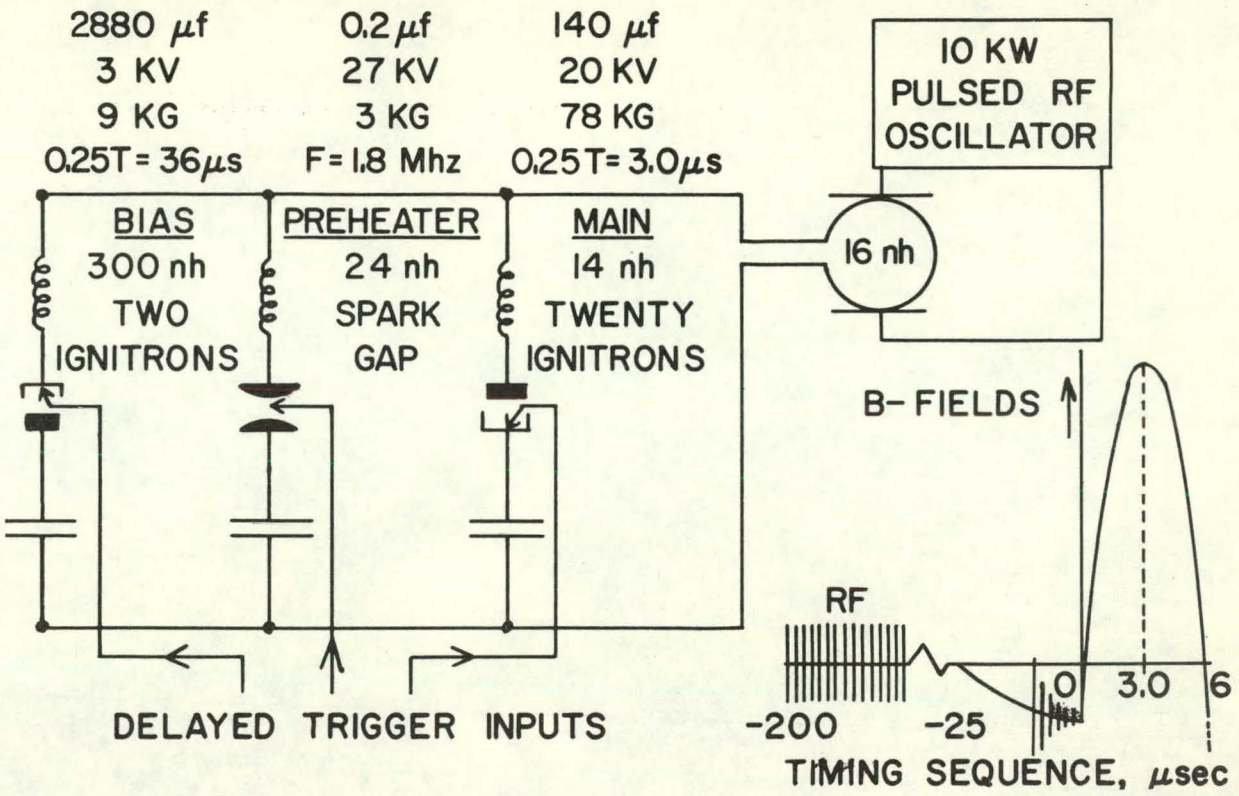

Fig. 2. Schematic of the four-stage θ-pinch.

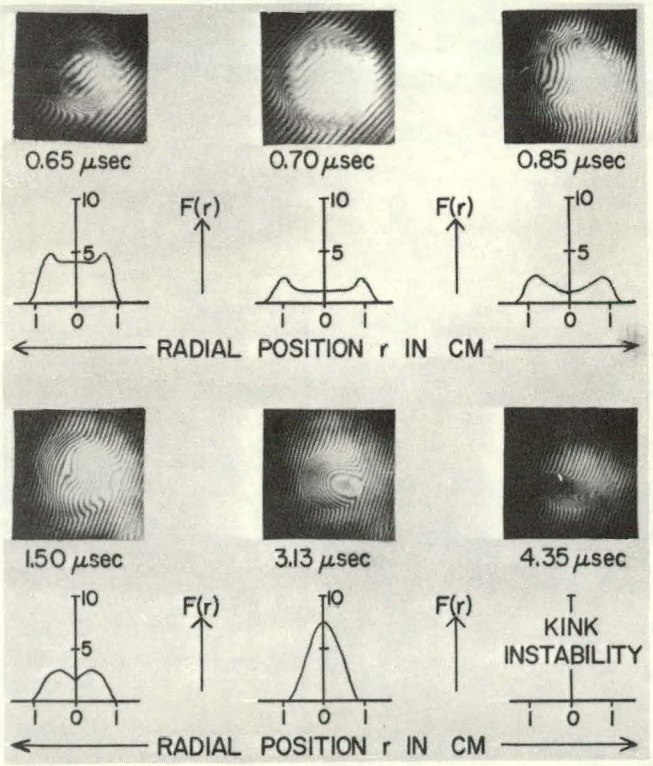

Fig. 3. Mach-Zehnder interferographs and the corresponding radial fringe shift profiles for 50 kG peak field, 4 kG reverse bias, 0.08 torr deuterium.

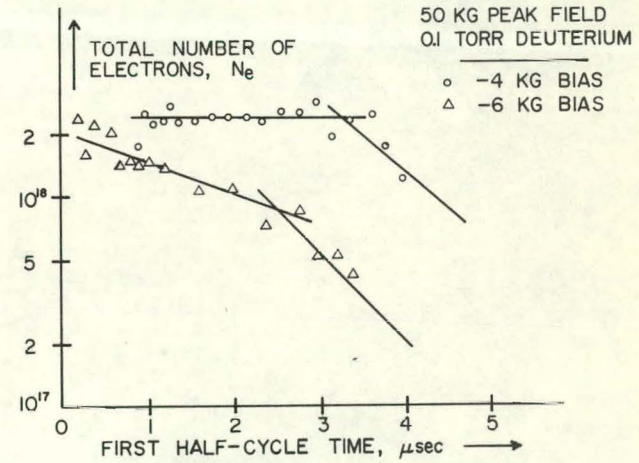

FIG. 4. TOTAL NUMBER OF ELECTRONS VERSUS TIME DURING THE FIRST MAIN FIELD HALF-CYCLE.

Fig. 4. Total number of electrons versus time during the first main field half-cycle.

MEASUREMENT OF θ-PINCH END LOSS USING A GAS LASER INTERFEROMETER*

by

K. S. Thomas

Los Alamos Scientific Laboratory, University of California
Los Alamos, New Mexico

ABSTRACT

A He-Ne gas laser interferometer[9,12] has been used to make plasma density measurements outside the central plasma core of a θ-pinch plasma. At the θ-pinch coil midplane, the average plasma density is less than the sensitivity of the interferometer, that is, less than $5 \times 10^{13} cm^{-3}$. Outside the ends of the coil line densities (particles per cm of tube length) of the order of $10^{15} cm^{-3}$ are measured. When compared to previous data[8] from the same θ-pinch, a streaming velocity out the coil ends in the neighborhood of the ion thermal velocity is obtained.

I. INTRODUCTION

End loss is apparently the dominant loss mechanism in the present generation of large θ-pinches[1]. Measurements of the total amount of plasma present as a function of time have given plasma loss rates[2,3,4,5]. Direct measurements of plasma escaping out the ends of θ-pinches have been made in several ways; direct photography[1,6], pressure probes[4], and measurement of the energy spectrum and flux of axially escaping ions[7]. This paper reports a measurement of the plasma density outside the end of the θ-pinch coil using a gas laser interferometer.

The end loss measurements were performed on Scylla III, a 150 kJ θ-pinch which has a coil 20 cm long and 10 cm in diameter, with a geometric mirror ratio of 1.3. The θ-pinch was operated in the low pressure regime (no bias field, 20 mtorr filling pressure) at a main bank voltage of 73 kV. Extensive measurements of the Scylla III plasma under these operating conditions have been reported previously[8].

II. INTERFEROMETER

The gas laser interferometer consisted of a He-Ne gas laser (Spectra Physics, Model 115) modulated by an external cavity. This type of interferometer was first used by Ashby and Jephcott[9]. The short duration of a θ-pinch plasma requires a fast time response, so the 3.4 μ laser radiation is monitored by means of an InAs detector[10,11]. A gas laser interferometer with a rotating corner reflector feedback system has been used on Scylla III[8]. This system works well when the fringe shifts are large, the limit of sensitivity being about 0.1 fringe, which is equal to an integrated electron density of $3.28 \times 10^{15} cm^{-2}$. A method of measuring smaller amounts of plasma, developed by Hammel and Rode[12], was used in this experiment. It is similar to the technique of Hooper and Bekefi[13] but has the advantage of being able to be applied to single plasma discharges. The interferometer uses, for a feedback system, a mirror mounted on an audio speaker with its acoustic cone removed. This mirror is modulated at a frequency of 1 khz to give a change of path length in the external cavity of about 0.1 λ. If the modulation is monitored just prior to the θ-pinch shot, the output signal of the detector may be calibrated in terms of plasma density. The frequency response of the interferometer and detector system was flat from several hundred hz to at least 5 Mhz so the difference in frequencies of the modulation and plasma signals should not introduce any appreciable error.

As would be expected, the interferometer was very sensitive to ambient vibrations. By mounting the interferometer on a frame which was well isolated from the θ-pinch and from the floor, the interferometer modulations caused by ambient

vibrations were mostly of several hundred hz or less, and these were rejected by introducing, in the detector system, a low-frequency cutoff of 300 hz. With this arrangement, usable data was obtained on about half the θ-pinch shots.

III. MEASUREMENTS

The measurements were made with the laser beam transverse to the discharge tube axis. The path of the laser beam through the 8 cm diameter quartz discharge tube is given by coordinates of a reference system centered on the discharge tube axis at the coil midplane. z is the distance of the laser beam from the coil midplane in the axial direction, x the perpendicular distance of the beam from the discharge tube axis, and y is along the beam path. Measurements were made at z = 0 and z = 11.5 cm (1.5 cm beyond the coil end). Measurements were attempted transversely at a point 5 cm outside the coil and axially along the discharge tube outside the main plasma core. In both cases large plasma effects were observed, regardless of the value of x, of the order of $2 \times 10^{16} cm^{-2}$. These were probably due to bombardment by hot plasma of the discharge tube wall outside the coil region. Framing pictures taken by an image converter camera confirm wall bombardment in this region.

Oscillograms of typical data at z = 0, x = 2.35 cm, with and without plasma, and at z = 0, x = 1.65 cm are shown in Figure 1. The upper trace shows the magnetic field in the coil and the lower the interferometer output. In the no plasma case, a small amount of magnetic pickup in the detector system is observed. This pickup, unfortunately, is not completely reproducible from shot to shot and constitutes the sensitivity limit of the interferometer. For the plasma cases, the plasma present before the main bank is fired is due to the preionizer. After the main bank is fired, the plasma level rises slightly due to increased ionization and then drops quickly to below the limits of sensitivity of the interferometer as the plasma is swept toward the center of the discharge tube by the compression field. The drop in plasma signal occurs 0.3 μsec later at x = 1.65 cm than at x = 2.35 cm.

Figure 2 shows oscillograms of data taken outside the coil for z = 11.5 cm, and x = 0 cm, 0.4 cm and 1.95 cm. The preionized plasma level is lower in these cases. For approximately 0.5 μsec after the main bank is fired, an increase in plasma signal occurs for all values of x. This plasma signal varies greatly from shot to shot and is probably due to ionized wall material. The rising magnetic field sweeps away this plasma and also prevents further bombardment of the walls in this region. At later times the end loss plasma is seen.

The results of the measurements outside the coil are shown in Figure 3 where the integrated plasma density is plotted vs. x for various times after the firing of the main bank. The data for x = 0.1 cm were taken with the laser beam passing on the opposite side of the discharge tube axis from the other points in order to insure that the peak was at x = 0. Each point is the average of about a half dozen readings and the error bars show the average deviation. A possible source of error lies in the fact that the laser beam diameter is about 3 mm, which is an appreciable fraction of the width of the peak. If the solid curves in Figure 3 are assumed and the data is Abel inverted, the results shown in Figure 4 are obtained where density is plotted as a function of radius for different times. These values may be used to calculate the line density (particles per cm of tube length) and the results are shown in Figure 5. The error bars indicate the values which would be obtained from curves such as are shown by the dotted lines in Figure 3 for T = 1.5 μsec.

IV. END LOSS RATE

The measurements at z = 0 show that, after the compression of the plasma by the magnetic field, the plasma density outside the central plasma core is less than the interferometer sensitivity, that is, less than about 0.01 λ or $3.3 \times 10^{14} cm^{-2}$. Thus the average plasma density along the 7 cm path length inside the discharge tube is less than $5 \times 10^{13} cm^{-3}$. The much higher densities ($\sim 10^{15} cm^{-3}$) outside the coil ends provide evidence that most of the plasma loss is end loss. The line density of plasma outside the coil ends, N_o, is related to the decay of plasma inside the coil by the following equation:

$$N\ell/\tau = 2vN_o \qquad (1)$$

N is the line density inside the coil, ℓ the length of the plasma, τ the e-folding time for plasma loss, and v the average streaming velocity of the escaping ions.

For the operating conditions used in this experiment N has been measured[8] at T = 1.8 μsec to be $4.3 \pm 0.8 \times 10^{16} cm^{-1}$. Although the exact length of the Scylla III plasma has not been measured, neutron yield and an extrapolation from the known plasma lengths in the Scylla I and Scylla IV θ-pinches both indicate a plasma length of 5 cm. τ as measured from the data of Figure 5 is 2.25 μsec. Earlier magnetic probe data[8] gives τ = 1.8 μsec.

Figure 5 gives, for T = 1.8 μsec , $N_o = 1.5 \times 10^{15} cm^{-1}$. If this is inserted in equation 1, the results for the two values of τ are: $v = 4.0 \times 10^7 cm\ sec^{-1}$ (τ = 1.8 μsec), and $v = 3.2 \times 10^7 cm\ sec^{-1}$ (τ = 2.25 μsec).

The measured ion temperature, T_i, for Scylla III is 1.8 keV[8], which corresponds to an average ion thermal velocity of $4.3 \times 10^7 cm\ sec^{-1}$. Thus the measured plasma densities are consistent with streaming velocities in the neighborhood of the ion thermal velocity.

V. ACKNOWLEDGEMENTS

It is a pleasure to acknowledge the helpful suggestions of J. E. Hammel concerning the construction of the interferometer, the valuable assistance of M. H. Thomas in constructing and performing the experiment, and useful discussions with G. A. Sawyer and F. L. Ribe.

REFERENCES

1. H. Griem, H. Grad, D. Crove, C. Hartman, R. Kilb, N. Lazar, and F. Ribe, USAEC Report TID-23705 (1967) p. 31.

2. E. M. Little, W. E. Quinn, and G. A. Sawyer, Phys. Fluids 8, 1168 (1965).

3. W. E. Quinn, E. M. Little, F. L. Ribe, and G. A. Sawyer, in Plasma Physics and Controlled Nuclear Fusion Research (International Atomic Energy Agency, Vienna, 1966) Vol. I, p. 237.

4. H. A. B. Bodin, T. S. Green, A. A. Newton, G. B. F. Niblett, and J. A. Reynolds, in Plasma Physics and Controlled Nuclear Fusion Research (International Atomic Energy Agency, Vienna, 1966) Vol. I, p. 193.

5. A. C. Kolb. W. H. Lupton, R. C. Elton, E. A. McLean, M. Swartz, M. P. Young, H. R. Griem, and E. Hintz, in Plasma Physics and Controlled Nuclear Fusion Research (International Atomic Energy Agency, Vienna, 1966) Vol. I, p. 261.

6. E. A. McLean, Naval Research Laboratory, Private Communication to F. L. Ribe, April 1966.

7. R. L. Bingham, L. M. Goldman, and R. W. Kilb, in Plasma Physics and Controlled Nuclear Fusion Research (International Atomic Energy Agency, Vienna, 1966) Vol I, p. 301.

8. G. A. Sawyer, V. A. Finlayson, F. C. Jahoda, and K. S. Thomas, Phys. Fluids 10, 1564 (1967).

9. D. E. T. F. Ashby and D. F. Jephcott, Appl. Phys. Letters 3, 13 (1963).

10. D. A. Baker, J. E. Hammel, and F. C. Jahoda, Rev. Sci, Instr. 36, 395 (1965).

11. R. F. Gribble, J. P. Craig, and A. A. Dougal, Appl. Phys. Letters 5, 60 (1964).

12. J. E. Hammel and D. L. Rode, Los Alamos Scientific Laboratory Report LA-3730 (1967).

13. E. B. Hooper, Jr. and G. Bekefi, Appl. Phys. Letters 7, 133 (1965).

* Work performed under the auspices of the U. S. Atomic Energy Commission.

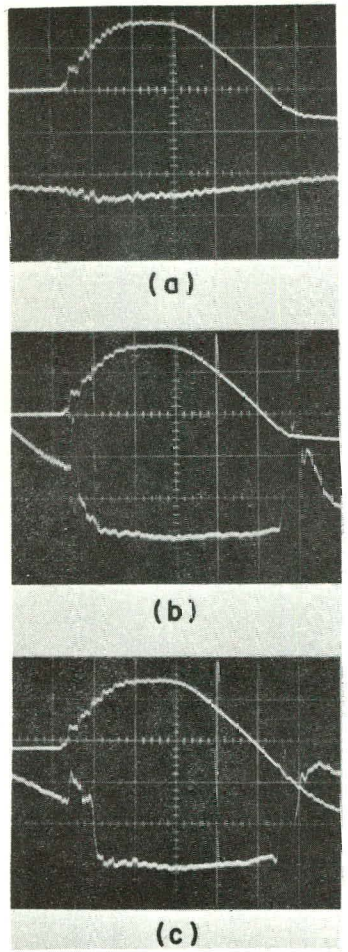

Fig. 1. Oscillograms for z = 0. The upper trace shows the magnetic field in the coil, and the lower, the interferometer output. Swell speed is 1 μsec/cm.
(a) x = 2.35 cm, no initial gas filling
(b) x = 2.35 cm
(c) x = 1.65 cm.

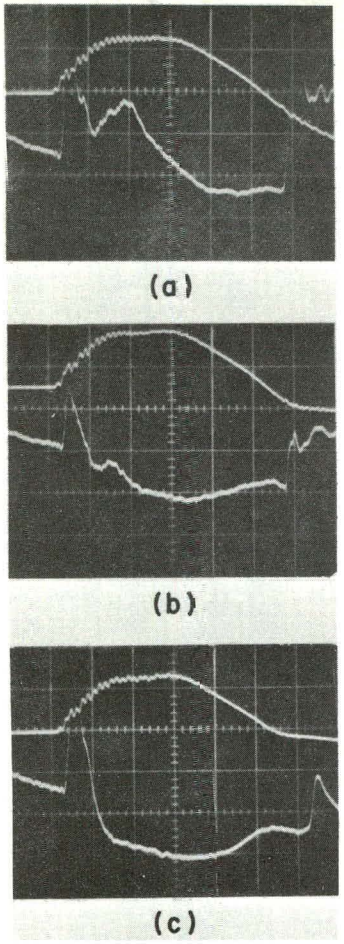

Fig. 2. Oscillograms for z = 11.5 cm (1.5 cm outside coil).
(a) x = 0
(b) x = 0.4 cm
(c) x = 1.95 cm.

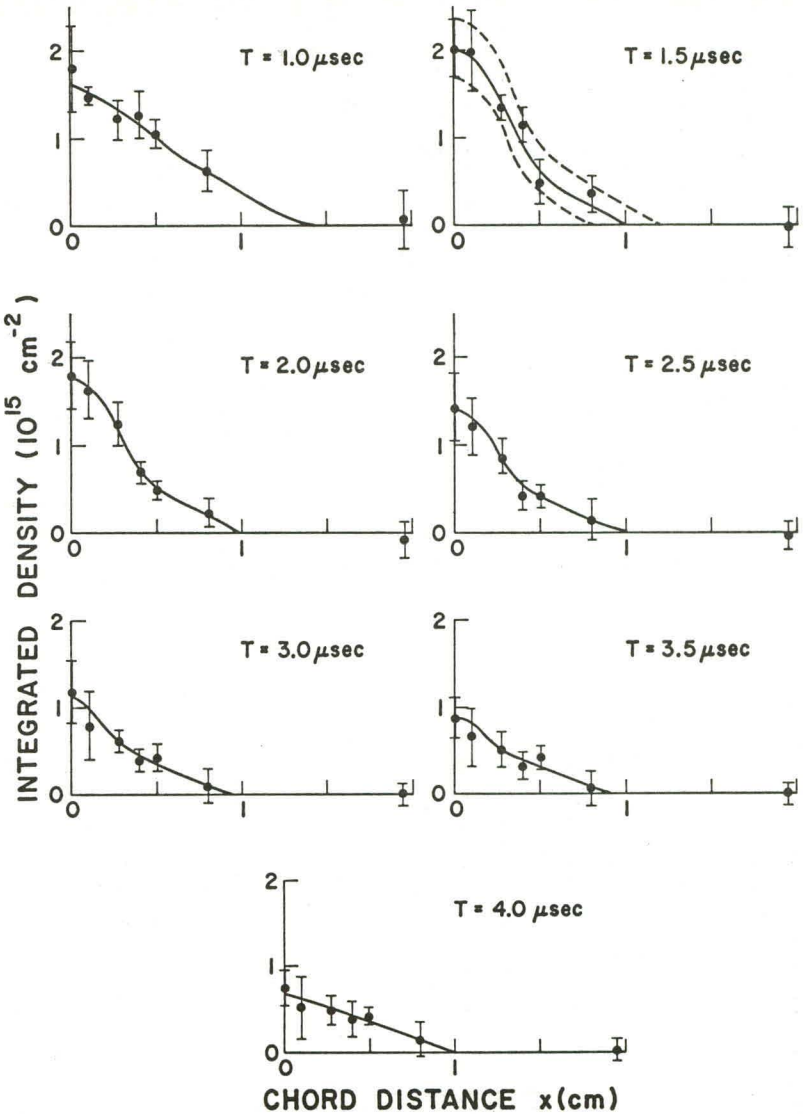

Fig. 3. Integrated plasma density vs. chord distance, x, from discharge tube axis for different times, T. z = 11.5 cm.

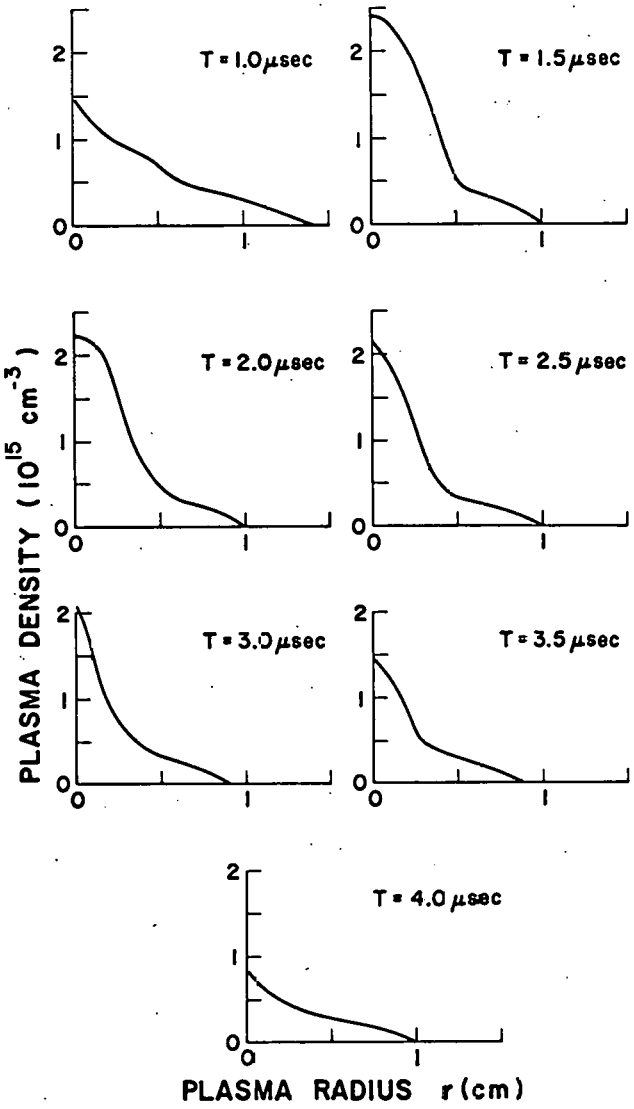

Fig. 4. Plasma density vs. radius for different times, T. z = 11.5 cm.

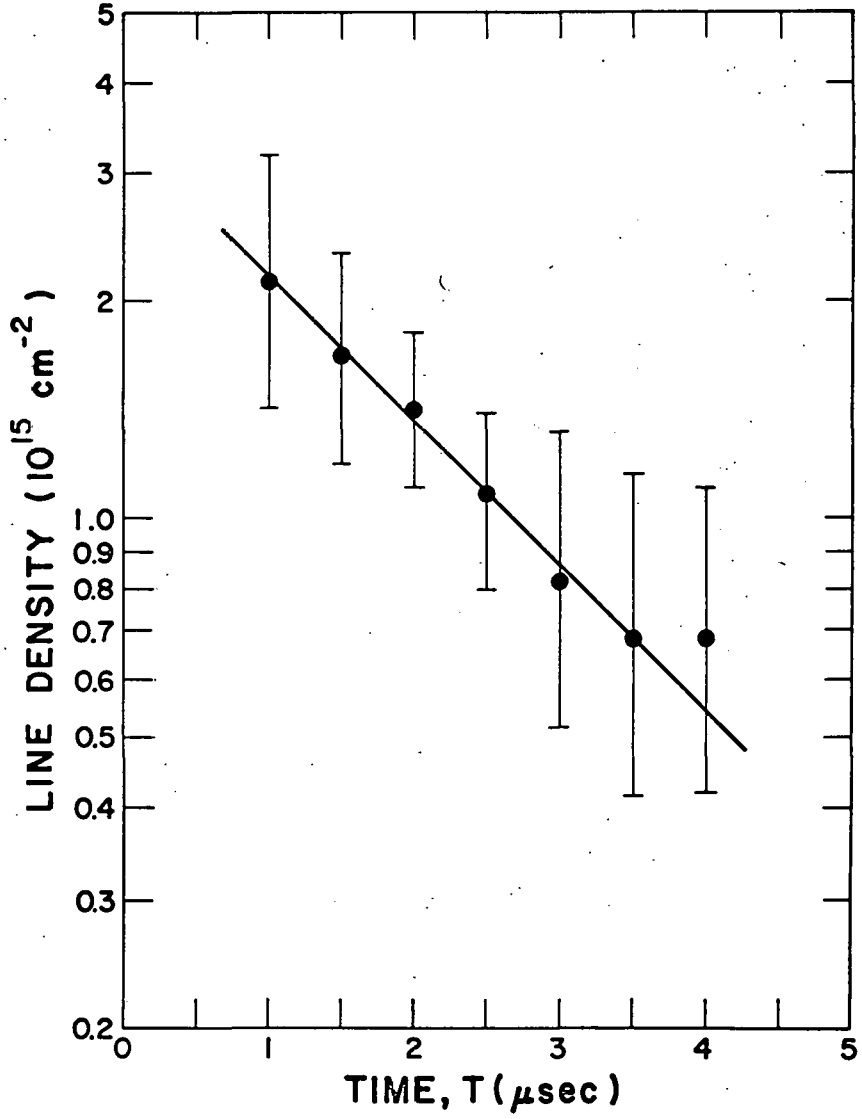

Fig. 5. Line density at z = 11.5 as a function of time, T.

A Low Energy Theta Pinch*

by

A. W. DeSilva and H.-J. Kunze

University of Maryland

College Park, Maryland

ABSTRACT

A low energy theta pinch device, constructed to provide a convenient spectroscopic source, has produced an interesting and useful plasma. The discharge tube has an inside diameter of 15cm and the coil is 32cm long. The main bank energy is 9 kJoule at 40 kV, and the current rings with a 7.5 μsec period. Plasma conditions have been investigated for a filling gas pressure of .012 Torr H_2 or D_2 and an antiparallel bias field of 500 gauss using light scattering, time and space resolved emission spectroscopy in the visible and soft X-ray regions of impurity lines (~1%C, 3%O), streak photography and neutron emission. These reveal that following the initial compression the plasma forms a stable cylinder about 4.5cm in diameter which persists for about 1.5 μsec. The electron temperature, determined by light scattering, is about 260 eV. Absolute continuum emission and light scattering measurements show the average electron density to be $4 \times 10^{15} cm^{-3}$. The temperature of carbon impurity ions is determined to be 1.3 keV by Doppler broadening, and neutron emission with a deuterium filling indicates an ion temperature of about 700 eV.

*Supported by the Atomic Energy Commission

I. INTRODUCTION

Theta pinch devices provide an excellent and very simple means to produce dense, high-energy plasmas. During the last ten years, research oriented to nuclear fusion has demanded larger and larger machines, and devices having capacitor banks capable of storing energies up to several magajoules have been constructed. Questions of confinement and heating were the main problems to be investigated.

In contrast, we describe a small setup which was built primarily as a light source for various spectroscopic studies. Confinement is of minor importance for this purpose; the idea was to obtain large-volume plasmas of high electron and ion temperatures using only modest facilities. This goal was reached in the present arrangement, which uses a main bank of only 9 kJoule stored energy at a voltage of 40 kV.

In the following, we describe the apparatus, the operating conditions and the plasma properties as obtained by various diagnostic techniques. A description of theta pinches themselves and a review of the literature is given by Quinn[1]; the most recent developments in this field can be found,e.g., in Ref. 2.

II. APPARATUS

Overall design of the θ-pinch device was aimed at maximum accessability to the plasma volume combined with simplicity and economy of construction. The compression coil has a 17.5 cm diameter and is 32 cm long, with a 12 mm slot in the midplane for diagnostic purposes. A fused quartz discharge tube of 15.2 cm inside diameter allows spectroscopic observations to be made conveniently in the UV region. To provide maximum accessability for diagnostic equipment, the coil is fed from a vertical collector plate connecting to an overhead capacitor bank. Pumping is through a pyrex tee section at one end, so that both ends and three sides of the coil are available for observation.

The main bank consists of three capacitors totaling 9.1 kJoule, and is switched into the collector plate by a single vacuum switch. In order to provide complete flexibility in selecting the initial conditions of plasma density and internal "bias" magnetic field, separate capacitor banks are used in the usual way to form the plasma (the preheater) and to generate the bias field. The preheater and bias bank are separately switched by means of pressurized trigatron switches. Figure 1 shows schematically the arrangement. In addition to the banks shown, it was found that reproducability was better when a preionizing pulse of R.F. was applied initially to the tube.

The preionizer is 16 ohm pulse line two meters

long (3 parallel 50Ω coaxial cables), with the center conductor at one end capacitively coupled to the gas in the tube by means of a pair of wires wrapped around the discharge tube, one on each side of the compression coil. This conductor is charged to 30 kV, and about 3 μsec prior to firing the preheater the far end of the pulse line is short-circuited by a trigatron switch. A burst of R.F. at 14 MHZ appears at the discharge tube and a small percentage ionization results.

The bias bank consists of two 60 μf capacitors with 10 kV rating connected in parallel through an inductance of 11 μH to the coil. The period is 220 μsec, which is sufficiently long so that the field is essentially constant during the fast compression that follows. The field is adjustable from +1 kG to -1 kG (The sign indicates polarity with respect to the main compression field).

The preheater, a 0.5 μf 40 kV low inductance capacitor, is normally fired on the rising side of the bias field, and its polarity is such as to cause a temporary field reversal. Breakdown occurs as the field passes through zero. Streak camera pictures of the preheater discharge show that the stability and uniformity of the plasma is sensitive to the charge voltage on the preheater capacitor and to the applied bias magnetic field. Under certain conditions the plasma bounces violently as the current rings through zero, and the light emission indicates the release of impurities into the plasma volume. This effect may be in part due to the similarity of the preheater frequency (0.45 MHZ) to the dynamic bounce frequency. It is usually possible to find a condition where the plasma oscillates gently a few times and then settles down to a more or less uniform column, with no wall emission visible. The preheater discharge damps out in about 19 μsec (at a filling pressure of 12 mTorr hydrogen), after which the main compression bank is fired.

The main compression bank consists of three 40 kV capacitors, each 3.8 μf with internal inductance of 20 nHenry. They are connected via six cables each to the vacuum switch. The quarter period of this bank is 1.77 μsec, and peak current is 4×10^5 amps, producing a peak compression field $B_z \simeq 13$ kGauss and a maximum $dB/dt \simeq 1.1 \times 10^{10}$ Gauss/sec. The electric field strength just inside the tube is 430 V/cm.

The cable terminations at both ends were very much simplified by departing from a strictly coaxial construction to connect the coax center conductor to the capacitor can, with the cable braid carrying the high voltage and being switched. The cables (B.I.C.C. type 50 P.2/I) have 40 kV on the braid whenever the bank is charged, and no cable failures attributable to this usage have occured in two years operation.

Use of a single vacuum switch has eliminated those problems associated with multiple switching. The limitation to this type of use seems to be the amount of bank energy that can safely be connected to a single terminal.

The switch is of the type described by Baker[3] suitably modified at his suggestions for switching the braid. A schematic of the switch and collector plate construction appears in Fig. 2. The thirteen stainless steel plates divide the bank potential to about 3 kV per gap. This rises to about 5 kV per gap during the reverse half cycles of the preheater discharge. The switch pressure is adjusted to ten to twenty millitorr (air), which is too low to allow the development of breakdown avalanches prior to triggering. At the center of each stainless steel plate is a brass insert with three "venetian blind" slots. These serve as pumping ports to evacuate the switch, and as communication path for the charged particles that initiate breakdown. It is important that no optical path through the switch be open or it will not hold off D.C. voltage.

A spark plug at the negative end triggers the switch, which fires after a short delay with less than 20 nsec jitter. The firing delay is variable with switch pressure, becoming, e.g., 800 nsec at a pressure of 2.5 mTorr. Increasing the (air) pressure to about 60 mTorr reduces the firing delay to 175 nsec. Further increase of pressure places the operating point too low on the Paschen curve and the switch will break down at D.C. voltages below 3 kV per gap.

The insulators between plates are of Teflon, which has the desirable property of simultaneously providing a vacuum seal, grading the potential, and remaining clean indefinitely. The switch is held together by a wrapping of fiberglass impregnated

with epoxy. The wrapping is applied after the switch assembly has been pumped down for about 24 hours, to allow the Teflon insulators to "creep" to a stable configuration. If this procedure is not followed, the Teflon insulator may subsequently separate from the laminate, allowing a breakdown to occur in the opening so formed.

Switch inductance, as deduced from observed bank ringing period, is of the order of 5 nanohenry. Closure time of the switch is about 80 nsec from the beginning of current flow. A slightly resistive phase (R~50 milliohm) lasts another 200 nsec and causes a small reduction of the dI/dt for this time. The switch shown has operated over 3000 shots with no maintenance or failure.

The discharge tube is evacuated by a turbomolecular pump to a base pressure of 10^{-6}Torr. Hydrogen is admitted through a palladium leak valve to the usual working pressure of 12 millitorr, and is flushed after each shot. A capacitance bridge type pressure gauge allows accurate monitoring of the pressure. The operational sequence of the machine is the following: 30 μsec after applying the bias bank field to the coil the preionizing R.F. pulse appears at the tube, 3 μsec later the preheater bank is discharged and after another 19 μsec the main bank.

III. OBSERVED PLASMA PROPERTIES

Although plasmas could be produced using filling pressures ranging from 5 mTorr to 10 Torr hydrogen, most measurements were performed with an initial pressure of 12 mTorr. First half-cycle operation was chosen with a negative bias field of 500 Gauss. The preheater capacitor was charged to 30 kV. Streak pictures (side-on and end-on taken with an STL camera) as well as observation of lines from higher ionization stages of impurity atoms revealed that this operation condition gave a grossly stable and reproducible plasma. In the following all measurements referred to will be for this condition, except where otherwise stated.

Comparison of measured plasma properties with theoretical calculations require, in principle, a detailed knowledge of the initial plasma parameters and of their radial distribution. For this reason the electron temperature was measured during the preheater discharge using the H_β line-to-continuum intensity ratio method[4]. At the midplane of the discharge tube the plasma column was imaged on a 1/2 meter grating monochromator. Radiation passing through the exit slit was divided by means of small mirrors into eight elements of equal height and passed to separate photomultipliers. Thus the plasma radiation was recorded simultaneously from eight chords of the plasma column, and using the Abel integral equation and assuming radial symmetry local emission coefficients were obtained. The same setup was also used for the determination of the electron density from measurements of the half-width of the H_δ line, see also Ref. 4. These measurements showed that the time of the ignition of the main discharge (i.e. ≈19 μsec after the beginning of the preheater discharge) the plasma was reasonably homogeneous over the radius of the discharge tube having an electron temperature of ≈2eV and an electron density of ≈ 2×10^{14}cm^{-3}.

Electron densities and temperatures during the main discharge were derived from the analysis of laser light scattered by the plasma. In principle a value for the electron density could also be obtained from measurements of the absolute intensity of the continuum emission in the visible using the multichannel arrangement as applied for the preheater studies. While this method yields quite reliable results at higher densities, the densities obtained at our low density mode operation were always higher than those obtained from light scattering. This can be attributed to the relatively high percentage of impurities present in the plasma at low densities. Adding known amounts of carbon and oxygen to the filling gas, the background concentration was found to be 3.6% for oxygen and 1.3% for carbon. While this determination of impurity concentration is straightforward at higher filling pressures, it is not quite as simple at low filling pressures, since selective injection or loss to the walls can be more important during the preheater phase[5]. Furthermore, it was not possible to determine the silicon concentration, which would be expected to ionize to a charge of X or XI; a concentration of around 0.5% could then account for the remaining difference between the electron densities obtained from light scattering and from the continuum intensity. In view of this fact the density obtained by the

scattering method was assumed to be the most reliable one.

A general description of the scattering technique can be found, e.g., in Ref. 6. We mention only that the light source was a Q-switched ruby laser operated at power levels between 100 and 200 MWatt and that the scattered light was observed at an angle of 90° in the midplane of the coil. The calibration of the system was carried out using Rayleigh scattering in N_2. Figures 3a and 3b display the results: the time histories of the electron density and electron temperature are shown on the axis of the discharge tube as well as radial distributions at two different timepoints. The experimental values are always the average values of several discharges. The profiles of the scattered light showed no deviations from a Gaussian shape within the experimental errors, thus justifying the assumption of true kinetic electron temperatures.

The plasma forms at first a hollow cylinder which still exists at 1.09 μsec. At this time the electron temperature on the axis is already 180 eV and in the plasma ring we measure even 260 eV. Density and temperature distribution show great similarity. At earlier times the density and temperature on the axis are considerably low, but judging from the radial distribution at 1.09 μsec we can assume that densities and temperatures will already be higher in the plasma sheath than on the axis. (At these early times no light scattering measurements were performed. The study of the implosion phase of theta pinches operated at the low densities is subject of a separate investigation, see DeSilva and Stamper[7]. Due to the relatively high impurity concentration these measurements are difficult since during the implosion phase strong line radiation from lower ionization stages of impurity atoms increase the plasma radiation background considerably.) At 1.45 μsec the temperature shows a nearly homogeneous distribution, whereas the density profile seems to be still somewhat influenced by radial plasma oscillations. The measurements clearly show a plasma column having a diameter between 4.5 and 5 cm. We further note that the density rise on the axis occurs more slowly than the temperature rise. Plasma losses and cooling become considerably after 2.4 μsec. (Maximum B-field is reached at 1.8 μsec.) The maximum density obtained is about $3.8 \times 10^{15} cm^{-3}$.

A direct measurement of the ion temperature was not performed for the hydrogen plasma. The only method which could yield reliable temperatures of the protons would have been the analysis of laser light scattered at very small angles. However, for the present plasma parameters a scattering angle of 2° or less would be necessary in order to obtain scattered spectra where the ion line dominates. Since at these small angles both experimental difficulties and the uncertainty in the width of the ion line (due to finite apertures) increases greatly, the corresponding measurement was not attempted.

However, filling the discharge tube with deuterium allows an estimate of the deuteron temperature from measurements of the neutron yield resulting from D-D reactions. For this purpose a neutron detector consisting of scintillator and multiplier was placed near the theta pinch coil. Performing discharges in hydrogen and shielding the detector with lead assured that the signals were really due to neutrons, and that no contributions from hard X-rays or from γ's falsified the measurement. The time-resolved measurements show that the neutron emission starts 1.4 μsec after the ignition of the discharge and peaks around 2.0 μsec, i.e., shortly after peak field. The total yield obtained is ~6000 neutrons. With a plasma volume of around 150 cm^3 and an average density of $3 \times 10^{15} xm^{-3}$ we obtained (see Ref. 8) an average deuteron temperature of 700 eV. In principle, the derivation of this temperature from the neutron yield could be questioned since at this low temperature the few fusion reactions are caused by deuterons far out on the tail of the Maxwellian[9] velocity distribution, and small deviations from this distribution could account for observed neutrons. However, further support for ion temperatures of this magnitude is obtained by measurements of the Doppler profiles of lines emitted by carbon ions.

Using a 1 1/2 meter grating spectrograph viewing along the axis of the discharge tube the width of the 2271 Å CV line was measured photographically. This yielded an average ion temperature over the first half cycle, since photoelectrical observations showed no appreciable CV emission from later times in the discharge. The Doppler temperature obtained

was 1.3 keV. The width of the CV line was also measured side-on. There an 8 mm high chord from the center of the plasma column was imaged on to a 1/2 meter grating monochromator and the spectrum was determined photoelectrically, scanning from discharge to discharge. This yielded the time history of the CV Doppler temperature and the results can also be seen on Fig. 3a. From about 800 eV at 1.0 μsec the temperature rises to about 1.55 keV at 2.35 μsec. These values compare fairly well with the average temperature obtained end-on. This implies a spatially homogeneous velocity distribution for the CV ions at the time of observation.

Quite different results were obtained for earlier times of the discharge when the profile of the 2297 A CIII line was measured side-on (also observing only the center chord of the plasma column). Figure 4 shows the spectra as measured at various times. The instrumental function is of triangular shape, with a half-width of 0.5 Å. Besides a central line, which becomes broader with time, we obtain two symmetrical satellites shifted by $\approx$ 1.2 Å from the central line. According to the direction of observation we can interpret this shift only as a radial velocity component for carbon ions, which amounts to $v \approx 1.5 \times 10^7$ cm/sec and corresponds to a directed radial kinetic energy of 1.4 keV for the carbon ions. This velocity agrees well with the velocity of the first implosion phase as obtained from streak pictures and as deduced from the time of the 1st maximum compression (observed on the continuum emission.)

It is interesting to see that shortly after the first maximum compression (occurring at $t \approx 0.45$ μs) the profile still reveals a low C III Doppler temperature of $\approx$65 eV and shows only a small fraction of C III ions having the distinct radial velocity component. 200 nsec later the ion temperature is considerably higher, and also a larger fraction of the ions shows the directed motion. This indicates a rapid heating occuring during this time interval. However, it is in principle not possible to obtain more quantitative results, e.g., on the fraction of the carbon ions having this velocity component, without detailed knowledge of the radial distributions of electron density, electron temperature and carbon ion concentration. Not only does the excitation rate for the observed line depend strongly on local temperatures and densities but also the rate for further ionization, thus producing locally different concentrations of the various ionization stages during times of rapid heating.

Finally, the length of the hot plasma core was determined by observing the CV 2271 Å line through equidistant holes in the coil. The length changes slightly with time; at the time of maximum B-field we obtain a length of $\approx$8.5 cm between the points, where the CV line intensity drops to 50%, or a length of 11.5 cm if we take the points where the intensity drops to 10%.

IV. SUMMARY AND DISCUSSION

Using a large diameter theta pinch coil, a large volume plasma (150 cm^3) is produced with a main bank energy of only 9 kJoule. The filling pressure was 12 mTorr hydrogen and the applied bias field - 500 Gauss. Electron temperatures and densities were obtained as a function of time and radius from the analysis of laser light scattered by the plasma. The maximum electron temperatures rise to 260 eV and the densities vary between 3 and 4 x $10^{15} cm^{-3}$. These measurements and also the analysis of the continuum radiation in the visible show that the plasma forms at first a hollow cylindrical column. From the initial condition and from considerations of pressure balance, it follows that there is a reverse trapped field on the axis. The zero field region appears to be at a radius of about 2 cm. This configuration persists well past the first compression, disappearing somewhat after 1.1 μsec. The field decay time is over an order of magnitude faster than the classical decay time.

At the position of field zero, the plasma β must be equal to one and this can be used to deduce an approximate value for the ion temperature. Let us consider, e.g., a volume element at the radius $r \approx 2$cm. at $t = 1.09$ μsec. Neglecting impurities, the equation of pressure balance yields an average temperature of the protons of around 750 eV. This agrees fairly well with the observed CV Doppler temperature, although the temperature of the deuterons deduced from the neutron yield is somewhat lower, namely around 500 eV at 1.4 μsec (derived under the assumption of a three-dimensional Maxwellian velocity distribution). At this later

time, a similar pressure balance consideration on the axis of the plasma column yields around 800 eV for the ions while the CV Doppler temperature has increased to 1.1 keV. If one includes impurities in these considerations (1.3% C and 3.6% O_2) the proton temperatures derived from pressure balance will be lower and the discrepancy to the temperature derived from the neutron yield will become smaller.

Considering the deuteron-deuteron collision time which for plasma conditions of $T_D \approx 500$ eV and $n_D \approx 3.10^{15}$ cm^{-3}, are around 5 μsec[10], the assumption of a Maxwellian velocity distribution after times of 1 μsec is extremely questionable. On the other hand, for a two-dimensional mono-energetic velocity distribution the neutron yield would require kinetic energies of the deuterons to be higher than 1 keV, which violates pressure balance.

From this fact we can draw the conclusion that if the ions were created preferentially mono-energetic, there has to be a mechanism involving ion wave instabilities to convert the directed motion into a random motion in times short compared to the binary collision time.

This explanation is supported substantially by measurements of the Doppler profiles of CV ions. Starting 1 μsec after the beginning of the discharge, the profiles were measured photoelectrically viewing side-on along a diameter of the plasma column; end-on, they were recorded photographically. The result is that for both directions of observation, the profiles are of Gaussian shape with the average width being the same (corresponding to a temperature of 1.3 keV). This observation cannot be explained on the basis of binary collisions, the carbon-carbon collision time being ~10 μsec and the carbon-proton collision time being ~2 μsec.

ACKNOWLEDGEMENTS

The initial suggestion for constructing this device came from Dr. Hans R. Griem, and we are indebted to him for his continuing interest and encouragement. We are grateful to Mr. Kenneth Diller for his enthusiastic support in the construction and operation of the machine.

REFERENCES

1. W. E. Quinn, in C.L. Longmire, J.L. Tuck, and W.B. Thompson, Eds., Plasma Physics and Thermonuclear Research, Pergamon Press, New York 1963, p. 150.
2. Plasma Physics and Controlled Fusion Research, Conference Proceedings, Culham 1965, (IAEA, Vienna, 1966) Vol. I.
3. W. R. Baker, Rev. Sci. Instr. 30, 700 (1959).
4. H. R. Griem, Plasma Spectroscopy McGraw-Hill, New York 1964.
5. A. H. Gabriel and H.-J. Kunze, to be published.
6. H.-J. Kunze, "The Laser as a Tool for Plasma Diagnostics.", chapter in Plasma Diagnostics, ed. by Lochte-Holtgreven and to be published by North Holland Publ. Co.
7. A. W. DeSilva and J. A. Stamper, to be published in Phys. Rev. Letters.
8. S. Glasstone and R. H. Lovberg, Controlled Thermonuclear Reactions, Van Nostrand, Princeton, New Jersey, 1960.
9. In the case of two-dimensional mono-energetic distribution, the above neutron yield would correspond to a kinetic energy of the deuterons roughly twice as high as the temperature derived above.
10. L. Spitzer, Jr., Physics of Fully Ionized Gases Interscience Publishers, New York, 1962.

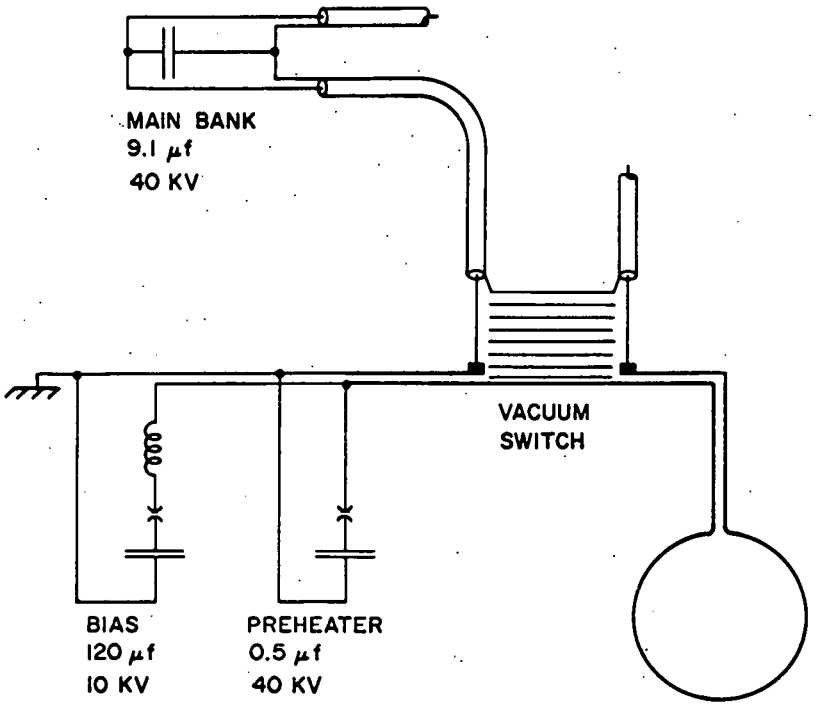

Fig. 1. Electrical circuit.

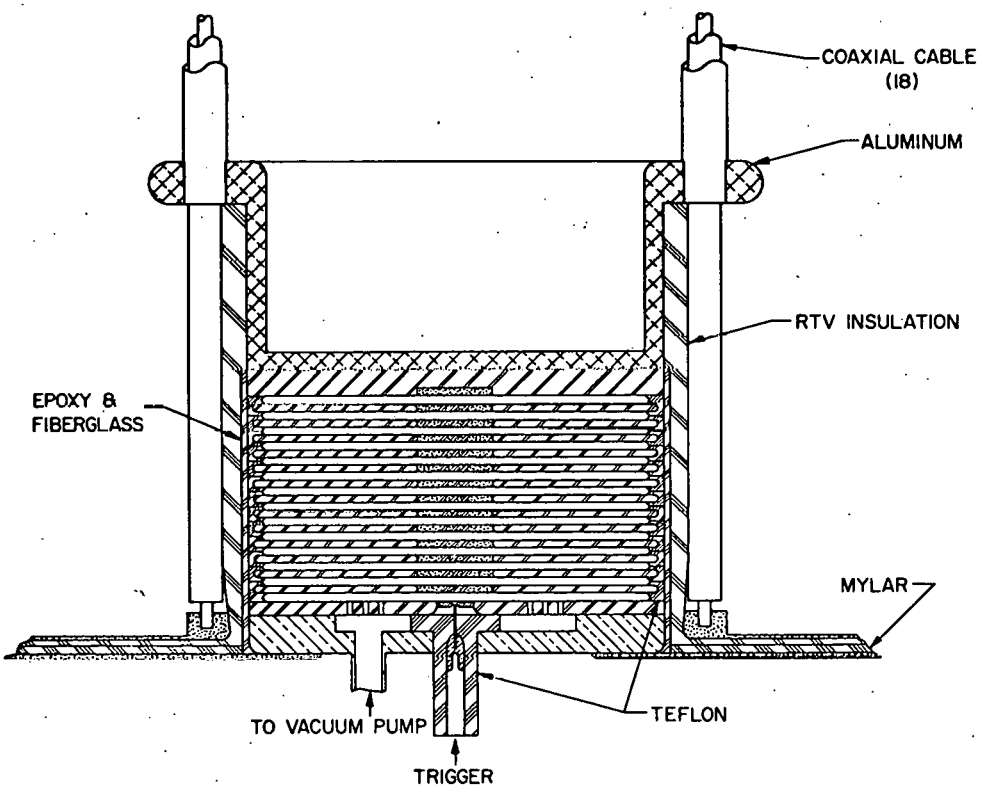

Fig. 2. Schematic diagram of vacuum switch. Some constructional details are omitted for clarity.

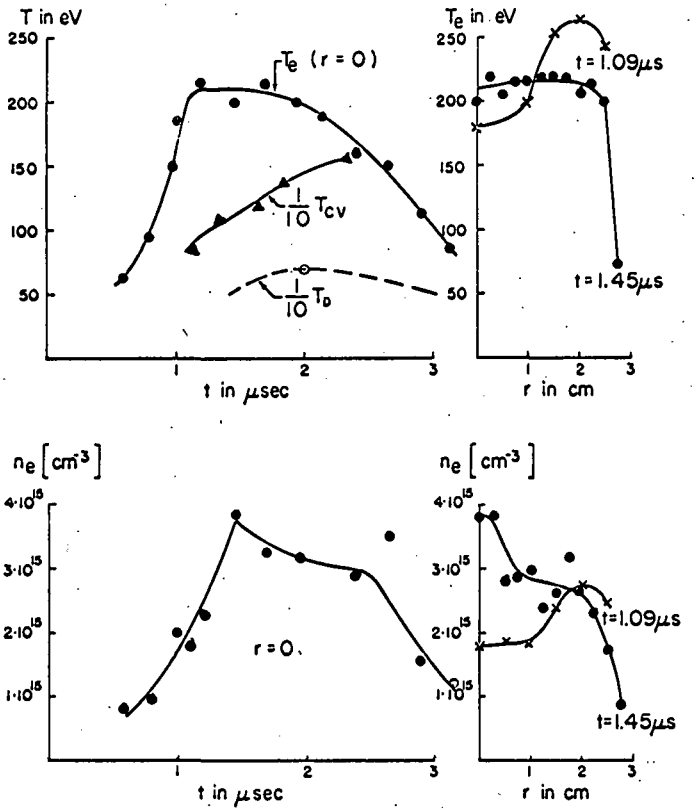

Fig. 3. Results of light scattering measurements. Time is measured from initiation of main bank current. (a) shows the time history of the electron density on the axis as well as radial distribution at two different time points. (b) shows the corresponding electron densities. Additional curves on (b) show the CV Doppler temperature and the deuteron temperature derived from neutron yield.

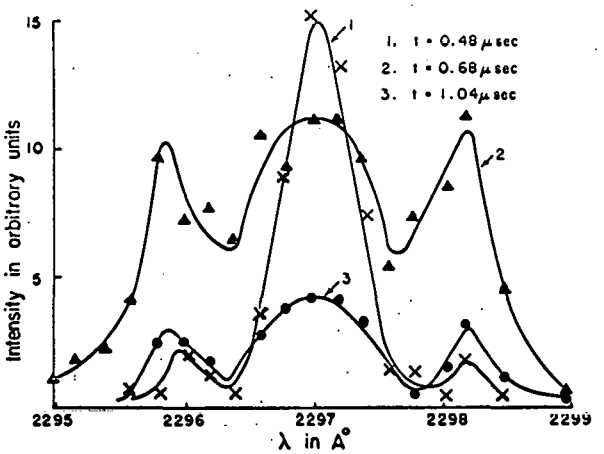

Fig. 4. Doppler profiles of C III, λ2297 Å at various times, taken along a tube diameter.

BREMSSTRAHLUNG OF DENSE, HOT PLASMA IN THE WAVELENGTH RANGE 0.25 TO 25 μ

P. Bogen, K.H. Dippel, D. Rusbüldt

Institut für Plasmaphysik der Kernforschungsanlage Jülich des Landes Nordrhein-Westfalen e.V.

ASSOCIATION EURATOM-KFA

ABSTRACT

Experiments have been carried out on a thetapinch ($\tau/4$ = 0.75 μsec, B_{max} = 45 kG) in order to compare the absolute intensity of the bremsstrahlung as well as its wavelength dependence with the theoretically expected values. Side-on interferometric measurements (Mach-Zehnder interferometer and Abel inversion) yielded the radial density distributions. These, together with measured electron temperatures, lead to a "theoretically" expected intensity. Quantitative agreement with observed values in the visible spectrum was found, when $T_e \leq 10^6$ °K and $N_e \leq 3 \cdot 10^{17}$ cm^{-3}. The observed values are significantly larger when $T_e > 10^6$ °K and smaller when $T_e < 10^6$ °K and $N_e > 3 \cdot 10^{17}$ cm^{-3}.

The wavelength dependence of the intensity between 0.25 and 25 μ has been measured with a time resolution of 20 nsec using an InAs photodiode and a copper-doped germanium photoresistive detector in the infrared, and a photomultiplier in the visible and ultraviolet domains. Side-on, the emission signals were at all times and for all wavelengths proportional to one another, whereas end-on some shape differences were observed, presumably, because of refractive index effects. The experiments confirm the theoretical prediction, that the Gaunt-factor should vary by a factor two in the investigated wavelength domain.

---

1. Introduction

In the long wavelength domain ($h\nu \ll kT$), the bremsstrahlung intensity I_ν depends strongly on the electron and ion densities N_e and N_i and only weakly on the electron temperature T and frequency ν. One has practically:

$$I_\nu = C \cdot (kT)^{-\frac{1}{2}} g_{ff}(\nu, T)\, Z^2\, N_e\, N_i\, \ell \qquad (1)$$

($C = 6.36 \cdot 10^{-47}$ cgs units, $g_{ff}(\nu, T)$ = Gaunt factor [1] for free-free emission, Z = ion charge number; ℓ = length of the optical layer.)

This equation should be valid, when reabsorption is negligible, when the refractive index is near one, and when the electrons have a Maxwellian velocity distribution. These conditions are rather fulfilled for thetapinch discharges in hydrogen when $N_e \approx 2 \cdot 10^{17}$ cm^{-3} and $T_e \approx 10^6$ °K.

This paper describes experiments carried out to measure the frequency dependence of I_ν resulting from the Gaunt factor, and to compare the observed value of I_ν with those expected from independent N_e and T measurements. N_e has been deduced from refractive index measurements, carried out side-on using a Mach-Zehnder interferometer [2, 3, 4], T_e from the pressure balance equation and from soft X-ray measure-

ments[5,6].

2. Experimental arrangement and calibration

A 4.5 kJoule thetapinch with a maximum field of 45 kGauss and a half-cycle of 1.5 μsec has been used; the coil diameter is 4 cm, its length 15 cm. For the side-on interferometer measurements plane quartz windows were cemented (Fig. 1) to the discharge tube. The interferometer fringes were recorded by a smear camera giving a time resolution of $2 \cdot 10^{-8}$ sec. The optical arrangement is shown on Fig. 1.

The bremsstrahlung intensity has been measured side-on and end-on with photomultipliers between 0.25 μ and 1 μ, with InAs photodiodes between 0.8 μ and 3.4 μ, and with a Cu-doped Ge-photoresistive detector between 2 μ and 25 μ. For the infrared measurements up to 25 μ a small quartz pipe bearing a KBr end-window was fused radially to the discharge tube. The time constant (1/e decrease of the signal $< 2 \cdot 10^{-8}$ sec) of the InAs diode and the Cu-Ge detector[7] was somewhat longer than that of the multiplier signal which was limited by the oscilloscope. The detectors were calibrated with a carbon arc between 0.25 μ and 6 μ, and with a blackbody of T = 1 800 °K between 3 μ and 25 μ. Interference filters yielded the spectral resolution. Spectral lines have not been detected in the investigated domain, except H_α and H_β at the beginning of the discharge.

3. Comparison between intensity and refractive index measurements

The fringe shifts caused by the plasma lead, after Abel-inversion, to the electron density profile (Fig. 2). The similitude ($\pm$ 10%) of the right and left part of the fringe shift profile indicates a reasonable symmetry of the plasma column. The azimuthal symmetry has been further checked by interferograms with infinite fringe width taken end-on with a Kerr-cell shutter[2,4].

To compare the theoretical and experimental values of I_ν, we defined the ratio

$$\eta = J_\nu / C \cdot (kT)^{-1/2} g_{ff}(\nu, T) \int_0^\ell N_e N_i \, ds \qquad (2)$$

J_ν is the observed intensity value, measured here at 0.4, 0.5, and 0.55 μ, N_e the electron density from refractive index measurements, and T the essentially radially independent[5] temperature deduced from soft X-ray measurements or from pressure balance. A value $\eta = 1$ implies good agreement.

On figures 3 and 4, η is plotted as a function of time for one particular discharge, and as a function of T for a set of different discharges. The overall error, resulting from intensity calibration, temperature measurement, fringe shift determination and Abel inversion, is estimated to be less than 50%. Although η is centered around one, there are deviations higher than expected. No satisfying explanation has yet been found for this discrepancy.

The presence of impurity ions would lead to values of $\eta > 1$. The oxygen concentration in the plasma is about 0.2%. This would increase the intensity of the visible continuum by less than 10% for $T = 1.5 \cdot 10^6$ °K. Silicon lines have not been detected in the first half-cycle of the discharge. If SiO_2 had been evaporated from the quartz walls, one would except a concentration of about 0.1% of Si. This should have an average value $Z \approx 12$, and might thus lead to an additional contribution of about 10%. The presence of small amounts of other high Z ions would also increase η, but seems improbable, since, for instance, the addition of 0.3% of argon perturbs significantly the stability of the discharge and its spectrum.

The observation of $\eta < 1$ values might be used as an argument against impurity effects. These values lie however rather close to the error limits. They are observed either at the end of

the first implosion of the pinch, when the plasma diameter is small, or at high initial densities when the driving magnetic field reaches its maximum. In the second case, the cylindrical symmetry of the plasma is not always perfect, so that a final conclusion about the reliability of the $\eta < 1$ values has not yet been reached.

4. Frequency dependence of the bremsstrahlung intensity

The interpretation of the absolute values of I_ν involves assumptions on the geometry and the impurity level; the relative variation of I_ν with frequency is less strongly dependent on the assumptions. It was therefore followed over a wide spectral range.

Fig. 5 shows the intensity signals at 0.54 and 5.8 /u observed end-on. Although Eq. 1 predicts a similar behaviour at all wavelengths, the time dependences are different: at 5.8 /u, the signal decreases more sharply at the end of the half-cycle. Our interpretation of this phenomenon is that the detectors do not explore identical regions of the plasma. At long wavelengths refraction effects become important. The light paths are bent by the cigar-shaped plasma boundary which acts as a lense.

Side-on observation gives more reliable results: the observed plasma layers are shorter, and the light path are approximately parallel to the density gradient. Fig. 6 shows the oscillograms of the intensity at λ = 0.3 /u, 3.2 /u, and 21 /u. The frequency response of the IR detectors being lower than that of the multiplier, the ratio of maxima to minima during the radial oscillation of the plasma column appears somewhat smaller in the IR than in the UV. The mean values show, however, at all wavelengths and during the full half-cycle a similar behaviour. In order to minimize the errors resulting from the irreproducibility of the discharge (± 15%) a light beam splitter was inserted and a signal at 3.2 /u was used as monitor for all measurements.

The observed relative variation of the Gaunt factor as function of wavelength is plotted on Fig. 7. It agrees with the theoretical prediction [1] within the error limit of ± 10%. This limit results from the uncertainty of the intensity standard, the experimental irreproducibility, and the oscilloscope accuracy. An unexpected significant correction results from the absorption of the observation windows, especially near the absorption limits in the UV and far IR, which varies after a number of discharges.

The good agreement of the frequency dependence of the Gaunt factor with the quantum mechanical single encounter calculations seems to justify the neglection of screening effects and three body encounters, which has been discussed by several authors [8, 9, 10]. The IR measurements have not shed further light on the problem of the discrepancy between intensity and refraction measurements in the visible.

References

1 W.J. Karzas and R. Latter
Astrophys. J. Suppl. VI, 167 (1961)

2 H.J. Belitz, P. Bogen, K.H. Dippel, H.L. Jordan, E. Kugler, A. Miyahara, P. Noll, J. Schlüter, H. Witulski
Plasma Physics and Controlled Nuclear Fusion Research, Vol. I, 287, IAEA, Vienna 1966

3 K.H. Dippel
Proc. Seventh Int. Conf. Phen. Ionized Gases, Vol. III, 228, Belgrad 1966

4 K.H. Dippel
Berichte der KFA Jülich, JÜL-493-PP, Juni 1967

5 P. Bogen, J. Schlüter
Comptes Rendus de la VI. Conférence sur les Phénomènes d'Ionisation dans les Gas, Vol. II, 561, Paris 1963

J. Schlüter
Berichte der KFA Jülich, JÜL-413-PP, September 1966

6 P. Bogen, J. Schlüter
Nucl. Fusion 5, 251 (1965)

7 P. Bogen, H. Conrads, D. Rusbüldt
Z. Phys. 186, 240 (1965)

8 G. Burkhardt, G. Elwert and A. Unsöld
Z. Astrophys. 25, 310 (1948)

9 L. Oster
Rev. Mod. Phys. 33, 525 (1961)

10 J. Dawson and C. Oberman
Phys. Fluids 5, 517 (1962)

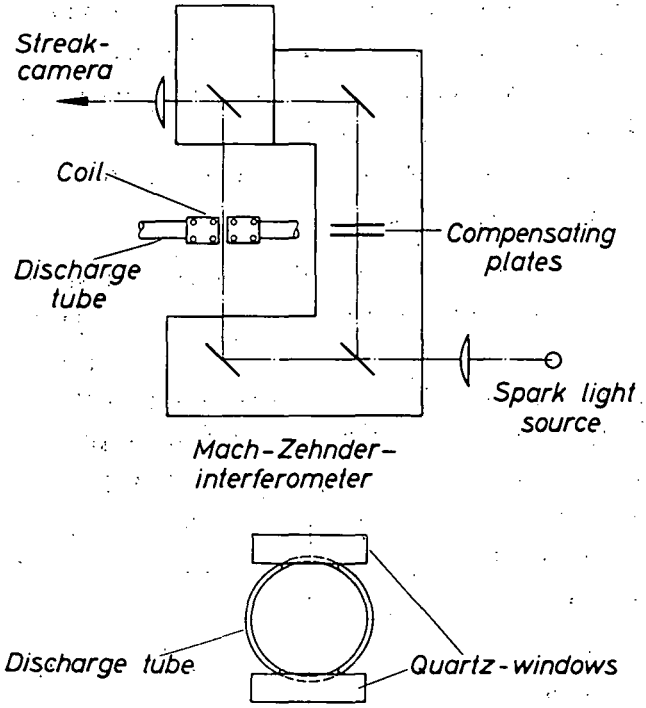

Fig. 1. Optical arrangement for side-on Mach-Zehnder interferometer measurements.

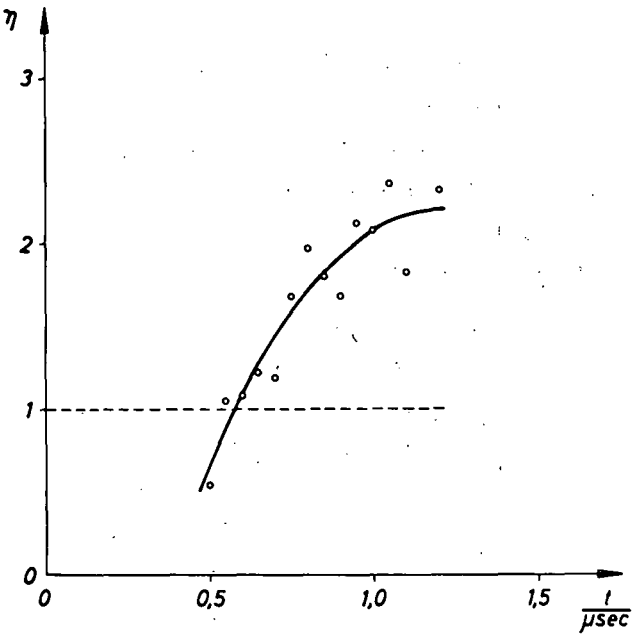

Fig. 3. Ratio η as a function of time t for a given experiment. p_o = 0.25 Torr H_2.

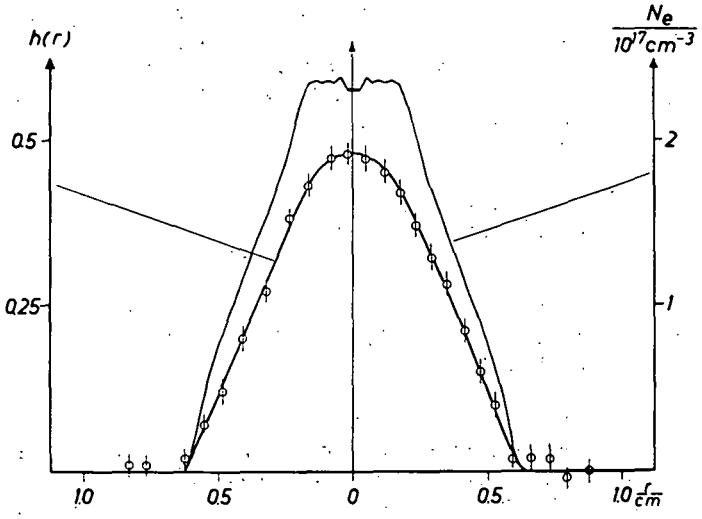

Fig. 2. Fringe shift h(r) as a function of radius before Abel inversion, and electron density N_e as a function of radius after Abel inversion.

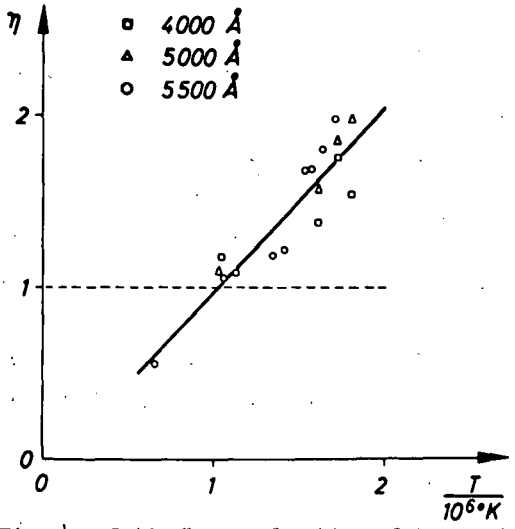

Fig. 4. Ratio η as a function of temperature T for different experiments at various wavelengths and p_o values.

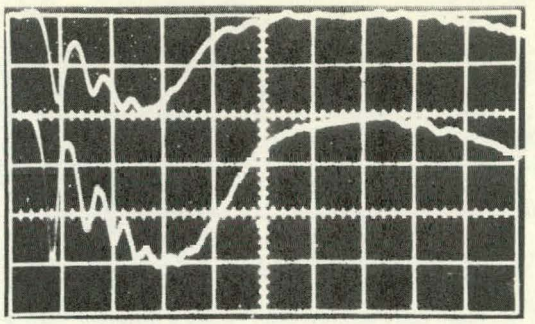

Fig. 5. End-on oscillograms of the continuum intensities at 0.54 and 5.8 μ. Time scale 0.2 μsec/div.

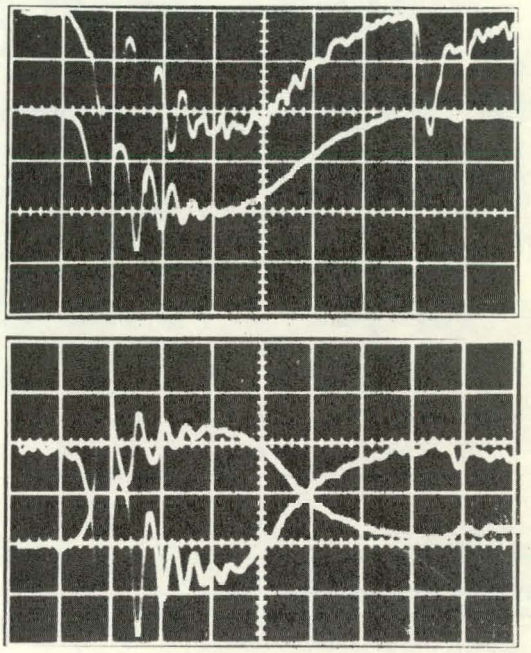

Fig. 6. Side-on oscillograms of the continuum intensities at 0.3 μ, 3.2 μ, and 21 μ. Time scale 0.2 μsec/div. The mean values of the intensities between the fifth maximum and minimum has been evaluated for Fig. 7.

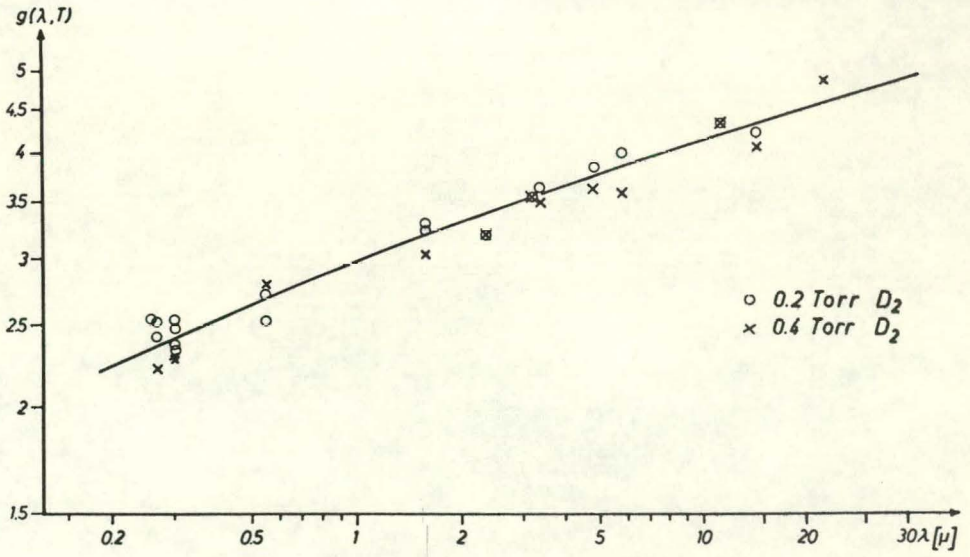

Fig. 7. Gaunt factor g(λ, T) as function of wavelength. At 3.2 μ the observed value of g has been fitted to the theoretical curve (solid line).

o p_o = 0.2 Torr D_2 ≙ $N_e = 2 \cdot 10^{17}$ cm^{-3}

× p_o = 0.4 Torr D_2 ≙ $N_e = 4 \cdot 10^{17}$ cm^{-3}

DIRECT MEASUREMENT OF MASS PICKUP IN A LOW ENERGY THETA PINCH*

by

Robert W. Harris
Sandia Laboratory, Albuquerque, New Mexico

ABSTRACT

A balanced magnetic probe technique has been used to determine the drive force acting on the plasma sheath during the first pinch. The sheath motion was studied with the probe technique, and with image converter framing pictures. The sheath mass was determined from the velocity and the time integral of the drive force. The results indicate an average pickup coefficient of 0.82 ± 0.06 for the first half of the pinch. Electron density and temperature were determined during the first half of the pinch by measurement of the H_β line profile. Combination of the spectroscopic and mass data indicates an average sheath ionization lower than predicted by theory, but the experimental error in the ionization determination precludes a definite conclusion to this effect.

INTRODUCTION

Mass pickup coefficients in theta pinches have been derived from the frequency of radial oscillations[1,2,3] using Taylor's theory.[4] For high energy machines this has indicated complete gas collection.[1,3]

In our case, peak electron temperature is only ~ 10 eV, and most of the trapped magnetic flux leaks out during the pinch because of the comparatively low plasma conductivity.[5] This suggests that complete mass pickup might not occur.

Mass pickup has been studied using a balanced magnetic probe technique,[5] which measures the magnetic field of the plasma current alone, at the center of the bottle and at a point outside the drive loop. The double field measurement determines both the plasma current and radius vs. time.

The plasma current and drive current yield the $\vec{j} \times \vec{B}$ force acting on the plasma; time integration of this force yields the momentum of the sheath. Dividing by the velocity of the sheath from the slope of the radius vs. time curve, the sheath mass is determined.

The mass pickup coefficient is the ratio of the sheath mass to the total mass initially outside the sheath inner radius. The inner radius was measured from framing pictures.

H_β line profiles were also taken and electron density and temperature were derived from them.

EXPERIMENTAL DETAILS

The theta pinch and balanced probe systems have already been described;[5] they will not be discussed here. Table I gives the experimental parameters.

Eighteen framing camera pictures were taken in six firings, using an STL-TRW image converter camera with 5-nanosecond exposure. The magnetic probe signals showed good repeatability during these firings.

The H_β line profiles were taken in 18 firings, using a Bausch and Lomb model 33-86-40 monochromator (dispersion 66 Å/mm) and a Dumont KM2485 S-20 photomultiplier. The monochromator slits could be set for 5-Å measured resolution. The photomultiplier time resolution was measured to be ~ 20 nsec. The photomultiplier linearity was checked with neutral density filters.

DISCUSSION OF DATA

Figure 2 shows the inner and outer radii from the framing pictures and the plasma current radius from the magnetic probe measurements. It was found that the radii did not vary significantly with θ,

*Work supported by the Atomic Energy Commission.

except at peak compression, where plasma instabilities become significant.

The horizontal lines at t_1 and t_2 represent the thickness required for the plasma current in order that the conductivity calculated from the spectroscopic temperatures measured at these times be consistent with the observed plasma current.[5]

Figure 3 shows the H_β line profiles at t_1. The theoretical line shape was taken from calculations by Hill,[6] based on the S(α) values of Griem.[7] The electron density from the fractional intensity widths and the temperature from the line-to-continuum ratio (page 281, reference 7) are given in Table II.

ANALYSIS AND RESULTS

The drive force acting on the plasma sheath is derived from the magnetic field energy,

$$W_B = \frac{1}{2} L_D I_D^2 + M_{DP} I_D I_P + \frac{1}{2} L_P I_P^2 \quad . \qquad (1)$$

Here L_D is the self inductance of the drive current, L_P is that of the plasma current and M_{DP} is their mutual inductance.

The force (in the +r direction) is simply[8]

$$F_r = + \frac{\partial W_B}{\partial r} = \frac{\partial M_{DP}}{\partial r} I_D I_P + \frac{1}{2} \frac{\partial L_P}{\partial r} I_P^2 \quad , \qquad (2)$$

where r is the sheath radius. The inductances are (page 318 of reference 8)

$$\begin{pmatrix} M_{DP} \\ L_P \end{pmatrix} = \frac{\mu_o \pi r^2}{\ell^2} \left\{ \sqrt{\ell^2 + \left(\frac{a}{r}\right)^2} - \left(\frac{a}{r}\right) \right\} \qquad (3)$$

where a is the drive current radius and ℓ is the length of the drive loop and plasma sheath, assumed equal. From Eq. (2) and (3),

$$F_r = \frac{2\mu_o \pi r I_P^2}{\ell^2} \left\{ \frac{\frac{1}{2}\ell^2 + \frac{3}{4}r^2}{\sqrt{\ell^2 + r^2}} - \frac{3}{4}r + \frac{I_D}{I_P} \left(\sqrt{\ell^2 + a^2} - a \right) \right\} \quad . \qquad (4)$$

Figure 4 shows the drive force from Eq. (4) and the sheath momentum for a typical firing. Mass pickup data for four firings is shown in Table III. The average coefficient of 0.82 ± 0.06 corresponds to the first half of the implosion, up to the time t_2.

From Table III, the average sheath mass at t_2 is (4.0 ± 0.3) x 10^{-9} kg. From Table II, the average electron density at t_2 is (1.7 ± 0.4) x 10^{16} cm^{-3}. Using the sheath thickness of (0.62 ± 0.22) cm indicated for t_2 by the framing pictures, the indicated ionic mass is (1.9 ± 0.8) x 10^{-9} kg. Using the mean values for the total mass and ionic mass the indicated percent ionization would be 47 percent. However, the estimated error in the ionization determination is much greater than the error in the mass pickup coefficient, since the ionization determination involves the electron density and sheath thickness which are not involved in the mass pickup coefficient. The errors in these quantities and in the total mass are such that the ionization at t_2 could be as high as ~ 90 percent. Theoretical calculations[9] would indicate complete ionization.

In calculating the ionic mass, the electron density from the spectroscopic measurement was taken as an average for the entire thickness of the sheath. The distribution of electron density within the sheath is probably highly nonuniform; the spectroscopic value of n_e may not be a good average for such a distribution. The numerical calculations of Düchs[10] do indicate that n_e is extremely nonuniform across the sheath in a theta pinch under conditions similar to the present case. Also, the theoretical H_β profile from which n_e was determined assumes LTE, which probably does not hold for this plasma; for optically thin hydrogen plasmas complete LTE requires $n_e > 10^{17}$ cm^{-3} for $kT_e > 1$ eV (p. 151, ref. 7). For these reasons the present data cannot be interpreted as indicating conclusively that the ionization is less than 100 percent for the time t_2.

CONCLUSION

The results for the first half of the implosion indicate that most of the gas is picked up, (82 ± 6) percent, even in our low energy machine. This supports the evidence of complete pickup obtained for high energy machines by indirect methods.[1,3]

There is good agreement between the plasma current radius, determined by the balanced probe method, and the mean visible radius, at least during the first half of the implosion. The

apparent thickness of the plasma current, determined from the conductivity and temperature, is slightly less than the visible sheath thickness. This is reasonable, since the current thickness calculation is based on the assumption of a uniform current density j(r) existing over the thickness calculated, while the actual current density will, of course, be peaked at the center of the sheath.[10]

The apparent ionic mass midway through the implosion (t_2) is a factor of two lower than the apparent total mass at the same time. However, there is nearly a factor of two estimated error in the determination of the percent ionization (although not in the determination of the pickup coefficient), so that it cannot be stated conclusively that the ionization at this time is less than complete.

ACKNOWLEDGEMENTS

The author is grateful to Everett H. Beckner, Ronald A. Hill, and Glenn H. Miller, who reviewed the manuscript and offered helpful suggestions for improvements.

REFERENCES

1. H. A. B. Bodin, T. S. Green, et al., Nuclear Fusion, 1962 Supplement, Part 2, p. 521.
2. T. S. Green, Nuclear Fusion 2, 1, 2, 92 (1962).
3. H. A. B. Bodin, T. S. Green, et al., Plasma Physics and Controlled Nuclear Fusion, Vol. I, p. 193, (International Atomic Energy Agency, Viena, 1966).
4. J. B. Taylor, Proceedings of a Conference on Theoretical Aspects of Controlled Fusion Research, Gatlinburg, Tennessee, April 1959, United States Atomic Energy Commission, Report No. TID-7582, p. 26.
5. R. W. Harris and J. E. McClintock, Physics of Fluids 9, 11, 2274 (November 1966).
6. R. A. Hill, "Fractional Intensity Widths and Stark Broadening Formulas for the Hydrogen Balmer Lines," Journal of Quantitative Spectroscopy and Radiative Transfer 7, 401 (1967).
7. H. R. Griem, Plasma Spectroscopy, (McGraw-Hill Book Company, Inc., New York, 1964).
8. W. R. Smythe, Static and Dynamic Electricity, (McGraw-Hill Book Company, Inc., New York, 1950), p. 310.
9. D. R. Bates, A. E. Kingston, and R. W. P. McWhirter, Proc. Roy. Soc. (London) 267A, p. 297 (1962).
10. D. Düchs, Comptes Rendus de la VI Conference Internationale sur less Phenomenes D' Ionisation dans les Gaz, Paris 1963, Vol II, p. 567, Fig. 2.

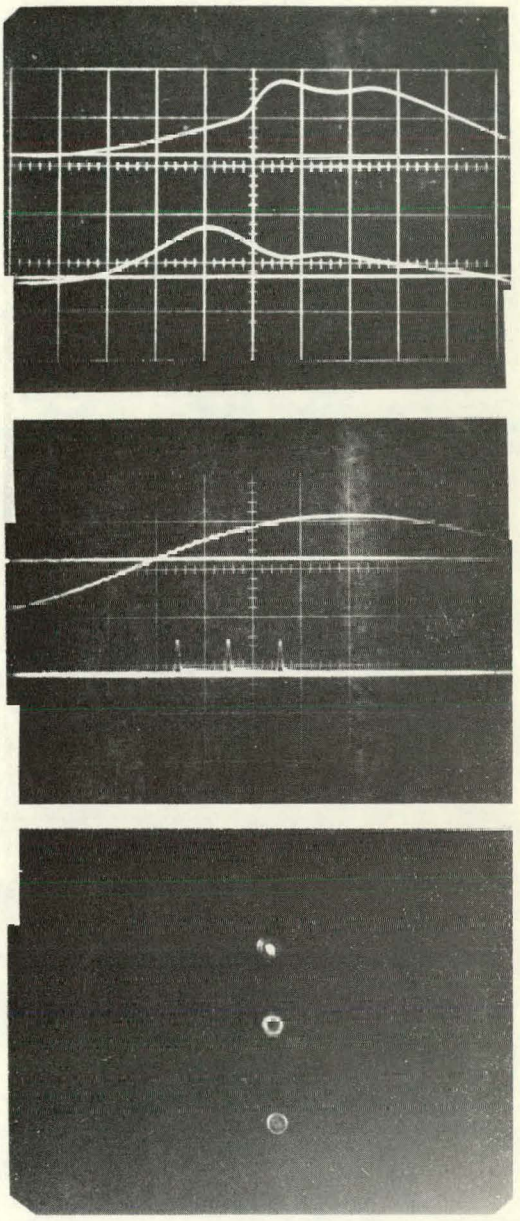

Fig. 1. Typical firing in radius and drive force measurement series: (a) center plasma field (top) and external plasma field (bottom), at 0.2 μsec/cm, sweeps delayed 3.06 μsec from start of drive current. (b) drive current monitor signal (top) and framing camera monitor pulses (bottom), same time scale as (a). (c) framing camera pictures, first frame on bottom. The outer radius in the first frame is 2.5 cm, the inner radius of the bottle.

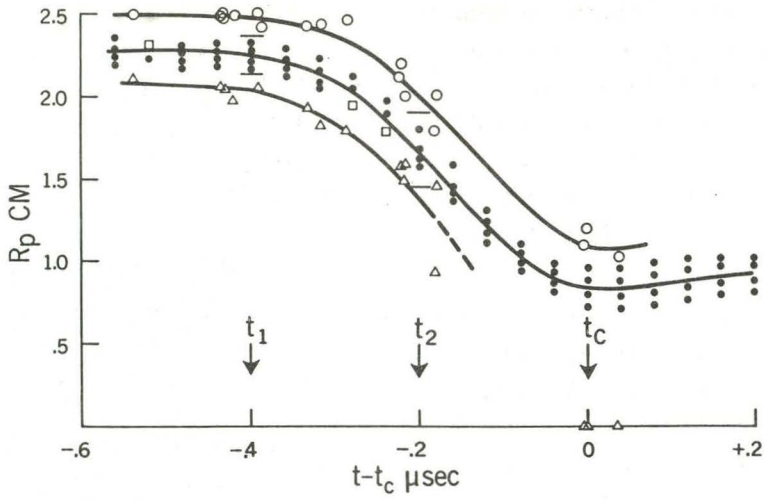

Fig. 2. Plasma sheath radius vs. time, showing outer radius from framing pictures (o), plasma current radius from balanced probe data (•), and inner radius from framing pictures (Δ). Boxes indicate overlapping magnetic probe data points. The times are relative to the time of peak center plasma field, t_c = 4.16 μsec from the start of the drive current. The times t_1 and t_2 correspond to the H_β profiles of Figs. 3 and 4. The horizontal lines indicate the thickness of a uniform current for agreement between the spectroscopic and conductivity temperature.

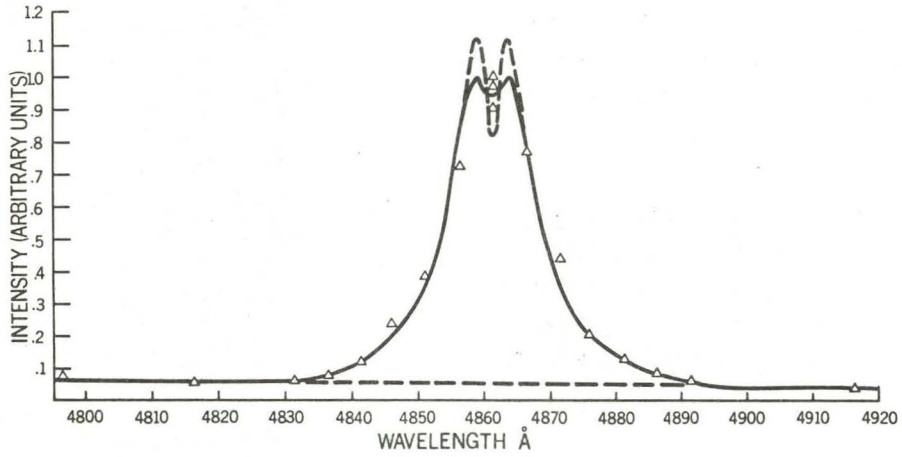

Fig. 3. H_β profile at $t_1 = t_c - 0.4$ μsec, showing data points (Δ) and theoretical line profiles for $n_e = 1.7 \times 10^{16}$ cm^{-3}. The curve with the dashed top corresponds to perfect resolution; the solid top is corrected for a 5-Å wide, square slit function.

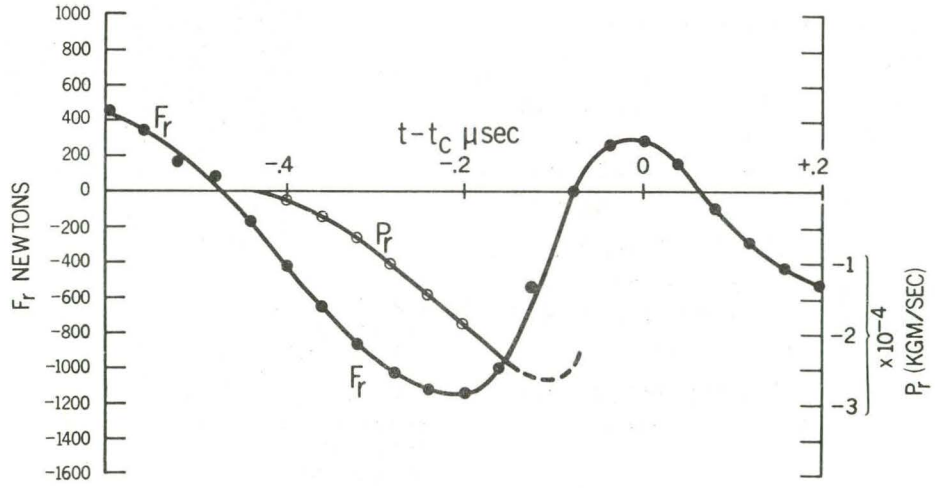

Fig. 4. Magnetic drive force and sheath momentum for a typical firing. Force computed from Eq. (4).

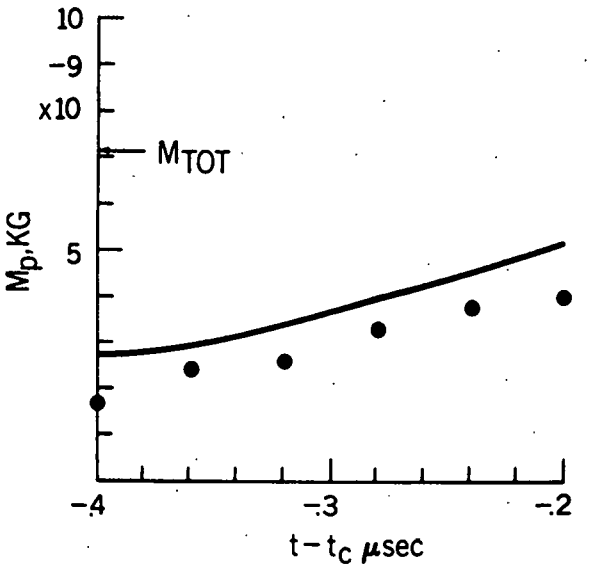

Fig. 5. Sheath mass vs. time for first half of the implosion, same firing as in Fig. 5. The solid curve corresponds to complete pickup of the mass initially outside the inner radius of the sheath at the time in question.

TABLE I

Experimental Parameters

Initial Bank Energy	= 4 kJ (50 kV)
Ringing Period	= 3.56 μsec (281 kc)
Initial Gas Pressure	= 300 μ H_2 (changed after each firing)
Firing Voltage	= 51.7 kV

TABLE II

Plasma Properties from H_β Measurements

Time	n_e	T_e
$t_1 = t_c - 0.4$ μsec	$(1.7 \pm 0.4) \times 10^{16}$ cm^{-3}	5.8 eV
$t_2 = t_c - 0.2$ μsec	$(1.7 \pm 0.4) \times 10^{16}$ cm^{-3}	9.0 eV

TABLE III

Effective Mass Pickup Coefficient

Firing	$M_P(t_2)$	$r_{IN}(t_2)$	$M_{\alpha=1}(r_{IN})$	α_{eff}
1	3.90×10^{-9} kg	1.32 cm	5.10×10^{-9} kg	0.765
2	4.01×10^{-9}	1.31	5.11×10^{-9}	0.785
3	4.29×10^{-9}	1.37	4.93×10^{-9}	0.870
4	3.91×10^{-9}	1.51	4.51×10^{-9}	0.867
				$\langle\alpha\rangle = 0.82 \pm 0.06$

t_2 = $t_c - 0.2$ μsec

M_P = plasma sheath mass

r_{IN} = inner radius of sheath

$M_{\alpha=1}(r_{IN})$ = mass corresponding to complete pickup of gas initially at $r > r_{IN}(t_2)$

$\alpha_{eff} \equiv M_P/M_{TOT}$

THE INFLUENCE OF STRONG MAGNETIC MIRRORS ON THE STABILITY AND CONTAINMENT OF A THETA PINCH PLASMA +)

by

A. Heiss, H. Herold, E. Unsöld
Institut für Plasmaphysik
Garching b. München, Germany

ABSTRACT

Magnetic mirrors with R = 1.1, 1.6 and 3.1 are applied to a theta pinch coil (30 cm long) fed by a 80 kJoule bank. The resulting plasma properties are compared with those of a mirrorless coil at various filling pressures (10 to 50 μHg, D_2). The application of mirrors does not cause detectable instabilities during the time of observation (5 usec$\simeq$T/2) provided that the mirror region is not too short. Rotational instabilities are observed occasionally in cases with mirror coils as well as with mirrorless coils, especially at higher filling pressures. The interferometrically determined particle number in the mirror coils shows an initial phase with reduced losses due to axial compression followed by a time of exponential decay which lasts up to the end of the half wave. The e-folding times are compared with those predicted by loss models for collissionless and collision dominated outflow and with those obtained from numerical two-dimensional magneto-hydrodynamic one-fluid computations. The results of the 3 loss models differ only slightly and there is good agreement with the experimentally observed e-folding times. For scaling purposes $t_N \sim R\ell / T_i^{1/2}$ is found to be a good approximation for theta pinch plasmas characterized by a m.f.p. of the ions from 10 to 1000 cm, T_i = 2 to .5 keV and β = .3 to .8.

The experiments were performed on an 80 kJ theta-pinch device where a straight coil and mirror coils with different mirror ratios R were applied. The data of the device are listed in Fig. 1. Fig. 2 shows a sketch on a reduced scale of the applied mirror coils together with the magnetic fields measured at the axis of the coils at current maximum. To change the mirror ratio only the end sections of the coils were exchanged along with the quartz tube which fitted in each case the contours of the coils. Coils with R > 3 could not be used, since in this case the preionization by a short current pulse in the z-direction did not work properly, particularly at low filling pressures. Wall discharges like slide sparks occurred in the throat of the tube. In this case the plasma in the subsequent Θ-discharge was observed to be unstable.

All mirror coils were driven with the same total energy in the capacitor bank. To compare the plasma outflow in terms of the plasma properties, T_i, T_e, n_e and the total particle number in the confined plasma N were measured for each mirror coil at different filling pressures (p = 10 to 30 μ Hg, D_2; in some cases also 50 μ Hg). T_e was measured using the foil absorption technique, T_i was deduced from the neutron emission. N(t) and $n_e(t)$ were determined by means of a Mach-Zehnder interferometer.

Experimental Results: Containment and Drift

Concerning the plasma containment with mirrors three stages can be distinguished during the half-wave of the compression

field. At the beginning of the discharge the conical mirror coils cause an axial compression of the theta pinch plasma. The velocity of the incoming compression wave (area shock wave) increases with higher mirror ratios and has values of 6 to 10 x 10^6 cm/secs for R = 1.1 to 3.1 at p = 20 μ. During the axial compression the total particle number N(t) in the coil stays nearly constant for about 1 to 1.4 usecs depending on the mirror ratios. This can be seen in Fig. 3 where the decay of the particle number in the coil is plotted for different R. The next stage is characterized by an exponential decay of N which generally lasts up to the end of the half-wave. The e-folding time t_N is increased by the application of mirrors.

t_N is taken to be characteristic of the plasma losses and will be compared with the results of loss models. Finally, in the region of zero field the measured particle number drops very fast.

The plasma drift toward the current feed in the straight coil, which is about 3 to 8 mm, is not altered much for R = 1.1 and 1.6, but for R = 3.1 the direction of the drift is reversed. This can be explained by a divergent current flux necessary to feed the mirrors in the rectangular adapter[1].

Stability

The application of mirrors generally does not cause observable instabilities during the observation time of about 5 usecs. Rotational instabilities which occur occasionally at high filling pressures (30 to 50 μ) are observed both in the mirror coils and in the straight coil. These statements are based on the following investigations:

a) Observation of the plasma at different cross-sections along z including the mirror regions with streak cameras. One example for stability is shown in Fig. 4.

b) Observation of the distribution and radial symmetry of the interference fringes (Fig. 5).

c) Investigation of the time resolved neutron emission of $T_i(t)$ and $T_e(t)$ and of the decay of particle number in the coil.

No indications of mirror induced instabilities could be detected by these methods. One exception is the mirror coil R = 1.6 in some cases. This mirror is very short and has a discontinuity in its cross section. In Fig. 3 an exceptionally high plasma loss for R = 1.6 is indicated. This may be due to an instability. However no gross disturbance of cylindrical symmetry is visible during the period of enhanced plasma loss (Fig. 4; 30 μ).

Very preliminary results with increased time scale were obtained after the installation of crowbar switches. For R = 3.1 and pressures $\leqslant$ 20 μ a confined and undisturbed plasma column can be observed on streak pictures up to 12 μsecs. With higher pressures rotational instabilities develop about 7 μsecs after the start of the discharge.

These times may be compared with the approximative growth times for instabilities taken from the theory of Wobig[2] for a bumpy theta pinch. Considering only the measured curvature of plasma inside the coil times of about 1 μsec are obtained. Therefore it is likely that at the experiments an additional stabilizing influence of effects outside the coil (plasma curvature, cold gas and wall effects) exists.

Comparison with Loss Models

For the purpose of choosing among the various loss models proposed the experimentally produced plasmas can be described as follows: The values for the mean free path of the ions (90° collisions among thermal ions) are between 7 cm (R = 3.1; p = 30 μ) and 1100 cm (R = 1; p = 10 μ). At least for the lower filling pressures the plasma can be considered to

be collisionless. The plasma β varies from o.3 to o.8 for p = 1o μ to 3o μ at all coils. The plasma particles are assumed to have an isotropic Maxwellian distribution at the beginning of the outflow. This is reasonable if one regards the strong axial motion and compression.

In the first model, collisionless effusion of the plasma ions along the magnetic field lines from a stationary isotropic Maxwellian distribution is assumed. The propability of the particles escaping is proportional to 1/R. The e-folding time is

$$t_N = N/(dN/dt) = R \cdot l / \langle v_z \rangle$$

where $\langle v_z \rangle = (2kT_i/m\pi)^{1/2}$ is the mean velocity parallel to the axis of the coil, l = plasma length.

For the collision dominated case t_N is compared with the results of a loss model of Taylor and Wesson[3] where the outflow is treated as a stationary hydrodynamic flow through a flexible nozzle formed by the magnetic field lines.

In Fig. 6 the experimental values of t_N are compared with those calculated from the two models. Furthermore the t_N resulting from numerical calculations with a two-dimensional one-fluid theory are plotted[4]. These calculations start with initial conditions measured in the theta pinch plasma after the dynamic phase. The one-fluid model describes the plasma axially and radially resolved assuming infinite electrical conductivity and isotropic pressure and taking thermal conductivity into account.

Good agreement is obtained between the calculated and measured e-folding times. The region of data covered by the experiments is R = 1 to 3.1; $n_{e\ max}$ = 5 x $1o^{15}$ to 5 x $1o^{16}$, with correlated T_i = 2 to .5 keV and $T_{e\ max}$ between 2oo and 3oo eV. Since the results of the applied models differ only slightly one cannot get information on which outflow mechanism is present. At p = 1o μ (Fig. 6) the calculated t_N are always lower than the measured t_N. Probably the assumption of an isotropic Maxwellian distribution for the ions made in the first model is not fulfilled in this case, and the containment times are influenced by relaxation phenomena.

Models for collisionless outflow from cusps (sheath models) where the equivalent loss hole cross section is proportional to r_g^2 or r_g x r (r_g = ion gyroradius, r = plasma radius)[5,6] are not applicable and do not fit the experimental results.

+) This work was performed as part of the joint research program of the Institut für Plasmaphysik, Garching and Euratom.

References

1 F. Pohl, Report IPP 1/57 (1967)
2 H. Wobig, Report IPP 6/57 (1967)
3 J.B. Taylor, J.A. Wesson, Nucl. Fus. 5 159 (1965)
4 W.H. Schneider, F. Hertweck, 2nd Europ. Conf. on Contr. Fus. and Plasma Physics Stockholm (1967)
5 W. Grossmann, Jr., Phys. Fluids 9, 2478 (1966)
6 J.B. Taylor, CLM-R 58 (1966)

Energy of bank (at U_o = 40 kV)	= 80 kJ
Total inductance with straight coil	= 35 nHy
Max. compression field	= 76 kG
Half period	= 5.9 usecs
Preionization by pulsed z-discharge	
Pulse length	= 400 nsecs
Max. z-current	= 15 kA

Fig. 1. Data of the theta-pinch device with straight coil.

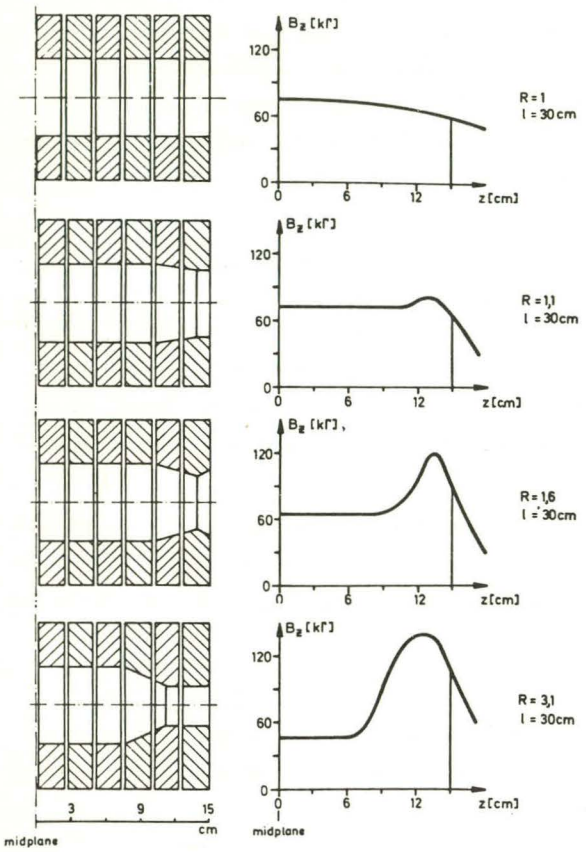

Fig. 2. Mirror coils applied at the experiment and field distribution on the axis of the coil at current maximum.
Max. coil diameter = 7.1 cm.
Coil length = 30 cm.

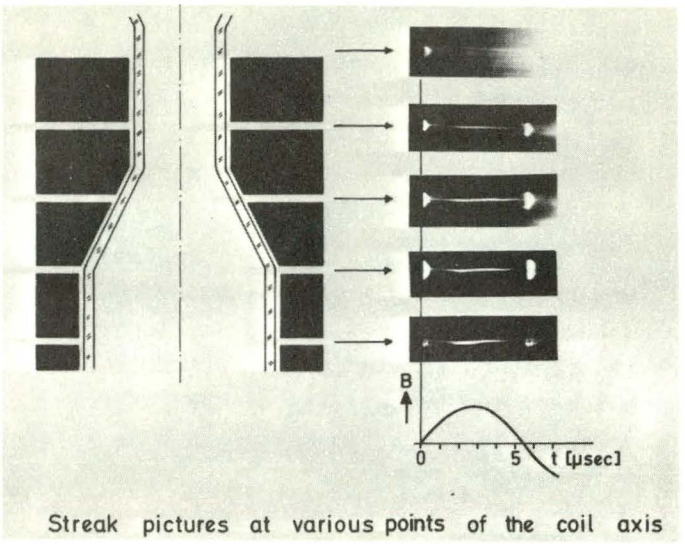

Streak pictures at various points of the coil axis

Fig. 4. Streak pictures at different cross sections along z showing a stable plasma. R = 3.1; p = 50 μ Hg, D_2.

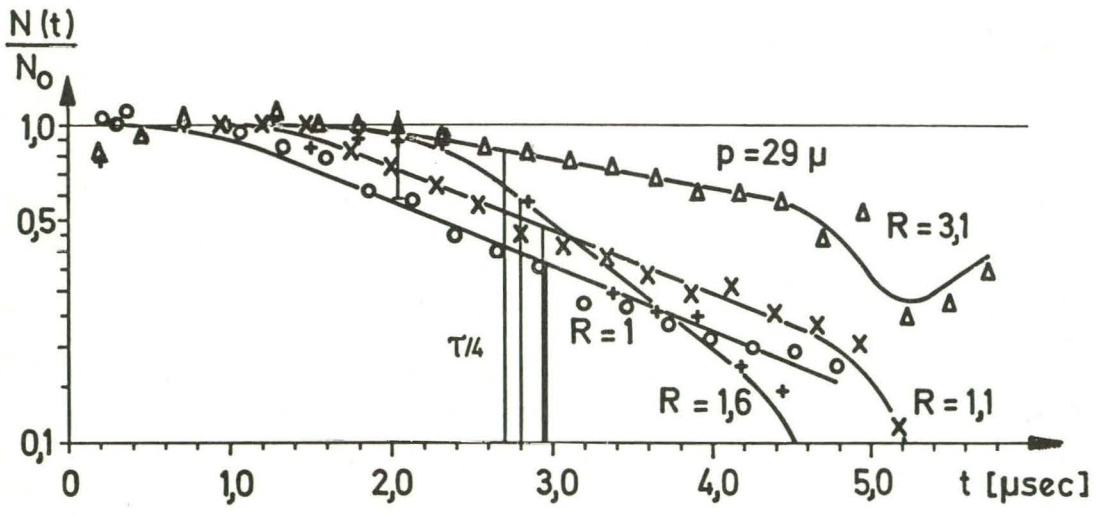

Fig. 3. Decay of total particle number in the coil with time $N(t)/N_o$ for different mirror ratios R.

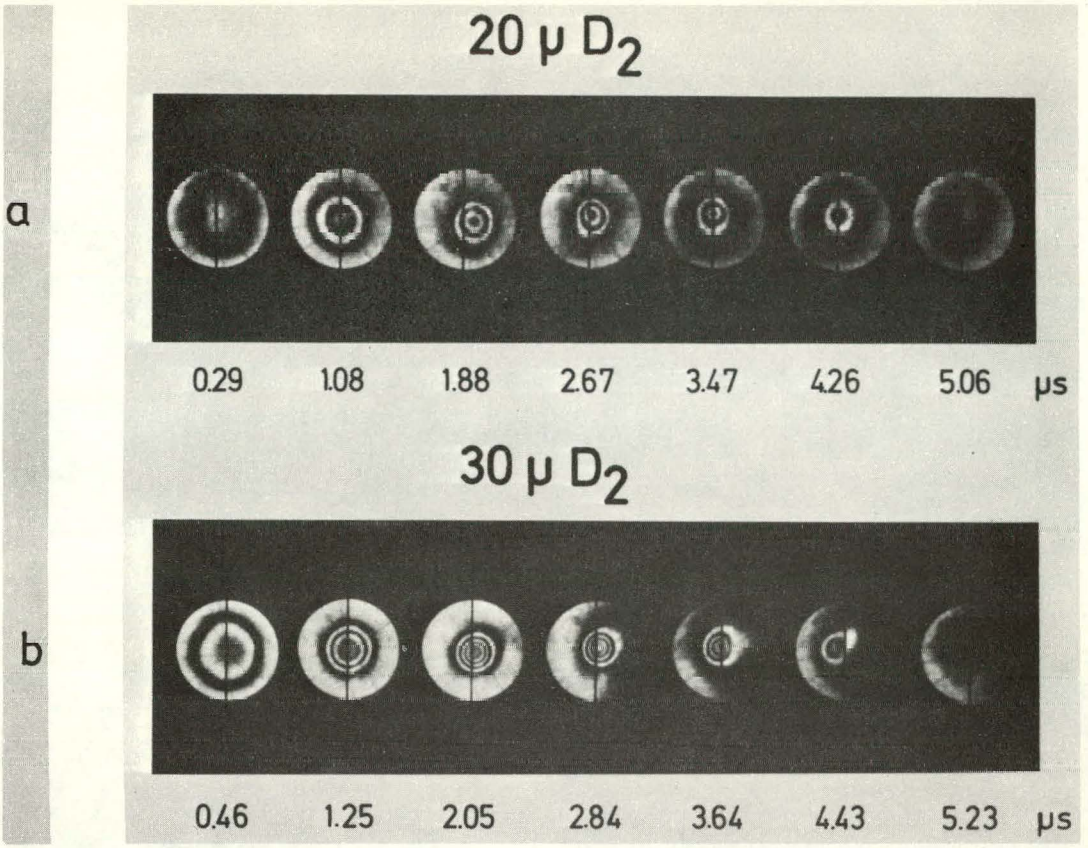

Fig. 5. Framing pictures of interference fringes (zero order):
a) stable plasma R = 1.6; p = μ
b) exceptional plasma loss starting at t = 2 μsecs (see also decay curve in Fig. 3) p = 30 μ; R = 1.6.

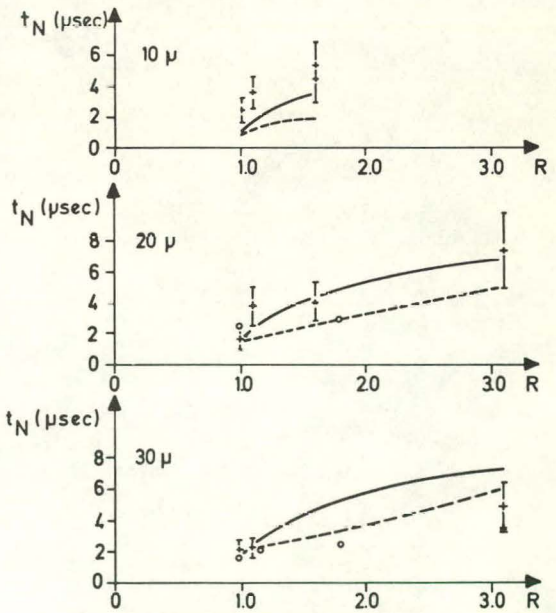

Containment time t_N as a function of the mirror ratio R for different initial pressures

Fig. 6. E-folding times for particle loss as a function of the mirror ratio.
+ experimental values
—— magnetohydrodynamic model of Taylor and Wesson[3]
--- collisionless effusion model
o one-fluid theory[4]

IMPULSION HEATING OF PLASMA IN THE BILLE-EN-TETE EXPERIMENT

by

P. EVRARD, J. JACQUINOT, C. LELOUP, J.P. POFFE, M. DE PRETIS, F. WAELBROECK

Groupe de Recherches de l'Association EURATOM - CEA sur la Fusion

ABSTRACT

A plasma column ($v_o < 5.10^6 cm.s^{-1}$, diameter $\approx$ 4.5cm) is injected along the axis of a simple magnetic bottle (mirror ratio 1.7) and heated by a fast condenser bank (0.5 μF, $\leqslant$ 100 kV) discharged into a single turn coil ($\emptyset$ = 16cm, ℓ = 40cm)surrounding the plasma. During the first quarter-period (0.4μsec), the initially static magnetic field (usually 1 700 gauss) decreases; the plasma expands ; the field reincreases rapidly thereafter ; during this recompression phase, plasma heating is observed. After the first half-cycle, the circuit is crowbarred. The initial plasma parameters were varied between : $10^{13} cm^{-3} > n > 10^{12} cm^{-3}$; $5eV < T_e < 15eV$; $10eV < T_i < 150eV$. After the heating, hot ions ($T_i \simeq 400eV$) and electrons (T_e = 12 $\pm$ 3keV) are detected. The radius is 2cm and the plasma volume is about 1,5 litre. The ions disappear in a few tens of μsec. During their life-time, the plasma appears turbulent and noisy. At lower densities, the hot electron population decays regularly ($\tau_{1/e} \geqslant$ 1msec). At higher densities, τ is still several hundreds of μsec, but sporadic bursts of instabilities are detected leading simultaneously to : large plasma energy losses ; a decrease of the pressure anisotropy ; radial and axial electron-losses ; strong polarized emission at ω_{ce} and at higher frequencies ; and rapid flute-like motions of the plasma column. Two different types of instability are distinguished.

--- - ---

I. INTRODUCTION

The capture and the containment of plasma injected into simple or more complicated magnetic mirror bottles has been investigated by many authors /1 to 10/. In some of those experiments /1 to 3/, no heating is applied after the capture and the trapped plasma is studied in an essentially constant magnetic field. One difficulty often encountered is that some plasma still streams through the configuration and it is experimentally difficult to distinguish between trapped and streaming plasma. This difficulty is partially avoided in other devices where the captured plasma is heated by a slow magnetic compression /4 to 7/. In this case, however, the study of the energy confinement time presents some difficulties since the compression acts as a positive energy source and modifies the plasma anisotropy and its geometry. A third approach, first followed by Ioffe /8/, consists in heating the plasma rapidly in a static configuration within the magnetic bottle itself. More recently, the development of "Turbulent" heating techniques /9 to 13/ has led to new experiments in this direction.

Considerable progress has been made towards the understanding of the behavior of plasma in such traps. In the absence of flute instabilities, one observes for both hot ion and hot electron plasmas that above certain critical densities, the plasma energy decreases step wise, each jump being of short duration and accompanied by rapid particle losses and by bursts of high frequency emission in the vicinity of the corresponding cyclotron frequency.

The connections between the theoretically proposed instability mechanisms and the observed events are often difficult to make unequivocally. It seems therefore that further experimental research is justified.

We present here experimental studies on the pulse heating of a low density plasma and on the behavior of the resulting hot ions and electrons in a simple magnetic mirror trap. An injected cold plasma is heated in a very short time ($\pm$ 0,5 μs) by a fast magnetic compression technique inside the magnetic bottle itself. Thereafter, the heated plasma decays in a static magnetic configuration. The working conditions were such that the collisional scattering of the hot particles into the loss cone is small during several milliseconds and we study the collective effects occuring during this time and their consequences on energy losses.

II. THE EXPERIMENTAL PROCEDURE

The experimental set up is shown on Fig. 1. It consists of :

- The injection region where a conical theta pinch gun [13] injects a single blob into an increasing magnetic field.

- The confinemcnt region, usually a simple magnetic mirror bottle of ratio 1.7 . The length between mirrors is 160cm and the diameter of the pyrex chamber is 15cm. The static magnetic field B_o in the mid-plane can reach 5kG and was usually 1.7kG

- An expansion chamber which reduces the influence of the neutral gas produced by the plasma striking the end walls. If need be, a second gun at the end of this chamber can be fired at any desired time.

A fast condenser bank (0.5 μF $\leqslant$ 100kV) is discharged into four single turn coils connected in parallel. The maximum oscillating magnetic field is 3.2kG. The discharge is usually crowbarred after the first half cycle (0.9 μs) . The residual oscillations are damped out in a few microseconds.

The operating sequence is the following :

a) The fast valve is opened, the expanding gas is preheated, the gun is fired and crobarred after the first quarter cycle.

b) After the head of the plasma blob ($v \simeq$ 14cm/μsec) has gone through the confinement region, the heating field is applied to the slow moving plasma tail ($v \leqslant$ 6cm/μsec). Its polarity is antiparallel to that of the initial field so that, in vacuum, the total field crosses twice the zero value.

Until now, the heating phase has not been investigated in details. For high initial densities (10^{14}cm^{-3}), the growth and the propagation of a large amplitude wave ($M_A \simeq 4$) has been observed [14] during the recompression phase. The average temperature increase of an electron ion pair in the magnetic bottle was $\Delta (T_e + T_i)_\perp \simeq$ 200eV. No long time confinement could be observed. By increasing the bank voltage and energy and by working at lower initial densities, the formation of low density hot confined plasmas has been achieved (cf. Fig. 2).

With these initial conditions ($10^{12} < n_e = n_i < 10^{13}$cm^{-3}) the Alfvén velocity and the collision free skin depth evaluated before the recompression phase are such that one does not expect and indeed does not observe any magnetic discontinuity during the recompression. As in other experiments [15 to 16], the observed heating could be partially explained in terms of non adiabatic effects, as the field crosses the zero, followed by some adiabatic compression effects.

In those conditions, the initial electron temperature varies from 15 to 7eV, and the initial ion temperature from 150 to 10 eV. After heating the $\frac{P_{\perp \text{hot}}}{P_{\perp \text{cold}}}$ ratio is usually larger than 10 .

III EVOLUTION OF THE HOT ION POPULATION

Information about the hot ion population has been obtained with a fast neutral analyser. The charge exchange fast neutrals are reionized within a helium gas cell and then analysed in energy [17]. The analyser detects only the neutrals with $V_{//} \ll V_{\perp}$. The mean energy of the fast neutrals is 500 eV and assuming charge exchange on atomic deuterium, one deduces a hot ion mean energy of about 400eV. At the lower initial base pressure (5×10^{-7} torr), the e-folding time of the fast neutral signal is 35 μs. It has been checked that charge exchange is not the essential loss mechanism : The fast neutral reciprocal life time does not extrapolate to zero for zero background pressure and the integral of the fast neutral signal increases when the background pressure is increased.

During the existence of hot ions, capacitive probe signals detect a noise in the 1 to 10 MHz range. The duration and the amplitude of this noise is strongly correlated (Fig. 3) with the ion life time and the amplitude of the fast neutral signals : When we increase the background pressure, the two durations are reduced proportionally.

After about a 100 μs, the hot ions have disappeared. A hot electron plasma remains, the confinement of which depends strongly on its density.

IV. EVOLUTION OF THE HOT ELECTRON PLASMA

Diamagnetic loops measuring the line density of the perpendicular energy show that energy confinement time depends very much on initial conditions. Four diamagnetic signals corresponding to increasing initial densities are shown on Fig. 2 a-d. Before the application of the heating at time t_o, the diamagnetic signals result from the passage of the injected plasma; after t_o, it is caused almost entirely by the hot electron plasma. In the case a (Fig. 2a) the electron temperature was obtained by three independent methods which agree with the value 12 ± 3keV

The first was to measure the energy of the hot electrons escaping by bursts through one mirror with a scintillator probe [18] covered with aluminum foils of different thicknesses ; we have also analyzed the spectrum of X-rays emitted by electrons striking radially the walls of the pyrex tube ; we have finally measured the decrease of the confinement time when a probe is lowered into the plasma, assuming that the azimuthal electron was only caused by the curvature and grad B drifts. This last method also yields a value of the plasma radius $r_p = 2$cm in the mid-plane.

From this measurement and assuming that the electronic temperature has approximately the same value at higher densities, we deduce from the diamagnetic signal amplitude that the maximum density is : $n_e = 2.5 \times 10^{10}\,cm^{-3}$ for case a and respectively 8×10^{10}, 1.3×10^{11} and 2.1×10^{11} for cases b, c, and d.

In the low density case (a), the plasma looks quiescent according to the diamagnetic signals with a decay time $\tau_{1/e} \geqslant 1$ msec.

At higher densities, instabilities occur in bursts leading to rapid plasma losses. One observes that the plasma remains quiescent when the density has fallen below a critical value of about $3 \times 10^{10}\,cm^{-3}$. Two different types of instability have been identified. At low densities (somewhat above $3 \times 10^{10}\,cm^{-3}$) a velocity space instability occurs with important particle scattering into the loss cone. At higher densities (about $1.5 \times 10^{11}\,cm^{-3}$), the plasma exhibits a motion in one radial direction and a considerable amount of plasma is lost on one side of the vacuum chamber.

V. THE VELOCITY SPACE INSTABILITY

Fig. 4 shows an example of the first type of instability. In this case 19 % of the plasma transverse energy is lost in 2 μs. Simultaneously, a burst of electrons is detected outside the mirrors. Absolute calibration of this detector shows that the

observed longitudinal losses can account for the amplitude of the transverse energy step. This is confirmed by the fact that no X-rays are emitted from the walls and that probes indicate no large radial motion of the plasma column. A burst of microwave radiation in the neighbourhood of the electron cyclotron frequency is also detected during the instability. This radiation is polarized in a plane perpendicular to B. A rapid decrease of the plasma anisotropy in velocity space is also observed during the instability. The anisotropy was determined [19] by measuring the longitudinal profile of the diamagnetic flux with a set of 9 magnetic loops surrounding the plasma at different axial positions. Finally the detector measuring the end losses was moved radially and we verified that the electrons were emitted from the central part of the plasma. Therefore, the instability occurs probably in the bulk of the plasma and not in regions of large Δn.

VI. INSTABILITY WITH RADIAL LOSSES

At higher densities, the instability has a very different behavior (Fig. 5): Nearly 50 % of the plasma is lost in about 5 μs after a period of more or less quiescent behavior. The plasma column moves radially but apparently does not rotate. The direction of motion is very irreproducible and in this case, the plasma went to the East side of the chamber. Simultaneously, with the instability, we observe a large X-ray emission from the East side of the chamber and diamagnetic signals on the three magnetic probes located on the East side near the walls. No end losses are recorded on the axis and also no signals from other magnetic probes located near the walls but at different azimuthal positions. The amplitude of both the X-ray emission and the magnetic signals indicate that the plasma column indeed came into contact with the wall. It looks like an $m = 1$ flute instability, but the correlation along a line of force is far from perfect. The signals of the two probes located on the same line of force but 48 cm apart from each other can differ by as much as a factor of five.

Surprisingly, H.F. emissions are observed in the neighbourhood of the electron cyclotron frequency ant at higher frequencies. One notices that this emission does not always occur when the losses are maximum but also when the diamagnetism decreases smoothly (cf. Fig 4).

In this case also, the plasma anisotropy in velocity space decreases about 15 % during the instability.

CONCLUSION

Different types of plasma instabilities have been observed in our impulsion heated plasma.

One of these occurs in velocity space and is in many respects analogous to the instability reported by Perkins and Barr [4]. They identified the phenomenon as a cyclotron double distribution instability. In our case, however, other possibilities can not be ruled out. It could also be for instance a Whistler mode [20] unstable for frequencies slightly below the electron cyclotron frequency.

The instability with radial losses is probably an $m = 1$ flute instability. A possible explanation for the associated high frequency emissions might be the high frequency "loss cone" flute instabilities inherent to two component plasma described by Pearlstein, Rosenbluth and Chang [21]. It could also qualitatively explain the decrease of anisotropy in velocity space.

Finally, flute instabilities appear as a likely candidate for the quick disappearance of hot ions in the initial phase.

REFERENCES

[1] G. FRANCIS, J.W. HILL, and D.W. MASON Conf. Proc., Culham, (1965), CN-21/30

[2] F.R. SCOTT, T.H. JENSEN, and C.B. WHARTON Conf. Proc., Culham (1965), CN-21/84

[3] P. EVRARD, J. JACQUINOT, C. LELOUP, J.P. POFFE, F. WAELBROECK, Rapport CEA-R 3000 and Nuclear Fusion, Vol. 6, N° 2 (1966)

[4] W.A. PERKINS and W.L. BARR, Conf. Proc. Culham (1965), CN - 21/93

[5] A. BIGUET, P.BLANC, R. GRAVIER, H. LUC, P. LECOUSTEY, C. RENAUD, J. TACHON and D. VERON, Conf. Proc.,Culham (1965) CN - 21/67

[6] H. COENSGEN, W. CUMMINS, W. NEXSEN and A. SHERMAN, Phys. Fluids 9, 187-194 (1966)

[7] A.P. BABICHEV, E.M. BURIAK, and E.F. GORBUNOVA, Conf. Proc., Culham, (1965), CN - 21/162

[8] YU.V. GOTT, M.S. IOFFE and E.E. YUSHMANOV, Conf. Proc., Culham 1965 CN - 21/143

[9] M.V. BABIKIN, P.P. GAVRIN, L.I. RUDAKOV, V.A. SKORYUPIN and E.K. ZAVOYSKY, Conf. Proc., Culham (1965), CN-21/154

[10] V.A. SIMONOV, V.V. ABOZOVIK, and V.V. IGNATIEV, Conf.Proc., Culham (1965) CN - 21/167

[11] R.KH. KURTMULLAEV, YU.E. NESTERIKHIN, V.I. PILSKY and R.Z. SAGDEEV, Conf. Proc. Culham (1965), CN - 21/218

[12] BABIKIN and Al., IAE 667, Kurchatov Instit. Moscow (1964)

[13] F. WAELBROECK et Al., Nuclear Fusion 1962 Suppl., Part 2, 663

[14] J. JACQUINOT, C. LELOUP, J.P. POFFE, M. de PRETIS, and F. WAELBROECK, Abstr. in the 8th Annl. Meetg. of the A.P.S., Boston, 1966

[15] K.S. SUH, G. SCHMIDT, and J. FUTTERMAN Phys. Fluids, Vol. 8 N°6, (1965)

[16] A.BARIAUD, R. GRAVIER, M. KORMAN, H. LUC, C. RENAUD and J. TACHON, Phys. Fluids, Vol. 7, N°9, (1964)

[17] C. RENAUD, Proc. of the 7th I.C.P.I.G, Vol. III, (Beograd 1966)

[18] R.E. ELLIS and N.W. CARLSON, Rev. of Sci. Instr., 32 (1961), 1367

[19] J. JACQUINOT, F. WAELBROECK, to be published

[20] J. E. SCHARER, Phys. Fluids, Vol. 10, N° 3,(1967)

[21] L.D. PEARLSTEIN, M.N. ROSENBLUTH, and D.B. CHANG, Phys. Fluids, Vol. 9, N° 5, (1966)

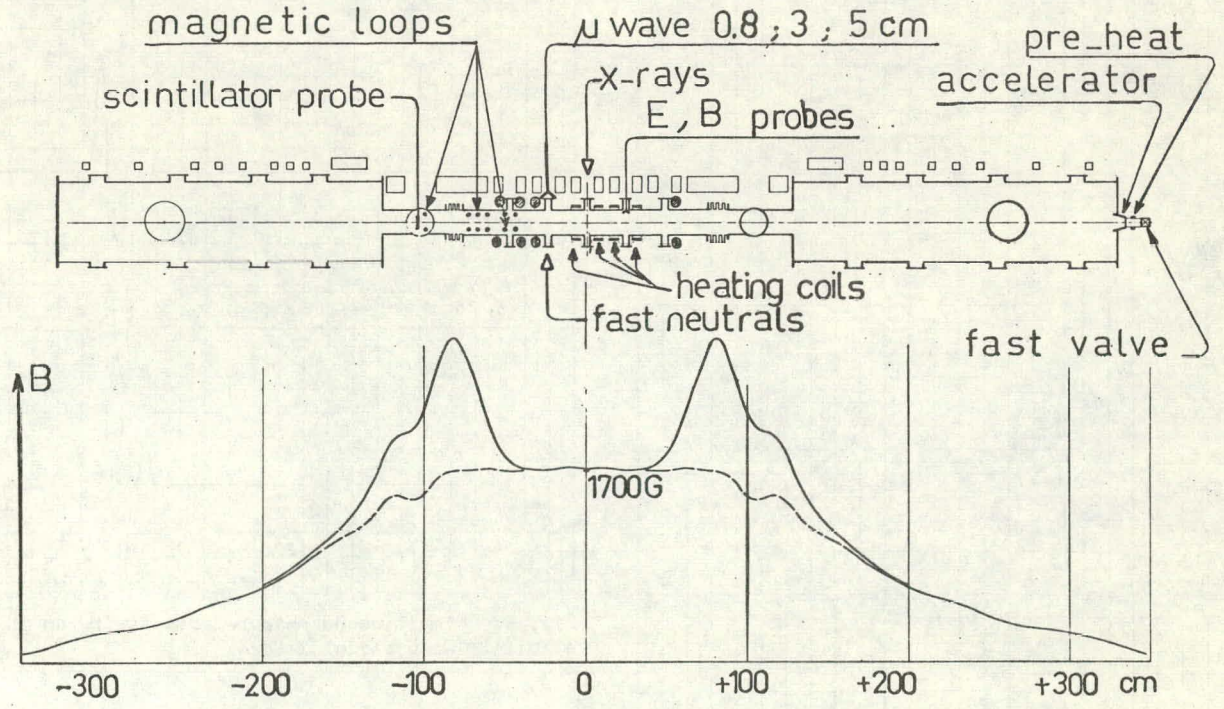

Fig. 1. The B.E.T. apparatus.

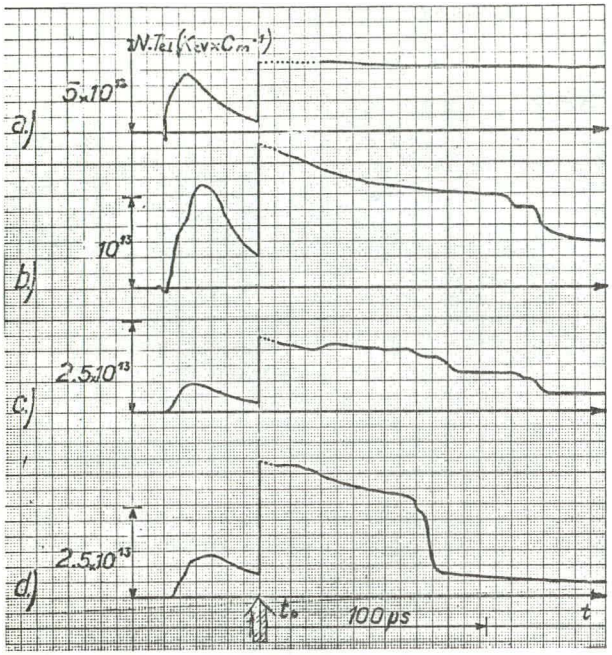

Fig. 2. Diamagnetic flux signals for 4 different cases of increasing initial densities. (a) stable case, density after heating, $n_e \simeq 2.5 \times 10^{10} cm^{-3}$; (b) case with velocity space instability, $n_e \simeq 8 \times 10^{10} cm^{-3}$; (d) case of instability with radial losses, $n_e \simeq 2.1 \times 10^{11} cm^{-3}$; (c) intermediate case, $n_e \simeq 1.3 \times 10^{11} cm^{-3}$. Heating is applied at time t_o.

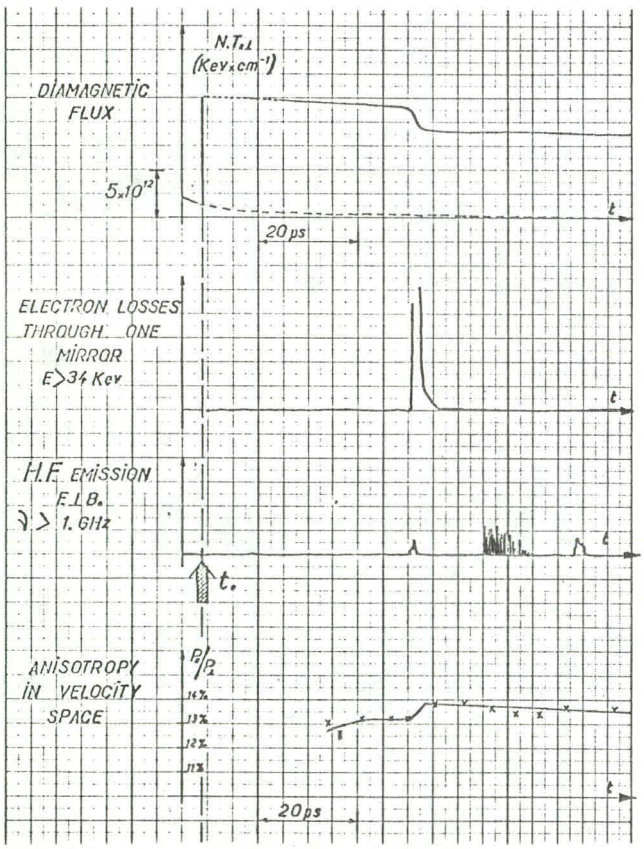

Fig. 4. Simultaneous measurements during a velocity space instability.

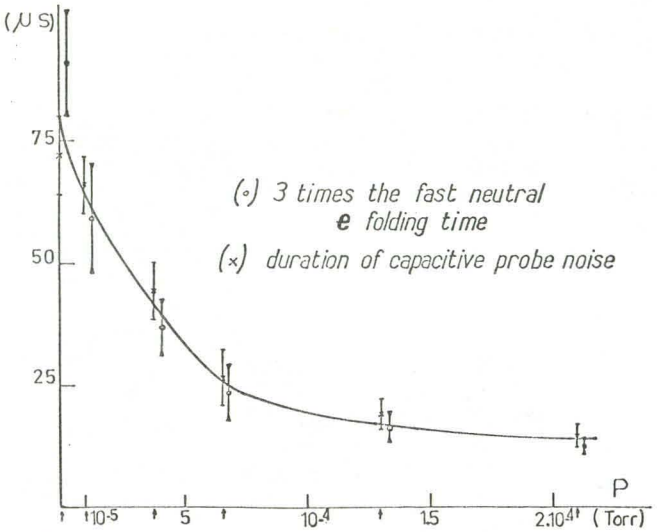

Fig. 3. Correlation between the duration of the capacitive probe noise and the fast neutral e-folding time.

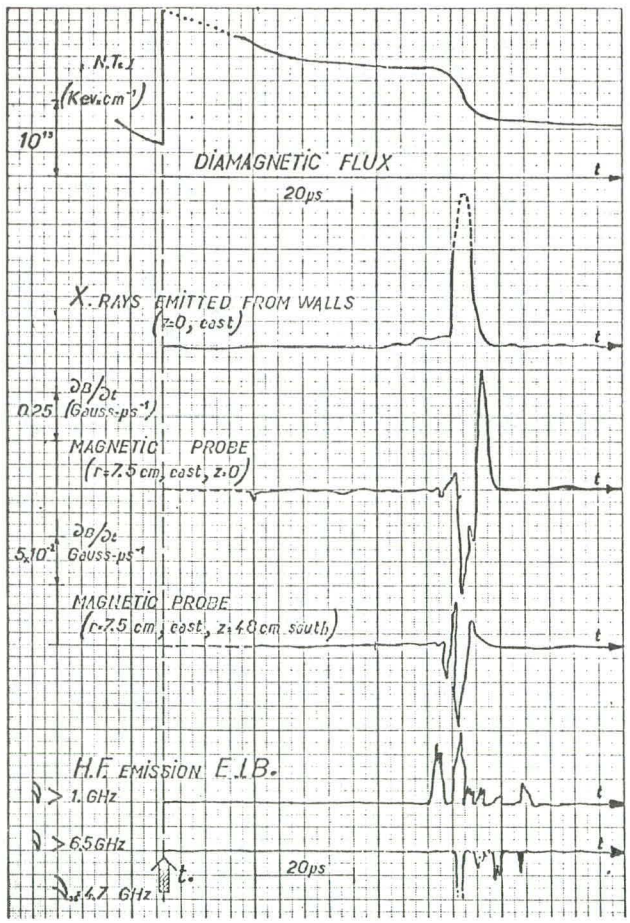

Fig. 5. Simultaneous measurements during an instability with radial losses.

COAXIAL GUN DEVELOPMENT*

I. Henins, P. S. Henry**, J. Lohr† and J. Marshall
Los Alamos Scientific Laboratory
University of California
Los Alamos, New Mexico

ABSTRACT

In the past the coaxial gun has been used to produce an energetic (10 keV) plasma with a total yield of approximately 5×10^{17} deuterons.[1] Our aim has been to increase the energy and quantity of the fast plasma. To increase the energy, a higher voltage than our usual 20 kV needs to be applied to the gun. This is difficult because of insulation problems at the current feed through the vacuum tank wall. One way to overcome this is to store the energy in a magnetic field inside the vacuum tank and then use this field energy to generate the necessary voltage and current to accelerate plasma. Various methods of this kind of energy storage have been investigated, but we have not yet been able to apply this to a practical gun design. The quantity of plasma should increase with increased gun dimensions and capacitor bank energy. A large coaxial gun, twice the linear dimensions of the previous one, has been built and its behavior is being investigated.

I. INTRODUCTION

We report here a set of experiments all aimed at the development of pulsed plasma guns toward larger plasma production. Our object is to find whether the output of energetic plasma can be increased to the point where a gun might be used to charge a thermonuclear reactor. The standard coaxial gun in use at Los Alamos at the beginning of this program is shown in Fig. 1. It produces about one kilojoule of fast plasma, 10^{18} deuterons with ~ 6-keV kinetic energy for instance, when it is driven by a 5.4-kilojoule capacitor bank at 19 kV. The fast plasma represents about 2% of the injected gas, the other 98% emerging subsequently from the gun muzzle with kinetic energies in the 100-eV region. The standard gun has been useful as a plasma source for a variety of experiments. To make it useful for charging a reactor we assume that the fast plasma production will have to be increased by a factor 10^3 or 10^4. It is quite plain that this cannot be done simply by raising the energy of the capacitor bank, whether by increasing the capacity, the voltage, or both. The problem is similar to one of impedance matching, but more complicated, and involves at least the necessity of transferring a substantial fraction of the bank energy through the gun terminals before the fast plasma is produced at the muzzle. The difficulty centers on the back emf of the moving discharge which opposes the flow of energy into the terminals. It seems quite likely that if the general shape of the gun and the current system inside it is to be retained, the dimensions of the gun, the density of the injected gas load, the voltage and the capacity of the capacitor bank will all have to be increased by substantial factors. Unfortunately, it is technically difficult to increase the voltage by a very large factor, and in the standard gun the gas density cannot be greatly increased without crowbarring the discharge on the insulator. It appears then that

* Work performed under the auspices of the U. S. Atomic Energy Commission.

** Present address: Physics Department, Princeton University, Princeton, New Jersey.

† Present address: Physics Department, University of Wisconsin, Madison, Wisconsin.

[1] Marshall, J., and Henins, I., Plasma Physics and Controlled Fusion Research (International Atomic Energy Agency, Vienna, 1966) p. 449.

simple scaling will not be practicable, but that means will have to be found of achieving progress toward one or more of the following objectives:

1) Improve the insulator design so that higher gas densities can be used without crowbarring,

2) change the geometry so as to store more energy magnetically inside the gun in such a way that it can subsequently be transferred to kinetic energy of plasma,

3) understand better physically the hydromagnetic processes inside the gun and in the fast plasma acceleration and energy conversion process.

Some progress has been made in all three of these directions but unfortunately not in such a way that it leads as yet toward one improved device having the desired characteristics. This has been done in the course of three series of experiments, the last of which is still in progress and will presumably continue for some time. We discuss the insulator design and two of these series of experiments below. The third, the "Snowplow" series, will be only briefly mentioned, since it is the subject of another paper in this conference.

II. GENERAL EXPERIMENTAL ARRANGEMENT AND INSULATOR DESIGN

All experiments discussed here were performed in a large sectional vacuum tank 48 in. in diameter. Either two or three 40-in.-long sections have been used to give a total length of 80 in. or 120 in. The high-voltage electrode in all cases was inserted through the center of one of the end plates and is insulated therefrom by a ceramic tube surrounding its stem. The electrode is connected to the negative high-voltage side of a low-inductance, ignitron-switched capacitor bank storing up to 24 kJ at 20 kV. After some false starts the insulator is at present connected to the bank cable header and vacuum sealed by a viton O-ring joint, pressurized with SF_6 as indicated in Figs. 2 and 4. Since the high-voltage electrode is fed by a hard core through the insulator the discharge tends to develop as an inverse pinch which is driven away from the insulator surface so long as energy is flowing inward through the terminals. This seems to be a design capable of standing very high-voltage gradients (at least 6 kV/cm) without crowbarring. It has been run over a wide range of pressures, from below breakdown to 50 torr with no problems. In all cases the end of the insulator has been protected from direct contact with the discharge by an overlapping skirt on the hot electrode. In the inverse pinch insulator configuration we follow practise of dense plasma focus experiments (Fillipov et al, Mather et al) where clean breakdown behavior has been obtained at high gas density.

So far as prevention of high pressure crowbarring is concerned the inverse pinch insulator configuration seems to be ideal. If initial breakdown is at the insulator it seems to lead initially, at least, to a snowplow current sheath discharge. We are not yet certain whether such an initial discharge is compatible with good gun behavior, so the inverse pinch insulator may or may not solve the high gas density problem in a gun. At least, under conditions usable with the former design it performs better.

III. "MUSHROOM", AN INVERSE PINCH ENERGY STORAGE EXPERIMENT

In this series of experiments attempts were made to achieve large internal magnetic energy storage by using an inverse pinch configuration running radially outward between a disk-shaped, high-voltage electrode and a flat or conical electrode attached to the wall of the vacuum chamber. The idea was that because of the 1/r dependence of the B_θ field inside an inverse pinch, the field strength at the current sheath would be relatively low. This would lead to a slow outward snowplow so that long times would be available for transfer of energy from an external source in the B_θ field, and so that relatively little energy would appear as kinetic energy of moving plasma. An inverse pinch is an inefficient method of accelerating a plasma to high speed, and therefore is a good method of storing magnetic energy.

It was expected that arrival of the current sheath at the outer edge of the high-voltage disk or "mushroom hat" electrode would lead to a violently unstable situation. The sheath would expand radially inward and axially outward into an evacuated region with high velocity because of the low density of the gas there and the increasing magnetic field with approach toward the axis. The rapid increase of inductance accompanying the bursting of the magnetic bubble would cause a back emf such as to reduce the current in the system, reduce the energy stored magnetically behind the hat and transfer a large part of it into kinetic energy of plasma in the expanding current sheath. The dynamics of the accelerated plasma in

the space beyond the hat should be similar to the fast plasma acceleration dynamics at the muzzle of a coaxial gun except that everything would be on a larger scale.

Several experiments with different electrode shapes and dimensions were tried, where with each change an attempt was made to increase the stored energy and/or to improve the plasma acceleration process. After a succession of experiments which went through about 10 models, it became apparent that the apparatus was developing in the direction of (1) larger hat diameter; (2) increased amounts of injected gas; and (3) shaping of the electrodes so as to provide more axial length for energy storage at small radii and decreased loss of gas by diffusion outward.

One of the late models is shown in Fig. 2, and a set of oscillograms obtained with it in Fig. 3. The oscillograms show the sudden decrease of current when the bubble bursts, and the output of two scintillation neutron detectors, one arranged to observe neutrons produced in the volume axially just beyond the hat, and the other to observe wall target neutrons at the far end of the tank, two meters from the hat. Neutron collimation experiments and magnetic probing have been interpreted to indicate the presence of a fireball of deuterium plasma, occupying a volume of about 10^5 cm^3 in front of the hat, with a density of $\sim 10^{13}$/cm^3 and an average particle energy of perhaps 20 keV. This would be a total energy of ~ 4 kJ. Analysis of terminal current and voltage indicates that at spillover time approximately 10 kJ out of the original 24-kJ bank energy is converted from stored magnetic energy to plasma motion. Approximately 10^8 neutrons per shot are produced in the fireball. The plasma characteristics quoted above would account for a yield smaller than this by nearly two orders of magnitude. We are forced to conclude that a cold gas of relatively high density coming from gas injection must occupy the same volume as the fireball.

IV. SCALED-UP COAXIAL GUN

It appeared during the Mushroom experiments that it would have been desirable to raise the gas density considerably near the edge of the hat while reducing, if possible, the amount escaping to the region outside. This is a most difficult distribution to achieve with the large hat perimeter and wide gap apparently required for large energy of plasma acceleration. It appeared that perhaps it would be more fruitful for high-energy gun development to return to the coaxial geometry with long cylindrical electrodes, investigate the behavior of the current front, and find out whether the inverse pinch insulator configuration could be used. The first experiments were performed with no external electrode except for the tank wall and are described elsewhere in this conference. We found that, at least with a static gas filling, the current front was always a snowplow, and that when it spilled over the end of the electrode it led to a dynamic pinch with a large neutron yield in deuterium. We then modified the system for pulsed gas admission and added an external electrode (Fig. 4). The resulting arrangement is almost identical to our standard gun, except that it is scaled up by a factor 2 in linear dimensions, and uses the inverse pinch insulator configuration.

The scaled-up gun appears to behave very much like the standard gun in current wave form and emission of fast plasma, although nothing like a complete set of diagnostics has been performed. The larger dimensions of the gun make probing of the discharge between the electrodes much easier than on the standard gun, and most of the experimental effort has gone into this. When it is operated in a good plasma-producing mode there is not perfect reproducibility of the discharge, and this has complicated the problem. However, multiple probe techniques have allowed us to measure current streamlines in some detail on individual shots. Clearly the external electrode affects the discharge strongly, but at the time of this report the situation remains complicated and not thoroughly understood.

ACKNOWLEDGMENTS

We wish to thank Dr. J. L. Shohet for communicating the results of computations regarding an outward moving sheath similar to that in the Mushroom experiment.

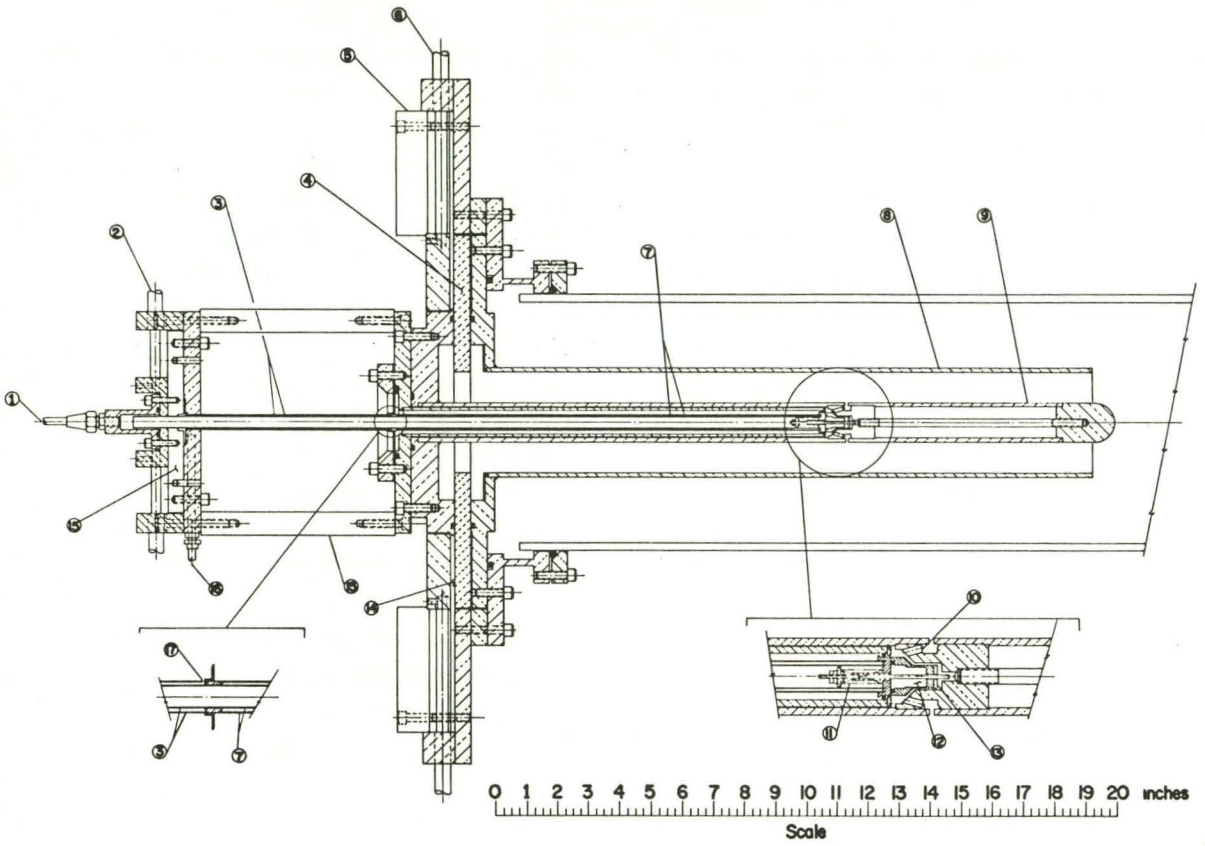

Fig. 1. Standard coaxial gun.

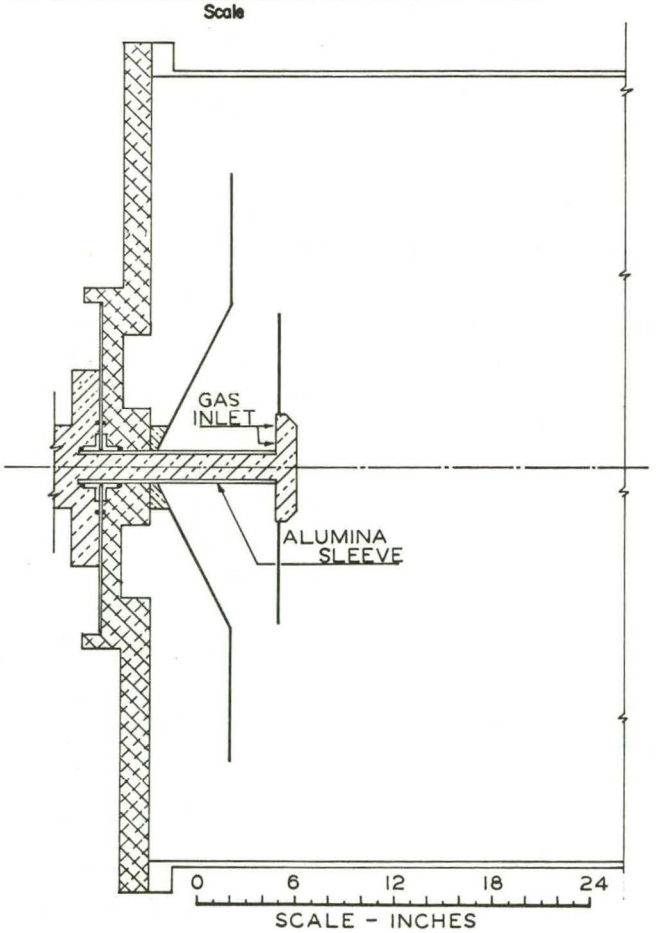

Fig. 2. Mushroom V inverse pinch energy storage gun.

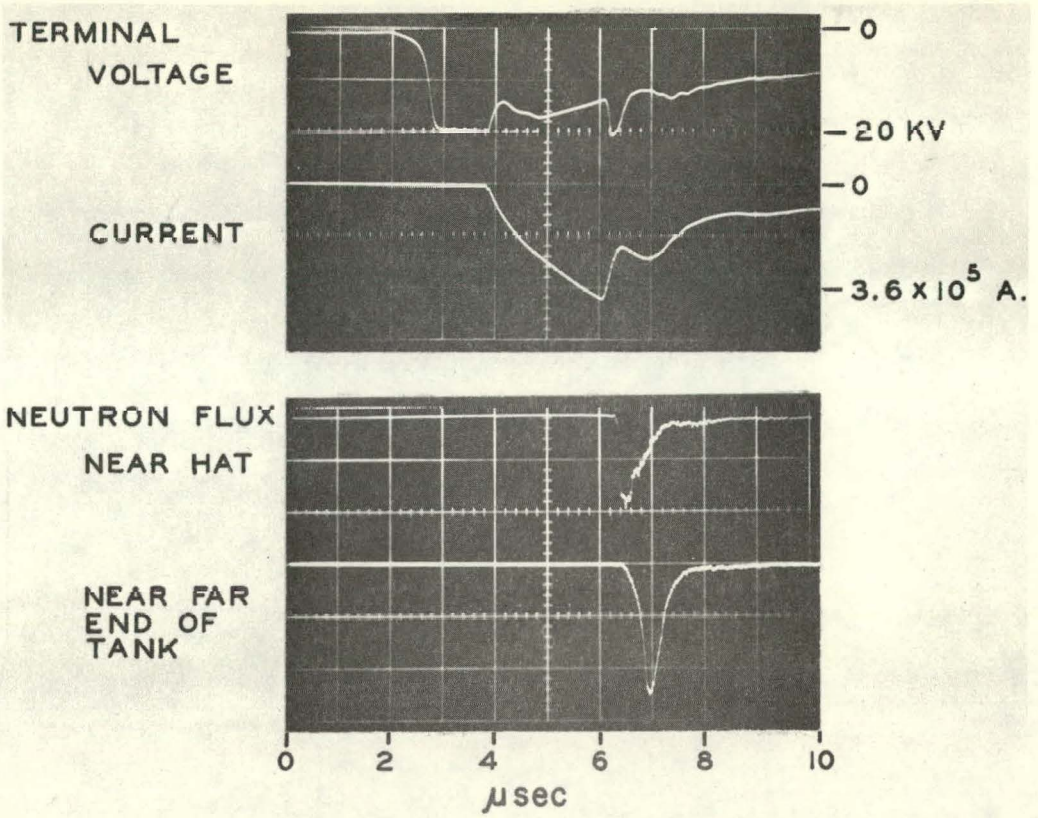

Fig. 3. Voltage, current and scintillation neutron detector signals, Mushroom V.

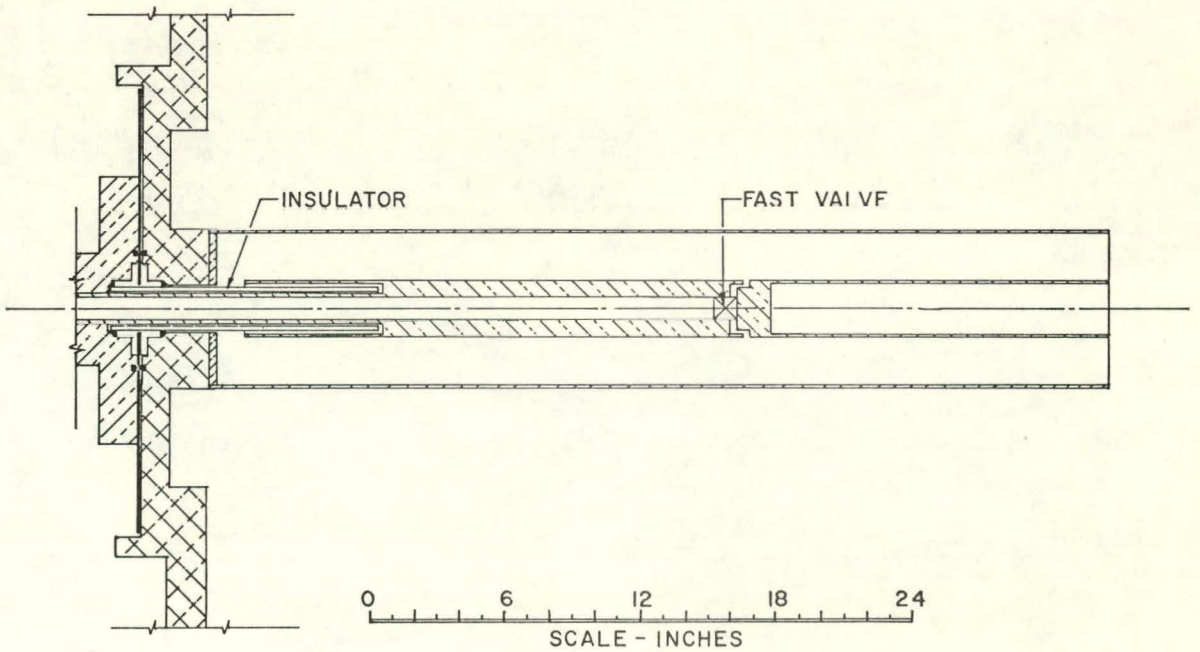

Fig. 4. Scaled-up coaxial gun.

PROPERTIES OF THE SPOKES IN COAXIAL AND PARALLEL - PLATE PLASMA ACCELERATORS

by

W. Prior, W. H. Bostick, L. Grunberger, P. Palmadesso, J. Zorskie

Stevens Institute of Technology
Hoboken, New Jersey

ABSTRACT

Image converter photographs[1] have shown that the "spokes" produced in the plasma coaxial accelerator at 2 mm hydrogen pressure are produced in pairs. Magnetic probe measurements indicate that the spokes have roughly the magnetic structure of a quasi-force-free configuration. Although the structures are too small in diameter (1mm) to make ion-density-flow probe measurements of their profiles, there are compelling reasons to predict that these structures have mass flow patterns which are roughly parallel to the quasi-force-free magnetic structure. Schlieren and spectroscopic techniques for measuring ion density profiles of the vortices will be described. Spectroscopic techniques for measuring rotational velocity profiles will also be described. Theoretical attempts to understand these structures as minimum energy configurations will be set forth.

Two types of filamentary plasma-magnetic field structures[2,3,4] which concentrate the plasma density, the rotational plasma flow density, the amperian currents, and the perturbation magnetic fields have now been observed by image-converter photography to be produced in pairs.[1] These filamentary plasma structures are judged to be relatively stable since they observed not to exhibit kink or sausage instability, to exhibit only a moderate amount of flute instability, and since they spontaneously arise in a fraction of a microsecond and endure for many microseconds. These structures are called vortices because of their rotational nature. Both of these types of vortices are created in a background magnetic field. One type of structure has its filamentary axis lined up parallel to the background magnetic field ($||$-to-B_o vortec) and may be regarded as the result of a large amplitude, non-linear ion acoustic wave or collisionless shock wave. The other type of structure has its filamentary axis lined up perpendicular to the background magnetic field ($\perp$-to-B_o vortex) and may be regarded as the result of a large-amplitude, non-linear Alfven wave. This $\perp$-to-B_o vortex has been produced and studied extensively in the conical θ pinch experiments[3,4,5] where the filament becomes a torus and where the measurements of perturbation magnetic fields and ion-density flow patterns show that the field- and flow-patterns have the shape roughly of a force-free configuration.

The spokes which have been observed, sometimes as an annoyance, for years in plasma coaxial accelerators can now be identified as $\perp$-to-B_o plasma vortices. With hydrogen at 2mm pressure these vortices can be produced in pairs in a spectacular way if the center conductor of the coaxial accelerator is not circular but, for example hexagonal, as in Figure 1. The spokes emanate, not from the corners, as one would naively expect, but from the flat sides of the hexagonal center conductor. Magnetic probe measurements show that there are perturbation magnetic fields directed along the filamentary axis of these vortices photographed in Figure 1. The formation of these vortices in pairs may be understood in a phenomenological way by means of Figure 2. Here the magnetic field is weaker on the flat and stronger at the corners of

the hexagonal center conductor. The magnetic field of the coaxial accelerator which is ordinarily purely azimuthal, "gives" where it is weakest to form a kind of pocket at the flat of the coax. The mass of gas rushing into the current sheath in the current sheath frame of reference starts to circulate in two vortices in this pocket and at the same time flows toward the outer conductor because of the "bullet shape" of the current sheath. The resulting plasma flow density in each vortex of the pair is helical, one being right-handed, the other left-handed. The background magnetic field lines which are ordinarily azimuthal are apparently "spun" into helical filaments by these plasma mass flows.

The striations which have been seen in the θ pinches by Bodin[6] and Kvartskhava[7] and Z pinches by Kvartskhava[7] are very likely examples of $\perp$-to-B_o vortices. A preprint received from Kolesnikov and the Filippovas[8] shows similar striations being produced in pairs.

It has thus far proved impractical to try to delineate with ion flow probes the flow patterns and density profiles of these $\perp$-to-B_o vortices in the coaxial accelerator because the dimensions of the vortices are so small ($\sim$ 1 mm in diameter). Instrumentation has now been constructed to measure the density profiles of these vortices with Schlieren photography. The Schlieren techniques will first be employed with the parallel plate accelerator where the "windows" can easily look at the vortices. It is also planned to use Stark broadening to measure density profiles of the vortices and doppler shift on impurity lines for measuring rotational profiles.

A "Plasma camera" technique for measuring ion densities has been effectively employed for studying the properties of $\parallel$-to-B_o plasma vortices produced by firing a two-wire button gun in a magnetic field (see Fig. 3). Efforts are underway to adapt this technique for measuring the $\perp$-to-B_o vortices.

Initial theoretical attempts following Woltjer[10] to describe plasma vortices with MHD equations where the energy is made an extremum subject to certain constraint integrals lead to magnetic field and flow configurations which are roughly of a general force-free type. However, this approach can be used only to demonstrate equilibrium (energy extremum) not stability (energy minimum), and it depends upon assumptions about boundary conditions at infinity which are not realistic. An approach which uses orbit equations for a two-species of particles appears much more promising.

ACKNOWLEDGEMENT

The research reported in this paper was sponsored by the Air Force Office of the Scientific Research, Grant AF-AFOSR-265-67, the National Aeronautics and Space Administration, Grant NsG-596 and by the Air Force Cambridge Research Laboratories, Office of Aerospace Research, under contract F19628-67-C-0265. It does not necessarily constitute the opinion of the sponsoring agencies. This is report number SIT-208.

REFERENCES

1. W. H. Bostick, W. Prior, L. Grunberger and G. Emmert. Phys. Fluids, 9, 2029, (1966).
2. W. H. Bostick, G. Emmert, E. Farber, L. Grunberger, A. Jermakian, W. Prior, J. Zorskie, P. Casale, and A. Deshmukh, in Proceedings of the Seventh International Conference on Ionization Phenomena in Gases (Gradevinska Knjiga, Beograd, Yugoslavia) 1965.
3. D. R. Wells, Phys. Fluids, 5, 1016, (1962).
4. D. R. Wells, Phys. Fluids, 9, 1010, (1966).
5. R. L. Small and W. H. Bostick, Report RE 284, Grumman Aircraft Engineering Corp., Bethpage, N.Y.
6. H. A. B. Bodin, Nucl. Fusion, 3, 215, (1963); also private communication.
7. I. C. Kvartskhava, K. N. Kervalidze, Yu. S. Gvaladze, and G. G. Zukakishvili, Nucl. Fusion 5, 181, (1966).
8. U. A. Kolesnikov, N. V. Filippov, and T. I. Filippova, Dynamics of a Noncyclindrical Plasma Shell in the Stages Prior to the Concentration of the Current in a Z-Pinch (Kurchatov Institute of Atomic Energy, Moscow, 1966).
9. T. Gold and F. Hoyle, Monthly Notices Roy. Astron. Soc. 120, 89 (1960).
10. L. Woltjer, Proc. of Nat. Academy of Science, 44, 833, (1958).
11. K. D. Sinel'nikov, B. G. Safronov, V. G. Padalka, and I. I. Dimidenko, Soviet Journal of Tech. Ph. 8, 786, (1964).

12. F. H. Coensgen, W. F. Cummins, W. E. Nexsen, Jr., and A. E. Sherman R.S.I. 35, 1072(N) (1964).

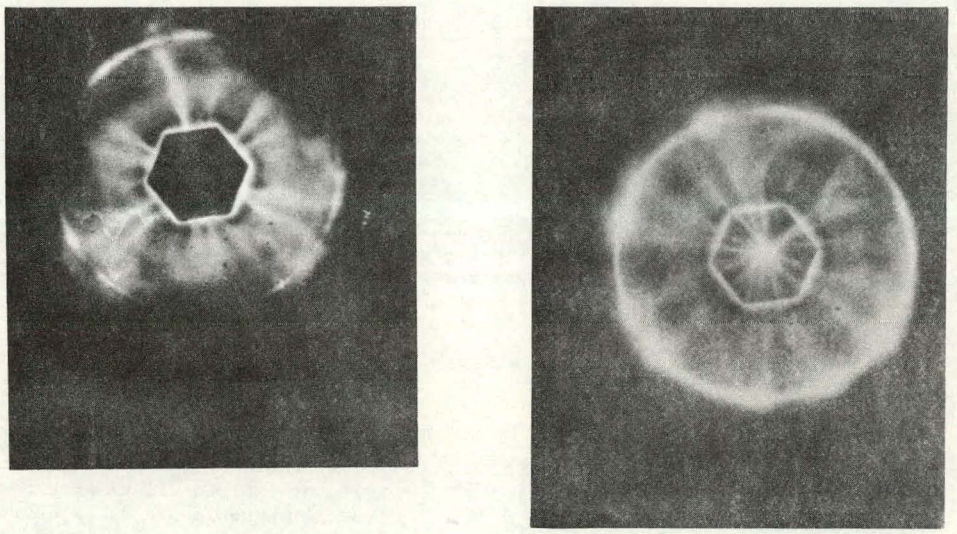

FIG. 1. Image converter photographs, end on, of a plasma coaxial accelerator, o.d. 5 cm, where the center conductor which is 4 cm long, is hexagonal. The accelerator is operated with H_2 gas at a static pressure of 2 mm. The formation of pairs of perpendicular-to-B vortices at each flat side of the hex is striking. The peak current in the accelerator is 150kA, the half-cycle is 1.5 μsec. The left photograph is taken 0.8 μsec after the beginning of the current half-cycle; right photograph taken at about 1.0 μsec when the vortices have coalesced in the pinch at the end of the center conductor. The authors suggest that the coming together of these force-free type filaments at the end of the center conductor is analogous to the process which produces solar flares[9] in the solar atmosphere.

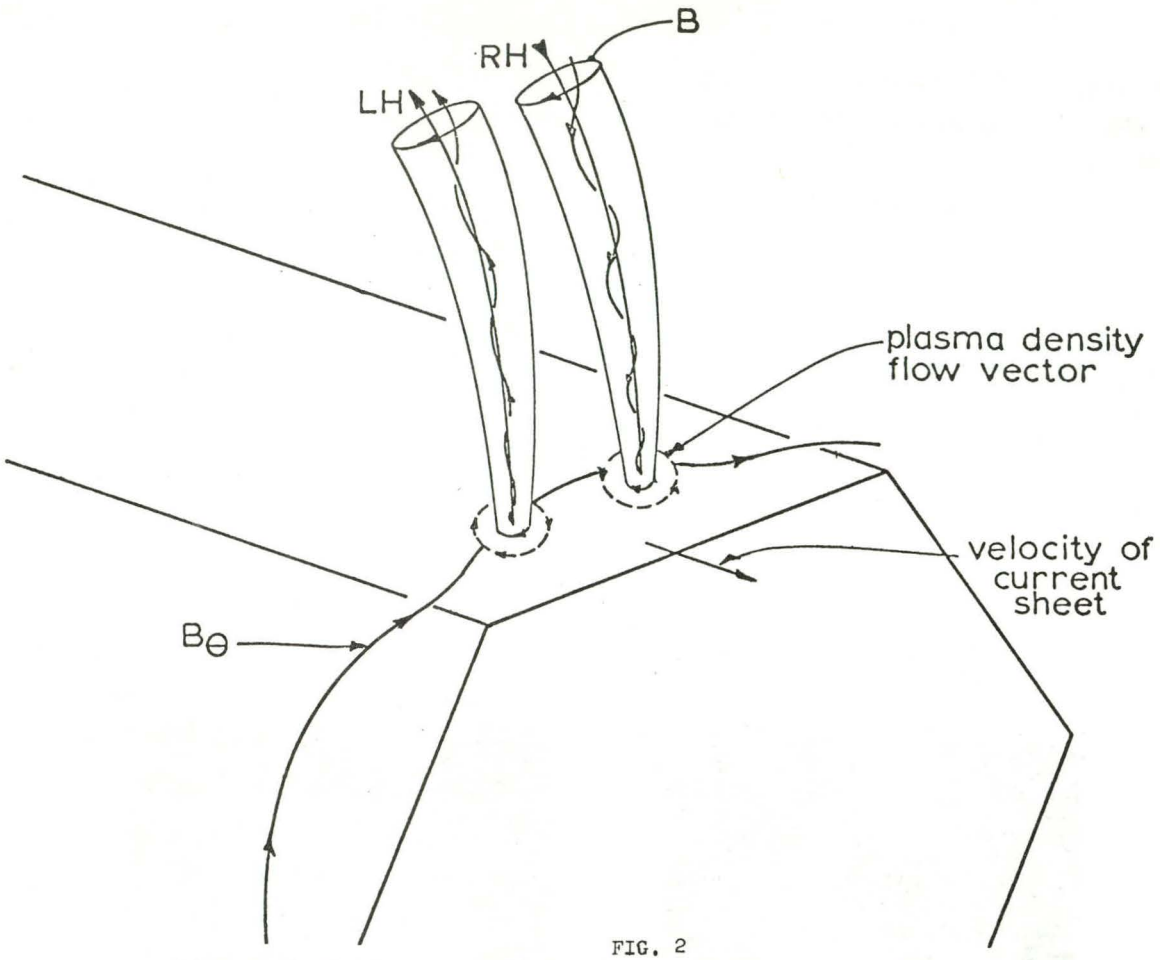

FIG. 2

Diagram showing how perpendicular-to-B_θ vortices may be expected to develop in pairs in the plasma coaxial accelerator with a hexagonal center conductor. The general geometry is somewhat similar to that expected from resistive instabilities in the tearing mode.

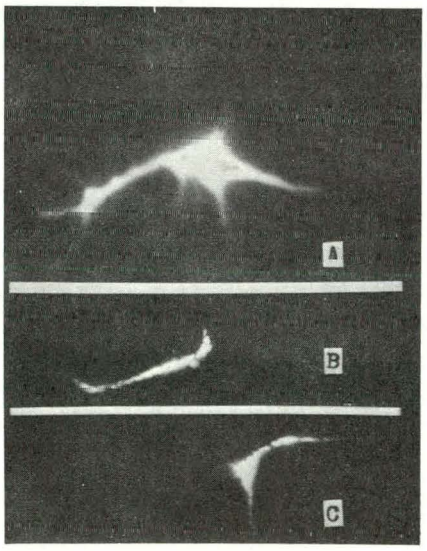

Fig. 3. Illustrates the technique of recording plasma density with a "Plasma camera".[11,12] The camera consists of two accelerating grids and a plastic scintillator (NE102) all aligned perpendicular to the magnetic field. A short (0.2 μsec) pulse is applied to the grids so as to drive electrons from the plasma into the scintillator. The pattern of illumination is thus representative of the plasma density near the front grid at the time of the pulse. In the following photographs peak plasma density is estimated to be 10^{13}/cc. PHOTO A. A copper two-wire button gun with upper electrode negative fires anti-parallel to the magnetic field toward the plasma camera which is ¼" away. The tiny gun is in the center of the photograph, the field is 400 Gauss and goes into the plane of the photograph. Note complicated striations which develop at these low magnetic fields.
PHOTO B. Same as above with B=1600 Gausses. Note the tendancy for the plasma to be driven in the jXB direction.
PHOTO C. Same as Photo B. but with gun polarity (i.e. j) reversed. Plasma is driven in the opposite direction.

DEPOLARIZING CURRENTS IN A DENSE PLASMA INJECTED ALONG A DOUBLE BEND MAGNETIC FIELD

by

D. VERON

Groupe de Recherches de l'Association EURATOM-CEA sur la Fusion

Fontenay-aux-Roses (Hauts-de-Seine) France

ABSTRACT

A coaxial gun with an inverse pinch like preionization system and an axial magnetic field produces a dense, high velocity plasma. By varying the parameters of the gun, the fast component mean velocity can be set from 10^8 to 2×10^8 cm/sec and the density from 0.4 to 3×10^{13} ions cm^{-3} . The plasma is injected parallel to the axis of a metallic tube having two identical oppositely curved sections, each extending over 1/8 of circumference. The radius of curvature is 1m, and the diameter of the tube is 30cm. The longitudinal guiding field is 3 kgauss in most of the experiments reported here. The electric drift of the plasma can be strongly reduced by increasing the transverse conductivity between the gun and the first curvature. In such conditions, the circulation of electron currents along the field lines has been evidenced. The depolarizing circuits of the plasma have been determined as a function of time. At first, the electrons flow towards the gun. Then, when the ion drift currents of each bend regions are equal (with reversed signs), the current circulating towards the gun vanishes, and, as expected, a self depolarization of the whole plasma is obtained by an electron flow between the two oppositely curved regions. The magnitude of the measured electron currents agrees with the ion drift current calculated from the plasma profile density at a given time.

---

1. INTRODUCTION

When a plasmoid is injected parallel to the lines of force of a bend magnetic field (fig.1a), the particles experience a drift normal to the plane of curvature. The ion and electron drift velocities are opposit in sign, so an electric field develops normal to the plane of curvature. Consequently, a radial drift of the whole plasma occurs. However, if a conducting circuit is attached to the polarized sides of the plasma blob, the charges accumulated by the curvature drift can be cancelled by an electron flow in the circuit. Two possible cases are sketched on fig.1. In the first one (fig.1b), the electrons can circulate along the lines of force towards a region of good transverse conductivity constituted by a metallic grid. In the second one, there is a self depolarization of the plasma by electrons flowing between the two oppositely bend regions (1c) Calculations show that the radial electric drift can be strongly reduced if the impedance of the circuit is small enough. When the curvature radius of the trajectory can be taken equal to the curvature radius R of the field line the equilibrium of the Laplace and the centrifugal forces can be written

$$\vec{J}_z \wedge \vec{B} = \frac{m\, n\, V_{//}^2}{R^2}\, \vec{R}$$

where J_z is the ion drift current density along the z-axis, B the field strength, m the ion mass, n the ion density and $V_{//}$ the directed velocity.

In the present paper, the ion drift current normal to the field lines is called polarization current. The electron current which flows along the field lines and cancels the charges accumulated by the polarization current is called depolarization current.

II. EXPERIMENTAL SET UP (fig.2)

The hydrogen plasma is generated by a coaxial gun with an inverse pinch like preionization system. The gun is located in the guiding field of 3kgauss strength. The mean velocity of the fast puff is 10^8 cm/sec and the density is in the 10^{13} range. A grid is placed in the straight part of the machine. In these conditions the radial electric drift measured at the inflexion point is found to be sensibly zero.

III. DEPOLARIZING CIRCUITS.

They will be deduced from two different ways : at first by the study of the polarization currents as a function of time, and then, by direct measurement of the electron currents along the field lines.

1) Study of the polarization currents. The ion drift current I which flows through the 1cm large surface S containing the magnetic axis (fig.3) is given by

$$\int_{x_1}^{x_2} J_z(x)\,dx = \frac{m}{BR}\int_{x_1}^{x_2} n(x)\,V_{//}^2(x)\,dx \quad (1)$$

$n(x)\,V_{//}^2(x)$ may be calculated from a Faraday cup signal, since the plasma is collisionless and instantaneously emitted. The J_z distribution along the magnetic axis is shown on fig.4 at different times. The shaded surfaces are proportional to the polarization currents I_1 and I_2 corresponding to the two successive curved parts of the field. When the plasma enters the machine, $I_2 = 0$ and the electrons can only flow towards the grid (fig.4a). At a later time, part of the depolarization current can flow between the two parts of the machine (fig.4b). When $I_1 = I_2$, the grid current should vanish and a self depolarization of the plasma occurs (fig.4c). Then $I_1 < I_2$ and electrons flow again towards the grid (fig.4d).

2) Measurement of the electron currents. Three Faraday cups are placed as indicated fig.5. They are able to detect electrons flowing towards the gun. The successive circuits a, b, c, d can be established by looking at the oscillograms. During the time interval a, C_1 and C_2 detect no current. The corresponding circuit is sketched on fig.5a. Then, a signal appears on C_2 indicating that a current flows between the two curved regions (fig.5b). During time interval c, the C_3 signal vanishes and the C_1 signal stays nul. As previously expected by observing the equality of I_1 and I_2 plasma depolarizes itself by the circuit of fig.5c. Finally, an electron current towards the grid appears again as detected by C_1 (the C_3 signal stays nul) (fig.5d). The circuits d and b are similar, but the grid currents are reversed in sign. After time interval d, the C_2 signal indicates that slow plasma is still flowing in the machine with $I_1 = I_2$. The depolarization circuit is similar to fig.5c.

IV. DETERMINATION OF THE CURRENTS INTENSITY.

1) The density $J_x(z)$ of the electron current coming from the second curved region can be calculated from the ion density distribution along the z-axis at the inflexion point (fig.6). It may be seen that the deviation from the measured (with Faraday cups) current profile is small.

2) The total current flowing through the 1cm large surface S' (fig.7) is equal to $\int_o^{z_o} J_x(z)\,dz$ On the other hand, the polarization current through the surface S is given by the relation (1). The numerical results obtained by the two methods are compared (fig.8).

V. CONCLUSION

The quantitative agreement between the calculated and measured currents shows that the complete depolarization is obtained only by the determined circuits. It should be noted that the depolarization circuit is all contained inside the plasma when the ion drift currents are equal in each bend region.

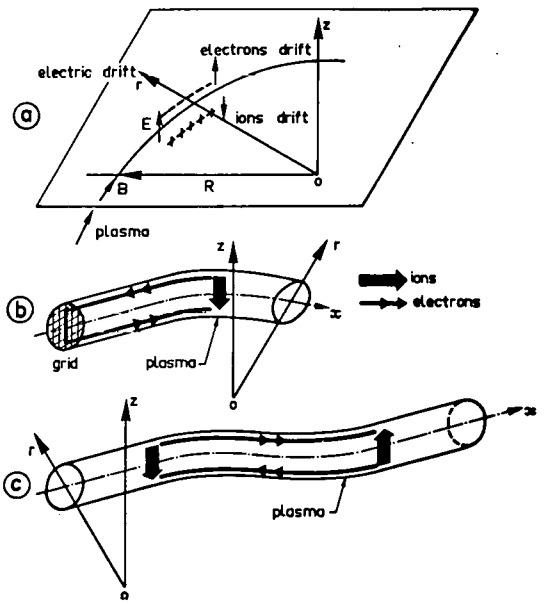

Fig. 1. Definitions.

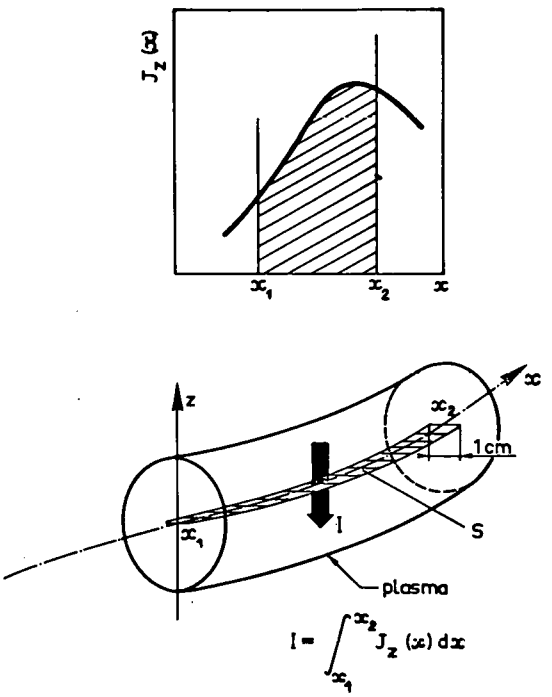

Fig. 3. Ion drift current.

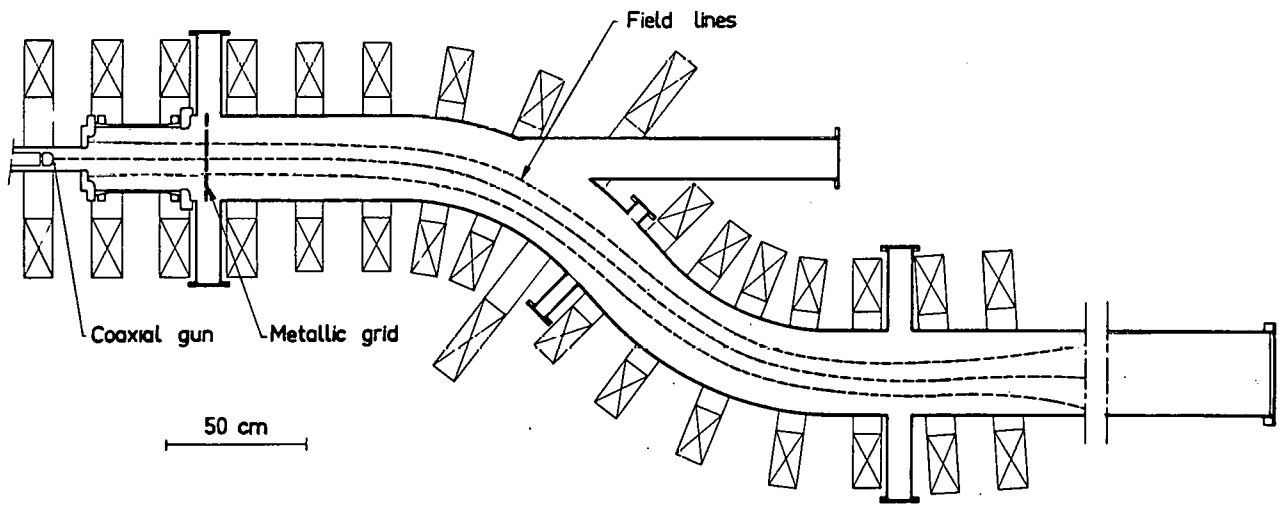

Fig. 2. Experimental set up.

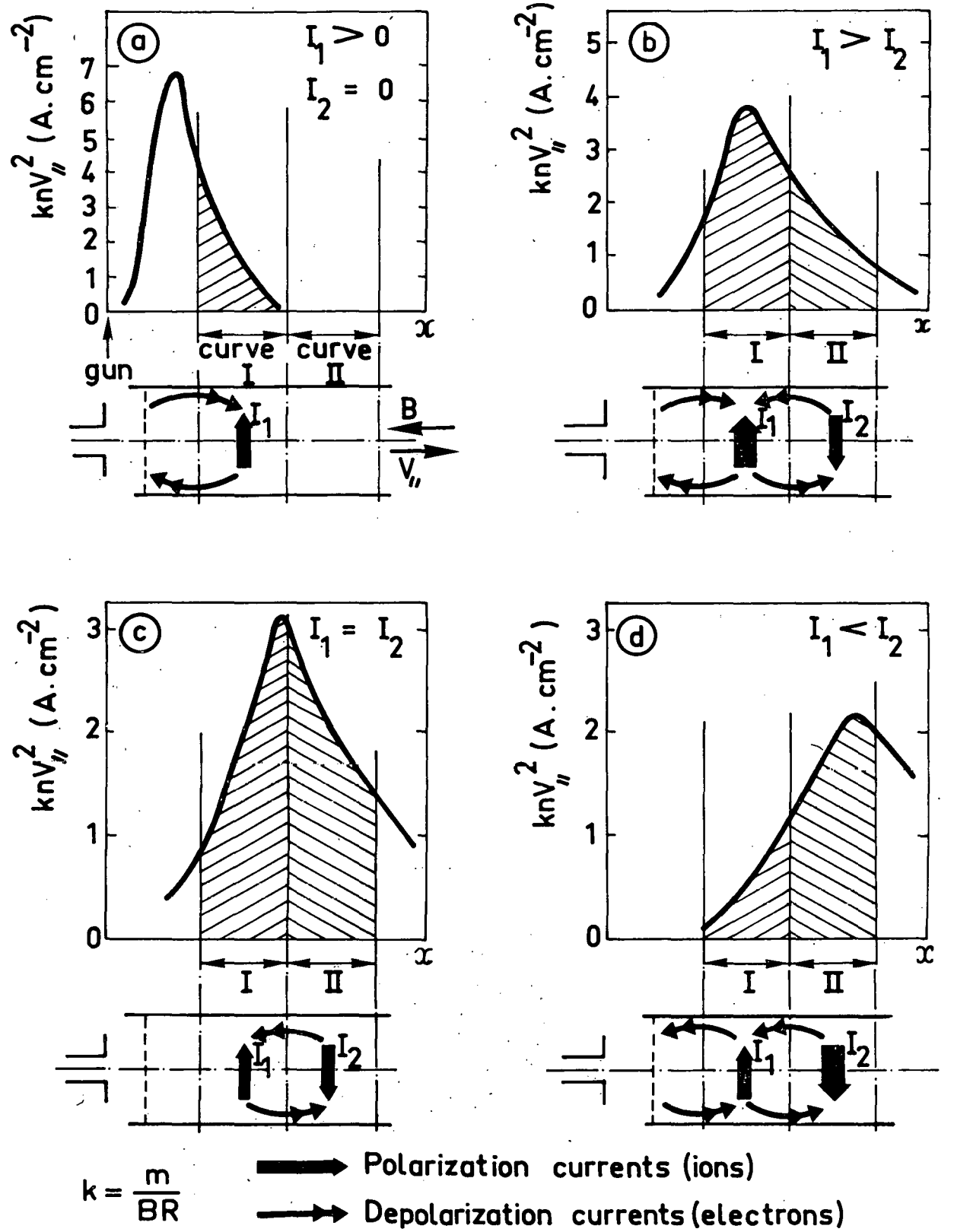

Fig. 4. Polarization currents study.

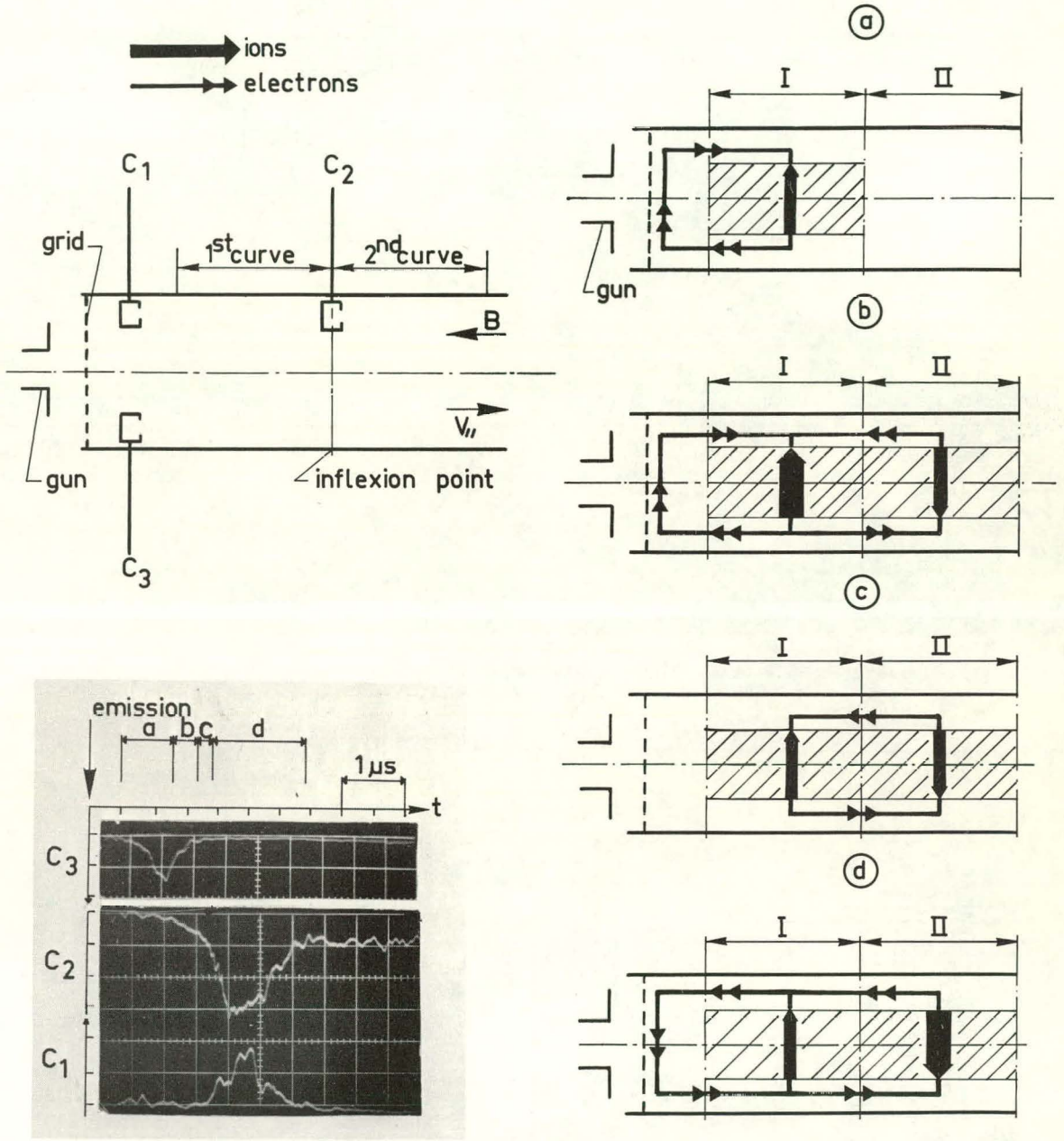

Fig. 5. Determination of the depolarization circuits.

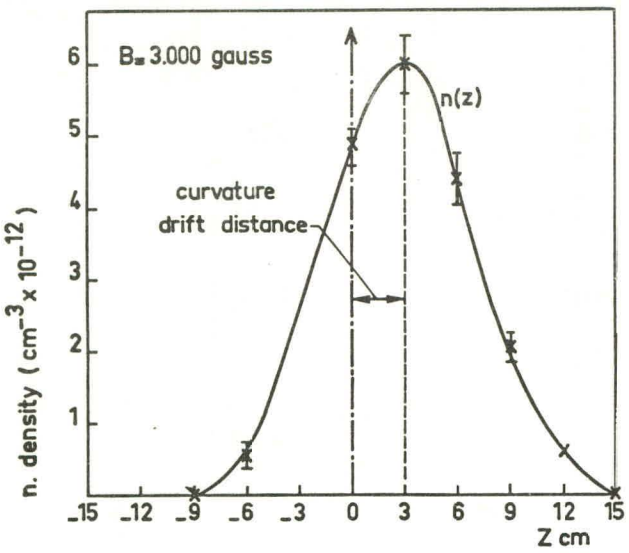

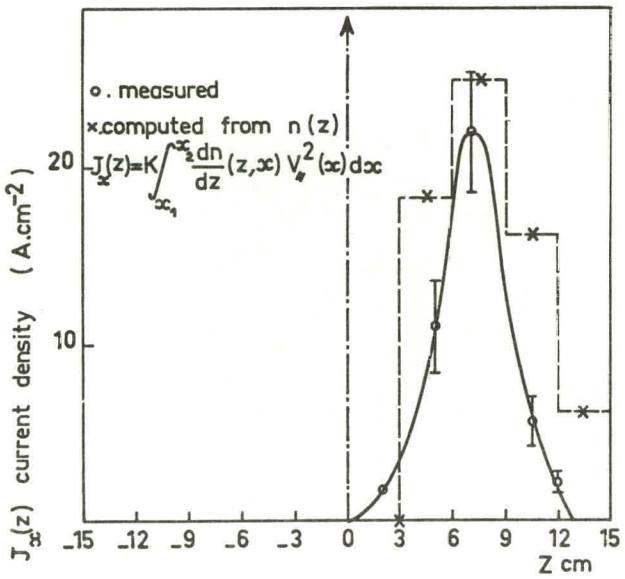

Fig. 6. Depolarization current.

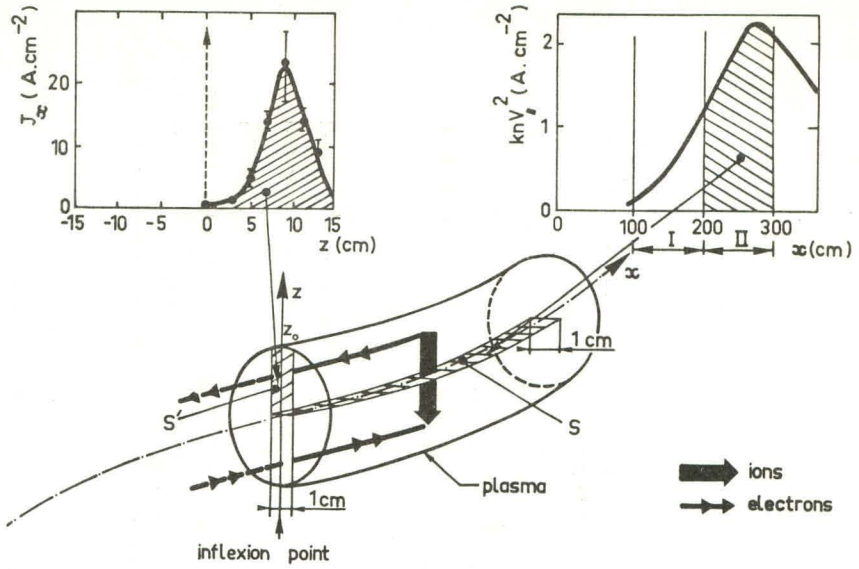

Fig. 7. Current calculation.

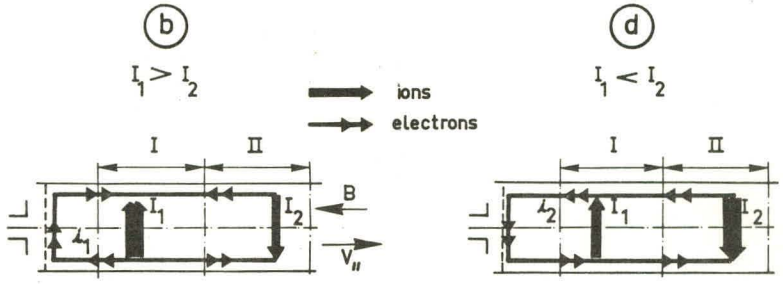

	i_1 (A. cm^{-1})
$\int J(z)\,dz$	167 ± 30
$k\int n(x) V_{//}^2(x)\,dx$	185 ± 37 ($I_1 - I_2$)

	i_2 (A. cm^{-1})	I_2 (A. cm^{-1})
$\int J(z)\,dz$	60 ± 11	172 ± 31
$k\int n(x) V_{//}^2(x)\,dx$	55 ± 11 ($I_2 - I_1$)	182 ± 36

Fig. 8. Comparison of the results.

PRE-IONIZATION PHENOMENA IN PULSED PLASMA ACCELERATOR

by

T. N. Lie, M. J. Rhee and C. C. Chang
Department of Space Science and Applied Physics
The Catholic University of America
Washington, D. C.

ABSTRACT

Appreciable level of pre-ionization in the cold gas ahead of the propagating current-sheet in both accelerators of coaxial and parallel plate geometry was detected using monochromators and probes for four different working gases. The origin of the pre-ionization is inferred to be due to a prebreakdown ionization build-up in the whole electrode gap. The ionization grows rapidly to a point of breakdown but since the breakdown usually occurs near the insulator, the remaining part of the electrode gap maintains the ionization until it encounters the current-sheet and undergoes intense heating. The pre-ionized media ahead of the current-sheet may cause unexpected behavior of the current-sheet. A possible explanation using the experimental results is given for the current-sheet tilt in the parallel plate accelerator and for the polarity effect in the coaxial accelerator.

I. Introduction

The question of the existence of appreciable pre-ionization ahead of the propagating current-sheet in the pulsed plasma accelerator is important since the presence of the ionized gas may significantly alter the expected current-sheet behavior. In the present study, the pre-ionization observed in the plasma accelerators of coaxial and parallel plate geometry are shown. The possible mechanisms for the pre-ionization process are discussed. Finally, the interaction between the current-sheet and the pre-ionized media are described in the light of experimental results.

II. Accelerators

The parallel plate plasma accelerator used in this investigation consisted of a pair of copper plates 6 cm wide, 8 cm long and 3.5 cm apart enclosed in a quartz tube 6 inches in diameter (Fig. 1). The discharge was driven by a 15 μF capacitor charged to 10 kV and triggered by a pressurized switch. The ringing frequency of the discharge is about 130 kHz. The coaxial plasma accelerator consisted of two cylindrical electrodes, the inner electrode being 1.6 cm in diameter by 12 cm long and the outer electrode being 5 cm in diameter by 6.5 cm long. The electrodes were enclosed in a 4 inch diameter quartz tube for optical observation. The quarter cycle time of the discharge current was about 0.6 μsec.

III. Pre-ionization

A. Parallel plate accelerator

The spectral radiation emitted from pre-ionized gas was detected with monochromators and the photoelectric signals were displayed on an oscilloscope screen. Fig. 1 illustrates the optical arrangement for the observation and Fig. 2 the signal wave-forms and the time correlation between them at various locations in the electrode gap when the accelerator is filled with helium gas at $p = 0.5$ Torr. Immediately evident are the signals of the He I 5876 Å, He I 4471 Å, O II 3135 Å and N III 3367 Å lines which start at the very beginning of the discharge current and whose amplitudes are comparable to those at the current-sheet which arrives at a much later time. None of the He II lines were observed here but there is reason to believe that a considerable amount of pre-ionization of ambient gas atoms takes place. The pre-ionization is detected not only in the electrode gap but also as far as 20 cm beyond the electrode end. Nitrogen ($p = 0.07 - 0.2$ Torr) and argon ($p = 0.05 - 0.15$ Torr) show essentially the same tendency and the spectral lines from ionized species such as N II, N III and A II are detected in the pre-ionized media.

The level of pre-ionization is rapidly increased as the gas pressure decreases. In the case of hydrogen filling, no pre-excited hydrogen lines were detected even with a wider slit width of the monochromator and the impurity lines which would be detected with the other working gases were not observed in the pressure range $P > 0.3$ Torr.

B. Coaxial Accelerator

The same pre-ionization phenomena have been observed in the coaxial accelerator but with a polarity effect this time. Fig. 3 and 4 shows the optical arrangement and the waveforms and time correlation of the photoelectric signals respectively. The pre-ionization signals are particularly high in the vicinity of the outer electrode when the polarity of the center electrode is negative. When the polarity is reversed, the pre-ionization signal at the outer electrode (negative) is usually a very sharp pulse at the beginning of the discharge and decays rapidly.

A magnetic probe and a miniature Rogowski coil were found to respond to the current carried by the pre-ionized gas in the coaxial accelerator. Fig. 5 shows a sketch of the Rogowski probe signals obtained at $r = r_2$ (radius of outer electrode) and at $r = r_1$ (radius of center electrode). In the case of helium, argon and nitrogen filling, always $J_{r=r_2} > J_{r=r_1}$ ahead of the current-sheet indicating there is a current of axial component at the positive outer electrode. As can be seen in Fig. 5, hydrogen showed a sharp rise at the current-sheet even at $r = r_2$ and the media ahead of the current-sheet does not seem to carry much current. The pre-ionization in a discharge chamber has been reported [1] previously and its electron densities were measured by microwave techniques.

C. Mechanism

Obviously, the pre-ionization is not related to the initial heavy current discharge near the insulator and has nothing to do with the radiation emitted by the shock driving discharge. The exact mechanism for the pre-ionization phenomena is not clear, however, it is inferred to be caused by the Townsend pre-breakdown ionization growth, because the ionization actually starts even before the breakdown. When the accelerator is triggered, the whole length of the electrode gap undergoes pre-breakdown discharge and with some secondary processes, the ionization grows rapidly to the point a breakdown. The breakdown usually takes place only in the vicinity of the insulator and the remaining part of the electrode gap is left ionized until it encounters the current-sheet and rigorous heating occurs. The secondary process which is mainly responsible for the pre-ionization is not certain. The cathode process, particularly photoelectric emission, is most likely, judging from rapid build-up of the ionization.

IV. Pre-ionization and the current-sheet

There seems to be evidence that the pre-ionized media alters expected current-sheet behavior in both types of accelerators. The current-sheet tilt in the parallel plate accelerator [2 3] and the electric polarity dependence of the current-sheet shape in the coaxial accelerator [4 5] are both well-known. These two unexpected phenomena obviously represent the same tendency and possibly have the same origin.

Fig. 6 shows frame photographs from an image converter camera taken to see what is happening in the vicinity of the electrode immediately after the breakdown in both accelerators. The aperture of the camera was wide open to admit enough light for the photograph and part of the electrode was covered to shield it from the intense light of the current-sheet in the parallel plate accelerator. The first frame of the photograph is exposed when the current-sheet is still near the insulator. As can be seen, a luminosity covers the whole surface of the anode at this moment and gets brighter until the current-sheet finally appears. These photographs together with the Rogowski coil data described in a previous section imply that a surface current along the anode exists after the main discharge. The surface current which seems to develop in a very short time is possible because there is enough pre-breakdown ionization buildup in the gap. If the current-sheet close to the anode in the early stages of the main discharge is considered, the current path at this location is not only perpendicular to the anode surface but also there is a component parallel to the anode surface and this part of the current-sheet experiences a $j \times B$ force directed toward the cathode which in turn results in the current-sheet tilting as a whole. The existence of an axial current component along the anode surface is probably due to the fact that there is an unusually high anode fall [6] in the current-sheet. The anode surface current must be hampered when the level of pre-ionization in the gap is too low, if the above assumption is valid. As was described in a previous section, the level of pre-ionization depends on the species of working gas and its pressure and the shape of the current-sheet may be affected accordingly. This was checked with the current-sheet produced by the coaxial accelerator. The shape of the electron density front which is found to be sharply defined except at the anode region were examined by varying gas pressure and the polarity of the electrode with the optical arrangement shown in Fig. 3. The density front was found by observing the continuum intensity peak or by checking a peak which gives the maximum width of the spectral line under observation. Table 1 showing the polarity and pressure dependence gives the propagation velocity "V" of leading front and the distance "d" between the density front at the center electrode and the outer electrode - "d" is derived from the delay time and velocity. As can be seen, the density front is inclined or canted for all gases used regardless of their pressure if the center electrode has positive polarity in agreement with previous works. [4 7 8] When the center electrode is negative, however, a distinct pressure effect of the working gas is apparent, i.e., the density front is nearly flat when the gas pressures are low but with the higher gas pressure the front is inclined as much as in the positive case. This indicates that the flatter current-sheet is produced only when the gas pressures are low where the intense pre-ionization and hence the current along the anode surface are most likely.

In the case of hydrogen filling ($p = 0.3 - 2$ Torr), the current-sheets produced in the coaxial accelerator and

also in the parallel plate accelerator behave differently from other working gases, i.e., it does not show distinct polarity effect [7,8,9] in the former accelerator and produces a planar current sheet [2] instead of a tilted one in the latter accelerator. This is considered to be caused by the fact that there is far less pre-ionization in this range of hydrogen pressure.

Acknowledgement: The work is supported by National Aeronautics and Space Administration under Research Grant NGR-09-005-025.

References:

1. G. F. Brand, S. K. Chung, and L. C. Robinson, Nuclear Fusion 6 41, (1966).
2. R. H. Lovberg, IEEE Trans. Nucl. Sci. NS-11 187 (1964).
3. R. B. Johansson, Phys. Fluids 8 866 (1965).
4. J. C. Keck, Phys. Fluids 5 630 (1962).
5. T. N. Lie, A. W. Ali, E. A. McLean, and A. C. Kolb, Phys. Fluids 10 1545 (1967).
6. R. H. Lovberg, AIAA Journal 4 1215 (1966).
7. R. H. Lovberg, Phys. Fluids 8 177 (1965).
8. J. W. Mather, Phys. Fluids 8 366 (1965).
9. T. N. Lie, A. W. Ali, E. A. McLean, and C. C. Chang, 2nd Semiannual Progress Report NASA NGR-09-005-025, (1967).

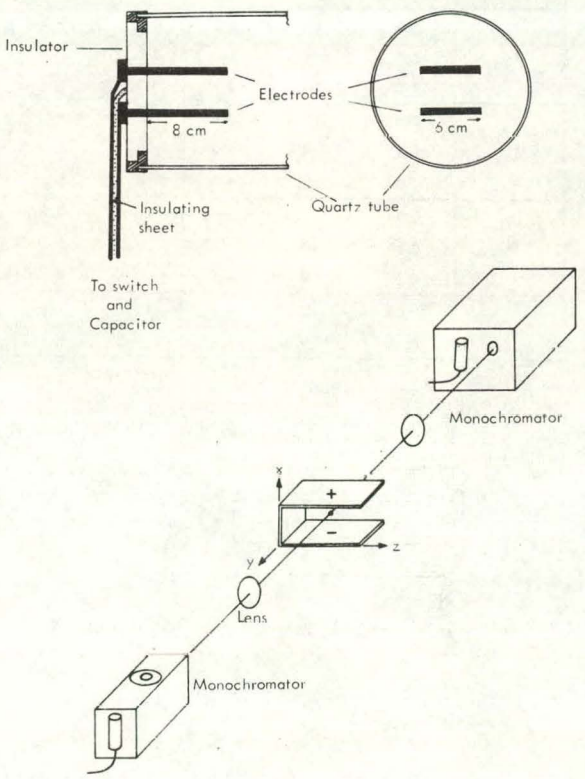

Fig. 1. Schematic diagram of parallel plate plasma accelerator and optical arrangement.

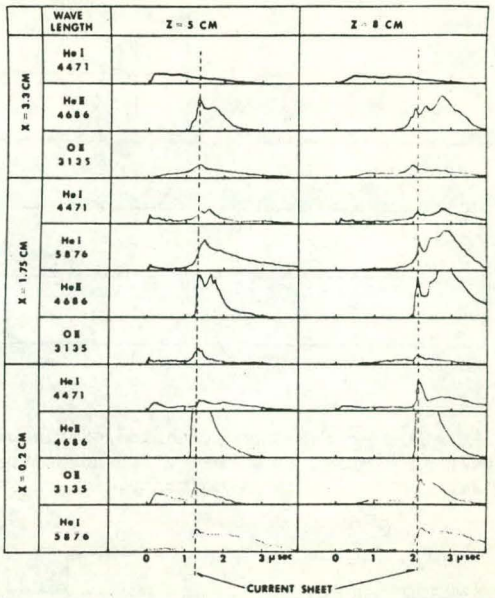

Fig. 2. Time correlation of photoelectric signals observed in parallel plate accelerator at various locations in the electrode gap.

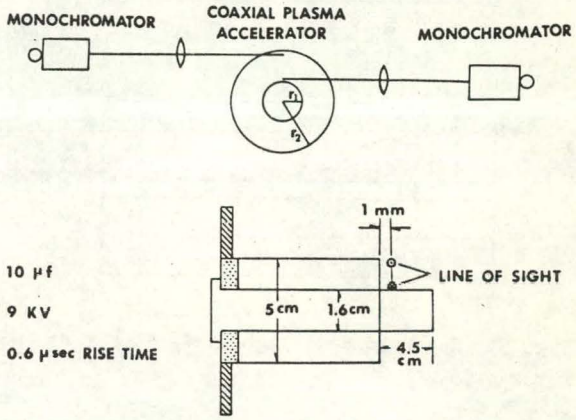

Fig. 3. Optical arrangement for the coaxial accelerator.

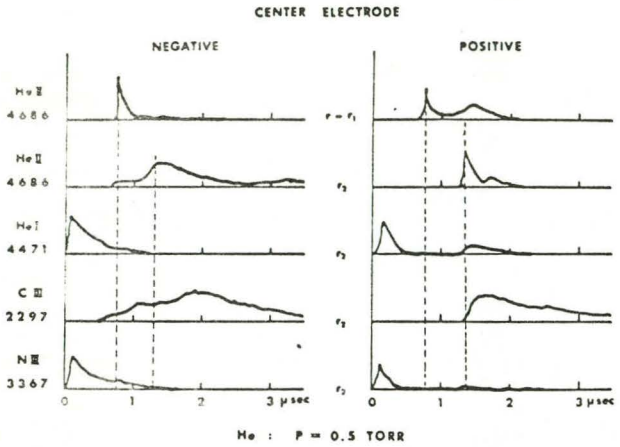

Fig. 4. Time correlation of photoelectric signals observed in coaxial accelerator for negative and positive center electrode polarity.

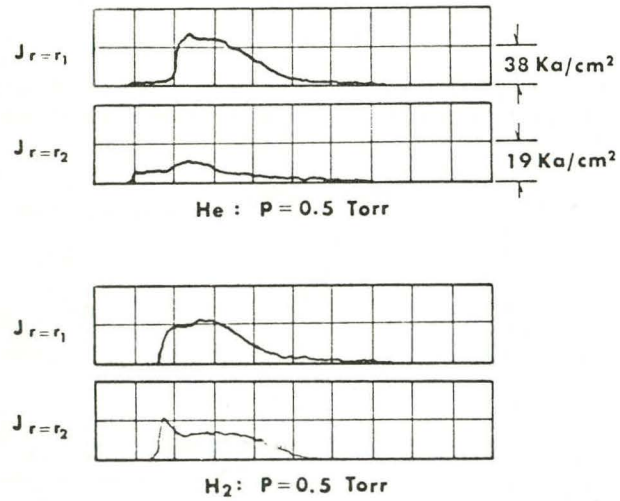

Fig. 5. Rogowski coil signals J_r at $r = r_1$ and $r = r_2$.

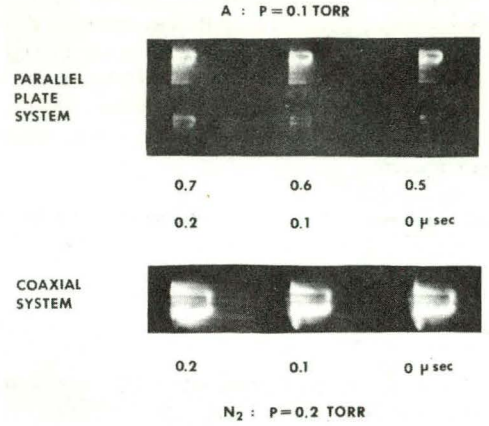

Fig. 6. Frame photographs taken prior to emergence of current sheet.

Table 1. Polarity and Pressure Dependence of the Velocity V and of the Inclination of the Density Front.

		CENTER ELECTRODE POSITIVE		CENTER ELECTRODE NEGATIVE	
GAS	P TORR	V CM/μSEC	d CM	V CM/μSEC	d CM
H_2	0.3	19	4.2	20	~ 1-2
	0.5	13.5	4	12.5	2.5
	1.0	10	3.5	10	3
He	0.4	13.5	5.4	12.5	0-1.5*
	0.5	9.4	4.3	9	3.9
	1.0	8.6	4.5	8.1	3.6
N_2	0.07	11.5	5	11	0.8
	0.1	10	5	9.3	2
	0.2	9	4.5	8.6	4
A	0.05	12	4.4	12	1.8
	0.15	9.3	5.1	9.3	5.1

* UNSTABLE

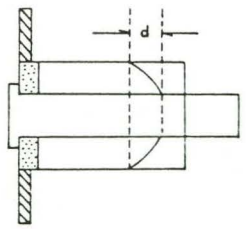

TRANSIENT SPECTRAL STUDY OF DISCHARGES IN COAXIAL PLASMA GUNS

by Charles J. Michels and Henry J. Hettel

Lewis Research Center
National Aeronautics and Space Administration
Cleveland, Ohio

ABSTRACT

Time-varying spectra of argon plasma in a coaxial plasma gun are measured for two geometries. One geometry, operating self-crowbarred, exhibits a fully ionized argon plasma (relatively "clean") for the first moving discharge in the gun. Performance agrees well with earlier snowplow model theory and experiment.

In contrast, the other geometry which operated in the multiple moving puff mode, exhibits a contaminated discharge with no propellant lines observed. A pyrex gas baffle is the source of contaminants. Performance does not agree with theory.

Introduction

The spectrum of the discharge of a coaxial plasma gun is a useful diagnostic tool in correlating experimental results with a theoretical model. Time-integrated spectra (for 25 superimposed shots) were described by Michels and Johansen (ref. 1) and contaminants were noted. It could not be determined from these spectral measurements when the contamination occurred during a shot. The present report describes the time-varying spectra as the discharges move past a viewing window in the gun barrel.

The theory for predicting kinetic efficiency of gun exhaust and exhaust velocity is given in Ref. 1 and 2. It employs the snowplow model and allows for variable mass distribution along the gun barrel, as well as various losses from the plasma. The theory indicates important parameters for efficient gun design. One such parameter is the non-dimensional mass loading parameter, $\mathcal{M} = (2l/L'Q_o^2)M_o$, where l is gun length in meters, L' is gun inductance per unit length in H/m, Q_o is original stored charge in coulombs, and M_o is the total mass swept up in kg.). It was found in Ref. 2 that theory and experiment could best be compared by plotting the plasma velocity and kinetic efficiency of the gun as functions of this mass loading parameter. Operating characteristics of the guns used in the present experiments were surveyed as a function of $\mathcal{M}$ and compared to theoretically predicted performance. Transient spectra were taken at highest efficiency points for each gun. The viewing windows were located at a point where maximum discharge luminosity and definition occurred.

Apparatus

Capacitor Bank

The guns were energized by a 10 kilojoule bank which had a resistance of 3.8 milliohms, an inductance of 14 nanohenries, and capacitance of 24.2 microfarads. Eleven GL-7703 ignitrons, switched synchronously, connect the bank to the gun.

Gun Geometries

Figure 1 is a view of the apparatus. The bank cables are shown connected to the copper gun electrodes at the far left. A controlled, 100 μ sec. duration puff of argon gas was admitted into the evacuated gun annulus. The gas diffused for 1100 μ secs. before bank voltage was applied.

The dimensions and electrical characteristics of both gun geometries are given in figure 2.

Instrumentation

Gun exhaust energy was measured as the temperature rise of a calorimeter cup. Probes for the measurement of azimuthal magnetic field were inserted in the gun annulus. Time of flight measurements of the magnetic front between probe stations determined magnetic front velocity.

The streak spectra are obtained by coupling an image converter camera, used in streak mode, in tandem with a grating polychromator shown in figure 1. The discharge radiation is focused via two lenses (one of which serves as the gun barrel window) on the polychromator entrance slit. The spectrum produced at the focal plane of the polychromator is viewed via the mirror by the electronic image converter camera. The attachment of a +3 diopter lens to the face of the camera lens, together with the use of the polychromator in second order, permitted a reciprocal linear dispersion of 70.4 A/mm to be obtained on the film record. The usable wavelength range per exposure is 250A and the total range is from 3800 to 5500A (380 to 550 nm.). Streak duration is 10 μ secs. Four successive shots were therefore necessary to examine the spectra between 3850 and 4700A$^{\circ}$ (385 to 470 nm.). This range includes the wavelengths of all the expected elements.

Results and Discussion

Gun Performance

The experimental and theoretical kinetic efficiencies and velocities determined for both guns are presented as a function of the mass loading parameter in figure 3. Efficiencies calculated from the theory of Ref. 1 and 2 are presented for both the simplified and loss models. The simplified model excludes losses due to the interaction of plasma with the wall, and also the ionization and radiation effects. It does include ohmic losses and losses due to shock heating. The loss model includes wall drag, ionization, radiation, ohmic, and shock heating losses. The choice of typical values of the loss parameters is discussed in Refs. 1 and 2.

The solid data symbols are for experimental data obtained in the present investigation. The open data symbols are for data given in Ref. 1 for similar but not identical guns.

Figure 3(a) presents the data for the noncrowbarred geometry. The new efficiency data are much higher than the originally reported data. This efficiency increase appears to result from the difference in the gas baffle designs employed.

Figure 3(b) presents the data for the selfcrowbarred geometry. The new data lie near the loss model theoretical data and extend the previous data to more optimum values of the mass loading parameter.

Transient Spectra

For the noncrowbarred gun, the plasma was viewed at the muzzle window and the spectra are shown in figure 4. Gun current starts at T_o. Analysis of the spectrum reveals that the plasma is composed of singly ionized silicon and oxygen ions, with minor amounts of SiIII, CII, and CIII present. The plasma consists of pyrex gas-baffle materials. As the plasma passes the muzzle window, it consists of a main front trailed by decreasing density plasma residuum. If any multiple fronts formed upstream, they decayed before reaching the window.

For the self-crowbarred gun operation, the plasma was viewed at the mid-barrel window (see fig. 2). A typical spectral record is presented in figure 5. The streak spectra in the lower portion of the figure show multiple fronts. Higher resolution non-time-resolved exposures were subsequently made under gun conditions matching those of the streak spectra. These integrated spectra are presented

above the streak spectra in figure 5, and each is the total integrated record of 10 gun shots. The reciprocal linear dispersion of these integrated spectra was 16.2A /mm . The higher resolution integrated spectra were used as an aid in line identification.

The spectra in figure 5 (along with other spectra records not presented here) reveal that the primary moving front consists of a fully developed ArII spectrum, with faint traces of ArIII, SiIII, and SiIV. The second front contains SiIII, SiIV, and OII spectrum with no ArI or ArII observed. The third and subsequent fronts are primarily SiII, SiIII, and OII. No CuI or CuII lines were detected even though the gun electrodes were copper. Wavelength limitations did not allow for a CuIII or CuIV search in the fronts.

Concluding Remarks

The transient spectra for two different gun geometries using argon propellant have been obtained.

The geometry which exhibits relatively noncontaminated fully ionized argon spectra shows good performance reproducibility with earlier data. New data correlate well with theory described by Michels, Heighway, and Johansen (ref. 2). Spectral identification shows the moving front in the gun consists of a fully developed ArII spectra with faint ArIII lines. No neutral lines are present, but SiIII and SiIV appear weakly. The second moving front is basically an energetic silica discharge. The remaining fronts are contaminant laden. No electrode material is noted in the plasma in the wavelength region observed.

In contrast, for the other geometry examined, the first moving plasma front consists primarily of the constituents of the pyrex gas baffle placed near the gas ports. This geometry would not be expected to accurately follow the theory proposed, and it does not.

The two different geometries have helped show the value of transient spectra diagnostics in determining when gun theory can be correctly applied to an experiment.

REFERENCES

1. C. J. Michels and A. E. Johansen, NASA Technical Note D-3 69 (1966).

2. C. J. Michels, J. E. Heighway, and A. E. Johansen, AIAA J. 4, 823 (1966).

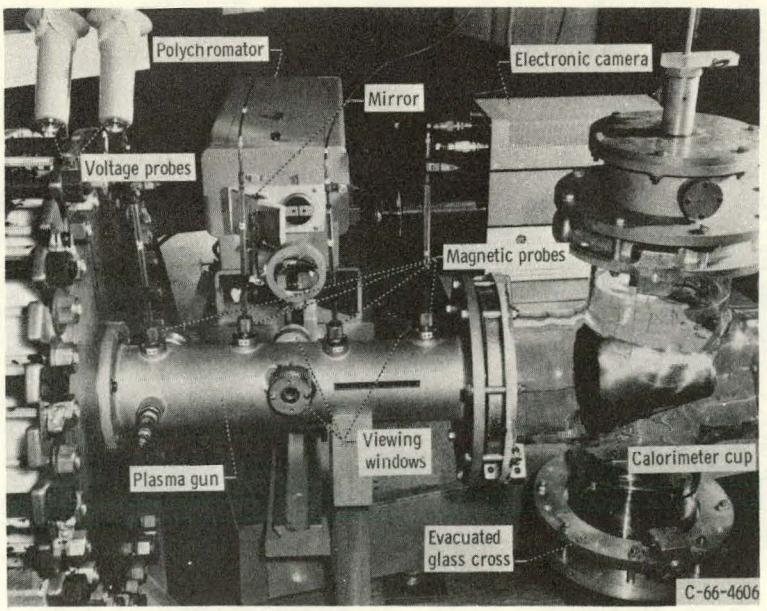

Fig. 1. View of apparatus for measuring time-varying plasma spectra

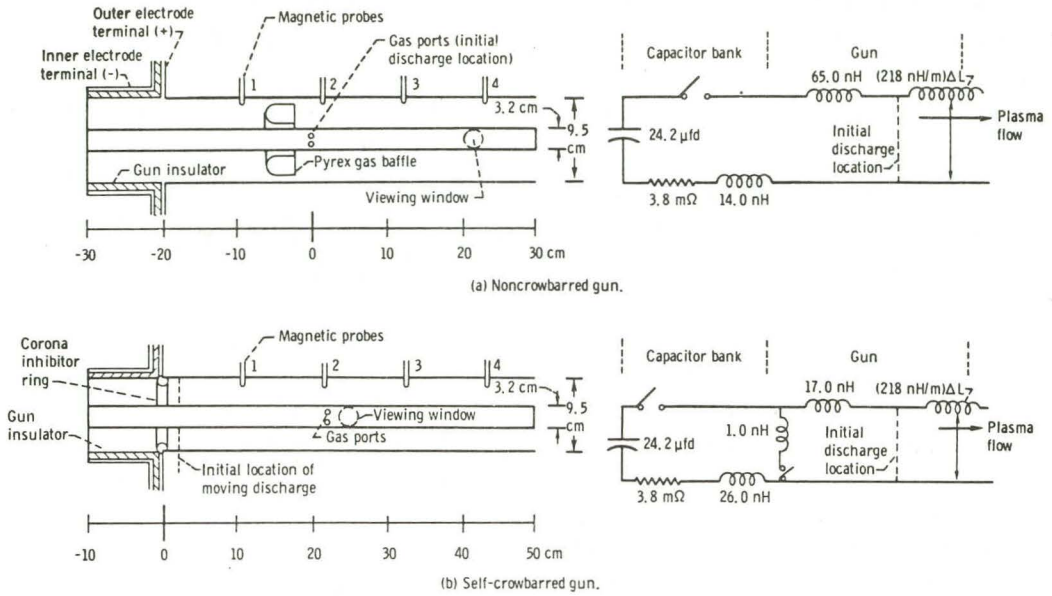

Fig. 2. Gun Geometries and electrical characteristics

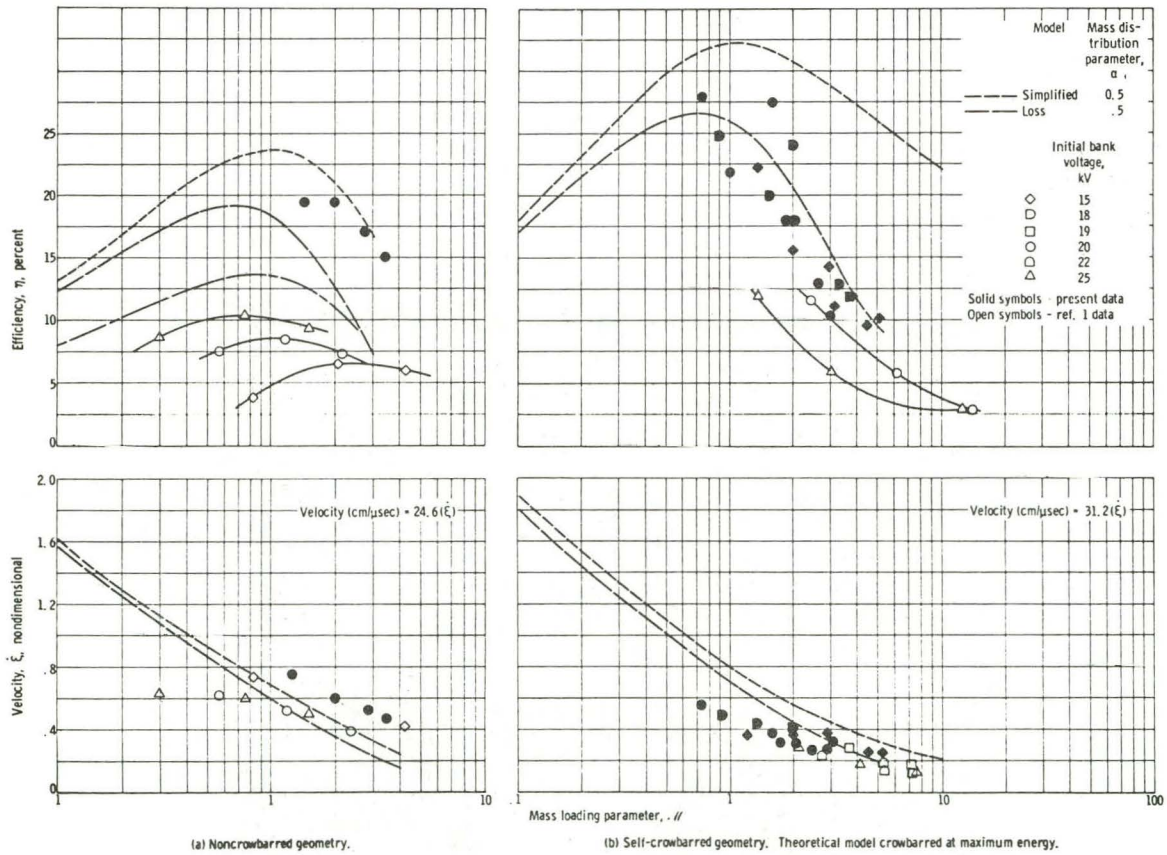

Fig. 3. Theoretical and experimental performance of plasma-gun geometries

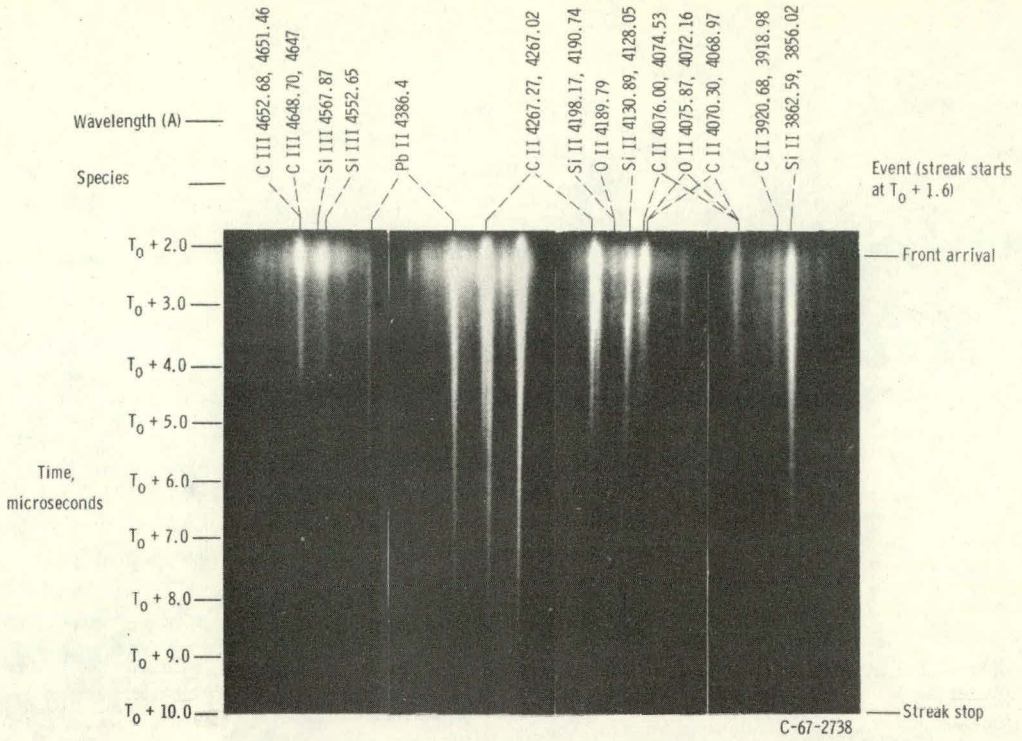

Fig. 4. Streak spectra for noncrowbarred geometry

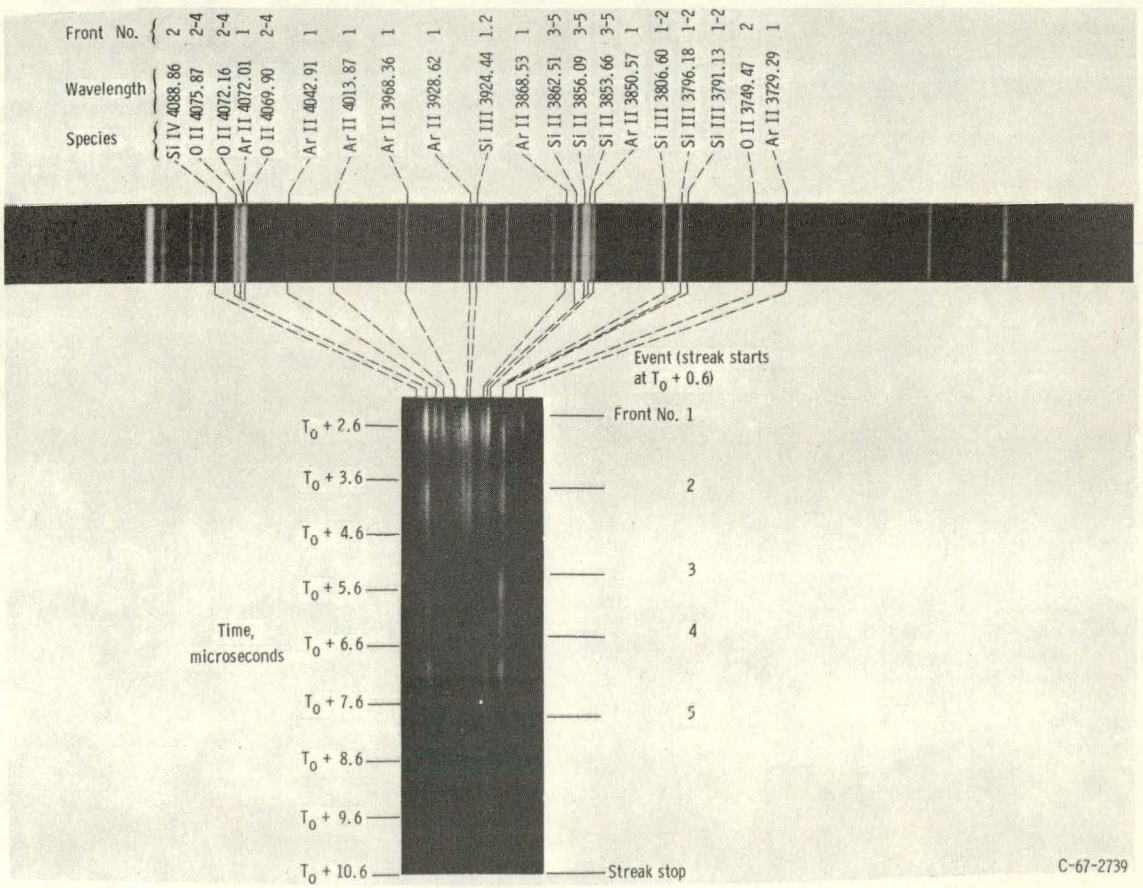

Fig. 5. Self-crowbarred gun streak spectrum, 3900A center wavelength

INVESTIGATIONS OF A CESIUM PLASMA ACCELERATOR WITH OPTICAL DIAGNOSTICS IN THE VISIBLE AND VACUUM ULTRAVIOLET*

by

D. R. Simon
D. A. Hill
M. E. Levy
Vitro Laboratories
West Orange, New Jersey

ABSTRACT

The cesium plasma generated by a low inductance coaxial accelerator has been previously investigated** using electrical probes. Time-of-flight measurements with these probes indicated plasma velocities of 3×10^8 cm/sec. In order to confirm the existence of the fast plasma front and establish the constituents of it, a series of spectroscopic experiments has been conducted in the visible and vacuum ultraviolet. A high-dispersion spectrum of the discharge was obtained to identify the species present. Photoelectric detection was used to observe the radiation from the leading and trailing plasma fronts with submicrosecond time resolution. In order to estimate the density of the cesium in the plasma, records of the 926 Å ground state transition of the cesium ion were obtained in the vacuum ultraviolet with a Seya-type 0.5 meter monochromator equipped with a 1200 line/mm platinum coated grating blazed for 700 Å. The total number of cesium ions in the 10^8 cm/sec velocity range is shown to be 10^{13} to 10^{14} per pulse. The analysis of the 926 Å data coupled with the supporting data in the visible and quartz ultraviolet indicates that the ejected plasma consists of a fast leading edge of cesium ions with an average velocity of 2.5×10^8 cm/sec and a slow trailing region of cesium and electrode material such as tungsten and thoria. Hydrogen was not detected at any time as an impurity in the measurements, indicating that Ly-β radiation did not enhance the cesium ion ground state radiation.

INTRODUCTION

The physical configuration of the coaxial plasma accelerator we have used resembles that of the units operated by J. Marshall[1], R. H. Lovberg[2] and many others. The unit differs in that it uses cesium as the working fluid, which is partially ionized by contact ionization, and an extremely fast energy discharge system permitting much of the energy to be delivered early in the acceleration process. A diagram of the accelerator is shown in Figure 1. The injected cesium is initially deposited upon the cold tungsten surfaces on the

* The work reported in this paper was sponsored by Picatinny Arsenal, Dover, New Jersey under Contract DA-28-017-AMC-2173(A).

** K. C. Rogers and D. R. Simon, "Operation of an Alkali Metal Plasma Gun," presented at the 5th Annual Meeting of the Division of Plasma Physics of the American Physical Society, November 6-9, 1963, San Diego, California.

split portion of the center electrode. The outer electrode is fabricated of tantalum in order to allow contact ionization to occur at this surface. The trigger discharge occurs between the two split segments of the center electrode and drives an ionized plasma toward the outer electrode thus breaking down the main discharge loop. In previous work[3] we have measured the plasma velocity by means of electrical plasma probes. A two-electrode probe (following McLaren's design[4]) was built that responds to local plasma conductivity. Using a pair of these probes spaced 25 cm apart, we have measured a flight-time of 0.8×10^{-7} sec for the initial plasma burst; i.e., a plasma velocity of 3×10^8 cm/sec. In a similar manner, a pair of Faraday cups were used to measure axial ion current and time of flight corresponding to a velocity of 2×10^8 cm/sec. Thus all indications pointed to a frontal velocity consistently greater than 10^8 cm/sec. Several accounts have appeared in the literature on devices accelerating plasmas to 10^7 cm/sec or better; however, all of these devices that we are aware of accelerate low Z plasmas. The question then arises whether our observations are caused by a low Z contaminant. A particular effort has been made in the present work to identify the components in our plasma and for that purpose optical techniques appeared to be the most powerful and specific.

OPTICAL DIAGNOSTICS

High Dispersion Spectroscopic Analysis of Cs Accelerator Discharge

The plasma accelerator discharge was viewed end-on through a quartz window. An image of the cross-sectional area intersecting the trigger gap was focused with quartz optics onto the entrance slit of a three meter grating spectrograph. Spectrographic plates were used to record the spectra of several superimposed discharges in the spectral region between 4350 Å and 5750 Å. This region is of interest because it contains the strong neutral cesium lines at 4555 Å and 4593 Å. (Glass slides transmitting above 3500 Å were used to short our first and second order U. V. spectra.) An analysis of the spectra obtained has yielded the following line identification:

CESIUM ION LINES

Measured Wavelength	Identification	
4650.1 Å	Cs	4651.1 Å
4647.3	CsII	4646.5
4446.8	Cs	4447.6
4411.2	Cs	4410.2
4374.5	CsII	4373.0
2598.3	Cs	2598.7
2512.2	Cs	2512.1
2478.7	CsII	2477.6

IMPURITY LINES

Measured Wavelength	Identification (Source)	
2837.8 Å	W	2837.8 Å (Spk)
2836.9	Th	2837.3 "
2835.8	W	2835.6 "
2802.9	W	2802.9 "
2795.7	W	2795.6 "
2755.9	W	2755.9 "
2749.5	Th	2749.5 "
2746.7	W	2746.7 "
2739.7	W	2739.4 "
2599.3	WII	2599.6 "
2509.2	W	2509.4 "

The appearance of thorium and tungsten lines was not surprising, since the inner electrode of the coaxial accelerator is constructed of 2% thoriated tungsten. It is important to note that no neutral cesium lines were seen and that hydrogen impurities are absent from the plasma.

From the above data it was concluded that the initial cesium plasma created at the trigger cap of the accelerator before the acceleration process is started is composed of ionized cesium and electrode material. The lack of neutral cesium lines indicated a fully ionized cesium plasma and the absence of hydrogen lines indicate a discharge free of hydrogen impurities.

Time Resolved Emission Spectroscopy in the Visible

Small-aperture high-resolution experiment.

For this experiment a three-meter grating spectrograph was used in an arrangement shown in Figure 2. The spectrograph was aligned so that the field

of view intersected the plasma beam 30 cm downstream from the accelerator. The radiation was detected by a 1P21 photomultiplier with an exit slit field of 10 Å. The photomultiplier tube was connected to an emitter follower and a current amplifier. The photoelectric recording was obtained from oscilloscope traces. The exit slit of the spectrograph was set on the CsII 5349 Å line by using a cesium vapor lamp as a standard.

Control discharges were fired initially without injecting cesium into the accelerator at a pressure of 10^{-6} torr. Figures 3(a) and 3(b) are typical records of the radiation signal seen by the photomultiplier as the plasma went by the observation port. The data shows that no radiation is seen during the first twenty microseconds from the initiation of the current flow. A slow luminous plasma front traveling at about 10^6 cm/sec is seen at a later time. The slower front contains electrode material.

The oscilloscope data shown in Figures 3(c) and 3(d) were obtained from a discharge in an ambient pressure of 10^{-6} torr with a cesium charge on the inner electrode. The radiation observed in the first few microseconds is consistent with emission from a cesium plasma traveling at 10^7 - 10^8/sec.

Although the fast luminous front detected here can not be due to spurious electrical noise (as the discharge recorded with the entrance slit of the spectrograph closed shows) there are other spurious effects such as multi-surface reflections which cannot be rulted out. A conclusion drawn from this experiment is that the slow plasma front appears in discharges whether or not a cesium charge has been placed in the accelerator.

Time Resolved Emission Spectroscopy in the VUV

Experimental setup. A VUV spectroscopic system has been used for monitoring the emission spectra of the cesium plasma fronts. A Seya-Namioka type VUV monochromator was set up, utilizing a sodium salicylate phosphor screen and photomultiplier detector. There are no windows in the system, and the dispersing element is a 1200 line/mm grating coated with magnesium fluoride and blazed for 1500 Å. The wavelength of interest in this experiment is the resonance transition of CsII at 926 Å. The cesium gun chamber and the monochromator are at a pressure of 10^{-5} torr. Figure 4 is a block diagram of the apparatus. Figure 5 is a photograph of the assembled system.

Observations in the VUV are desirable for several reasons: (a) Since the plasma is fully ionized initially, it is expected that the cesium ions will be a large constitutent in the plasma front downstream. (b) The problem of reflected light produced by the initial arc and interfering with measurements of light emission from the plasma front is minimized due to the poor reflectance of materials at wavelengths below 1000 Å.

Initial studies were performed by observing the CsII 926 Å line in emission approximately 50 cm downstream from the cesium accelerator nozzle. Only the slow plasma front was observed in this experiment. It would be expected that by the time the fast front reached the observation point, most excited ions would have already reached the ground state configuration, thus terminating their radiative transitions. The observation port was therefore moved to a distance of 5 cm from the accelerator nozzle. With the fast plasma front traveling at 10^8 cm/sec, the cesium ions would still exist in excited states 5 cm away from the accelerator.

Determination of ion density from 926 Å emission. The total density of excited cesium ions can be calculated from a determination of the absolute intensity of the 926 Å CsII line as the fast plasma front travels past the entrance slit of a vacuum monochromator. A Seya-Namioka half-meter monochromator was positioned with the entrance slit viewing the plasma flow 5 cm downstream from the accelerator nozzle. A 1200 line/mm platinum coated grating blazed for 700 Å was used.

The reflectivity of the grating at 926 Å is estimated as 5%.

The photomultiplier used was an EMI 9514'S' with dark current of $1\text{-}5 \times 10^{-8}$ amperes for voltages between 1500 and 2000 volts. This photomultiplier was calibrated using an NBS standard lamp.

The VUV radiation was converted by a sodium salicylate phosphor screen whose conversion efficiency is estimated at 1%. The contribution of scattered light originating at wavelengths above 1600 Å was determined by using a fused quartz filter in front of the phosphor screen. The insertion of the filter eliminated the fast front signal at the sensitivities which we were using.

During this experiment an entrance slit of 0.05 mm wide and 1.0 cm high was used. The slit was on the average 30 cm away from the observed plasma volume, subtending a solid angle which is approximately 4.4×10^{-7} of the total 4π solid angle illuminated. The sensitivity of the monochromator-detector system, including the phosphor efficiency, the grating efficiency, and the photomultiplier efficiency is estimated to be 28 volts per milliwatt of 926 Å radiation accepted by the entrance aperture.

A typical set of data is shown in Figure 6. The upper trace is the current signal from the capacitor discharge and the lower trace the photomultiplier signal. The radiation signal has a height of 5 volts and a half width of 0.2 μ seconds. The integrated radiant energy at 926 Å detected by the monochrometer as the fast front traverses the region of observation is given approximately as

$$\frac{\text{pulse height} \times \text{half width}}{\text{sensitivity}} = \text{radiant energy}$$

$$\frac{5 \text{ volts} \times 0.2 \times 10^{-6} \text{ sec}}{28 \times 10^{3} \text{ volts per watt}} = 3.6 \times 10^{-11} \text{ J}$$

The entrance slit of the spectrograph is 30 cm away from the observed plasma volume and 50 cm from the 3 cm square grating. From the above consideration we can construct a geometric model, Figure 7, from which a calculation can be made to determine the number of excited ions capable of radiating at 926 Å. This determination turns out to be independent of the density distribution in the fast front.

The total number of photons collected from the entire pulse is

$$N_t = \int_0^\infty R\, dt = \int_0^\infty n(x)\, A(x)\, \ell\, \Omega\, K\, dt$$

$$= \ell\, \Omega\, K \int_0^\infty n(x)\, A(x) \left(\frac{dx}{dt}\right)^{-1} dx$$

where R is the number of photons collected per second and n the density of atoms (in upper state), A the cross sectional area of the plasma pulse, ℓ the length of the observed region, Ω the solid angle of the collector, and K the decay rate of the upper state.

For uniform velocity, $dx/dt = v$ = constant, and the total number of photons collected can be written as

$$N_t = \frac{\ell \Omega K}{v} \int_0^\infty n(x)\, A(x)\, dx$$

where $\int_0^\infty n(x)\, A(x)\, dx$ turns out to be the total number of ions (in the upper state) in the entire pulse. Considering that a 926 Å photon contains 13.4 ev of energy, the N_t from Figure 7 becomes 1.7×10^{7} photons, and the total number of excited ions is calculated to be 4.8×10^{13}. It should be borne in mind that this calculation is only accurate to order of magnitude.

Assuming an average velocity of 2.5×10^{8} cm/sec for the fast front, the kinetic energy imparted by the accelerator can be calculated. This is in the vicinity of 32 J. The corresponding energy input to the accelerator is 125 J.

Discussion of Possible Radiation Mechanisms from Ambient Cesium Atoms

The observation of weak luminous fronts due to electromagnetically accelerated plasmas is usually complicated by other phenomena which could be mistaken for the plasma front. A discussion of such phenomena follows.

If the chamber in which the plasma is accelerated were completely evacuated (an im-

practical task), then any particle or photon flux emanating from the region of the initial plasma arc would travel the length of the chamber without interacting. Under such conditions one would only be concerned about reflected radiation from chamber walls or the interaction of fast particles with the walls. In the present experiments (emission in the UV and VUV), care has been taken to focus the spectrograph slit on a volume element located near the center of the accelerator chamber, thus obtaining a high rejection ratio for the radiation originating outside this volume. A further check is afforded by a comparison of the intensity-time characteristics of the radiation emitted by the fast plasma front with the radiation emitted at the initial arc region in the gun. The two signals do not have similar characteristics, thus providing a strong case for the relative unimportance of reflected light.

The analysis must take into consideration the fact that there is an ambient neutral cesium atmosphere downstream from the coaxial gun that would interact with particles or photons emitted by the initial current arc, and therefore could produce luminous effects that could be misinterpreted as plasma fronts of high velocity. Let us consider the effects of such a situation.

Assuming an ambient temperature of 300 ^{o}K the vapor pressure of cesium is calculated to be 1.6×10^{-6} torr which corresponds to a density of 6×10^{10} atoms cm^{-3}. Is this density adequate to provide the observed optical signal? The energy radiated over 4π steradians by the plasma coupled with an absorption length of 10^3 cm at the ambient cesium density results in a source radiance which is higher than that possible with the energy available in the capacitor.

Conclusions

The observation of the cesium fast front by the luminosity at 926 Å can be interpreted quantitatively only if extraneous sources of radiation are unimportant. We have experimentally determined the total 926 Å output integrated over the pulse width and 4π steradians to be 1×10^{-3} J. The possible sources of energy at the measured wavelength are:

a) direct plasma luminosity

b) radiation entering the spectrograph multiple reflections

c) radiation transport in the ambient cesium background from the gun discharge.

Reflections at these wavelengths may be discounted immediately since the coefficient of reflectivity in the VUV is less than 1% for the materials in the system. Multiple reflections would imply a source radiation level many times greater than that available in the energy storage system.

Radiation diffusion through the ambient cesium population (6×10^{10} atms/cc) requires that a mean free path of a photon be of the order of centimeters. This requirement is not satisfied, since the absorption length at the ambient CsII density is 10^3 cm.

We conclude that:

a) Cesium is a major constituent of the fast front traveling at about 2.5×10^8 cm/sec.

b) The kinetic energy of the cesium plasma is about 30 J as estimated by indirect methods. The corresponding input energy to the accelerator is 125 J.

c) Tungsten and thorium as well as cesium are constituents of the subsequent slow front traveling at $1\text{-}5 \times 10^6$ cm/sec.

d) No spectroscopic evidence is found for hydrogen or carbon in the plasma.

REFERENCES

(1) J. Marshall, T. F. Stratton, Nuclear Fusion, 1962 Supplement, Part 2, 663.

(2) R. H. Lovberg, Phys. of Fluids, 8, 177-85, January 1965.

(3) K. C. Rogers, D. R. Simon, "Operation of an Alkali Metal Plasma Gun," presented at the 5th Annual Meeting of the Division of Plasma Physics of the American Physical Society, November 6-9, 1963.

(4) T. I. McLaren, J. N. Fox, R. M. Hobson,
Nature, 198, 1264, 1963.

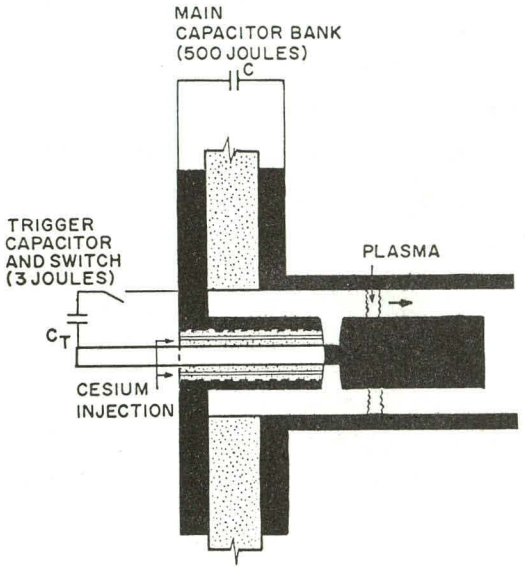

Fig. 1. Cesium gun.

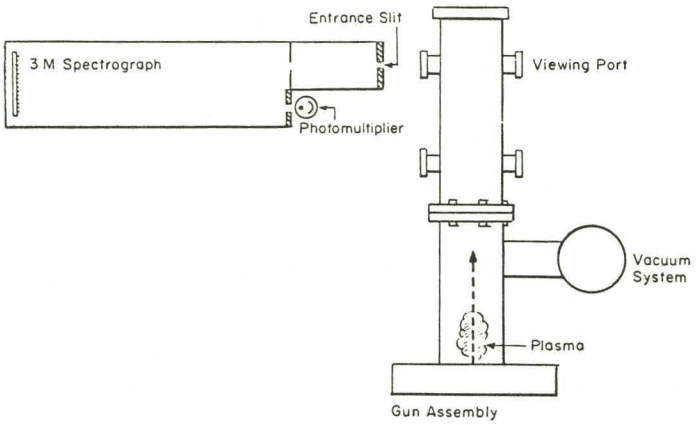

Fig. 2. Experimental arrangement.

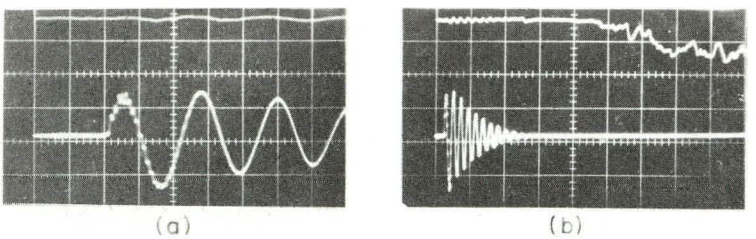

Upper Beam P. M. Tube
Lower Beam Rogowski Coil

Time (a) .5 μsec/div, (b) 5 μsec/div

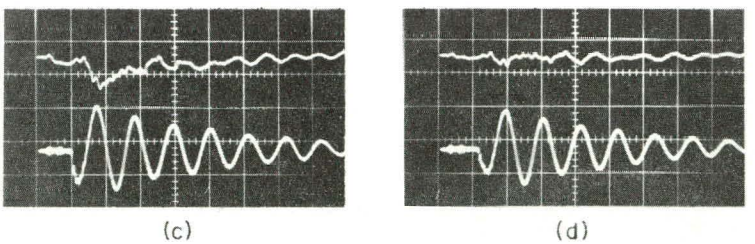

Upper Beam P. M. Tube
Lower Beam Rogowski Coil

Time (c) & (d) 1 μsec/div

Fig. 3. Optical emission at 5349 Å.

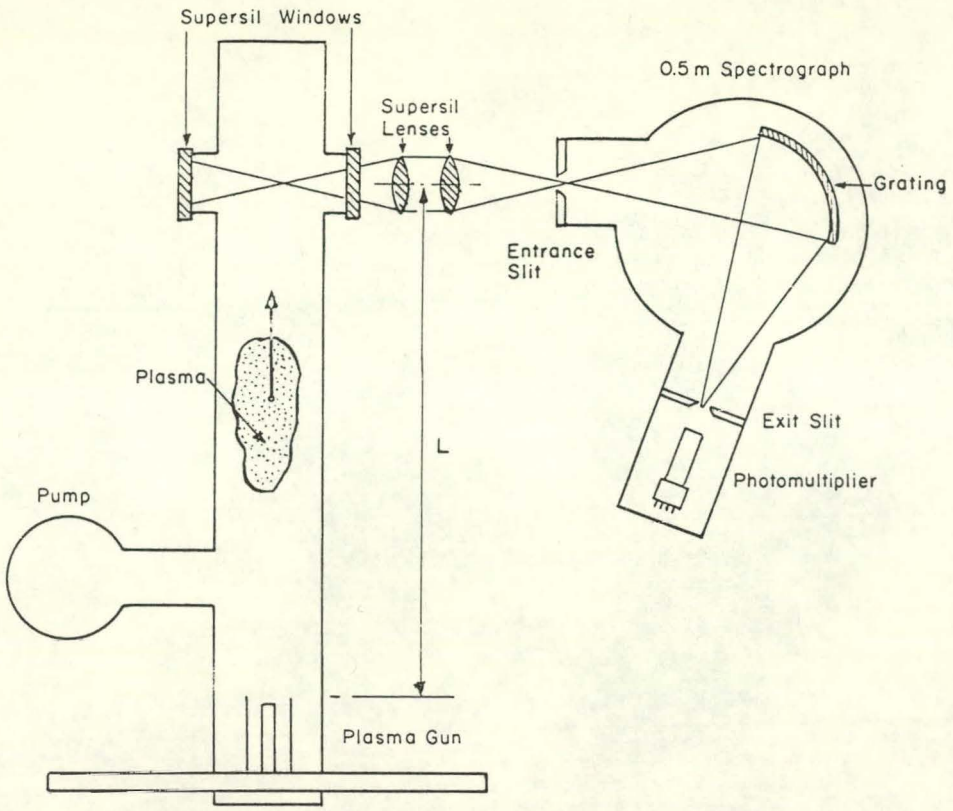

Fig. 4. Experimental configuration.

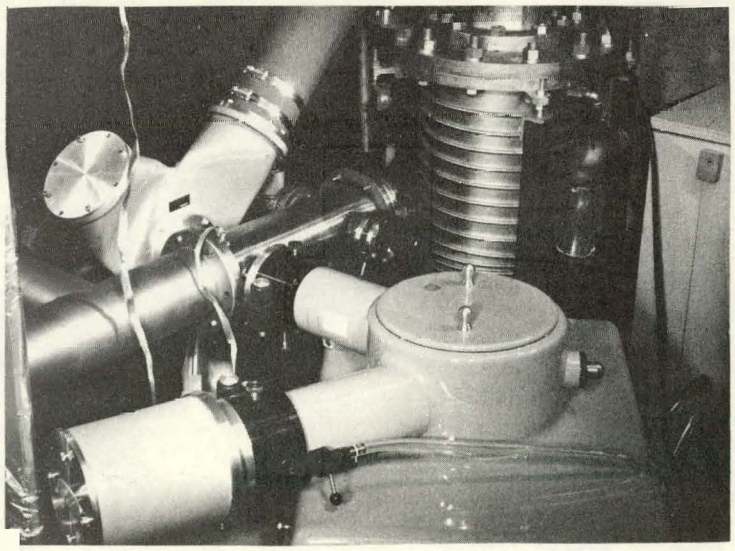

Fig. 5. Experimental apparatus.

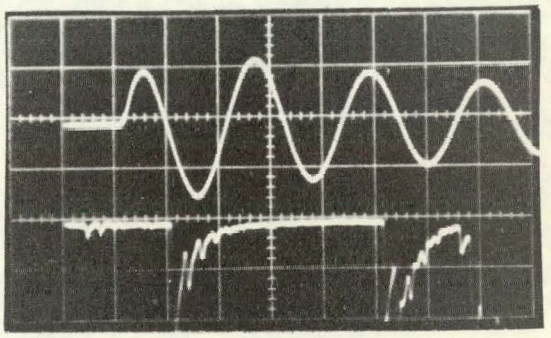

Fig. 6. Optical emission at 926 Å.

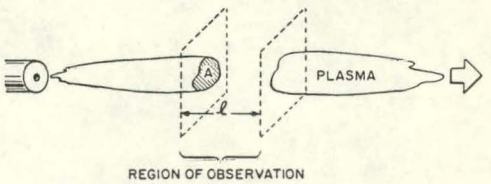

NO. OF PHOTONS COLLECTED PER SECOND, $R = n A \ell \Omega K$

n = DENSITY OF ATOMS (IN UPPER STATE)

A = CROSS SECTIONAL AREA OF PLASMA

ℓ = LENGTH OF OBSERVED REGION

Ω = SOLID ANGLE OF THE COLLECTOR

K = DECAY RATE OF UPPER STATE

Fig. 7. Model used for interpretation of data.

EXPERIMENTAL INVESTIGATIONS OF NORMAL IONIZING SHOCK WAVES

by
Leslie S. Levine and Robert A. Gross
Columbia University
New York, New York

ABSTRACT

Experiments have been conducted on normal ionizing shock waves produced in a coaxial electromagnetic shock tube. Steady shock velocities were measured as a function of initial gas pressure, drive current, and applied axial magnetic field. The speeds agreed well with theoretical values. Shocks propagating at transAlfvenic speeds ($u_{Alf_1} \lesssim u_s \lesssim 3u_{Alf_1}$) were studied. Measurements were made of the upstream transverse electric field and the switch-on magnetic field. Their magnitudes were in good agreement with the predictions of the Chapman-Jouguet hypothesis. Further support for this theory was provided by the measured compression ratio across the shock front. It was concluded that transAlfvenic normal ionizing shocks exhibited Chapman-Jouguet behavior with current flow in the shock front, and no separation of shock and drive currents. In contrast, superAlfvenic shocks ($u_s \gtrsim 3u_{Alf_1}$) appear to be gas dynamic in nature. Spectroscopic measurements and shock reflection studies demonstrated the presence of a nonluminous front and shock heated gas preceding the drive current in this regime. The luminosity front acts as a contact surface separating the unequilibrated shock from the luminous current. Finite transverse electric fields have been observed at superAlfvenic shock speeds. This effect was attributed to the finite conductivity of the plasma.

INTRODUCTION

A strong shock wave, propagating into an initially nonionized gas, can convert the gas into a highly conducting dense plasma. If there is an applied magnetic field normal to the plane of such an ionizing shock wave, and if the shock speed u_s is within the limits $u_{Alf_1} \lesssim u_s \lesssim 3u_{Alf_1}$ (where u_{Alf_1} is the Alfven velocity in the preshock gas), then ionizing switch-on shock behavior is predicted.[1] The present state of experimental and theoretical understanding of ionizing shocks has been reviewed recently.[2]

The most distinctive feature of ionizing shocks is the ability of the preshock gas to sustain an electric field parallel to the shock front. The value

of this transverse electric field critically effects the shock jump equations but cannot be determined a priori from the conservation equations. The indeterminacy is similar to the situation found in classical detonation theory, and the analogy has been employed to suggest a Chapman-Jouguet like hypothesis for ionizing shocks.[3] This additional assumption permits a unique solution for the properties of ionizing shock waves with a magnetic field normal to the front. The nature of Chapman-Jouguet behavior has been further elucidated by Taussig in a detailed study of these normal ionizing shocks driven by currents in an electromagnetic shock tube.[1] Taussig's results suggested that, at shock propagation speeds of less than about three times the upstream Alfven velocity, Chapman-Jouguet behavior should be observed. Such shocks are predicted to exhibit a unique value of upstream electric field, postshock transverse (or switch-on) magnetic field and compression ratio across the front. They should also show no growing uniform plasma region between the shock front and drive currents, as the shock and drive current front speeds are predicted to be the same.

Earlier experiments produced normal ionizing shocks in a coaxial geometry[4], but only recently has there been any experimental verification of Chapman-Jouguet behavior. Heywood[5] has reported measurements of the upstream radial electric field that are in qualitative agreement with theoretical predictions. Miller[6] has measured the azimuthal switch-on magnetic field produced by the shock front current. Its value, together with the observed lack of separation from the drive current, gives added confirmation to the Chapman-Jouguet hypothesis.

In the present research we measured the electric and magnetic fields, together with the density compression ratio across the front of normal ionizing shocks which were moving at speeds such that Chapman-Jouguet behavior was expected.

EXPERIMENTAL APPARATUS

The coaxial metallic shock tube, shown schematically in Figure 1, is similar to the system described by Miller.[6] Steady shocks were produced by constant drive currents of up to 100 KAmp and propagated into room temperature hydrogen gas at a uniform pressure of several hundred millitorr. Normal magnetic fields of up to several kilogauss were applied along the axis. The measurement of front velocities and azimuthal magnetic field distributions has been discussed by Miller. The steady electric field was determined from measurements of the potential difference across the annulus using a high voltage probe at the upstream end of the tube. The postshock gas density was deduced from electron number densities obtained from measured halfwidths of the Stark broadened H_β line. Such profiles were scanned on a shot-to-shot basis by a calibrated photoelectric monochromator. Further details of the experimental arrangement may be found in Reference 7.

EXPERIMENTAL RESULTS

Wave speeds were measured over a wide range of initial conditions. The variation of the observed steady shock velocity with initial gas pressure, drive current and applied axial magnetic field, was found to be in agreement with the predictions of Taussig's analysis.

The upstream radial electric field was measured as a function of shock speed at two different values of axial magnetic

field, and the results are shown in Figure 2. The speed was varied by changing the drive current while keeping the initial gas pressure constant. The solid curves in the figure represent the values of electric field predicted by Taussig's calculations for ionizing shock waves assuming Chapman-Jouguet behavior. Agreement with theory is good, particularly at speeds above 5 cm/μsec. At lower speeds, the disagreement is probably due to the low value of the postshock electrical conductivity. The fact that the measured electric field increases with applied magnetic field and with decreasing drive current clearly demonstrates that the field is a real plasma effect and not one associated with capacitor bank voltage.

The azimuthal magnetic field profiles were obtained from the electronically integrated outputs of magnetic probes inserted into the annulus. They showed a characteristic step corresponding to the switch-on field (or, equivalently, to the shock front current) before reaching a steady value behind the drive current. The magnitude of the switch-on field was measured as a function of shock speed for a fixed axial magnetic field and gas pressure, by varying the drive current. The results are shown in Figure 3 together with the predicted variation. Again, agreement with theory is rather good. No evidence was found of a current-free region between the shock and drive currents in the regime where Chapman-Jouguet behavior is predicted.

Electron densities were measured spectroscopically as a function of time as the luminous plasma moved past a particular axial position in the tube. Simultaneously the temperature was measured from the ratio of the H_β line intensity to the intensity of the 100 Å wide band of continuum radiation centered about the line center. In the temperature range that was observed (~2 to 3.5 x 10^4 °K), the plasma should be nearly fully ionized and the total mass density can be determined immediately from the electron density. The theoretical value of the mass compression ratio expected across an ionizing shock is a very sensitive indicator of Chapman-Jouguet behavior.

The density profile at a particular shock speed and initial conditions is shown in Figure 4. The compression ratio across the shock was deduced from an extrapolation of the experimentally derived density profile to the time corresponding to the onset of luminosity at the front. To within the experimental error, agreement was found between the theoretical value of compression calculated with the Chapman-Jouguet hypothesis, and the extrapolated data (at $t_{LAB}=0$). It also can be shown from the spectroscopic density profile that the drive current is effective in sweeping up nearly all of the gas initially in the annulus.

In Table I, all of the measurements made at one set of conditions are compared directly with the theoretical predictions of Taussig, assuming Chapman-Jouguet behavior. No additional physical assumptions have been employed. The agreement between theory and experiment is good.

At shock speeds of greater than about three times the upstream Alfven speed, theory predicts a gas dynamic shock with a separation between current and shock front and no upstream electric field. However, no luminous plasma was detected ahead of the drive current at these speeds,

although shock reflection studies indicated that there was a nonluminous front preceding the main luminosity front. This is in contrast to the situation observed in shocks in the Chapman-Jouguet regime, where there was no resolvable separation between the shock front (as seen in reflections), and the luminosity or current fronts. Spectroscopic investigations in the gas dynamic shock regime suggest that the luminous front behaves, not as a shock front, but rather like a contact discontinuity, separating the luminous drive current from the nonluminous unequilibrated postshock gas.

Even in this regime of gas dynamic shock behavior, a small value of upstream electric field (~15 V/cm) was always measured. Ideal theoretical analysis does not predict this.[1] It is believed that this effect is due to the finite conductivity in the postshock region.

CONCLUSIONS

Measurements have been made of the electric and magnetic fields which are in agreement with the predictions of ionizing shock theory over a range of experimental conditions within the Chapman-Jouguet regime. A careful and detailed comparison with theory was made at one set of conditions and good agreement was found.

ACKNOWLEDGEMENTS

It is a pleasure to acknowledge the continuing advice and assistance of Professor C. K. Chu, Dr. Bennett Miller, Dr. Robert T. Taussig, and Mr. Richard Meehan. The work described in this paper was supported by the Air Force Office of Scientific Research under Contract AF 49(638)-1634 at the Columbia University Plasma Laboratory.

REFERENCES

1. R. Taussig, Phys. Fluids 8, 1616 (1965); Phys. Fluids 9, 421 (1966).
2. R. A. Gross, Revs. Modern Phys. 37, 724 (1965).
3. W. B. Kunkel and R. A. Gross, in Plasma Hydromagnetics, D. Bershader, Ed. (Stanford University Press, Stanford, 1962), p.58.
4. R. Patrick, Phys. Fluids 2, 589 (1959).
5. J. Heywood, Phys. Fluids 9, 1150 (1966).
6. B. Miller, Phys. Fluids 10, 9 (1967).
7. L. S. Levine, Ph.D. Thesis, Columbia University (1967).

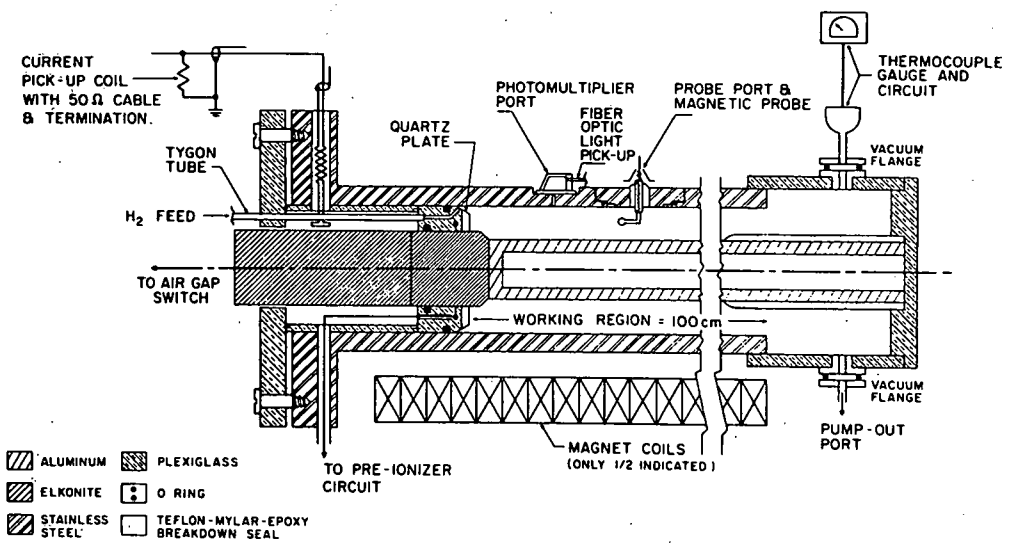

Fig. 1. Schematic of coaxial electromagnetic shock tube

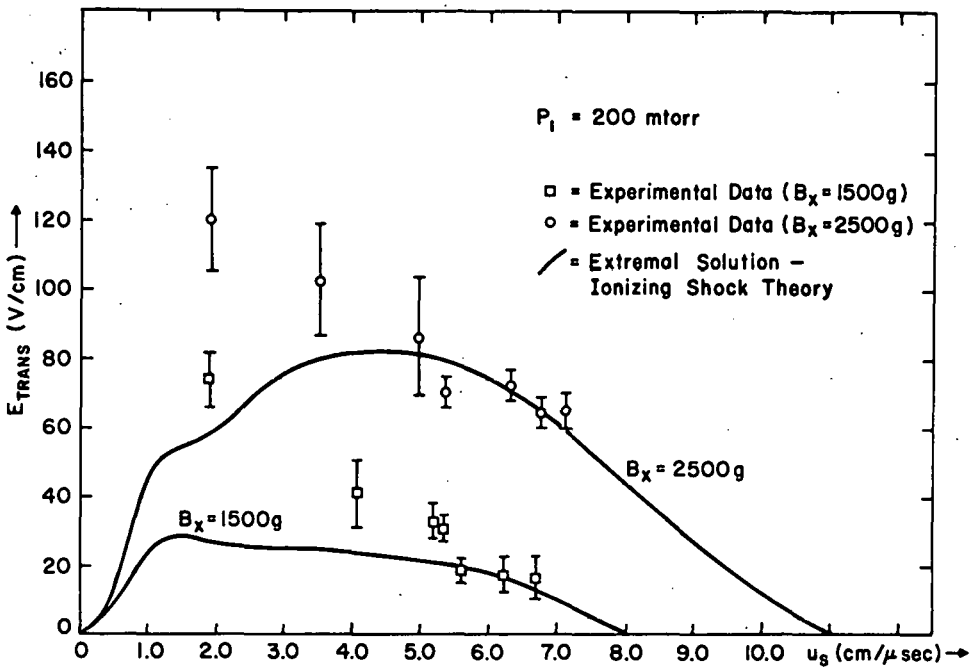

Fig. 2. Transverse electric field as a function of shock speed and axial magnetic field

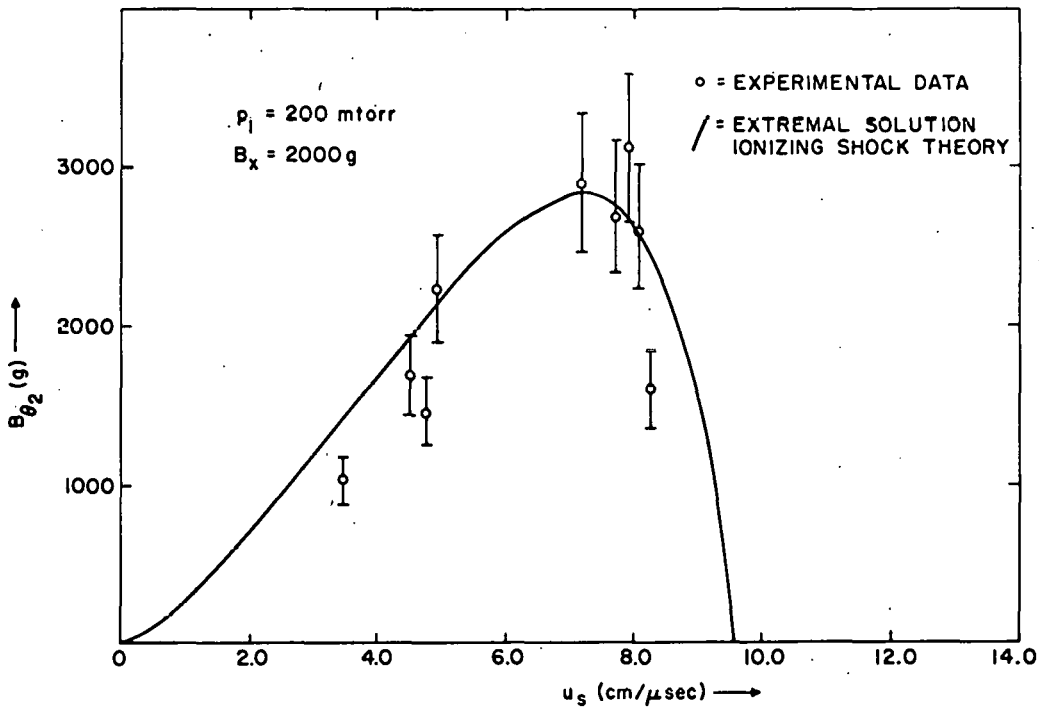

Fig. 3. Switch-on magnetic field as a function of shock speed

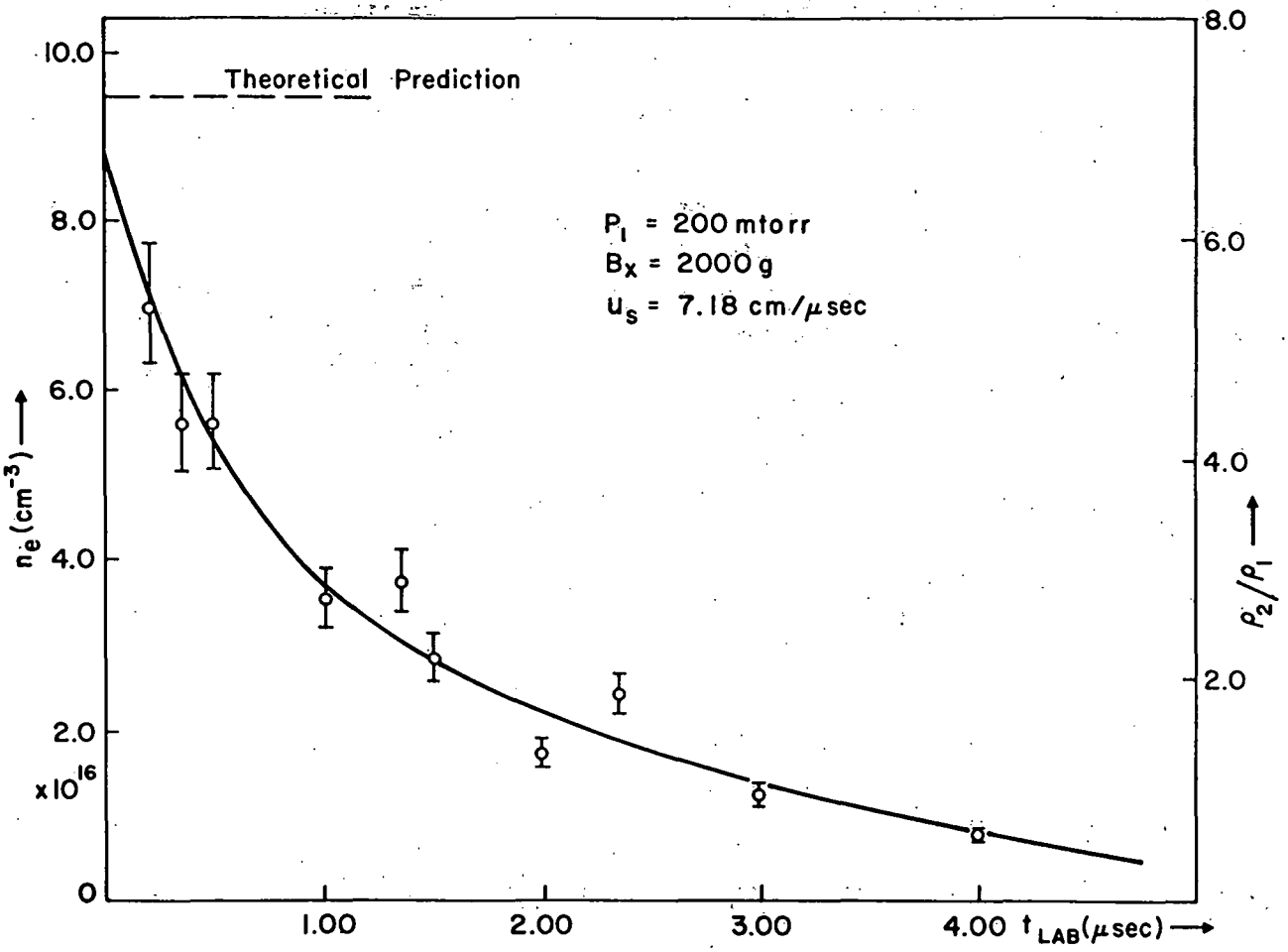

Fig. 4. Profile of electron density and compression ratio

TABLE I

COMPARISON OF THEORETICAL AND EXPERIMENTAL PARAMETERS FOR A NORMAL IONIZING SHOCK WAVE

Given conditions: p_1=200 mtorr; B_x=2000 g; u_s=7.18 cm/μsec=1.87 u_{Alf_1}

Property	Experimental Value	Theoretical Value (Chapman-Jouguet Solution)
I_{drive}	70 ± 7 KAmp	65 ± 6 KAmp
B_{sw-on}	(2.90 ± .45)x10^3 g	(2.86 ± .29)x10^3 g
E_{trans}	38 ± 14 V/cm	34.5 ± 3.5 V/cm
ρ_2/ρ_1	6.6 ± .8	7.3 ± .7
T_2	(16.0 ± 2.6)x10^3 °K	(25.0 ± 2.5)x10^3 °K

COMPARISON OF ION PROBE AND DOUBLE LANGMUIR PROBE MEASUREMENTS ON PLASMA BLOBS

by

D.G. Fearn and E.R. Wooding

Department of Physics
Royal Holloway College
(University of London)
Englefield Green,
Surrey, England

ABSTRACT

A comparison has been made of electron densities and temperatures determined from a Faraday-cup ion probe[1] and a double Langmuir probe under conditions where the latter has been reported to give results consistent with spectroscopic measurements[2]. Both probes were inserted into the plasma ejected at about 10^6 cm/sec from a conical z-pinch plasma gun[3]. Saturation of the ion probe collector current occurred only with apertures less than about 0.025 cm in diameter or low density plasmas. The double probe yielded n_e = 1 to 4 x 10^{15} cm^{-3} and T_e = 1 to 3 x 10^4 deg. K, whilst values of n_e from the ion probe were lower by a factor 10, with T_e greater by a factor 3. Calorimeter measurements of the total plasma energy were consistent with the double probe results when an allowance was made for the presence of neutral particles.

Introduction

The Faraday-cup ion probe[1] used to measure ion and electron number densities n_i and n_e[4,5] in plasma blobs consists of a collector electrode situated behind an aperture of diameter d, which defines a beam of plasma flowing into the probe with velocity v. When biased to collect only ions, the electrode current is

$$i = \frac{\pi}{4} d^2 \, e \, v \, n_e \qquad (1)$$

where e is the electron charge. If v and the ion charge Ze are known n_e, n_i, and the ion energy distribution may be evaluated.

It has been assumed previously that equation (1) is correct, provided that the collector repels all electrons[1]. In the present work, however, full voltage-current characteristics for an ion probe in the exhaust of a conical z-pinch plasma gun[3] indicated that this assumption is invalid. Further measurements were therefore made using a double Langmuir probe.

Description of the Probes and Plasma Gun

The ion probe (Fig.1a) had an aperture with a diameter variable from 0.09 to 1.0 mm. The bias voltage V_a was applied between the collector and shield. When plasma entered the probe a current i flowed, and a voltage V_e = iR appeared across resistance R; the bias was then $V_b = V_a - V_e$. The circuit was electrically floating, since the electrical interference was increased by earthing the shield, whereas i was unchanged.

The double Langmuir probe (Fig.1b) consisted of two platinum wires of 0.05 cm diameter sealed into a glass double capillary tube. The bias circuit incorporated a reversing switch, and the resistance R was divided equally between the two leads. As found by others[6], i was drastically reduced by surface contamination, so the platinum surfaces were cleaned by ion bombardment before each measurement was made, giving a reproducibility better than 10%.

The probes were placed 35 cm from the ring

electrode of a conical z-pinch plasma gun[3], which was fired 500 μsec after the admission of 10^{-4} gm of argon. It produced two plasma blobs, the first being formed from the radial current sheet at the ring electrode, and the second by the expulsion of the pinched plasma from between the electrodes. A calorimeter[7] indicated that the total plasma energy was 1.2 J/cm^2 at the probe position.

The usual time-of-flight method[1,4,5] of deducing flow velocities is valid only if this time is much longer than the plasma emission time. This was true for the first plasma blob, in which v varied from 1.8 to 1.2 cm/μsec, but the second was emitted over about 7 μsec, causing the derived velocities, of 1.2 to 0.5 cm/μsec, to be approximate.

The Ion Probe Experiment

A series of oscillograms was taken of V_e as V_a was increased from 0 to 70 V, with several aperture sizes, and the peak current for each plasma blob was plotted against V_b. If equation (1) is valid, these characteristics should rise to a saturation value of i, but, as seen in Fig.2, saturation only occurred with the smallest apertures. Moreover, when saturation did occur, the bias required depended on the aperture diameter.

From integration of equ.(1), the areas of the oscillograms of V_e were proportional to the total number of ions entering the probe if all electrons were repelled by the collector. These areas were therefore expected to be constant for sufficiently high V_b, but this prediction was not confirmed experimentally.

When saturation of the probe current occurred, calculations indicated that n_e reached 8×10^{13} cm^{-3} in the first plasma blob, and 4×10^{14} cm^{-3} in the second. Assuming that the rise of the characteristics to saturation was explainable by Langmuir probe theory, and that kT_e was much greater than the electron directed energy, T_e was found to be 4 to 6 eV. The total directed ion energy, 0.03 J/cm^2, was a factor 40 smaller than the calorimeter result. As this discrepancy was too large to be attributed to thermal energy or to the presence of fast neutral atoms, a comparison with another measurement technique was desirable. The double Langmuir probe was chosen as it is simple to construct and use, and it has been shown to give results consistent with spectroscopic measurements[2] in conditions similar to those investigated here.

The Langmuir Probe Experiment

Double probe voltage-current characteristics were plotted for a number of positions along the plasma column using oscillograms taken of V_e as V_a was varied from 0 to $\pm$ 25 V. These characteristics, which were of the expected symmetrical shape with slight slopes in the saturation regions, yielded values of n_e a factor 10 greater than given by the ion probe, reaching 2.5×10^{15} cm^{-3} in the first plasma blob, and 4×10^{15} cm^{-3} in the second (Fig.3). T_e fell from 3×10^4 °K at the luminous front to 10^4 °K in the second plasma blob, then rose slightly. These values were considerably lower than those deduced from the ion probe. Assuming Z = 1 and the ion and electron temperatures to be equal, the directed energy of the ions was estimated to be 0.37 J/cm^2, and the plasma thermal energy to be 0.06 J/cm^2.

A basic assumption of the usual probe theory is that ion and electron mean free paths are much larger than the probe size. However, calculations using the information in Fig.3 showed that these mean free paths were, in the present case, considerably smaller than the probe diameter. In a stationary plasma, resulting errors in derived values of T_e are small, but n_e is reduced in the vicinity of the probe[8]. A diffusion analysis is then necessary to obtain values of n_e appropriate to the undisturbed plasma. Czech and Theenhaus[2] have, however, compared double probe and spectroscopic measurements in an electromagnetic shock tube, and obtained agreement for $n_e \leq 10^{16}$ cm^{-3}, suggesting that the present results are reliable. This conclusion was supported by an analysis of the diffusion of particles to the probe, which showed that insufficient time was available for a significant depletion of n_e to occur in a plasma element crossing the probe end, due to the high flow velocity.

The probe response time of 0.1 nsec. defined as the time for an ion to cross a sheath of a Debye length thickness[9], was appreciably less than the flow time across the probe end, 0.3 to 1.0 μsec.

Discussion

The double probe measurements gave a value of the total plasma energy, about 0.4 J/cm^2, in reasonable agreement with the calorimeter result of 1.2 J/cm^2. The discrepancy may be explained if fast neutral atoms carried 60 to 70% of the energy received by the calorimeter.

It was concluded that the ion probe gave erroneous results under the present conditions. Time-resolved photographs of the flow distortion caused by the probe (Fig.4a) showed that this was due to the collection of dense stagnant plasma in front of the probe. This reduced the amount of plasma flowing into the aperture, causing derived densities to be low, and only the faster electrons were admitted, explaining the high temperatures deduced from the voltage-current characteristics. This flow perturbation, which was predicted earlier by Demidenko et al.[4], will be of importance in any device admitting plasma through a small aperture[1, 10], except when the aperture lies in a wall normally containing the plasma.

Photographs of the flow perturbation caused by the double probe indicated that this was very small near the exposed platinum surfaces, except possibly in the most dense region of the second plasma blob (Fig.4b). The disturbance in front of the ion probe was always considerably more severe.

Conclusions

Voltage-current characteristics for an ion probe in a flowing plasma exhibited saturation only when small apertures were used, suggesting that the simple theory was invalid. The total plasma energy derived from these results was a factor 40 below that from calorimeter measurements, whereas a double Langmuir probe yielded densities and energies consistent with the calorimeter experiment if the plasma was 30 to 40% ionised.

It was concluded that the ion probe gives quantitatively significant results only for $n_e << 10^{14}$ cm^{-3}. The double Langmuir probe is probably more accurate if density perturbations can be accounted for.

Acknowledgements

The authors thank the Ministry of Technology for supporting this work. They are also indebted to Mr P.R.J. Smith and Mr G. Roberts for assistance in constructing the apparatus.

References

1. Ashby, D.E.T.F., Gooding, T.J., Hayworth, B.R., and Larson, A.V., A.I.A.A.J., 3, 1140-1142 (1965).
2. Czech, J., and Theenhaus, R., Proc.7th Int. Conf.Ionis.Phen.Gases, Belgrade, 2, 774-777 (1966).
3. Fearn, D.G., and Wooding, E.R., Brit.J.Appl. Phys., 18, 213-218 (1967).
4. Demidenko, I.I., Lomino, N.S., Padalka, V.G., Safronov, B.G., and Sinelnikov, K.D., J.Nucl. En., Pt C, 8, 433-445 (1966).
5. Little, P.F., and Avis, B.E., J.Nucl.En., Pt C, 8, 11-20 (1966).
6. McLaren, T.I., Fox, J.N., and Hobson, R.M., Nature, 198, 1264-1265 (1963).
7. Azovskii, Yu.S., Guzhovskii, I.T., and Safronov, B.G., Sov.Phys.- Tech.Phys., 9, 784-785 (1964).
8. Little, R.G., and Waymouth, J.F., Phys.Fluids, 9, 801-808 (1966).
9. Nation, J.A., and Simpson, D., Brit.J.Appl. Phys., 16, 1705-1709 (1965).
10. Mason, D.W., J.Nucl.En., Pt C, 6, 553-558 (1964).

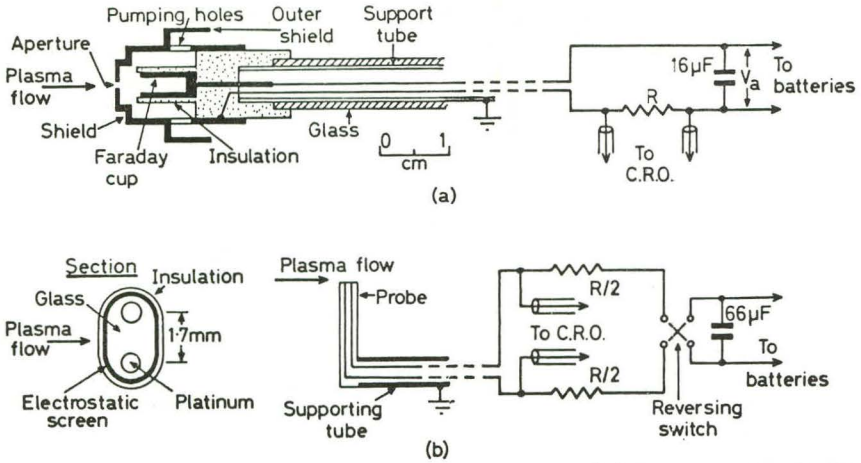

Fig. 1. (a) The ion probe and bias circuit, and (b) the Langmuir double probe and bias circuit.

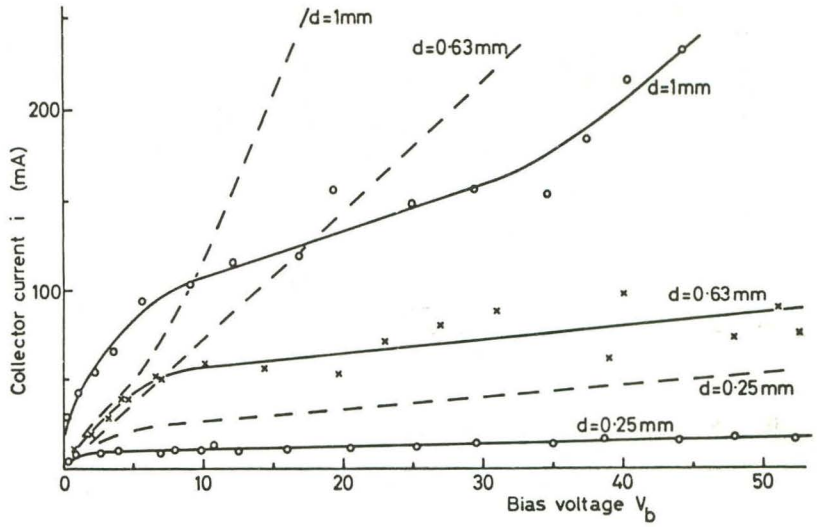

Fig. 2. Ion probe voltage-current characteristics. The full lines and experimental points are for the first plasma blob, and the dashed lines are for the second.

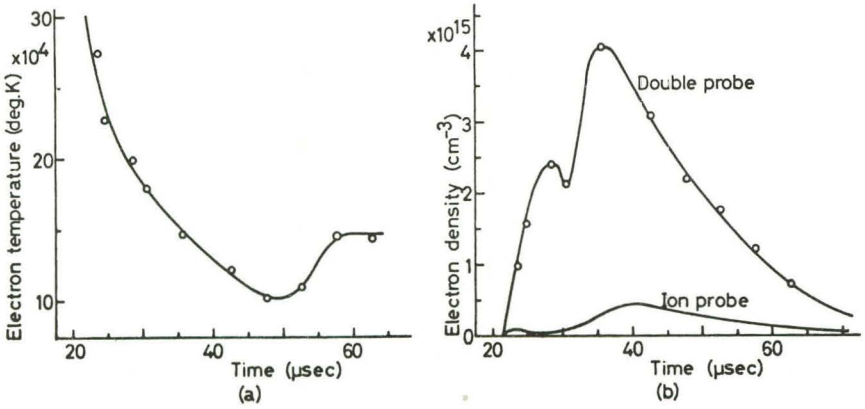

Fig. 3. Measured properties of the plasma column. (a) Electron temperature from the double probe, and (b) electron number density from the double probe and the ion probe. Time is with respect to breakdown in the plasma gun.

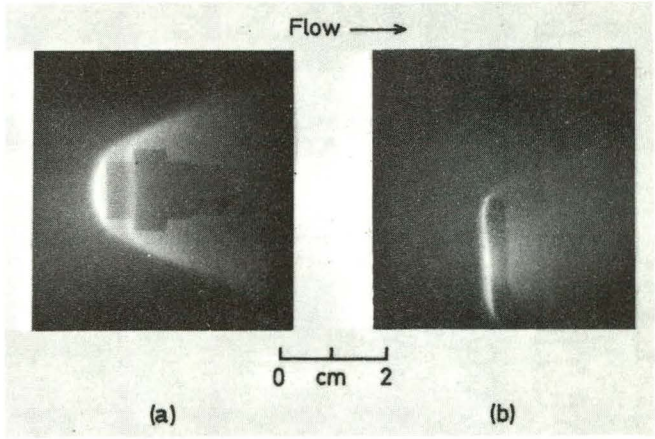

Fig. 4. Photographs of the plasma flow around (a) the ion probe, and (b) the double Langmuir probe, 38 μsec after breakdown in the plasma gun. Exposure times are 1 μsec.

NUMERICAL CALCULATIONS IN MAGNETOHYDRODYNAMICS

by

Klaus Hain*
Naval Research Laboratory
Washington, D.C. 20390

ABSTRACT

Numerical solutions for one-dimensional time-dependent problems in magnetohydrodynamics are widely used for the interpretation and planning of experiments. Since the extension of these calculations to more dimensions is now feasible, it is appropriate to summarize the basic assumptions and numerical methods for the solution of one-dimensional fluid dynamic problems. Computing schemes for two-dimensional magnetohydrodynamics are discussed. A simple implicit difference scheme is developed. The boundary conditions are treated by means of Green's functions.

Introduction

Numerical solutions of one-dimensional plasma problems in the magnetohydrodynamic approximation have been successfully compared with experiments.[1-5] They have been and still are a powerful tool for analyzing and interpreting θ-pinch experimental data, for example, time and space resolved measurements can be compared with the calculations in order to determine if classical diffusion exists in a plasma.

Several programs have been developed for this purpose;[6-7] and the Culham program (D. Fisher, K. V. Roberts) is especially well documented and easy to use. It is only necessary to specify the initial parameters for density, temperature, etc., and the characteristics of the external magnetic field.

As computers become more powerful and the measurements become more accurate and detailed, it is necessary to carry out the magnetohydrodynamics calculations in more than one dimension. The basic numerical procedures and boundary conditions will be discussed in this paper.

*Work performed while at the NASA Goddard Space Flight Center.

Before examining the details of the general problem it seems appropriate to review briefly the basic fluid dynamic assumptions and by so doing to clarify their range of applicability. Generally speaking, the fluid equations are moment equations obtained from the Boltzmann or Fokker-Planck equation. If the fluid is near thermal equilibrium the expansion can be terminated so that only the moment equation for density, momentum and energy remain (the pressure may be a tensor for a plasma in a strong magnetic field). It turns out that a higher moment expansion (i.e. the 13 moment expansion) only gives good results if the fluid is near thermal equilibrium.

The fluid approximation, as it will be here understood, has only three moments and is strictly valid for fluids near thermal equilibrium, which means that there must be enough collisions to establish a Maxwell velocity distribution in times short compared with times in which the macroscopic quantities change.

In the case of a nonthermal, turbulent plasma an effective particle-wave collision frequency can be introduced in an adhoc fashion for comparison

with observations. Fluid dynamic's equations describe the macroscopic behaviour of the plasma. Measurements correspond to an average over a volume and a certain time interval (i.e. time resolution of magnetic probes, satellite measurements of plasma temperature and densities during a finite flight interval). Microinstabilities give rise to disorder in a finite volume, and entropy changes in a macroscopic system.

An average will be defined here by

$$\bar{A}(x,t) = \int d^3\xi\, d\tau\, A(x+\xi, t+\tau) f(\xi,\tau)$$

where $f(\xi,\tau)$ is a weight function and

$$\int d^3\xi\, d\tau\, f(\xi,\tau) = 1$$

An average entropy defined in this way can be increased. The interaction of these plasma elements have to be calculated to determine the transport coefficients, but the basic structure of the equations will not be changes. For extension of the magnetohydrodynamic equations see for example; C. F. Kennel, J. M. Green[10] and A. Simon, W. B. Thompson[11].

II Fluid Equations

The fluid equations for one specie are:

$$\frac{\partial \rho}{\partial t} + \vec{\nabla}(\rho\vec{v}) = \rho \cdot S$$

$$\frac{\partial}{\partial t}(\rho\vec{v}) + \vec{\nabla}(\rho\vec{v}\cdot\vec{v}) + \vec{\nabla}p + \frac{e\rho}{m}(\vec{E}+\vec{v}\times\vec{B}) = \vec{\pi} \qquad (1)$$

$$\frac{\partial}{\partial t}\left(\tfrac{1}{2}\rho v^2 + \frac{1}{\gamma-1}p\right) + \vec{\nabla}\left[\left(\tfrac{1}{2}\rho v^2 + \frac{\gamma}{\gamma-1}p\right)\vec{v}\right] + \frac{e\rho}{m}(\vec{E}\cdot\vec{v}) = \varepsilon$$

where S is a source term, $\vec{\pi}$ the momentum interchange, ε the energy interchange and the other symbols have their usual meaning.

$$\vec{\pi}^K = \vec{\pi}^{(o)K} + \sum_j d_p^{jK}(\vec{v}^j - \vec{v}^K) n_j n_K$$

$$\varepsilon^K = \varepsilon^{(o)K} + \sum_j d_\varepsilon^{jK}(T^j - T^K) n_j n_K + \varepsilon^{(3)K} \qquad (2)$$

$$n_j = \rho_j / m_j$$

the indices indicate different fluids with d_p^{ik} the coefficient for momentum interchange d_ε^{ik} the coefficient for energy interchange, ε_S radiation loss, π_o viscosity term, ε_o heat conduction. Eq. (1) can be written also in the following way with $T = p/\rho$.

$$\left(\frac{\partial}{\partial t} + \vec{v}\vec{\nabla}\right)\rho + \rho\, div\,\vec{v} = \rho S$$

$$\rho\left(\frac{\partial}{\partial t} + \vec{v}\vec{\nabla}\right)\vec{v} + \vec{\nabla}p + e\cdot n(\vec{E} + \vec{B}\times\vec{v}) = \vec{\pi} - \rho S\cdot\vec{v} \qquad (3)$$

$$\left(\frac{\partial}{\partial t} + v\vec{\nabla}\right)T + (\gamma-1)T\, div\,\vec{v} = \frac{\gamma-1}{\rho}\left[\varepsilon + \tfrac{1}{2}\rho S v^2 - \frac{1}{2}\vec{\pi}\vec{v}\right]$$

The Maxwell equations complete the set:

$$\frac{\partial \vec{B}}{\partial t} = \vec{\nabla}\times\vec{E}$$

$$div\,\vec{E} = \Sigma e_j n_j$$

$$\vec{j} = \vec{\nabla}\times\vec{B} \qquad (4)$$

Here the displacement current is neglected since the Alfvèn velocity is generally small compared to light velocity. If the frequencies under consideration are less than the plasma frequency, $\omega_p = \sqrt{\frac{4\pi e^2 n_e}{m_e}}$ or if the lengths are greater than v_s/ω_p, where v_S is the sound speed, then the assumption of quasineutrality can be made

$$\Sigma e_j n_j = 0 \qquad (5)$$

which replaces the second equation in (4). By computing $\vec{E}$ from equation (3) the validity of this assumption can be checked.

The plasma equations in the limit $m_e/m_i \to o$ are

$$\frac{\partial \rho}{\partial t} + \vec{\nabla}(\rho\vec{v}) = \rho\cdot S$$

$$\frac{\partial}{\partial t}(\rho\vec{v}) + \vec{\nabla}(\rho\vec{v}\cdot\vec{v}) + \vec{\nabla}\left(p^i + p^e + \frac{B^2}{2}\right) - \vec{\nabla}(\vec{B}\cdot\vec{B}) = \vec{\pi}^p + \sum_j d_p^{jp}(\vec{v}_j - \vec{v})$$

$$\frac{\partial}{\partial t}\left(\tfrac{1}{2}\rho v^2 + \frac{1}{\gamma-1}(p^i + p^e)\right) + \vec{\nabla}\left[\left(\tfrac{1}{2}\rho v^2 + \frac{\gamma}{\gamma-1}(p^i + p^e)\right)\vec{v}\right] + \vec{E}\cdot\vec{j} = \varepsilon \qquad (8)$$

$$\vec{E} + \vec{v}\times\vec{B} = \mu\cdot\vec{j} + \frac{1}{en}(\vec{B}\times\vec{j} + \vec{\nabla}p^e)$$

$$\mu = \frac{1}{e^2}\left(d^{ie} + \frac{n^e}{n} d^{oe}\right)$$

Inertia terms in the modified Ohm's law can be neglected if the drift kinetic energy of the electrons remains small. It may be of importance in very fast pinches or if the resistive skin depth is large compared to the "collisionless" skin depth c/ω_{pe}.

Maxwell equation

$$\left(\frac{\partial}{\partial t} + \vec{v}\vec{\nabla}\right)\vec{A} = \overleftrightarrow{\mu}\cdot\vec{j} \qquad (9)$$
$$\vec{B} = \vec{\nabla}\times\vec{A}$$

with the condition

$$\vec{\nabla}\vec{A} = 0$$

and

$$\vec{j} = \vec{\nabla}\times\vec{B} = \nabla^2\vec{A}$$

For one-dimensional problems the last two terms in the modified Ohm's law disappear. For a multidimensional flow the surface of constant temperature and that of constant density are not necessarily the same. This may be important in a rotating star; i.e. if the temperature is constant along the surface and the pressure is a function of the latitude θ, this would start a current system with r,θ components which in turn causes a rotation v_φ which is a function of θ. This could cause a turbulent plasma flow field which may be responsible for the sunspots. In laboratory plasmas the importance of the Hall term $\vec{j}\times\vec{B}$ for explaining plasma rotation in a θ-pinch has been shown by A. C. Kolb and P. C. Thoneman.[22]

One can write the plasma equation in an integral form, which may be useful for the utilization of higher order computation schemes. Let dV be a volume element and $\vec{df}$ the surface element with the unit vector pointing outward, then

$$\frac{\partial}{\partial t}\int \rho\, dV = -\int \vec{df}\,\rho\vec{v} + \int \rho S\, dV$$

$$\frac{\partial}{\partial t}\int \rho\vec{v}\, dV = -\int \vec{df}\left[(p^i+p^e) + \frac{B^2}{2}\right] - \int \vec{df}\,(\rho\vec{v}\cdot\vec{v} - \vec{B}\cdot\vec{B}) + \int \vec{\pi}\, dV$$

$$\frac{\partial}{\partial t}\int\left(\frac{1}{2}\rho v^2 + \frac{1}{\gamma-1}(p^i+p^e) + \frac{B^2}{2}\right)dV \qquad (10)$$
$$= -\int \vec{df}\left[\left(\frac{1}{2}\rho v^2 + \frac{\gamma}{\gamma-1}(p^i+p^e)\right)\vec{v} + \vec{E}\times\vec{B}\right] + \int \varepsilon\, dV$$

These equations may be also written in a more familiar way by using the temperature

$$\left(\frac{\partial}{\partial t} + \vec{v}\vec{\nabla}\right)\rho + \rho\, div\,\vec{v} = \rho S$$

$$\left(\frac{\partial}{\partial t} + \vec{v}\vec{\nabla}\right)\vec{v} + \frac{1}{\rho}\left[\vec{\nabla}(p^i+p^e) + B\times j\right] = \vec{\pi} - \rho S\vec{v}$$

$$\left(\frac{\partial}{\partial t} + \vec{v}\vec{\nabla}\right)(T^i+T^e) + (\gamma-1)(T^i+T^e)\, div\,\vec{v} \qquad (11)$$
$$= \frac{\gamma-1}{\rho}\left[\varepsilon - \frac{1}{2}\vec{\pi}\vec{v} + \left[(T^i+T^e)\rho S - \frac{1}{2}\rho v^2 S\right]\right]$$

and

$$\left(\frac{\partial}{\partial t} + \vec{v}\vec{\nabla}\right)(T^e - T^i) + (\gamma-1)(T^e-T^i)\, div\,\vec{v} = \varepsilon'\frac{\gamma-1}{\rho}$$

(ε' includes ohmic heating)

These equations can be written in the general form

$$\left(\frac{\partial}{\partial t} + \vec{v}\vec{\nabla}\right)\eta_j + \sum_K \eta_K \overleftrightarrow{A}_{Kj}\vec{\nabla}\cdot\vec{\sigma} = \sum_K D_{jK}\eta_K + \varepsilon_j \qquad (12)$$

$$\left(\frac{\partial}{\partial t} + \vec{v}\vec{\nabla}\right)\vec{v} + \sum_K \overleftrightarrow{g}_K\vec{\nabla}\eta_K = D_\sigma\vec{v} + \vec{\pi}$$

where

$$\eta_j = \begin{pmatrix} \rho \\ T^i+T^e \\ T^e-T^i \\ \vec{B} \end{pmatrix}$$

$$D_{jK} = \alpha_j^{(1)}\vec{\nabla}\overleftrightarrow{\alpha}_{jK}^{(2)}\vec{\nabla} \qquad (13)$$

III Numerical Procedures

If the diffusion coefficient d is of the order $d \approx \Delta x\cdot\sigma_c$, where Δx is the mesh actually used and v_c the characteristic velocity, the purely hydrodynamic terms and their properties will dominate. Since the diffusion terms are small one can solve the Eq. (12) in two separate steps; first the diffusion term, then the hydrodynamic terms [8,13]. The diffusion equation (in the simplest form) is

$$\frac{\partial\eta}{\partial t} = \mu\nabla^2\eta + \varepsilon \qquad (14)$$

In one-dimension one solves this problem by the implicit method for the space points x_i

$$\eta_i^{t+\delta t} - \eta_i^t = \frac{1}{2}\mu \frac{\delta t^2}{\Delta x^2}\left(\eta_{i+1}^{t+\delta t} - 2\eta_i^{t+\delta t} + \eta_{i-1}^{t+\delta t} + \eta_{i+1}^t - 2\eta_i^t + \eta_{i-1}^t\right) \quad (15)$$

In two-dimensions the alternating direction method is used to obtain $\eta_{j,K}^{t+\delta t}$

$$\eta_{j,K}^{t+\delta t/2} - \eta_{j,K}^t = \frac{1}{2}\mu \frac{\delta t}{\Delta x^2}\left(\eta_{j+1,K}^{t+\delta t/2} - 2\eta_{j,K}^{t+\delta t/2} + \eta_{j-1,K}^{t+\delta t/2} + \eta_{j,K+1}^t - 2\eta_{j,K}^t + \eta_{j,K-1}^t\right)$$

$$\eta_{j,K}^{t+\delta t} - \eta_{j,K}^{t+\delta t/2} = \frac{1}{2}\mu \frac{\delta t}{\Delta x^2}\left(\eta_{j+1,K}^{t+\delta t/2} - 2\eta_{j,K}^{t+\delta t/2} + \eta_{j-1,K}^{t+\delta t/2} + \eta_{j,K+1}^{t+\delta t} - 2\eta_{j,K}^{t+\delta t} + \eta_{j,K-1}^{t+\delta t}\right) \quad (16)$$

Appropriate boundary conditions should be applied with the same accuracy as the difference scheme used, which requires the use of second order formula in space and time. If the boundary conditions are less accurate the accuracy will be reduced. Both schemes are unconditionally stable.

The characteristics $\vec{\lambda}$ along which hydrodynamic waves travel are:

$$\vec{\lambda} = \vec{v}$$
$$\vec{\lambda} = \vec{v} + \vec{e}\sqrt{\vec{e}\sum_{j,K} \overleftrightarrow{A}_{j,K}\cdot\overleftrightarrow{g}_K\cdot\vec{e}}, \quad (17)$$

where $\vec{e}$ is a unit vector. For a plasma this gives

$$\vec{\lambda} = \vec{v} + \vec{e}\sqrt{\gamma T + (\vec{e}\times\vec{B})^2/\rho}$$

which reduces to the Alfven speed along the direction $\vec{e}$.

The hydrodynamic equations for one variable η are

$$\left(\frac{\partial}{\partial t} + \vec{v}\vec{\nabla}\right)\eta + A(\eta - q)\,\mathrm{div}\,\vec{v} = 0$$
$$\left(\frac{\partial}{\partial t} + \vec{v}\vec{\nabla}\right)\vec{v} + g\vec{\nabla}\eta = \vec{\nabla}\cdot q. \quad (18)$$

These equations for only one variable do not limit the generality of the following discussion.

The characteristics are real and given by

$$\vec{\lambda} = \vec{v} + \vec{e}\,v_c$$
$$v_c = \sqrt{A\cdot g}$$

In a time interval Δt disturbances travel a distance Δr

$$\Delta r^2 = \Delta t^2(\vec{v} + \vec{e}\,v_c)^2$$

As this system has only real characteristics it is an initial value problem. The number of boundary conditions to be specified is the number of characteristics which cross the boundary.

Equations of this type with variable characteristic and viscosity $q = 0$ do not have a continuous and unique solution in space. It is well known that every disturbance will develop shock fronts and other discontinuities. To determine the solution uniquely one has to specify that the entropy should always increase through the shock. Equation (18) is reversible in time without shocks.

As for the simplicity in the computation scheme one usually wants to work with continuous solutions. Fitting procedures on shock fronts (or other discontinuities) are very cumbersome. If the natural viscosity is not big enough one uses the von Neumann[13] term:

$$q = 0 \quad \text{if } (\mathrm{div}\,\vec{v}) \geq 0$$
$$= -N_s^2\Delta x^2(\mathrm{div}\,\vec{v})^2 \quad \text{if } (\mathrm{div}\,\vec{v}) < 0 \quad (19)$$

which ensures energy conservation and entropy increase and gives a shock transition in N_s meshpoints.

It is important to use implicit computation schemes, if possible, which are not restricted by the requirement

$$\Delta t < |v_c|\,\Delta x$$

This can be done by using the future values $\eta^{t+\delta t}$, $v^{t+\delta t}$ of the next time step together with the values of the last step to compute the new $\eta^{t+\delta t}$, $v^{t+\delta t}$ instead of using solely the old points.

Before going into details in the discussion on feasible computing schemes for one and two-dimensional problems one has to compute the convection terms $\vec{v}\,\vec{\nabla}$ (which may include centrifugal and coriolis forces).

These convection terms are actually obtained by interpolation using the vector $\vec{v}\,\Delta t/\Delta x$. If such an interpolation is done very often it can introduce an extra diffusion which can completely obscure the real diffusion. In one-dimension one employs a Langrangian scheme and infrequent interpolation backwards if the mesh is too distorted[8]. Applying the same technique in two or more dimensions would imply using a non-orthogonal net. The formulas for that method are somewhat lengthy and could cause the computer time to go up considerably. The other alternative is to interpolate in each time step.

Using higher order interpolation formulas may cause artificial spikes (or dips). One scheme which seems to work satisfactorily is the following:

Let $\eta\ i+1$, $\eta\ i$, $\eta\ i-1$ be the variable points for interpolation and $d = -v\,\Delta t\ /\ \Delta x$ the interpolation factor, then

$$\tilde{\eta} = \eta_i + \tfrac{1}{2} d\,(\eta_{i+1} - \eta_{i-1} + d(\eta_{i+1} - 2\eta_i + \eta_{i-1})) \qquad (20)$$

if

$$\tfrac{1}{4} < (\eta_{i+1} - \eta_i)/(\eta_i - \eta_{i-1}) < 4$$

else

$$\tilde{\eta} = \eta_i + d(\eta_{i+1} - \eta_i) \quad \text{if } d \geq 0$$

$$\tilde{\eta} = \eta_i + d(\eta_i - \eta_{i-1}) \quad \text{if } d < 0$$

IV One-dimensional Programs

Choosing η at integral space points x_j and v at half integral space points $x_{j+1/2}$, Eq. (18) yields the following difference equation in Langrangian form.

$$\hat{\eta}_j - \eta_j + \frac{A\cdot\Delta t}{2\cdot\Delta x}\left(\hat{v}_{j+1/2} - \hat{v}_{j-1/2} + v_{j+1/2} - v_{j-1/2}\right)\cdot\tilde{\eta}_j = 0$$

$$\hat{v}_{j+1/2} - v_{j+1/2} + \frac{\Delta t}{2\Delta x}\,\tilde{g}_{j+1/2}\left(\hat{\eta}_{j+1} - \hat{\eta}_j + \eta_{j+1} - \eta_j\right) = 0. \qquad (21)$$

Here $\sim$ denotes a mean value and Λ the value after $t+\Delta t$.

Substitution of the first equation into the second gives a second order difference equation for $\hat{v}$

$$\hat{v}_{j+1/2} - v_{j+1/2} + \frac{\Delta t}{\Delta x}\,\tilde{g}_{j+1/2}(\eta_{j+1} - \eta_j) + \tfrac{1}{2}\frac{\Delta t^2}{\Delta x^2}\,v^2_{c_{j+1/2}}\left[\hat{v}_{j+3/2} - 2\hat{v}_{j+1/2} + \hat{v}_{j-1/2}\right] \qquad (22)$$

This scheme is unconditionally stable with the amplification factor $|\sigma|=1$. The equation can be iterated to obtain improved mean values for $\tilde{g}_j$ and $\tilde{\eta}_j$. The iteration converges very fast, usually at the second iteration step. Due to the iteration procedure the computation time per timestep takes longer, but the increased timestep compensates for this.

The earlier schemes used a fixed but nonuniform mesh with fixed boundaries[12]. The method developed at the Culham Laboratory has a variable boundary and is essentially Langrangian. Mesh adjustments are made infrequently so that the interpolation errors which give rise to increased mass and diffusion are negligible compared to errors in older Eulerian schemes.

V "1.5 Dimensional" Programs

In some problems the time variation in one dimension can be considered as quasistationary; namely, in cases with a strong magnetic field. If the Alfven velocity v_a perpendicular to the field lines is so high that

$$t_c \gg R/v_a$$

where R is a characteristic dimension perpendicular to the magnetic field and t_c is some characteristic time. In this case the inertia terms in this direction can be neglected. Also as relatively few mesh points are needed in this direction, the computation is relatively fast. Numerical calculations for a Theta-pinch with parallel fields have been carried out earlier[14].

VI Two-dimensional Programs

Calculations in more than one dimension are simplest with an Eulerian scheme with a fixed othogonal net. This method requires interpolation in each timestep for the convective terms.

As pointed out before changes in the variables are relatively small in time intervals $\Delta t = \Delta x/v_c$.

Therefore one should use either explicit formulas with high accuracy in the space dimension or implicit formulas where the timestep is limited by the specified truncation error.

Explicit schemes using higher order difference formulae have been developed by K.V. Roberts.[15] These difference schemes are based on the integral conversation laws as given in Eq. (10). Although it is difficult to estimate the overall error it has been shown that the unphysical distortion by convection could be greatly reduced.

A simple implicit scheme, second order in time and space is given below.

The equations for the two-dimensional case are:

$$\frac{d\gamma}{dt} + A\gamma \operatorname{div}\vec{v} = 0$$
$$\frac{dv_1}{dt} + g_1 \frac{\partial \gamma}{\partial x_1} = 0 \qquad \frac{dv_2}{dt} + g_2 \frac{\partial \gamma}{\partial x_2} = 0 \tag{23}$$

Let ∇, Δ designate the difference operators

$$\nabla (j) = (j) - (j-1)$$
$$\Delta (j) = (j+1) - 2(j) + (j-1) \tag{24}$$

Intermediate values for the velocities v_1 and v_2 are computed in the following way

$$\left(1 - \frac{v_c^2 \Delta t^2}{4 \Delta x_1^2} \Delta_1\right) \bar{v}_1 (j+1/2, k) = \left(1 + \frac{v_c^2 \Delta t^2}{4 \Delta x_1^2} \Delta_1\right) v_1 (j+1/2, k) + \frac{v_c^2 \Delta t^2}{2 \Delta x_1 \Delta x_2} \nabla_1 \nabla_2 v_2 (j+1, k+1/2) - \tilde{g}_1 \nabla_1 \gamma$$

$$\left(1 - \frac{v_c^2 \Delta t^2}{4 \Delta x_2^2} \Delta_2\right) \bar{v}_2 (j, k+1/2) = \left(1 + \frac{v_c^2 \Delta t^2}{4 \Delta x_1^2} \Delta_2\right) v_2 (j, k+1/2) + \frac{v_c^2 \Delta t^2}{2 \Delta x_1 \Delta x_2} \nabla_1 \nabla_2 v_1 (j+1/2, k+1) - \tilde{g}_2 \nabla_2 \gamma (j, k+1) \frac{\Delta t}{\Delta x} \tag{25}$$

Comparison with the one-dimensional equation the above obvious.

Values at t + Δt are then computed from

$$\left(1 - \frac{v_c^2 \Delta t^2}{4 \Delta x_1^2} \Delta_1\right) \hat{v}_1 (j+1/2, k) = \left(1 + \frac{v_c^2 \Delta t^2}{4 \Delta x_1^2} \Delta_1\right) v_1 (j+1/2, k) + \frac{v_c^2 \Delta t^2}{4 \Delta x_1 \Delta x_2} \nabla_1 \nabla_2 \left(\bar{v}_2 (j+1, k+1/2) + v_2 (j+1, k+1/2)\right) - \tilde{g}_1 (j+1/2, k) \frac{\Delta t}{\Delta x_1} \nabla_1 \gamma (j+1, k)$$

$$\left(1 - \frac{v_c^2 \Delta t^2}{4 \Delta x_2^2} \Delta_2\right) \hat{v}_2 (j, k+1/2) = \left(1 + \frac{v_c^2 \Delta t^2}{4 \Delta x_2^2} \Delta_2\right) v_2 (j, k+1/2) + \frac{v_c^2 \Delta t^2}{4 \Delta x_1 \Delta x_2} \nabla_1 \nabla_2 \left(\bar{v}_1 (j+1/2, k+1) + v_1 (j+1/2, k+1)\right) - \tilde{g}_2 (j, k+1/2) \frac{\Delta t}{\Delta x_2} \nabla_2 \gamma (j, k+1) \tag{26}$$

$$\hat{\gamma}(j,k) - \gamma(j,k) = -\frac{1}{2} A \Delta t \left(\frac{\nabla_1}{\Delta x_1} \hat{v}_1 (j+1/2, k) + v_1 (j+1/2, k) + \frac{\nabla_2}{\Delta x_2} \left(\hat{v}_2 (j, k+1/2) + v_2 (j, k+1/2)\right)\right)$$

The amplification matrix for numerically stability is

$$H = \frac{1}{(1+\gamma_1^2)^3 (1+\gamma_2^2)^3} \begin{pmatrix} 1-\gamma_1^2+\gamma_2^2+\gamma_1^2\gamma_2^2-2\gamma_1\gamma_2 & 2i\gamma_1 & \\ -2\gamma_1\gamma_2 & 1+\gamma_1^2-\gamma_2^2+\gamma_1^2\gamma_2^2 & 2i\gamma_2 \\ 2i\gamma_1(1+\gamma_1^2\gamma_2^2) & 2i\gamma_2(1+\gamma_1^2\gamma_2^2) & (1-\gamma_1^2)\cdot(1-\gamma_2^2) \end{pmatrix}$$

with

$$\gamma_1 = \frac{1}{2} \frac{v_c \Delta t}{\Delta x_1} \sin (k_1 \Delta x_1 / 2)$$
$$\gamma_2 = \frac{1}{2} \frac{v_c \Delta t}{\Delta x_2} \sin (k_2 \Delta x_2 / 2)$$

where k_1, k_2 is the wavelength of the propagated disturbances.

To obtain stability it is necessary and sufficient that the eigenvalues of this matrix are less than unity[13]. The eigenvalues are:

$$\sigma_1 = 1$$
$$\sigma_{2,3} = \frac{(1-\gamma_1^2)(1-\gamma_2^2) \pm i\sqrt{(1+\gamma_1^2)(1+\gamma_2^2) - (1-\gamma_1^2)(1-\gamma_2^2)}}{(1+\gamma_1^2)(1+\gamma_2^2)}$$

with

$$|\sigma_{2,3}| = 1$$

The amplification factor is unity, as in the one-dimensional case.

VII Boundary Conditions

For problems with an external driven field acting on the plasma the boundary conditions are determined by the magnetic flux and the energy flux into the plasma. For a given coil configuration the plasma acts as an electrical circuit with time dependent resistance and inductance. If the plasma conductivity is finite there are no surface currents and one can work with fixed boundaries. In two dimensions this simplifies the problem considerably. (For a free boundary problems compare computations for the magnetosphere[16]).

For one-dimensional problems, the condition for the continuity of the magnetic field through the boundary between plasma and vacuum (or discharge tube) together with the circuit equation are sufficient to give the value of the magnetic field or the magnetic flux at the plasma boundary.

The same condition for the continuity of the magnetic field also applies for the two-dimensional case. In order to avoid computing the vacuum field outside the plasma one has to introduce Green's functions with the proper boundary conditions.

These Green's functions for a fixed boundary have only to be computed once.

Every vector potential field, such as the magnetic field, is given by its singularities and the boundary conditions at infinity. Because of the divergence-free structure such singularities can only be current loops (magnetic dipoles). One can construct closed surfaces which may or may not include these singularities. The magnetic field outside is then given by Green's functions which fulfill the proper jump conditions. A construction of a magnetic field which has only components parallel to the surface is only possible if this surface allows a construction of an orthogonal coordinate net without singularities[19]. This condition is sufficient and necessary. Such a surface has the topological structure of a torus. The function for the magnetic field can be constructed from the Biot-Savart law. The discussion which follows is quite general, but in order to avoid unnecessary complications it will be restricted to an axisymmetric case.

Assume an axisymmetric coil with a cross section bounded by the curve S_c and a plasma torus with a cross section bounded by the curve S_p. (For a plasma with another topology the discussion is more complicated but the results are essentially the same.) The curves S_c and S_p must be doublepoint free and must have continuous radii of curvature. To be definite, consider the θ-pinch configuration. The integration along the θ direction can be performed analytically to give a Green's function for a j_θ current. This function contains a logarithmic singularity. In order to compute the magnetic field at the plasma boundary, integral equations must be solved. For numerical computations these integral equations are replaced by matrix equations. Let the n_c points on S_c be characterized by roman indices and n_p points on S_p be characterized by greek indices. As the Green's function contains a logarithmic singularity the integration over the singularity has to be performed analytically. This can be done by expansion of the Green's function in a finite Fourier series and then expressing the Fourier coefficients by means of the function at the given points[17]. Integrals of the form

$$F(s) = \int g(s,s') f(s') ds'$$

can then be written as

$$F_k = g_{kj} f_j$$

With this indexing g_{kj} is the Green's function at the coil surface itself, $g_{\alpha\beta}$ the Green's function on the plasma surface $g_{\alpha k}$, $g_{k\alpha}$ are the Green's function from the coil to the plasma surface and vice versa, the superscripts t, p indicate the tangential and perpendicular components respectively. Since the jump in the parallel magnetic field B^t at any surface is proportional to the current, and the jump in the perpendicular field B^p is proportional to the surface layer of magnetic monopoles, the surface current and the surface monopole density are expressed by the magnetic fields themselves.

At $t = 0$ let the magnetic field be the vacuum field generated by a superconducting coil with the total current I. The magnetic field is then given by $I\ B^t_k(0)$, where fulfills the equation

$$B^t_K(0) = g^{tt}_{Kj}\, B^t_K(0) \tag{29}$$

with

$$\sum_K B^t_K(0)^2 = 1 \tag{30}$$

(For proof of the existence of such a solution and a description of the computing procedure see Martensen[17,18].)

For a change of the external current during each small timestep the plasma will almost act as a superconductor. The induced net current integrated over the plasma surface will be zero. The magnetic field of this superconducting plasma and the coil will be given by the solution of the following equations:

$$\begin{aligned} b^t_K &= g^{tt}_{Kj}\, b^t_j + g^{tt}_{K\alpha}\, b^t_\alpha \\ b^t_\alpha &= g^{tt}_{\alpha j}\, b^t_j + g^{tt}_{\alpha\beta}\, b^t_\beta \end{aligned} \tag{31}$$

where

$$b_K^t = B_K^t - B_K^t(0) \tag{32}$$

The restrictions imposed are

$$B_K^t(0) b_K = 0 \ , \quad B_\alpha^t(0)\, b_\alpha^t = 0, \quad b_K^t\, g_{K\alpha}^{tt}\, b_\alpha = 1 \tag{33}$$

where b_α^t is the tangential magnetic field at the plasma surface and $B_\alpha^o = g_{\alpha\beta}\, B_\beta^o$. These equations are to be solved for b_α and b_k subject to the constraints (33). At a time t let

$$I = B_K^t(0) \left\{ g_{K\alpha}^{tt} B_\alpha^t + g_{K\alpha}^{tp} B_\alpha^p \right\}$$
$$I_p = b_K^t\, g_{K\alpha}^{tt}\, B_\alpha^t \tag{34}$$

Then I gives the total current induced at the coil by the plasma and I_p the part of the current for which the plasma acts as a superconductor. B_α^t and B_α^p are the magnetic field at this time at the plasma surface. Now let

$$\delta B_\alpha^t = B_\alpha^t - I\, g_{\alpha K}^{tt}\, B_K^t(0) - I_p\, b_\alpha^t$$
$$\delta B_\alpha^p = B_\alpha^p - I\, g_{\alpha K}^{pt}\, B_K^t(0) \tag{35}$$

The change in the current distribution in the coil surface is obtained from the solution of

$$\delta B_K^t = g_{Kj}^{tt}\, \delta B_j^t + g_{K\alpha}^{tt}\, \delta B_\alpha^t + g_{K\alpha}^{tt}\, \delta B_\alpha^p \tag{36}$$

with the constraints

$$B_K^t(0)\ \delta B_K^t = 0 \qquad b_K^t\, \delta B_K^t = 0 \tag{37}$$

As the magnetic field B_α^t and B_α^p are produced by the same current distribution they must be linearly related. Thus, at the plasma surface the magnetic fields are determined by the equations

$$\delta B_\alpha^t = g_{\alpha\beta}^{tt}\, \delta B_\beta^t + g_{\alpha\beta}^{tp}\, \delta B_\beta^p + g_{\alpha K}^{tt}\, \delta B_K^t$$
$$\delta B_\alpha^p = g_{\alpha\beta}^{pt}\, \delta B_\beta^t + g_{\alpha\beta}^{pp}\, \delta B_\beta^p + g_{\alpha K}^{pt}\, \delta B_K^t \tag{38}$$

with the constraints

$$\delta B_\alpha^t\, g_{\alpha K}^{tt}\, B_K^t(0) = 0 \ , \quad b_\alpha^t\, \delta B_\alpha^t = 0, \quad \delta B_\alpha^p\, g_{\alpha K}^{pt}\, B_K^t(0) = 0 \tag{39}$$

This equation together with Eq. (36) can be solved for δB_α^t and gives a linear relation of the form

$$\delta B_\alpha^t = H_{\alpha\beta}\ \delta B_\beta^p. \tag{40}$$

(One can also express this as a linear relation between the instantaneous magnetic flux and the magnetic field.)

The computation proceeds in the following way. Let B at time t be specified at plasma boundary and the coil surfaces. Then one solves the plasma equations with the boundary condition

$$\bar{B}_\alpha^t = B_\alpha^t + \Delta I b_\alpha^t$$

Solving the plasma equations then gives $\bar{B}_\alpha^p$, the approximate field at the boundary at $t + \Delta t$. Then Eq. (34) is used to compute new currents $\bar{I}$, $\bar{I}_p$. Equation (35) now determines δB_α^p, and at last Eq. (40) together with Eq. (35) is used to compute B_α^t for the next timestep.

VIII Concluding Remarks

One-dimensional magnetohydrodynamic calculations have been employed with success in comparing the theory and experiments. Two-dimensional calculations are only beginning to reach this point of sophistication. Also there are different approaches to this problem which need further evaluation. F. Hertweck and K. V. Roberts[21] have started two dimensional calculations, using an explicit scheme, (the angle derivative method) and applied periodic boundary conditions for the magnetic field. Since the boundary conditions were oversimplified no direct comparison with experiments could be made. Nevertheless, the numerical results gave considerable insight in the dynamic behavior of the plasma.

N. O. Weiss's[20] two-dimensional calculations of expulsion and twisting of magnetic field lines are also very impressive (and have been shown as a movie).

The author started two-dimensional calculations for a plasma emerging from a dipole (to simulate the solar wind). This is an attempt to solve a stationary problem by the relaxation of dynamic processes.

Representation of the results is a major problem. A movie can give good insight into the dynamics of a plasma. Because of the large amount of experimental data and numerical output direct comparison of two-dimensional calculations with time and space resolved measurements should also be made by computers.

References

1. G. Hain, K. Hain, W. Koppendörfer, K. V. Roberts, S. J. Roberts; Fully Ionized Pinch Collapse, Zeitschr. Natur Bd. 15a, 1039-1050, (1960)
2. K. Hain, A. C. Kolb; Fast θ Pinch, Salzburg Conf. Vol. II, 561-569, (1962)
3. H. Fisser, J. Schlüter; A Comparison between Numerical Calculations of a Linear z-Pinch Discharge and Measurements by Magnetic Probes, Salzburg Conf. Vol. II Page 571-576 (1962)
4. D.E.T.F. Ashby, K. V. Roberts, S. J. Roberts; Experimental and Theoretical Observations on Fast Linear Pinches Plasma Phys. Accelerators Thermonuclear Res., Vol. 3, 162-166, (1960)
5. F. L. Ribe, R. M. Gilmer, H. C. Hoyt, G. Hain, K. Hain; Comparison of Computed and Measured Behavior of Fast θ Pinches, LAMS-2911 (1963)
6. D. Düchs, H. R. Griem; Computer Study of the Dynamic Phase of a Small θ Pinch, Phys. of Fluids, Vol. 9, 1099-1109, (1966)
7. A. Eberhagen, M. Keilhacker; Time and Space Resolved Measurements of Electro Derivaties from Continuum Emission of a θ Pinch.
8. D. Fisher; Culham Reports
9. D. Düchs; Three Fluid Model for a Partially Ionized Plasma in a θ Pinch Discharge, CR VI Conf. Internat. Phénomenes d'Ionization dans les Gax, Paris S.E.R.M.A., Vol. 2, 573-580, (1963)
10. C. F. Kennel, J. M. Green; Finite Larmer Radius Hydromagnetics, Ann. Phys. Vol. 38. 63-94, (1966)
11. A. Simon, W. B. Thompson; Hydromagnetic Equation with Viscosity for a Collisionless Plasma, Plasma Phys. Accelerator-Thermonuclear Research, Vol. 8, 313-316 (1966)
12. K. Hain; Pinch Collapse, A.E.R.E. Report 3383 (1961)
13. R. Richtmyer; Difference Methods for Initial Value Problems, New York, Interscience Publishers (1957)
14. K. Hain; Numerical Solutions for 1.5 Dimensional Magnetohydrodynamics Problems, Symposium Williamsburg, NASA Publications (1967)
15. K. V. Roberts; N. O. Weiss; Convective Difference Schemes, Culham Report CLM-P76 (1965)
16. J. C. Baker; D. B. Beard, J. C. Young; Self Consistent Method of Determining the Boundary Shape between a Plasma and a Magnetic Field, Phys. of Fluids, Vol. 7, 504-510, (1964)
17. W. Martensen; Zur Numerischen Behandlung des Inneren Neumannschen and Robinschen Problems, Zeitschr. f. angew. Math. Mechanik Band, 39, 377-380, (1959)
18. W. Martensen; Harmonische Vektorfelder, Arch. Rational Mech. Annal., 5, 46-75, (1960)
19. R. Kippenhahn; Plasma Figurationen mit Oberflächenströmen, die von einem Magnetfeld im Gleichgewicht gehalten werden, Zeitschr. f. Naturf. Band, 13a 260-267, (1958)
20. N. O. Weiss; The Expulsion of Magnetic Flux by Eddies Proc. Roy. Soc. A Vol. 293, 310-328, (1966)
21. K. V. Roberts, F. Hertweck, S. J. Roberts; Thetatron, A Two dimensional Magnetohydrodynamic Computer Program, U.K.A.E.A. CLM-Report 20, (1963)
22. A. C. Kolb, P. C. Thonemann; Plasma Rotation and Instability in the θ Pinch Due to Transverse Magnetic Fields, Phys. Fluids, Vol. 7, 1455-1461, (1964)

COMPUTER SIMULATION OF THE THETA PINCH*

by

Thomas A. Oliphant, Jr.

Los Alamos Scientific Laboratory, University of California
Los Alamos, New Mexico

ABSTRACT

A preliminary calculation of the dynamics of the theta-pinch during its initial compression was discussed in a previous paper.[1] That calculation represented a feasibility study of the methods used. We have subsequently refined our calculation by including Joule heating, electron heat flow, and electron-ion temperature equipartitioning. This allows us also to include a realistic estimate of the ion-ion collision frequency. Thus, we are prepared to make quantitative predictions with the present numerical program. In our preliminary calculation we allowed a z-dependence of the magnetic field in order to obtain a qualitative estimate of the effect of a mirror field on end losses. For our first quantitative problem we have taken the simpler case of a z-independent theta-pinch without end losses. The physical problem studied was the same Scylla-III experiment which was discussed in connection with a purely M.H.D. calculation.[3] While the overall result of the pinch compression is the same with our new approach, there are noticeable differences in detail, the most important of which is the structure of the shock front. In the present calculation we see the snow-plow effect much more realistically than it was seen in the M.H.D. calculation. We have followed the calculation through the first reflection of the shock wave from the center of the plasma.

INTRODUCTION

The numerical calculations of θ-pinch dynamics reported earlier[1] was primarily a feasibility study for the methods used. In order to study the physical model in more detail, we have imposed z-symmetry and included three additional effects, namely, Joule heating, electron heat flow, and electron-ion temperature equipartitioning.

THEORETICAL EQUATIONS

Our basic model is the same as the one discussed earlier. We will recapitulate the basic equations here making the necessary changes as we go along for the present calculation. The equation for the field quantity,

$$\psi = rA \tag{1}$$

is

$$\frac{\partial^2\psi}{\partial r^2} - \frac{1}{r}\frac{\partial\psi}{\partial r} - \xi\left(\frac{\partial\psi}{\partial t} + u\frac{\partial\psi}{\partial r}\right) = 0 \tag{2}$$

where

$$\xi = \frac{4\pi}{\eta}\ , \tag{3}$$

η is the electrical resistivity, and u is the fluid velocity. The electric and magnetic fields are given by

$$E_\theta = -\frac{1}{r}\frac{\partial\psi}{\partial t} \tag{4}$$

and

$$B_z = \frac{1}{r}\frac{\partial\psi}{\partial r} \tag{5}$$

The boundary condition on ψ are

$$\left.\frac{\partial\psi}{\partial r}\right|_{r=a} = aB_z(a,t) \tag{6}$$

and

$$\psi(0,t) = 0 \tag{7}$$

where a is the outer boundary of the plasma containing tube.

The electron temperature equation is

$$\frac{\partial T}{\partial t} + u\frac{\partial T}{\partial r} - \frac{(\gamma-1)T}{\rho}\left(\frac{\partial \rho}{\partial t} + u\frac{\partial \rho}{\partial r}\right) - \frac{(\gamma-1)}{R\rho}\frac{1}{r}\frac{\partial}{\partial r}\left(r\kappa\frac{\partial T}{\partial r}\right) - \dot{T}_D + \left(\frac{T-\tau}{t_{eq}}\right) = 0 \qquad (8)$$

where T is the electron temperature, τ is the ion temperature, R is the gas constant, κ is the electron thermal conductivity, t_{eq} is the electron-ion equipartition time, and $\dot{T}_D$ is the Joule heating term given by

$$\dot{T}_D = \frac{(\gamma-1)\eta}{(4\pi)^2 R\rho}\left(\frac{\partial B}{\partial r}\right)^2 \qquad (9)$$

The boundary condition on T is simply that no heat is allowed to flow into or out of the plasma.

A Monte-Carlo calculation has been set up to simulate the effects of ion-ion collisions. On the average an ion takes a time t_c to be deviated by 90° by the cumulative effects of small angle encounters with other ions. Using a probability based on this time we make a number of actual 90° collisions between some ions and their nearest neighbors.

The acceleration of the Lagrangian point particles is given by

$$\vec{a} = \hat{e}_r\left[\frac{q\, v_\theta B_z}{m} - \frac{B_z}{4\pi\rho}\frac{\partial B_z}{\partial r}\right] + \hat{e}_\theta\frac{q}{m}(E_\theta - v_r B_z) \qquad (10)$$

The coefficients η, κ, t_{eq}, and t_c are taken from Spitzer.[2]

SPECIFIC EXAMPLE

The example considered was similar to the Scylla III problem discussed earlier[3] on the basis of an MHD program. The magnetic boundary field was taken to be a sine wave of a quarter period of about 1.2μ-sec. In this example we suppressed the collision mechanism so that we are solving the Vlasov equation. The end-on projections of the space densities of particles and the magnetic field profiles are plotted at three different times during the first pinch compression in Figs. 1 through 6. Figure 3 clearly illustrates the formation of the snow-plow moving inward. During this inward motion, some magnetic field penetrates to the axis and subsequently gets highly compressed so that a pronounced central field spike occurs at maximum compression.

The present problem was run with 1000 mesh points. A mesh refinement study was made by using 500 and 2000 mesh points. There was very little difference among these three runs. The main difference was a less than 3% increase in speed of the snow-plow. The central magnetic field spike persisted essentially unchanged as did the form of the snow-plow. Thus we feel that the collisionless model has been calculated correctly. Incidentally, a similar magnetic field spike has been observed in the collisionless model by Kilb.[1]

Since the magnetic field spike is not observed in Scylla experiments here at LASL, we are led to believe that some collisional heating mechanism must be responsible for repressing it. With our collision mechanism we are only able to slow the snow-plow down, but we are not able to suppress the field spike. Thus, we have doubts about the adequacy of our present collision mechanism. Since our old MHD code adequately suppressed the field spike, we feel that some sort of collisional heating calculation should ultimately be able to overcome this deficiency.

REFERENCES

1. Symposium on Computer Simulation of Plasma and Many-Body Problems", Williamsburg, Virginia, April 19-21, 1967.
2. L. Spitzer, Physics of Fully Ionized Gases, Interscience, New York, New York, 1962.
3. T. A. Oliphant, Numerical Studies of the Theta Pinch, LAMS-2944, (1963).

* Work performed under the auspices of the U. S. Atomic Energy Commission.

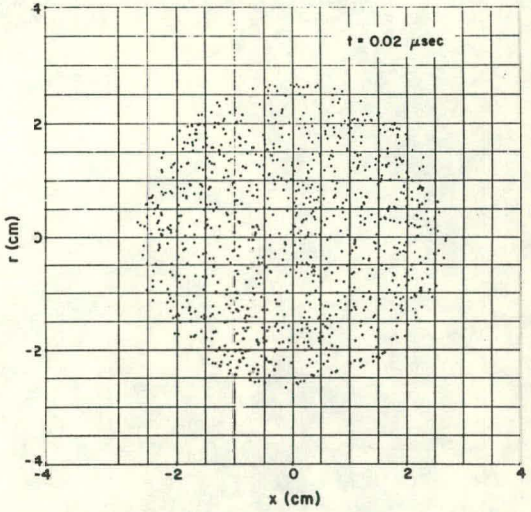

Fig. 1. Projection along the z-axis of the space distribution of the Lagrangian mass points at 5 = .02 μsec.

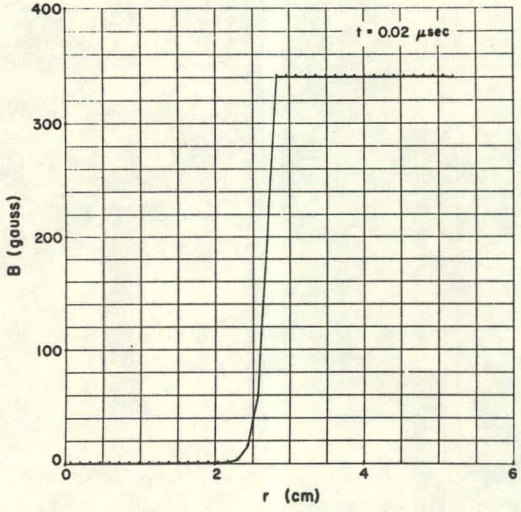

Fig. 2. Profile of magnetic field (z-directed) vs. radial distance r from the axis at t = .02 μsec.

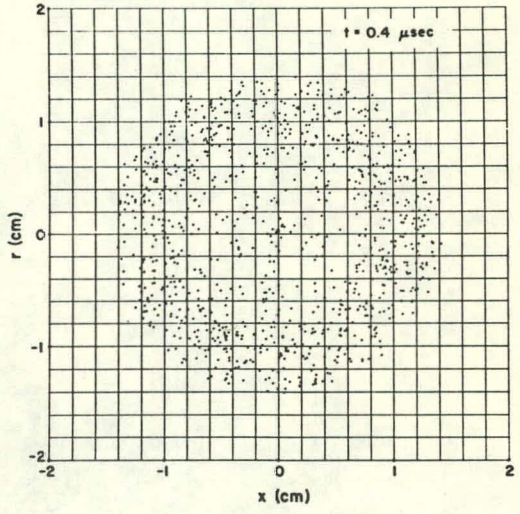

Fig. 3. Projection along the z-axis of the space distribution of the Lagrangian mass points at t = .4 μsec.

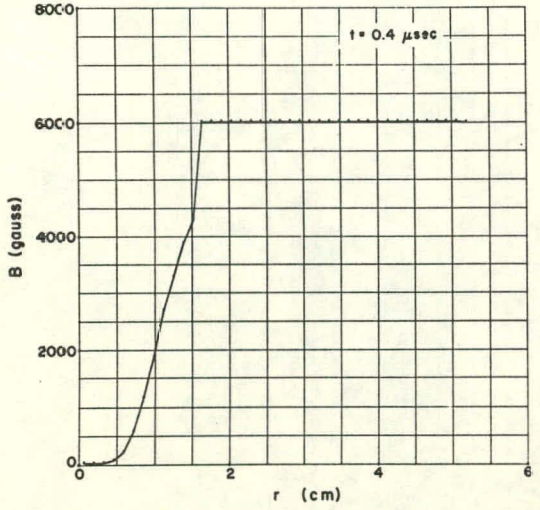

Fig. 4. Profile of magnetic field (z-directed) vs. radial distance r from the axis at t = .4 μsec.

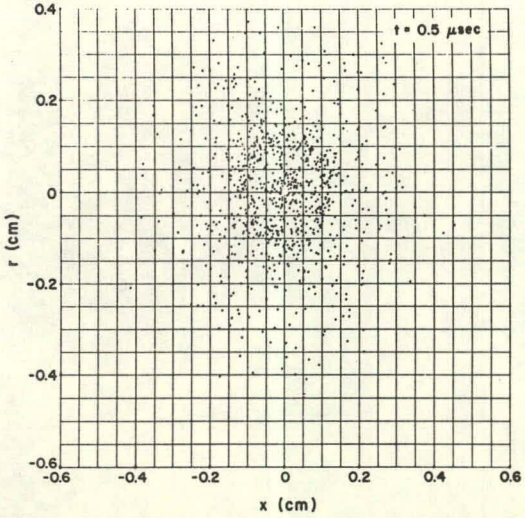

Fig. 5. Projection along the z-axis of the space distribution of the Lagrangian mass points at t = .5 μsec.

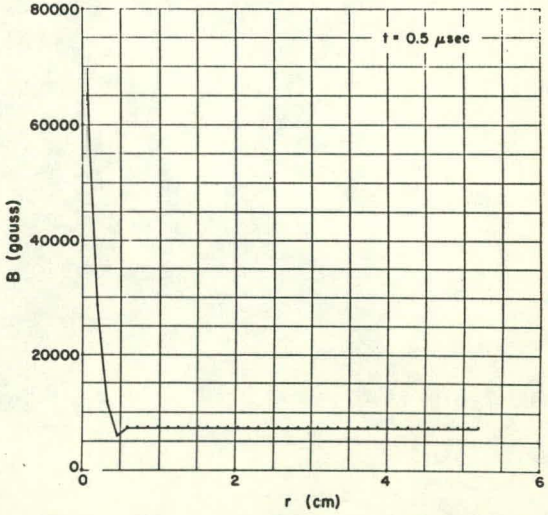

Fig. 6. Profile of magnetic field (z-directed) vs. radial distance r from the axis at t = .5 μsec.

SHEATH STABILITY*

by

R. L. Morse
Los Alamos Scientific Laboratory, Los Alamos, New Mexico

ABSTRACT

A class of finite-β marginally stable modes is considered, which are related to plasma density gradients. Perturbed currents and fields are calculated for a sheet pinch confined by a magnetic field which has the same sign on both sides of the plasma. This paper separately considers the numerical simulation of mirror instabilities in θ-pinch plasmas and the resultant increase in thermal motion along field lines.

INTRODUCTION

The perturbation calculation which follows begins from a stationary solution of the Vlasov equations in which the electrons are taken to be cold and distributed so as to neutralize ion charge and the ions have an unperturbed distribution

$$f_0 \sim \exp\left[- (\varepsilon + \alpha P_y^2/2M)/T_i \right]$$

where $\varepsilon = M\bar{V}^2/2$ and $P_y = M(V_y + A_y)$. The B field has only a z component everywhere and all quantities vary only in the x direction. If A_y $(x = 0) = 0$, then $x = 0$ is the center plane of the pinch. Hence P_y is a constant of particle motion and f_0 is in principle a stationary solution. In the limit that the ion density at $x = 0$, $n_0 \ll B_z^2/8\pi T_i$ (the low β limit),

$$n = n_0 \exp\left[- \alpha\Omega^2 x^2 \right],$$

where $\Omega = \frac{qB_z}{Mc}$. For more general β, $n(x)$ and $B_z(x)$ are obtained by numerical integration.

When f_0 is expanded in terms of velocities, it can be seen that there are really two different temperatures

$$T_x = T_z = T_i \text{ and } T_y = T_i/(1 + \alpha).$$

The calculation was done in the limit $\alpha \ll 1$ where this transverse anisotropy is small and where first order drift theory gives a satisfactory approximation to unperturbed ion trajectories. Perturbations of the form

$$\delta B_z = \delta B_z(x) e^{i(k_y y + k_z Z + \omega t)}$$

are considered with a similar form for $\delta\bar{E}$ and δB_y. The perturbed distribution function, f_1 is obtained by the method of characteristics

$$f_1 = -q/M \int_{\infty}^{0} dt (\delta\bar{E} + \bar{V} \times \delta\bar{B}/c) \cdot \nabla_V f_0$$

where the integration is along unperturbed trajectories. In the limit $k_z, \omega \to 0$, the $V_x \delta B_z$ term in the cross product does not vanish. The dominant parts of this term come from denominators of the form

$$\frac{1}{k_y V_D + k_z V_z - \omega + n\Omega}$$

in which n, the coefficient of Ω, is zero. V_D is the ∇B drift velocity in the y direction.

The W.K.B. method is applied to $\delta B_z(x)$, terms up to $\delta B_z''$ are kept and a perturbed J_x is calculated from the resulting f_0. An eigenvalue equation for k_y is obtained when J_x is plugged into the field equation for $\delta B_z(x)$ in the limit $k_z, \omega \to 0$;

$$\delta B_z = (1+\alpha)^{3/2} e^{-\alpha^2 X^2/r_L^2} \left[(1 - k_y^2 r_L^2 \delta B_z/2) + r_L^2 \delta B_z'' \right]$$

where $r_L = u/\Omega$ is the mean ion gyro radius. The $k_y^2 r_L^2$ term is a finite Larmor radius correction term. The interpretation of this equation in terms of marginal stability depends on the existence of $k_z \neq 0$ or some equivalent "line tying mechanism," and may be significantly modified by the resulting electron motion when time dependence is introduced. However, with this reservation, these modes resemble the transverse anisotropy modes obtained with the bounce model, and as pointed out in the first reference[1], are mathematically related to the "mirror" and "fire hose" instabilities which have been treated by Furth[2], Grad[3], Rosenbluth[4], and others.

θ-PINCH PLASMA SIMULATION COMPUTATIONS

A P.I.C. type[5] computer code has been written for simulation of axisymmetric high β plasmas. Simulation "particles" move in r and z. The "particles" are initially given a distribution of canonical P_θ which are then held fixed and used in computing the effect of solenoidal E fields on θ currents and the centrifugal force term in the equation of motion. The phase space which is treated here is therefore five dimensional. The magnetic fields are computed from particle currents through the vector potential by successive overrelaxation starting from an initial guess which is extrapolated from field solutions at previous times. The field iteration is found to require only about 1/10 of the total cycle time; most of the expense is in the particle motion and cell quantity computation.

The code has been applied to end loss, rotational instabilities, and mirror instabilities. The latter is discussed here. Recall that if in a high β plasma, pressure perpendicular to field lines, $P_\perp$, is sufficiently greater than $P_\parallel$, then in spite of the stabilizing effect of the magnetic field, perturbations of magnetic field and particle density varying as a function of position along field lines will grow unstably[1,2,3,4]. In most cases, the destabilizing term is proportional to $(P_\perp/P_\parallel - 1)$.

In the final adiabatic compression of a θ-pinch plasma, if not in the initial shock phase, it is expected that most of the energy of compression goes into motion perpendicular to field lines, thus leaving $P_\perp \gg P_\parallel$. On the other hand, θ-pinch end losses are seen to proceed as if parallel and perpendicular thermal velocities were approximately equal from early times[6]. Ion-ion collisions are not sufficiently rapid to explain this result. It is worthwhile, therefore, to investigate the nonlinear effects of mirror instabilities which are caused by the anisotropy in question. Fig. 1 shows three frames of a run of the simulation code starting from a distribution which is initially in equilibrium in the perpendicular coordinates (initial field pure B_z) but with $P_z = 0$. The first frame shows 8000 "particles" in the initial configuration. Frames 2 and 3 show the bunching of particles as the mirror instabilities develop. The interval between frames is about one ion gyro period, or about 10^{-7} sec for a typical θ-pinch plasma. At the time of the last frame, the r.m.s. z velocity is about 1/3 of the r.m.s. perpendicular velocity, which suggests that mirror instabilities may have a strong effect on longitudinal thermal velocities and end losses in θ-pinches.

REFERENCES

1. R. L. Morse, Phys. Fluids 10, 1017 (1967).
2. H. P. Furth, Nucl. Fusion Suppl. Pt. 1, 169 (1962).
3. H. Grad, Phys. Fluids 9, 498 (1966).
4. M. N. Rosenbluth, Los Alamos Report LA-2030.
5. F. H. Harlow, Proceedings Symposia in Applied Mathematics 15, 269 (1963).
6. K. S. Thomas, paper D3, these proceedings.

*Work performed under the auspices of the United States Atomic Energy Commission.

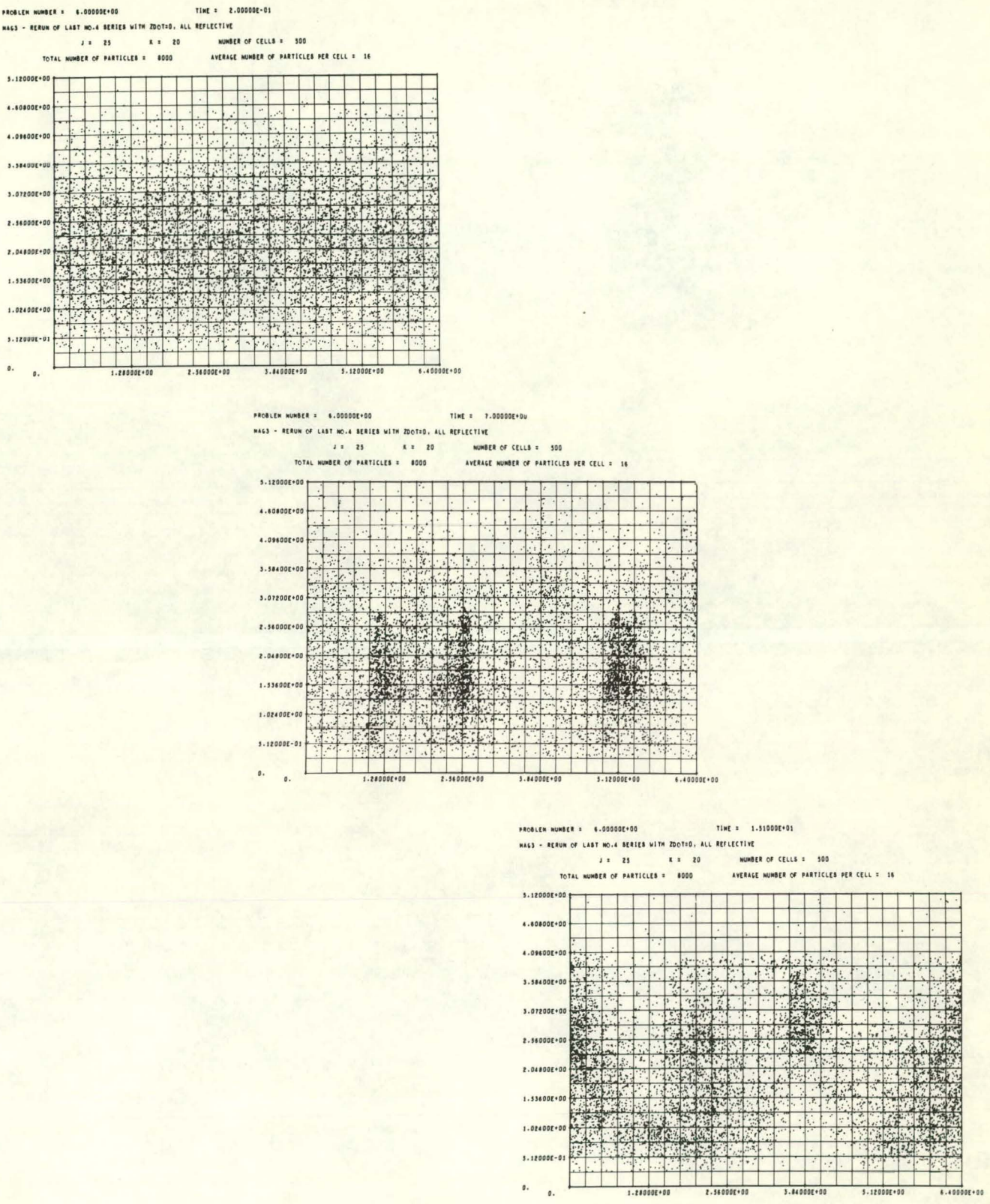

Fig. 1. Particles plotted against r (vertical) and z (horizontal) after 0, 1, and 2 gyro periods. Periodic boundary conditions are imposed in z and the outer r boundary conserves flux.

A VARIATIONAL APPROACH TO THE CLASSIFICATION OF NONLINEAR MAGNETOHYDRODYNAMIC WAVES AND PLASMOIDS

by

Daniel R. Wells
Department of Physics, University of Miami
Coral Gables, Florida

and

Joseph Norwood, Jr.
Magnetohydrodynamics Section, National Aeronautics
And Space Administration, Langley Research Center
Hampton, Virginia

ABSTRACT

Variational methods are used to determine the structure of dynamically stable plasmoids. The total energy of the plasmoids is varied subject to a set of constraint integrals on the flow. It is demonstrated that the resulting flow structure in an azimuthally symmetric geometry results in a plasmoid of the type observed experimentally when the angular momentum of the plasmoid is not conserved. This is the colinear vortex structure. New experimental results are presented which clearly demonstrate that the structures observed in mirror trapping experiments are of the type predicted by the variational calculation. The colinear plasmoid structures are shown to be members of a class of nonlinear transverse waves that trap and transport fluid mass. It is also demonstrated that a modification of these solutions that assumes conservation of angular momentum of the plasmoid describes another type of vortex structure which is centered on the magnetic field lines and moves at right angles to the field. This is the H-centered vortex structure. It corresponds to the vacuum field limit of the classical weak magnetoacoustic wave solutions.

From the linearized one-fluid hydromagnetic equations assuming the velocity, $\vec{v}$, and the perturbation magnetic field, $\vec{b}$, to be small quantities, one derives the wave equations

$$\left(\frac{\partial^2}{\partial t^2} - (V_A)_o^2 \frac{\partial^2}{\partial z^2}\right) \vec{b} = 0$$
$$\left(\frac{\partial^2}{\partial t^2} - (V_A)_o^2 \frac{\partial^2}{\partial z^2}\right) \vec{v} = 0 \quad , \qquad (1)$$

where $(V_A)_o^2 = B_o^2/\rho\mu_o$, defines the Alfvén speed. By taking the curl of these equations, another set of wave equations is produced for $\vec{j}$, the current density, and $\vec{\zeta}$, the vorticity.

The perturbing fields obey the classical wave Equations (1) to all orders in the perturbation. This equation is a linear mode of the full set of first order nonlinear hyperbolic equations describing the standard model of magnetohydrodynamic phenomena. Equations (1) are actually valid

to all orders in $\vec{B}$ and $\vec{V}$ if one assumes the equipartition solution[1]. This comes about because the first order perturbation calculation automatically discards all convective acceleration terms in the momentum equation. This, in turn, yields a hyperbolic partial differential equation which is simply the classical wave Equations(1). The equipartition solution automatically discards the convective acceleration terms and yields the same wave equation without the use of perturbation techniques. We will show that a large disturbance which generates a nonlinear wave solution can be an equipartition solution and be a stable mode. This special solution also results in the classical wave equation. There is a very important difference between the solutions obtained by perturbation theory and those obtained with the equipartition solution. The former are superposable, the latter are not and complex interactions occur when two of these nonlinear modes are localized in the same region of flow.

It is well known that in a perfect fluid conductor the magnetic lines of force are frozen into the fluid. Thus the current density vector is convected with the flow. The vorticity of the mass flow is also frozen into the fluid for certain types of flow fields[2]. It can be shown that

$$\frac{\partial \vec{\zeta}}{\partial t} - \nabla\times(\vec{v}\times\vec{B}) = \nabla\times\frac{1}{\rho}(\vec{j}\times\vec{B}) \quad . \tag{2}$$

The fluid will be transported with the vorticity of the mass flow field if the right hand side of Equation (2) can be shown to vanish.

Equation (2) may be referred to as the generalized Helmholtz vorticity conservation relation since in the limit of vanishing right hand side it reduces to the Helmholtz relation of ordinary hydrodynamics. We will return to this special requirement for mass transport of fluid later in the discussion.

We now turn to a description of the type of plasmoid which is discussed in reference 3. One has a sphere or spheroid of fluid moving parallel to the magnetic guide field. It maintains its identity and all of the mass of fluid inside the sphere is carried along with the disturbance. The fluid outside the sphere is not carried along with the disturbance and thus is merely perturbed and undergoes a wave-like undulation (see Figure 1). We now associate this propagating disturbance (plasmoid) with a nonlinear Alfvén wave. We base our discussion on a global dynamic stability analysis suggested by Chandrasekhar and Woltjer[4,5,6].

The hydromagnetic equations allow certain integrals of the motion. A given hydromagnetic system cannot change into an arbitrarily different system but only into systems characterized by the same integrals. Thus these integrals act as a set of constraints on the equations of motion. If the energy of the system has an extremum compatible with these constraints, then the system must be in hydromagnetic equilibrium. By minimizing the energy with respect to the available class of Lagrange multipliers (which are spatial constants due to the integral nature of the constraints) the field equations for a global, dynamically stable equilibrium may be obtained. A change of configuration would then be impossible since there is no external source of energy available to the system.

The integrals as given by Woltjer are

$$I_1 = \int_V \vec{A}\cdot\nabla\times\vec{A}dV \tag{3}$$

$$I_2 = \int_V \vec{B}\cdot\vec{v}dV \tag{4}$$

$$I_3 = \int_V \hat{i}\times\vec{r}\cdot\rho\vec{v}dV \tag{5}$$

$$I_4 = \int_V \hat{j}\times\vec{r}\cdot\rho\vec{v}dV \tag{6}$$

$$I_5 = \int_V \hat{k}\times\vec{r}\cdot\rho\vec{v}dV \tag{7}$$

$$I_6 = \int_V \rho dV \quad , \tag{8}$$

where $\hat{i}$, $\hat{j}$, and $\hat{k}$ are unit vectors in an ordinary Cartesian coordinate system and $\vec{r}$ is the radius vector. $\vec{A}$ is the magnetic vector potential, ρ is the fluid density.

Woltjer[6] gives a proof for the constancy of these integrals where the volume of integration is a closed system surrounded by a rigid conducting spherical surface. It can be shown[7] that a similar proof holds for the geometry of the nonlinear wave that is observed experimentally and described below. The plasmoid is shown in Fig. 1. At the spherical surface, the boundary conditions are

$$\begin{aligned} \vec{B}\cdot\hat{n} &= 0 \\ \vec{v}\cdot\hat{n} &= 0 \quad . \end{aligned} \tag{9}$$

A straightforward calculation shows that the integrals I_1 through I_6 are constants of the motion both for the closed system of the plasmoid itself and for the surrounding plasma considered as a separate flow region. It is then only necessary to match the boundary conditions at the surface of the plasmoid utilizing Equations (9).

We will demonstrate that if the variational calculation is carried out with the constraint integrals I_3, I_4 and I_5 not included, (non-conservation of angular momentum of the plasmoid) the nonlinear Alfvén wave results. If these integrals are included (conservation of angular momentum of the plasmoid) a structure is found which can rotate approximately as a rigid body and corresponds to another type of plasmoid observed by Bostick[8] and others. The plasmoid transported by the nonlinear Alfvén wave exchanges angular momentum with the surrounding fluid. While Equations (9) indicate that there is no interchange of fluid between the plasmoid and its surroundings, momentum transfer can be accomplished by means of pressure gradients during the period of nonsteady flow of the fluid as the plasmoid is reaching its stable equilibrium state. The second type of plasmoid does not exchange angular momentum with its surroundings because it polarizes and moves across the magnetic guide field.

We consider first the nonlinear Alfvén wave or colinear plasmoid. The two integrals that concern us here are I_1 and I_2. The energy integral is

$$E = \int_V \left(\frac{\rho V^2}{2} + \frac{B^2}{2\mu_0} \right) dV \quad , \tag{10}$$

where we are considering an incompressible medium of constant density and the gravitational potential is ignored. One now looks for the condition for energy extrema, i.e. equilibrium states compatible with the constancy of I_1 and I_2,

$$\delta E - \frac{\alpha}{2\mu_0} \delta I_1 - \rho\beta\delta I_2 = 0 \tag{11}$$

where α and β are Lagrangian multipliers. Expanding Equation (11), one finds for the equations of motion

$$\nabla\times\vec{B} = \alpha\vec{B} + \rho\mu_0\beta(\nabla\times\vec{v}) \tag{12}$$

$$\vec{v} = \beta\vec{B} \quad . \tag{13}$$

Equations (12) and (13) define a set of equilibrium solutions. A subset of these solutions is found by expressing the energy in terms of I_2

$$E = \left(\rho\beta + \frac{1}{\mu_0\beta} \right) \frac{I_2}{2}$$

and minimizing E with respect to β. One then finds

$$\beta^2 = \frac{1}{\mu_0\rho} \quad . \tag{14}$$

This is the equipartition solution and is a set of stable solutions corresponding to colinear flow[7]. The stability of this solution has also been demonstrated by Chandrasekhar[9] in a linearized analysis.

Combining Equations (12) and (13) to eliminate $\vec{v}$,

$$\nabla\times\vec{B} = \left(\frac{\alpha}{1 - \mu_0\rho\beta^2} \right) \vec{B}$$

from which, with Equation (14), $\alpha = 0$ corresponds to the only non-trivial solution. If one designates the ratio $\left(\frac{\alpha}{1 - \mu_0\rho\beta^2} \right)$ as κ, one has

$$\nabla\times\vec{B} = \kappa\vec{B} \quad . \tag{15}$$

This is the equation for a force-free field. Thus the stable plasmoid propagating as a nonlinear Alfvén wave has colinear fields with flows having Alfvén velocity. The Lorentz-force, $(\vec{j}\times\vec{B})$, is identically zero everywhere inside the boundary of the structure and the condition for trapping fluid particles in the wave, Equation (2), is met. The fields $\vec{j}$, $\vec{\zeta}$, $\vec{v}$ and $\vec{B}$ are all mutually parallel. These solutions are sufficient to determine a dynamically stable equilibrium.

If the fluid is compressible, and the angular momentum is not conserved, the constraint integrals to be used are I_1, a modified form of I_2, and I_6. It can be shown that I_2 may have its integrand multiplied by any analytic function of ρ and the integral will still be a constant of the motion. Thus I_2 can be written in general form as

$$I_{2n} = \sum_n \int \vec{v} \cdot \vec{B}\, \rho^n dV \quad .$$

If the variation is then carried through, one again finds that the flow is colinear and force-free just as in the case of the incompressible fluid model. In this case, however, additional information is obtained about the pressure, density, and tempera-

ture distribution within the plasmoid. This then is the compressible colinear plasmoid. It corresponds to a nonlinear transverse magnetohydrodynamic wave.

If we consider the structure that results if one takes $\delta\rho = 0$ and assumes that angular momentum is conserved (i.e., one considers a constant density incompressible fluid) the resulting flow equations become

$$\nabla\times\vec{B} = \frac{\alpha\vec{B}}{2} + \mu_0\beta(\nabla\times\vec{v})$$
$$\vec{v} = \frac{\beta}{\rho}\vec{B} + \omega r\hat{\theta} \quad . \tag{16}$$

For a cylindrical, axisymmetric system, the resulting field structure is given by

$$B_\theta = A^* J_1(\kappa r) \tag{17}$$

$$V_\theta = \frac{\beta A^*}{\rho} J_1(\kappa r) + \omega r \quad . \tag{18}$$

α, β, and κ can be evaluated by means of appropriate boundary conditions. The result yields

$$\beta = -\frac{\omega}{\nu} \pm \sqrt{\frac{\omega^2}{\nu^2} + \frac{\rho}{\mu_0}} \tag{19}$$

$$\alpha = \frac{2\mu_0}{\rho R} \cdot \beta \cdot \left(\frac{\omega}{\nu}\right) , \tag{20}$$

where ν is a constant determined by the boundary conditions. From Equation (19) we see that as $\omega \to 0$, the solution goes to the Alfvén speed and flow may occur symmetrically either parallel (corotational) or antiparallel (contrarotational) to the field. As ω becomes very large $\beta \to 0$ and all of the energy available in the flow is energy of rigid rotation. This apparently approximates the plasmoids which have been observed by Bostick and co-workers. These are the H-centered vortices.

Recent experiments performed at the University of Miami using the apparatus described in Reference 3 indicate that in mirror trapping experiments the plasmoids observed have structures which are accurately predicted by Equations (14) and (15). The symmetries of the flow structures within the plasmoids are exactly those predicted by the theory. That is, they are co and contrarotational and at least approximately force-free structures.

References

1 H. Alfvén and C. Falthammer, Cosmical Electrodynamics, Oxford Press, 1963.

2 V.C.A. Ferraro and C. Plumpton, Magneto Fluid Dynamics, Oxford Press, 1961.

3 D.R. Wells, Phys. Fluids, 9, 1010-1021, (1966).

4 L. Woltjer, Proc. Nat. Acad. of Sci. 44, 489 (1958).

5 L. Woltjer, Proc. Nat. Acad. of Sci. 44, 833 (1958).

6 L. Woltjer, Proc. Nat. Acad. of Sci. 45, 769 (1959).

7 D.R. Wells and J. Norwood, Jr., "Production and Propagation of Plasmoids in a Nonlinear Alfvén Wave", Phys. Fluids (to be published).

8 W.H. Bostick, H. Byfield, and A. Jermakian, Phys. Fluids 9, 2287-88 (1966).

9 S. Chandrasekhar, Hydrodynamic and Hydromagnetic Stability, Oxford (1961) pp. 551-6.

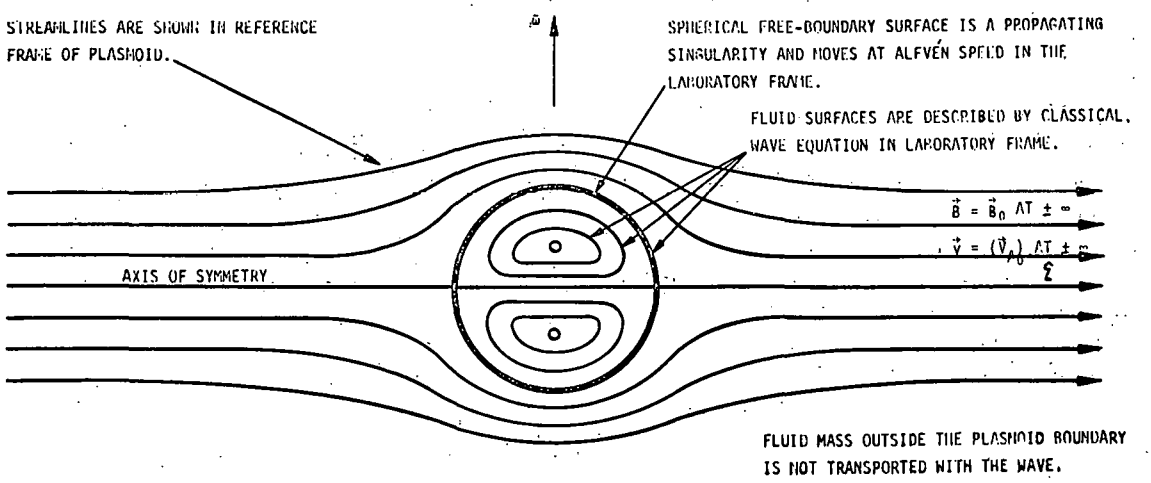

Fig. 1. The nonlinear Alfvén wave (plasmoid).

PRODUCTION AND MAGNETIC FIELD CONFINEMENT INVESTIGATIONS OF LASER IRRADIATED SOLID PARTICLE PLASMAS*

by

Alan F. Haught and Donald H. Polk
United Aircraft Research Laboratories
East Hartford, Connecticut

ABSTRACT

The focused beam of a Q-spoiled ruby laser has been used to form a high-temperature, high-density plasma from a single 10-20 μ diameter particle of lithium hydride, which is electrically suspended in a vacuum environment. From time resolved charge collection measurements, the plasma expands as a ball and is essentially spherically symmetric in both density and expansion velocity. Velocities up to 4×10^7 cm/sec, corresponding to average plasma energies of over 200 eV, have been measured. Calculations of the plasma formation and expansion have been made using both a spherically symmetric hydrodynamic model and an integrated similarity model, and give results in very good agreement with those observed experimentally. Measurements have been carried out examining the interaction of these plasmas with confinement magnetic fields of mirror and minimum-B geometry at field strengths up to 8 kG. The results obtained indicate the confinement of a $\sim$ 200 eV thermalized plasma with a density of $\sim 10^{13}$ cm^{-3} for times of respectively 5 and 10 μ sec in the 8 kG mirror and minimum-B magnetic fields.

I. APPARATUS

To produce experimentally an isolated, high-density plasma, a small particle of the lithium hydride from which the plasma is generated is electrically suspended in vacuum at the focus of the lens where it is vaporized, ionized, and heated by the focused high-intensity beam of a Q-spoiled laser.[1] A schematic of the apparatus used for these studies is shown in Fig. 1. Particles of the lithium hydride stored in the particle injector are projected up into the suspension region by means of a spring flipper wire. These particles are charged by electrons emitted from a hot filament and are captured in the suspension electric field produced by a cubical array of electrodes, opposite pairs of which are each connected to one of the terminals of a Y-connected, three-phase ac supply. By suitable adjustment of these ac potentials and of dc potentials also applied to the electrodes, all but one of the particles are ejected from the suspension field, and the remaining particle is positioned at the point near the center of the one liter cubical suspension volume where the size of the particle orbit is a minimum--approximately 2-3 times the particle diameter. Using a set of three orthogonal slides which support the suspension electrode array through a vacuum tight bellows coupling, the electrode array is positioned so that the particle, in its minimum orbit, is located at the lens focus. The focused giant pulse beam from a Q-spoiled ruby laser is then used to vaporize and ionize the atoms of the particle, resulting in the production of a high-temperature, high-density plasma.

II. FREE PLASMA EXPANSION - THEORY

The plasma, since it is formed in a vacuum, immediately begins to expand. This expansion lowers the plasma density, decreasing the plasma absorption coefficient, and eventually terminating the heating by the laser beam. The hydrodynamic equations for the plasma expansion, taking into account the energy input to the plasma from the laser beam, have been solved numerically for the plasma energy and the time history of the plasma

expansion by dividing the plasma into a series of concentric spherical shells, and computing the density, expansion velocity, and temperature within each shell.[3,4] From the results of these calculations, very early in the laser pulse the plasma temperature becomes uniform throughout the plasma and the density and velocity profiles within the expanding plasma assume forms which do not subsequently change with time. In Fig. 2, the calculated similarity density and velocity profiles are plotted as functions of normalized radial position within the plasma, $u = r/R$, where R is the time dependent outer boundary radius of the plasma.

The results of the hydrodynamic calculations suggest an integrated similarity model in which the asymptotic forms of the density and velocity profiles are assumed throughout the plasma growth, and the expansion equations are similified by integration over the plasma volume.[3] During the initial stages, when the similarity conditions do not strictly apply, the energy absorbed is small, and any discrepancies resulting from the use of this model do not materially affect the results. The expansion time history and values of plasma energy obtained from both the integrated similarity model and the hydrodynamic model are virtually indistinguishable over the entire range of conditions of experimental interest, justifying the use of the simpler integrated similarity model for extensive calculations with different values of the experimental parameters. In addition, the simpler equations obtained with the integrated similarity model permit the use of a more exact energy absorption term than employed in the hydrodynamic equations, allowing the effects on the energy absorption of the plasma density profile and the chord path of the laser radiation through the spherical plasma to be taken into account.

The free expansion plasma time history given by the integrated similarity model (and the hydrodynamic model as well) is shown in Fig. 3 along with the laser pulse waveform, Φ, and plasma energy absorption rate, W. For the case shown in Fig. 3 a 1 GW, 10 nsec laser beam focused to a $100\,\mu$ focal spot radius irradiating a $10\,\mu$ radius lithium hydride particle gives an asymptotic average plasma energy, ϵ, of 200 eV/plasma constituent. It is observed that the peak plasma temperature characteristically is approximately 1/5 the average energy of the plasma, i.e., even when the plasma temperature is a maximum, four times the thermal energy is present in the form of kinetic energy of radial expansion. As a result of the rapid plasma expansion, the maximum power absorbed from the laser beam generally occurs well before the laser pulse maximum, and the total energy absorbed by the plasma is only ~ 1-2 percent of the total energy available in the laser pulse.

Calculating the plasma energy over a range of particle sizes, R_0, and laser focal spot sizes, Γ, gives a plasma energy surface for a given laser beam power and pulse time history such as that shown as a contour map in Fig. 4. Such calculations carried out for different laser beam powers and pulse durations all display a "ridge", or characteristic R_0, Γ region, along which the plasma energy is a maximum and away from which the plasma energy decreases rapidly. In general, the maximum plasma energy is obtained when $2R_0 \leq \Gamma \leq 5R_0$ and $R_0 < 50\mu$, illustrating the necessity for careful control of the experimental conditions if maximum plasma energy is desired. Calculations of a number of plasma energy surfaces like that of Fig. 4 have been made for different values of the peak laser beam power, Φ, and laser pulse halfwidth, τ, (a Gaussian shaped pulse is assumed). For pulse powers greater than 1 MW and pulse durations greater than 1 nsec, the maximum plasma energy is given by the empirical relation $\epsilon_{max} = 80\ \text{eV}\,(\Phi\,\text{MW})^{1/3}(\tau\,\text{nsec})^{-1/2}$. With a 20 MW laser pulse of 20 nsec duration, the calculated maximum plasma energy is 50 eV and for a 1 GW, 10 nsec laser pulse, an energy of 250 eV is predicted.

III. FREE PLASMA EXPANSION - EXPERIMENTAL[3]

Charge collectors have been used to measure experimentally the ionization and spherical symmetry of plasmas produced by laser beam irradiation of single 10-20 μ radius lithium hydride particles. Using six charge collectors, simultaneous observations were made of the charge density of the expanding plasma in six directions relative to the laser beam axis. The charge collection (and thus the amount of plasma expanding) in the direction of the laser beam is somewhat lower than observed in the other directions. The maximum difference, however, is less than a factor of two, and the charge density distribution in the expanding plasma is essentially spherically symmetric. Using two charge collectors located at different distances from the plasma origin, measurements of the time delay between the arrival of the plasma at the two probes can be used to determine the plasma expansion velocity. Using three sets of probes, simultaneous time-of-flight measurements were made of the plasma expansion in three directions relative to the laser beam. Within 10-20 percent, the plasma time of flight in the three directions is the same, and the expansion velocity distribution of the plasma is essentially spherically symmetric. These results establish that the freely expanding plasma produced in the experiments is essentially spherically symmetric in both density and expansion velocity despite the unidirectional energy input to the plasma and justify the simplifying assumption of spherical symmetry employed in the theoretical models.

From Fig. 3, after the plasma radius exceeds ~ 10^{-1} cm, the plasma temperature is greatly decreased from its peak value and nearly all of

the plasma energy is in the form of kinetic energy of radial expansion. Consequently integrating the kinetic energy density as determined by the profile of Fig. 2 over the plasma volume, the average energy of the plasma ions and electrons is uniquely related to the expansion velocity of the plasma boundary. In the experiments, plasma expansion velocities in excess of 4×10^7 cm/sec have been obtained. This expansion velocity corresponds to an average plasma energy of 220 eV, in good agreement with the 250 eV energy predicted by the theoretical calculations for the 1 GW peak power, 10 nsec halfwidth laser pulse used. Experimental studies have been made for three widely differing sets of laser power-focal spot size conditions. In each case the plasma energies obtained are in good agreement with the theoretically predicted values, serving as strong support for the theoretical models employed.

IV. MAGNETIC FIELD CONFINEMENT INVESTIGATIONS[3]

The laser irradiated single particle plasma is a spherically expanding free plasma, produced in vacuum with no supports, background gas, net mass motion, or net currents present. As a result, this plasma is particularly suitable for studying the interaction of a plasma with magnetic containment fields. With megagauss magnetic fields, pressure balance would be obtained at a plasma density greater than 10^{19} cm^{-3}. At these densities, the plasma is still opaque to the laser beam, and a much larger fraction of the total laser beam energy would be absorbed, giving rise to a plasma energy greater than that of the freely expanding plasma. However, the production of megagauss magnetic fields is a difficult problem in itself and, as a result, a second regime of interest has been investigated in the studies reported here. In these studies the plasma is allowed to expand in magnetic fields of kilogauss field strength giving a plasma of $\sim 10^{13}$ cm^{-3} density. Such experiments permit the examination of the capture, thermalization, and subsequent decay of an initially spherical plasma in mirror, cusp, and minimum-B containment fields.

For these studies no injection of the plasma is required. With the particle suspended in place, the magnetic field is turned on. The suspension voltages are then removed, and the particle is irradiated with the laser beam, producing the plasma which then expands within the magnetic field. Since the plasma energy absorption and formation occur while the plasma is so small (see Fig. 3) that no appreciable interaction with the magnetic field occurs, the plasma develops as if the magnetic field were not present, and the spherical field-free plasma expansion forms the initial conditions for the plasma interaction with the magnetic field.

To produce the magnetic fields for these studies, three independent ignitron-switched capacitor bank power supplies are used to power three pairs of magnet coils, one coil located immediately behind each of the particle suspension electrodes as shown in Fig. 1. The magnetic field configurations produced with these coils are shown in Fig. 5. In Fig. 5 directions are identified which, along with "up" and "down" are used to define the location of the charge collector and time-of-flight diagnostics and the orientation of the magnetic fields in the experiments. A pair of coils is used to form a mirror (mirror ratio 4.3) or a cusp magnetic field and, using all six coils, a minimum-B magnetic field is generated. The present experiments have been carried out in mirror and minimum-B magnetic fields at central field strengths up to 8 kG.

Shown in Fig. 6 are the results of measurements of the plasma density symmetry with no magnetic field (free plasma expansion), in an 8 kG mirror field, and in an 8 kG minimum-B magnetic field. The charge collector probes register the ion flux through the probe aperture (apertures of all probes equal). For a given probe the integrated charge collection, recorded as a voltage signal on a capacitor, represents the amount of plasma which has expanded in the direction of that probe. With no magnetic field, the integrated charge collection as a function of time is essentially the same (i.e., within a factor of two) for each of the six probes, displaying the spherically symmetric density distribution discussed in Part III. With either a mirror or a minimum-B magnetic field, however, the charge collection, and thus the plasma flux, transverse to the magnetic field (all collectors except South) is greatly reduced, while the plasma flux along the mirror axis in the direction of the mirror loss cone (South) is greatly enhanced. With no magnetic field, the plasma observed by the charge collectors is received over a time interval of less than 1μ sec. With either the mirror or the minimum-B magnetic field, the charge collection is observed to occur over a time interval of 5-10μ sec. Both the strong asymmetry in the direction of the loss cone and the increase in charge collection time indicate that a substantial fraction of the plasma did not expand freely through the magnetic field but was contained within the field and only gradually leaked out.

Time-of-flight measurements of the plasma expansion rate were made for the free plasma expansion and for the expansion in magnetic fields to examine the variation in the plasma expansion velocity caused by the plasma-magnetic field interaction. Two time-of-flight probes measuring the plasma expansion rate in the South and Upper West directions were used for these studies giving the data of Fig. 7. With no magnetic field, the plasma time of flight, and thus expansion velocity, for both of these directions is very nearly the same--the essentially spherically symmetric free plasma expansion discussed in Part III. In both the simple

mirror and the minimum-B magnetic field, the time of flight across the magnetic field is greatly increased indicating a very low plasma velocity transverse to the magnetic field. Along the mirror axis (South), the plasma time of flight is not only much shorter than that across the magnetic field but also shorter than obtained with no magnetic field. This result is suggestive of a plasma-magnetic field interaction which restricts the plasma expansion in the transverse directions, changing the three-dimensional free plasma expansion to a one-dimensional expansion and resulting in a larger plasma velocity along the magnetic field lines.

Using a 6 mm microwave interferometer, measurements have been made of the attenuation and phase shift of a beam transmitted through the plasma, from which information regarding the plasma density decay can be derived. Calculations of the microwave amplitude and phase shift signals were carried out for the free plasma expansion and show that the transmitted microwave beam is initially attenuated by the expanding plasma but that transmission again occurs when the plasma density decreases below cutoff ($n_c = 3 \times 10^{13}$ cm^{-3}). During the time of large attenuation, the phase shift introduced by the plasma is surpressed. Only after the plasma density decreases below cutoff is modulation of the phase signal observed, and in general only a single phase shift maximum occurs, at the time when the line of sight density through the plasma is 10^{13} cm^{-2}. From Fig. 8 with no magnetic field, in agreement with these calculations, the expanding plasma rapidly attenuates the microwave beam, but transmission is recovered again in approximately 0.4 μ sec. One phase shift maximum is observed, corresponding to a line of sight density, $\int ndr$, of 10^{13} cm^{-2}, and appears at a time only 0.3 μ sec after the plasma production. With a mirror magnetic field, however, the microwave signal is strongly attenuated for 5 μ sec, and the final phase shift maximum occurs at 5.5 μ sec, indicating that the mirror magnetic field preserves a plasma density of $> 10^{13}$ cm^{-3} for a time as long as 5 μ sec compared with the 0.3 μ sec for the free expansion case. Similar results out with still longer lifetimes are obtained with a minimum-B magnetic field. In particular, at a central minimum-B magnetic field strength of 8 kG, plasma is observed at a density of $> 10^{13}$ cm^{-3} for as long as 10 μ sec following the plasma formation, and from the finite slope of the attenuation trace, substantial plasma is still in evidence as late as 80 μ sec.

Cold background plasma produced by the expanding plasma striking the walls of the containment region could produce the microwave and charge collector results obtained. However, the collisional scattering loss time of such a cold ($\sim$ 1 eV) plasma at the required density of $\sim 10^{13}$ cm^{-3} is only 10^{-7} sec, and the cold plasma would not remain within the confinement region for the 5-10 μ sec evidenced by Fig. 8. For the thermalized laser produced plasma ($\sim$ 100 eV) at a density of $\sim 3 \times 10^{13}$ cm^{-3} the scattering loss time constant is 10 μ sec, in reasonable agreement with the experimentally observed plasma lifetime. In addition, a cold background plasma at a density of $\sim 10^{13}$ cm^{-3} would rapidly diffuse across the magnetic field due to the short scattering time, and it would not be expected that the magnetic field configuration would have an appreciable effect on the plasma decay rate. The increased plasma lifetime in the minimum-B magnetic field shows that field geometry effects are important and further indicates that the plasma contained by the magnetic field is the thermalized laser produced plasma.

V. REFERENCES

*Portions of this work were supported by the U. S. Atomic Energy Commission under Contract AT(30-1)-3578. The results presented in this paper are discussed in greater detail in Ref. 1 and in two reports to the A.E.C., Refs. 2 and 3.

1. Haught, A. F. and D. H. Polk, Phys. Fluids, 9 2047 (1966).

2. Haught, A. F. and D. H. Polk, "Production of Plasmas for Thermonuclear Research by Laser Beam Irradiation of Solid Particles," Quarterly Report, June, 1966, E920365-4, NYO-3578-4, prepared under Contract AT(30-1)-3578 for the U. S. Atomic Energy Commission, June, 1966.

3. Haught, A. F., D. H. Polk, and W. J. Fader, "Production of Plasmas for Thermonuclear Research by Laser Beam Irradiation of Solid Particles," Annual Review Semiannual Report, June, 1967, F920365-6, NYO-3578-6, prepared under Contract AT(30-1)-3578 for the U. S. Atomic Energy Commission, June, 1967.

4. Fader, W. J., "Hydrodynamic Model of Spherical Plasma Produced by Laser Irradiation of a Solid Particle," to be published in Physics of Fluids.

VI. FIGURES

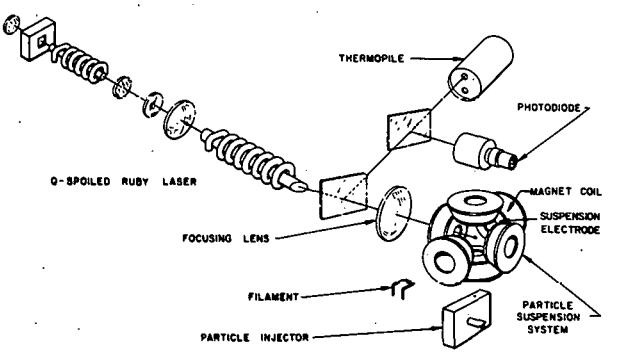

Fig. 1 - Particle Plasma Apparatus

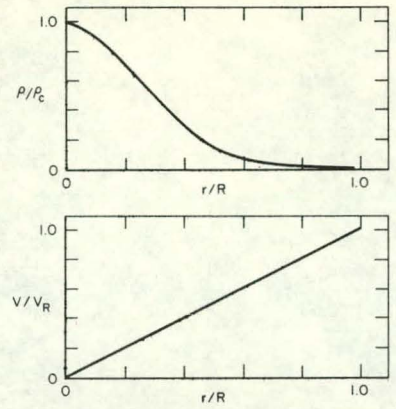

Fig. 2 - Density and Velocity Profiles

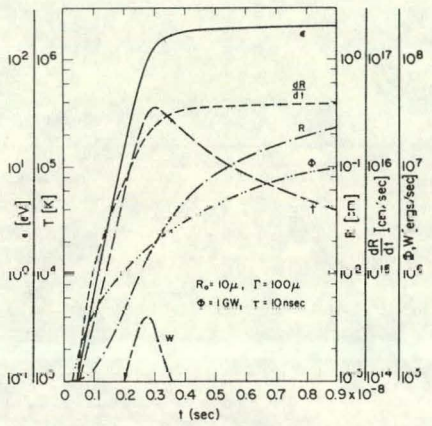

Fig. 3 - Plasma Time History

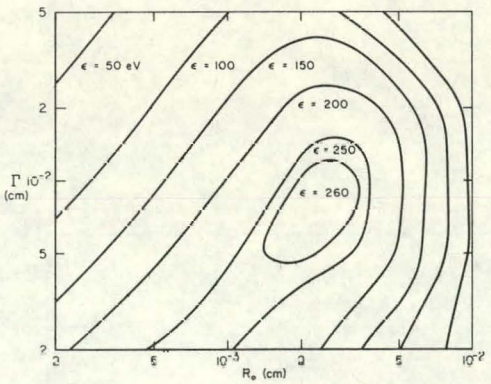

Fig. 4 - Plasma Energy Surface

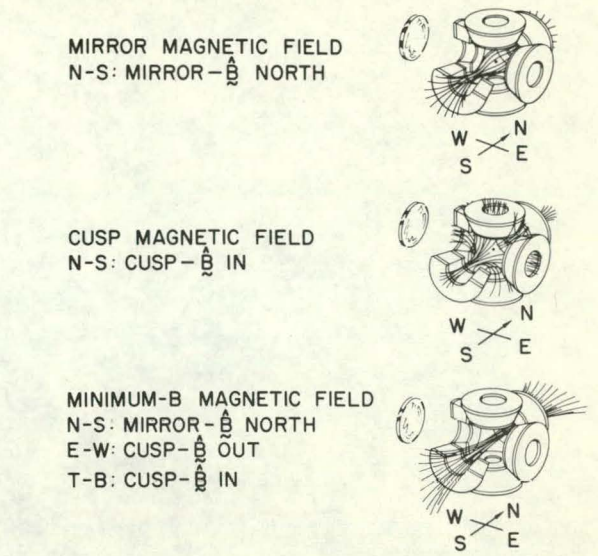

Fig. 5 - Containment Magnetic Field Geometries

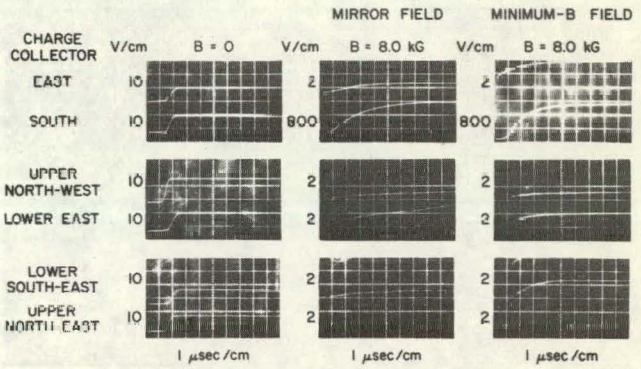

Fig. 6 - Plasma Density Symmetry

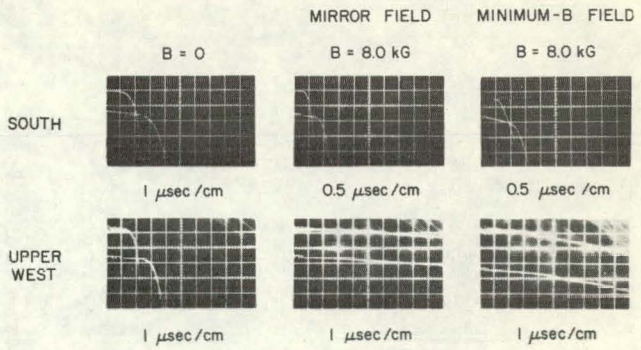

Fig. 7 - Plasma Expansion Velocity

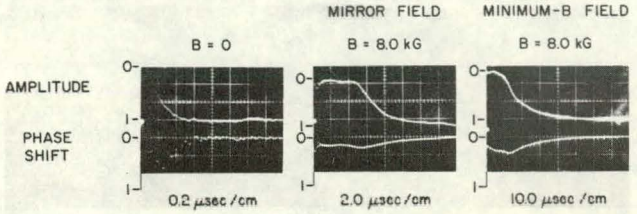

Fig. 8 - Plasma Density Decay

LASER - THERMONUCLEAR FUSION EXPERIMENT

by

J. C. Bryner and G. H. Sichling
North American Aviation, Inc.
Space Division
Downey, California

ABSTRACT

A series of experiments has been carried out to demonstrate the feasibility of producing thermonuclear reactions by heating fusionable material with an intense laser beam. The plasma was produced in a 10^{-7} torr vacuum by a 500 megawatt pulsed, ruby laser. The laser pulse width was measured at 10 to 15 nanoseconds. A specially designed lens system focused the laser beam onto a LiD pellet of about 0.1 mm dimension, which resulted in an intensity of about 4.5×10^{12} watts/cm^2. Time-of-flight measurements indicated velocities which were sometimes in excess of 10^7 cm/sec and kinetic energies of several kilovolts per ion in the expanding plasma cloud. A special purpose integrating scintillation counter was constructed to detect neutrons produced in D-D reactions. No neutrons were detected by this device in any of the experiments. This result indicates that fewer than 1000 thermonuclear reactions took place and that the peak plasma temperature was below 330 electron volts.

Introduction

The concept of heating material to thermonuclear temperature by means of a focused laser beam has been suggested by several investigators.[1,2,3] Within North American's Space Division the idea was first suggested in early 1963 in pursuance of studies in advanced energy sources for space power and propulsion systems. A small, theoretical investigation was subsequently initiated in an attempt to determine the feasibility of the concept for use in the space program. The conclusions of this study completed in November 1963 were:

1. Temperatures in the thermonuclear range (1 to 10 kev) are possible using state-of-art ruby laser equipment.
2. An experiment should be performed to demonstrate the feasibility of the basic concept.

Because of the enormous potential of thermonuclear power for use in the space program plans for a feasibility experiment were made and eventually became a reality.[4,5] These experiments are the subject of this paper.

Equipment

Most of the equipment used in these laser-fusion experiments was designed and built at North American's Space Division. Following is a brief description of the major items.

Laser. The laser we used consists of two almost identical sections, one of which is a Q-spoiled oscillator, the other a single-pass amplifier. Both sections use 6 inch x 3/8 inch ruby rods mounted in reflective cavities and illuminated by PEK XE 16-6 xenon flash lamps. The laser may be seen in the upper, central portion of Figure 1. Q-spoiling is accomplished by the use of passive dye (Victoria Blue B) which was dissolved in alcohol (ethyl or isopropyl) and deposited on a spinning, 2 x 3-inch microscope slide. The thickness of the dye deposited on the slide could be controlled by varying the concentration of dye in the alcohol and the rotational speed of the slide. Experiments with the laser revealed that there is an optimum dye thickness for high power output.

Measurement of the laser power was accomplished with a type 929 photodiode which was calibrated using an NBS standard quartz-iodine lamp. The results of this calibration was checked by measuring the laser Q-spoil energy with a TRG thermopile and calculating the power from an oscillogram of the output laser light. The two methods agree fairly well and show that about 300 megawatts of beam power are produced in the 6-inch ruby oscillator and up to about 500 megawatts in the oscillator-amplifier combination.

Focusing Optics and Telescope. This lens system was designed and built especially for focusing ruby laser light. Additionally, a retractable telescope serves to view the target surface and, through the use of a filar micrometer, measure the characteristics of the impacted area. Crater diameters of less than 0.10 mm have been measured with this device which were produced by 200 to 300 megawatt laser pulses. The maximum intensity on the target surface under these conditions is about 4.5×10^{12} watts/cm^2.

Vacuum System. The vacuum system, shown in the lower, central portion of Figure 1, provides a 10^{-7} Torr vacuum in a cubical chamber about 10 inches on an edge. It is pumped by a 6-inch oil diffusion pump and a rotary roughing pump. The focusing optics attach to one wall of the chamber. In order to preserve the surface of the final lens element, a flat window is mounted in the chamber wall. The chamber is constructed of aluminum.

Remote Target Positioning Assembly. The target holding and remote positioning assembly is mounted on the top plate of the vacuum chamber, as can be seen in Figure 1. It provides a continuous, micrometer adjustment of the target in three, independent directions, and hence can position it at a given point in the chamber. Since the target material (LiD) changes its properties with exposure to the air, a scheme has been incorporated which permits the target material to be enclosed in a small handling container with an appropriate inert atmosphere. This holder is inserted in the positioning assembly. As the chamber is pumped down, the cover of the holder is removed, thus exposing the material for laser irradiation without risking contamination in the handling process.

Neutron Detector. The neutron detector used in these experiments consists of a 5-inch diameter, 5-inch long cylinder of "Pilot A" scintillating plastic material coupled to an RCA 8055 photomultiplier tube. It can be seen attached to the left-hand side of the vacuum chamber in Figure 1. The nuclear event which it was designed to monitor would take place in less than 10^{-8} seconds. Since we were only interested in the total number of events and not the time history of the neutron flux, an integrating circuit with a time constant of about 240 microseconds was built into the photomultiplier circuit. The detector was calibrated using 14.1 Mev neutrons from a D-T reaction.

Attempts to Produce Thermonuclear Reactions

In November 1965, three separate attempts were made to detect thermonuclear neutrons from a lithium-deuteride (LiD) plasma. In each case, small crystals of LiD were suspended in the vacuum chamber on a 0.001 inch thick strip of mylar tape placed approximately at the laser focus. Final focusing and alignment was accomplished after the air was evacuated from the chamber by means of the Remote Target Positioning Assembly. Radiation calculations were made for the worst case (the whole target undergoing fusion reactions), and neutron shielding was applied to protect personnel in this case. A photograph of the experimental configuration during one of these tests is given in Figure 1. The 5-gallon cans contain a water-borax solution for neutron shielding.

An oscillogram of one of these neutron tests is shown in Figure 2. The measured laser power for this particular shot is 450 megawatts. The expansion velocity is 3.2×10^7 cm/sec which corresponds to an average kinetic energy per ion of about 2.2 kev. The neutron detector sensitivity is about 3×10^4 neutrons/major division. As no indication is seen at the time of the laser pulse, something less than 10^3 neutrons must have been produced. The small wiggles seen after the laser pulse are probably some kind of electrical pickup since nearly identical wiggles appear on the laser detector output also.

The reaction rate of a D-D reaction can be written[6]

$$R_{DD} = 1/2\, n_D^2\, (\overline{\sigma v})_{DD} \qquad (1)$$

where n_D is the deuterium density and[7]

$$(\overline{\sigma v})_{DD} = \frac{2.33 \times 10^{-14}}{T^{2}/_{3}} \exp\left(-\frac{18.76}{T^{1}/_{3}}\right) \frac{cm^3}{sec} \qquad (2)$$

The temperature T is measured in kilo-electron volts (kev). In the solid form of LiD the atomic density of deuterium is approximately 5×10^{22} atoms/cm^3. Since measured expansion velocities are on the order of 10^7 cm/sec, the number density would be expected to reduce by approximately an order of magnitude in one or two nanoseconds however. For a rough estimate we assume that $n_D = 5 \times 10^{21}$ cm^{-3}.

If we assume further that the portion of the target volume which is hot enough to undergo thermonuclear reactions is $V = 10^{-6}$ cm^3 and that high temperatures exist for approximately $t = 10^{-9}$ seconds, the total number of reactions N can be written:

$$N \approx R_{DD} V t$$

$$= 1/2\ (5 \times 10^{21})^2\ \frac{2.33 \times 10^{-14}}{T^{2}/_{3}}\ \exp\ (-\ \frac{18.76}{T^{1}/_{3}})$$

$$\times 10^{-6} \times 10^{-9} = \frac{2.91 \times 10^{14}}{T^{2}/_{3}}\ \exp\ (-\ \frac{18.76}{T^{1}/_{3}})$$

reactions (3)

The D-D reaction can go either of two ways, each with about equal probability:

$$D + D \begin{cases} \nearrow\ H_e^3 + n\ (3.27\ \text{Mev}) \\ \searrow\ T + P\ \ (4.03\ \text{Mev}) \end{cases} \qquad (4)$$

Only the upper path creates a neutron; however, the tritium (T) reacts at a considerably faster rate by the following reaction to produce another neutron:

$$D + T \rightarrow H_e^4 + n\ \ (17.6\ \text{Mev}). \qquad (5)$$

We therefore assume that every D-D reaction produces a neutron, and the rate of neutron production is also given by Eq. 3. A plot of the number of neutrons produced as a function of plasma temperature T is given in Figure 3. It can be seen here that fewer than 10^3 neutrons are produced (under the assumptions stated above) whenever the plasma temperature remains below about 330 ev. Temperature was not measured directly in any of these experiments however.

We now calculate our plasma temperature according to some later work in which plasma temperatures have been determined.[7,8] Equation 6 gives the plasma temperature T_p (in degrees Kelvin) as a function of molecular weight M and laser intensity P:[7]

$$T_p = 0.5\ M^{0.8} P\ (0.6/M^{0.09}) \qquad (6)$$

For a hot plasma of LiD, the average molecular weight M is 4.5 g/mole. The highest intensity recorded in any shot is 4.5×10^{12} watt/cm^2. Using these two numbers in Equation 6, the plasma temperature $T_p \approx 600$ ev, which agrees rather poorly with the estimate from the neutron production. Part of the disagreement may be because Equation 6 was generated using Be, Al and Pb, while we have applied it to LiD.

Radiation losses from the hot plasma will tend to lower the temperature. The specific power loss from a hot plasma under the preceding conditions may be written:

$$P_{br} = 5.35 \times 10^{-31}\ n_e \sum (n_i Z^2)\ T_e^{1/2}$$

$$= 5.35 \times 10^{14}\ T^{1/2}\ \text{watts/cm}^3 \qquad (7)$$

where $n_e = 2 \times 10^{22}$ cm^{-3}, $n_D = n_{Li} = 5 \times 10^{21}$ cm^{-3} and $T = T_e$.

At a temperature of 330 ev, $p_{br} \approx 3 \times 10^{14}$ watts/cm^3. At the same time, however, the laser is supplying about 5×10^8 watts. Assuming that all of this power is absorbed in the 10^{-6} cm^3 target volume, the specific power input from the laser is 5×10^{14} watts/cm^3. The Bremsstrahlung losses, therefore, are seen to be large enough to limit the temperature somewhat below the preceding estimates.

Acknowledgement

The authors express indebtedness to W. E. Banios, Chief of Power and Propulsion, for his continuous direction, encouragement and technical support during the course of this study.

References

1. Basov and Krokhin, Proceedings of the Conference on Quantum Electronics, Feb. 11-15, 1963, Paris.
2. Dawson, J. M., Phys. of Fluids 7, 981 (1964), also Plasma Physics Lab. Report MATT-22, 18 September 1963, Princeton, N.J.
3. Engelhardt, A. G., Westinghouse Research Lab Report 63-128-113-R2, 9 October 1963.
4. "High Temperature Dense Plasma Induced by Laser," G. H. Sichling and J. C. Bryner, SID65-540, North American Aviation, April 1965.

5. "Preliminary Laser-Fusion Application Study," W. K. Luckow, SID65-852, North American Aviation, July 1965.

6. Controlled Thermonuclear Reactions, Glasstone and Lovberg, D. Van Nostrand Co., 1960.

7. "Plasma Temperatures Generated by Focused Laser Giant Pulses," David W. Gregg & Scott J. Thomas, J. Appl. Phys. 38, 1729 (15 March 1967).

8. "Vacuum Ultraviolet Radiation from Plasmas Formed by a Laser on Metal Surfaces", A. W. Ehler and G. L. Weissler, Appl. Phys. Letters 8, 89 (15 February 1966).

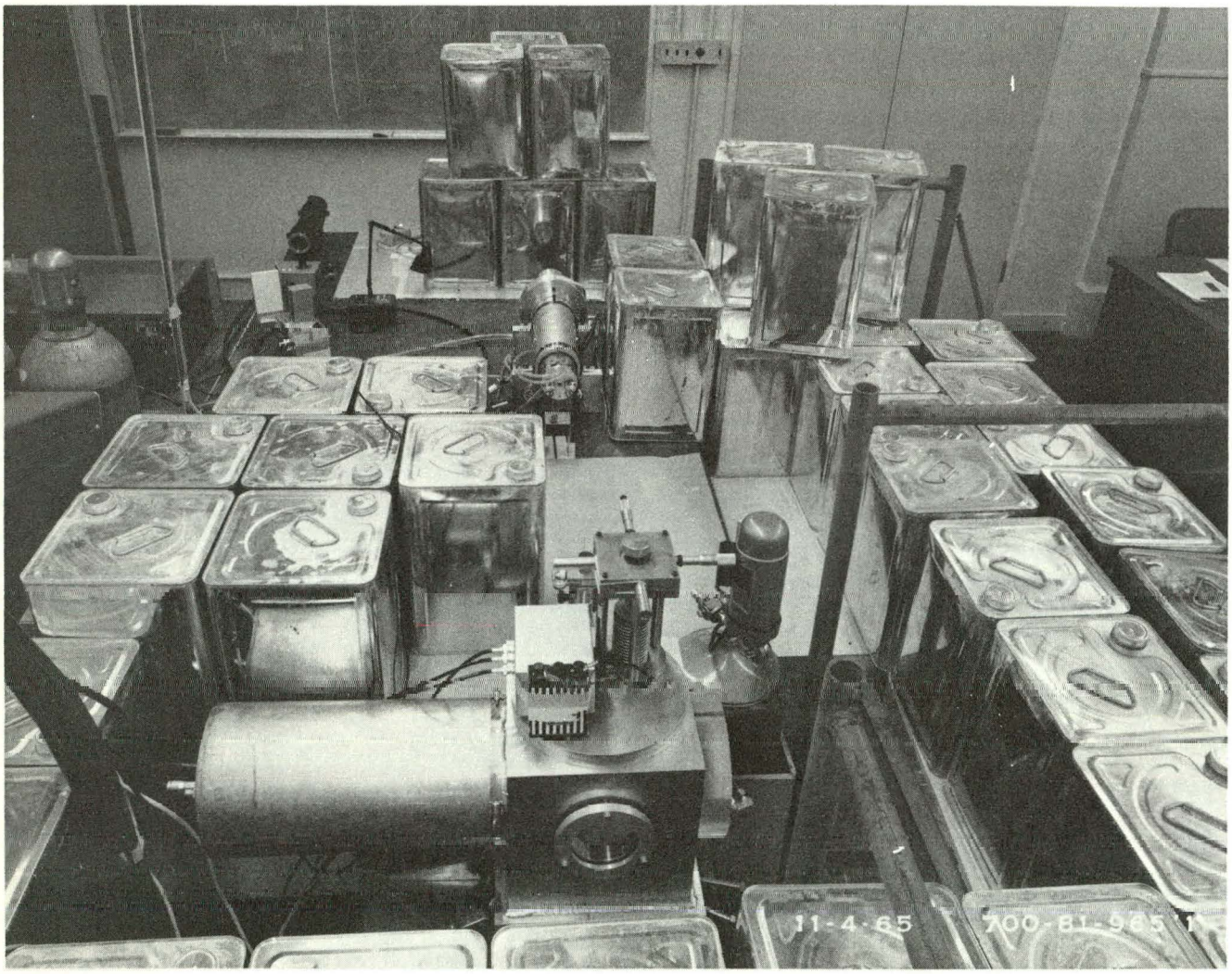

Fig. 1. Equipment arrangement for thermonuclear reaction experiments

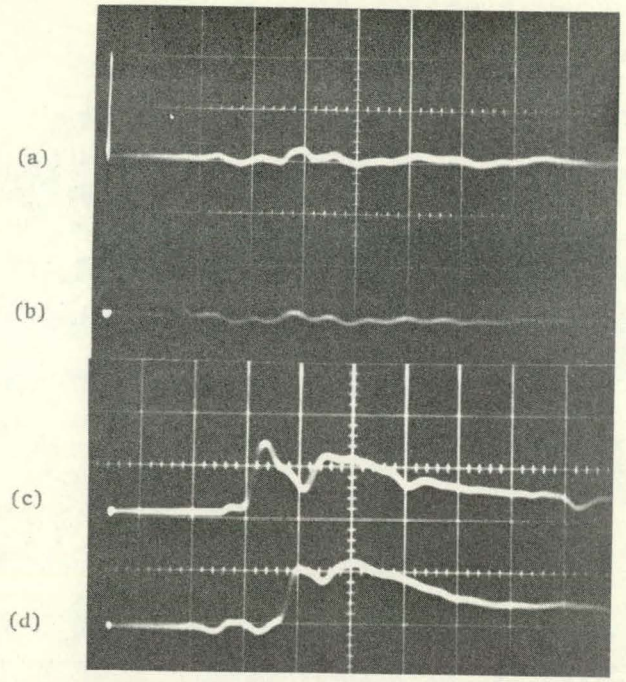

Fig. 2. Oscillograms of neutron test performed in November 1965.
(a) Neutron Detector - 3×10^4 neutrons/major division,
(b) Laser Pulse - 250 Mw/major division,
(c) Position Probe No. 1,
(d) Position Probe No. 2.
Position probes were placed 2.26 cm apart. Time scale is 0.1 nsec/major division.

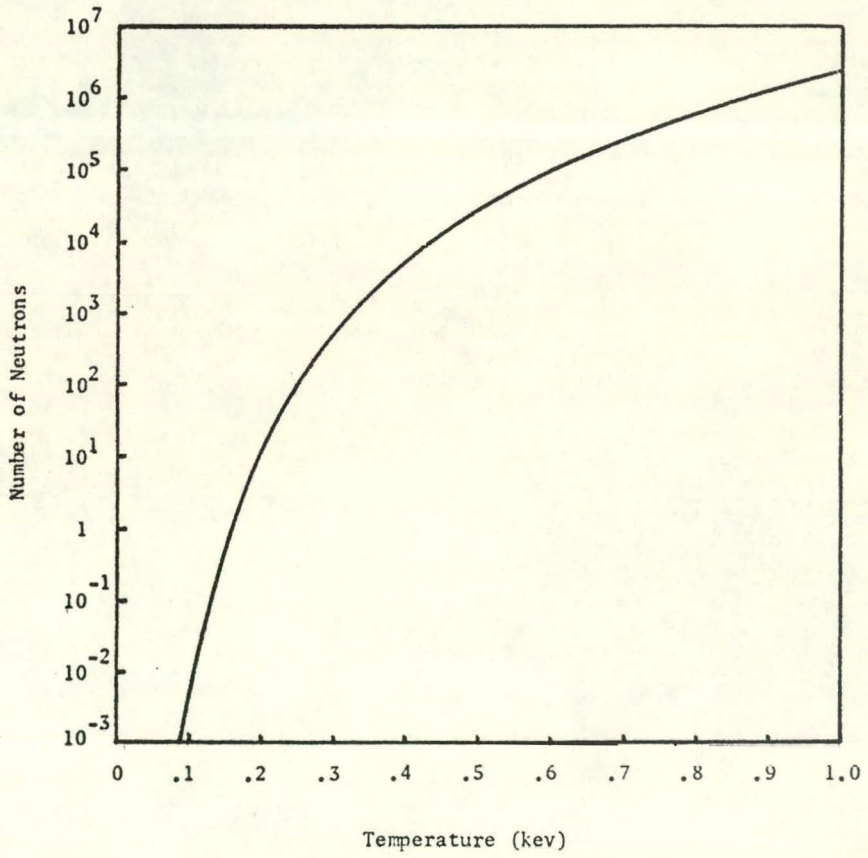

Fig. 3. Theoretical neutron yield from 10^{-6} cm^3 of LiD plasma of density 5×10^{21} cm^{-3} in 10^{-9} seconds.

THE 15-METER SCYLLAC θ PINCH*

by

E. L. Kemp, W. E. Quinn, F. L. Ribe, and G. A. Sawyer

Los Alamos Scientific Laboratory, University of California
Los Alamos, New Mexico

ABSTRACT

The Scyllac θ pinch is being designed in two phases: a 15-m linear device, followed later by a 5-m diameter torus. These will successively occupy a common building, power supply, and control system. Engineering progress in designing the large system is described, as well as component development of the basic 60-kV, 2-μF capacitor, the coaxial cables, and the "start" and "crowbar" switches. The "M and S," or free-boundary, problem of toroidal plasma equilibrium has been solved to first order in the aspect ratio of the plasma torus, yielding equilibrium solutions for thin-skinned plasmas with and without internal magnetic fields. Actual coil configurations to produce corresponding transverse stabilizing fields of $\ell = 0$ and $\ell = 1$ azimuthal symmetry with suitable longitudinal wavelengths have been constructed and measured. Corresponding experiments with $\ell = 0$ and $\ell = 1$ "bumps," excited at the center of the 100-cm Scylla IV compression coil, are being carried out to study ballooning-instability growth rates and practical problems of transverse field excitation.

I. THE TOROIDAL θ PINCH

The 15-m Scyllac θ Pinch[1,2] is being designed in two phases: a preliminary 15-m linear device, followed later by a 5-m diameter torus. The object is to investigate the micro- and macro-instability limitations of closed systems using collisionless high-β plasmas with ion temperatures in the 2-10-keV range.

In the case of a sharp plasma - magnetic-field boundary, the static "M and S" toroidal equilibrium,[3] illustrated in Fig. 1a, requires the inner magnetic lines to be sufficiently wavy that their lengths are equal to those of the outer lines. This necessarily introduces periodic regions of bad curvature which, in this high-β case, lead to macroscopic ballooning instabilities (flute modes of finite longitudinal wavelength, localized near the regions of bad curvature). Additional dynamic stabilization[1,2,4] is therefore necessary in order to produce macroscopic stability.

II. ENGINEERING DEVELOPMENT

1. The Overall System

The Scyllac θ pinch embodies the same basic technology as that used in the present high-voltage Scylla IV,[5] but with a 15-fold proliferation of components, as well as some necessary new component development. It requires a new experimental area of 30 × 30 meters housed in a building 3 stories high, designed to accommodate first the 15-m linear machine (Fig. 2) and then the 5-m torus (Fig. 3). The energy-storage system is being designed so that the capacitor racks and collector plates of the former can be rearranged to accommodate the torus. Preliminary designs have been completed of the building and all sub-systems, exclusive of dynamic stabilization. Both the torus and the linear device are split into 15 sections, each driven by 216 capacitors rated at 1.9-μF, 60-kV. The primary energy system will have the following parameters: B_{max} = 110 kG, E_θ = 1100 V/cm at 4.75-cm radius, rise time = 4 μsec, L/R decay time > 100 μsec. Its total energy is 10 MJ.

2. Component Development

A new 1.9-μF, 60-kV capacitor is being developed with the aid of the capacitor industry and a new high-voltage, low-inductance coaxial cable with the cable industry. In addition, a new 60-kV spark gap, similar to the Scylla IV 50-kV gap but with several unique features, is being developed

locally for the 60-kV capacitors. A scale-model prototype of two sections of Scyllac has been built to evaluate the new components and engineering concepts to be incorporated into the large system.

A crucial item is a "crowbar" switch for extending the magnetic-field duration to times greater than 100 μsec. At present the exploding-foil dielectric switch shown in Fig. 4 has been tested on a 90-kJ θ pinch (Scylla I-A) and shows promise. The oscillograms of Fig. 5 show it carrying 1.5 MA with an e-folding time of 1.2 msec in this system without plasma.

3. The Linear System

This θ pinch (Fig. 2) will provide a collisionless plasma of such length that end loss and line tying will be negligible for about 30 μsec. This should allow ample time to observe microinstabilities and corresponding anomalous diffusion if its magnitude is greater than about 0.03 the Bohm value. The central 2 meters of the compression coil will be excited with periodic $\ell = 0$ and $\ell = 1$ magnetic bumps of the type to be used in the torus. This will allow the measurement of ballooning growth rates. In addition, the amount of M and S excitation necessary to give a sidewise acceleration sufficient to overcome the expected drift due to toroidal curvature can be determined. Preliminary dynamic stabilization experiments are also envisioned.

III. MAGNETIC-FIELD EXCITATION TO PROVIDE TOROIDAL EQUILIBRIUM

1. Theoretical Treatment of Thin-Skinned Magnetic Equilibrium

Although the original Meyer-Schmidt treatment[3] showed the existence of plasma shapes for these equilibria, it remained until recently[6,7] to solve the problem in terms of known periodic applied fields. This has been done at high aspect ratio (for Scyllac $R/a \approx 300$) in terms of transverse magnetic fields with sinusoidal longitudinal periodicity whose angular dependence is of the form $\cos \ell\theta$. As might perhaps be expected, the problem resolves itself mainly into the superposition of $\ell = 0$ (periodic mirroring) and $\ell = 1$ (wavy) fields, as shown in Fig. 1b; although higher ℓ values enter weakly. The essentials of the solution of Ref. 7 are shown in Fig. 6 for typical Scyllac parameters. The abscissa δ_o represents the fractional excursion $\delta a/a$ of the mirror bumpiness; δ_1 the corresponding quantity for waviness; and δ_2 the fractional excursion from a circular plasma cross section into an elliptical one. For $\delta_1 \approx \delta_o$ (the case shown in Fig. 1a) a value $\delta_o \approx 0.2$ suffices, and δ_2/δ_1 is small. As seen from the ratios δ_o/C_o and $2\delta_1/C_1$, the required fractional periodic field variations are smaller, strikingly so for the $\ell = 1$ fields.

2. Practical Coils for Driving Periodic $\ell = 0$ and $\ell = 1$ Fields

Considerable modeling has been done to find coil configurations which give periodic vacuum-harmonic fields in a θ-pinch coil under realistic skin-effect conditions. A model coil giving a reasonable approximation to the $\ell = 1$ harmonic (periodically reversing transverse field) is shown in Fig. 7. This design has been constructed in a reinforced epoxy structure which is excited from vertical current collector plates driven by capacitors. Thus the coil can be driven from narrow vertical slots in the compression coil and its excitation timed to occur after the initial θ-pinch shock implosion is over. This "adiabatic" excitation of the M and S fields is considered essential in the Scyllac design.

Model measurements show that a periodic set of these $\ell = 1$ coils produces a peak transverse field of 15 mG per A of driving current. Each section has an inductance of 50 nH. For an assumed plasma β of 0.8 and the Scyllac value of main compression field, $B_o = 110$ kG, the current necessary to give $\delta_1 = 0.2$ $(= \delta_o)$ is therefore approximately 270 kA. The capacitor energy necessary to furnish this current at 50% transfer efficiency to the coil is 3.4 kJ. This is approximately 3% of the Scyllac primary capacitor-bank energy for the same periodicity length.

It presently appears to be impracticable similarly to excite $\ell = 0$ bumps from slots in the compression coil. One must instead produce spatially periodic changes in the current of the main compression coil. The principle for doing this adiabatically is shown in Fig. 8 for an isolated perturbation at the center of the Scylla IV coil. The series coil causes a reduction of the current drawn to its compression-coil section from the collector plate. However, field is excluded from the series coil by a hollow carbon cylinder for its skin-penetration and L/R time, which can be set to the ~ 2 μsec required for the shock implosion phase of the discharge to elapse. Measurement

show the bump to have $\Delta B_z/B_o = -0.15$. The corresponding plasma surface excursion is $\delta_o \approx 0.3$ for the non-periodic bump.

IV. BALLOONING OF BUMPY PLASMA COLUMNS

1. Collisionless and Collision-Dominated Plasma Regimes

The sensitivity of theoretical predictions of ballooning growth rates to the plasma model employed has been pointed out previously.[8,9] Collisionless (bounce-model) plasmas[10] have ballooning growth rates for $m > 1$ which are one to two orders of magnitude slower than those computed on the collision-dominated, incompressible-fluid model[4,11] The practical consequence of such a difference is that for very weakly growing instabilities one might employ dynamic stabilization fields in a configuration different than that which gives the static M and S equilibrium.[1] On the other hand, fast-growing instabilities would probably require oscillation of the M and S fields themselves.[4] The frequency of the high-Q dynamic stabilization circuit is also reduced for weakly growing instabilities. This is an important consideration in procuring the high-Q capacitors.

2. Ballooning Experiments on Scylla IV

There is now direct evidence in the case of a collision-dominated plasma with no line tying[12] that an $\ell = 0$ bump gives $m = 1$ ballooning in agreement with the incompressible-fluid prediction.[4] In this case, the ion-ion mean free path, λ_{ii} is 0.4 cm, and $\lambda_{ii}/2\pi r_L \approx 0.7$ ($\lambda_{ii}/2a \approx 0.4$). A similar experiment is in progress in the collisionless case of Scylla IV for which $\lambda_{ii}/2\pi r_L \approx 300$ ($\lambda_{ii}/2a \approx 300$), using the $\ell = 0$ arrangement of Fig. 8, as well as an $\ell = 1$ coil similar to that of Fig. 7. In this case, the absence of line tying is not assured, and its presence or absence must be demonstrated. In particular, collision-dominated plasmas will also be generated to see if ballooning similar to that of the Culham experiment[12] is encountered.

REFERENCES

1. F. L. Ribe, W. E. Quinn, G. A. Sawyer, D. A. Baker, R. L. Morse, T. A. Oliphant, W. B. Riesenfeld, E. L. Kemp, R. S. Dike, and A. S. Rawcliffe, Los Alamos Scientific Laboratory Report LA-3487-MS (1966).
2. H. Griem, H. Grad, D. Grove, D. Hartman, R. Kilb, N. Lazar, and F. Ribe, Report of Ad Hoc Panel on Scyllac, Report TID-23705 (USAEC Division of Technical Information, 1966).
3. F. Meyer and H. V. Schmidt, Z. Naturforsch. 13a, 1005 (1958).
4. J. Wesson, Paper B1, these proceedings.
5. E. M. Little, W. E. Quinn, and G. A. Sawyer, Phys. Fluids 8, 1168 (1965).
6. T. A. Oliphant, Los Alamos Scientific Laboratory Report, LA-3749-MS (1967).
7. J. L. Johnson, R. L. Morse, and W. B. Riesenfeld, Paper B2, these proceedings.
8. G. H. Wolf, Institut für Plasmaphysik (Garching bei München) Report IPP-163 (1967) p. 31.
9. F. L. Ribe, Nuclear Fusion 7, No. 2/3 (1967).
10. R. L. Morse, Phys. Fluids 10, 1017 (1967).
11. H. Wobig, Proceedings Euratom Symposium on Theoretical Plasma Physics, Varena, I, 135 (1966), p. 31.
12. H. A. B. Bodin and A. A. Newton, Paper A2, these proceedings.

* Work performed under the auspices of the U. S. Atomic Energy Commission.

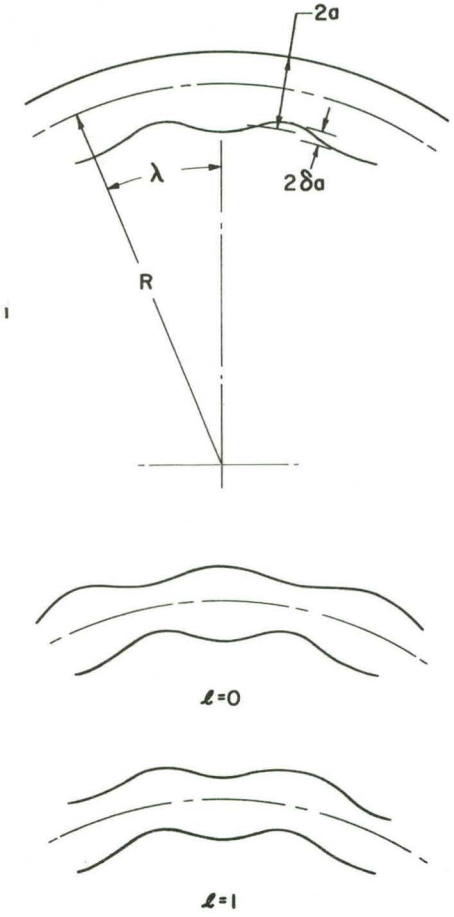

Fig. 1. (a) Schematic view of the equilibrium shape of a toroidal, high-β plasma. (b) Field line patterns of $\ell = 0$ (mirrored) and $\ell = 1$ (wavy) harmonic magnetic-field components which result in the equilibrium of (a).

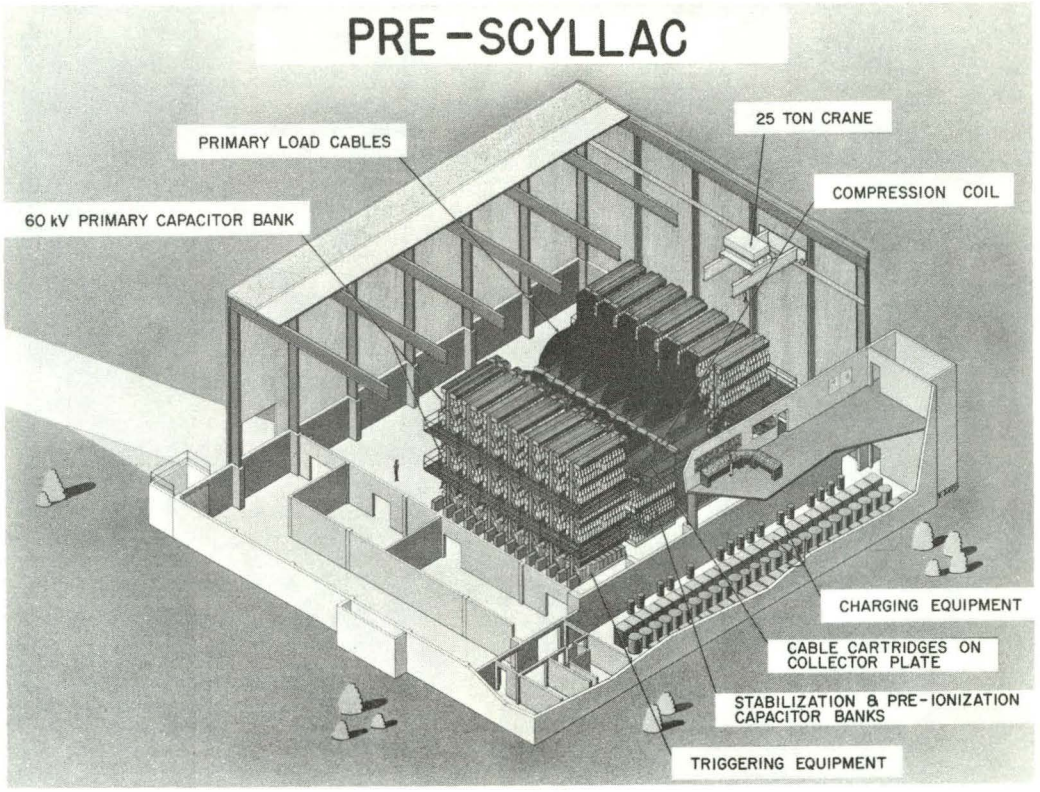

Fig. 2. The projected Scyllac facility, showing the preliminary phase of a 15-M linear θ pinch.

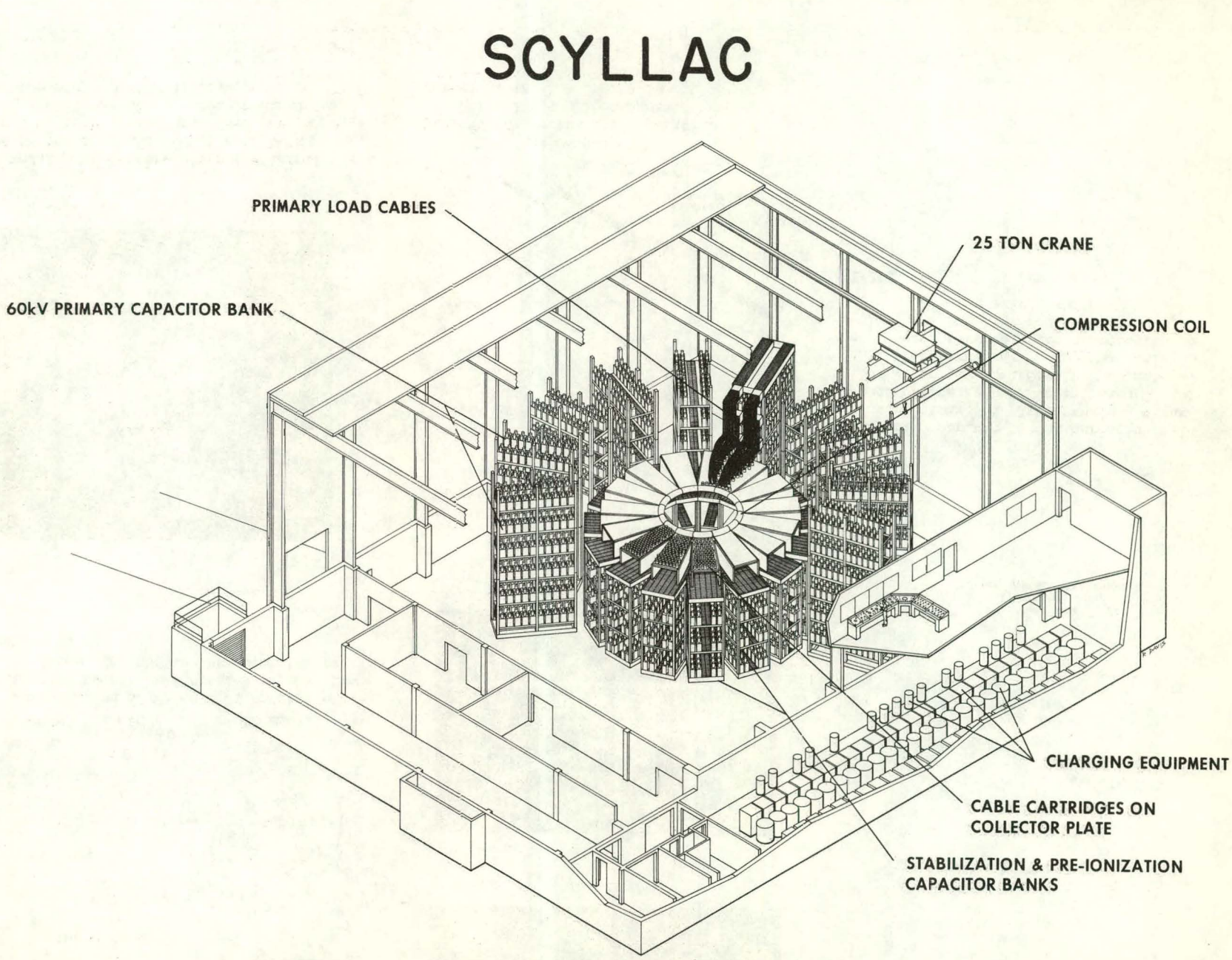

Fig. 3. The projected Scyllac facility, showing the final phase of a toroidal θ pinch with 5-m diameter.

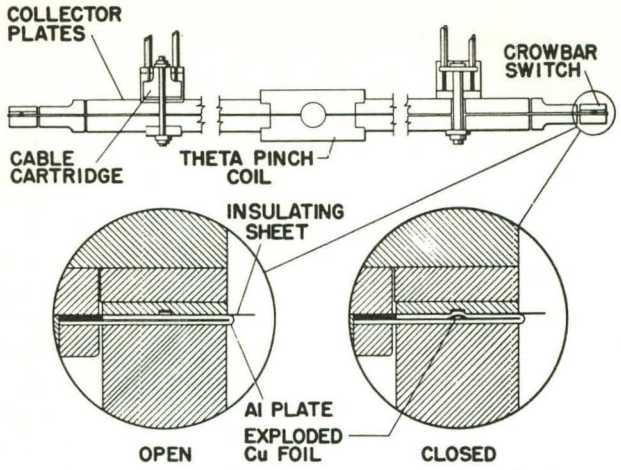

Fig. 4. Illustration of the use of an exploding-foil, dielectric switch on a small θ pinch. Two switches are shown for the series capacitor bank arrangement.

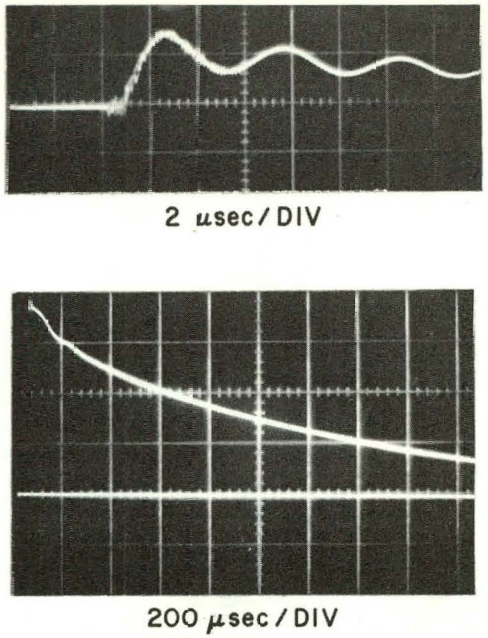

Fig. 5. Oscillograms showing the Scylla I-A current crowbarred by the exploding-foil dielectric switch.

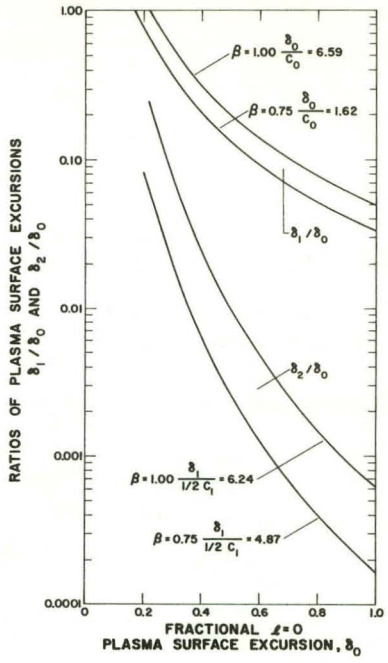

Fig. 6. Computed vacuum harmonic field perturbations and plasma surface excursions necessary to give an M and S equilibrium for typical Scyllac parameters. The parameters are: a (plasma radius) = 0.75 cm, λ (wavelength of perturbation) = 13.5 cm, R (major radius) = 250 cm, $C_o = \Delta B_z/B_o$ (on axis), and $1/2\ C_1 = B_{trans}/B_o$ (on axis).

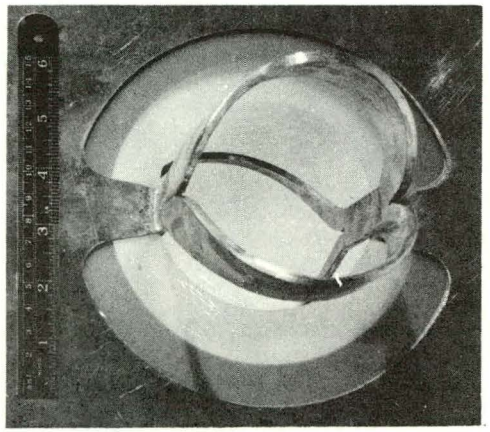

Fig. 7. Model of a center-driven $\ell = 1$ coil connected to copper plates capable of being driven in a θ-pinch coil slot. When used with others, this coil excites one longitudinal period of the field perturbation.

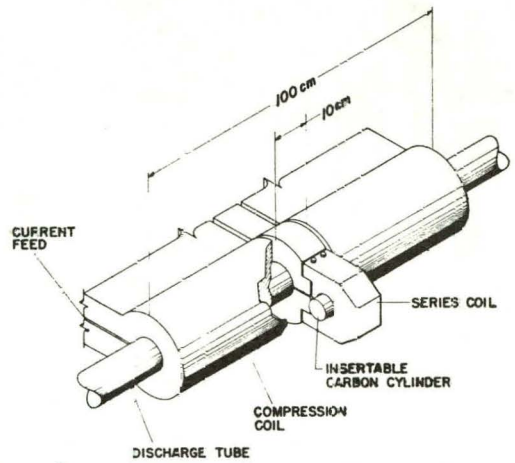

Fig. 8. Apparatus for generating an $\ell = 0$, adiabatically applied magnetic bump in the center of the 1-m Scylla IV coil.

ANISOTROPY AND ITS RELAXATION IN A FAST MEGAJOULE THETA PINCH +)

by

C.Andelfinger, E.Fünfer, G.Lehner, F.Pohl
U.Seidel, J.Sommer, M.Ulrich
Institut für Plasmaphysik
Garching b. München, Germany

ABSTRACT

Due to the fast radial theta pinch compression one expects a strongly anisotropic ion velocity distribution. Theoretical considerations based on the Fokker-Planck equation taking into account both ion-ion and ion-electron collisions and their influence on the relaxation of the ion anisotropy are presented (G.Lehner, in press, Z.f. Physik). Theory shows that for an anisotropic plasma the neutron flux and energy spectrum from D-D reactions is anisotropic, too (G.Lehner, F.Pohl, IPP Report 1/6o (1967), in press Z.f.Physik). These predictions are compared with recent measurements on the Isar I megajoule theta pinch (C.Andelfinger et al., IPP Report 1/67 (1967)). The measurements concern the anisotropy and axial distribution of the neutrons. Particle densities and end losses were studied by interferometric means. These measurements yield the perpendicular and parallel temperatures and the particle densities as functions of time. The maximum perpendicular ion temperatures are about 5 keV. The parallel ion temperatures taken from the rate of end losses are small in the beginning and increase quite fast after about a quarter-cycle. Detailed computations on the relaxation using the above-mentioned theoretical results are in very good agreement with the observations.

1. Introduction

In the present paper we discuss experiments with the Isar I MJ theta pinch, which has been modified by a longer collector to reduce the drift and by crowbar switches. In a fast theta pinch one expects a strongly anisotropic plasma. We investigate the temporal behaviour of both the perpendicular and the parallel temperature of the ions and the relaxation of the anisotropy. The experiments were performed with a bank energy of 1.5 MJ at an initial pressure of $8\ \mu\ D_2$. A more detailed description is given elsewhere[1].

2. Measurements

The neutrons produced by an anisotropic plasma carry with them a lot of information on the velocity distribution of the deuterons[2]. We wanted to make use of this fact and made the following measurements.

a) The total neutron flux ($\approx 10^{12}$ neutrons/sec cm^3) was used to evaluate $T_{\perp i}$ under the assumption $T_{\parallel i} \ll T_{\perp i}$, i.e. a two-dimensional Maxwellian for the deuterons.

b) For an anisotropic plasma the energy spectrum of the neutrons depends on the direction of observation. Therefore we exposed nuclear plates side-on and end-on to measure $T_{\perp i}$ and $T_{\parallel i}$ respectively. This yields time averaged temperatures. Practically one measures the values corresponding to the time of maximum neutron flux, however.

c) Due to the strong anisotropy[3] of the D(d,n)He^3 the neutron flux depends on the direction of observation also[2]. The ratio of the fluxes side-on and end-on depends on $T_{\perp i}$ and $T_{\parallel i}$ (Fig. 1). This ratio was measured with scintillators side-on and end-on.

The axial distribution of neutrons was investigated by six small scintillators placed close to the plasma column in holes of the coil. The measured profiles were unfolded to give the real axial distribution (Fig. 2).

Additional information was obtained mainly by interferometric means. Fig. 3 presents examples of the interferograms together with streak photographs. Fig. 4 shows the resulting density profiles for different times covering the confinement time of more than 10 μsec and Fig. 5 the total number of electrons N_e, the maximum densities on the axis $\bar{n}_{ea}$, and the mean parallel velocity $v_{\parallel}$ of the ions as functions of time. If we assume collisionless outflow of particles and a Maxwellian distribution of the parallel ion velocities $T_{\parallel i}$ is related to $v_{\parallel}$ by

$$(1) \qquad \frac{1}{2} k T_{\parallel i} = \frac{m_i}{2} v_{\parallel}^2 \frac{\pi}{2}$$

3. Theory

At least for parallel trapped fields the electron temperatures in theta pinches remain relatively small[4], $T_e \approx T_i/10$. Under these conditions the relaxation of the anisotropy cannot be described by ion-ion collisions only. One has to consider electron-ion collisions also. On the other hand, T_e is not so small that collective interactions become important[5]. The problem can be treated with the help of the Fokker-Planck equation, therefore. Assuming an elliptic distribution

$$(2) \qquad f(\vec{u}) = \left(\frac{m_i}{2\pi k}\right)^{3/2} \frac{1}{T_{\perp i} T_{\parallel i}^{1/2}} \cdot \exp\left[-\left(\frac{m u_{\perp}^2}{2kT_{\perp}} + \frac{m u_{\parallel}^2}{2kT_{\parallel}}\right)\right]$$

Kogan[6] obtained for ion-ion collisions

$$(3) \qquad \left(\frac{dT_{\perp i}}{dt}\right)_{ii} = -\frac{2\lambda e^4 n}{T_{\perp i} - T_{\parallel i}} \left(\frac{\pi T_{\parallel i}}{m_i}\right)^{1/2} \cdot \left\{(3+\xi)\phi(\xi) - 3\right\}$$

$$(4) \qquad \left(\frac{dT_{\parallel i}}{dt}\right)_{ii} = -2\left(\frac{dT_{\perp i}}{dt}\right)_{ii}$$

where

$$(5) \qquad \phi(\xi) = \begin{cases} \dfrac{\operatorname{arctg}\sqrt{\xi}}{\sqrt{\xi}} & (\xi \geq 0) \\ \dfrac{\ln \frac{1+\sqrt{-\xi}}{1-\sqrt{-\xi}}}{2\sqrt{-\xi}} & (\xi \leq 0) \end{cases}$$

$$(6) \qquad \xi = \frac{T_{\perp i} - T_{\parallel i}}{T_{\parallel i}}$$

n is the particle density and λ the Coulomb logarithm. The problem has been treated for ion-electron collisions also on the assumption of eq. (2) for the ions and an isotropic Maxwellian for the electrons[7]. The results are very unwieldy, however. They can be simplified if we assume

$$(7) \qquad m_i T_e \gg m_e T_i$$

so that

$$(8) \qquad \left(\frac{dT_{\perp i}}{dt}\right)_{ie} \approx -\frac{8\lambda e^4 n}{3m_i} \left(\frac{2\pi m_e}{T_e^3}\right)^{1/2} \left(T_{\perp i} - T_e\right)$$

$$(9) \qquad \left(\frac{dT_{\parallel i}}{dt}\right)_{ie} \approx -\frac{8\lambda e^4 n}{3m_i} \left(\frac{2\pi m_e}{T_e^3}\right)^{1/2} \left(T_{\parallel i} - T_e\right)$$

Taking into account the rate of heating due to the magnetic field we finally describe the relaxation process by

$$(10) \qquad \frac{dT_{\perp i}}{dt} = \frac{T_{\perp i}}{B_i} \frac{dB_i}{dt} + \left(\frac{dT_{\perp i}}{dt}\right)_{ii} + \left(\frac{dT_{\perp i}}{dt}\right)_{ie}$$

$$(11) \qquad \frac{dT_{\parallel}}{dt} = + \left(\frac{dT_{\parallel i}}{dt}\right)_{ii} + \left(\frac{dT_{\parallel i}}{dt}\right)_{ie}$$

B_i is the magnetic field in the plasma. It is related to the external field by

$$(12) \qquad B_i = B_a \sqrt{1-\beta}$$

4. Results

These theoretical predictions can be compared with experimental results. The values of T_e are extremely important here. We have no detailed knowledge of $T_e(t)$. For $t = 5$ μsec we have values from laser scattering experiments between 300 and

4oo eV. Furthermore, it is known from other experiments that T_e is almost constant. We use T_e as a constant parameter in the computations, therefore.

Figs. 6, 7 give an example of the comparison between experimental data and the computations. These start at 4.9 μsec with the first experimental value $T_{\perp i}$ = 3.3 keV. $T_{\parallel i}$ is not well known at this time. From Fig. 5 and eq. (1) we know that $T_{\parallel i}$ is a few 1oo eV. The computation shows that the initial value of $T_{\parallel i}$ has almost no influence on the result. In each case $T_{\parallel i}$ rises to about 1 keV, a value which is almost independent of T_e also. On the other hand, the behaviour of $T_{\perp i}$ changes drastically with T_e. If we neglect the ion-electron relaxation in eq. (1o) and (11) $T_{\perp i}$ is almost proportional to B_a because the ion-ion relaxation is not very effective and because the decrease of β is just a small correction (β decreases due to energy and particle losses while the trapped magnetic flux is constant within the limits of error). If ion-electron relaxation is taken into account the computed values of $T_{\perp i}$ are in very good agreement with the experimental values for T_e = 3oo to 4oo eV while for T_e = 2oo eV they are too low. The maximum temperatures $T_{\perp i} \approx 4$ keV and $T_{\parallel i} \lesssim 1$ keV agree also with the results of nuclear plate measurements. The maximum neutron output coincides with both the maximum $T_{\perp i}$ and the maximum neutron flux ratio side-on to end-on as one expects (Fig. 8).

+) This work was performed as part of the joint research program of the Institut für Plasmaphysik, Garching and Euratom.

References

1 C. Andelfinger et al., IPP Report 1/67 (1967)
2 G. Lehner, F. Pohl, IPP Report 1/6o (1967), in press Z.f.Physik
3 D.L. Booth et al., Proc. Phys. Soc. 69A, 265 (1956)
4 T.S. Green et al., Report CLM-P124 (1966)
5 C.S. Wu et al., Phys. of Fluids 8, 1126 (1965)
6 V.J.Kogan, Plasma Physics and the Problem of Controlled Thermonuclear Reactions, Pergamon Press, N.Y. 1961, Vol. 1, 153, ed. M.A. Leontovich
7 G. Lehner, in press Z.f.Physik

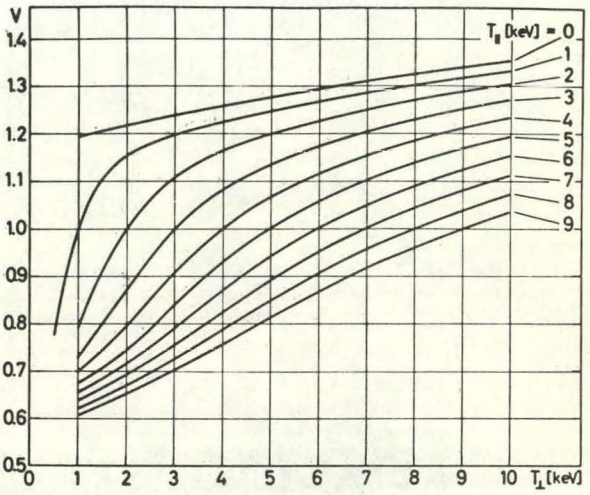

Fig. 1 Ratio of neutron fluxes side-on to end-on

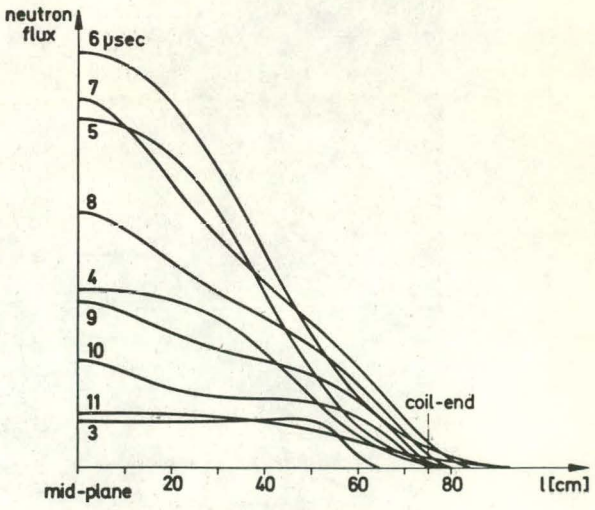

Fig. 2 Unfolded axial neutron flux distribution (1.5 MJ, 8 μ D_2)

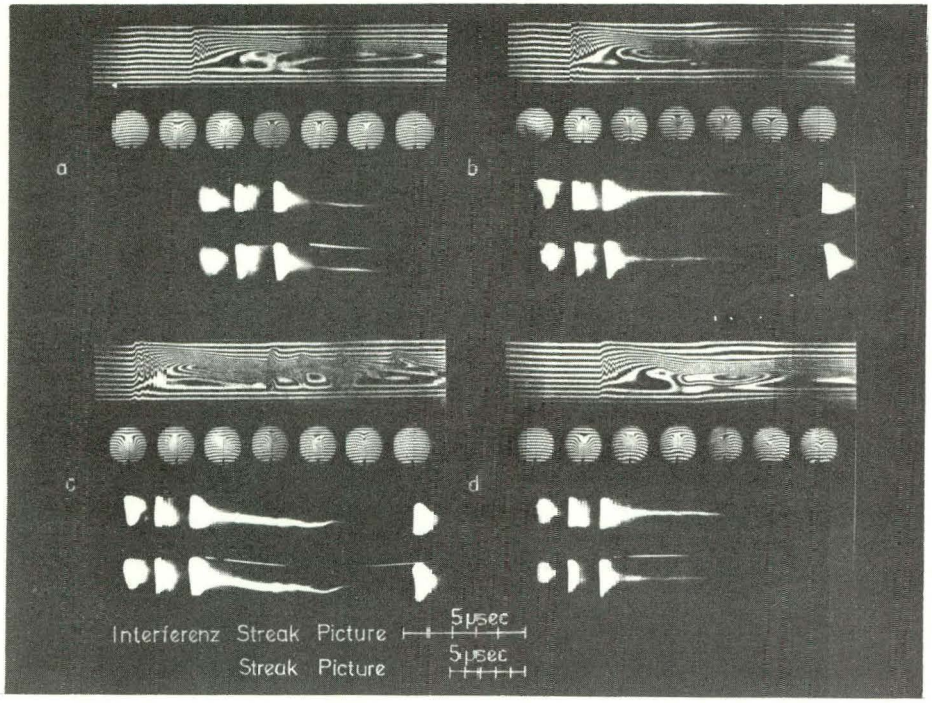

Fig. 3 Examples of interferograms and streak photographs
a) 0.5 MJ, 8 µ D_2;
b) 0.5 MJ, 15 µ D_2;
c) 0.5 MJ, 15 µ D_2;
d) 1.5 MJ, 8 µ D_2

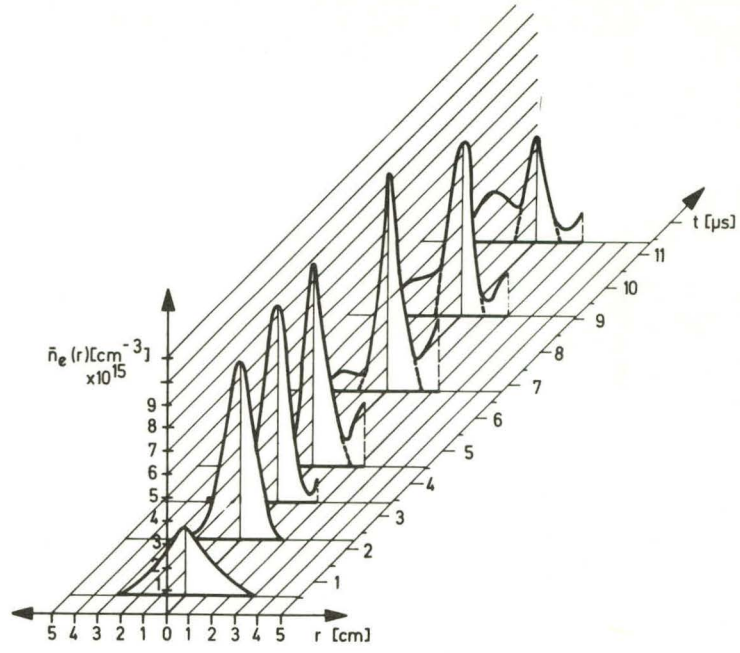

Fig. 4 Electron density profiles (1.5 MJ, 8 µ D_2)

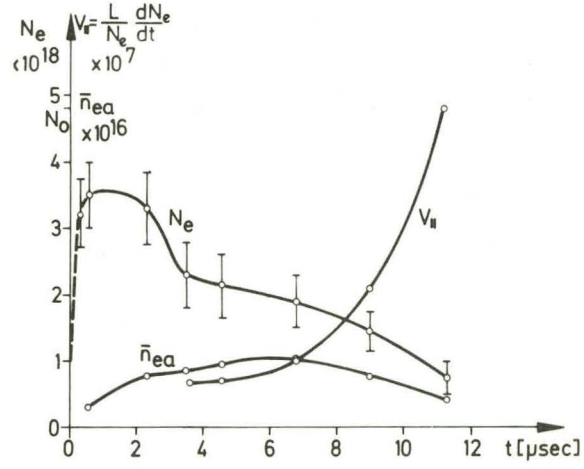

Fig. 5 Total number of electrons N_e, maximum electron density $\bar{n}_{ea}$ and parallel ion velocity $v_{||}$ (1.5 MJ, 8 µ D_2)

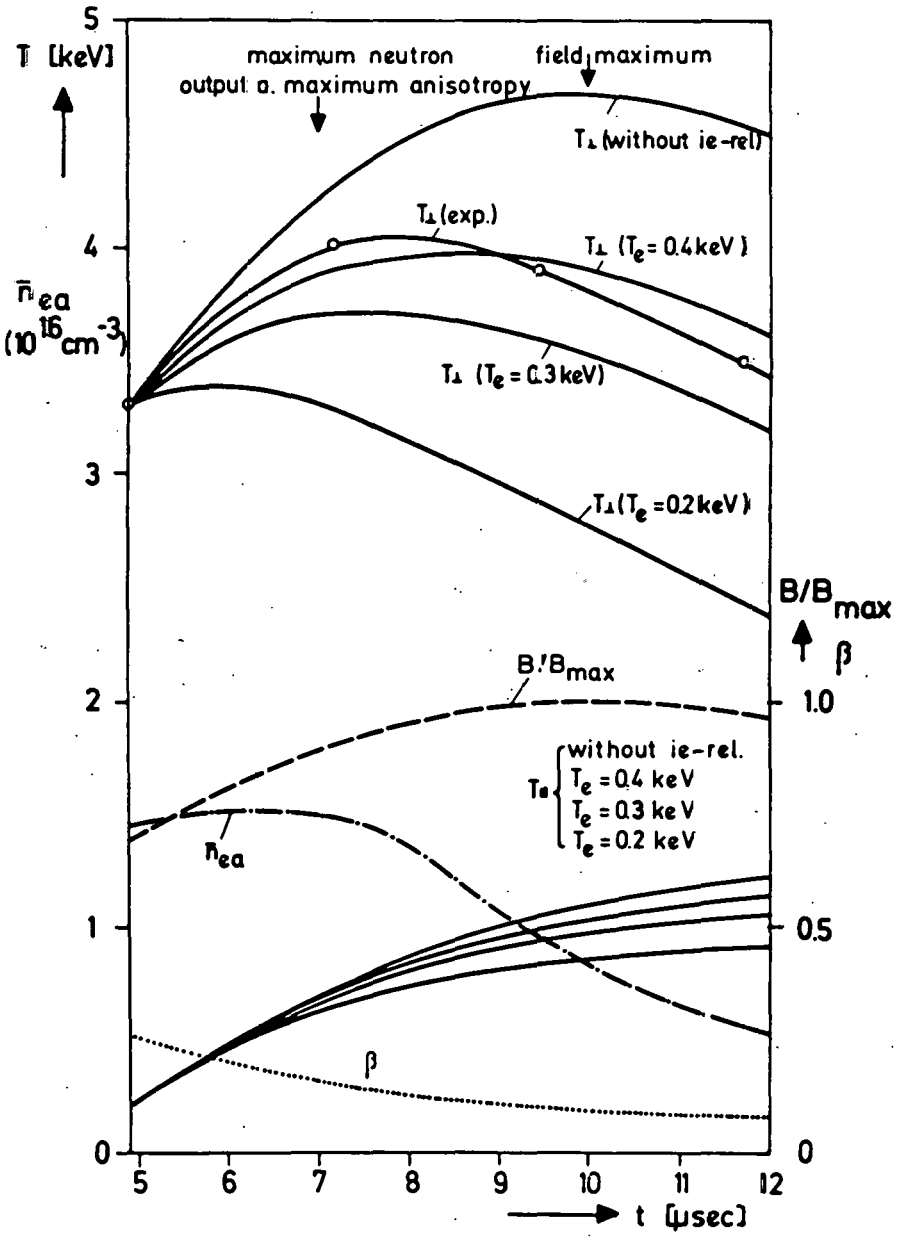

Fig. 6 Comparison between experimental and theoretical temperatures

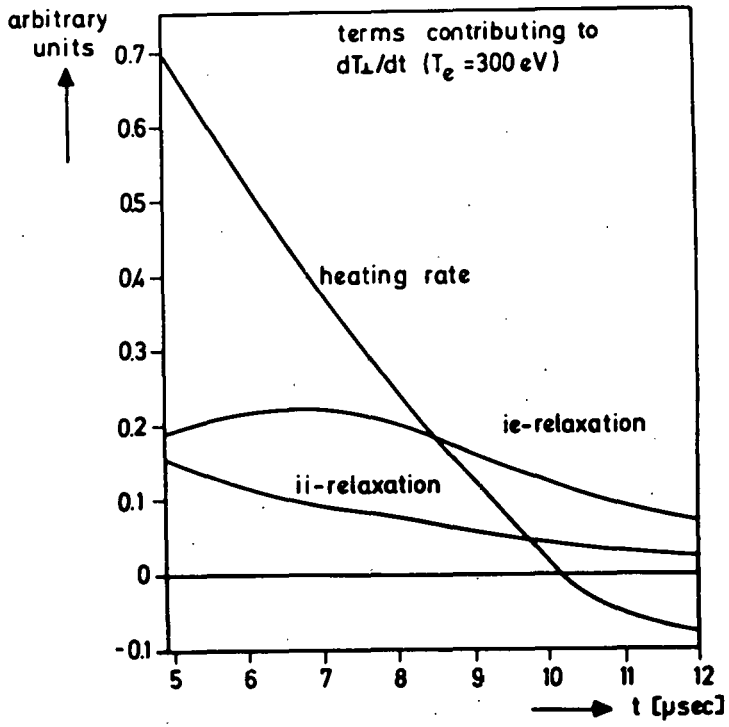

Fig. 7 Heating and relaxations rates for the example of T_e = 300 eV in Fig. 6

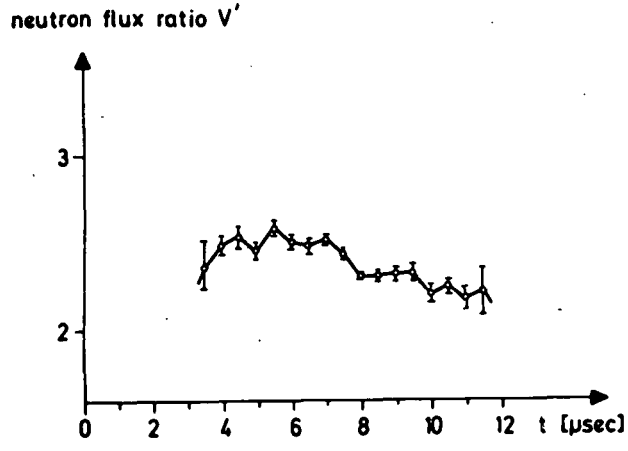

Fig. 8 Measured ratio of neutron fluxes side-on to end-on

COLUMBA - A HIGH TEMPERATURE Z-PINCH EXPERIMENT*

J. A. Phillips, A. E. Schofield, J. L. Tuck
Los Alamos Scientific Laboratory
University of California
Los Alamos, New Mexico

ABSTRACT

So far the existence of elevated temperatures (~ 5 keV) in z-pinches has not been established though in θ-pinches, especially in those of high E_θ, such temperatures are well known and appear to impart good behavior. In the Columba experiment we attempt to use the high temperature plasma of a θ-pinch as the starting point for a z-pinch compression. The θ-pinch is of conventional Scylla design: tube length 28 cm, inside diameter 8 cm, with B_z magnetic field rising to a peak of 56 kG in 2 μsec. The z-pinch, turned on at selected times in the θ-pinch cycle, can provide currents of 400 ka with rise times of 8 μsec. The experiment is in the preliminary stages of operation. The indications are that the initial z-pinch current does not flow along the discharge tube wall as in conventional z-pinches but along the B_z magnetic lines joining the z-pinch electrodes. At low B_z fields and z-currents the z-pinch radius then closely follows the θ-pinch field, i.e. minimum radius with maximum B_z pressure and maximum radius when the B_z field passes through zero. At high B_z fields and z-currents the added magnetic pressure from the z-current further compresses the plasma column and reduces the B_z field between the plasma and the coil.

I. INTRODUCTION

The purpose of the Columba experiment is to produce for study a z-pinch having a temperature in the thermonuclear (~ 5 keV) region. For reasons not yet clear, these high temperatures have probably not been produced in simple z-pinches although in certain high E_θ θ-pinches[1,2], the achievement of such temperatures is well established. (The plasma concentration phenomenon [2,3] may turn out in fact to be z-pinches and have a high temperature: this has yet to be confirmed.) It is further known that θ-pinches at kilovolt temperatures are better behaved and less unstable than at low temperatures (< 1 keV): this may be due to the effects of (1) high β, (2) finite lamor radius effects and (3) suppression of finite resistivity effects. It would be interesting to determine if such favorable effects take place for the more hydromagnetically unstable z-pinch.

In the Columba experiment, the high temperature plasma from a θ-pinch is used as the starting point for a z-pinch. At predetermined times in the θ-pinch cycle the z-pinch is initiated on this plasma and, it is hoped, will confine and further compress the hot plasma. Of immediate concern is the question whether the z-pinch will form on the dense hot plasma core or on low density plasma outside the central region or remain trapped on the discharge tube wall. This paper presents evidence that the z-pinch does not form on the wall but appears to compress the plasma column.

II. EXPERIMENTAL APPARATUS

The θ-pinch is of conventional Scylla design, Fig. 1, coil length 28 cm, inside diameter 8 cm, and ~ 56 kG peak magnetic field with rise time of 2 μsec. The coil is fed at two points diametrically opposite. The z-pinch, 56 cm spacing between electrodes, is centered along the θ-pinch axis and is energized by two low inductance capacitor banks in series, Fig. 1. Peak currents of 400 ka with half period 16 μsec are obtained. The z-pinch ground return consists of eight insulated 1.25 cm copper rods (Fig. 1) which allow the B_z flux to pass around the θ-pinch coil.

Diagnostics on the θ-pinch are two pick-ups loops, one measures the B_z field at the midplane of the θ-pinch coil and the second measures the flux Ø passing through the coil. The ratio of the

*Work performed under the auspices of the U.S. Atomic Energy Commission.

signals from these loops, B_z to ϕ, gives a measure of plasma radius.

From the voltage V_z across the z-pinch and z-current I_z together with the assumption of zero resistance the inductance L of the discharge is given by

$$\frac{\int_o^t V_z\, dt}{I_z(t)} = L(t) + L_o$$

With the added assumption of uniform pinch radius between the electrodes a pinch radius can be calculated.

The total neutron yield is monitored with a standard Ag-counter, and a fast phosphor-photomultiplier detector gives the time behavior of penetrating radiation.

III. RESULTS

1) Small I_z, small B_z fields.

With small z-currents (< 100 ka) and small θ-pinch fields (~ 30 kG) the z-pinch inductance follows the θ-pinch field, Fig. 2. The z-pinch was fired ~ 1 μsec after the start of the θ-pinch cycle and has initially a high inductance (small radius). The z-pinch expands, contracts, and expands again in phase with the B_z magnetic pressure.

From this behavior we infer that the z-pinch discharge initially flows along those B_z lines which pass close to the z-pinch electrode. As plasma is heated the z-pinch expands. The subsequent contractions and expansions of the discharge column is due to variations in the magnetic pressure of the θ-pinch field. No breakdown along the discharge tube wall is evident.

2) Low I_z, high B_z.

In Fig. 3 the calculated radius of five z-discharges are plotted versus time. The z-discharges were fired at different times (T_o) in the θ-pinch cycle; curve F. We note the following,

a) With the start of the z-pinch in the θ-pinch first half cycle, curve E, the initial radius is small $\lesssim$ 0.1 cm and then expands as was the case in Fig. 2.

b) Starting of the z-pinch about a B_z field zero, curves B and D, the initial pinch radius is large $\gtrsim$ 0.8 cm and quickly compresses as with a z-pinch alone.

c) Starting at a B_z field maximum, curves A and C, the pinch radius is $\approx$ 0.5 cm which possibly reflects those B_z field lines along which the z-current flows are displaced away from the axis by the θ-pinch plasma.

d) In all cases when the B_z field passes through the first zero after the z-pinch is fired the calculated z-pinch radius drops to small values $\leq$ 0.2 cm. At this time the z-current takes a sudden drop $\leq$ 30%. This drop may be due (1) to an interchange instability in the region of diffused B_z and B fields, or (2) the inability of the z-pinch magnetic field to contain the hot plasma. At higher z-currents > 200 ka, this drop is small, $\leq$ 5%, or absent.

3) High I_z, high B_z.

With the θ-pinch run at high voltages (~ 50 kG) and the z-pinch at 34 kV (> 300 ka) the results are shown in Figs. 4 and 5.

With a θ-pinch and vacuum the ratio of the B_z field at the midplane and B_z flux ϕ in the coil is constant with time. The ratio B_z/ϕ is subject to exaggerated errors in the vicinity of t ± 0.4 μsec and should be disregarded.

With a θ-pinch and plasma Fig. 4, the B_z/ϕ ratio increases near the end of the first half cycle presumably due to plasma heating. (The expanding plasma compresses the B_z field between it and the wall.) The ratio remains fairly constant over the second half cycle. Two typical neutron pulses are also shown. (These signals must be corrected for neutron time of flight to the detector [3.6 m distant].)

When z-pinches are fired 1.2 - 1.4 μsec in the θ-pinch second half cycle, Fig. 4, the B_z/ϕ ratio drops as the z-current rises. This we interpret as a compression of the plasma by the added B_θ pressure allowing the B_z field lines between the plasma and θ-pinch coil to expand.

When a radius is calculated the results are shown in Fig. 5. The initial radius, ~ 0.7 cm, is that expected for the θ-pinch plasma and becomes smaller as the z-pinch pressure increases. We also

show the total B field and magnetic pressure ($\sim B^2$) in the plasma surface using these values of radius and β unity. The efficiency of the z-pinch for producing high magnetic pressures shows up strongly.

The signals from the fast scintillation detector show a marked increase as the magnetic pressure rises, as would be expected if the z-pinch further compresses the plasma. At the present time, however, we have not completely ruled out two other possibilities. The z-pinch alone produces neutrons up to ten times that of a θ-pinch and the observed increase may be neutrons by z-pinches near the electrodes. Also, on $\sim$ 25% of the discharges we have observed short bursts ($\lesssim$ 0.2 μsec duration) of hard X-rays. The fraction of the increase in signal due to these two sources has not yet been determined.

From the Ag counter the neutron production of a θ-pinch is increased when the z-pinch is fired during the second half cycle. Maximum yields are generally obtained when the z-pinch is started near a B_z field minimum (screw pinch[5]).

IV. DISCUSSION

From the results to date it appears that a z-pinch when applied to the hot plasma from a θ-pinch behaves as expected. The z-current flows along those B_z lines which pass close to the electrodes and forms about the hot plasma. There is evidence that the added magnetic pressure exerted by the z-pinch further compresses the plasma.

V. ACKNOWLEDGMENTS

It is with pleasure that we acknowledge the able help and assistance of W. Bowman, R. Holm, and P. Parker together with T. Dolan, W. Hones, and P. Roensch during the summer, who have assembled and run the experiment. The help of R. Dike in designing the experiment is gratefully acknowledged.

REFERENCES

1. K. Boyer, W. C. Elmore, E. M. Little, W. E. Quinn and J. L. Tuck, Phys. Rev. 119, 831 (1960).
2. F. C. Jahoda, E. M. Little, W. E. Quinn, F. L. Ribe and G. A. Sawyer, Journal of Applied Physics, 35, 2351 (1964).
3. Filippov, N.V., Filippova, T. I., and Vinogradov, V. P., Nucl. Fusion Suppl. Pt. 2 (1962) 577.
4. J. W. Mather, Plasma Physics and Controlled Nuclear Fusion Research, Vol. II Conference Proceedings, Culham 6-10 Sept., 1965.
5. S. A. Colgate, J. P. Ferguson, H. P. Furth, and R. E. Wright, Proc. Second U.N. Conf. on Peaceful Uses of Atomic Energy 32, 140 (1958).

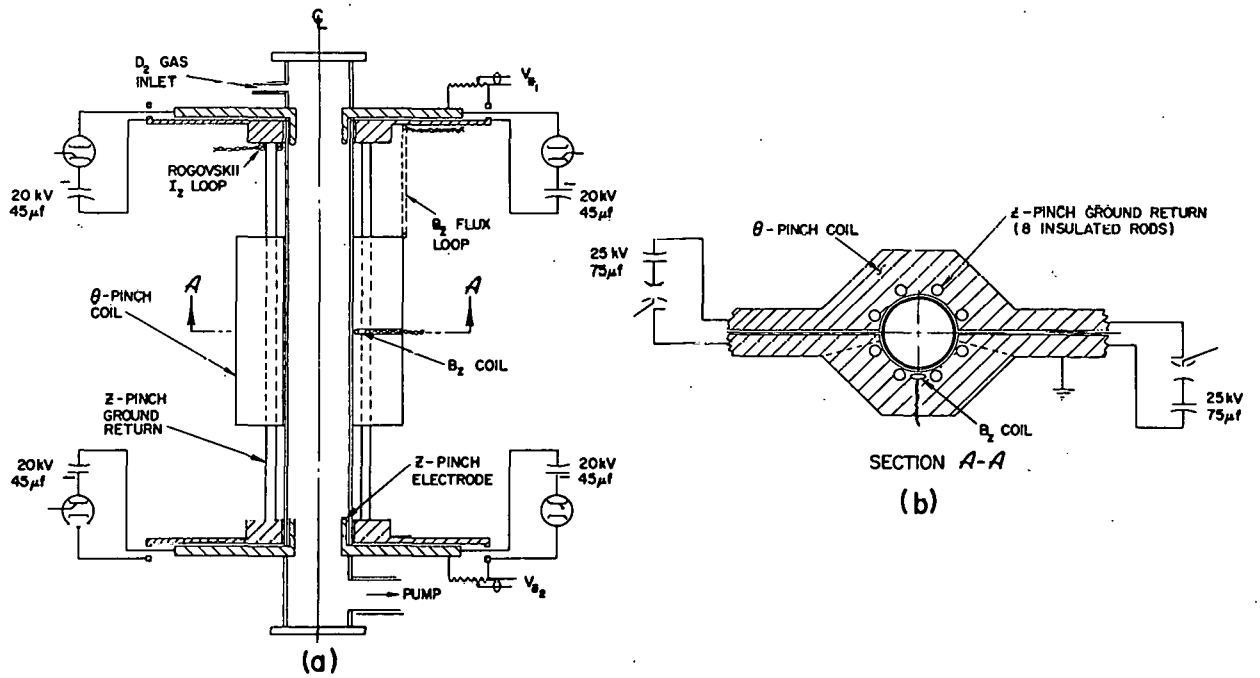

Fig. 1. Schematic drawing of the Columba experiment showing the position of the θ-pinch coil on the z-pinch discharge.

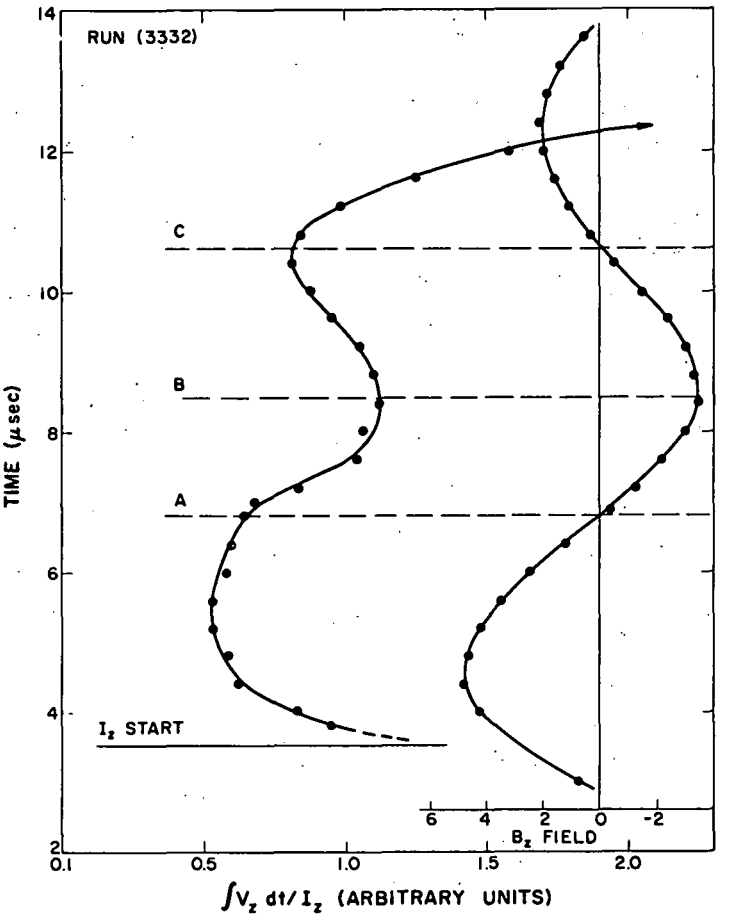

Fig. 2. The calculated z-pinch inductance ($\sim \int V_z dt/I_z$) as a function of time per low z-currents and low B_z fields. The z-pinch was initiated 1.0 μsec after the start of the θ-pinch cycle. Note the variations in inductance with the B_z field.

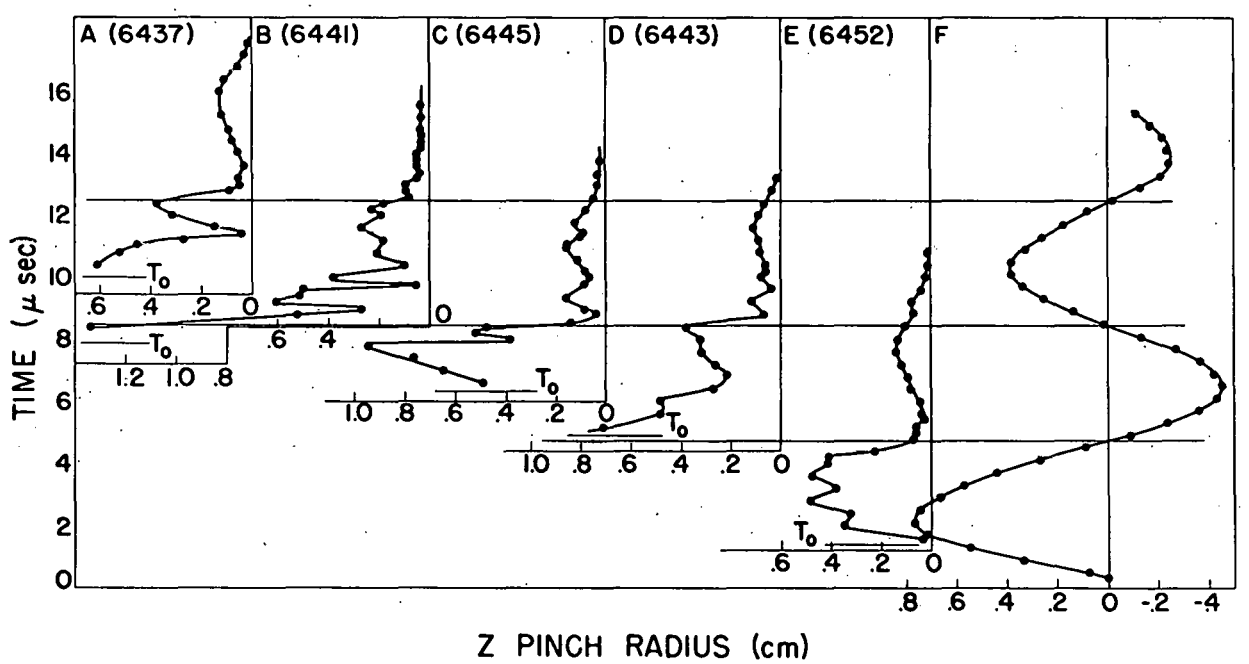

Fig. 3. Time dependence of the calculated radius of the z-pinch for small z-currents and high θ-pinch fields. The z-pinch was fired at time T_0 in the five shots. Curve F is the B_z field from the θ-pinch.

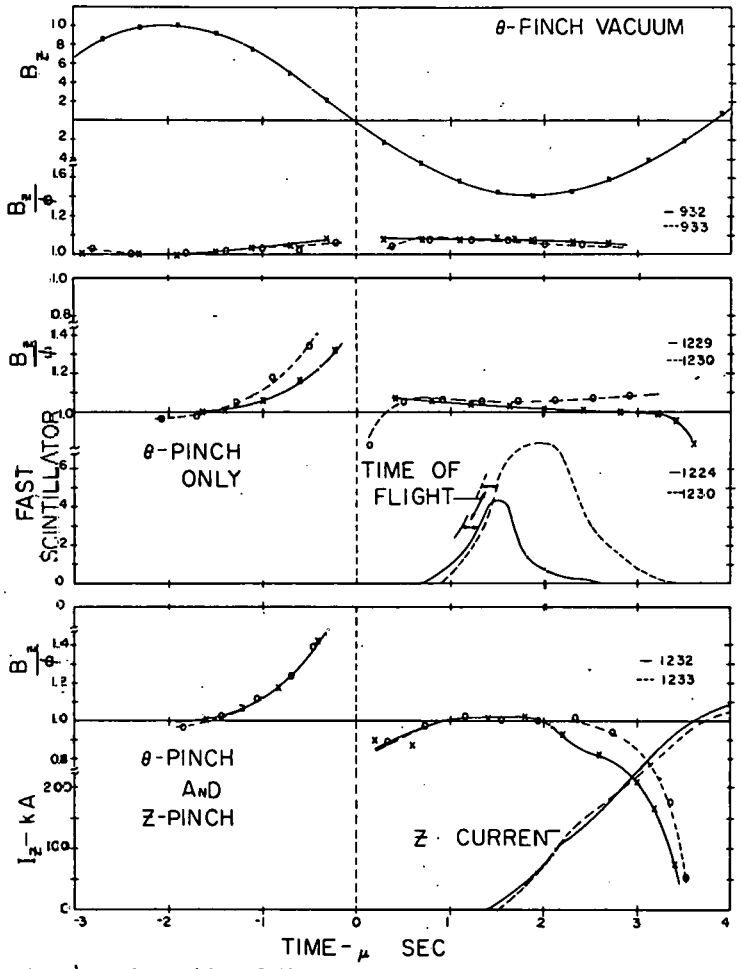

Fig. 4. The ratio of the B_z field at the midplane to the magnetic flux ϕ in the θ-pinch coil as a function of time for three cases (1) θ-pinch and vacuum (2) θ-pinch and plasma, and (3) θ-pinch and z-pinch which is fired ~1.4 μsec after the start of the second half cycle of the θ-pinch. The B_z field neutron production with a θ-pinch, and z-current are also shown.

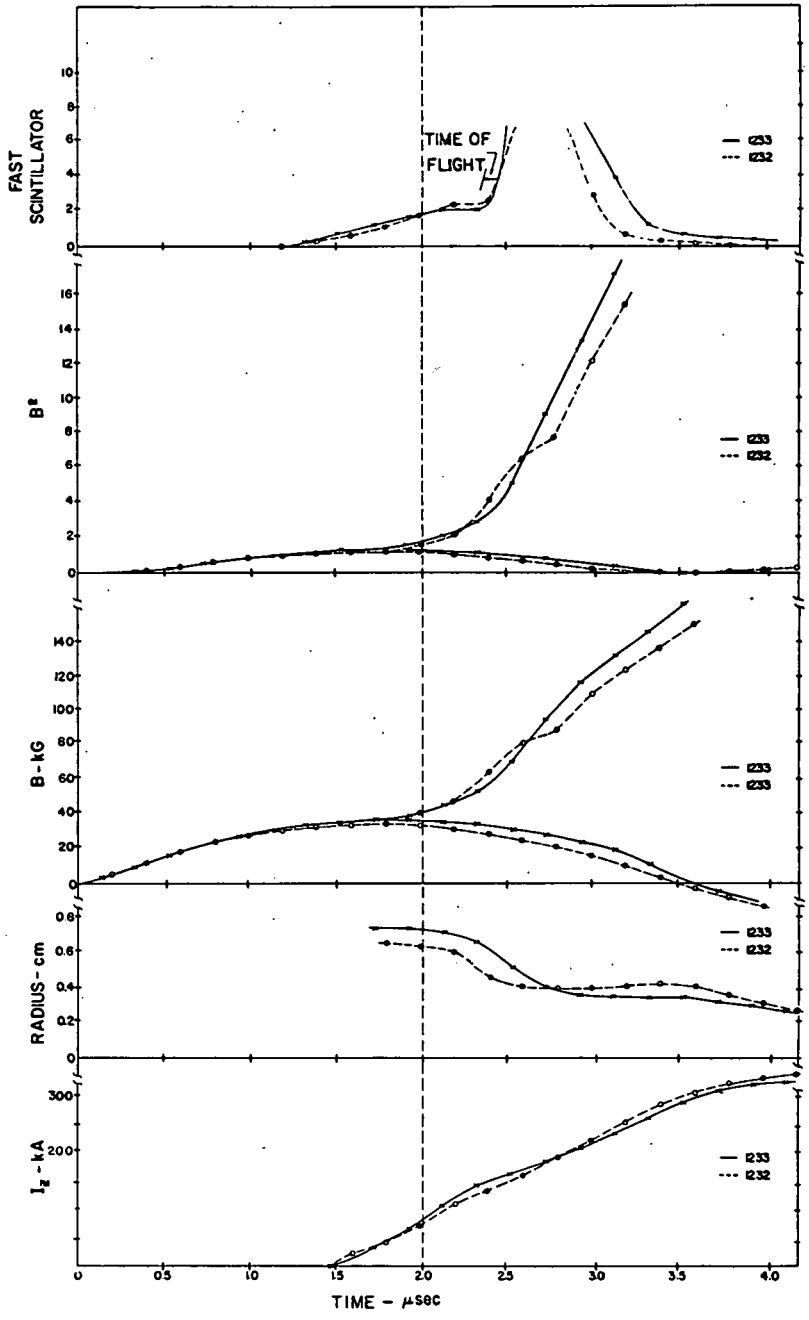

Fig. 5. The behavior of the high current z-pinch when fired in the second half cycle of a θ-pinch. The time dependence of the z-current, calculated pinch radius, calculated total B, and pressure (~B^2) on the pinch surface (B = 1 assumed) are shown. The signals from the fast scintillator detector are included.

'LONG-CUSP' CONTAINMENT EXPERIMENT

by

T.K. Allen, H. Coxell, M. Hill and I.J. Spalding

UKAEA Research Group, Culham Laboratory, Abingdon, Berkshire, England.

ABSTRACT

A cusp-ended theta-pinch experiment (CENTAUR) is described. The 100 kV θ-pinch, 50 cm long and of coil diameter 19 cm, reaches a peak field of up to 21 kG in 2.1 μsec. The cusps are energised at either end independently to give fields of up to 40 kG and 65 kG at the ring and spindle cusps respectively, with a rise time of 2.1 μsec. Both the cusp and θ-pinch fields fall to some 70% of their peak value in 15 μsecs.

The stability and containment time of a simple θ-pinch is examined for various values of β. At low β an $m = 1$ instability is predicted and observed, but at high β the plasma appears to be stable, in agreement with theory[1]. Plasma temperatures and densities are typically 150 eV and 10^{16} cm^{-3} in these experiments, and so the calculated Bohm pump-out time is significantly less than the $\beta = 1$ collision-free loss time through an ion gyro radius hole. The observed containment times are consistent with Bohm diffusion (in common with other published θ-pinch experiments), but this interpretation is not unique in the present experiment until β has been measured with greater accuracy. Preliminary observations with the cusps are described.

INTRODUCTION

Previous experiments[1] on the containment of high β plasma in spindle-cusp geometry have shown that: (i) Plasma can escape through a hole as small as two ion gyro-radii ($2r_i$) at the ring cusp when the electron temperature (Te) is high enough to avoid classical diffusion. (ii) The ring and point cusp losses are of comparable magnitude. (iii) There is no observable rotation. The first result is consistent with the hypothesis that the strong space-charge electric fields associated with a collision-free sheath are short-circuited[2] so that the characteristic length is an ion gyro-radius rather than an electron gyro radius. Both (i) and (ii) are also in good agreement with a steady-state statistical model of cusp containment in which electric fields are neglected[3]. However, more recent measurements[4] of the electric fields developed across the cusps when $\beta = 1$ plasma blobs are injected into DC cusp fields[5] provide no evidence of wall short-circuiting.

The cusp hole size is closely related to the stability of the plasma sheath if $\beta \sim 1$, and so if diffusion is anomalously rapid and the plasma dimensions are above a critical value, the hole size is increased. It was shown that Bohm diffusion might provide an alternative explanation for the previous results[2], and so a new experiment (CENTAUR, a cusp-ended theta-pinch) has been designed to give a Bohm pump-out time significantly less than the $\beta = 1$ collision-free end-loss time. The experiment also provides a comparison, under similar conditions, of the stability and containment time of the MHD stable cusp geometry with that of a θ-pinch possessing a variable mirror ratio. The configuration has the flexibility required for the investigation of some predicted causes of plasma rotation, which may affect the MHD stability of both the cusp and θ-pinch geometries.

APPARATUS

CENTAUR, Fig.1, consists of a θ-pinch coil 50 cm long, 19 cm diameter with additional axially-fed cusp/mirror coils at either end[6]. The θ-pinch coil, which is constricted at the ends to give a more uniform B_z along the axis, is fed by a 100 kV, 100 kJ capacitor bank with single solid-dielectric switches for make and clamp duty. The peak B_z field of 22 kG is reached in 2.1 μsec and then falls to 67% in 1.5 μsec. The cusp/mirror coils have separate 40 kV, 30 kJ banks, and are capable of giving fields of 40 kG and 65 kG at the ring and spindle cusps respectively, with waveforms almost identical to that of the theta-pinch.

Radio frequency preionization and a bias field of ± 700 G, can be applied with either of two alternative preheat banks, namely:

(i) A 100 kV, 500 J, 1 kG θ-pinch ringing at 1.1 Mc/s

(ii) A 40 kV, 640 J z-pinch giving 22 kA critically damped in 2.6 μsec.

In the range 0.01 - 0.03 torr ionization is at least 30 - 50% at zero bias with either system, and Te is 2 eV. Theta-pinch parameters calculated from the Hain-Roberts code are given in Table 1.

TABLE 1

100 kV THETA-PINCH PARAMETERS

Bank Inductance	27 nH		
Start Switch	10 nH	Coil Length	50 cms
Coil Inductance	42 nH	Coil Radius	9.5 cms
Total Inductance	91 nH		

$\tau_{\frac{1}{4}} = 2.1$ μsec

$B_z = 16.5$ kG (at 75 kV)

$E = 520$ V/cm (at 75 kV)

PLASMA PARAMETERS (Hain-Roberts Code)

20 μ D_2, Te = 2 eV, fully ionized; Bank voltage 75 kV

Initial Plasma Radius 8.5 cm.

$\bar{T}e = 130$ eV

$\bar{T}i = 270$ eV

$n_e = 1.7 \times 10^{16}$ at peak field ($t = 2.1$ μsec)

$\tau_{sound} = 1.4$ μsec

Parallel Thermal Conduction Time ~ 0.5 μsec (uniform cylinder)

$\omega_{ce}\tau_{ei} \sim 300$

THEORY

Models of Containment

(i) A $\beta = 1$ cylindrical θ-pinch of length L and radius R loses plasma by effusion through point cusps of radius $(3\pi/2)^{\frac{1}{4}}(r_i R)^{\frac{1}{2}}$ in a time[3]

$$\tau_1 \geq 0.92\ (R/r_i)(L/\bar{c}) \qquad \ldots (1)$$

where r_i is the RMS ion gyro radius and $\bar{c}$ is the mean ion velocity.

(ii) When $\beta \neq 1$, but $(1-\beta)$ is assumed to be uniform and small, a fluid model of transient axial flow[7] indicates that the line density (N) on the midplane remains constant for a time

$$\tau_2 = 0.435\ (1-\beta)^{-\frac{1}{2}}(L/\sqrt{\bar{c}^2}) \qquad \ldots (2)$$

and then drops rapidly. Thus, $\tau_2 < \tau_1$ unless $(1-\beta)^{-\frac{1}{2}} > 2(R/r_i)$.

(iii) A third model relevant to both a $\beta = 1$ and a reversed field θ-pinch is that of diffusion across the confining field followed by axial flow[7] in the $\beta < 1$ sheath of width Δ. Then

$$2\pi RL \cdot \alpha D \cdot \frac{n}{\Delta} = 4\pi R\Delta \cdot \frac{n\bar{c}}{4} \qquad \ldots (3)$$

where αD is the effective diffusion coefficients, and $D = 10^8$ kTe(eV)/16 B (G) is the Bohm coefficient. Thus

$$\Delta = (2\alpha DL/\bar{c})^{\frac{1}{2}} \qquad \ldots (4)$$

The corresponding containment time is given by

$$\frac{\pi R^2 Ln}{\tau_3} = 4\pi R\Delta \cdot \frac{n\bar{c}}{4}$$

i.e.

$$\tau_3 = R(L/2\alpha D\bar{c})^{\frac{1}{2}} \qquad \ldots (5)$$

with the parameters given in Table 1.

$\tau_1 = 41$ μsec

$\tau_2 = 3$, 4, 5·7, or 13 μsec for $\beta = 80$, 90, 95 or 99% respectively

$\tau_3 = 12$ μsec for $\alpha = 1$, i.e. Bohm diffusion.

Thus if $\beta = 99\%$ the line density at the midplane should not decrease rapidly in times of the order 5 μsec unless the diffusion coefficient is much greater than the classical value.

STABILITY

Stability is predicted[8] for a perfectly conducting parallel-field θ-pinch of uniform β for modes $m \geq 1$ when

$$\beta > \frac{1}{1 + (R/Rw)^{2m}} . \qquad \ldots (6)$$

More severe stability criteria are given for a diffuse pinch[8].

Although the cusp geometry is MHD stable for a non-rotating plasma in equilibrium[9], Kaye[10] predicts that collision free plasma having an ion gyro radius sheath escapes through a $\beta = 1$ spindle cusp with a preferred direction of angular momentum, so that (a) a simple spindle-cusp (as in ref.1) does not rotate; (b) a $\beta = 1$ theta pinch rotates in the ion direction in a characteristic time $\frac{r_i}{R} \cdot \tau_1$; (c) the hybrid geometry of Fig.1 rotates in the reverse direction to (b) in a time dependent on the mirror ratios, but of order $\frac{r_i}{R} \cdot \tau_1$.

DIAGNOSTICS

Continuum radiation over a 36 Å bandwidth centred at 4743 Å was imaged on to a 13-channel photomultiplier assembly to measure the radial density profile either in the midplane (z=0) or at z = 12.5 cm. Uncalibrated streak pictures were taken in the plane z = 12.5 or z = 0 cms respectively and balanced loops measured the plasma diamagnetism within a few mm of these positions. Simultaneous measurements of T_e were made by viewing axially with a 4-channel soft X-ray absorption spectrometer using foils of thickness 2.6 - 12 mg/cm^2. Provision is made for interferometric measurements of line density, Faraday rotation measurements of plasma β, and Thomson scattering measurements of n_e and T_e, but data from these techniques is not

yet available.

The stability of the θ-pinch as a function of $\bar{\beta}$ has been investigated in some detail, but the cusp data is still preliminary. In the work described below the ringing θ-pinch preheat was employed at a fixed filling pressure of 0.02 torr of D_2.

MEASUREMENTS

Simple θ-pinch without Mirrors

Radial density profiles at the midplane ($z = 0$) are shown in Fig.2; zero and negative bias give a flat-topped density profile with a sharp edge, whereas positive bias produces a more diffuse boundary. The line density and plasma diamagnetism measured at the same position are plotted in Fig.3 together with Te. An average beta ($\bar{\beta}$) is deduced from the diamagnetic signal and the maximum plasma radius. The latter quantity provides the present experimental uncertainty in $\bar{\beta}$.

At zero bias, $\bar{\beta} = 90\binom{+10}{-15}$ per cent from times (t) of 3 - 9 μsec after firing the θ-pinch, while N and $\bar{T}_e$ both fall steadily from their computed value at $t = 3$ μsec. Although a very small amount of negative flux is trapped from the preheat at 'zero bias', a marked change in behaviour is observed as the external bias is increased progressively to - 720 G. At this value $\bar{\beta}$ is of order 100% for 15 μsecs, the line density and diamagnetic signals show a weak oscillation, and $\bar{T}_e$ exceeds the computed value for over 15 μsec, following a $B^{4/5}$ adiabatic dependence on B_z quite closely. At + 650 G bias $\bar{\beta}$ = 50 - 70% at 3 μsec, $\bar{T}_e$ rises to ~ 140 eV and the X-ray signals then fall very rapidly in a manner consistent with electron thermal conduction cooling (see Table 1).

Radial streak pictures (Fig.4) show an $m = 1$ drift at positive bias, with an e-folding time of 4 μsec. The predicted growth time is roughly 6 μsec[8]. With negative bias very stable plasmas are observed for some 15 μsec after the initial implosion, and a rapid rotation in the ion gyro detection is then detected with 45° stereoscopic pictures. Assuming $m = 2$, a rotation frequency of 6×10^4 c.p.s. i.e. roughly $2\left(\frac{r_i}{R}\right)^2 \omega_{ci}$, is measured.

With Cusps

With 11 kG in the θ-pinch, 20 kG at the ring cusp and 37 kG at the point cusp, little change is observed in the diamagnetism and soft X-ray emission from the comparable θ-pinch condition. In the reversed field case, where rotation is observed most readily in the θ-pinch, the cusps do not alter the direction of rotation.

CONCLUSIONS

Stability

A low β (positive bias) θ-pinch is predicted and observed to be $m = 1$ unstable, with a growth time 50% less than the predicted (uniform β) value[8]. It is concluded, by analogy, that 'line-tying' does not account for the stability of the high β (zero bias) θ-pinch, for which the $m = 1$ mode is predicted to be stable when $\bar{\beta} > 90\%$ (equation 6) This latter plasma has a measured $\bar{\beta} = 90\binom{+10}{-15}$ percent and is stable for some 6 sound-transit times. The negative bias θ-pinch is grossly stable for 11 sound-transits, until the onset of a rotational instability at roughly the Bohm type. The rotational instability in the negative bias case is not stabilized (nor reversed in direction) by the cusps.

Containment

Observations over the central half of the coil indicate little loss of plasma in the reversed-field θ-pinch for some 15 μsec. Further measurements are required to establish whether the particle containment time is in fact greater than 15 μsecs, i.e. whether plasma has escaped from the outer ($|z| =$ 12.5 to 25 cm) regions of the coil. A Bohm containment time of 14 μsec is predicted from equation (5).

The rapid decrease in line density observed in the zero-bias θ-pinch is also consistent with Bohm diffusion is a high β boundary layer, but a more accurate assignment of β (e.g. by Faraday rotation) is required to distinguish between diffusion and end losses by axial flow. (Energy losses do not directly affect this comparison.)

Cusp

Preliminary measurements on cusp containment and rotation are not inconsistent with anomalously rapid diffusion, so that plasma is lost preferentially through the ring cusps. Further work is in progress to examine whether field assymetries or a low β can account for the observations. Finally, it is noted that equations (4) and (5) with $\alpha \sim 1$ (i.e. Bohm diffusion) appear to account for many features of other theta-pinch experiments[11-13].

ACKNOWLEDGEMENTS

The authors wish to acknowledge the encouragement of Drs R.S. Pease and R.J. Bickerton, the vigorous support of T.E. James' engineering group, useful discussions with Mr A.S. Kaye, and the able assistance of M.J. Eden, R.S. Alphey and A.J. Hawkes.

REFERENCES

1. T.K. ALLEN, et al. Phys. Fluids, 9, 1394 (1966)

2. G.D. HOBBS and I.J. SPALDING. Culham Laboratory Report CLM-R 57 (1966)

3. J.B. TAYLOR. Culham Laboratory Report CLM-R 58, (1966)

4. F. INSINGER and I.J. SPALDING. First European Meeting on Controlled Fusion and Plasma Physics (unpublished) 1966. (Munich)

5. T.K. ALLEN, et al. Proceedings of the VIIth Conference on Ionization Phenomena in Gases, vol.II, 171, Belgrade (1966).

REFERENCES (continued)

6. T.E. JAMES, et al. Second International Conference on Magnet Technology, Paper 60, Oxford. (1967).

7. J. WESSON. IAEA Conference on Nuclear Fusion, Culham, (1965), vol.1, 223.

8. F.A. HAAS and J.A. WESSON, to be published in Phys. Fluids, (1967) and CLM-P 136.

9. H. GRAD, Prog. Nucl. Energy, Series XI, Plasma Physics, vol.2, 189, (1963)

10. A.S. KAYE, Culham Laboratory, private communication.

11. A.C. KOLB, et al. IAEA Conference on Nuclear Fusion, Culham 1965, vol.1, 249.

12. W.E. QUINN, et al. Ibid, vol.1, 237.

13. H.A.B. BODIN, et al. Ibid, vol.1, 193

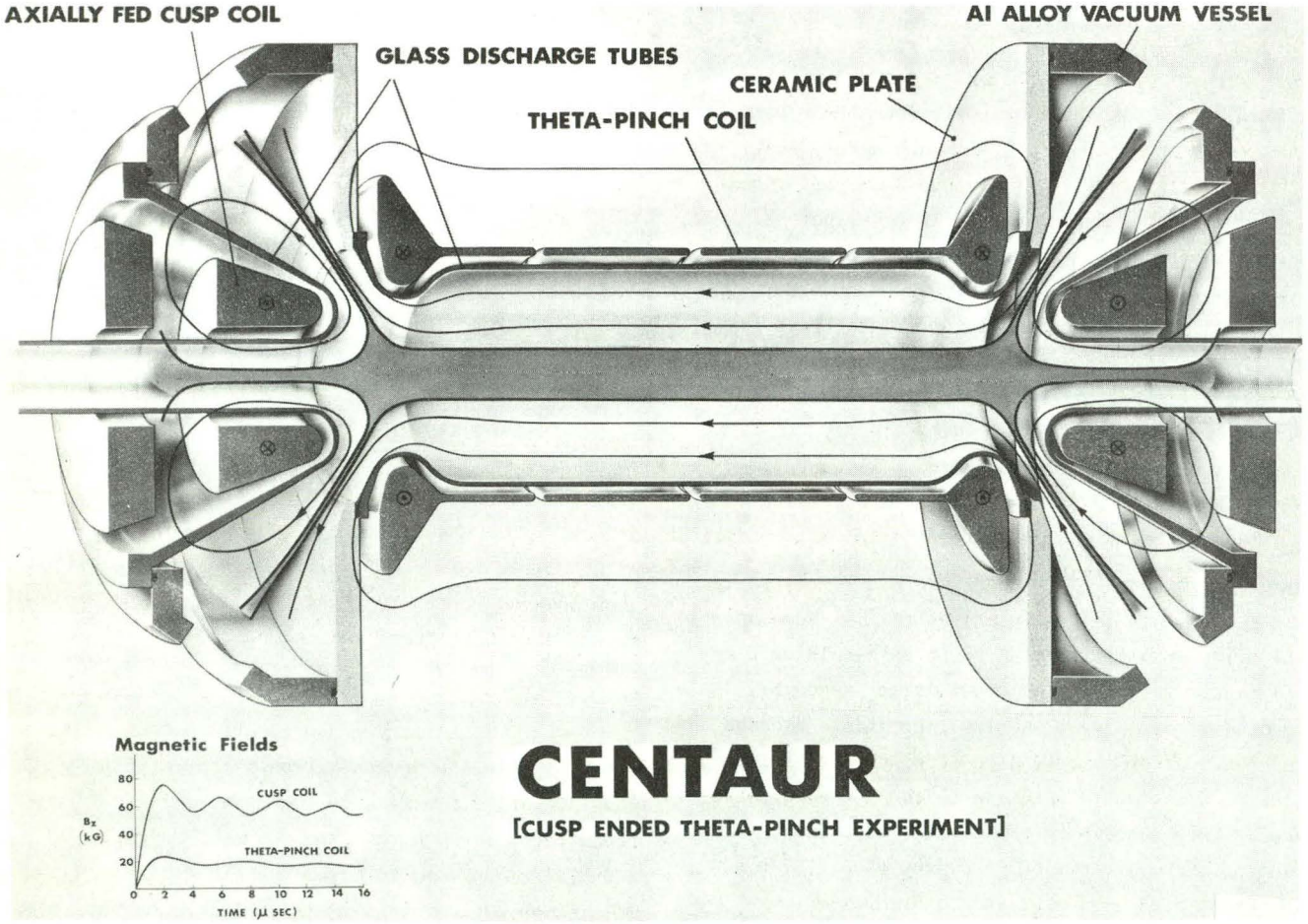

field lines, and plasma position (roughly to scale). The θ-pinch and point cusp B_z are plotted for bank voltages of 100 kV and 40 kV, respectively.

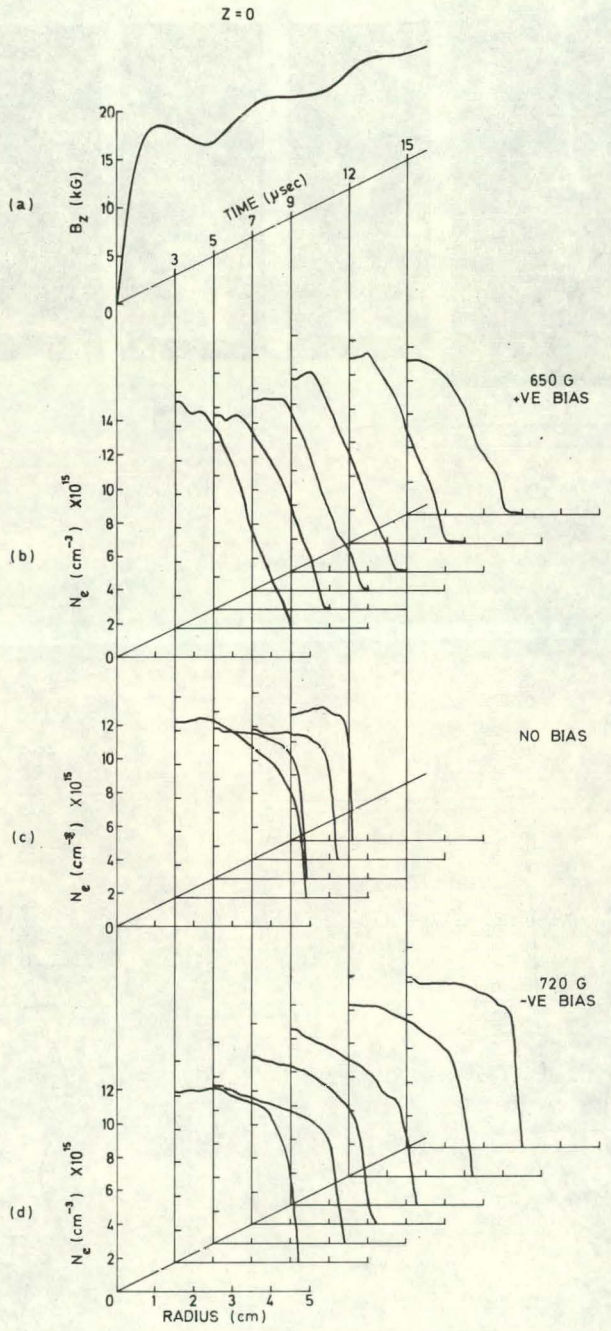

Fig. 2. Midplane radial density profiles at time t = 3 to 15 μsec after firing the θ-pinch at 75 kV. (No cusps, 0.02 Torr D_2): (a) B_z waveform; (b) +650G bias; (c) Zero bias (a small - ve flux is, however, trapped from the preheat); (d) -720G bias.

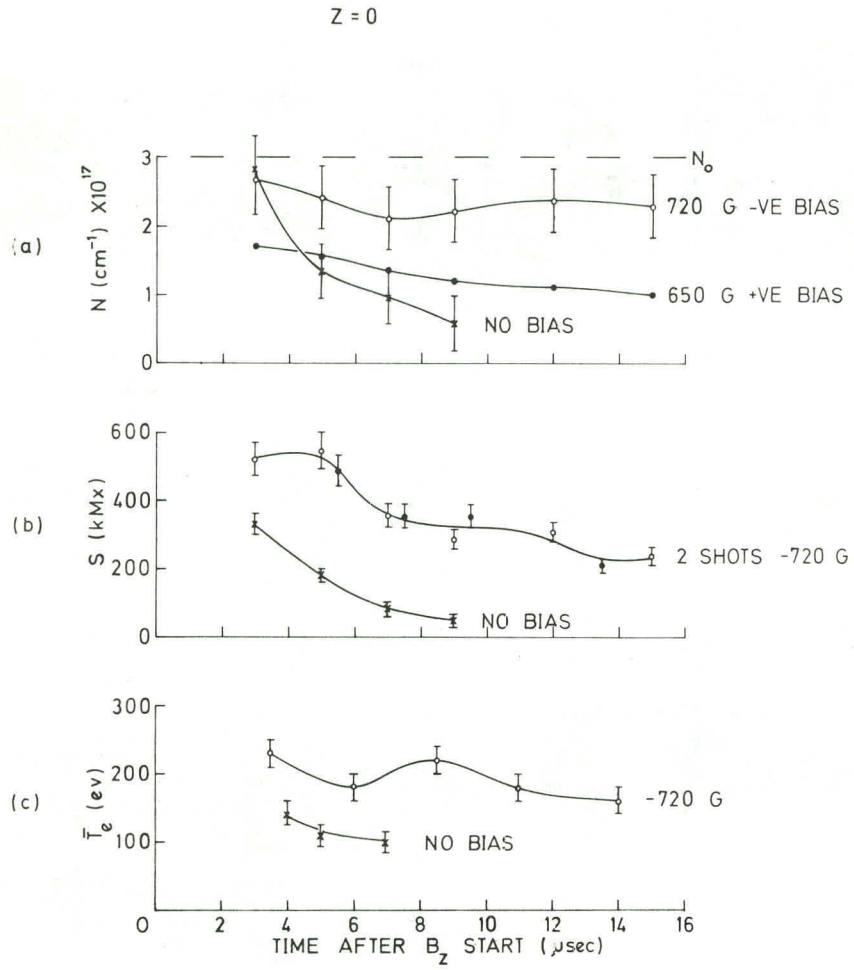

Fig. 3. (a) Line density N_e for -720G, 0, +650G bias; (b) Diamagnetic signal S (kilo Maxwells) for -720G, and zero bias; (c) Soft X-ray temperatures T_e for -720G and zero bias. (θ-pinch 75 kV, no cusps, 0.02 Torr D_2).

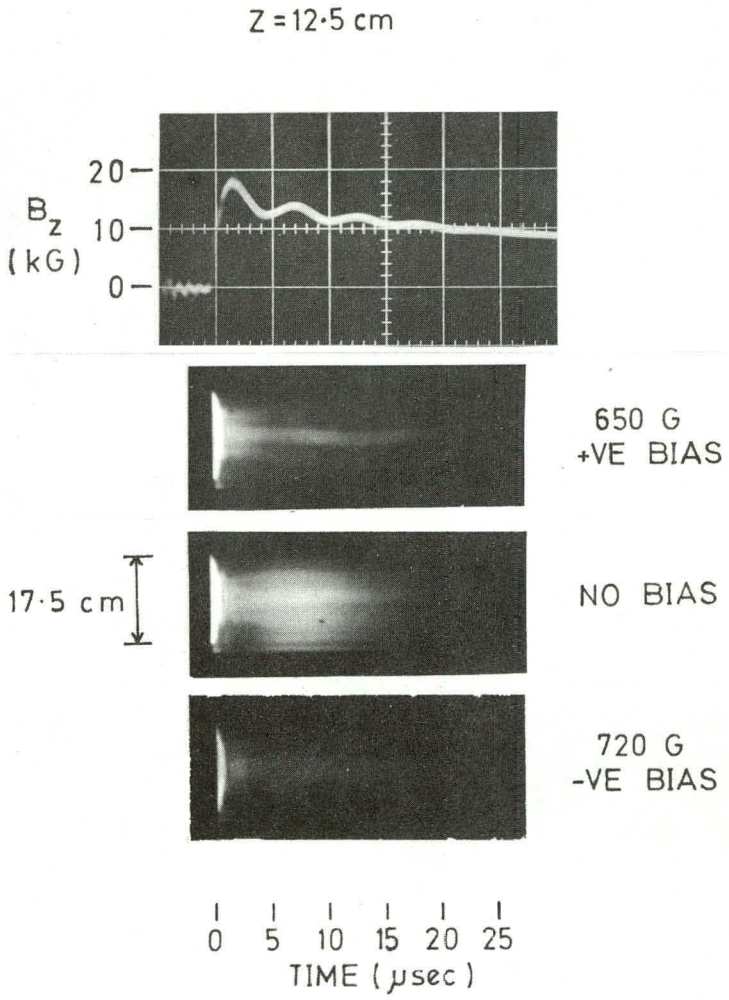

Fig. 4. Radial streak photographs at Z = 12.5 cm (perpendicular to transmission line) for -720G, 0, and +650G bias. (θ-pinch 75 kV, no cusps, 0.02 Torr D_2).

HARD CORE THETA-PINCH WITH REVERSE TRAPPED MAGNETIC FIELD

by

A. C. Kolb, M. P. Young, and E. A. McLean

Naval Research Laboratory
Washington, D. C. 20390

ABSTRACT

A rotating flute instability has previously limited the confinement time in Pharos to ~ 15 μsec. The experiment has been modified by (a) increasing the quartz tube i.d. from 8.7 cm to 17 cm, (b) increasing the main bank energy from 1.3 MJ to 2 MJ, and (c) inserting a 4 cm diameter insulated conductor on the axis, connected to a 700 kJ, 100 kV capacitor bank (a clamped 5-stage Marx generator). The relevant design parameters are: B_z = 80 kG, rise time 25 μsec, L/R decay time 200 μsec; B_θ = 50 kG at 3 cm from magnetic axis, rise time 25 μsec, L/R decay time 150 μsec. The experiment is designed to study high shear, high-β plasma in a closed field geometry. The confinement time without the hard core is considerably longer in the case of the larger tube. Preliminary results with 50 and 100 kJ of the hard core capacitor bank show that the time the plasma is held off the rod increases with increasing hard core current.

OBSERVATIONS ON A LARGE DIAMETER θ-PINCH WITHOUT HARD CORE

Earlier observation of the confined plasma in Pharos with a 8.4 cm diameter tube showed that instabilities would develop within 10-15 μsec. The predominant modes were the rotating flute and m = 1 drift.

When the tube diameter was increased by a factor of about two (17 cm) the stability was greatly improved: i.e. the rotating flute mode was delayed to 30 μsec, typically. With a reverse bias field the losses are relatively small during the first ~ 15 μsec. Thereafter, the loss rate is large and can be accounted for by flow out the ends through a constricted aperture in combination with radial losses at the Bohm rate[1]. In Fig. 1 the behavior during the first 15 μsec is compared with that during latter phases of the discharge. As in the small tube case, where the loss rate is at least an order of magnitude slower than the Bohm rate during the first 15 μsec, the losses during early times appear relatively small.

In Fig. 2 two streak photographs for the 8.4 and 17 cm tubes are compared; bias field-5.8 kG and - 4.3 kG, respectively. The general improvement in confinement due to increasing the dimensions is evident. However, there is now an indication of resistive tearing after three or four dynamic bounces when the bias field is reduced to -1.7 kG (See Fig. 3).

The effect of the initial reverse bias field is shown in Fig. 3. Without a bias field the plasma is lost out the ends somewhat faster than in the case of reverse bias field. Also the temperature is lower since CV radiation does not appear. With -0.8 kG bias field there are hair-like wisps which leave the plasma surface. With higher bias field these disappear, but the tearing mode develops early in time and then washes out. Finally with -4.3 kG bias field the tearing mode is no longer evident and the plasma is macroscopically quiescent for ~ 30 μsec, at which time a rotating flute is frequently observed.

Under circumstances where the tearing mode is evident ($B_z \approx$ -1.7 kG), the increasing of the bank energy has little effect on the gross behavior

[1] E. A. McLean, A. D. Anderson and H. R. Griem, another paper presented at this conference.

(Fig. 4), but does influence the severity of the rotating flute after ~ 25 μsec and the tearing mode at ~ 5 μsec.

These various observations show that while the confinement has been greatly improved with a large tube, that various macroscopic instabilities still develop. Also after 15 μsec (when the plasma appears macroscopically stable) there appear to be fast Bohm-like radial losses[1].

OBSERVATIONS ON A HARD CORE, HIGH SHEAR, θ-PINCH

In an attempt to stabilize the various instabilities described above and to extend the initial period (the first ~ 15 μsec) of low loss rates to later times, a rod carrying a high current was placed along the axis (Fig. 5). With this arrangement the effect of large shear on high-β, θ-pinch plasmas, with closed field lines in the case of reverse bias field, can be studied. The energy of the main capacitor bank was also increased to 2 MJ from 1.3 MJ in order to maintain high B_z fields in the larger coil. The parameters of the entire system are listed below:

Compression Bank		Hard Core Bank	
E	2 MJ		700 kJ
I_o	12 MA	I_z	750 KA
$\tau_{\frac{1}{4}}$	25 μsec		25 μsec
L/R	200 μsec		150 μsec
V	20 kV		100 kV
B_z	80 kG	B_θ	50 kG at r = 3 cm

To date only 100 kJ of the hard core capacitor bank have been utilized. Current wave forms for the 100 kJ case are shown in Fig. 6.

With 50 kJ energy in the hard core bank, the plasma could be held off the rod for ~ 4 μsec after the switching of the compression bank. The optimum result was obtained when the hard core was fired 2 μsec ahead of the main bank. With a reverse bias field and no hard core current, the plasma would hit the rod , with an influx of impurities, at earlier times - see Fig. 7. The bright flash of luminosity is impurity radiation when the plasma diffuses onto the rod.

Increasing the energy in the hard core bank from 50 kJ to 100 kJ (the latter for one shot) increased the time before impurities flood the system by 50% (Fig. 8). However, the hard core was fired 2 μsec after the main compression bank and did not reach a maximum until t = 9 μsec in Fig. 8. By optimizing the timing of the two banks, further improvement at the 100 kJ level can be expected, judging from the 50 kJ results (Fig. 7)[2]. In Fig. 8 one can also see that some impurities are introduced at the times of maximum compression during the dynamic bouncing.

To summarize, using 1/7 of the available energy in the hard core system the bulk of the plasma could be held off the rod for ~ 6 μsec and this time depends strongly on the hard core current. There is every indication that it will be possible to study high-β, shear-stabilized plasmas for times in excess of 10 μsec. Whether or not the fast losses after 15 μsec observed without a hard core can be suppressed by shear remains an open question.

[2] This could not be shown because the tube broke shortly before the conference.

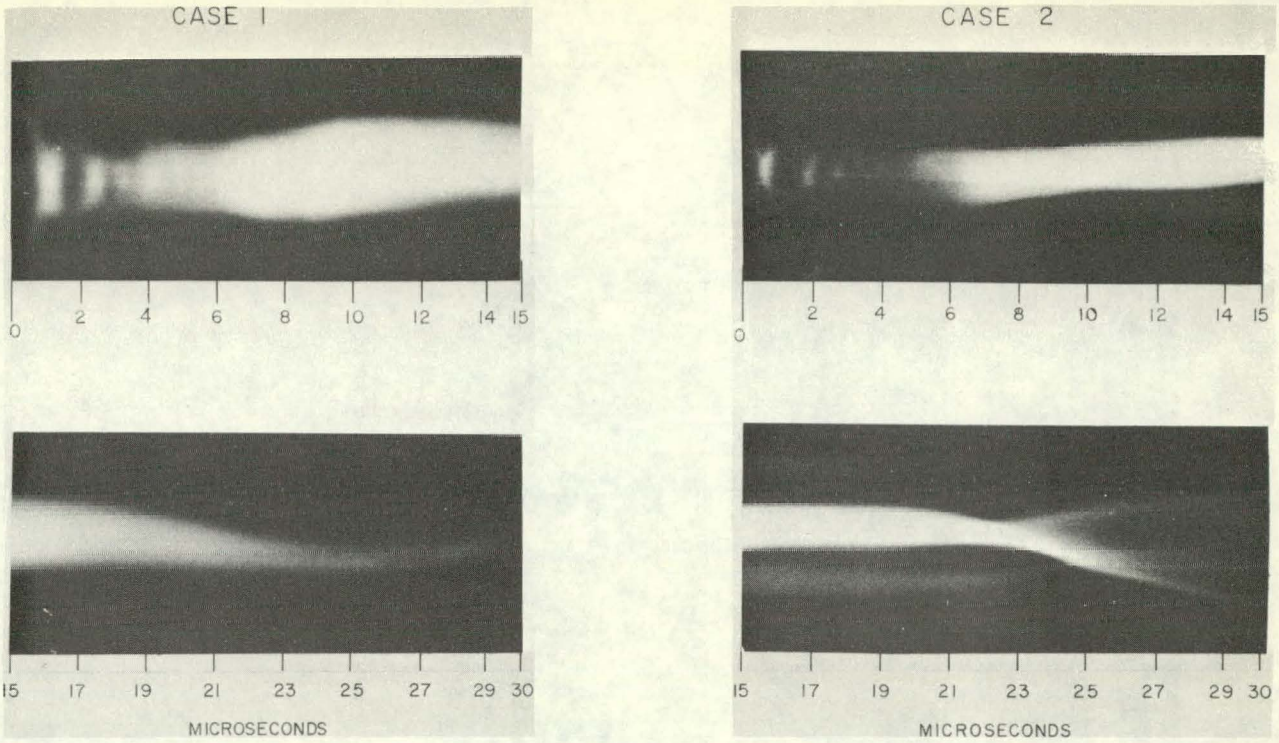

Fig. 1. Comparison of early and late stages of the discharge in a 17 cm tube. The losses are much less during the first 15 μsec. These photographs also indicate the day-to-day reproducibility. P_o = 60 μD_2, B_z max = 30 kG at 14 μsec, $N_{av} \approx 6 \times 10^{16}/cm^3$, $T_e \approx 100$ eV.

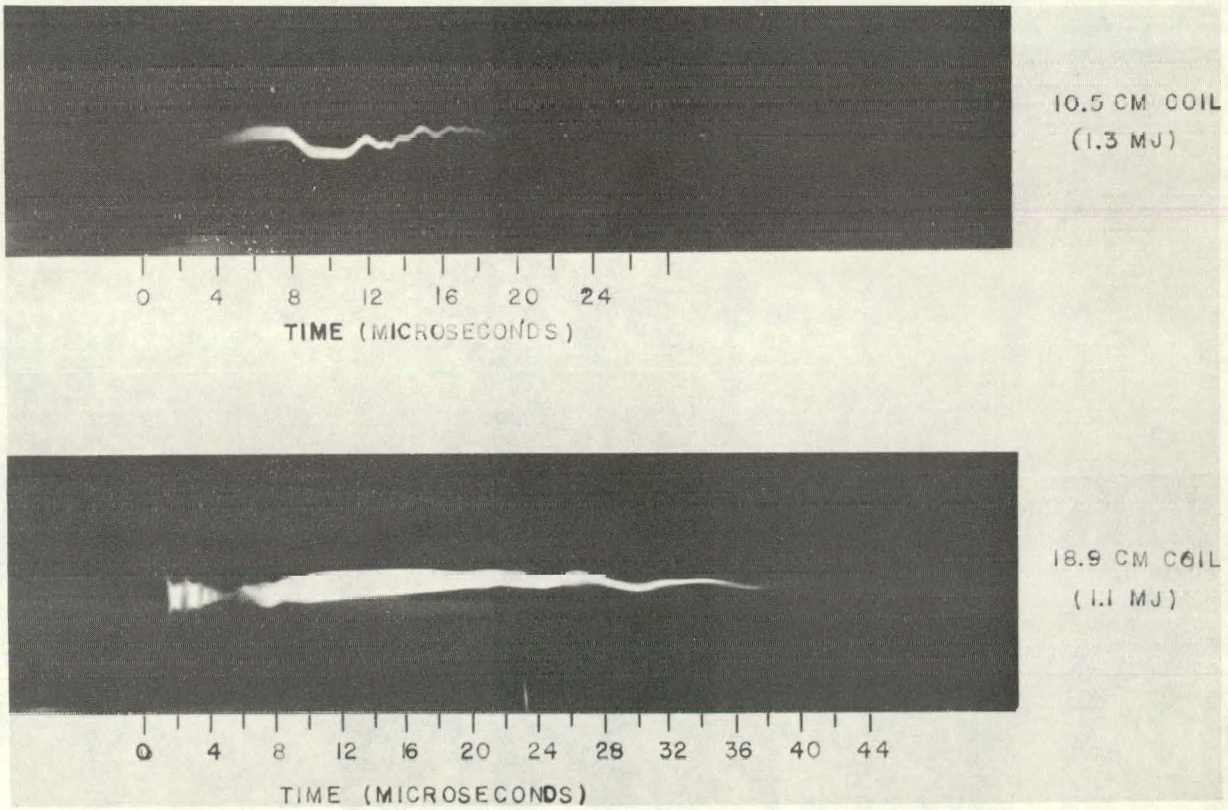

Fig. 2. Comparison of 8.4 cm and 17 cm diam. cases. With larger tubes the m = 1 drift and m = 2 rotating flutes are greatly suppressed. For the 17 cm case, B_z = -1.7 kG and there is some evidence for a resistive tearing mode after ~ 5 μsec.

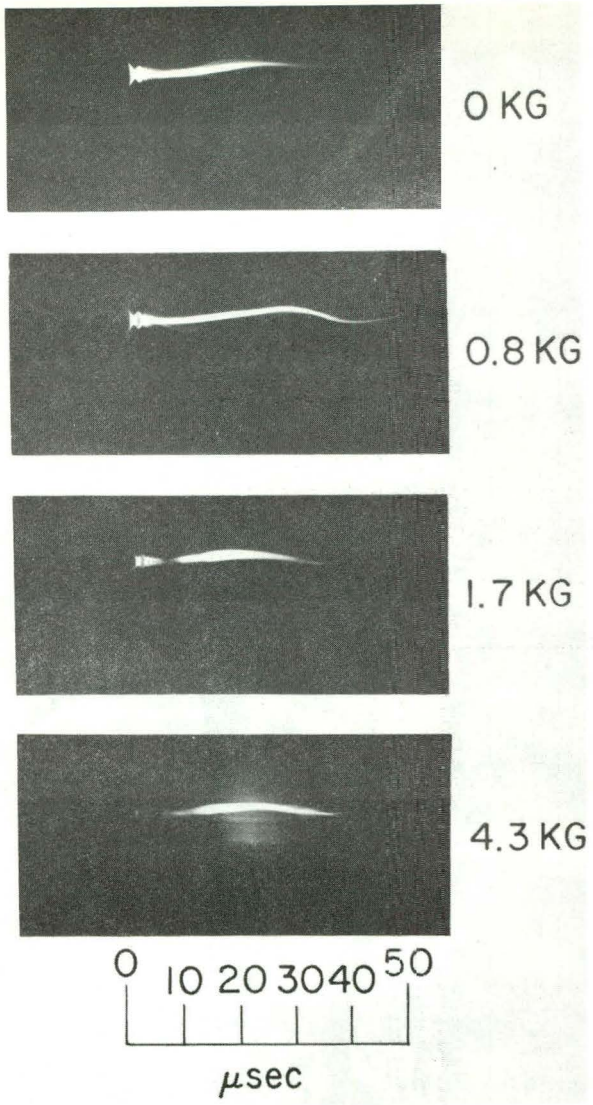

Fig. 3. Influence of bias field. P_o = 60 μD_2, B_z max = 30 kG in 14 μsec.

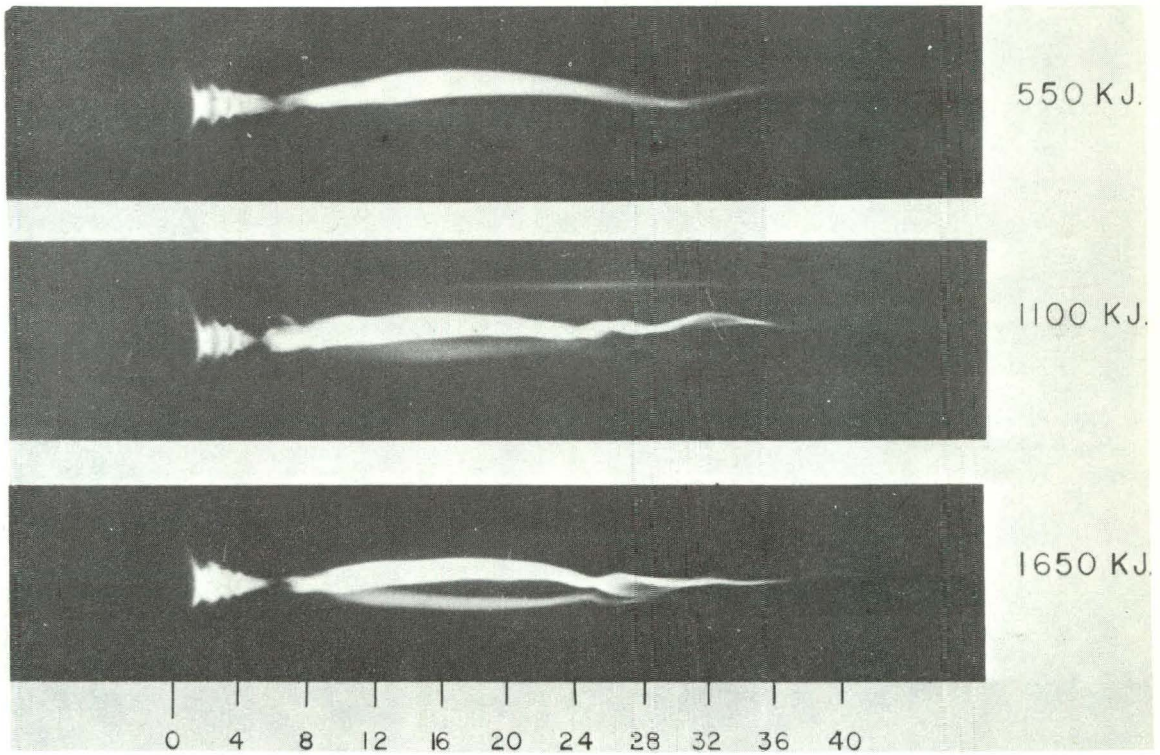

Fig. 4. Influence of capacitor bank energy for an initial bias field of -1.7 kG: The second image is reflected light.

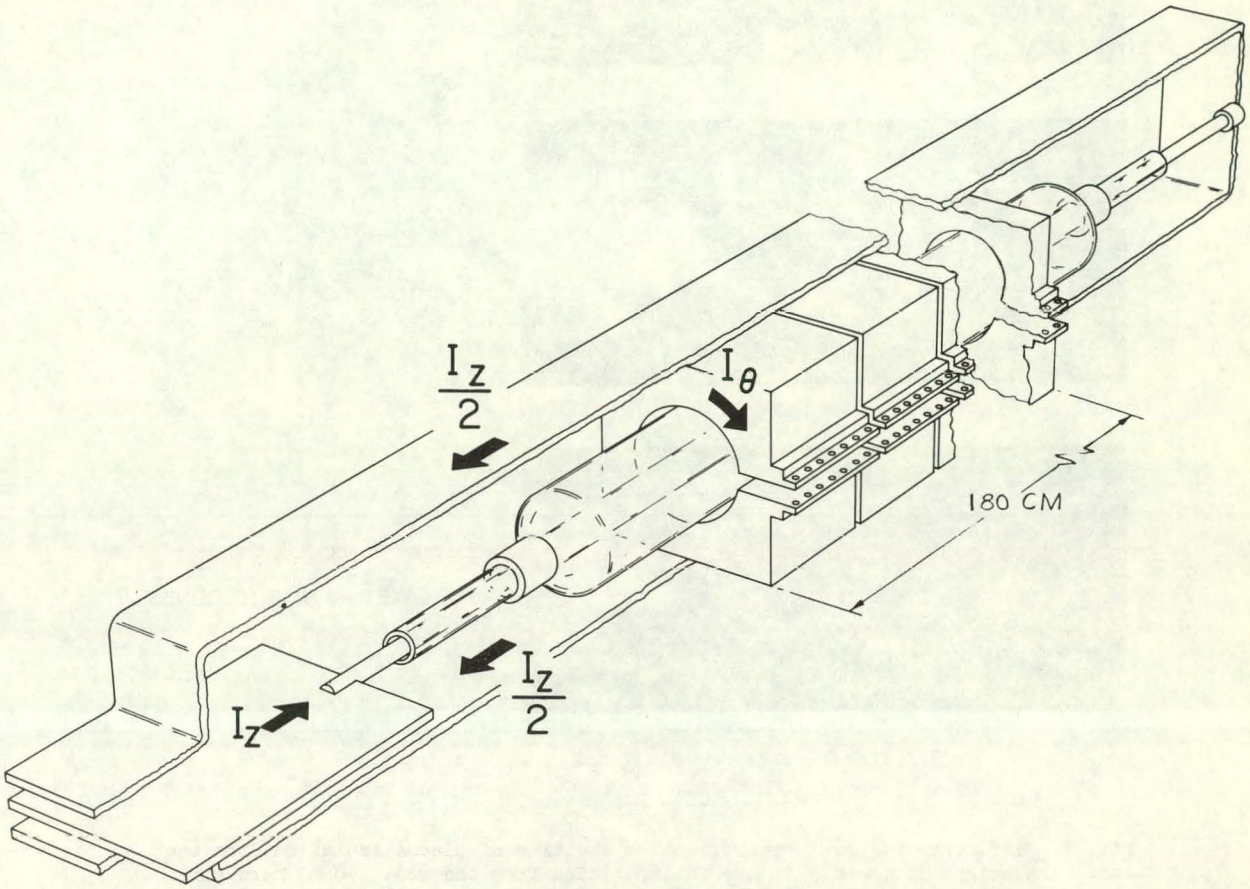

Fig. 5. θ-pinch with hard core. Rod radius = 2.0 cm. Maximum current = 750 KA.

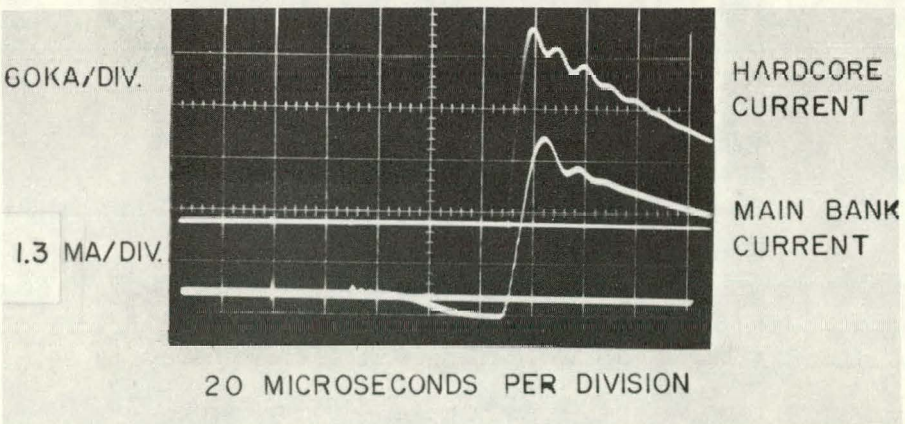

Fig. 6. Current wave forms for 100 kJ hard core bank and 550 kJ compression bank.

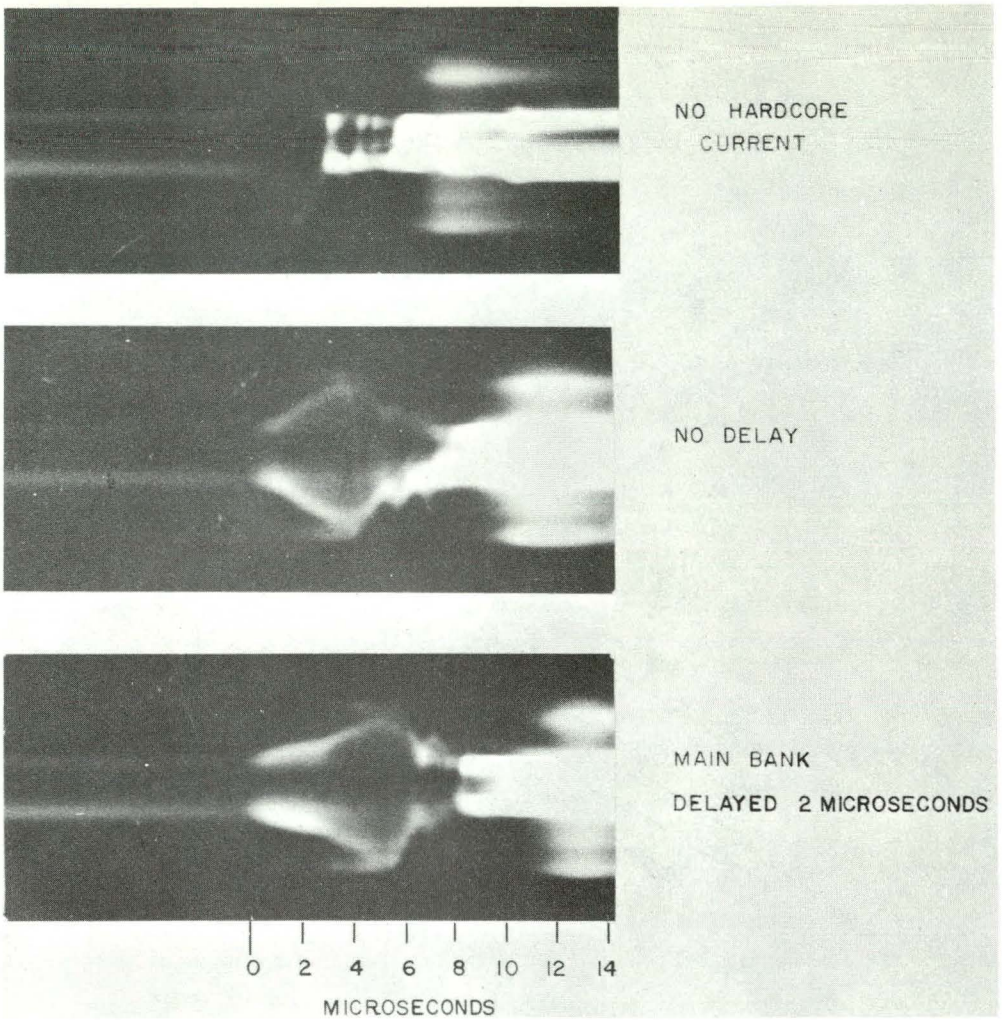

Fig. 7. Influence of hard core current on the time of plasma isolation from the rod. The bright luminosity is due to impurities from the rod. 50 kJ hard core with I_z = 165 KA, B_z max = 18 kG in 11 μsec, bias field = -4.3 kG, P_o = 60 μD_2.

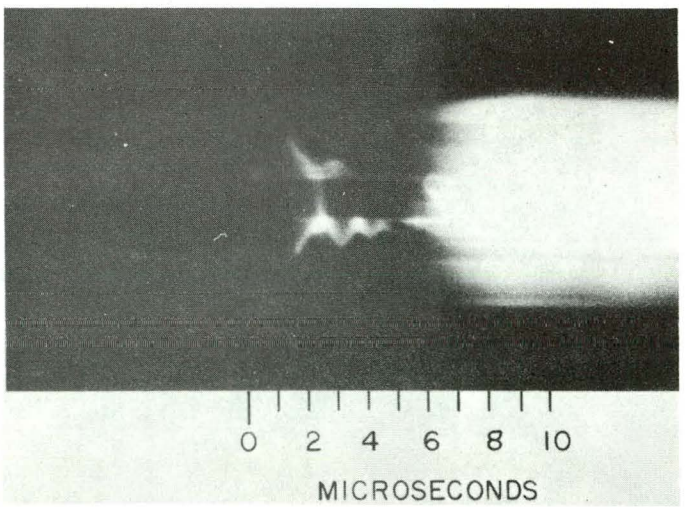

Fig. 8. 100 kJ hard core bank with B_z max = 30 kG and -4.3 kG bias field. (See Fig. 6). The bulk of the plasma is held off the rod for 6 μsec.

HARD-CORE THETA PINCH AND ITS TOROIDAL EQUILIBRIUM

S. Yoshikawa
Plasma Physics Laboratory, Princeton University,
Princeton, New Jersey

ABSTRACT

A hard-core theta pinch should have an advantage for confinement over an ordinary inverse theta pinch in that the plasma is stable against the overall macroscopic instability. The equilibrium and overall stability of this plasma are considered using the well-known equilibrium equation. Estimates are made of the critical β for the finite-β ballooning instability.

HARD-CORE THETA PINCH

1. Introduction

Theta pinches, as compared with low-β toroidal or open-ended devices, have the advantage that the time constant required to contain the plasmas for thermonuclear reaction is much shorter than in other devices. This reduces considerably the number of classes of instabilities that are detrimental to confinement. In particular, the drift instabilities may not limit the high-β plasmas.[1] Experimental results presented so far appear to support this view.

The experiments on conventional theta pinches, however, are so far limited by the particle loss through the end. That is, the plasma is not in equilibrium and the confinement time is determined by $\tau = (B_e/B_c)\, L/V_s$, where B_e and B_c are the magnetic field strength at the mirror and the center, respectively, L is the machine length, and V_s is the sound velocity (high density case).

The "Scyllac" proposal is to rectify this difficulty by making the linear pinch into a toroidal one to eliminate the particle loss from the ends. However, this experiment, of necessity, requires a large device, and the problem of toroidal equilibrium and stability comes into play. One approach to supply the toroidal equilibrium and the stability against $k_{\parallel} = 0$ flute instability is to use the M and S geometry modified by Pfirsch and Wobig.[2] A rather complex configuration and somewhat incomplete theoretical understanding, however, make this approach less than ideal.

2. Azimuthally Symmetric Toroidal Theta Pinches

An alternative approach is to use a Tokamak configuration for toroidal theta pinch. This configuration automatically has an equilibrium, and it is shown by Ware and Haas[3] that the plasma has stability against $k_{\parallel} = 0$ mode up to $\beta \sim a^2/4R^2$ where a is the minor radius and R is the major radius. Although the assumptions to derive this criterion fail, if $a/R \sim 1$, the relation $\beta \sim a^2/4R^2$ is expected to hold approximately.

In theta pinches, a/R can be increased to unity with little difficulty. So-called inversed field theta pinches are, in fact, toroidal plasmas with $a/R \sim 1$. Somehow, inverse pinches are in disfavor because of the possibility of positional instabilities and/or kink instabilities. The

inverse theta pinch, however, offers a true confinement in that plasmas are trapped in closed magnetic field lines. To avoid positional instabilities and/or kink instabilities, a hard core can be introduced to convert the inverse theta pinch essentially into a large a/R, high-β Tokamak. This was suggested by Kolb and Yoshikawa and independently by Kilb . The configuration is sketched in Fig. 1. Initially, a uniform magnetic field in the -z direction and a weak toroidal field are applied. After preionization of the gas, a $+B_z$ field and a large toroidal field B_t can be applied to compress the plasma. If the ratio B_z/B_t is kept approximately a/2R during the compression, the plasma should remain in a stable equilibrium against the interchange mode.

3. Stabilization against Positional Instability

By shaping the external B_z-producing coil, it is possible to eliminate the positional instability. The positional instability is defined as the instability of the plasma ring as a whole. A plasma ring can move either sideways or axially in the z direction, depending upon whether the B field is convex or concave at the plane of symmetry. By shaping the B_z field as shown in Fig. 1 (i.e., convex)[4] the plasma is unstable against the sideways motion if no toroidal field is present. This instability can be stabilized by a strong toroidal field, because the plasma has a tendency to follow the magnetic field line, or else one can say that the sideway motion increases the magnetic energy by deforming it, hence the displacement is energetically unfavorable.

Experimentally the inverse theta pinch without toroidal field is usually unstable against the sideways motion, unless extreme care is exercised to avoid any asymmetry. If the B_z field becomes concave, the ring is expected to flip as was reported by Clark and Wuerker.[5]

Finally, the ring major radius should remain constant. The stability calculation, neglecting the toroidal field effect, has been done previously. The conclusion is similar to the betatron stability condition. It is concluded that, if the externally applied B_z is proportional to R^{-n} with $0 \leq n \leq 1.5$, the plasma major radius is expected to remain constant.[4] The presence of the toroidal field should not change this stability criterion.

As long as the ratio B_p/B_t does not exceed a/2R, the plasma is also stable against low-m kink (Kruskal - Shafranov) instability. It is not clear whether the plasma is stable against high-m kink instabilities. Experimental evidence in Tokamak, however, suggests that the plasma, even if no high-m kink instability may exist, does not suffer any catastrophic particle loss.

The plasma equilibrium configuration has been calculated by Shafranov,[6] Suydam,[7] and others.[4] The main conclusion of these calculations is that the plasma pressure is limited to the poloidal magnetic field pressure. If the pressure exceeds this value, the plasma equilibrium is no longer possible. From a very general consideration, it can be shown that the current in the toroidal direction is necessary to maintain the toroidal equilibrium.[4]

4. Stability against the Ballooning Stability

Although the toroidal theta pinch can be operated at any desired value of β, because of the stability condition and the equilibrium condition it is desirable to operate at $\beta \sim B_p^2/2B_t^2 \sim a^2/2R^2$, where B_p is the poloidal magnetic field. Although the system is stable against a $k_{\parallel} = 0$ flute instability, the plasma can become unstable against so-called finite-β ballooning instability.[8] The instability appears if the growth time becomes

shorter than the time an Alfven wave covers the distance in the region of the unstable curvature (modified by a well-depth parameter h). Thus the plasma becomes unstable if $\beta > (4h/1 + 3h)(aR_b/L^2)(\pi^2/(1 - h)^2)$ where R_b is the radius of the bad curvature section and $h/(1 - h)$ is the ratio of the average good curvature to the bad curvature[7] ($h \leq 1$). In view of the experimental configuration we can let $R_b \sim R$, $L \sim 2\pi R$, and $h \sim 1/2$. Thus, $\beta \geq a/R$. In general, the plasma can be made stable if $\beta < a/R$. This result does not contradict the fact that $\beta = 1$ plasma is always unstable against the interchange, because the calculation under that condition is usually based on the assumption that the plasma-vacuum interface is infinitesimally thin, i.e., $a = 0$.

5. Effect of Resistivity

The discussion is so far based on an infinitely conducting plasma model. In reality, the plasma conductivity should be taken into consideration for equilibrium. The current required to hold the plasma must be kept constant to maintain the equilibrium. The current decays with the time constant determined by $\tau = a^2(\text{cm})\, T_e^{3/2}(\text{eV})\, 2\pi \times 10^{-8}[\ln(8R/a) - 7/4]$ sec. Thus the decay time is 7 msec if $a = 2$ cm, $T_e = 1000$ eV, and $\ln(8R/a) - 7/4 \sim 1$. This decay time can be increased by means of the toroidal electric field coupled through an air core transformer (Fig. 1) if necessary. The decay time is increased by a factor (B_t^2/B_p^2) by this method. The finite resistivity may introduce a new type of instability (e.g., resistive g mode). The growth rate for the resistive g mode is estimated to be (for $k_\perp = 10/a$, $n = 10^{15}$/cc and $B = 50$ kG) $9 \times 10^3/T^{1/2}\,\text{sec}^{-1}$.[8] Thus, during the time of interest (~ 1 msec), this instability is not expected to be dangerous at $T_e = 1000$ eV.

6. Conclusion

The hard-core theta pinch should be stable against interchange and positional instabilities, with adequate choice of β and the ratios B_p/B_t and a/R. This choice of the parameters also should bring about the stability against low-m kink instabilities. We have not considered the effect of the shear to the stability of plasma instability because no adequate theory is available to consider the effect of shear on high-β plasmas.

If we relax the condition of the azimuthal symmetry, the stable plasma condition is expected to be relaxed further. The modified M and S geometry of Pfirsch and Wobig[2] can be considered as the extension of this azimuthally symmetric hard-core theta pinch.

This work was performed under the auspices of the U. S. Atomic Energy Commission, Contract AT(30-1)-1238.

References

1. N. A. Krall and M. N. Rosenbluth, Phys. Fluids 8, 1488 (1965).
2. D. Pfirsch and H. Wobig, in Plasma Physics and Controlled Nuclear Fusion Research (International Atomic Energy Agency, Vienna, 1966), Vol. 1, p. 757.
3. A. A. Ware and F. A. Haas, Phys. Fluids 9, 956 (1966).
4. S. Yoshikawa, Phys. Fluids 7, 278 (1964).
5. G. L. Clark and R. F. Wuerker, Phys. Fluids 5, 1503 (1962).
6. B. D. Shafranov, Soviet Phys.--JETP 6, 545 (1958); 10, 775 (1960).
7. B. R. Suydam, LAMS-2571, Los Alamos (1961).
8. B. Coppi and M. N. Rosenbluth, in Plasma Physics and Controlled Nuclear Fusion Research (International Atomic Energy Agency, Vienna, 1966), Vol. 1, p. 617. Also H. P. Furth, J. Killean, M. N. Rosenbluth, and B. Coppi, ibid. Vol. 1, p. 103.

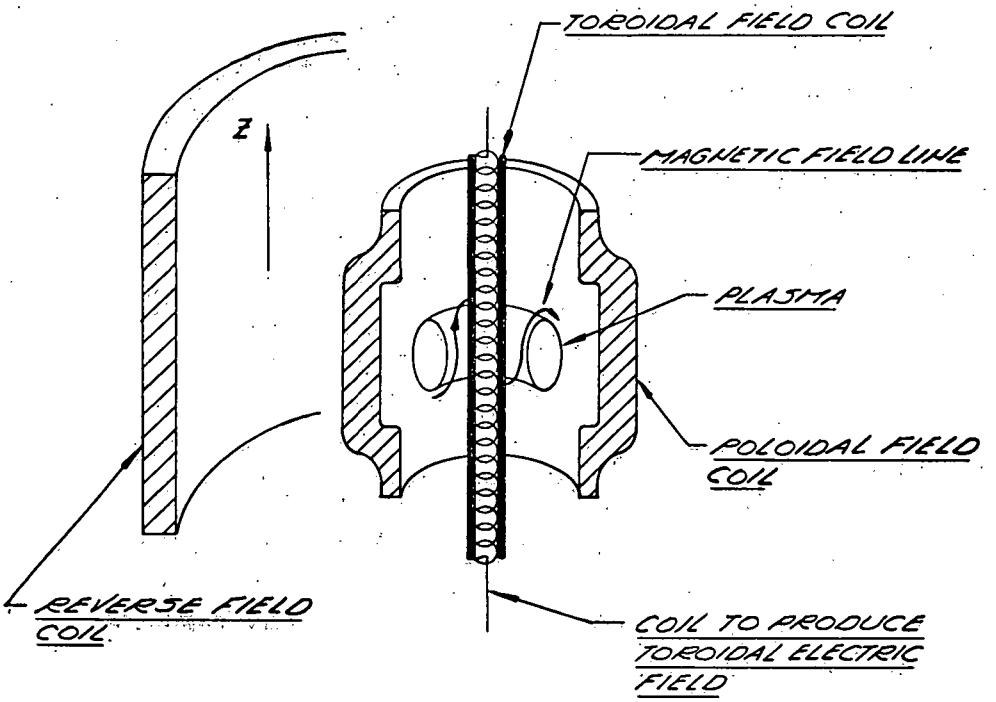

Fig. 1. Schematic drawing of hard-core theta pinch.

OBSERVED ANOMALOUS PLASMA LOSS FROM A MINIMUM-B SYSTEM*

by

F. H. Coensgen, W. F. Cummins,
R. E. Ellis, F. R. Kovar and W. E. Nexsen, Jr.

Lawrence Radiation Laboratory, University of California
Livermore, California

ABSTRACT

Plasma losses from either simple magnetic mirror or minimum-B confinement geometries have been studied in an 18 in. diameter plasma injected system. For conventional vacuum conditions (base pressure $\lesssim 5 \times 10^{-7}$ torr) plasma which is diverted to the wall in forming a minimum-B field introduces an influx of neutral gas which gives rise to plasma losses from impurity generated instabilities as well as atomic processes. By reducing the base pressure to the 10^{-9} torr range and evaporating titanium throughout the entire chamber the neutral influx can be reduced and at least one instability suppressed. Plasma with density up to 5×10^{13} cm^{-3} is formed under conditions where lifetime in a quasi-stationary minimum-B field is not limited by ion-ion scattering, electron cooling, charge-exchange or interchange instabilities. From the presence of high frequency fluctuations, sporadic end loss and anomalously high attenuation of transmitted microwave beams the plasma is known to be turbulent. In this range from 3×10^{13} to 5×10^{12} cm^{-3} the characteristic decay time lies between 400 and 500 μsec. Below 5×10^{12} cm^{-3} the density decay proceeds in an obviously stepwise fashion indicating intermittent stability. Evidence suggests that the stabilizing effect is also present at higher densities but that the length of the stable periods decreases with increasing density.

INTRODUCTION

In the 2X experiment plasma containment in open-ended systems is studied by rapidly creating a plasma then making time dependent measurements of plasma parameters such as density, ion energy, electron temperature, end losses, cross field transport and radiation. Obviously the first point of interest is a comparison of particle and energy loss rates from the plasma with those expected from atomic processes (coulomb collisions, charge-exchange and radiation). If anomalous losses are found it is then important to determine their origin and, if possible, suppress them by changes of one or more of the following factors: the magnetic field, the plasma density gradients, the ion velocity and/or energy distributions, the electron temperature, the ratio of the average ion gyroradius to plasma dimensions, or the boundary conditions (e.g., coupling of the plasma to the walls by external plasma).

When operated as a simple mirror system, particle losses as determined from microwave density measurements and DD reaction rate histories were found to proceed approximately exponentially with a 300 μsec characteristic lifetime.

In this operation the absence of low order instabilities was ascribed to "line tying". Although the observed losses were faster than the estimated scattering and charge-exchange rates and rf signals were detected, the effect of high frequency instabilities could not be determined as the anomalous rate could have been associated with higher order interchange modes.

In the present experiments the question of hydromagnetic instabilities is avoided through the use of a minimum-B containment field. Indeed, the first result was a confirmation of the suppression of interchange instabilities by the complex field.

Plasma injection into the minimum-B system proceeds on the following schedule. At time t = 0 plasma is injected along dc field lines by firing seven Ti-hydride guns which are located in the dc

field at one end of the vacuum chamber five meters from the containment volume. Plasma is trapped in simple mirror geometry by initiating the pulsed mirror and compression magnets at 30 μsec. At 60 μsec current is initiated in an orthogonal quadrupole magnet so that the minimum-B field is formed by 70 μsec. All magnet currents reach their maximum at 200 μsec at which time they are crowbarred and the central field decays exponentially with an 8.5 msec characteristic time.

PLASMA LOSS DUE TO NEUTRAL CONTAMINANTS

Initially a rapid, catastrophic plasma loss started about 30 μsec after the quadrupole field was applied. From an examination of the magnetic field lines after transition to minimum-B geometry it was evident that the mirror points along field lines which cross the midplance at radial distances greater than a limiting value r_ℓ were outside of the vacuum chamber. Thus, plasma trapped at radial distances greater than r_ℓ was diverted to the walls by superposition of the quadrupole. Also, plasma lost through the mirrors resulted in an unavoidable wall bombardment as most of the lines of the minimum-B field pass through the wall shortly after the mirror position. Such plasma losses can increase the density of the neutral background not only through recombination but to a much greater extent by desorption of occluded gas. The resultant influx of neutral particles into the trapped plasma was dramatically signaled by a rapid increase of light and of energetic charge exchange neutrals accompanied by equally rapid declines in density and reaction rate. This very rapid plasma loss was eliminated by restricting the injected plasma column diameter to 15 cm and providing the entire internal surface of the vacuum chamber with an uncontaminated titanium coating prior to each containment run. At 10^{-8} torr, the monolayer-forming time is approximately 30 seconds. To insure clean surfaces the experiment was run within 6 seconds after the heater currents in the 25 Ti sublimators were terminated.

The improvement of the energetic plasma lifetime is evident by the extension of the prompt neutron and fast atom signals, (Fig. 1). For the conditions of this experiment the total charge-exchange flux is independent of the plasma density, and proportional to the surrounding neutral density, as the mean free path for ionizing thermal neutrals, λ_{ce} is less than the plasma column radius, r_p. Thus, the nearly constant magnitude of the fast atom signal shown as curve FA_c in Fig. 1 indicates a constant background neutral density. Actually as shown by the curves in Fig. 2 the plasma density continually decreased in time, so it is probable that the rapid decline of the fast atom signal after 800 μsec (FA_c, Fig. 1) occured at the density where $\lambda_{ce} \gtrsim r_p$.

Previously the rapid plasma loss accompanying the transition to minimum-B geometry was attributed to charge-exchange, but, the fast atom data from 2X does not substantiate this hypothesis. First, when the injected plasma column was restricted in diameter to 15 cm the magnitude of the fast atom signal was reduced without a comparable extension of the reaction rate. Also, gettering the system which increases the duration of both fast atom and neutron signals does not change the magnitude of the charge-exchange signal for the first 300 μsec (Fig. 1) which implies that neutral background density at the center is not changed. Thus, it appears that the active surface reduces the detrimental effect of plasma lost through the mirrors. Without the active walls such losses could generate cold plasma ions near the ends of the plasma column. If the cold plasma density becomes great enough an ion-ion instability[2] due to a double-humped ion energy distribution should develop. Actually, a rf signal at or slightly greater than ω_{ci} is detected during the rapid plasma loss. Furthermore, during this period there is a rapid reduction of the mean energy of the trapped ions which may indicate a shift of the energy spectrum similar to that reported by Perkins[3].

In the gettered system the trapped ion energy spectrum is nearly constant, no signals at ω_{ci} are found and the rapid loss is suppressed.

PLASMA CONTAINMENT IN GETTERED SYSTEM

The density decay rate has been studied as a function of the injected density by varying the potential applied to the plasma guns, which changes the output of the guns without changing the injected mean ion energy. At higher injected densities

(curves I, II, III, Fig. 2) the decay exhibits three distinct regions. From 200 to 350 μsec $\tau \tilde{=} 100$ μsec. From 350 μsec to densities below 2×10^{12} cm^{-3} the decay is nearly exponential with τ between 350 to 500 μsec. Finally the decay proceeds in a stepwise manner made up of rather long "stable" periods separated by shorter periods of fast loss. Closer examination of the microwave interferograms showed that the decay during the latter part of the second period also proceeds in a stepwise manner, at least up to densities of 8×10^{12} cm^{-3}. The duration of the flat portions decreases earlier in time when the density is greater.

The faster decay of the first period has been found to be due to the disappearance, beyond 350 μsec, of a large diameter (and presumably colder) plasma cylinder outside of the main hot plasma. It is suspected that this external plasma is due to ionization of neutrals during compression and/or late plasma from the guns.

After 350 μsec, for plasma densities up to 10^{13} cm^{-3} the trapped D^+ energy range was found to extend from 2 keV to 50 keV and remain nearly constant as long as these signals could be measured (about 1 msec). Mean ion energies derived for various assumptions of background gas are in the range from 6 to 8 keV. This is in good agreement with the 6 keV value obtained from total neutron production, microwave density and estimated plasma volume. Also for very good operation, the reaction rate decayed at twice the density decay rate which is consistent with a one component hot plasma. During this period, the constancy of the average ion energy rules out electron cooling as a major loss mechanism.

Charge-exchange times of the order of 10 msec are expected on the basis of the measured pressure rise when the guns are fired in the gettered system. This value is consistent with the 8.5 msec decay rate found during the "stable" periods. If the vacuum conditions are allowed to deteriorate slightly, the decay during "stable" periods is faster.

Radio frequency radiation at ion cyclotron harmonics, high attenuation of microwave beams, and sporadic plasma bursts along field lines beyond the mirror are strong evidence of turbulence during this period of anomalous plasma loss (t > 350 μsec). Loss cone instabilities are, of course, the first suspected origin of the turbulence, but electromagnetic modes as well as other electrostatic modes are also theoretically possible.

The 2X plasma never satisfies the Post-Rosenbluth[3] condition for stability against the density gradient driven drift-cyclotron instability. However, frequencies near .4 ω_{ci} which correspond to the fastest growing modes of this instability have not been found. Neither is there evidence of preferential loss from regions of steep density gradients.

The 2X plasma satisfies the stability criterion for the Post-Rosenbluth type A instability below 10^{13} cm^{-3}, if one assumes no reflection of the waves at the mirrors. If there is enough reflection so that the system is unstable initially, it is possible that the "stable" regions at lower densities might be due to crossing this threshold and subsequent steps might be due to energy loss which lowers the mean Larmor radius to the point where the plasma is again unstable. We have made an intensive search for radiation or fluctuations at the ion plasma frequency but have not found evidence of this activity which should characterize the instability. At this time the stepwise structure seems to indicate a stabilizing mechanism instead of a threshold phenomenon.

With clean walls only a single frequency which is about 1.5 Mc less than ω_{ci} is observed at 150 μsec when the rf signal is first detected. Within 100 μsec the fundamental disappears and is replaced by the second harmonic. Increasingly higher content of higher harmonics appear later in time. To date, the rf data is consistent with Harris - like modes[2] where the frequency shift to higher harmonics could be due to electron heating (through instabilities) and consequent damping of the lower harmonics.

We have no direct measurement of the ion energy during the later stepwise decay. The decay rate (> 8.5 msec) during the "stable" periods is consistent either with mean ion energies greater

than 2 keV or room temperature ions. However, the loss rate between steps (Fig. 2) demands ion velocities corresponding to at least a few hundred eV. The previously mentioned fact that the decay rate during the "stable" periods was increased for higher background pressures also indicates that the ion energies are greater than room temperature.

SUMMARY AND CONCLUSIONS

Losses arising from neutral contamination are due primarily to instabilities. Such losses could be important for all plasma confinement systems since they lower the energy of the plasma ions.

Plasma of density $\leq 5 \times 10^{13}$ cm^{-3}, mean ion energy 6 to 8 keV, and electron temperature $T_e > 100$ eV has been established in a minimum-B field (plasma diameter 6 cm, distance between mirrors 160 cm). This plasma is turbulent and is lost along field lines due to cooperative effects rather than atomic processes. In the range from 2×10^{13} to 2×10^{12} cm^{-3} the density decays exponentially with a characteristic lifetime in the range of 350 to 500 μsec.

The rf data is consistant with Harris like modes.

The origin of the obvious steplike decay at lower densities is as yet undetermined. It could be due to an intermittant suppression of instabilities due to changes of one or more factors such as ion energy distribution, electron temperature, or boundary conditions external to the magnetic mirrors.

REFERENCES

[1] F. H. Coensgen, W. F. Cummins, W. E. Nexsen, Jr., and A. E. Sherman, Phys. Fluids 9, 187 (1966).

[2] L. S. Hall, Warren Heckrotte and Terry Kammash, Phys. Rev. 139, A1117 (1965).

[3] W. A. Perkins and W. L. Barr, Cyclotron Instability in a Hot Electron Plasma with a Double-Humped Velocity Distribution, UCRL-70103 Preprint, June 26, 1967.

[4] R. F. Post and M. N. Rosenbluth, Phys. Fluids 9, 273 (1966).

*Work performed under the auspices of the U.S. Atomic Energy Commission.

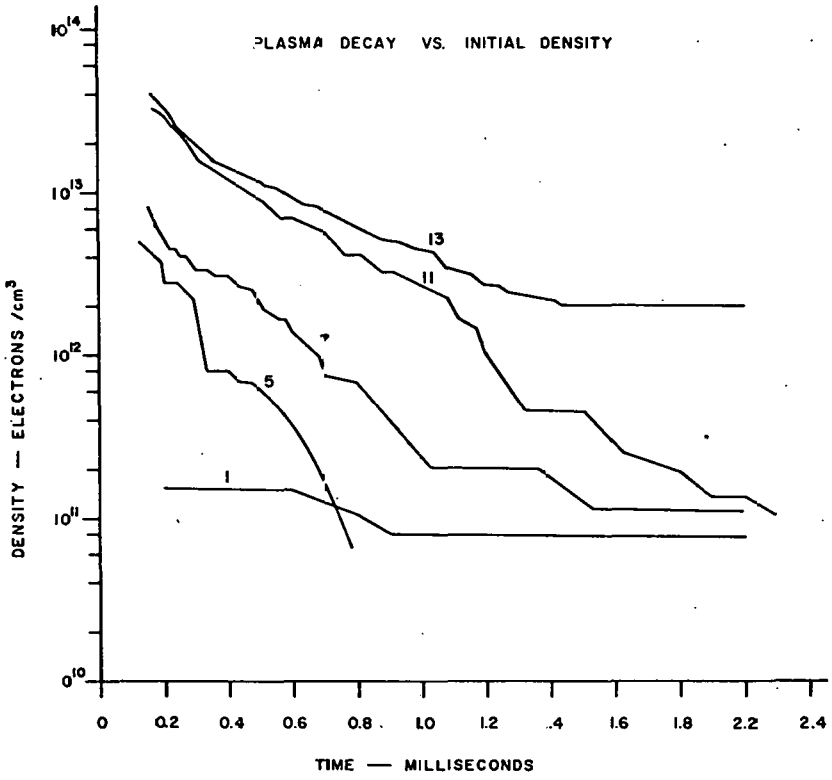

Fig. 1. Effect of gettering on plasma lifetime.
Curve N_D is the reaction history in ungettered chamber
Curve N_c is the reaction history in gettered chamber
Curve FA_D is the r keV D° flux, ungettered chamber.
Curve FA_c is the 4 keV D° flux, gettered chamber.

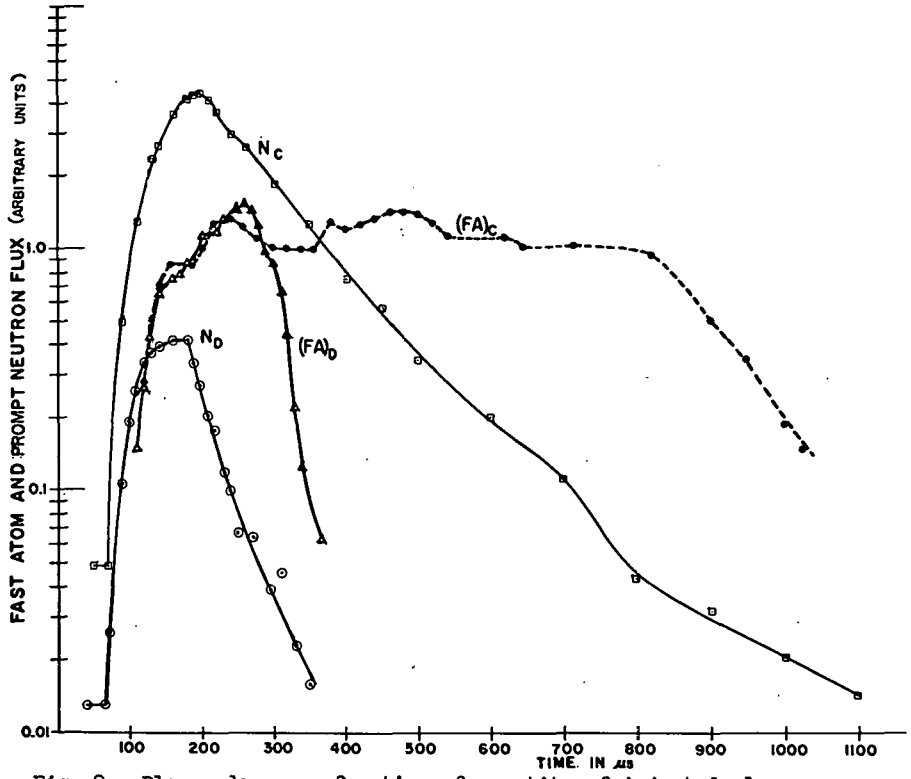

Fig. 2. Plasma decay as function of quantity of injected plasma. The quantity of injected plasma is proportional to the square of the gun potential which is indicated in kilovolts on the curves.

BREAKDOWN AND PREIONIZATION STUDIES FOR A MEGAJOULE THETA PINCH AT LOWER DENSITIES +)

by

A.Eberhagen, W.Köppendörfer and M.Münich
Institut für Plasmaphysik
Garching b. München, Germany

ABSTRACT

Two fast z-pinches of 8o and 12o kV charging voltage as a preheating system have been examined. The 8o kV pulse provides breakdown down to a pressure of 5 micron. This discharge collapses extremely rapidly at low electron densities and forms a narrow discharge channel which lacks reproducibility. The 12o kV z-pinch then heats the gas and brings up ionization. By proper timing of this discharge reproducibility could be established for pressures down to 1o micron.

1. Introduction

Axial current discharges are used at Culham[1], at General Electric[2] and at Garching, as preheaters for Megajoule theta pinches in order not to be limited in the charging voltage of the preionizer.

Since about two years high voltage z-pinches of short duration have been found superior to the earlier used z-pinches fed by transmission lines. The relatively long current duration of the latter led to the development of kink instabilities and to a turbulent plasma. When the main discharge then was triggered after the turbulences had decayed the plasma consequently was already considerably contaminated by wall contact.

Schumacher and Wilhelm[3] for the first time applied a 12o kV z-pinch pulse less than 1 µsec long to heat and compress the gas in one single rapid compression. It was the idea to have the main discharge being fired then before the freely expanding plasma could reach the walls. The merit of this method was an about a factor of ten smaller oxygen content in the plasma as compared to the earlier used transmission line preheaters.

However, it was soon found out that the trapping of mass was less efficient[4] and the neutron yield smaller[5] than in those cases where the plasma was allowed to be reflected at the walls before starting the main discharge. But this procedure in turn increased the impurity content of the plasma again. All these discharges became irreproducible at filling pressures below 2o mTorr.

To investigate the properties of such fast discharges in more detail at low pressures we have assembled an experiment. In order to prevent the irreproducibilities of the breakdown to affect the preheating discharge two consecutive z-pinch discharges have been chosen. In addition a fast low

energy theta pinch discharge was applied subsequently to simulate the early compression phase of a theta pinch.

2. The Experimental Setup

The silica discharge tube is 3 m long and has an inner diameter of 8.8 cm. Stainless steel electrodes are attached to the ends.

A two stage Marx generator of 8o kV voltage serves for breakdown. The discharge is damped by nonlinear resistors to a 9 kA current pulse of about 2 μsec duration.

For preheating a three stage Marx generator of 12o kV voltage is fired about 6 μsec after breakdown. The current pulse reaches 16 kA and is damped out after 1.2 μsec again by nonlinear resistors.

The theta pinch coil is one meter long and covers the middle part of the length of the discharge tube. It is fed by a small condenser bank. The ringing frequency is 66o Kcycles. It reaches a dB/dt of 1.6 x $1o^{1o}$ T/sec and a maximum field of 4 kT.

These discharges have been investigated by magnetic probes, diamagnetic loops, microwave interferometers, spectrometers and by a streak camera with a highly intensifying image converter to observe the discharges in the light of different spectral lines.

3. Results

3.1 The Breakdown

The breakdown occurs within some nanoseconds, whereas the delaytime from switching the voltage to the electrodes to breakdown depends strongly on the filling pressure. Close to 5 mTorr the delaytime rises steeply and it proved impossible to achieve breakdown below this pressure. We did not obtain so far substantial improvements of the breakdown properties either by altering the electric field configuration or by stimulating field emission at the electrodes. Therefore we have no indication yet that achievement of breakdown can be expected below 5 mTorr.

3.2 The Plasma Properties After Breakdown

From streak camera pictures a bright shining plasma ball about the center of the tube can be seen running out in irreproducible streamers. The electron density after breakdown was measured with a 4 mm microwave interferometer. In addition the current density distribution over the radius was evaluated from measurements of the azimuthal field. In Fig. 1 the microwave signal is presented together with the discharge current and also is the current density over the radius at two characteristic times: early after breakdown and shortly after maximum current.

Early in the discharge an approximately uniform current density is to be seen. This justifies the assumption of a homogeneous electron density for the first 2oo nanoseconds after breakdown also. The microwave signal and current density measurements can then be interpreted by a plasma which starts to contract at a density of $1o^{13}$ within about 5oo nanoseconds to a thin column of 1.5 cm diameter. The bulk of the gas remains essentially unaffected by the discharge.

After one microsecond the plasma channel becomes unstable and moves about in an irreproducible way as indicated by magnetic probe measurements. When the discharge current damps out after 2 μsec the plasma expands rapidly as seen from the streak camera pictures.

With help of the image converter and corresponding interference filters the discharge could be observed in the monochromatic light of D_β, a C II and a O II line.

A thin plasma column is clearly indicated by these monochromatic smear pictures with a radius getting the smaller the higher the ionization potential of the species observed. This evidences a hot core in the center of the discharge tube. This region of high temperature coincides with the region of current density.

To learn about the temperature and the electron density spectroscopic measurements have been made. Because the results of these measurements from the breakdown discharge have much in common with those from the preheater they will be presented jointly after the description of the preheating discharge.

In the whole range from 1o to 5o mTorr the general features of the breakdown discharge are the same as described before. According to the microwave measurements with 2.5 and 4 mm wavelength there are regions with electron densities well above cutoff, i.e. 2 x $1o^{14}$ per cc., but as can be seen from the other measurements the ionization is inhomogeneous and limited to a narrow channel in the center.

To further increase the ionization the second, preheating discharge (PD) was fired after a proper delay of 6 μsec from breakdown, thereby allowing the instabilities to damp out and the hot and cold plasma to mix.

3.3 The Preheating Discharge

In contrast to the breakdown discharge magnetic probe measurements exhibit a current density distribution in an annulus at the beginning of the preheating discharge (Fig. 2). This plasma annulus is compressed within about twice the time as compared to the interval the discharge channel was formed before in the breakdown discharge. This finding here indicates a higher efficiency in the trapping of the mass.

After compression a plasma column is formed again. Its diameter, however, is slightly larger than in the breakdown discharge. During all these phases the regions of high temperatures in the plasma could again be illustrated with help of the image converter plus interference filters.

After 1.5 μsec the bank current is damped out. But as seen from Fig. 2 at 1.5 and 2.o μsec currents are still trapped within the plasma. They in fact can be followed up to about 3.5 μsec. Afterwards the trapped fields are smaller than 3o G. No irreproducibilities were registered in this discharge. The main reason for this evidently is a shorter current pulse and a larger plasma diameter at the time when the current is high.

3.4 Spectroscopic Measurements

Information on the degree of ionization, on the temperatures and on the impurity degree in the plasma is of main interest in this present context. Since microwave measurements could only exhibit electron densities up to an upper limit of 2 x $1o^{14}$ per cc. extensive spectroscopic investigations have been carried out.

Evaluation of the electron density distribution from the continuum radiation of the plasma proved impossible here due to the considerable intensity contributions from H^- continuum and H_2 molecular lines. Every information therefore had to be derived from line emission of the plasma, particularly from the Balmer lines D_α, D_β, D_γ, D_δ. Their absolute intensities and their profiles were registered.

Since for the present plasma conditions the upper levels of at least D_γ, D_δ proved to be well above the collision limit and the equilibration time to be short compared to the risetime of the plasma parameters values on electron temperatures and densities could first be derived from the absolute intensities of these lines. Independently information on electron temperatures was also obtained from the halfwidth time of these lines.

Finally the profile measurements yielded two informations. While D_α predominantly proved to be Doppler broadened the D_δ line essentially exhibited a Stark profile. Therefore information could be obtained on the ion velocities and electron densities. These figures, however, ought to be considered as upper limits only as no unfolding of the profiles with

respect to the different broadening factors has been undertaken yet.

In order to obtain a preliminary spatial resolution all intensity measurements were done for the middle part of the discharge and the outer regions separately.

The spectroscopic results are essentially compiled in Table 1.

Apart from information on the impurity content in the plasma the most important statement from them is the appearence of two distinct electron temperatures. Whereas the higher values of 6 - 1o eV are substantiated by the fact that pronounced ionization of the plasma does occur and that in addition to the Balmer lines C II and O II lines could also be observed in both z-discharges, the lower values of o.1 - o.4 eV agree with the experimental finding that the bremsstrahlung continuum is strongly overcome by H^--continuum and H_2-lines. The spatial resolution undertaken in the intensity measurement contradict the supposition that the two different temperatures belong to different plasma regions. On the other hand the Balmer lines must fade out here in plasma regions where the high temperature value is present for longer than about two microseconds. This actually is indicated by the spectroscopic measurements for the plasma channel.

4. Conclusions

It should be mentioned here that considerably more information is at hand than described before especially from 2.5 mm microwave measurements and from studies on the subsequent theta pinch discharge.

It was found advantageous to split up the problem of breakdown and preionization by using two separate discharges. This way the preionization could be established in a reproducible way even at 1o mTorr filling pressure.

The degree of ionization could not reliably be measured. All estimates based on measurements point toward more than 3o% in the case of 1o mTorr filling pressure.

Still several interesting questions remain open to interprete for instance the explanation of plasma temperature.

As a final remark we recall that the current cannot exceed much more than 15 kA in amplitude and one microsecond in time without creating kink instabilities. We can therefore state that prolonged high axial currents dont help ionization.

+) This work was performed as part of the joint research program of the Institut für Plasmaphysik, Garching and Euratom.

Acknowledgement

The authors are grateful for the assistance in the microwave measurements of Dr. H. Hermansdorfer.

References

1 A.A. Newton, Culham Laboratory Report CLM-R 62

2 L.M. Goldman et al., Phys. Fluids 8, 3 522 (1965)

3 U. Schumacher and R. Wilhelm, Phys. Verhandlungen, Vol. 5 (1966)

4 T.S. Green, A.A. Newton and S.E. Segre, Culham Laboratory Report CLM-P 93

5 U. Schumacher and R. Wilhelm, private communication

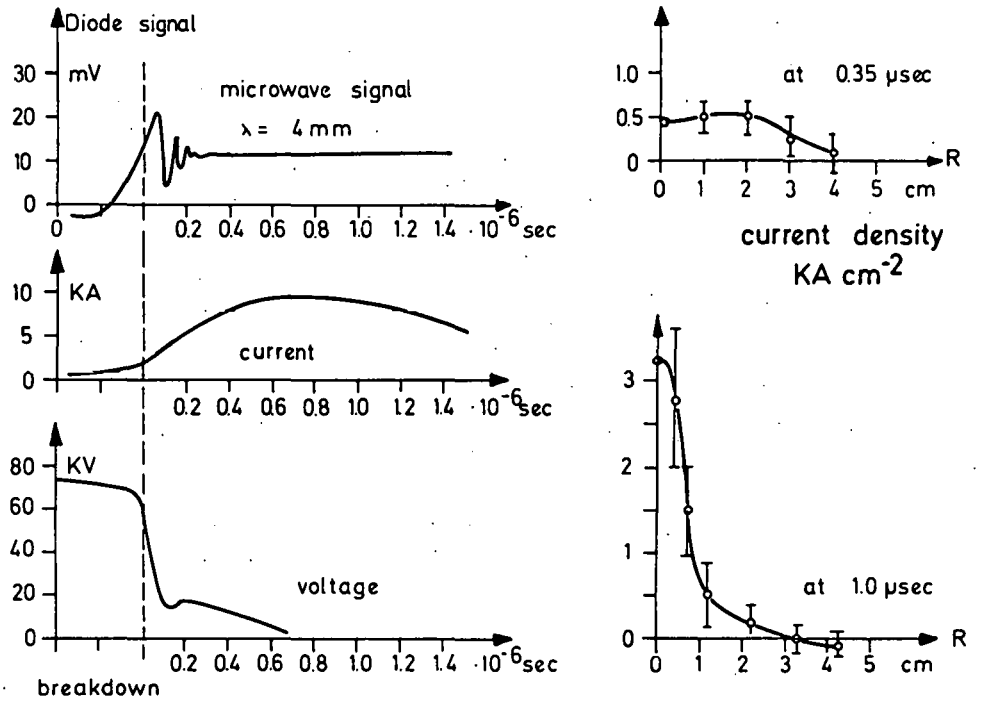

Fig. 1. Breakdown discharge. Current, voltage and microwave transmission versus time. On the right the current density over radius for two times.

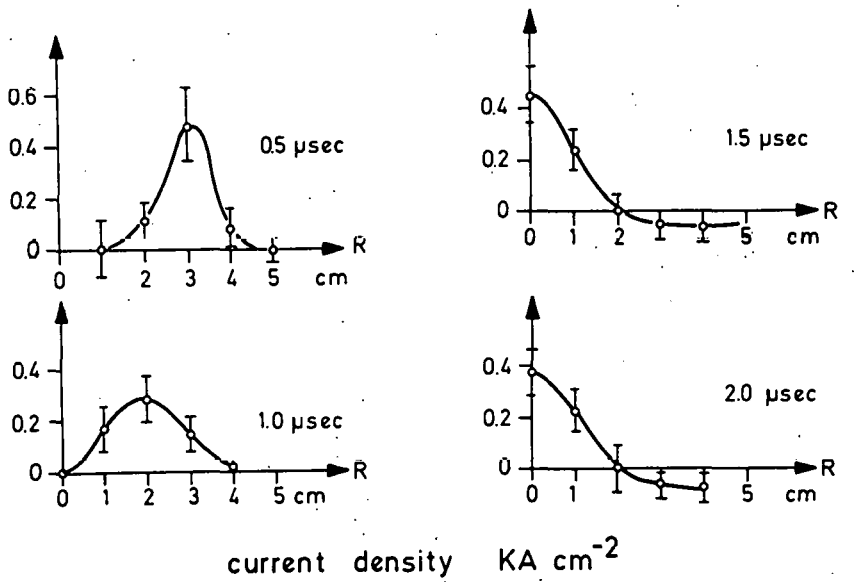

Fig. 2. Preheating discharge. The current density versus radius for four distinct times of the discharge.

Filling Pressure	Discharge	Form Balmer Line Intensitie		Form Halfwidth Time of Balmer Lines	Form Profiles of Balmer Lines		Carbon Impurity	Oxygen Impurity
		kT_e (eV)	N_e (cm^{-3})	kT_e (eV)	v_i (cm/sec)	N_e (cm^{-3})		
10μ	Breakdown Discharge	0.2 – 0.3	$2\text{-}3\times10^{14}$	7 – 10	$\leq 3\text{-}4\times10^{6}$	$\leq 3\times10^{14}$	0.2%	— (0.3%)
10μ	Preheating Discharge	0.2 – 0.3	$2\text{-}4\times10^{14}$	7 – 10	$\leq 4\text{-}5\times10^{6}$	$\leq 4\times10^{14}$	0.5%	— (1.0%)
10μ	Theta-Pinch	0.2 – 0.3	$3\text{-}4\times10^{14}$	10 – 20	$\leq 6\text{-}7\times10^{6}$	$\leq 4\times10^{14}$	2.0%	0.1% (3.0%)
50μ	Breakdown Discharge	0.2 – 0.3	$1\text{-}2\times10^{14}$	6 – 9	$\leq 3\text{-}4\times10^{6}$	$(\leq 5\times10^{14})$		
50μ	Preheating Discharge	0.2 – 0.3	$1\text{-}2\times10^{14}$	7 – 10	$\leq 4\text{-}5\times10^{6}$	$(\leq 6\times10^{14})$		
50μ	Theta-Pinch	0.2 – 0.4	$4\text{-}8\times10^{14}$	10 – 20	$\leq 7\text{-}8\times10^{6}$	$(\leq 2\times10^{15})$	0.02%	0.03% (3.0%)

Table 1. Electron densities and electron temperatures as measured from line intensities and line profiles for the breakdown and preheating discharge.

AN EXPLOSIVE GENERATOR-POWERED θ-PINCH*

by

D. B. Thomson, R. S. Caird, K. J. Ewing, C. M. Fowler and W. B. Garn
Los Alamos Scientific Laboratory, University of California
Los Alamos, New Mexico

and

J. C. Crawford and R. A. Damerow
Sandia Corporation
Albuquerque, New Mexico

ABSTRACT

A recently developed, explosively-driven generator has been used to create neutron-producing plasma in a conventional θ-pinch coil. A spiral-wound, flux-compression device, loaded with 5 lbs. of explosive, was used with an exploding-wire, high-voltage switch to produce a crowbarred current of 2.6 MA in a 15 nH θ-pinch coil. The rise time was 2.5 μsec and the peak rate 3 MA/μsec. This current produced 114 kG in the θ-pinch coil (25.5 cm long x 6.6 cm i.d.). Five plasma shots have been fired, each using a 40 kA linear discharge preionizer, a 1.7 kG reverse field and 85 microns of deuterium in a preconditioned discharge tube. Malfunctions occurred on two shots, and the others produced neutron yields of 2×10^3, 2×10^4 and 5×10^5. The yield rate peaked one μsec before maximum field, with a one μsec half width, suggesting typical short coil losses. The results also show that efficient high-voltage switching is essential to neutron production. Experiments are now in progress to use this switching technique and a 5 MA generator to produce 150 kG in a 35.5 cm long coil with similar plasma initial conditions.

INTRODUCTION

Past attempts to apply explosively-produced magnetic energy to θ-pinch plasma experiments have involved the direct implosion of the θ-pinch coil.[1] In the experiments reported here, an explosively-driven electrical generator[2] was used to provide the energy for a conventional,[3] nonimploding, θ-pinch plasma device.

The report follows in six parts: first, a general description of the particular generator used for these experiments; second, the switching circuit necessary to shape the output pulse of the generator to the θ-pinch requirements; third, a description of the plasma initial conditions and the precautions that were necessary because of the single-shot nature of the experiments; fourth, a summary of the experimental results; fifth, the

conclusions that can be drawn from this exploratory series; and finally, a discussion of experiments that are now in progress.

EXPLOSIVELY-DRIVEN GENERATOR

The energy released by detonation of high explosives can be used to produce short pulses of electromagnetic energy. Of the several types of generators available for accomplishing this task, the helical type[4] was chosen as most appropriate for these experiments. A sketch of this type of generator is shown in Fig. 1.

After an initial current is established (by an external capacitor bank) in the helical winding, the inductance of the generator is forcibly reduced by explosively expanding the armature. A rapidly rising current pulse I(t) is produced which may be described by the following equation:

$$I(t) = \frac{L_o I_o}{L(t)} \exp\left[-\int_o^t \frac{R(t,I)}{L(t)}\, dt\right], \quad (1)$$

where L(t) is the circuit inductance, R(t, I) is the circuit resistance and the zero subscripts refer to values at the beginning of the generator operation. The generator shown in Fig. 1 has a 16 cm nominal diameter, a length of 40 cm, and uses 5 pounds of high explosive to produce a 3 MA current pulse in its normal operating time of 27 μsec. The explosive is detonated simultaneously at both ends; hence, the output terminals are located at the center of the helix.

For inductive loads of 65 nH or less, the generator produces its maximum output current of 3 MA. Joule heating of the helical conductors tends to limit the current to this value. A generator of this type produces an exponentially rising current pulse with current and voltage very nearly in phase. When the current has reached its maximum value, the generator is effectively "crowbarred"; and the current then decays at a rate determined by the L/R time constant of the load.

SWITCHING TECHNIQUE

A switching circuit has been devised that shapes the output current pulse from the explosive generator to produce the high values of dI/dt necessary for a successful θ-pinch. This switch produces dI/dt values of 3×10^{12} amps/sec from the generator which without the switch characteristically has a peak rate of 0.4×10^{12} amps/sec.

An equivalent circuit of the θ-pinch experiment is shown in Fig. 2(a). The operating sequence is as follows: the detonator switch (S_1) is closed, and the capacitor bank discharges through the generator (L_g). At peak capacitor bank current, the explosive crowbar switch (S_2) is closed and the generator begins its operation. Approximately 2.5 μsec before completion of generator operation, the fuse wires burst and produce enough voltage (35 kV) to break down the dielectric (S_3) switch. Current in the exploding fuses then quickly falls to zero (approximately 1 μsec), and all the generator current is then driven through the dielectric switch and the θ-coil (L_θ) with a risetime of 2.5 μsec. This circuit, therefore, makes the explosively-driven power supply compatible with a wide range of plasma experiments.

The sketch in Fig. 2(b) shows geometrically how this circuit was constructed, and Fig. 3 shows a photograph of the actual device on the firing table. The generator was connected to fuse wires through a parallel plate transmission line. The fuse assembly consisted of 26, No. 22 copper wires, each 5 inches long, connected in parallel with a 35 kV mylar breakdown gap. This section was connected to the θ-coil through a second parallel plate transmission line.

GENERATOR DRIVEN θ-PINCH EXPERIMENTS

The Initial Conditions

The utilization of the switched generator current to achieve an intense high temperature

θ-pinch requires initial conditions similar to those used for first half cycle neutron production in laboratory θ-pinch experiments. These conditions are a fully ionized, relatively pure deuterium plasma immersed in a suitable reverse field and discharge tube walls that have been adequately treated or warmed up by electrical discharges prior to application of the principal, fast-rising magnetic field pulse.

For the first five plasma shots reported here, the initial condition plasma was created in a 2 mm wall, 64 mm o.d. Pyrex tube, using a 40 kA linear discharge between two electrodes spaced 60 cm. apart. The coil length was 25.5 cm and the i.d. was 6.6 cm. The linear discharge was obtained from a 7.5 μF capacitor charged to 15 kV, crowbarred to minimize Z-current just prior to θ-pinch action. A separate coil pair, driven by 440 μF at 6 kV, was used to supply reverse field ($\sim$1.7 kG) prior to the preionization. The deuterium pressure ($\sim$85 microns), timing, reverse field strength, coil and tube dimensions, and warm-up procedures were based on earlier work.[1,3,5]

The shot procedure was to install a new Pyrex tube, with electrodes, at the firing point; give the system an overnight vacuum pumpdown (10^{-4} mm Hg); warm-up the tube with about ten θ-pinch shots from an auxiliary fast bank; then attach the explosive generator and fire it together with the preionization and reverse field banks.

Explosively Driven θ-Pinch Shots

A series of five plasma shots was fired with the type of generator described above. Figure 3 shows a typical shot setup at the firing point. Current pickups monitored the switched generator output; and a proton recoil neutron detector, shielded with lead, monitored the time history of the neutron yield. Figure 4 shows plots of B field and yield rate vs. time for the two best shots. Figure 5 summarizes results of all the plasma shots. Neutron yields of 2×10^3, 5×10^5, and 2×10^4 were obtained on shots 1, 2, and 5 respectively. On shot 3, the reverse field header broke down, giving $-B_o = 0$, which is believed sufficient reason for zero neutron yield. On shot 4, the switching malfunctioned, giving a stretched-out and reduced V_θ. This is believed sufficient reason for zero neutron yield.

CONCLUSIONS

These experiments lead to the following general remarks:

(1) The explosively-driven generators described here produce fast-rising high current outputs in standard heavy wall θ-pinch coils of such magnitude (2.6 MA) as to compare favorably with many high energy condenser banks used to drive modern high temperature[3,6,7] θ-pinches.

(2) The exploding wire dielectric switching delivers coil voltages sufficient to produce neutron emitting θ-pinches in the standard pressure regime (80-100 microns, with reverse field).

(3) The neutron yields appear to be sensitive to shot-to-shot variations in the voltage vs. time output of the high current switches.

(4) The short half width of the neutron yield rates shown in Fig. 4 ($\leq$1.2 μsec) is characteristic of the short coil (0.25 meters) and is most likely caused by flute instability or end-loss.

(5) The variation in yield magnitude between shots 2 and 5, Figs. 4 and 5, is similar to variations in "first-shot" yields studied earlier,[1,5] indicating that the low energy warm-up shots may not have been sufficient. It may be necessary to use a fast bank of sufficient energy and V_θ to produce neutrons during the tube conditioning shots, just prior to use of the generator, if the effect of warm-up is to be substantially reduced.

(6) The typical pump-down vacuum used here has been 10^{-4} mm Hg; it appears desirable to improve the vacuum.

EXPERIMENTS NOW IN PROGRESS

An explosively-driven generator, similar to the one described above, is now being used for higher energy experiments. This generator uses 17 pounds of high explosive to produce 6 MA into inductive loads up to 65 nH. The θ-coil for these experiments is 35.5 cm long and 7.2 cm i.d. To date, 4 MA have been successfully switched into the θ-coil with a rise time similar to that shown in Fig. 4.

These results indicate that further development of explosive generators and related θ-pinch experiments may lead to creation of suitably contained,[8] high temperature plasma in substantially stronger magnetic fields (>200 kG) than currently being used with large (megajoule) condenser banks.

ACKNOWLEDGMENT

The authors appreciate the excellent assistance of R. A. Klein of Sandia Laboratory in the assembly of the generators.

REFERENCES

1. "Proceedings of the Conference on Megagauss Magnetic Field Generation by Explosives and Related Experiments," Euratom, Brussels 1966, pp. 1-19, 491-514.
2. Details to be published by Sandia Laboratory at a later date.
3. E. W. Little and W. E. Quinn, Phys. Fluids 6, 875 (1963).
4. A. D. Sakharov, Uspekhi Fizicheskikh nauk 88, no. 4, April 1966, 725-734.
5. "Characteristics of the Scyllacita θ-Pinch," Los Alamos Report (to be published).
6. L. M. Goldman, et. al., Phys. Fluids 8, 522 (1965).
7. A. C. Kolb, et. al., Nuc. Fusion Suppl. Pt. 2, 553 (1962).
8. F. C. Jahoda, et. al., J. Appl. Phys. 35, 2351 (1964).

* **Work performed under the auspices of the U. S. Atomic Energy Commission.**

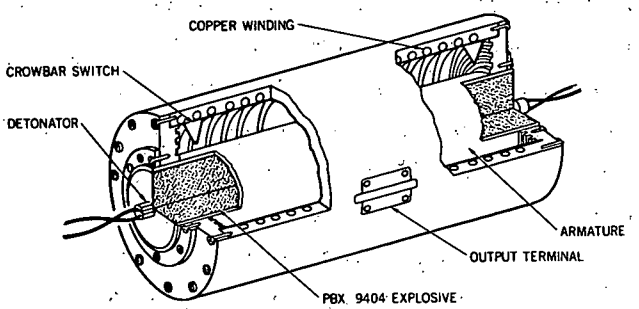

Fig. 1. Sketch of the Sandia Model 106 explosive magnetic generator.

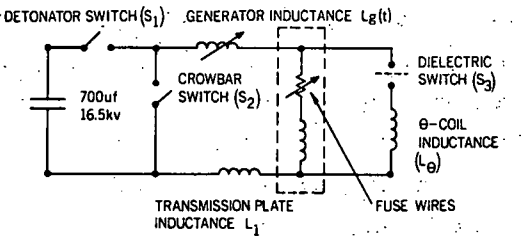

(a) EQUIVALENT CIRCUIT OF THE θ-PINCH EXPERIMENT

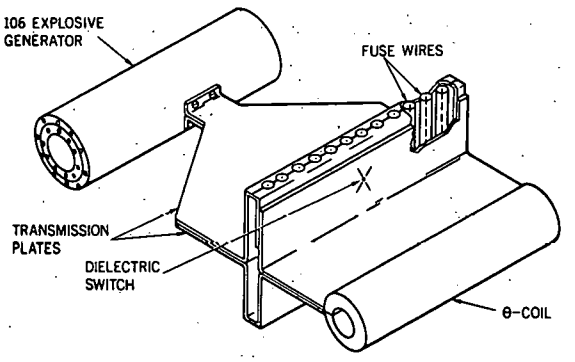

(b) EXPERIMENTAL DEVICE

Fig. 2. (a) Sketch of the equivalent circuit of the condenser bank, explosive generator, exploding wire switch, and θ-pinch load. (b) Sketch of the geometrical arrangement of the generator, switch, and θ coil.

(a)

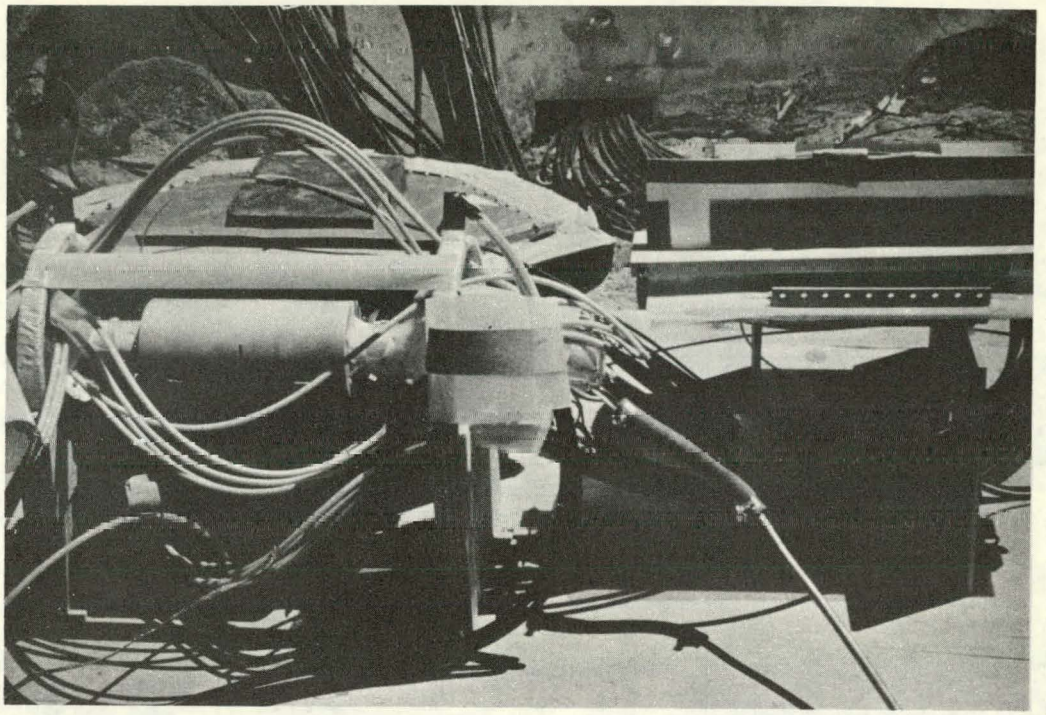

(b)

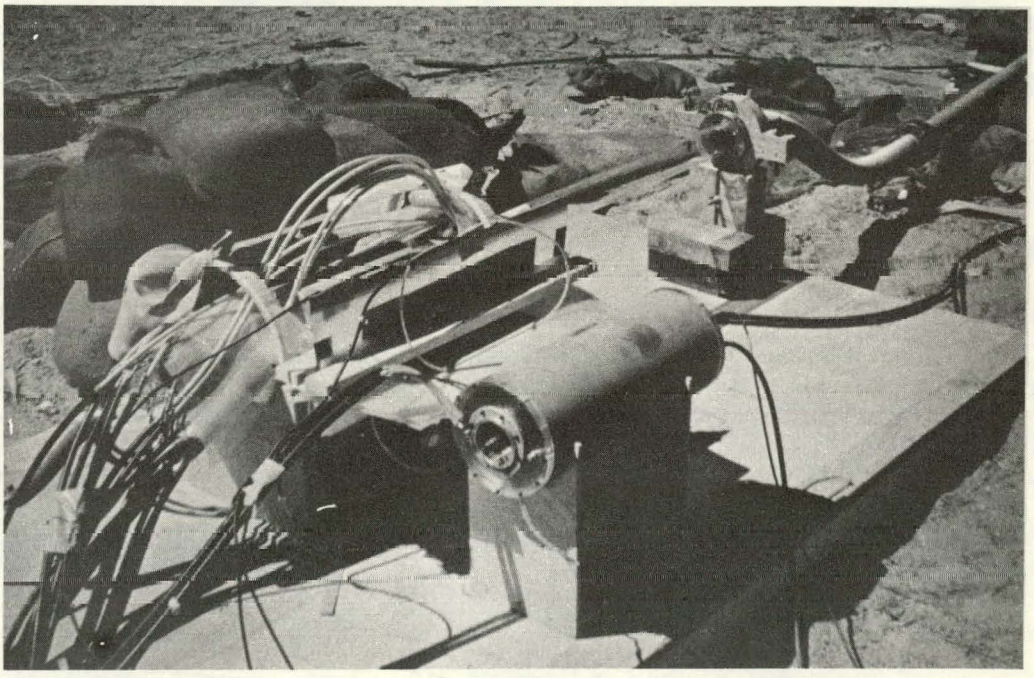

Fig. 3. Photographs of the complete experiment at the firing point. The top picture (a) shows the θ-pinch coil connected to the auxiliary fast bank, during warm-up, complete with discharge tube, preionization electrodes, and reverse field coils. The generator is in a ready position on the right. The bottom picture (b) shows the generator connected to the θ coil and ready to fire explosively.

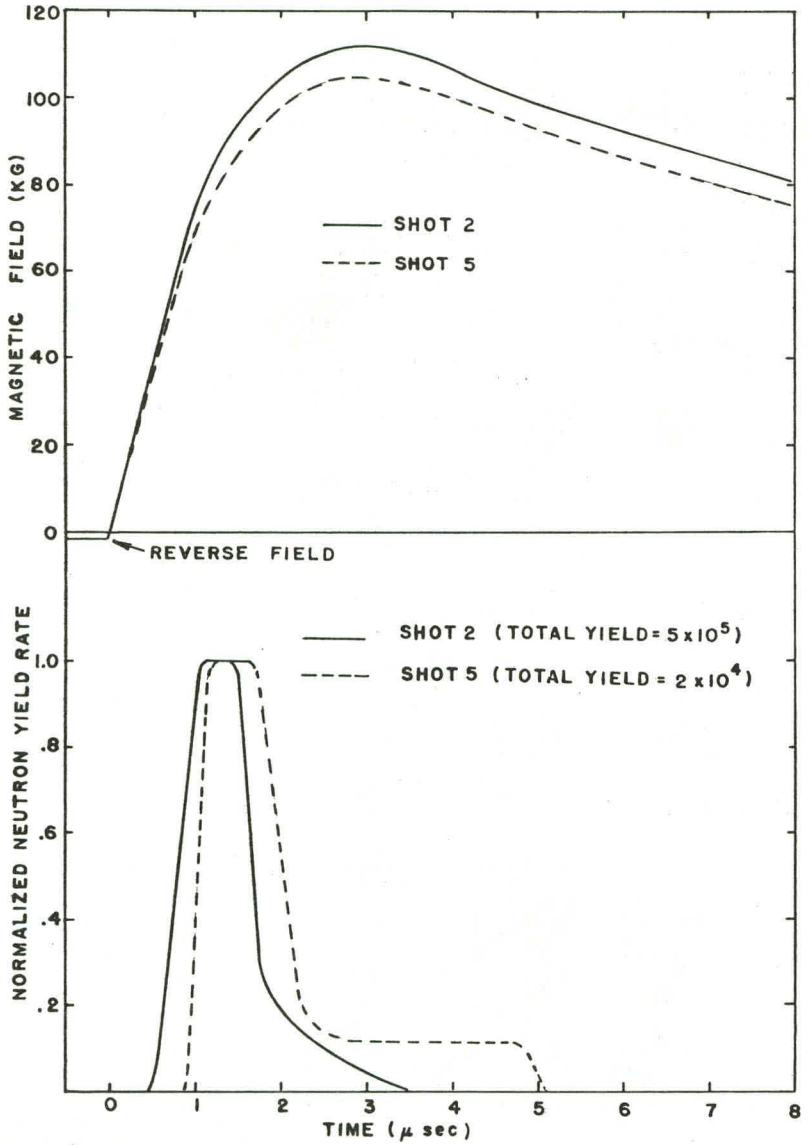

Fig. 4. Curves showing magnetic field vs. time and normalized neutron yield rate vs. time for the two best shots of the series.

NO. $\frac{dB}{dt}\left(\frac{kG}{\mu sec}\right)$ vs t(μsec)	PEAK FIELD (kG)	REVERSE FIELD (kG)	RISE TIME (μsec)	NEUTRON YIELD
1. 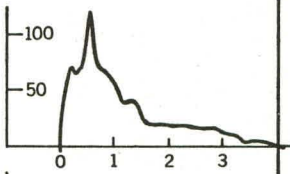	128	−1.7	2.1	2×10^3
2. 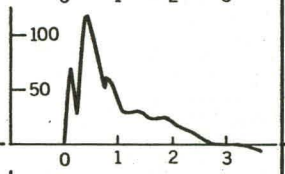	114	−1.7	1.6	5×10^5
3. 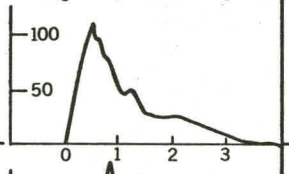	106	0	1.8	0
4. 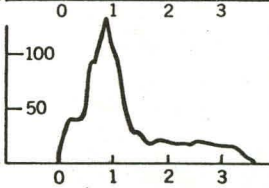	121	−1.7	2.7	0
5. 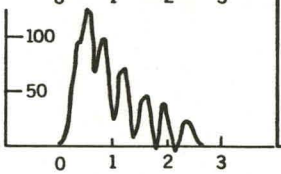	106	−1.7	1.6	2×10^4

SHOT SUMMARY

Fig. 5. Table summarizing results of the plasma shot series. Note: The rise times (4th column) are measured from 0 to 90% of B-field peak.

THEORY OF INERTIAL CONFINEMENT OF DENSE PLASMAS

by

J.G. Linhart, Ch. Maisonnier, J.P. Somon
Laboratori Gas Ionizzati (EURATOM-CNEN),
Frascati, Rome, Italy

ABSTRACT

Cylindrical devices in which a central medium (such as a magnetic field or a deuterium plasma) is compressed by means of a collapsing liner, are considered. The liner is supposed to be either a metallic shell, accelerated by explosives, or a polytropic plasma shell, accelerated by magnetic pressure. The results of several studies on the dynamics of the motion are presented. They give in particular the efficiencies of the energy transfers from the external source to the liner and from the liner to the central medium the confinement time, and the maximum energy density attainable in the compression. A more detailed analysis will soon be published.

1) J.P. Somon, Euratom Symposium on Theoretical Plasma Physics, Euratom 15, 1244 e, f (1966).
2) Ch. Maisonnier, M. Haegi, J.G. Linhart, Conf. on Plasma Physics and Controlled Nuclear Fusion Research, Culham 1965, 2, 345.
3) Proc. of the Conference on Megagauss Magnetic Field Generation by Explosives and Related Experiments, EUR 2750 e, Brussels (1966).

INTRODUCTION

The various devices which can produce plasmas of thermonuclear interest can be divided, for our purpose, into two classes:

- the "static" systems in which the structures producing the confining magnetic field are not destroyed after each shot, which limits the intensity of the field at the coil to less than 1/2 Megagauss.
- the "dynamic" systems in which the plasma density is so high that the plasma pressure cannot be balanced statically by magnetic and mechanical forces, so that the confinement time will be dictated mostly by inertia considerations.

As far as dynamic systems are concerned, it seems that a coherent analysis of the physical processes involved in the rapid transmission of large quantities of energy to a dense plasma has never been published. Our theoretical group in Frascati has been working on such problems for several years[1] and we will present very briefly a few of the results so far obtained, which will be published soon in more detail.

In the past, several methods to produce dynamically hot and dense plasmas have been studied. Interest in mechanisms such as ordinary dynamic z-pinches or converging

shock-waves has decreased; on the other hand the compression of plasma by a liner having a very high kinetic energy density seems more promising (fig.1), because in this case the life-time τ of the hot plasma in the state of maximum compression is increased due to the inertia of the heavy liner. We will define a confinement factor $\chi = \frac{\tau}{\tau_0}$ where τ_0 would be the life-time of the hot core if it were unconfined.

To this family of systems belong the plasma focus machines 2,4,5,6 and the compression of dense plasmas by liners driven by explosives [3]. The model that we have used is shown in fig.2: the liner and the central plasma are initially separated by vacuum or by a magnetic field; an energy source (condenser bank or explosives) is then used to accelerate the liner which later collapses on the central core; during this collapse, the kinetic energy of the liner will be transformed partly in internal energy of the liner, partly in magnetic energy (if there is a trapped magnetic field) and partly in thermal energy of the core.

For the two different cases of plasma liners accelerated by magnetic pressure and of metallic liners accelerated by explosives, we have studied the behaviour of the following quantities:

- the efficiencies η and ε
- the confinement factor χ
- the radius r_m of the compressed hot plasma
- the maximum energy density transmissible to the central plasma

which enter directly in the discussion of any property of this class of devices. As an example, fig.3 gives the minimum energy per unit length required in a fusion reactor working along these principles [2].

EVALUATION OF THE EFFICIENCY η

Plasma liners accelerated by magnetic pressure [7]

Numerical calculations have shown that in the case of a cylindrical liner coupled to a condenser bank, the efficiency could reach 100% if the liner were infinitely thin and conducting and if its mass and initial radius were properly matched to the characteristics of the condenser bank. When finite conductivity and thickness are taken into account, one shows that the optimum value of η can reach 70% in typical cases.

Moreover, it has been shown that, even if one starts with a thin solid liner, complete vaporisation will occur in all cases of interest before maximum compression, due to Joule heating.

Metallic liners driven by explosives [8]

Initially, an explosive shell (radii R_2, R_3) is placed around the liner (radii R_1, R_2) and the detonation is initiated on the outer boundary of the explosive (fig.4).

The liner acceleration has been studied using a plane approximation for the explosive products (valid when $R_3/R_2 < 3$), by a numerical treatment of the hydrodynamical equations. The results show that, in practice, the main part of the liner's kinetic energy is acquired very quickly, in a time small compared to the collapse time.

The efficiency η of the acceleration is given in fig.5 as a function of the geometrical ratio of the radii, for a copper li

ner accelerated by a composition B explosive. The curves have a closed shape which allows an optimisation of the parameters.

It may be concluded that liner velocities of the order of the detonation velocity and efficiencies η of the order of 5% to 20% can usually be reached.

DECELERATION OF THE LINER AND DISCUSSION OF $\mathcal{E}$, r_m, χ AND CENTRAL ENERGY DENSITY

Several studies have been made on the dynamics of a cylindrical liner which is not submitted to an outside pressure and collapses on a polytropic and adiabatic medium of various polytropic coefficients γ (for instance $\gamma = 2$, corresponds to a B_z magnetic field trapped within a liner of finite electrical conductivity)[3,9,10].

The internal medium is compressed by the liner until a maximum internal pressure is reached for a turn around radius r_m of the inner liner boundary. Successively the liner starts a diverging motion.

The liner is supposed to behave as a compressible perfect fluid and its motion is analyzed by means of some models or by solving numerically the equations of hydrodynamics. Under the assumption of a high compression ratio, one gets the following properties:

- during a long phase of the motion the internal pressure is negligible and the velocity of the inner liner boundary remains quite constant;
- then comes a very fast deceleration phase which is followed by a confinement phase of characteristic time t_c;
- if the liner thickness D is smaller than a certain critical thickness D_c, the internal and kinetic energies of the liner at the maximum compression are negligible compared to the initial kinetic energy. The efficiency $\mathcal{E}$ of the energy transfer from the liner to the compressed medium is then equal to unity and the energy conservation equation gives simply the maximum pressure;
- if the liner thickness D is greater than the critical thickness, the energy, kinetic or internal, which remains whitin the liner at the maximum compression is no more negligible and $\mathcal{E} < 1$.

To proceed further, the two different cases of plasma liners and of solid liners will have to be considered.

Plasma liner[10]

The liner is generally a heavy gas of high Z which is ionized continually and radiates under the influence of the compression. It is considered as a polytropic gas in which the polytropic coefficient γ can be adjusted in order to take approximately radiation into account (extra degrees of freedom, small $\gamma - 1$).

Due to the high Mach number (ratio of the initial velocity of the liner to the sound velocity in the liner) a "shock model" is valid. Some results of the dynamics are illustrated in fig.6 for an infinitely thick cylindrical liner. The motion of the liner surface is insensible to the value of γ until it is seriously decelerated. This happens for a pressure $p^* \simeq \rho_0 v_0^2 (R_1/r_1)$. On the other hand, the asymptotic pressure P_∞, as obtained by a self-similar solution, depends strongly on γ when $\gamma - 1$ is small, and different trajectory configurations are possible.

The pressure p^* is the maximum pressure practically obtainable, and it is reached for liners whose thickness is greater than the critical thickness D_c.

Under some unimportant simplifying assumptions, the results can be summarized as shown in fig.7.

In particular the variations of ε and χ in function of the liner thickness are shown in fig.8.

Solid liners[3]

At high pressure, metals behave as perfect fluids, whose equation of state is available from experimental data. The initial liner thickness is small and the liner velocities are of the same order as the sound velocities in metals.

The Mach number is small and shock models cannot be used as for plasma liners for which $M \gg 1$. As a consequence, the behaviour of thick solid liners will be different from the behaviour of thick plasma liners.

The main results are given in figs. 9 and 10. The factor of confinement χ is not given by any simple formula and has to be read in each case on the families of curves shown in fig.10.

CONCLUSION

To sum up very briefly, the main results are the following:

a) the efficiency η of liner acceleration can be practically up to about 70% if the energy source is a condenser bank, and up to 20% if it is an explosive.

b) the maximum energy density which can be efficiently communicated to the central core is of the order of the maximum kinetic energy density of the liner, for solid liners. For plasma liners, it is higher by the convergence ratio $\frac{R_1}{r_1}$.

c) the efficiency ε with which energy goes from liner to central core can be 100% if the liner is thin. It is much less for thick liners, whereas the coefficient of confinement χ varies in the opposite direction. At the critical thickness, $\chi\varepsilon$ reaches in all cases a maximum value which is

$$\chi\varepsilon = \frac{v}{V_0}$$

where v is the sound velocity in the compressed central plasma and V_0 is the maximum velocity of the liner.

There is no space here to apply these results to specific cases. Just to mention an example, a "dynamic" fusion reactor would need a liner whose initial parameters would have to satisfy the following relation:

$$\rho_0 V_0 R_1 > 10^7 \qquad \text{C.G.S.}$$

and a D.T. plasma core with an initial density $n_p(0)$ such that

$$n_p(0) > 10^{14} \frac{V_0 r_m}{R_1^2} \qquad \text{C.G.S.}$$

For the energy to be minimum, the liner would have to have the "critical thickness" defined before.

REMARKS

The effective coefficient of confinement will be smaller than the one just calculated from purely dynamic considerations if there are mechanisms by which the central core can loose an appreciable amount of energy, or particles, during the calculated life-time. Here we will just mention some loss mechanisms which could be important:

a) radial loss by particle diffusion and by thermal conductivity: a trapped magnetic

field, not high enough to insure the balance of pressure, but sufficient to reduce the thermal conductivity (cold blanket confinement) is required.

b) axial losses: the system should either be longer than

$$\chi . r_m$$

or some kind of axial confinement has to be provided (spherical collapse).

c) radiation losses: the problem of radiation in the field of very dense and sometimes impure plasmas (liner) is of paramount importance but it is also very complicated and up to now we have done very little about it.

d) Rayleigh-Taylor instabilities: they are dangerous in the acceleration as well as in the deceleration periods. The problem is complicated for thick liners (who have two boundaries) above all if they are compressible. A linear calculation shows that for uncompressible liners, large perturbations should appear only in the diverging phase of the motion. A more careful study has been undertaken in which the liner compressibility is taken into account and the fluid equations are numerically solved with a bidimentional (r, ϑ) program.

REFERENCES

4) J.W. Mather, P.J. Bottoms, A.H. Williams, This conference.

5) C. Patou, A. Simonnet, J.P. Watteau, This conference.

6) N.V. Filippov, Nucl.Fusion Suppl., part 2, 577 (1962)

7) G. Lehner, J.G. Linhart, Ch. Maisonnier, Report CNEN RTI/FI(64)2.

8) J.P. Somon, Report LGI 63/18.

9) G. Lehner, J.G. Linhart, J.P. Somon, Nucl.Fusion 4, 362 (1964).

10) J.P. Somon, Report LGI 66/11.

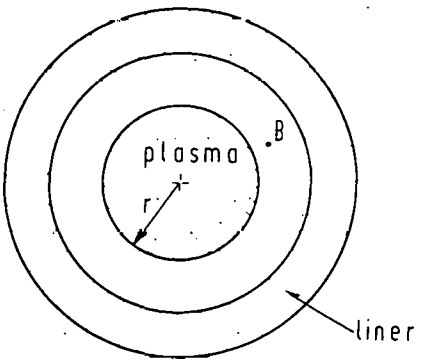

- Fig. 1 -

Compression of a plasma core by a collapsing liner.

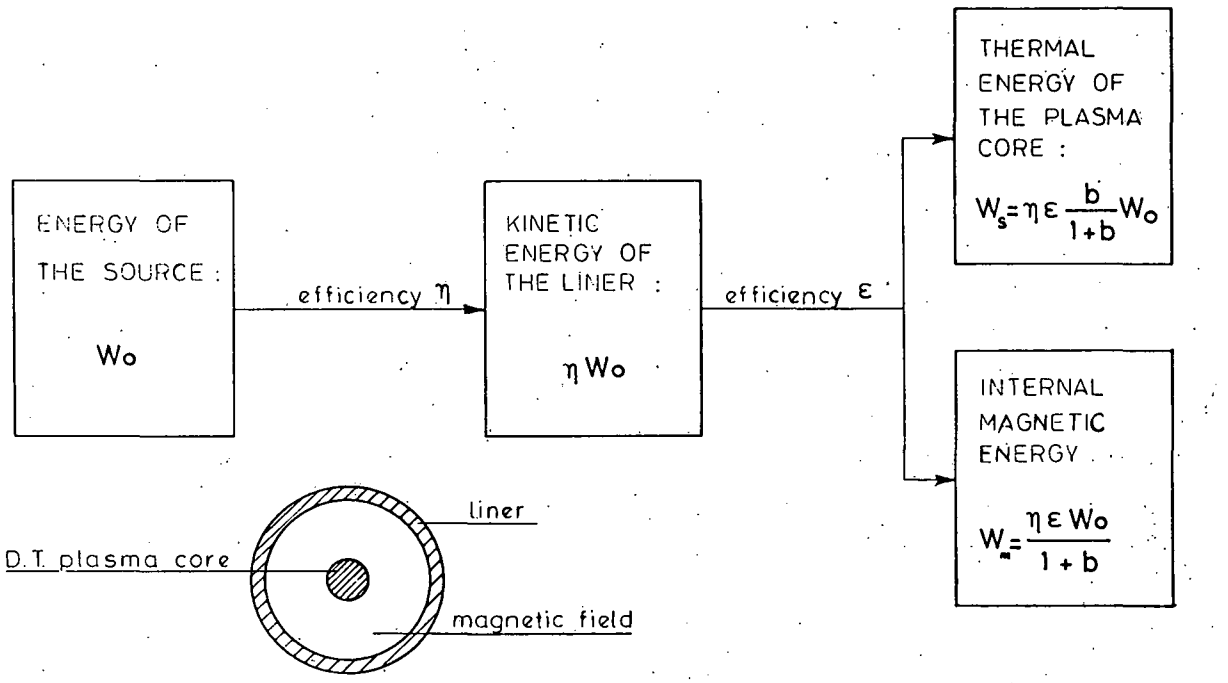

Fig 2 - Inertially confined pinch device (by definition $b = \frac{W_s}{W_m}$)

$$W_o \simeq 10^2 \left(\frac{1+b}{b} \right)^2 \cdot \frac{r}{\chi \varepsilon_o^2} \quad \text{M Joule/cm}$$

where :

r : radius of the hot plasma

ε_o : efficiency of the transfer of energy from the source to the hot plasma ; $\varepsilon_o = \eta \varepsilon$

b : $\frac{W_s}{W_m}$

χ : confinement factor

- Fig. 3 -

Minimum energy per unit length of a pulsed reactor

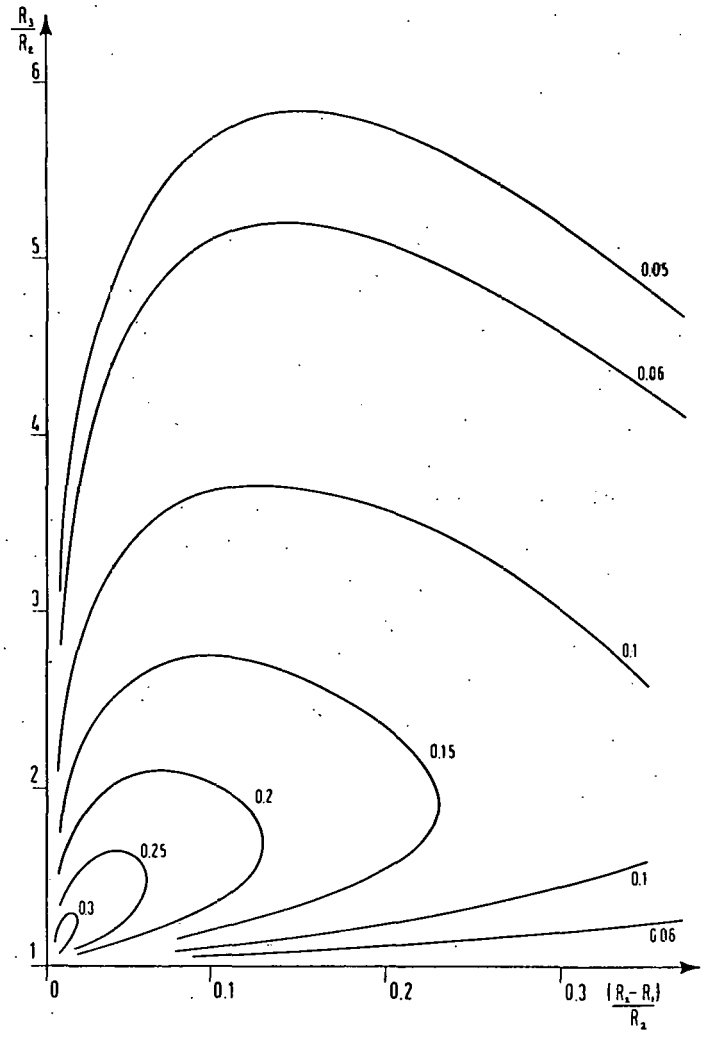

Fraction η of the chemical explosive energy transmitted to a cylindrical rigid liner

– Fig. 5 –

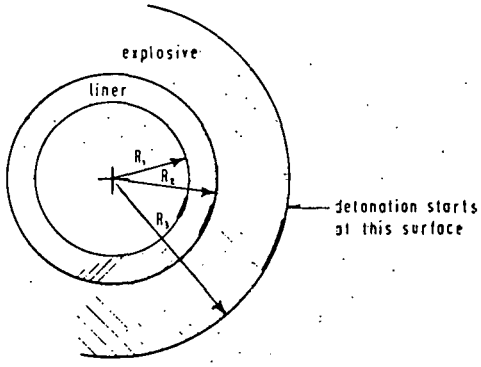

– Fig. 4 –

Initial configuration for the acceleration of a cylindrical liner

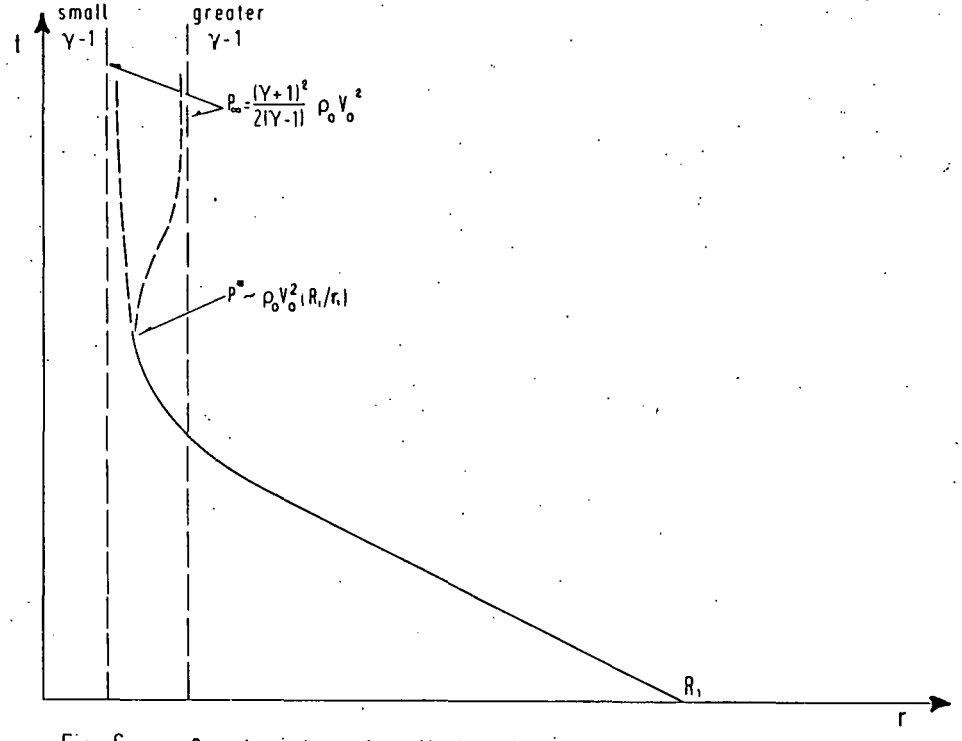

Fig. 6 – Deceleration of cylindrical plasma liners

		Thin liners $D \leq D_c$	Thick liners $D \geq D_c$
Reduced maximum pressure	$\frac{P_m}{\rho_o v_o^2}$	$\frac{1}{D_c}\left(\frac{D}{D_c}\right)^2$	$\frac{1}{D_c}$
Reduced minimum radius	$\bar{r}_m = \frac{r_m}{R_o}$	$D_c\left(\frac{D_c}{D}\right)^{1/2}$	D_c
Reduced confinement time	$\bar{t}_c = \frac{v_o t_c}{R_o}$	$\bar{r}_m$	D
Efficiency of the compression	ε	1	$\frac{D_c}{D}$
Confinement factor	X	$\mu^{1/2}$	$\mu^{1/2}\left(\frac{\mu}{\mu_c}\right)^{1/2}$

R_o = initial liner radius

ρ_o = initial liner thickness

v_o = initial liner velocity

P_o = initial plasma pressure

$D = \frac{d}{R_o}$ = initial reduced liner thickness

$D_c = \left(\frac{P_o}{\rho_o v_o^2}\right)^{1/3}$ = critical reduced liner thickness (for $\gamma_{plasma} = 2$)

$\mu = \frac{\text{liner mass}}{\text{plasma mass}}$

Fig. 7 - Cylindrical compression of an adiabatic plasma by a plasma liner

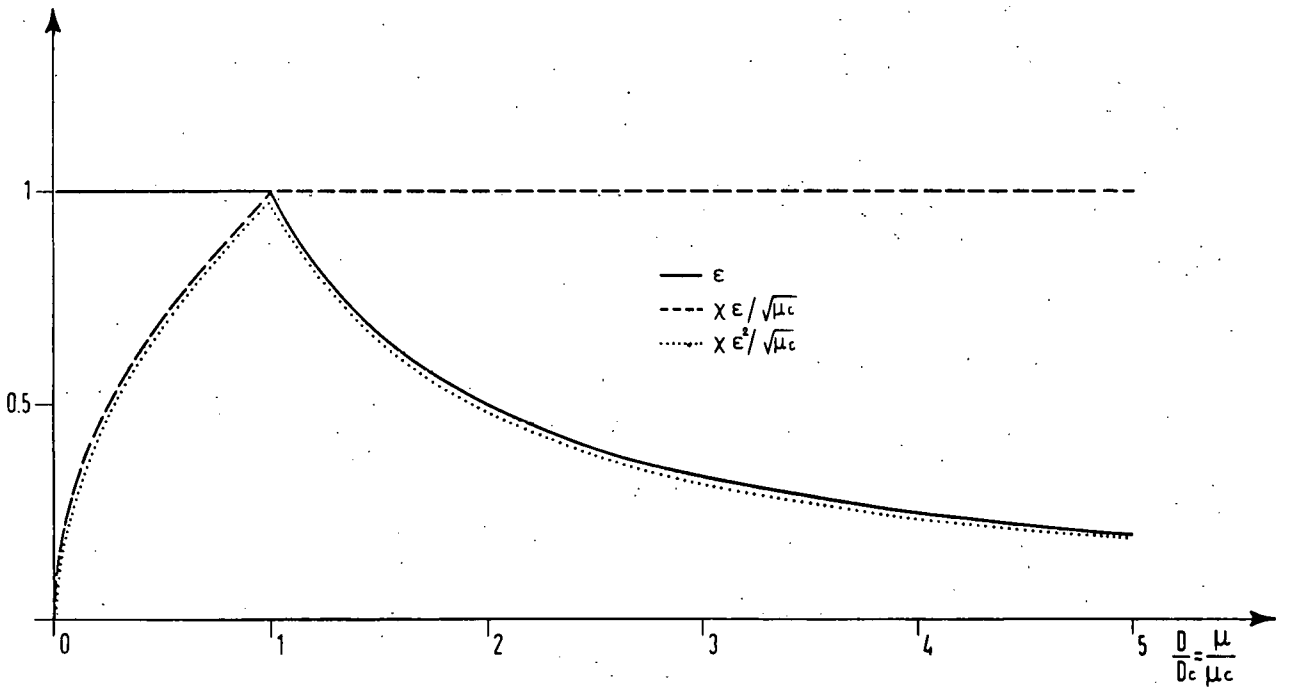

Various parameters for a plasma liner deceleration - ε = efficiency ; X = confinement factor

- Fig. 8 -

		Thin liners $D \leq D_c$	Thick liners $D \geq D_c$
Reduced maximum pressure	$\frac{P_m}{P_M}$	$\left(\frac{D}{D_c}\right)^2$	$\left(\frac{D}{D_c}\right)^{2/3}$
Efficiency of the compression	ε	1	$\left(\frac{D_c}{D}\right)^{2/3}$

ρ_o = initial liner density — P_o = initial plasma pressure

v_o = initial liner velocity — C_o = initial liner sound velocity

$D = \frac{d}{R_o}$ = initial liner reduced thickness — $M = \frac{v_o}{C_o}$ = Mach number

$D_c = \left(\frac{P_o}{\rho_o v_o^2}\right)^{1/2} \left(1.5 + \frac{1}{M}\right)^{1/2}$ = critical thickness

$P_m = \rho_o v_o^2 \left(1.5 + \frac{1}{M}\right)$ = maximum achievable pressure in plane geometry

- Fig. 9 -

Cylindrical compression of an adiabatic plasma by a metallic liner

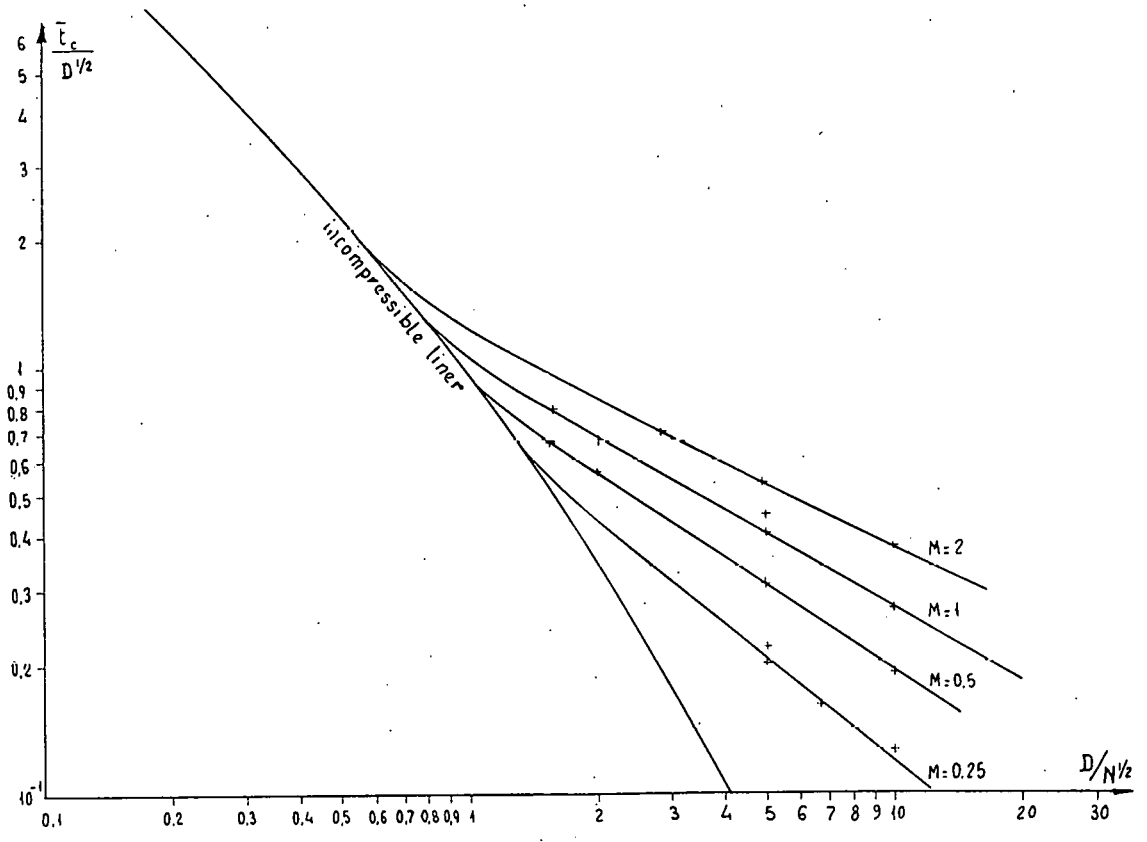

- Fig. 10 -

Cylindrical compression of an adiabatic plasma by a metallic liner : confinement time as a function of the liner thickness.

PULSED, HIGH DENSITY ELECTRON-HOLE PLASMAS IN THE LINEAR PINCH

Wen Shuh Chen and Betsy Ancker-Johnson
Boeing Scientific Research Laboratories and University of Washington*

ABSTRACT

A new diagnostic instrument has been built which makes possible determining the density distribution of nonequilibrium plasma within the bulk of indium antimonide to a high degree of temporal and spatial resolution. The diagnostic tool consists of a N_2-CO_2 CW laser, a Cu-doped germanium detector, and associated electronic apparatus. The absorption of the infrared by the plasma is proportional to the plasma density, since the wavelength of the radiation, 10.6 μ, falls between the absorption edge in InSb, ∿6 μ, and its lattice absorption cutoff, ∿18 μ. The small spatial resolution is achieved by making the diameter of the probing infrared beam very small (dia. ≤ 0.15 mm). The good temporal resolution (tens of nanoseconds) is possible both because the detector has a fast response and because sampling techniques may be used since conditions in the plasma are highly reproduced from pulse to pulse. Measurements show the build-up of the pinch from an essentially uniform density distribution at early times to a highly peaked distribution at later times, while the applied power is held constant. The smallest pinch radii at the modest power levels so far employed are 0.05 mm, which corresponds to plasma density of ∿3 x 10^{16} cm^{-3}.

I. Introduction

Measuring the electron-hole plasma density distribution within a semiconductor is more difficult than determining the distribution in a gaseous plasma, since one cannot place a probe inside a piece of solid. Two experiments have been performed to determine the plasma distribution during pinching in n-InSb.[1] Osipov and Khvoshchev[2] in Russia have measured the electron-hole recombination radiation in the wavelength range of 4-6 μ to determine the size of the pinch channel during very strong pinching. Toda[3] in Japan has scanned a sample at 220° K undergoing pinch with a microwave probe and measured the reflected signal which is related to the impedance of the contact between the probe and the sample and, thus, deduced the plasma distribution. There are several disadvantages inherent in both methods:

(1) They lack time resolution. The measurements represent some undetermined average over the pulse length.

(2) Neither method is capable of sufficient spatial resolution to measure the pinch channel.

(3) Measurements of the recombination radiation from a pinch channel are hindered by the absorption of the signal by the surrounding crystal. Applying a magnetic field to push the plasma near the surface, as the Russians did, introduces complexities. Furthermore, this method can only be used to detect high density plasmas such as very strongly pinched plasmas, since at lower densities the recombination radiation is too weak to be detected.

II. Description of the Plasma Density Probe

A new diagnostic tool to determine the spatial and temporal distribution of nonequilibrium electron-hole plasmas has been made utilizing a N_2-CO_2 CW laser and a Cu-doped Ge infrared detector. The absorption of such infrared radiation by a plasma in InSb is proportional to the plasma density since the wavelength of the radiation (10.6 μ) falls

* Research on plasmas in semiconductors at the University of Washington, Department of Electrical Engineering, is partially supported by The National Science Foundation.

between the absorption edge of InSb (6 μ) and its lattice absorption cutoff (∿18 μ).[4]

Figure 1 shows the experimental arrangement of the infrared density probe. The laser beam goes through the Irtran II window (1 mm thick, transmittance 70%) into a vacuum chamber. High spatial resolution is achieved by the small pinhole mask (0.15 mm currently, but it can be made smaller) in front of the sample. The intensity of the laser is very weak so that the plasma is not affected by it. The sample is attached to a moveable cold finger at ∿77° K. Its position relative to the pinhole is accurately adjusted by a micrometer. Hence, the infrared beam can be scanned across the sample. The plasma is injected from the cathode by a pulsed power supply. The pulse duration is approximately 1.5 μsec and the repetition rate is low, 30 Hz, to avoid heating the sample. The fast-response Cu-doped Ge detector is mounted on a cold finger in contact with liquid He. The detector signal is amplified and sampled. Noise from the laser, detector, and amplifiers, causes the signal-to-noise ratio at this point in the circuit to be very adverse. An automated integrator coupled to the sampling oscilloscope (integration time about 15 sec) averages out the noise so that it is negligible. The signals are then recorded on an x-y recorder. The time resolution is achieved by the fast response detector and the sampling technique. The limit of the time resolution has also not been determined, but it is at least in the tens of nsec range. Thus sequential measurements closely spaced in time are easily made.

Figure 2 shows the absorption of the infrared beam as a function of total current (total current = plasma current + ohmic current) while an injected and subsequently pinched plasma is produced in a p-InSb sample with an initial carrier density of 1.4×10^{14} cm^{-3} and resistivity of 5.4 Ωcm at 77° K. With the time of observation held fixed at 1.3 μsec after the applied power is turned on and with the laser beam passing through the center of a plasma slab, the infrared absorption and, hence, the plasma density is seen to increase mildly and then steeply as the applied power is increased. The solid line in Fig. 2 is the current-field strength characteristic taken at the same time. A comparison of these two curves shows that absorption starts to be detectable coincident with the injection of plasma. When the total current exceeds 3 A pinching begins and the absorption is much more pronounced, as expected, since the plasma density in the path of the laser is increasing steeply with small increases in current.

III. Results

Figure 3 shows some results as the laser beam is scanned across the plasma slab three times with the current held constant at three different magnitudes which are large enough to cause pinching. The shape of the (inserted) plasma conduction characteristic in the range of these current magnitudes indicates that weak pinching is occurring. The absorption curves exhibit marked peaking. With increasing current level (note that the 4.2 A absorption curve was detected with twice the sensitivity used to obtain the other two) the absorption and, therefore, the density strongly increases in the peak. The size of the pinch channel at the highest current in this series is 0.117 mm in diameter, which corresponds to a plasma density of $\sim 3 \times 10^{16}$ cm^{-3}.

Figure 4 shows a series of absorption curves with all parameters held constant except the time of observation during the pinching process. The inset is an oscillogram of the current through the sample and the voltage drop across it with the observation times indicated. These current levels correspond to weak pinching. The top absorption curve corresponds to the plasma density distribution 0.6 μsec after the pulse is turned on. The plasma has not yet pinched. As time progresses the pinch channel is gradually formed. The well formed pinch measured at 1.4 μsec has a diameter of 0.125 mm.

These preliminary results reveal several interesting aspects of pinching in electron-hole plasmas which require further investigation. For example, the location of the peak of the plasma distribution shifts as the self-magnetic field increases, Fig. 3, and as the time of observation progresses, Fig. 4.

Also, the pinch channel is not located symmetrically in the slab-shaped sample, Fig. 4, whereas it is in the square cross-section one, Fig. 3. Furthermore, the meaning of the apparent negative absorption on either side of the large absorption peaks in both sets of data is not yet understood.

IV. Summary

The unique features of this electron-hole plasma density probe are:

(1) It has definite, small spatial resolution which can be determined.

(2) It has a definite, very fast time resolution so that sequential measurements are easily possible.

(3) Only nonequilibrium plasma is detected because of the modulation by the pulsed power supply, thus the surrounding crystal and the thermal equilibrium carriers have no effect.

(4) It is sensitive enough to study electron-hole plasma even when not in the pinched state, hence it has a very wide range of application.

The first results on the plasma distribution in the linear pinch show that the pinch channel, even for modest pinching currents (4 to 6 A), is smaller than the currently used resolution. The measured radii are 0.05 mm, half the previous estimates.

V. Acknowledgment

It is a pleasure to thank R. W. Boice and R. M. Lantz for invaluable help in making this instrument.

References

1. B. Ancker-Johnson, "Plasmas in Semiconductors and Semimetals," *Semiconductors and Semimetals, Vol. 1*, ed. R. C. Willardson and A. C. Beer, New York, Academic Press (1966) pp. 379-481
2. B. D. Osipov and A. N. Khvoshchev, Zh. Eksperim. i Teor. Fiz. 43, 1179 (1962) [English transl: Soviet Phys. JETP 16, 833 (1963)].
3. M. Toda, Japan, J. Appl. Phys. 2, 467 (1963).
4. S. J. Fray, F. A. Johnson and R. H. Jones, Proc. Phys. Soc., (London) 76, 939 (1960).

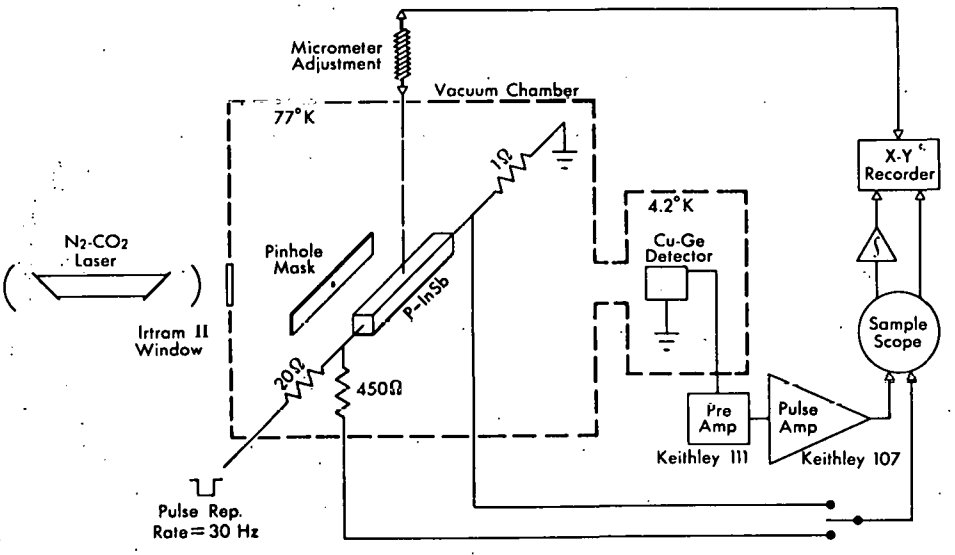

Fig. 1. Block diagram of the experimental arrangement.

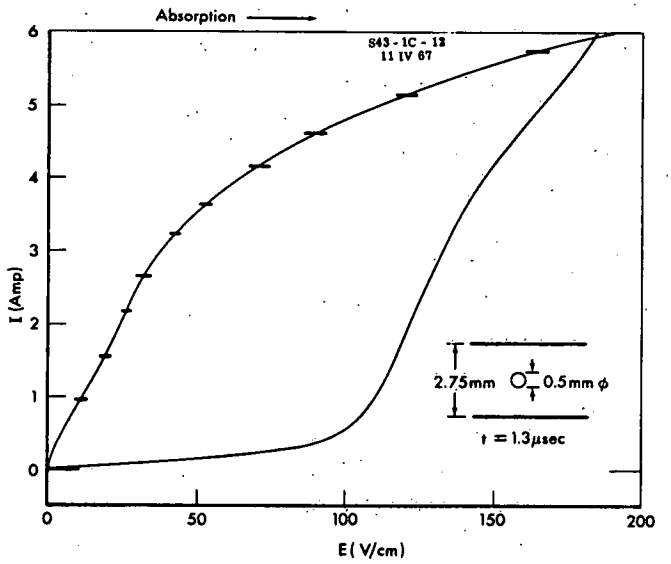

Fig. 2. Absorption as a function of sample current (dashed lines) along with the current-electric field strength characteristic (solid line). The sample dimensions are 10 x 2.75 x 0.61 mm^3.

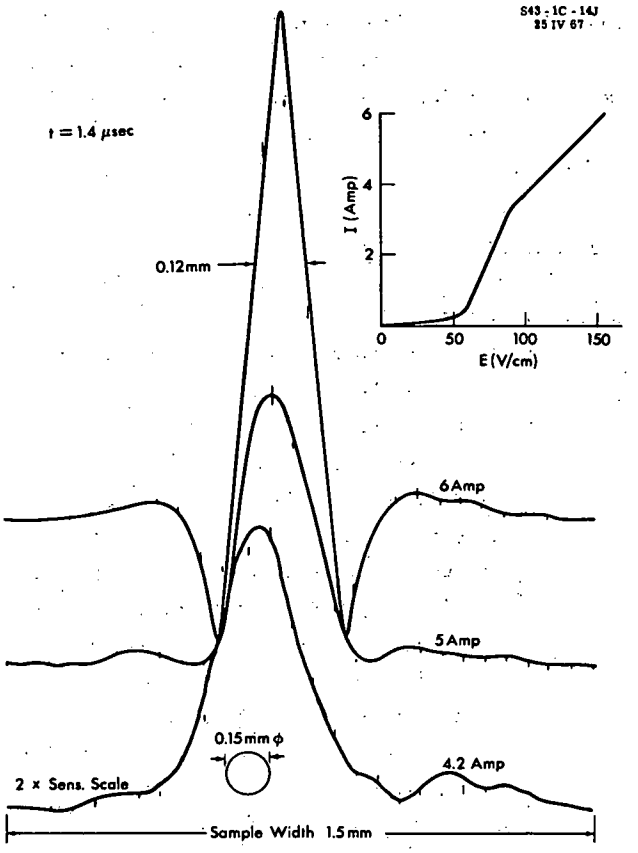

Fig. 3. Distributions of pinched plasmas at different current levels producing weak pinching. The inset shows the corresponding current-field strength characteristic. The sample dimensions are 9.6 x 1.5 x 0.71 mm^3.

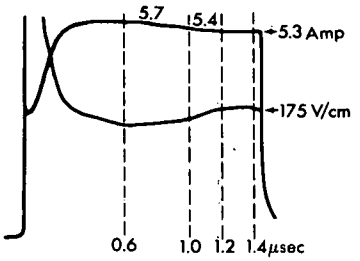

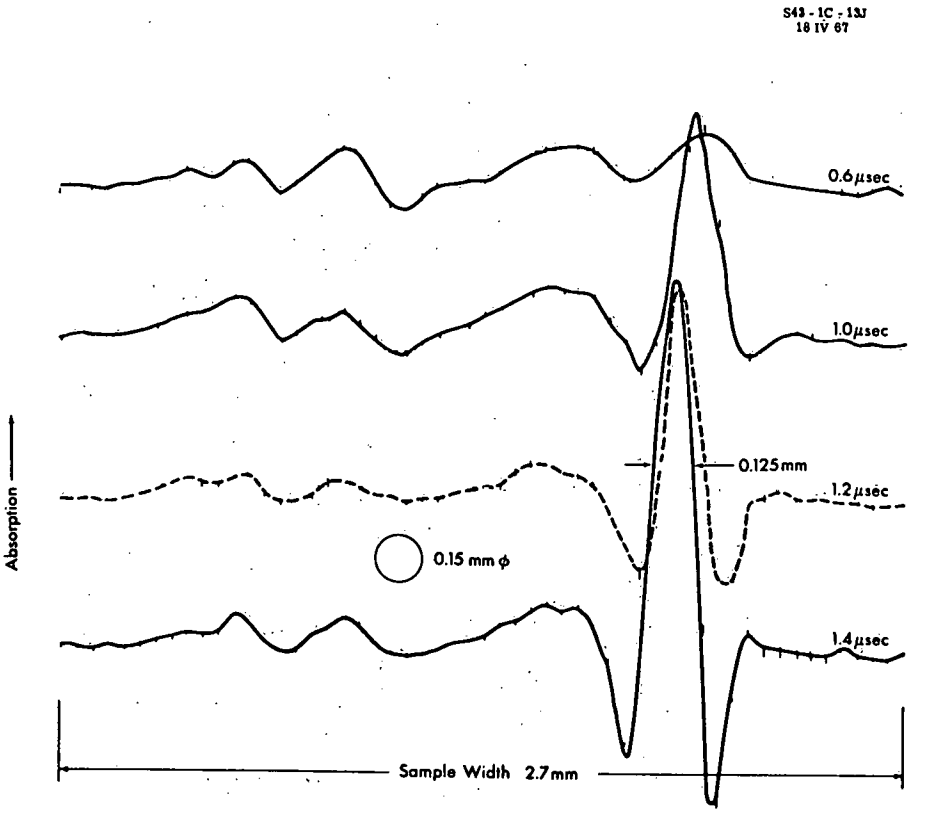

Fig. 4. Measurements of plasma absorption during plasma pinching for different times after the production of the plasma. The inset shows current and field strength as functions of time. The sample dimensions are 10.0 x 2.75 x 0.61 mm^3.

PREIONIZATION STUDIES IN A LARGE INVERSE PINCH

by

F. Y. Sorrell
Aerospace Engineering Sciences Department and
Joint Institute for Laboratory Astrophysics
University of Colorado

and

G. C. Vlases and E. A. Crawford
Aerospace Engineering Sciences Department
University of Colorado

ABSTRACT

This paper describes several approaches to the problem of preheating hydrogen in a 50 cm. diameter inverse pinch tube. The goal is to create a uniform, fully ionized plasma in equilibrium at a temperature of 1.5 e.v. or higher and a density on the order of 10^{15} electrons per c.c. for collisionless shock wave studies. Preionization is accomplished by discharging a preheat capacitor bank through the same electrode system as is used for the shock bank. Time and space resolved determination of the electron density has been made by measuring the Stark broadening of H_β with a scanning Fabry-Perot interferometer. The electron temperature is determined by photoelectric spectroscopic measurements of relative intensities. Finally, the total plasma density is estimated from the trajectories of shock waves propagating in the preheated gas. The measurements indicate that a high current, short duration discharge, in which the heating is primarily by strong shock waves, is more efficient in ionizing the gas than is a slow pulse in which the heating is primarily Ohmic. With shock heating it appears possible to achieve nearly full ionization at a temperature of 1.5 to 3 e.v. over about two thirds of the chamber. With a long, slow current pulse, either oscillating or crowbarred, densities are significantly lower even though the total energy in the bank may be several times that used in the fast pulse configuration.

Introduction

In experimental studies of collisionless shock waves it is important that the ambient (unshocked) gas be nearly fully ionized so that charge exchange and neutral-neutral collisions do not affect shock structure. It is also desirable that the ratio of mean free path to ion gyro radius exceed one ahead of the shock. This has, to our knowledge, not yet been accomplished in any of the various "pinch" experiments on collisionless shocks. However, wave thicknesses which are significantly less than the mean free path between shock heated particles and ambient charged particles have been reported[1,2] indicating that some form of collisionless heating mechanism is operating in the wave front.

This paper is concerned with the preheating phase of a proposed collisionless shock experiment. Preheating is accomplished by passing a large current through the test gas. Two limiting cases are studied. The first involves various types of relatively slow discharges where the heating is primarily Ohmic. The second utilizes a short, high current oscillatory discharge in which a series of shock waves is passed through the gas in order to

ionize it, after which the gas is allowed to relax back to a uniform state.

The device chosen for these studies is an inverse pinch tube which has a high degree of reproducibility and stability, and accessibility for probe and optical measurements. A schematic of the discharge tube is shown in Figure 1. It is 50 centimeters long. The operating parameters which are described in detail in Ref. (3), were chosen to provide the shock speeds, etc, necessary for the anticipated experiments. The preheating banks discussed in this paper are: 135 microfarads, 20 kilovolts max., with a period of 80 microseconds (slow bank) and 32 microfarads, 30 kilovolts max. with a period of ten microseconds (fast bank). The slow bank is operated in one of three configurations: oscillatory, crowbarred on the first current maximum, and crowbarred on the third current maximum. The current decays to 10% of its peak value in about 330 microseconds. The fast bank is operated in an oscillatory manner and decays to 10% current in about 45 microseconds. A small pre-preheat capacitor was used in some of the experiments.

Diagnostic Techniques

The diagnostic techniques are designed at measuring the electron density, electron temperature, and total gas density in the preheated gas.

The electron number density (n_e) is determined by measuring the width of the Stark broadened H_β line and relating the width to n_e by Griem's Theory[4]. The procedure measures total free electron density and remains valid even when some of the free electrons come from ionized impurities; it does not require thermodynamic equilibrium. The line profile was obtained by using a rapid scanning Fabry-Perot interferometer, as described by Cooper[5], with a Bausch and Lomb Model 33-86-25-02 monochromator.

Data were taken at three different radial positions from windows approximately 1/2 cm. by 2 cm. Typical scanning time for an individual line was 2 - 4 μ-sec and the profiles were measured with sufficient accuracy to give the electron number density within 10-15%.

The temperature is estimated by measuring the ratio of the intensity of H_β to 100 Å of underlying continuum. This requires that the fourth quantum level of Hydrogen be in equilibrium with the continuum radiation of the free electrons which calculations show to be true in the present work. Since collisions with free electrons is the major process that populates the n = 4 level, only the electron temperature is measured.

Electrons from impurities will increase the underlying continuum radiation without increasing the line radiation (H_β) and make the temperature appear higher than it actually is. We have not been able to accurately estimate the amount of the impurity radiation, hence, at present can only suggest when it is expected to be the cause of error.

The ratio of line to continuum radiation was measured by using a Jarrell-Ash 1.5 meter Wadsworth spectrograph fitted with a multichannel photoelectric readout head. Slit widths were 30 Å, centered on the line, and 5 Å for each of the continuum windows, at 5545 Å and 4715 Å. The continuum windows were checked to be free of impurities by using an overexposed film spectra and by scanning the windows with a monochromator, and all phototubes were calibrated simultaneously by using an NBS standard lamp. Data were typically taken at a radius of 12.5 cm from the center of the chamber and from an area approximately 0.5 cm by 2 cm.

Agreement of the two continuum windows was usually within 15% for the fast bank and 30-40% for the slow banks. H_β to continuum ratios were repeatable to within 10% for the fast bank and 20-30% for the slow banks, which gave a scatter in the temperature of 5-10% for the fast bank and 15-25% for the slow bank.

It was decided to try and measure the total gas mass density in order to determine whether

or not large amounts of impurities were present. Because of the disparate atomic weights of Hydrogen and the common impurity ions, a small impurity number density will appear as a relatively large increase in mass density. The technique used involves measuring the trajectories of various hydromagnetic waves produced by a second capacitor bank fired at a chosen time after initiation of the preheat discharge. When a large amplitude current is passed through the gas it produces, ideally, a magnetic piston travelling through the gas preceded by a magnetohydrodynamic shock wave. Knowledge of the shock and piston speeds produces, in principle, a redundant measurement of the gas density, provided the current wave form is known. The exact solution for a linearly rising current in an inverse pinch geometry was given by Greifinger and Cole[6], based on a single fluid infinite conductivity mhd model. Among other things, their analysis showed that the piston velocity is given quite accurately by the snowplow theory even when the shock is quite weak. In practice the technique is complicated by deviations of the actual conditions from those in the single fluid model, and by the fact that errors in velocity measurement produce large errors in apparent measured density.

Results

A. Preliminary Work. It was reported by Sorrell[7], in an earlier paper concerned with collision dominated shocks in a small inverse pinch, that a thick anode layer forms and destroys the shock-magnetic piston features when metal plates are used for electrodes. He reported further that this layer was effectively removed from the shock region by using button electrodes. It was thus decided to follow the same procedure in the present experiments if feasible. In order to reduce the possible contamination of the Hydrogen plasma by impurities, boron nitride and alumina discs were bonded to the pyrex top and the bottom plates of the chamber in the vicinity of the button electrodes. The measured electron density, however, was often greatly in excess of twice the filling density of Hydrogen molecules for the early phase of the discharge, indicating gross impurity contamination. Full copper discs were then substituted, and the problem was eliminated. A theory by Kantrowitz[8] gives the time required for the surface temperature of a given material to reach its melting or decomposition temperature when subjected to a constant heat input equal to the flux of particles striking the wall times the average energy per particle. Another theory by Ashby[9] in which the total heat dissipated in a linearly using current layer running on a surface is assumed to flow into the surface, gives a critical current at which melting or decomposition occurs. This theory may provide a realistic model for ablation during the current phase while Kantrowitz' theory would be expected to be applicable to the current free plasma decay period. The heating time based on a 10 ev plasma at 10^{15} cm^{-3} and "critical current" given by these two theories are listed in Table IV. From this it appears clear that no insulator is capable of withstanding currents generated by the fast bank without ablating substantially in agreement with our experimental results. On the other hand, the copper electrodes, which were used for all the results presented below, appear to be satisfactory for use either with the fast or slow banks on the basis of either theory.

B. Fast Bank. The results of interferometer measurements of density with a fast bank are shown in Figures 2 and 3. With an initial voltage of 20 kv the density is fairly low, corresponding to only about 30 to 50% ionization through most of the chamber volume. At 24 kv, however, the electron density is much higher, corresponding to about 80% ionization throughout the chamber at 40 microseconds. It is characteristic of the fast bank heating that the results are relatively independent of magnetic field. We are presently taking data at 28 kv and hope to achieve essentially complete ionization by this technique. The electron temperature, as

determined by the methods outlined above, is given in Table 3. Total density measurements with the fast bank have not yet been successfully completed; however, spectroscopic data does not indicate that large amounts of impurities are present.

C. Slow Banks. In contrast to the results of Paul[1], we have been unable to produce significant ionization of the plasma with any of the slow bank configurations. The electron densities obtained with the bank crowbarred on the third current maximum are shown in Figure 4. The total density was determined by firing the fast bank after the slow bank. The measured wave speed results in a calculated density of $5.5 \times 10^{-6} \pm 30\%$ kg/m^3, as compared with a filling density of 5.48×10^{-6} at 50 μ. This indicates that the degree of ionization is quite low, barring the possibility of the presence of a significant fraction, by mass, of impurities. The electron temperature, on the other hand, is quite high (Table 3). With the oscillating current configuration the electron temperature is observed to decrease to around 1 ev during current nulls, and to increase substantially during current maximum. The temperature is relatively high (2.5 to 4.5 ev) during the unidirectional current flow which occurs after clamping. The measured electron densities are very sensitive to the ambient field strength, in contrast to the situation which exists with a fast preheating bank. The same sensitivity is noticed, to a lesser extent with the electron temperature.

Film spectra we have taken have in general not shown any strong impurity lines with either bank, although the results are not yet conclusive. Some impurity lines have shown up in the 100 Å interferometer-monochromator window centered at H_β. These lines, which have not yet been positively identified, appear primarily during time of current flow and are believed to be CuII and NII. They have never been seen during the decay period of the fast bank plasma.

Conclusions

It is clear that two distinct heating mechanisms are at work in these experiments: shock heating and resistive heating. Shock heating predominates in the fast bank discharges while resistive heating is the more important with the slow bank.

The shock waves generated by the fast bank at 24 kv are sufficiently strong that the first one sent out ionizes the gas almost completely except at high ambient field strengths[10,11]. Waves generated on subsequent half cycles further heat the gas. After the gas has relaxed to its initial uniform density, the thermodynamic state is one of greatly increased entropy and hence increased temperature. The shock waves efficiently heat heavy particles as well as light ones, so that a near local thermodynamic equilibrium state is established. Finally, it should be mentioned, in connection with shock waves, that although the jump conditions certainly are dependent on the magnetic field for a given piston speed, the effect of B_{z_o} on the post shock temperature is not too strong[12]. This implies that the final conditons obtained with the fast bank should be relatively independent of the field, which is borne out by the data.

With each of the slow bank configurations, shock heating is negligible as the Lorentz forces are too small to produce strong waves; heating is thus expected to be nearly completely via resistive dissipation. During the long unidirectional current pulse of the crowbarred phase the current should diffuse throughout the entire chamber. The electrons are heated quite extensively, but because of the inefficient collisional energy transfer between electrons and heavy particles, it is doubtful that the protons and atoms are heated. The data also indicates that the electrons are hot only during current flow, and that they cool within a few microseconds when the electric field is removed. This is most apparent with the oscillatory bank where T_e

is high during current peaks and low during nulls. Furthermore, the energy addition with the long, low current waveform is apparently so slow that, because of radiation, diffusion, and conduction losses, an equilibrium highly ionized plasma is never created. The fast bank, on the other hand, creates a uniform plasma in a relatively short time, before losses are too severe.

Paul[1] has reported approximately 90% ionization for preheating with a slow bank that is quite similar to ours, both in energy stored per unit of chamber volume and in current waveform. The experiments differ principally in the fact that Paul used a linear Z pinch 1 meter long as opposed to our 15 cm long inverse pinch, and worked at somewhat lower densities. One might suspect that our plasma has disappeared to the ends of the chamber but the total density measurements indicate this is not correct. The apparent disagreement between Paul's results and ours is not understood at present. We therefore conclude that the fast bank is more efficient in putting energy into the gas and leaves it much closer to thermodynamic equilibrium. A bank which heats the gas by strong shock waves appears to be the best approach to pre-heating for collisionless shock studies in our experiments.

Acknowledgments

This work was supported jointly by the National Science Foundation under grant GK 1202, and the Advanced Research Projects Agency under contract No. DA-31-124-ARO (D)-139.

References

1. J. W. M. Paul et.al., Nature 208 135 (1965).
2. G. Goldenbaum and E. Hintz, Physics of Fluids 8 2111 (1965).
3. G. C. Vlases, Proceedings 5th International Shocktube Symposium, White Oak, Marylang, 1965. (Also JILA Rept. #49).
4. H. K. Griem, Plasma Spectroscopy, McGraw Hill, N.Y. (1964).
5. J. Cooper, J. Sci. Inst. 40 433 (1963).
6. C. Greifinger and J. D. Cole, Phys. Fluids 4 527 (1961).
7. F. Y. Sorrell, Ph.D. Thesis, Cal. Inst. Tech. (1966).
8. A. R. Kantrowitz, Paper presented at 15th Anniversary Salvay Conference, Brussels, Nov. 5-10 1962. Also AVCO R.R. 141 (1962).
9. D.E.T.F. Ashby, J. Nuclear Energy, Part C, 5 83 (1963).
10. G. C. Vlases, Physics of Fluids (to be published)
11. C. F. Stebbins, Ph.D. Thesis, U. of Colorado (1967).
12. See, for example, AVCO Everett R.R. 185 (1964) by A. R. Kantrowitz and H. E. Petschek.

Table I. Preheat Bank Parameters

Configuration	C (μF)	V (kv)	I_{max} (kA)	Period (μ sec)	Time of Crowbar (μ sec)	90% Decay Time (μ sec)
Fast: (a)	32	20	400	10	none	45
(b)	32	24	480	10	none	45
Slow: (a)	135	15	159	80	none	450
(b)	135	15	159	80	20	330
(c)	135	15	159	80	100	330

Table II. Ablation Parameters

Material	Melting Temp. (°C)	Time to Melt (Kantrowitz) (milliseconds)	Critical Current (Ashby) (kA)
Alumina	2000	24.0	255
Boron Nitride	1200*	4.9	172
Quartz	1600	2.4	144
Pyrex	700†	.2	76
Copper	1083	280.0	> 500

*Decomposition Temperature
†Softening Temperature

Table III. Electron Temperature in e.v.

Fast Bank

Voltage (kv)	Field (gauss)	Time (μ sec) 40	50	60	70
20	850	1.7	1.4	1.25	1.15
	2500	1.85	1.55	1.30	1.4
24	850	1.9	1.8	1.9	2.0

Slow Bank, Oscillating

Voltage (kv)	Field (gauss)	Time (μ sec) 80*	100†	120
15	2500	1.0	3.2	1.3
18	2500	1.9		1.7

*current null
†current max

Slow Bank, 1/4 Cycle Crowbar

Voltage (kv)	Field (gauss)	Time (μ sec) 80	100	120	140
18	0	1.5	2.1		
	1275	2.85	2.85	3.1	2.85
	2500	2.3	1.8	2.1	2.1

Slow Bank, 5/4 Cycle Crowbar

Voltage (kv)	Field (gauss)	Time (μ sec) 110	140	180
15	0	1.8	1.8	1.6
	850	2.9	2.6	2.2
	2500	2.1	1.6	1.6
18	0	2.3	2.1	2.7
	850	4.5	3.8	2.8
	2500	3.2	2.8	2.6

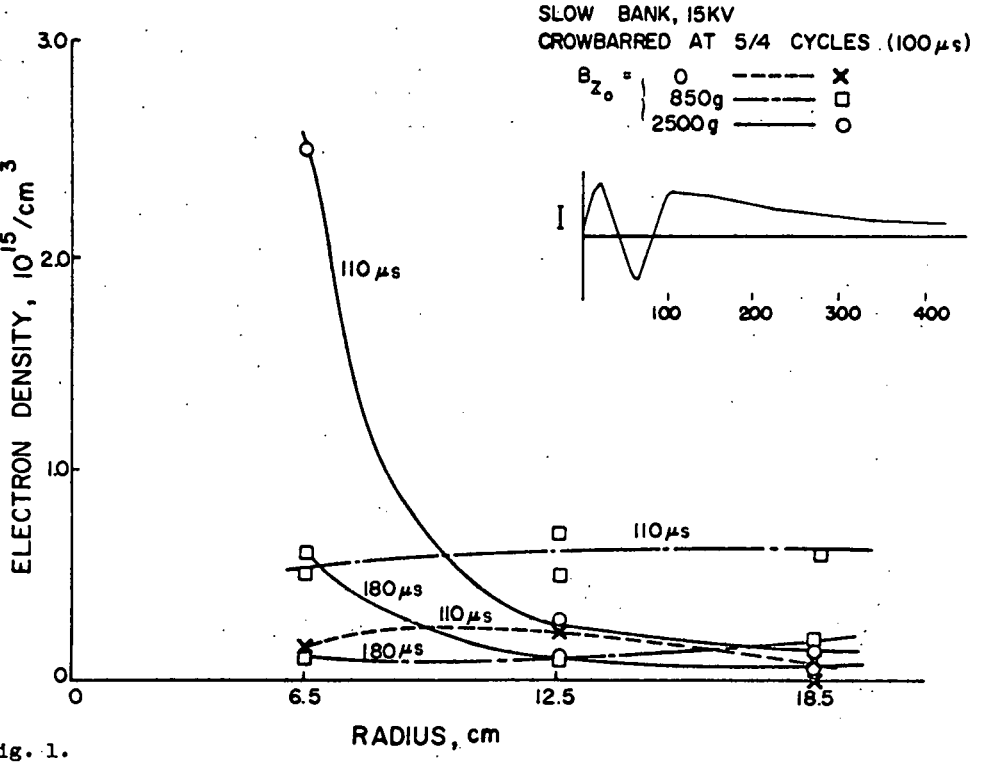
SLOW BANK, 15KV
CROWBARRED AT 5/4 CYCLES (100 μs)
B_{Z_o} = 0
850g
2500g
I
100
200
300
400
110 μs
110 μs
180 μs
110 μs
180 μs
ELECTRON DENSITY, 10^{15}/cm^3
3.0
2.0
1.0
0
6.5
12.5
18.5
RADIUS, cm

Fig. 1.

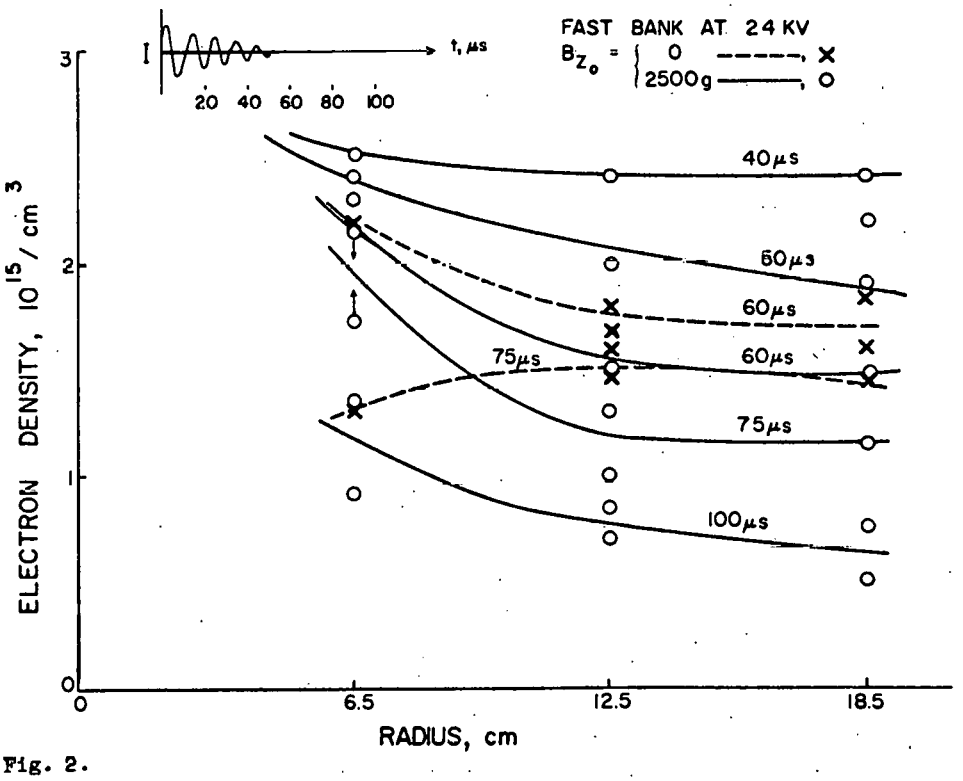
I
t, μs
20 40 60 80 100
FAST BANK AT 24 KV
B_{Z_o} = 0
2500g
40 μs
60 μs
60 μs
75 μs
60 μs
75 μs
100 μs
ELECTRON DENSITY, 10^{15}/cm^3
3
2
1
0
6.5
12.5
18.5
RADIUS, cm

Fig. 2.

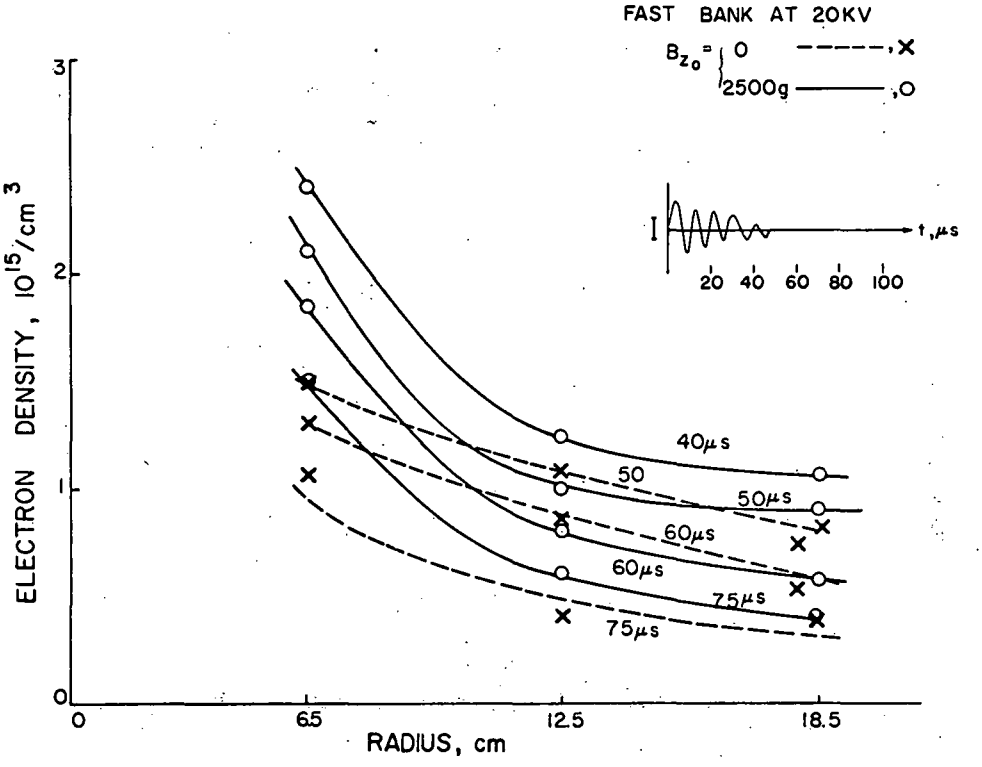
FAST BANK AT 20KV
B_{z_0} = 0 ------, ×
2500g ——— , o
I
t, μs
20 40 60 80 100
ELECTRON DENSITY, $10^{15}/cm^3$
3
2
1
0
40μs
50
50μs
60μs
60μs
75μs
75μs
0
6.5
12.5
18.5
RADIUS, cm

Fig. 3.

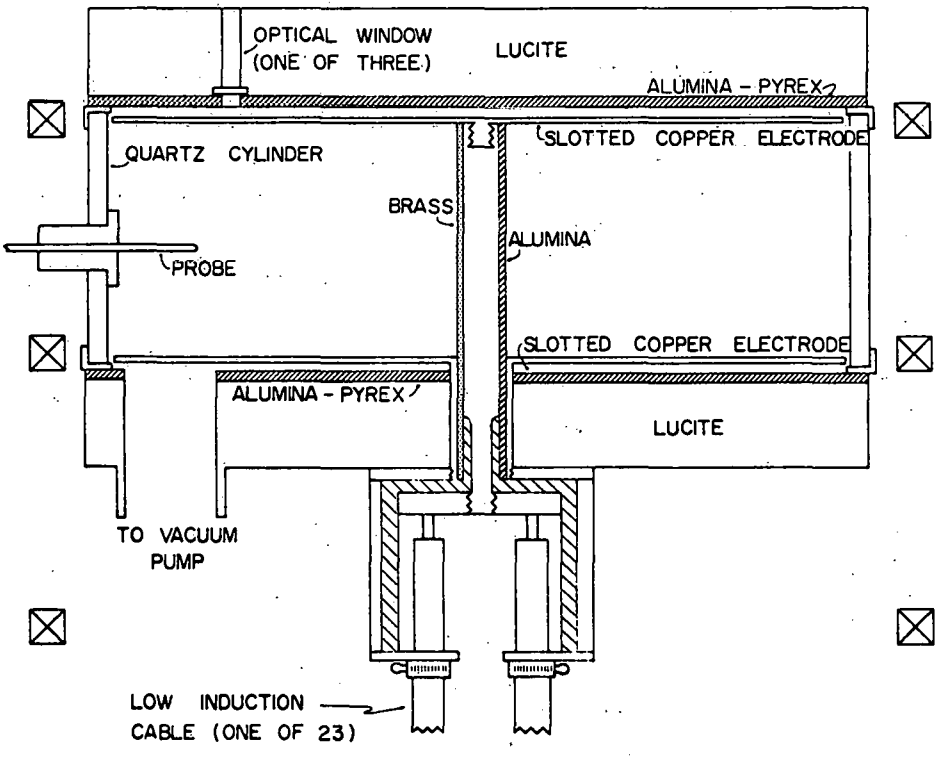
OPTICAL WINDOW (ONE OF THREE)
LUCITE
ALUMINA - PYREX
SLOTTED COPPER ELECTRODE
QUARTZ CYLINDER
BRASS
ALUMINA
PROBE
SLOTTED COPPER ELECTRODE
ALUMINA - PYREX
LUCITE
TO VACUUM PUMP
LOW INDUCTION CABLE (ONE OF 23)

Fig. 4.

HIGH DENSITY PLASMA INDUCED BY PULSED MICROWAVE*

by

R. B. Block†, D. L. Rode & O. K. Mawardi
Case Western Reserve University
Cleveland, Ohio

ABSTRACT

A high mirror-ratio coil used in a θ-pinch experiment was adapted as a spherical microwave resonator to produce intense preionization by a high power microwave discharge. The initial breakdown is triggered by an X-band pulse of .22 μsec duration and 325 kw peak power. This is followed by an S-band pulse 1.3 μsec long at 800 kw peak power. Theory shows that the transverse magnetic resonant modes yield the largest magnitude electric fields, these being radial. The predicted TM_{22m} and TM_{51m} modes have been observed experimentally to be well coupled to the cavity when the S-band pulse is incident upon a low density plasma. Electron densities are measured by Langmuir probes and an infrared wavelength interferometer**, the latter indicating densities of 10^{14} cm^{-3} at a base pressure of 80 μ in Helium, although breakdown occurs even well below 10 μ. In addition the skin depth, the electron temperature, and the Q of the cavity have been measured and are in close agreement with the theory. Substantially higher percentages of ionization are believed to be produced at the lower pressures as the total number of electrons produced is fairly insensitive to the base pressure and breakdown was observed to occur well below 10 μ.

Introduction

In several theta-pinch investigations it is common to preionize the gas prior to compressing it strongly. Customarily, the preionization is achieved by means of a weaker shock. However, some attempts have been reported in the literature[1] in which r.f. power was used to ionize the gas. The results, so far, have not been encouraging. The main difficulty resides in the gas breaking down in a thin layer on a surface corresponding to a region of high electric field strength. This layer whose thickness is of the order of the skin depth shields the rest of the gas from the electromagnetic field. Although electrons do diffuse from the layer and into the gas, the average electron densities and percentages of ionization which have been obtained thus far are much lower than the corresponding numbers found with shocks (electron densities $\sim 10^{14}$ to 10^{16} cm^{-3} and almost complete ionization). Conversely, the r.f. approach offers simplicity in application besides a relatively quiescent plasma free from trapped fields.

This paper describes a series of investigations, pertaining to r.f. ionization, aimed toward improving the coupling of high power microwave to a gas. The corresponding electron densities and fractional ionization produced are quite high. The general procedure and calculations related to the microwave apparatus are described below.

A high mirror-ratio coil used in a theta-pinch experiment[2] was adapted as a spherical microwave resonator. The neutral gas is contained in a fused quartz sphere placed inside this coil concentrically. A microwave pulse of 0.22 μsec duration and 325 kw

*Supported in part by the National Science Foundation

†Presently with Physics International, San Leonardo, Calif.

**D.L. Rode & J.E. Hammel, "Fractional Fringe-Shift Laser Interferometer" Bull, Am. Phys. Soc. 12, 793, (1967)

peak power in the X-band spectrum (8.5 to 9.6 GHz) is first applied to the cavity. This initiates the breakdown and the partial ionization of the gas. The formation of plasma, however, detunes the cavity thus reducing the further absorption of r.f. power at this frequency. The plasma also shields the central core of gas and hinders the ionization process.

To circumvent these drawbacks a subsequent pulse at a lower frequency is applied after a variable delay. This second pulse in the S-band (3.1 to 3.5 GHz, 1.3 μsec duration, 1 Mw peak power) is now chosen so as to resonate the cavity with the plasma present. Consequently, the cavity remains well-coupled and the ionization can be further intensified. Furthermore, at this lower frequency the skin depth is larger and the electric field can penetrate deeper into the plasma. The improved efficiency of this method has been corroborated by similar experiments reported by Dougal[3] in which he also observes an enhancement of the ionization. The general arrangement of the equipment for the S-band is shown in schematic form by Fig. 1. Not shown is a similar set-up for X-band apparatus.

Modes in the Sphere

Relevant to the present experiment are the normal modes for two cases which are theoretically similar; 1) vacuum sphere configuration, and 2) concentric sphere configuration. Prior to the gas breakdown the modes are like those of a conducting sphere whose interior is a vacuum. The TE and TM mode frequencies for this first case follow respectively from the characteristic values of[4]

$$j_n(k_{nm}r_o) = 0$$

$$[rj_n(k_{nm}r)]'_{r=r_o} = 0 \qquad (1)$$

In the above j_n is a spherical Bessel function, r_o is the radius of the sphere, and k_{nm} is the wave number of the mode. The first, second, etc. roots in order of increasing k_{nm} are denoted by m beginning with unity. These characteristic values are tabulated[5] and the vacuum sphere resonant frequencies follow simply. Non-trivial electric fields can result only if the ordinal number $n > 0$. Hence, these fields always vanish at the origin.

For easier breakdown, it is desirable to identify and utilize those modes that will yield the higher values of the electric field strength for a given input power. The electric field components for TE modes are given by

$$E_r = 0$$

$$E_\theta = -\frac{kp}{\sin\theta} j_n(k_{nm}r)Y_n^p(\theta,\phi)$$

$$E_\phi = -ik\, j_n(k_{nm}r)\frac{\partial}{\partial\theta} Y_n^p(\theta,\phi) \qquad (2)$$

where (r,θ,ϕ) stands for the usual spherical coordinates. On the other hand, the TM modes have

$$E_r = \frac{n(n+1)}{r} j_n(k_{nm}r)Y_n^p(\theta,\phi)$$

$$E_\theta = \frac{1}{r}\frac{\partial}{\partial r}[r\, j_n(k_{nm}r)]\frac{\partial}{\partial\theta} Y_n^p(\theta,\phi)$$

$$E_\phi = \frac{ip}{r\sin\theta}\frac{\partial}{\partial r}[r\, j_n(k_{nm}r)]Y_n^p(\theta,\phi) \qquad (3)$$

It is readily checked that the TM modes yield higher values of the total electric field for the allowable (S-band) frequency range. This is shown in a graphical way in Fig. 2.

The second case to be considered (viz., the cavity delineated by two concentric spherical conductors) refers to the situation inside the resonator after the gas has broken down to the extent that the cutoff density ($n_{co} = \frac{m\varepsilon_o}{e^2}\omega^2$, MKS units) has been surpassed. Here, the plasma is regarded as the inner conducting sphere. For the idealized situation of perfect conductors the mode frequencies are obtained from the zeros of

$$[z_n(k_{nm}r)]_{r=r_o,r_1} = 0 \quad \text{, TE modes}$$

and

$$\frac{\partial}{\partial r}[rz_n(k_{nm}r)]_{r=r_o,r_1} = 0 \quad \text{, TM modes} \qquad (4)$$

The function $z_n = j_n + c_n n_n$ where n_n is the spherical Neumann function, c_n is a constant, and r_o and r_1 are the outer and inner radii of the conductors. The inner radius r_1 corresponds to the size of the quartz container inside the spherical resonator. Since the roots of Eq. (4) for the range of interest to this investigation ($\frac{r_o}{r_1} = 1.66$, S-band spectrum) are not tabulated, these equations were solved on a computer. The appropriate modes suitable to the purpose of this investigation are as follows

TE mode : none

TM mode : $\nu_{5,1}$

The above calculations have been performed on the basis of the assumption that the resonator walls are perfect conductors - i.e., the equivalent Q is infinite. It is known, however,[6] that the resonance frequency ω_o for a finite Q differs slightly from ω_r, that for an infinite Q, according to the expression

$$\omega_o^2 = \omega_r^2(1 - \frac{1}{Q}) \quad . \qquad (5)$$

Since $Q \tilde{\sim} 40$, the expected correction is of the order of one per cent.

Experimental Results

a) Resonant Modes of the Cavity

In order to check on the characteristic frequencies calculated in the previous section a number of runs were performed in which the cavity standing wave ratio (SWR) was measured for very low power. This corresponds to the vacuum case. As it was more convenient to perform this part of the experiment at the S-band, the following results were for the range 3.1 to 3.5 GHz. Fig. 3. shows the SWR as a function of frequency. Since the signal strength was weak (of the order of a milliwatt) no ionization takes place in the sphere and the minima in the SWR curve correspond to better than one per cent with the predicted values. A noteworthy effect is the higher coupling for the TM modes as compared to the TE mode (SWR figures of 10.5 db and 0.5 db for the former as compared to 17 db for the latter).

The modes corresponding to the concentric spherical resonator require the appearance of plasma as the inner conductor. Accordingly, the megawatt pulse was applied to the sphere. At these power levels it is impractical to measure SWR by conventional techniques. Instead, the resonant frequencies were obtained by measuring the dependence of the electric field on the frequency. The relative magnitude of the electric field was inferred from the intensity of the light output from the discharge. Fig. 3 shows also the time-averaged output of a photomultiplier as a function of frequency. Here, it is seen that the modes corresponding to the hollow spherical resonator (vacuum mode) appear as well as the TM concentric sphere mode. The relative intensity of this mode, however, is much larger than that of the vacuum case. The resonant frequency checks closely with the value predicted in Section 2 within 1.2%. This discrepancy may be accountable by Eq. (5).

b) Power Absorption in the S-Band

Figs. 4(a,b,c) are oscillograms for the reflected power from the sphere at three different frequencies in the S-band. In Fig. (4a) the trace indicates almost complete rejection by the microwave cavity of the incident power. The frequency was chosen to be far from any of the resonant modes of the cavity. On the other hand, Fig. (4b) clearly demonstrates that although breakdown does occur earlier in the pulse most of the incident energy is still rejected. This is because the frequency corresponds to that of the vacuum mode and not to that of the concentric spherical mode. The oscillogram of Fig. (4c) clearly shows that the incident power is almost completely absorbed by the cavity subsequent to the initial breakdown and ionization of the gas. The frequency for this case corresponds to that of resonance at the concentric spheres configuration.

A measurement of the energy absorbed by the cavity indicates that it is 91% (±3%) of the incident 1 Megawatt pulse. For this case the quartz container was filled with Helium at 5 μ of pressure. This efficiency does not seem to be too sensitive to the pressure as it remained better than 88% when the pressure was varied from 5 to 100 μ.

c) Electron Density and Temperature

The ionization produced by the X-band pulse in Helium is quite weak. Double electric probe measurements show electron densities of 4×10^{11} cm^{-3} and electron temperatures of 5 to 7 eV. It was noted that the average percentage of ionization was not appreciably pressure dependent (over the range 500 μ to 50 μ) being at peak powers of the order of a few tenths of a percent. The electron temperature estimated from probe measurements is in agreement with the value obtained from spectroscopic data. The observed sheath thickness of 2 cm. at 5 torr agrees with the skin depth calculated for the 5 eV temperature.

The ionization produced by the S-band is more intense and the average electron densities that are now observed are approximately 4 to 6×10^{13} cm^{-3} at 80 μ in Helium. These numbers have been measured by means of a laser interferometer technique[7] previously reported in the literature. Preliminary measurements seem to indicate that the electron density is not very sensitive to the back pressure over the range (200 to 20 μ). The percentage of ionization so produced thus varies from about 0.8 to 8%.

Discussion of Results

The value of the electron density sensed by the laser interferometer is in fact the average over the whole optical path. If it is assumed that all of the electrons are concentrated in the skin depth, then one can estimate readily the percentage ionization in the skin depth.

Two possible formulae can be used. The first one corresponds to the situation where $\omega_p >> \omega >> \nu$ and ν is the relevant collision frequency for the electrons. Starting from the well known relation[8] for the penetration depth "δ" of an electromagnetic plane wave in an unmagnetized plasma and which is

$$\delta^{-1} = \frac{\omega}{c}\left[-\frac{1}{2}\left(1-\frac{\omega_p^2}{\omega^2+\nu^2}\right)+\frac{1}{2}\left(\left(1-\frac{\omega_p^2}{\omega^2+\nu^2}\right)^2+\left(\frac{\omega_p^2\nu}{(\omega^2+\nu^2)\omega}\right)^2\right)^{1/2}\right]^{1/2} \qquad (6)$$

it is found that for the above assumption

$$\delta \approx \frac{c}{\omega_p} , \qquad (7)$$

where c is in MKS units.

The other extreme case corresponds to a very dense plasma, i.e. $\omega_p >> \nu_{ie} >> \omega$ and here ν_{ie} is the electron-ion collision frequency. The skin depth now becomes

$$\delta \approx \frac{c}{\omega_p}\sqrt{\frac{2\nu_{ie}}{\omega}} \qquad (8)$$

Starting from these two extreme estimates and employing the appropriate values of ω_p, ω and ν, one finds that the percentage ionization would be greater than one hundred per cent. This therefore indicates that the electrons are not concentrated only in the skin depth but are diffused over a dimension much greater than δ. Since the measurements are taken over times short compared to the diffusion time, it is reasonable to state that the electrons are probably produced inside the bulk of the gas and that the ionization can take place because of non-linear effects which can enhance the effective skin depth.

REFERENCES

1. H. Beerwald, P. Bogen, T. El-Khalafewy, H. Fay, E. Hintz and H. Kever, International Conference on Plasma Physics and Controlled Nuclear Fusion Research, Fusion J. (Suppl.) 2, 595, (1962).
2. R. B. Block, Bull. Am. Phys. Soc. II, 12, 786, (1967).
3. A. A. Dougal, Bull. Am. Phys. Soc. II, 8, 131, (1963).
4. W. Panofsky and M. Phillips, "Classical Electricity and Magnetism," Addison-Wesley Publ. Co., Reading, Mass., (1962).
5. R. F. Harrington, "Time-Harmonic Electromagnetic Fields," McGraw-Hill Book Co., New York, N. Y., (1961).
6. J. C. Slater, "Microwave Electronics," D. Van Nostrand Co., New York, N. Y., (1954).
7. D. L. Rode and J. E. Hammel, Bull. Amer. Phys. Soc. II, 12, 793, (1967).
8. C. B. Wharton, UCRL-4836 (Rev.), Univ. of California Radiation Laboratory, Livermore, Calif., (September, 1957).

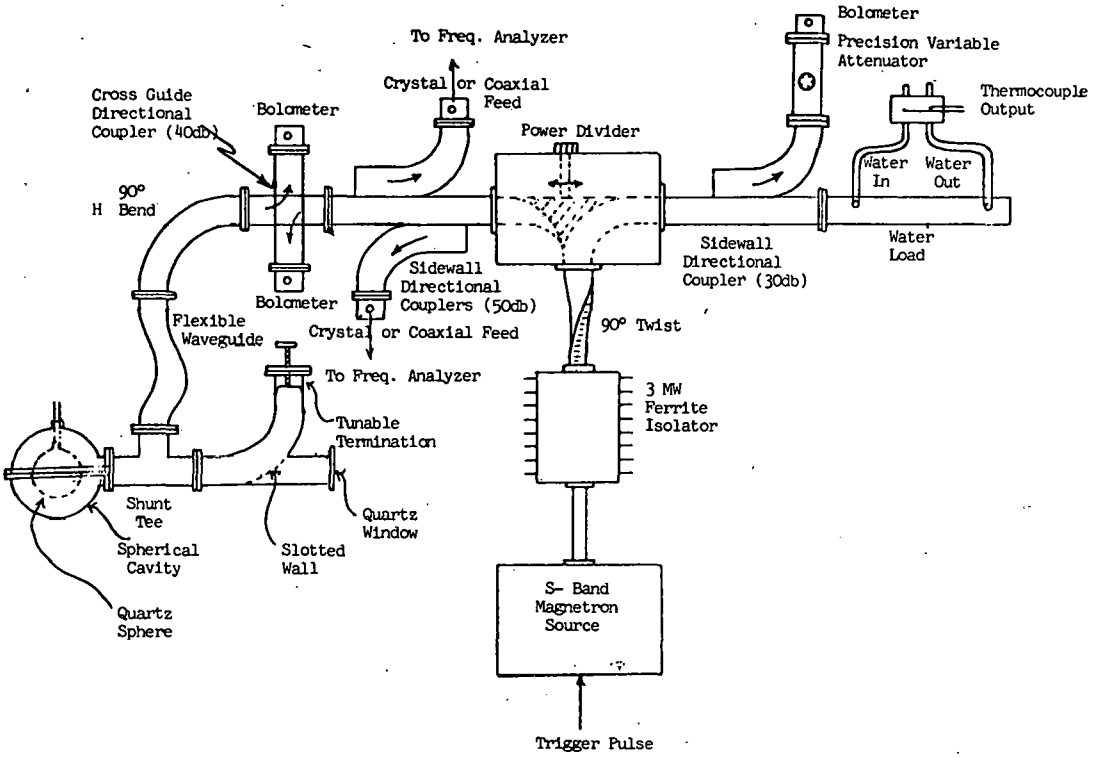

Fig. 1. Schematic of the S-band microwave heating experiment. Waveguides are all pressurized to approximately 30 PSI.

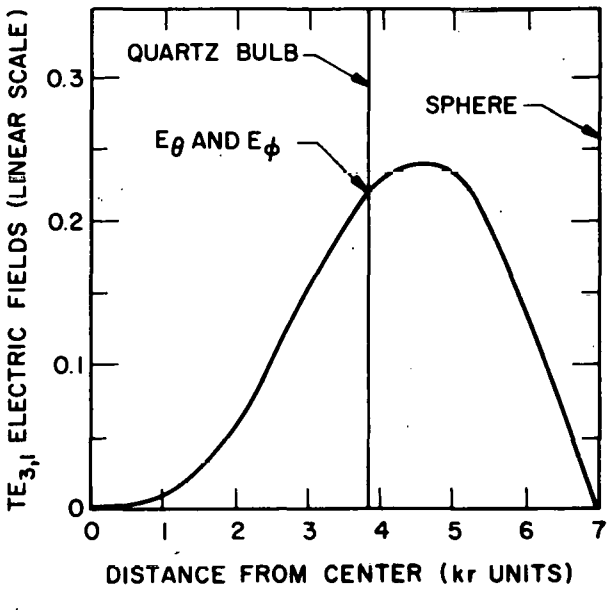

Fig. 2a. Transverse electric mode electric field components. The positions of the quartz bulb and inner wall of brass sphere are as marked.

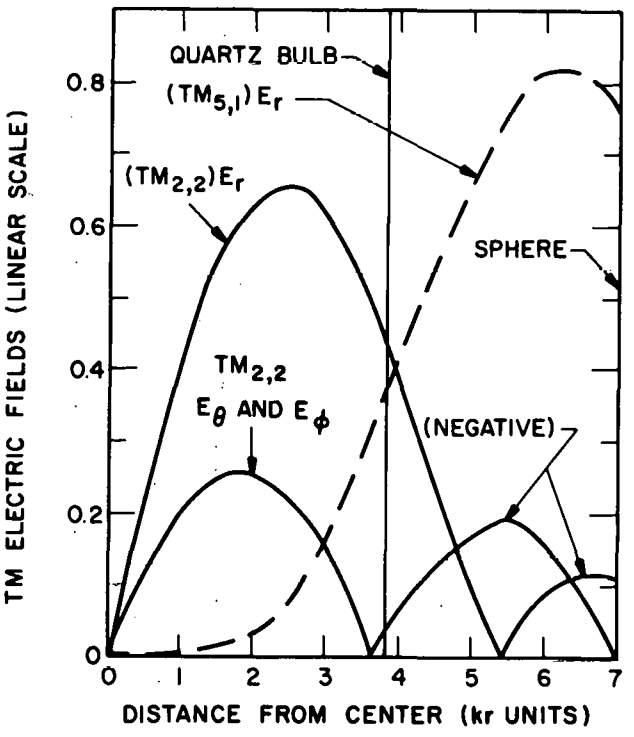

Fig. 2b. Transverse magnetic mode electric field components. The normalization is the same as that of Fig. 4a to allow a direct numerical comparison.

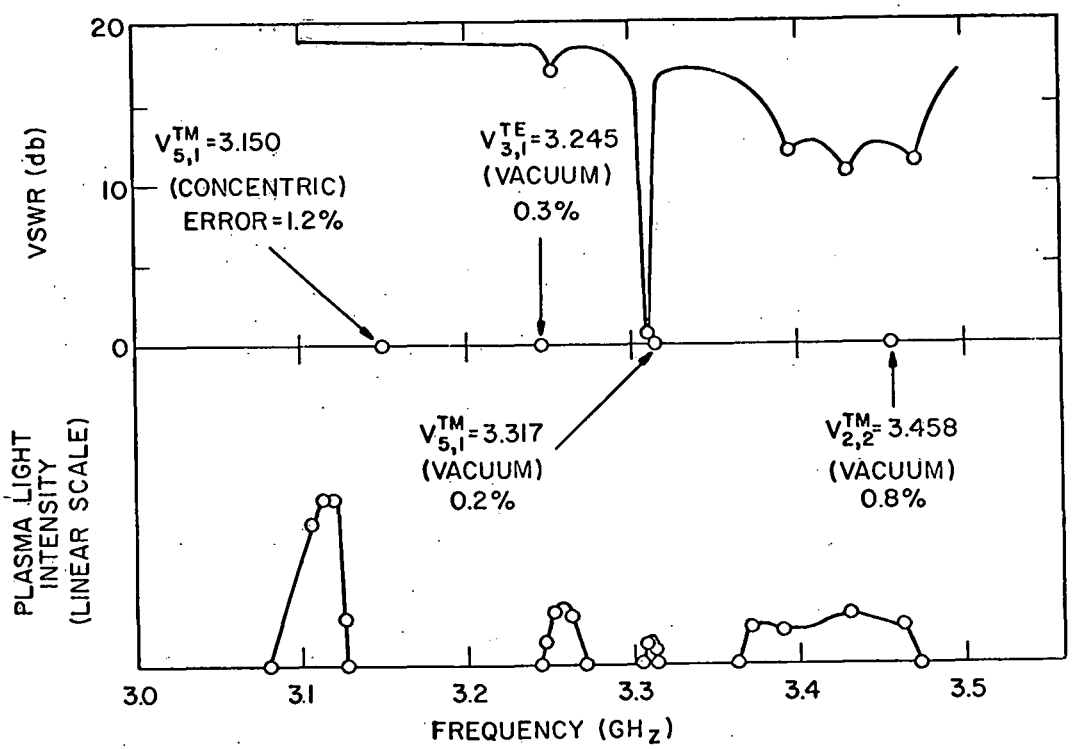

Fig. 3. Comparison of theory with experiment to identify vacuum and concentric spherical resonance. The VSWR curve is for no breakdown in the sphere while the Light Intensity curve is taken with a breakdown in 1 μ of helium. The $\nu_{n,m}$ values are theoretical.

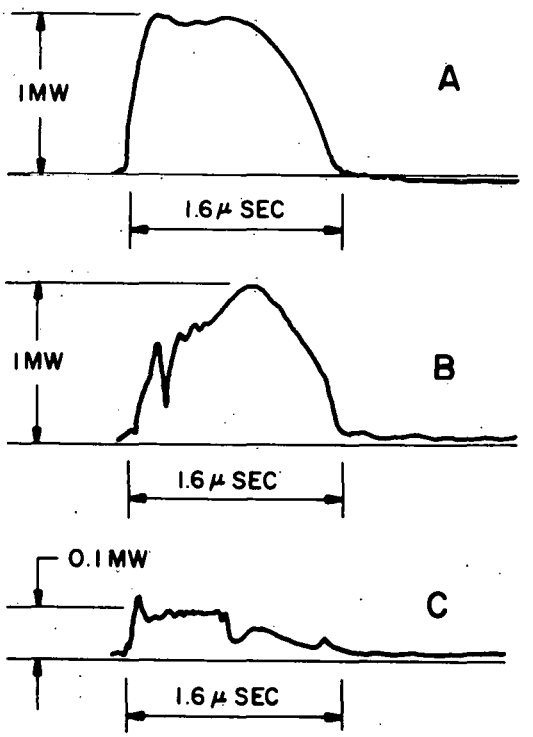

Fig. 4. (A) Fully reflected pulse far from resonance. This is also the incident pulse shape for all three curves. (B) Reflected pulse showing breakdown and reflection at a vacuum resonance. (C) Reflected pulse showing improved absorption over the duration of the pulse at a concentric spherical resonance.

ERRATA SHEET, LA-3770

Paper E-7

(1) Page 2 table:

"Cs 4651.1 Å should read Cs II 4651.1 Å"

"Cs 4446.8 Å should read Cs II 4446.8 Å"

"Cs 2598.7 Å should read Cs II 2598.7 Å"

"Cs 2512.2 Å should read Cs II 2512.2 Å"

Paper D-2

In the Abstract:

(1) Line 2 in parenthesis should read:
"1.15 mirror ratio" should read "1.10 mirror ratio".

(2) Below and left of center:
"6 - 10 rotating flutes" should read "6 - 10 flutes"
(i.e., delete "rotating").

In the text:

(1) Near the top of column 2, first page:
"1.15" should read "1.10".

(2) Near the top of column 1, second page:
"Insert a minus sign in front of the first integral sign in the un-numbered equation for $\frac{DL}{\lambda}$."

In the references:

(1) In Ref. 1, the number in parenthesis at the end of the reference should be changed as follows:
"(163)" should read "(1963)".

Paper D-7

On page 2, column 2, line 15 from the bottom:
"should read 0.1 instead of 1 μsec".

CONFERENCE PARTICIPANTS

Betsy Ancker-Johnson
Plasma Physics Laboratory
Boeing Scientific Research Lab.
P. O. Box 3981
Seattle, Washington 98124

Claus Andelfinger
Institut für Plasmaphysik
8046 Garching
bei München
Germany

Peter L. Auer
Cornell University
College of Engineering
Ithaca, New York 14850

Don A. Baker
Los Alamos Scientific Lab.
University of California
Los Alamos, New Mexico 87544

John R. Banister
Department 5120
P. O. Box 5800
Sandia Corporation
Albuquerque, New Mexico 87115

Everet H. Beckner
Department 5142
P. O. Box 5800
Sandia Corporation
Albuquerque, New Mexico 87115

James N. Benford
University of California, San Diego
Physics Department
La Jolla, California 92037

M. J. Bernstein
Aerospace Corporation
P. O. Box 95085
Los Angeles, California 90045

Roy J. Bickerton
University of Texas
Department of Physics
Austin, Texas 78712

H.A.B. Bodin
U.K. A.E.A.
Building E.1
Culham Laboratory
Culham
Abingdon, Bershire
England

Peter Bogen
Institut für Plasmaphysik
517 Jülich
Germany

Grenfell P. Boicourt
Los Alamos Scientific Lab.
University of California
P. O. Box 1663
Los Alamos, New Mexico 87544

Winston H. Bostick
Stevens Institute of Technology
Hoboken, New Jersey 07030

Paul J. Bottoms
Los Alamos Scientific Lab.
University of California
P. O. Box 1663
Los Alamos, New Mexico 87544

Jim Boyd
University of Texas
Dept. of Electrical Engineering
Austin, Texas 78712

Keith Boyer
Los Alamos Scientific Lab.
University of California
P. O. Box 1663
Los Alamos, New Mexico 87544

David Brown
Los Alamos Scientific Laboratory
University of California
P. O. Box 1663
Los Alamos, New Mexico 87544

Don C. Bryner
North American Aviation-Space Div.
Downey, California

Louis C. Burkhardt
Los Alamos Scientific Laboratory
University of California
P. O. Box 1663
Los Alamos, New Mexico 87544

R. S. Caird
Los Alamos Scientific Laboratory
University of California
P. O. Box 1663
Los Alamos, New Mexico 87544

Darrell Call
Los Alamos Scientific Laboratory
University of California
P. O. Box 1663
Los Alamos, New Mexico 87544

William Carlson
Ames Research Center
MTP Branch
Mail Stop 229-2
Moffett Field, California 94035

Chieh C. Chang
Space Science Applied Physics Dept.
Catholic University of America
Washington, D.C. 20017

Dah Yu Cheng
Ames Research Center
MTP Branch
Mail Stop 229-2
Moffett Field, California 94035

E. C. Cnare
Department 5141
P. O. Box 5800
Sandia Corporation
Albuquerque, New Mexico 87115

F. H. Coensgen
Lawrence Radiation Laboratory
P. O. Box 808
Livermore, California 94550

Darrell C. Collier
University of Arkansas
Physics Department
Fayetteville, Arkansas 72701

Gerald G. Comisar
Aerospace Corporation
P. O. Box 95085
Los Angeles, California 90045

Hans Conrad
NASA
Langley Research Center
Hampton, Virginia 23365

Maynard Cowan
Department 5141
P. O. Box 5800
Sandia Corporation
Albuquerque, New Mexico 87115

E. A. Crawford
University of Colorado
Boulder, Colorado 80302

John C. Crawford
Department 5143
P. O. Box 5800
Sandia Corporation
Albuquerque, New Mexico 87115

W. F. Cummins
Lawrence Radiation Laboratory
P. O. Box 808
Livermore, California 94550

Mark Daehler
Los Alamos Scientific Lab.
University of California
Los Alamos, New Mexico 87544

Richard A. Damerow
Department 5141
P. O. Box 5800
Sandia Corporation
Albuquerque, New Mexico 87115

David Ben Daniel
General Electric R & D Center
P. O. Box 8
Schenectady, New York 12301

Gernot Decker
Institut für Plasmaphysik
8046 Garching
bei München
Germany

James F. Decker
Bell Telephone Laboratories
Whippany, New Jersey 07971

Alan W. DeSilva
University of Maryland
Department of Physics
College Park, Maryland 20742

Robert S. Dike
Los Alamos Scientific Lab.
University of California
P. O Box 1663
Los Alamos, New Mexico 87544

Joseph N. DiMarco
Los Alamos Scientific Lab.
University of California
P. O. Box 1663
Los Alamos, New Mexico 87544

Thomas J. Dolan, Jr.
Los Alamos Scientific Lab.
University of California
P. O. Box 1663
Los Alamos, New Mexico 87544

Harry Dreicer
Los Alamos Scientific Lab.
University of California
P. O. Box 1663
Los Alamos, New Mexico 87544

Melvin Eisner
Physics Department
Texas A&M University
College Station, Texas 77843

Raymond C. Elton
Code 7721
Naval Research Laboratory
Washington, D. C. 20390

R. C. Etievant
Princeton University
Plasma Physics Laboratory
P. O. Box 451
Princeton, New Jersey 08540

A. E. Evans
Los Alamos Scientific Lab.
University of California
P. O. Box 1663
Los Alamos, New Mexico 87544

K. J. Ewing
Los Alamos Scientific Lab.
University of California
P. O. Box 1663
Los Alamos, New Mexico 87544

Val Finlayson
Los Alamos Scientific Lab.
University of California
P. O. Box 1663
Los Alamos, New Mexico 87544

Andrzej Folkierski
Physics Department
Univ. of British Columbia
Vancouver 8, B.C. Canada

Peter R. Foreman
Los Alamos Scientific Lab.
University of California
P. O. Box 1663
Los Alamos, New Mexico 87544

Harold K. Forsen
Dept. Nuclear Engineering
University of Wisconsin
Madison, Wisconsin 53706

C. M. Fowler
Los Alamos Scientific Lab.
University of California
P. O. Box 1663
Los Alamos, New Mexico 87544

J. R. Freeman
Department
P. O. Box 5800
Sandia Corporation
Albuquerque, New Mexico 87115

Jeffrey Freidberg
Los Alamos Scientific Lab.
University of California
P. O. Box 1663
Los Alamos, New Mexico 87544

Otto M. Friedrich, Jr.
Dept. of Electrical Engineering
University of Texas
Austin, Texas 78712

David A. Freiwald
Dept. 5141
P. O. Box 5800
Sandia Corporation
Albuquerque, New Mexico 87115

Ewald Fünfer
Institut für Plasmaphysik
8046 Garching
bei München
Germany

Alan H. Gabriel
University of Maryland
Department of Physics
College Park, Maryland 20742

Wray B. Garn
Los Alamos Scientific Laboratory
University of California
P. O. Box 1663
Los Alamos, New Mexico 87544

Duane C. Gates
Research Div.
Aerojet-General Nucleonics
San Ramon, California 94583

Robert A. Gerber
Dept. 5141
P. O. Box 5800
Sandia Corporation
Albuquerque, New Mexico 87115

Verle Gilson
Lawrence Radiation Laboratory
P. O. Box 808
Livermore, California 94550

Per Gloersen
Room L 9515
General Electric Space Sciences Lab.
P. O. Box 8555
Philadelphia, Pennsylvania 19101

L. M. Goldman
General Electric R & D Center
P. O. Box 8
Schenectady, New York 12301

William Gough
Controlled Thermonuclear Branch
Division of Research
U. S. Atomic Energy Commission
Washington, D. C. 20546

Paule Graf
35 - Avenue Mahieu
94 - Saint-MAUR
France

R. F. Gribble
Los Alamos Scientific Laboratory
University of California
P. O. Box 1663
Los Alamos, New Mexico 87544

Hans Griem
University of Maryland
Department of Physics
College Park, Maryland 20742

William Grossmann, Jr.
Courant Inst. of Mathematical Science
251 Mercer Street
New York, New York 10003

Lt. Richard Gullickson
Kirtland Air Force Base
Albuquerque, New Mexico 87115

Greg Haas
University of Houston
Cullen Blvd.
Houston, Texas 77004

Klaus Hain
NASA-GSFC
Laboratory for Theoretical Studies
Code 641, Bldg. 1
Greenbelt, Maryland

Kenneth W. Hanks
Los Alamos Scientific Laboratory
University of California
P. O. Box 1663
Los Alamos, New Mexico 87544

Jay E. Hammel
Los Alamos Scientific Laboratory
University of California
P. O. Box 1663
Los Alamos, New Mexico 87544

Robert Harris
Sandia Laboratory
(Org. 5835)
Sandia Base
Albuquerque, New Mexico 87115

Robin Harvey
Stevens Institute of Technology
Department of Physics
Hoboken, New Jersey 07030

Kenneth E. Harwell
Aerospace Engineering
Auburn University
Auburn, Alabama 36830

Alan F. Haught
United Aircraft Research Lab.
Silver Lane
East Hartford, Conn. 06108

Dale B. Henderson
Los Alamos Scientific Lab.
University of California
P. O. Box 1663
Los Alamos, New Mexico 87544

Ivars Henins
Los Alamos Scientific Lab.
University of California
P. O. Box 1663
Los Alamos, New Mexico 87544

Robert M. Henson
Los Alamos Scientific Lab.
University of California
P. O. Box 1663
Los Alamos, New Mexico 87544

Hans Herold
Institut Für Plasmaphysik
8046 Garching
bei München
Germany

Keith Hinrichs
Research Division
Aerojet-General Nucleonics
San Ramon, California 94583

Edward Hintz
University of Maryland
College Park, Maryland 20742

Herb Hollister
Kaman Nuclear
Garden of the Gods Road
Colorado Springs, Colorado 80907

Lewis L. House
High Altitude Observatory
Boulder, Colorado 80301

John Irving
Department of Natural Philosophy
University of Strathclyde
Royal College
George Street
Glasgow C1, Scotland

Franz C. Jahoda
Los Alamos Scientific Lab.
University of California
P. O. Box 1663
Los Alamos, New Mexico 87544

John L. Johnson
Princeton University
Plasma Physics Laboratory
Princeton, New Jersey 08540

Hugh J. Karr
Los Alamos Scientific Lab.
University of California
P. O. Box 1663
Los Alamos, New Mexico 87544

Edwin L. Kemp
Los Alamos Scientific Lab.
University of California
P. O. Box 1663
Los Alamos, New Mexico 87544

Herbert Kever
Institut Für Plasmaphysik Der
Kerforschungsanlage
Julich Des Landes
Nordrhein-Westfalen e.V.
Jülich, Germany

Ralph W. Kewish, Jr.
Los Alamos Scientific Lab.
University of California
P. O. Box 1663
Los Alamos, New Mexico 87544

Ralph Kilb
General Electric R & D Center
Nucleonics and Radiation
P. O. Box 8
Schenectady, New York 12301

Heinz Knoepfel
Laboratori Gas Ionizzati
Associazione Euratom-Cnen C.P. 65
Frascati (Roma)
Italy

Alan C. Kolb
Naval Research Laboratory
Code 7700
Washington, D.C. 20234

Walter Köppendörfer
Institut für Plasmaphysik
8046 Garching
Münich, Germany

H. J. Kunze
University of Maryland
Dept. of Physics and Astronomy
College Park, Maryland 20740

Ja Hyun Lee
NASA Langley Research Center
Hampton, Virginia 23365

Guenther W. Lehner
Institut für Plasmaphysik
8046 Garching
bei München
Germany

H. R. Lewis, Jr.
Los Alamos Scientific Lab.
University of California
P. O. Box 1663
Los Alamos, New Mexico 87544

Tong Nyong Lie
Catholic University of America
Dept. of Space Science
Washington, D. C. 20017

Edward M. Little
Los Alamos Scientific Lab.
University of California
P. O. Box 1663
Los Alamos, New Mexico 87544

Charles Maisonnier
Laboratori Gas Ionizzati
Associazione Euratom-Cnen
C.P. 65
Frascati (Roma)
Italy

Charles K. Manka
Sam Houston State College
Physics Dept.
Huntsville, Texas 77340

John Marshall
Los Alamos Scientific Lab.
University of California
P. O. Box 1663
Los Alamos, New Mexico 87544

Joseph W. Mather
Los Alamos Scientific Lab.
University of California
P. O. Box 1663
Los Alamos, New Mexico 87544

O. K. Mawardi
Physics Department
Case Institute of Technology
Cleveland, Ohio 44106

John Meissner
Los Alamos Scientific Lab.
University of California
P. O. Box 1663
Los Alamos, New Mexico 87544

D. A. Meskan
Aerospace Corporation
P. O. Box 95085
Los Angeles, California 90045

Donald E. Michael
Los Alamos Scientific Lab.
University of California
P. O. Box 1663
Los Alamos, New Mexico 87544

Charles J. Michels
Mail Stop 301-1
NASA Lewis Research Center
21000 Brookpark Road
Cleveland, Ohio 44135

Bennett Miller
Department of Physics
Columbia University
New York, New York 10027

Richard L. Morse
Los Alamos Scientific Lab.
University of California
P. O. Box 1663
Los Alamos, New Mexico 87544

Henry T. Motz
Los Alamos Scientific Lab.
University of California
P. O. Box 1663
Los Alamos, New Mexico 87544

Edgar A. McLean
Naval Research Laboratory
Code 7725
Washington, D.C. 20021

John McLeod
Los Alamos Scientific Lab.
University of California
P. O. Box 1663
Los Alamos, New Mexico 87544

William E. Nexsen
Lawrence Radiation Lab.
P. O. Box 808
Livermore, California 94550

G.B.F. Niblett
Physics Department
University of California
San Diego
La Jolla, California 92037

J. NiCastro
Dept. 5142
Sandia Corporation
P. O. Box 5800
Albuquerque, New Mexico 87115

Clair Nielson
Los Alamos Scientific Lab.
University of California
P. O. Box 1663
Los Alamos, New Mexico 87544

Peter Noll
Institut Für Plasmaphysik
517 Jülich
Germany

Thomas A. Oliphant, Jr.
Los Alamos Scientific Lab.
University of California
P. O. Box 1663
Los Alamos, New Mexico 87544

Melvin D. Olman
Dept.
Sandia Corporation
P. O. Box 5800
Albuquerque, New Mexico 87115

John A. Palsedge
Los Alamos Scientific Lab.
University of California
P. O. Box 1663
Los Alamos, New Mexico 87544

Edward L. Patterson
Dept. 5142
Sandia Corporation
P. O. Box 5800
Albuquerque, New Mexico 87115

Lt. Robert Parker
Kirtland Air Force Base
Albuquerque, New Mexico 87115

Nicol J. Peacock
Atomic Weapons Research Establishment
Nuclear Physics Division
Building N60
Aldermaston, Berkshire
England

James A. Phillips
Los Alamos Scientific Laboratory
University of California
P. O. Box 1663
Los Alamos, New Mexico 87544

Richard J. Plugge
Los Alamos Scientific Laboratory
University of California
P. O. Box 1663
Los Alamos, New Mexico 87544

Donald H. Polk
United Aircraft Research Lab.
Silver Lane
East Hartford, Conn. 06108

M. L. Pool
Department of Physics
174 W. 18th Avenue
Ohio State University
Columbus, Ohio 43210

Sidney D. Putnam
Physics International Company
2700 Merced Street
San Leandro, California 94577

Warren E. Quinn
Los Alamos Scientific Lab.
University of California
P. O. Box 1663
Los Alamos, New Mexico 87544

A. S. Rawcliffe
Los Alamos Scientific Lab.
University of California
P. O. Box 1663
Los Alamos, New Mexico 87544

F. L. Ribe
Los Alamos Scientific Lab.
University of California
P. O. Box 1663
Los Alamos, New Mexico 87544

Werner B. Riesenfeld
Los Alamos Scientific Lab.
University of California
P. O. Box 1663
Los Alamos, New Mexico 87544

Howard N. Roberts
Physics Department
University of Texas
Austin, Texas 78712

Anthony E. Robson
University of Texas
Physics Building 330
Austin, Texas 78712

Dan L. Rode
Case Institute of Technology
Cleveland, Ohio 44106

David Ross
University of Houston
Physics Dept
Cullen Blvd.
Houston, Texas 77004

Henry Rugge
Physics International Company
2700 Merced Street
San Leandro, California 94577

George A. Sawyer
Los Alamos Scientific Lab.
University of California
P. O. Box 1663
Los Alamos, New Mexico 87544

Aldred E. Schofield
Los Alamos Scientific Lab.
University of California
P. O. Box 1663
Los Alamos, New Mexico 87544

R. M. Scott
Case Institute of Technology
Cleveland, Ohio 44106

John Sheffield
University of Texas
Physics Building 311
Austin, Texas 78712

Richard E. Siemon
University of California, San Diego
Department of Physics
Revelle College
P. O. Box 109
La Jolla, California 92037

Donald R. Simon
Vitro Laboratories
200 Pleasant Valley Way
West Orange, N. J. 07052

David R. Smith
P. O. Box 5800
Sandia Laboratory
Sandia Base
Albuquerque, N. M. 87115

John P. Somon
Laboratori Gas Ionizzati
C.P. 65
Associazione Euratom-Cnen
Frascati (Roma)
Italy

F. Y. Sorrell
University of Colorado
Boulder, Colorado

Ian J. Spalding
U.K. A.E.A.
Culham Laboratory
Culham
Abingdon, Berkshire
England

Emory J. Stovall, Jr.
Los Alamos Scientific Lab.
University of California
P. O. Box 1663
Los Alamos, New Mexico 87544

Richard F. Taschek
Los Alamos Scientific Lab.
University of California
P. O. Box 1663
Los Alamos, New Mexico 87544

Fred Tenney
Princeton University
Plasma Physics Laboratory
Princeton, New Jersey 08540

Otto H. Theimer
New Mexico State University
Research Center
Box Y
University Park, N. M. 88070

L. H. Thomas
IBM(Watson Laboratory)
612 W. 115 Street
New York, New York 10025

Keith S. Thomas
Los Alamos Scientific Lab.
University of California
P. O. Box 1663
Los Alamos, New Mexico 87544

William B. Thompson
University of California
San Diego
La Jolla, California 92037

David B. Thomson
Los Alamos Scientific Lab.
University of California
P. O. Box 1663
Los Alamos, New Mexico 87544

James L. Tuck
Los Alamos Scientific Lab.
University of California
P. O. Box 1663
Los Alamos, New Mexico 87544

Robert Turner
Applied Physics Laboratory
The John Hopkins University
8621 Georgia Avenue
Silver Springs, Maryland 20910

D. Veron
Association Euratom-CEA
Fusion Controlee
Centre d'Etudes Nucleaires
Fontenay-aux-Roses
Boite Postale No. 6
Seine, France

F. Waelbroeck, Director
Institut für Plasmaphysik
Der Kernforschungsanlage, Jülich
Des Landes Nordrhein-Westfalen e.V.
Jülich, Germany

Jean-Paul H. Watteau
27 - Avenue de Stalingrad
Colombes - 92
France

Frederic Weigl
University of Texas
Austin, Texas 78712

D. M. Weldon
Los Alamos Scientific Lab.
University of California
P. O. Box 1663
Los Alamos, New Mexico 87544

Daniel R. Wells
University of Miami
Department of Physic
Coral Gables, Florida 33124

John Wesson
U.K. A.E.A.
Culham Laboratory
Culham
Abingdon, Berkshire
England

Arthur H. Williams
Los Alamos Scientific Lab.
University of California
P. O. Box 1663
Los Alamos, New Mexico 87544

Fred E. Wittman
Los Alamos Scientific Lab.
University of California
P. O. Box 1663
Los Alamos, New Mexico 87544

Randolph J. Wolf
National Center for Atmospheric Research
Boulder, Colorado 80302

Frederick L. Yarger
New Mexico Highland University
Department of Physics
Las Vegas, New Mexico 87701

George Yevick
Stevens Institute of Technology
Hoboken, New Jersey 07030

S. Yoshikawa
Princeton University
James Forrestal Research Center
Plasma Physics Laboratory
Princeton, New Jersey 08540

N. J. Zabusky
Bell Telephone Lab.
Whippany, New Jersey 07981

Eugene L. Zimmerman
Los Alamos Scientific Lab.
University of California
P. O. Box 1663
Los Alamos, New Mexico 87544

Otto Henry Zinke
Associate Prof. of Physics
University of Arkansas
College of Arts and Sciences
Fayetteville, Arkansas 72701

Joseph Zorskie
Stevens Institute of Technology
Hoboken, New Jersey 07030

Harmuth Zwicker
Institut für Plasmaphysik
8046 Garching
bei München
Germany

AUTHOR INDEX

A

Allen, T. K. G4
Ancker-Johnson, Betsy H5
Andelfinger, C. G2
Anderson, A. D. A5
Auer, P. L. B6

B

Beckner, Evert H. C4
Block, R. B. H7
Bodin, H. A. B. A2
Bogen, P. D5
Bostick, W. H. E3
Bottoms, P. J. C1
Bryner, J. C. F6
Butler, D. C7

C

Caird, R. S. H3
Chang, C. C. E5
Chen, Wen Shuh H5
Coensgen, F. H. H1
Comisar, G. G. C6
Coudeville, A. C3
Coxell, H. G4
Crawford, E. A. H6
Crawford, J. C. H3
Cummins, W. F. H1

D

Damerow, R. A. H3
de Pretis, M. E1
DeSilva, A. W. D4
Dippel, K. H. D5
Dougal, Arwin A. D2

E

Eberhagen, A. H2
Ellis, R. E. H1
Evrard, P. E1
Ewing, K. J. H3

F

Fearn, D. G. E9
Fowler, C. M. H3
Freidberg, J. P. B4, B7
Funfer, E. A1, G2

G

Garn, W. B. H3
Gribble, R. F. A3
Griem, H. R. A5
Gross, Robert A. E8
Grossmann, W., Jr. B4
Grunberger, L. E3

H

Hain, Klaus F1
Hamada, Shigeo A7
Harris, Robert W. D6
Harvey, Robin A6
Haught, Alan F. F5
Heiss, A. D7
Henins, I. C7, E2
Henry, P. S. E2
Hettel, Henry J. E6
Herold, H. D7
Hill, D. A. E7
Hill, M. G4

J

Jacquinot, J. E1
Johnson, J. L. B2
Jolas, A. C3

K

Kaleck, A. A4
Kawasaki, S. A8
Kemp, E. L. G1
Kever, H. A4, B3
Kilb, Ralph W. B5
Kinsinger, R. E. B6
Kolb, A. C. G5
Konen, L. A4
Köppendörfer, W. H2
Kovar, F. R. H1
Kunze, H.-J. D4

L

Lehner, G. G2
Leloup, C. E1
Levine, Leslie A. E8
Levy, M. E. E7
Lie, T. N. E5
Linhart, J. G. H4
Little, E. M. A3
Lohr, J. E2
Long, J. W. C5

M

Maisonnier, Ch. H4
Marshall, J. C7, E2
Mather, J. W. C1
Mawardi, O. K. B8, H7
McLean, E. A. A5, G5
Meskan, David Allan C6
Michels, Charles J. E6
Miyamoto, Tetsu A7
Morse, R. L. B2, B7
C7, F3
Münich, M. H2

N

Newton, A. A. A2
Nexsen, W. E., Jr. H1
Noll, P. A4
Norwood, Joseph, Jr. F4

O

Ohnishi, Haruyaki A7
Oliphant, Thomas A., Jr. .. F2
Opat, Henry A6

P

Palmadesso, P. E3
Patou, C. C2
Peacock, N. J. C5
Phillips, J. A. G3
Poffé, J. P. E1
Pohl, F. G2
Polk, Donald H. F5
Prior, W. E3

Q

Quinn, W. E. A3, G1

R

Rhee, M. J. E5
Ribe, F. L. G1
Riesenfeld, W. B. B2
Roberts, Howard N. D2
Rode, D. L. H7
Rusbüldt, D. D5

S

Sato, Masatomo A7
Sawyer, G. A. G1
Schiff, Morton A6
Schofield, A. E. G3
Schumacher, U. D1
Scott, R. M. B8
Seidel, U. G2
Sichling, G. H. F6
Simon, D. R. E7
Simonnet, A. C2
Sommer, J. G2
Somon, J. P. H4
Sorrell, F. Y. H6
Spalding, I. J. G4
Speer, R. J. C5
Sugita, K. A4

T

Thomas, K. S. D3
Thomson, D. B. H3
Tuck, J. L. G3

U

Uchida, T. A8
Ulrich, M. G2
Unsöld, E. D7

V

Van Paassen, H. L. C6
Véron, D. E4
Vlases, G. C. H6

W

Waelbroeck, F. A4, E1
Watteau, J. P. C2, C3
Weigl, Frederic D2
Wells, Daniel R. F4
Wesson, John B1
Wilcock, P. D. C5
Wilhelm, R. D1
Williams, A. H. C1
Witulski, H. A4
Wooding, E. R. E9

Y

Yevick, George A6
Yoshikawa, S. G6
Young, M. P. G5

Z

Zorskie, J. E3
Zwicker, H. D1